Université de Liège

Faculté des Sciences Appliquées

Collège de doctorat en Électricité, Électronique et Informatique

---

Standard and Mixed Finite Element Formulations for Systems with Type-II Superconductors

---

Doctoral dissertation presented by

Julien Dular

Submitted in partial fulfillment of the requirements for the degree of

Doctor of Philosophy (PhD) in Engineering Sciences

January 2023

Thesis committee

Prof. Benoît Vanderheyden (Université de Liège), Advisor

Prof. Christophe Geuzaine (Université de Liège), Co-advisor

Prof. Philippe Vanderbemden (Université de Liège), President

Prof. Francesco Grilli (Karlsruher Institut für Technologie)

Prof. Sebastian Schöps (Technische Universiteit Darmstadt)

Dr. Mariusz Wozniak (CERN)

Author contact information

Julien Dular

Electronics and Microsystems
Dept. of Electrical Engineering and Computer Science
Université de Liège

Montefiore Institute B28
Quartier Polytech 1
Allée de la Découverte 10
4000 Liège, Belgium

Email: julien.dular@uliege.be

Funding

This thesis was funded by the Fonds de la Recherche Scientifique (F.R.S.-FNRS).

Computational resources have been provided by the Consortium des Équipements de Calcul Intensif (CÉCI), funded by the Fonds de la Recherche Scientifique de Belgique (F.R.S.-FNRS) under Grant No. 2.5020.11.

This version was generated on July 20, 2023

Acknowledgements

First and foremost, I am immensely grateful to my two advisors, Prof. Benoît Vanderheyden and Prof. Christophe Geuzaine. Both have been admirably available and responsive throughout my thesis journey. Their priceless advice, continuous support and genuine kindness have definitively contributed to the fulfillment of this work. I am truly honored to have had the chance to learn with them.

More specifically, I thank Benoît for his insightful ideas, his in-depth feedbacks, and his investment in my thesis. Benefiting from his vast knowledge of physics and his remarkable rigor in mathematics was very precious and helpful. In addition to being an admirable scientist, Benoît is also a caring, patient and sincere person who creates a healthy and warm work atmosphere.

I thank Christophe for his unfailing ability to boost my motivation. I am grateful to his permanent and contagious enthusiasm. On the scientific side, his impressive mastery of finite element and mesh software as well as his faculty of finding clever modeling solutions in a minute were of invaluable help for the development of the numerical methods in this work.

I want to extend my thanks to Prof. Philippe Vanderbemden for introducing me to superconductivity. I had the pleasure to attend several of his world-class lectures and to receive his passion for science and engineering. In addition to Philippe, I also thank Sébastien Brialmont, Michel Houbart, and Jean-François Fagnard for the stimulating collaborations and numerous exchanges we had at the interface between numerical modeling and experimental measurements.

Regarding engaging collaborations, I am also grateful to Prof. Sebastian Schöps, of the Technische Universiteit Darmstadt, for his qualitative help on stability analyses and valuable comments and suggestions on mixed formulations, and to Mariusz Wozniak, of CERN, for his insights and knowledge on twisted cables, his enthusiasm about the developed models and for giving me the opportunity to present formulations at the GetDP workshop at CERN.

I thank Bruno de Sousa Alves, of Polytechnique Montréal, for his help on periodic cohomology functions and precious explanations about cut ordering, as well as Bruno Dular, of Bonn Universität, for clarifying concepts of algebraic topology. My gratitude also goes to François Henrotte, he helped me unravelling the intricacies of curl-free functions in helicoidal coordinates. I thank Lorenzo Bortot, Mané Harutyunyan, Kévin Berger, Erik Schnaubelt, and Albert Piwonski for the fruitful collaborations.

I thank the F.R.S.-FNRS for granting me the opportunity to freely research on numerical models, as well as the University of Liège for the comfortable workspace and the CÉCI for the computing clusters. I thank David Colignon for his help on using them wisely.

Next, my thanks go to my colleagues from ACE, without whom the life as a PhD student would definitely not have been the same. In particular, I think to Xavier, Nicolas and Anthony, with whom I've shared the boat since the beginning. I also warmly thank Pierre, Maxime, Kevin, Amaury, Vanessa, Jon, Matteo, Philippe, Ismail, Kaoutar, Boris, Florent, François, Véronique, David, Fabrice, Jean and Valera. Thursday's lunches with their unique coffees and Friday's post-newsletter declutching hours deserve their place in these acknowledgements.

I also thank Erik, Albert, Alix, Bruno and my mother for carefully proof-reading parts of this dissertation, and even its entirety for Alix. Their fresh minds and sharp thoughts helped me a lot to write the final version of this manuscript.

I am grateful to my mother, my two brothers, Tom and Bruno, and my friends for their steady encouragements. I save my warmest thank for Alix, my partner. She is an infinite source of energy, motivation and love.

Finally, I dedicate this thesis to my father, Patrick Dular. Among so many other things, I owe him my passion for science and nature, and my love for life.

Abstract

Type-II superconductors are of great interest in high magnetic field and electric power applications due to their unique magnetic and electric properties. The design and optimization of systems in these applications require devoted numerical modeling techniques. The main objective of this dissertation is to contribute to the development of robust and efficient finite element formulations suited for systems containing type-II superconductors, and possibly ferromagnetic materials. Type-II superconductors and ferromagnetic materials are described by nonlinear constitutive laws, that may cause distinct finite element formulations to present markedly different numerical behaviors.

In this work, we first present two standard finite element formulations for magnetodynamic problems (h-ϕ and a) and we analyze how the involved nonlinearities can be handled in the most efficient manner. Based on the analysis results, we then propose and present four dedicated mixed finite element formulations (h-ϕ-a, t-a, h-ϕ-b, and a-j). As these mixed formulations take the form of perturbed saddle-point problems, we pay a particular attention to their discretization so as to avoid numerical instabilities.

Next, we compare the performance of the six formulations on a collection of problems of increasing complexity, with geometries ranging from 1D to 3D. We highlight the fact that the best formulation is problem-dependent and we give general recommendations for obtaining efficient time-stepping and linearization techniques. We conclude by applying the formulations on two distinct problems featuring non-trivial geometries: cables made up of twisted multi-filamentary superconducting wires, and layered magnetic shields made up of a stack of a large number of superconducting tapes with a ferromagnetic substrate.

Résumé

Grâce à leurs propriétés électriques et magnétiques remarquables, les supraconducteurs de type II sont particulièrement intéressants dans le cadre d'applications à haut champ et de transport d'énergie électrique. La conception et l'optimisation de telles applications requièrent des méthodes de modélisation numérique dédiées. L'objectif principal de ce travail est de contribuer au développement de formulations éléments finis robustes et efficaces pour des systèmes incluant des supraconducteurs de type II, ainsi que, éventuellement, des matériaux ferromagnétiques. Ces deux matériaux sont décrits par des lois constitutives nonlinéaires, ce qui implique que des formulations éléments finis distinctes peuvent présenter des comportements numériques fortement différents.

Dans un premier temps, nous présentons deux formulations éléments finis classiques pour des problèmes de magnéto-dynamique (h-ϕ and a) et nous étudions comment traiter les nonlinéarités associées de la façon la plus efficace possible. À partir des conclusions obtenues, nous proposons ensuite quatre formulations éléments finis mixtes (h-ϕ-a, t-a, h-ϕ-b, and a-j). Ces formulations prennent la forme de problèmes au point-de-selle perturbés. Une attention particulière doit dès lors être portée à leur discrétisation afin d'éviter des instabilités numériques.

Dans un second temps, nous comparons les performances des six formulations pour un ensemble de problèmes de complexité croissante, impliquant des géométries 1D, 2D, et 3D. Nous mettons en évidence le fait que la formulation la plus performante est différente selon le problème. Nous formulons également des recommandations générales pour obtenir une intégration temporelle robuste et une linéarisation efficace. Nous concluons en appliquant les méthodes à deux problèmes présentant des géométries non-triviales : des câbles constitués de filaments supraconducteurs torsadés, et des écrans magnétiques creux réalisés à partir de l'empilement d'un grand nombre de rubans supraconducteurs comportant un substrat ferromagnétique.

Contents

Introduction 1
Context and motivation 1
Dissertation goals 4
Dissertation outline 4
Original contributions 6

1 Superconducting materials modeling 9
1.1 Magnetodynamic equations and constitutive laws 9
1.2 Superconducting materials 10
1.2.1 Meissner state 11
1.2.2 Mixed or vortex state 12
1.3 Ferromagnetic materials 15
1.4 Numerical modeling of type-II superconductors 17

2 Standard finite element formulations 19
2.1 Problem definition 19
2.1.1 Magnetodynamic equations 19
2.1.2 Initial and boundary conditions 20
2.1.3 Global constraints on voltage and current 21
2.1.4 Strong form of the magnetodynamic problem 23
2.2 Magnetic field formulation (h-ϕ-formulation) 23
2.3 Vector potential formulation (a-formulation) 26
2.4 Space discretization 28
2.4.1 Discretization of h the h-ϕ-formulation 28
2.4.2 Discretization of a and e_a in the a-formulation 31
2.5 Time integration 34
2.6 Linearization 35
2.6.1 The Picard iteration 37
2.6.2 The Newton-Raphson iteration 38
2.6.3 Hybrid iterations 39
2.7 Analysis of the treatment of material nonlinearities 39
2.7.1 Fixed points 40
2.7.2 Simple models for T2S and SFM nonlinearities 43
2.7.3 Iterations on the simple models for the T2S nonlinearity 44
2.7.4 Iterations on the simple models for the SFM nonlinearity 53
2.8 Summary and motivation for mixed formulations 55

3 Mixed finite element formulations **57**
3.1 Surface-coupled h-ϕ-a-formulation . . . 58
3.2 Thin-shell t-a-formulation . . . 61
3.3 Volume-coupled formulations . . . 65
  3.3.1 Volume-coupled h-ϕ-b-formulation . . . 66
  3.3.2 Volume-coupled a-j-formulation . . . 66
3.4 Space discretization and numerical oscillations . . . 67
  3.4.1 Surface-coupled h-ϕ-a-formulation . . . 68
  3.4.2 Thin-shell t-a-formulation . . . 72
  3.4.3 Volume-coupled h-ϕ-b-formulation . . . 77
  3.4.4 Volume-coupled a-j-formulation . . . 79
3.5 Basics of stability analysis of saddle-point problems . . . 80
  3.5.1 Spaces, norms and operators . . . 80
  3.5.2 Solvability and stability of unperturbed saddle-point problems . . . 81
  3.5.3 Solvability and stability of perturbed saddle-point problems . . . 82
  3.5.4 Numerical inf-sup test . . . 84
3.6 Stability analysis . . . 85
  3.6.1 Surface-coupled h-ϕ-a-formulation . . . 86
  3.6.2 Thin-shell t-a-formulation . . . 93
  3.6.3 Volume-coupled h-ϕ-b-formulation . . . 94
  3.6.4 Volume-coupled a-j-formulation . . . 100
3.7 Summary . . . 101

4 Numerical performance of the formulations **103**
4.1 T2S slab (1D) . . . 104
  4.1.1 Verification with a scaling solution . . . 105
  4.1.2 Possibility of using large time steps . . . 109
  4.1.3 Comments on the power law . . . 112
  4.1.4 Efficiency of the formulations . . . 112
4.2 T2S cylinder (2D) . . . 115
  4.2.1 Comparison of the solutions . . . 115
  4.2.2 Efficiency of the formulations . . . 119
4.3 T2S tape (2D) . . . 120
  4.3.1 Comparison of the solutions . . . 120
  4.3.2 Efficiency of the formulations . . . 123
4.4 T2S and SFM cylinders (2D) . . . 123
  4.4.1 Comparison of the solutions . . . 124
  4.4.2 Efficiency of the formulations . . . 125
4.5 T2S and SFM in a magnet motor pole (3D) . . . 128
  4.5.1 Source fields . . . 130
  4.5.2 Comparison of the solutions and efficiencies of the formulations . . . 131
4.6 Summary and general recommendations . . . 135

5 Two applications with a non-trivial geometry **137**
5.1 Problems with a helicoidal symmetry . . . 137
  5.1.1 Helicoidal change of variables . . . 139
  5.1.2 Practical implementation of a full h-ϕ-formulation in 2D . . . 141

5.1.3 Verification against a 3D model 145
5.1.4 Extension to non-helicoidally-invariant boundary conditions 151
5.2 Stacked-tape magnetic shield 159
5.2.1 Problem definition and experimental measurements 160
5.2.2 Simple model 162
5.2.3 Homogeneous model 163
5.2.4 Model comparison in axial field (2D-axi) 165
5.2.5 Model comparison in transverse field (3D) 172
5.2.6 Summary 178

Conclusions **179**

A Mathematical framework **183**
A.1 Elements of algebraic topology and function spaces 183
A.1.1 Chains and homology 183
A.1.2 Cochains and cohomology 184
A.1.3 Global currents and voltages associated with general geometries 186
A.2 Whitney forms 186
A.2.1 Node functions (0-forms) 187
A.2.2 Edge functions (1-forms) 187
A.2.3 Facet functions (2-forms) 188
A.2.4 Volume functions (3-forms) 188
A.2.5 Sequence of discrete function spaces 189
A.2.6 Higher order functions 189
A.3 Green's identities 190

B Additional developments **191**
B.1 Magnetic Gauss law 191
B.2 Centered finite difference approximations of order two 192
B.3 Jacobian derivations 193
B.4 Approached solution for first-flux penetration 194
B.5 Quasi-3D h-ϕ-formulation in helicoidal coordinates 196

C Additional figures **199**

Bibliography **204**

List of Figures

1 Different types of superconducting cables and wires. 2
2 Different types of superconducting systems. 3

1.1 Critical surfaces for type-I and type-II superconductors. 11
1.2 Reversible and irreversible superconductors. 13
1.3 Magnetization of a superconducting cylinder with the Bean model. 14
1.4 Power law for type-II superconductors. 15
1.5 Hysteresis curve of a ferromagnetic material. 16
1.6 Anhysteretic ferromagnetic material constitutive law. 16

2.1 General domain geometry, notations and global variables. 21
2.2 Source electric field sign convention. 22
2.3 Domains and conventions for the global term, volume integration. 25
2.4 Shape functions for $\boldsymbol{h}$ in the h-ϕ-formulation. 29
2.5 Illustration of cut supports in 2D and 3D problems. 30
2.6 Co-tree gauge for the magnetic vector potential in the non-conducting domain. . 32
2.7 Perpendicular edge functions in the reference triangle. 33
2.8 Unit source voltage shape function. 34
2.9 Extrapolation techniques for the first estimate or iterative methods. 36
2.10 Picard and Newton-Raphson (N-R) iterations. 38
2.11 Illustration of iteration cycles for T2S and SFM. 39
2.12 Iteration cycles for T2S - Residual and power estimate. 40
2.13 Fixed point iterations, three distinct situations. 42
2.14 One-degree-of-freedom setup for T2S. 43
2.15 One-degree-of-freedom functions for T2S. 44
2.16 One-degree-of-freedom functions for SFM. 45
2.17 T2S - h-ϕ-formulation - Picard and N-R as fixed point iterations. 46
2.18 T2S - Illustration of attracting iteration cycles. 47
2.19 T2S - h-ϕ-formulation - Picard and N-R number of iterations. 48
2.20 T2S - a-formulation - Picard and N-R as fixed point iterations. 50
2.21 T2S - a-formulation - Picard and N-R number of iterations. 51
2.22 T2S - a-formulation - Acceleration of Picard iterations with Aitken's technique. 52
2.23 T2S - a-formulation - Two ideas for improving N-R behavior. 53
2.24 SFM - h-ϕ and a-formulations - Picard and N-R number of iterations. 54
2.25 SFM - h-ϕ-formulation - N-R improvement with a hybrid technique. 55

3.1 Domain decomposition for the h-ϕ-a-formulation. 59

3.2 Domain definition and conventions for the t-a-formulation. 62
3.3 Domains and conventions for the global term, surface integration. 63
3.4 Support entities for degrees of freedom in the h-ϕ-a-formulation. 69
3.5 Second-order node functions in the reference triangle. 70
3.6 Curl of second-order perpendicular edge functions in the reference triangle. . . 70
3.7 Tangential traces of shape functions for $\boldsymbol{h}$ and $\boldsymbol{a}$ on the coupling boundary. . . 71
3.8 Simple geometry for the h-ϕ-a-formulation. 72
3.9 Numerical oscillations with the h-ϕ-a-formulation (magnetic flux density map). 73
3.10 Numerical oscillations with the h-ϕ-a-formulation (profiles near the interface). 73
3.11 Support of the global shape function for the t-a-formulation. 76
3.12 Numerical oscillations with the t-a-formulation (current density profile). 76
3.13 Simple geometry for the t-a-formulation. 77
3.14 Numerical oscillations with the t-a-formulation on a 3D problem. 77
3.15 Simple geometry for the inf-sup test - h-ϕ-a-formulation. 88
3.16 Inf-sup test - h-ϕ-a-formulation. 89
3.17 Eigenvalue distribution from the inf-sup test - h-ϕ-a-formulation. 90
3.18 Illustration of two eigenvectors from the inf-sup test - h-ϕ-a-formulation. . . . 90
3.19 Link with numerical oscillations - h-ϕ-a-formulation. 91
3.20 Inf-sup test - t-a-formulation. 95
3.21 Simple geometry for the inf-sup test - h-ϕ-b-formulation. 97
3.22 Inf-sup test - h-ϕ-b-formulation. 97
3.23 Eigenvalue distribution from the inf-sup test - h-ϕ-b-formulation. 98
3.24 Illustration of three eigenvectors from the inf-sup test - h-ϕ-b-formulation. . . . 99

4.1 T2S slab geometry (1D). 105
4.2 Verification of the h-ϕ-formulation on the 1D T2S slab problem. 106
4.3 Verification of the a-formulation on the 1D T2S slab problem. 108
4.4 Second-order elements for the a-formulation on the 1D T2S slab problem. . . . 109
4.5 Solutions obtained with large time steps on the 1D T2S slab problem. 110
4.6 Interpretation of the error induced by a finite difference approximation. 111
4.7 Accuracy obtained with large time steps on the 1D T2S slab problem. 111
4.8 Two distinct regions for the differential conductivity of the power law. 112
4.9 Applied source field for the 1D T2S slab problem. 113
4.10 Residual evolution with Picard and N-R iterations on the 1D T2S slab problem. 114
4.11 T2S cylinder geometry (2D-axi) 115
4.12 Magnetic flux density distribution for the 2D T2S cylinder problem. 116
4.13 Current density in the 2D T2S cylinder problem 117
4.14 Current density profiles for the 2D T2S cylinder problem. 118
4.15 Error on AC losses for the 2D T2S cylinder problem. 118
4.16 T2S tape geometry (2D) 120
4.17 Field profiles for the 2D T2S tape problem. 121
4.18 Error on AC losses for the 2D T2S tape problem. 122
4.19 Hybrid T2S-SFM cylinders geometry (2D-axi) 124
4.20 Field profiles in the T2S, for the 2D T2S-SFM cylinder problem (fine mesh). . 125
4.21 Field profiles in the SFM, for the 2D T2S-SFM cylinder problem (fine mesh). . 126
4.22 Error on AC losses for the 2D T2S-SFM cylinders problem. 126
4.23 Hybrid T2S-SFM motor pole geometry (3D) 128

4.24 Source and permeability curve for the 3D T2S-SFM motor pole problem. . . . 129
4.25 Magnetic flux density distribution for the 3D T2S-SFM motor pole problem. . . 133
4.26 Current density in the T2S for the 3D T2S-SFM motor pole problem. 133

5.1 Helicoidal change of variables. 139
5.2 General 2D problem in helicoidal coordinate system. 142
5.3 Problem with six twisted Nb-Ti filaments for verification. 145
5.4 3D reference problem with six twisted Nb-Ti filaments. 146
5.5 Periodic supports for the cut functions. 147
5.6 Support of the axial cut function. 147
5.7 Fields along a helicoidal fiber for the 3D reference model (fine mesh). 148
5.8 Field maps in the plane for the 2D model. 149
5.9 Current density in both coordinate systems for the 2D model. 149
5.10 Comparison of the magnetic flux density for the 2D and 3D problems. 150
5.11 Comparison of AC losses for the 2D and 3D problems. 151
5.12 Constant transverse field in both coordinate systems. 152
5.13 Magnetic flux density map for the quasi-3D model on linear materials. 156
5.14 Magnetic flux density in the plane for the quasi-3D and 3D models. 156
5.15 Magnetic flux density along a fiber for the quasi-3D and 3D models. 157
5.16 Fields along a helicoidal fiber for the 3D model with a transverse field. 158
5.17 Fourier mode amplitudes for the 3D model with a transverse field. 158
5.18 Fabrication process and sample A of the stacked-tape magnetic shield. 159
5.19 Saturation law and magnetic permeability of the ferromagnetic substrate. 160
5.20 Axial and transverse configurations. 161
5.21 Axial and transverse configurations - simple model. 162
5.22 Axial and transverse configurations - homogeneous model. 163
5.23 Coarse meshes in axial configuration - simple and homogeneous models. 166
5.24 Mesh dependence in the axial configuration - simple model. 167
5.25 Three formulations in the axial configuration - simple model. 167
5.26 Influence of N_s in the axial configuration - simple model. 168
5.27 Three formulations in the axial configuration - homogeneous model. 169
5.28 h-ϕ-formulation in the axial configuration - simple and homogeneous models. . 169
5.29 Current density in axial configuration - simple and homogeneous models. . . . 170
5.30 Coarse meshes in transverse configuration - simple and homogeneous models. . 172
5.31 Three formulations in the transverse configuration - simple model. 173
5.32 Magnetic flux density in the transverse configuration - simple model. 174
5.33 Influence of N_s in the transverse configuration - simple model. 175
5.34 Three formulations in the transverse configuration - homogeneous model. . . . 175
5.35 Magnetic flux density in the transverse configuration - homogeneous model. . . 176
5.36 Permeability in transverse configuration - simple and homogeneous models. . . 176

A.1 Topology of a torus. 184
A.2 Reference 0-, 1-, 2-, and 3-simplices and node numbering convention. 186
A.3 Node functions in the reference triangle. 187
A.4 Edge functions in the reference triangle. 188

B.1 Semi-infinite superconducting slab geometry. 194

C.1 Initial estimates for the h-ϕ and a-formulations on a 1D problem. 199
C.2 Evolution of N-R iterations for the h-ϕ-formulation on a 1D problem. 200
C.3 Evolution of Picard iterations for the a-formulation on a 1D problem. 200
C.4 Field profiles in the T2S, for the 2D T2S-SFM cylinders problem. 201
C.5 Field profiles in the SFM, for the 2D T2S-SFM cylinders problem. 201
C.6 Fields along a helicoidal fiber for the 3D reference model. 202
C.7 Shielding factors from 0 to 60 mT, axial and transverse, at 293 K and 77 K. . . 203
C.8 Shielding factors from 0 to 670 mT, axial, at 77 K. 203

List of Tables

4.1 Efficiency comparison on the 1D T2S slab problem. 114
4.2 Efficiency comparison on the 2D T2S cylinder problem. 119
4.3 Efficiency comparison on the 2D T2S tape problem. 123
4.4 Efficiency comparison on the 2D T2S-SFM cylinders problem. 127
4.5 Performance figures for the 2D T2S-SFM cylinders problem. 127
4.6 Dimensions and parameters for the 3D T2S-SFM motor pole problem. 129
4.7 Degrees of freedom involved in the 3D T2S-SFM motor pole problem. 131
4.8 Performance figures for the 3D T2S-SFM motor pole problem. 134

5.1 Performance figures for the 2D and 3D twisted filaments problems. 151
5.2 Performance figures for the 2D stacked-tape magnetic shield problem. 171
5.3 Performance figures for the 3D stacked-tape magnetic shield problem. 177

Introduction

Context and motivation

Superconductivity was first discovered in 1911 by Kamerlingh Onnes. He observed that the electrical resistivity of mercury suddenly drops to zero when it is cooled below a temperature of 4.2 K [1]. Many other elements, metallic alloys and ceramic compounds were then discovered to be superconductors and were intensively studied by scientists. In addition to their zero DC electrical resistivity, superconductors were found to exhibit unique magnetic properties [2, 3].

The electric and magnetic properties of a certain type of superconductors, known as irreversible type-II superconductors (T2S), allow them to carry large currents with smaller resistance than conventional conductors and to generate magnetic fields higher than the saturation field ($\approx$ 2 T) of ferromagnetic materials [4]. For these reasons, superconductors are fascinating materials that are being exploited in a wide variety of applications since their discovery [5] and that continue to offer promising perspectives in new technologies [6] as listed below.

Low-temperature superconductors (LTS) such as Nb-Ti and Nb_3Sn are widely used in commercial cables. They are typically manufactured in the form of multi-filamentary twisted wires ($\approx$ 100 filaments) and used in high-field applications, typically cooled with liquid helium [7]. Coils of Nb-Ti cables can generate fields up to 9 T at 4.2 K, or 11 T at 1.8 K, whereas Nb_3Sn cables open the possibility of generating fields up to $\approx$ 23 T [5]. These materials are used in applications including magnetic resonance imaging (MRI) systems, nuclear magnetic resonance (NMR) devices, magnetic levitation (Maglev) trains, particle accelerators [8], and tokamak fusion reactors [9].

High-temperature superconductors (HTS), i.e., superconductors with a transition temperature above the liquid nitrogen boiling temperature of 77 K, were discovered since 1987 [10, 11, 12]. While considerably reducing the refrigeration costs [13], high-temperature superconductors (HTS) push the limit of accessible fields beyond 20 T [14, 15]. Continuous improvements are being accomplished on manufacturing high-performance wires and tapes made of these materials [5], but they remain challenging and expensive to produce at a large-scale, so that a large part of recent technologies involving HTS is still in a development stage [13, 16].

In addition to wires and tapes, HTS can be used as bulk materials [23], including large single-grain pellets and sintered structures [24]. Bulk HTS are able to trap large magnetic fluxes permanently, involving fields that exceed 17.6 T at 26 K [25], or 10 T at 50 K [26]. The resulting "trapped-field magnets" are particularly attractive in applications such as rotating

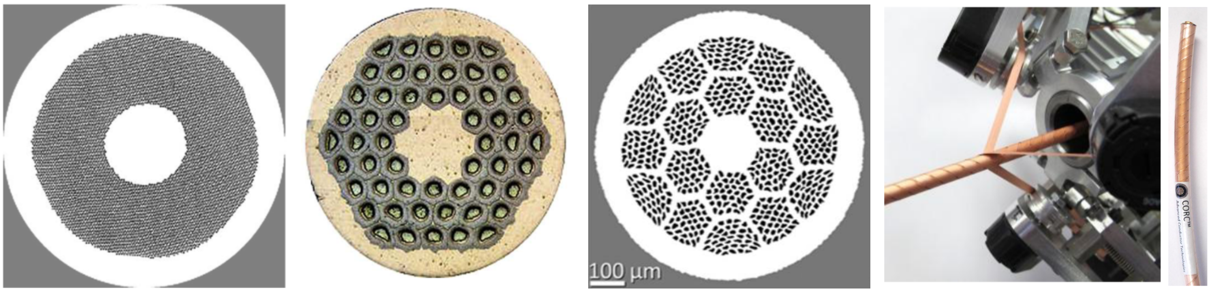

(a) Nb-Ti wire. (b) Nb_3Sn wire. (c) Bi-2212 wire. (d) CORC® cable.

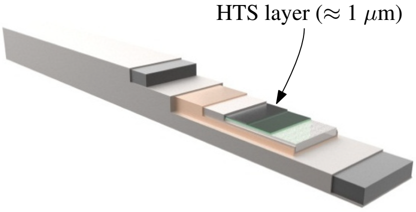

(f) Roebel cable.

(e) REBCO tape. (g) Twisted stacked tape conductors. (h) Bulk GdBCO.

Figure 1: Superconducting wires, tapes and bulks. (a)-(b) Multi-filamentary Nb-Ti and Nb_3Sn wire © 2015 Elsevier [17]. (c) Multi-filamentary Bi-2221 wire © 2019 IEEE [18]. (d) CORC® (conductor on round core) cable [19]. (e) REBCO tape © 2022 MDPI [20]. (f) Roebel cable [19]. (g) Twisted stacked tape conductors © 2022 IEEE [21]. (h) Bulk GdBCO sample © 2016 IEEE [22].

electric machines, magnetic separation devices, magnetic drug delivery systems, portable MRI and NMR systems, or Lorentz force velocimetry [26]. Bulk HTS can also be used as magnetic shields [27] or even as flywheels for energy storage systems [28].

With the development of the T2S technology, there is a strong demand for tools and methods capable of describing the behavior of complex superconducting systems in order to predict their performance [29]. Existing analytical methods are not accurate for realistic systems and experimental tests are oftentimes expensive, time-consuming, and can even be destructive [6]. By contrast, modern numerical methods provide a versatile and powerful solution that is becoming increasingly important for the design and optimization of superconducting applications [6, 30].

The finite element method (FEM) is the most commonly used method for superconductor modeling. For decades, it has proved to be a general and extremely flexible approach for finding approximate solutions to complex sets of equations describing various physics, in particular in electromagnetism [31]. Developing finite element models includes writing the differential problem describing the chosen physics into an alternative form, called a *formulation*, that is suited for a practical implementation of the finite element method. Establishing efficient and accurate finite element formulations suited for superconductor modeling is however not an easy task, for essentially two main reasons.

First, the equations describing the macroscopic (≈ 1 cm^3) magnetic response of superconductors are highly nonlinear. Constitutive laws may also be strongly anisotropic or be coupled with other highly nonlinear thermal parameters in the case of magneto-thermal coupling. Moreover, many superconducting systems also involve ferromagnetic materials [32, 33, 34, 35], whose magnetic response is also nonlinear. Handling all nonlinearities in a robust manner is not straightforward with classical finite element formulations and there is thus a need for dedicated methods to be designed [36].

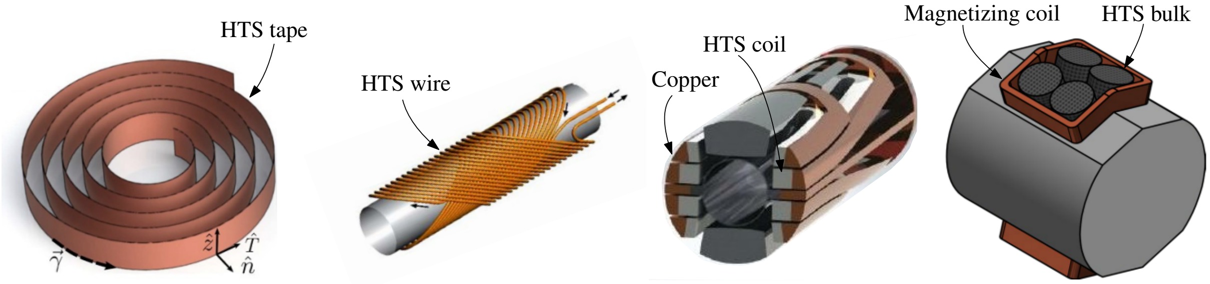

(a) No-insulation coil. (b) CCT magnet. (c) Feather M2 magnet. (d) HTS motor stator.

Figure 2: Examples of systems involving high-temperature superconducting tapes, wires or bulks. (a) No-insulation coil © 2020 IOP Publishing [37]. (b) Canted-Cosine-Theta (CCT) magnet © 2017-2022 CERN [38]. (c) Feather M2 magnet © 2014 IEEE [39]. (d) Stator of a HTS motor © 2018 IEEE [40].

Second, superconducting wires and tapes can display complex geometries, as shown in Fig. 1. Rutherford cables [41], Roebel cables [42], tri-axial HTS cables [43], twisted stacked tape conductors [44], or multi-layer CORC$^{®}$ cables (conductor on round core) [45] are good examples of intrinsically 3D geometries. Furthermore, many practical superconducting systems involve complicated windings or arrangements of wires and tapes, as shown in Fig. 2. Striking examples include layered structures made up of stacks of HTS tapes such as racetrack coils [46], no-insulation coils [47], and passive magnetic shields [48]. Dealing with a direct representation of such systems by a finite element model rapidly becomes computationally expensive and time-consuming. Dedicated and clever numerical methods are required to obtain reliable predictions of the behavior of these systems within a reasonable amount of computational time.

Different finite element formulations and methods exist and are being investigated for modeling the numerous types of superconducting systems [49, 29]. Relevant examples are thin-shell approaches for thin structures such as HTS tapes [50, 51], homogenization techniques for layered structures made up of a large number of tapes [52, 53], and mixed formulations for hybrid superconducting-ferromagnet systems or rotating motors [54, 55, 56]. All are promising avenues for an efficient treatment of the difficulties associated with the different kinds of superconducting applications.

Dissertation goals

The main goal of this work is to contribute to the development of efficient and reliable finite element formulations, in particular for modeling type-II superconductors (T2S, which includes both LTS and HTS) coupled with soft ferromagnetic materials (SFM), focusing on purely magnetic models. This main goal is decomposed in four objectives.

The first objective is to understand in detail how to handle in a robust manner the nonlinearities involved with T2S and SFM, in order to identify the principles on which new, better performing, formulations can be designed.

The second objective is to propose, or gather from the literature, finite element formulations that potentially present interests for hybrid systems with T2S and SFM, and to give indications on how to discretize them properly, avoiding numerical instabilities.

The third objective is to compare all the introduced formulations, and to try to give general recommendations on how to choose a method for obtaining accurate, robust and efficient resolutions. We shall see that no formulation outperforms all the others in all cases, so that a variety of different situations is worth considering.

The last objective is to apply and extend the proposed methods to two problems that present inherent complex geometries: a twisted multi-filamentary superconducting wire and a stacked-tape magnetic shield made up of T2S and SFM layers.

These objectives can be tackled one by one, leading to the following dissertation outline.

Dissertation outline

This dissertation is divided in five chapters.

In Chapter 1, we present the equations describing the macroscopic behavior of type-II superconductors and ferromagnetic materials. After introducing the magnetodynamic approximation of Maxwell's equations, we discuss the nonlinear constitutive laws associated with T2S and SFM. We then close the chapter with a brief overview of the state-of-the-art in numerical modeling techniques.

In Chapter 2, we start by fully defining the *strong form* of the mathematical problem we want to solve, based on the equations introduced in the previous chapter. The problem definition includes the introduction of global variables for imposing the voltage or the current in conducting regions. From the strong form, we then derive two distinct *weak forms* of the problem, the h-ϕ-formulation and the a-formulation, and describe their space and time discretizations, as well as their linearization for a practical implementation in a finite element solver. Both formulations are classical formulations for magnetodynamic problems that can be applied to systems with T2S and SFM. However, when applied to such systems, they are known to exhibit completely different numerical behaviors because of the nonlinearity of the equations. Therefore, we propose to analyze the treatment of the nonlinearities by investigating simplified versions of the formulations in the light of fixed point theory. The conclusions of the analysis suggest that none of the two formulations is optimal for handling systems with both T2S and SFM, which is one motivation to look for other formulations.

In Chapter 3, we propose four different mixed formulations. They all involve two main unknown fields that are coupled either via a common surface, the h-ϕ-a and t-a-formulations, or via a common volume, the h-ϕ-b and a-j-formulations. The t-a-formulation is relevant for thin T2S tapes whereas the other ones are primarily designed for handling systems containing both T2S and SFM. The four formulations enter the same framework of perturbed saddle-point problems, and their discretization necessitates to verify particular *stability conditions* to ensure well-posedness. We illustrate how naive discretization choices result in undesirable behaviors such as spurious oscillations in the numerical solution, and we propose choices that verify the stability conditions. We justify our results by the so-called *inf-sup test*, after introducing the basics of saddle-point stability analysis.

The first three chapters settle the theoretical basis and provide a collection of six different finite element formulations, together with different resolution techniques. The methods are ready to be used on systems with T2S and SFM. It is the subject of the next two chapters to compare them and assess their performance when applied on practical problems.

In Chapter 4, we compare the numerical performance of the different methods and formulations on problems with relatively simple geometries. We start by general observations on a 1D T2S bar problem. We continue with several 2D systems involving a T2S bulk cylinder, a T2S tape, and both T2S and SFM cylinders. We close the chapter by a 3D problem containing both T2S and SFM.

In Chapter 5, we consider two distinct problems with more complex geometries. A brute force modeling approach on these problems results in exceedingly long simulations and dedicated simplifications are therefore required for obtaining efficient models. The first application consists in evaluating AC losses in wires made up of twisted multi-filamentary superconducting wires. When these wires present a combination of translation and rotation symmetries, the dimension of the problem can be reduced from 3D to 2D by the introduction of a *helicoidal* change of variables, which drastically reduces the computational work.

The second application focuses on calculating the shielding effectiveness of magnetic shields made up of a stack of T2S tapes with a SFM substrate. The resulting system is a layered structure exhibiting both superconducting and ferromagnetic properties. We propose two simplified models to describe the magnetic behavior of this structure.

Original contributions

Below is a list of the main contributions that are considered to be, at least partly, original:

1. The analysis of the treatment of nonlinear laws involved in type-II superconductors and ferromagnetic materials by iterative techniques, in the light of fixed point theory. This analysis is presented in Chapter 2.

2. Several propositions for mixed formulations. The h-ϕ-a-formulation, applied on 2D and 3D problems, including a scalar magnetic potential; a derivation of the t-a-formulation including global variables for the total current and voltage in thin conducting domains; the a-j-formulation for 3D problems; and the h-ϕ-b-formulation, applied on 2D and 3D problems. These formulations are presented in Chapter 3 and applied in Chapters 4 and 5. Parts of these contributions are published in [36, 55, 57].

3. The stability analysis of the proposed mixed formulations in the light of perturbed saddle-point problem theory, as well as the identification of discrete function spaces that satisfy the stability conditions in order to obtain well-posed discrete finite element formulations. This is discussed in Chapter 3. Parts of the stability analysis are published in [55].

4. The presentation of the discrete function spaces associated with the h-ϕ-formulation under a change of variables from Cartesian coordinates to helicoidal coordinates, applied on helicoidally symmetric magnetodynamic problems. The presentation includes the treatment of nonlinear materials. Also, an extension to the treatment of non-helicoidally symmetric boundary conditions for linear materials, by means of a mode decomposition method, resulting in a quasi-3D problem, as well as a brief outlook of the applicability of this method on nonlinear materials such as type-II superconductors. This is presented in Chapter 5. A small part of this work is submitted for publication in [58].

5. A homogeneous and anisotropic model for describing the magnetic response of magnetic shields made up of a stack of superconducting tape annuli, and the comparison of the numerical performance of three formulations in axial (2D-axisymmetric) and transverse (3D) configurations. This is discussed in Chapter 5. The application of the homogeneous model is submitted for publication in [53].

The finite element formulations and the models developed in this thesis are part of the open-source Life-HTS toolkit. They are available online at:

`www.life-hts.uliege.be`.

Codes are implemented in GetDP, an open-source finite element software [59], and the geometry and mesh generation is performed by Gmsh [60], an open-source software as well.

Journal publications

- J. Dular, C. Geuzaine, and B. Vanderheyden, “Finite-element formulations for systems with high-temperature superconductors”, IEEE Transactions on Applied Superconductivity, vol. 30, no. 3, pp. 1–13, 2019. [36]
- J. Dular, M. Harutyunyan, L. Bortot, S. Schöps, B. Vanderheyden, and C. Geuzaine, “On the stability of mixed finite-element formulations for high-temperature superconductors”, IEEE Transactions on Applied Superconductivity, vol. 31, no. 6, pp. 1–12, 2021. [55]
- J. Dular, K. Berger, C. Geuzaine, and B. Vanderheyden, “What formulation should one choose for modeling a 3D HTS motor pole with ferromagnetic materials?”, IEEE Transactions on Magnetics, vol. 58, no. 9, pp. 1–4, 2022. [57]
- M. Houbart, J.-F. Fagnard, J. Dular, AR. Dennis, D. Namburi, J. Durrell, C. Geuzaine, B. Vanderheyden, P. Vanderbemden, “Trapped magnetic field distribution above a superconducting linear Halbach array”, Superconductor Science and Technology, vol. 35, no 6, p. 064005, 2022. [61]
- A. Piwonski, J. Dular, R. Silva Rezende, and R. Schuhmann, “2D eddy current boundary value problems for power cables with helicoidal symmetry”, IEEE Transactions on Magnetics, 2023. [58]
- S. Brialmont, J. Dular, L. Wéra, J.-F. Fagnard, B. Vanderheyden, C. Geuzaine, S. Hahn, A. Patel, and P. Vanderbemden, “Magnetic shielding up to 0.5 T at 77 K using a stack of high temperature superconducting tape annuli”, *in review* in Superconductor Science and Technology, 2023. [53]

Conference and workshop presentations

- J. Dular, C. Geuzaine, and B. Vanderheyden, “Finite element models for systems with high-temperature superconductors and ferromagnetic materials”. Oral presentation at the 22$^{\text{nd}}$ International Conference on the Computation of Electromagnetic Fields, Paris, France. July 2019.
- J. Dular, C. Geuzaine, and B. Vanderheyden, “Comparison of finite element formulations for HTS and ferromagnetic materials”. Invited poster presentation presented at the 14$^{\text{th}}$ European Conference on Applied Superconductivity, Glasgow, United Kingdom. September 2019.
- J. Dular, C. Geuzaine, and B. Vanderheyden, “Life-HTS - Finite element formulations for HTS, practice session”. Lecture at the 3$^{\text{rd}}$ International School on Numerical Modelling for Applied Superconductivity, Nancy, France. September 2020.
- J. Dular, “Superconductors in GetDP”. Two-hour lecture at the GetDP workshop, CERN, Switzerland (online). April 2021. (`https://videos.cern.ch/record/2766046` and `https://videos.cern.ch/record/2766047`)
- J. Dular, M. Harutyunyan, S. Schöps, B. Vanderheyden, and C. Geuzaine, “Stability of

HA and TA coupled formulations". Invited oral presentation at the 7th International Workshop on Numerical Modelling of High Temperature Superconductors, Nancy, France (online). June 2021.

- J. Dular, M. Harutyunyan, L. Bortot, S. Schöps, B. Vanderheyden, and C. Geuzaine, "Stability of HA and TA coupled formulations for HTS modelling". Oral presentation at the 12th symposium on electric and magnetic fields (EMF), Liège, Belgium (online). July 2021.
- J. Dular, M. Wozniak, A. Nicolet, B. Vanderheyden, and C. Geuzaine, "2D FEM calculation of AC losses in twisted superconductors with a helicoidal transformation". Poster presentation at the 23rd International Conference on the Computation of Electromagnetic Fields, Cancun, Mexico (online). January 2022.
- J. Dular, K. Berger, C. Geuzaine, and B. Vanderheyden, "What formulation should one choose for modeling a 3D HTS motor pole with ferromagnetic materials?". Poster presentation at the 23rd International Conference on the Computation of Electromagnetic Fields, Cancun, Mexico (online). January 2022.
- J. Dular, S. Brialmont, P. Vanderbemden, C. Geuzaine, and B. Vanderheyden, "3D finite element models of stacked tapes magnetic shields". Oral presentation at the 8th International Workshop on Numerical Modelling of High Temperature Superconductors, Nancy, France. June 2022.
- J. Dular, C. Geuzaine, and B. Vanderheyden, "Mixed finite element formulations for systems with superconductors and ferromagnetic materials". Oral presentation at the 8th international conference on Advanced Computational Methods in Engineering, Liège, Belgium. September 2022.

Chapter 1

Superconducting materials modeling

In this chapter, we present the physical framework in which type-II superconductor modeling takes place. In particular, we introduce the magnetodynamic approximation of Maxwell's equations and we present the power law, describing the electric behavior of type-II irreversible superconductors. We then give a brief overview of modeling techniques, with a focus on the finite-element method.

1.1 Magnetodynamic equations and constitutive laws

The electrodynamics in continuous media is described by Maxwell's equations,

$$\operatorname{div} \boldsymbol{b} = 0, \tag{1.1}$$

$$\operatorname{div} \boldsymbol{d} = \rho, \tag{1.2}$$

$$\mathbf{curl}\, \boldsymbol{h} = \boldsymbol{j} + \partial_t \boldsymbol{d}, \tag{1.3}$$

$$\mathbf{curl}\, \boldsymbol{e} = -\partial_t \boldsymbol{b}, \tag{1.4}$$

with $\boldsymbol{b}$ the magnetic flux density (T), $\boldsymbol{d}$ the electric displacement field (C/m^2), $\boldsymbol{h}$ the magnetic field (A/m), $\boldsymbol{e}$ the electric field (V/m), ρ the electric charge density (C/m^3) and $\boldsymbol{j}$ the electric current density (A/m^2) [62, 63]. These equations are usually referred to as Gauss's law of magnetism (1.1), Gauss's law of electricity (1.2), Ampère-Maxwell's law (1.3) and Faraday's law (1.4) respectively. The set of equations (1.1) - (1.4) is completed by constitutive relations [64]. For isotropic materials, three scalar parameters are introduced and define the relations

$$\boldsymbol{b} = \mu \boldsymbol{h}, \qquad \boldsymbol{d} = \varepsilon \boldsymbol{e}, \qquad \boldsymbol{j} = \sigma \boldsymbol{e}, \tag{1.5}$$

with μ the permeability (H/m), ε the permittivity (F/m) and σ the electrical conductivity (S/m). In general, constitutive relations are nonlinear and the three parameters μ, ε and σ can be complicated functionals or functions of, e.g., position, temperature, magnetic field, electric field or mechanical stress and strain. In this work, coupling with physics other than electrodynamics is not considered, and the parameters are assumed to be functions of electromagnetic fields only.

The magnetodynamic (or magneto-quasistatic) approximation of Maxwell's equations consists in neglecting the electric displacement current $\partial_t \boldsymbol{d}$ in the Ampère-Maxwell's law, Eq. (1.3)

[65, 66]. The modified equation, $\textbf{curl}\, \boldsymbol{h} = \boldsymbol{j}$, is referred to as Ampère's law and the resulting system of equations qualitatively changes in nature: the full Maxwell's equations describe wave phenomena, whereas the magnetodynamics equations define a diffusion problem.

The magnetodynamic approximation is valid for slowly time-varying fields, in the sense that their characteristic time constant τ, e.g., the inverse of the excitation frequency in the harmonic regime, is much larger than the transit time $\tau_{\text{em}} = \ell/c_{\text{m}}$ needed for an electromagnetic wave to travel over the spatial length ℓ of the system, at the speed of light in the medium c_{m} [67]. When $\tau \gg \tau_{\text{em}}$, wave propagation phenomena can be neglected and changes in field sources can be assumed to instantaneously affect all field quantities in the whole domain [67]. It is in the framework of the magnetodynamic equations that we conduct this research [26, 35].

To complete the magnetodynamic approximation, the permeability is assumed to be a known function of the magnetic field only, i.e., $\mu = \mu(\boldsymbol{h})$. In particular, we do not model magnetic hysteresis behaviors, for which the permeability depends on the history of the magnetic field. Moreover, the electrical conductivity is assumed to be a known function of the electric field and the magnetic flux density, i.e., $\sigma = \sigma(\boldsymbol{e}, \boldsymbol{b})$. With these assumptions, the problem is simplified and a closed set of equations for the magnetodynamic problem is obtained:

$$\begin{cases} \operatorname{div} \boldsymbol{b} = 0, \\ \textbf{curl}\, \boldsymbol{h} = \boldsymbol{j}, \\ \textbf{curl}\, \boldsymbol{e} = -\partial_t \boldsymbol{b}, \end{cases} \quad \text{with} \quad \begin{cases} \boldsymbol{b} = \mu(\boldsymbol{h})\boldsymbol{h}, \\ \boldsymbol{j} = \sigma(\boldsymbol{e}, \boldsymbol{b})\boldsymbol{e}. \end{cases} \tag{1.6}$$

This problem will be complemented by boundary and initial conditions in Chapter 2. Constitutive laws can also be inverted. Introducing the reluctivity $\nu = \mu^{-1}$ and the electrical resistivity $\rho = \sigma^{-1}$, constitutive laws are sometimes rewritten as $\boldsymbol{h} = \nu(\boldsymbol{b})\boldsymbol{b}$ and $\boldsymbol{e} = \rho(\boldsymbol{j}, \boldsymbol{b})\boldsymbol{j}$.

In vacuum, the permeability is constant, it is a fundamental physical constant that we approximate[1] to $\mu_0 = 4\pi \times 10^{-7}$ H/m. We denote by $\nu_0 = \mu_0^{-1}$ the reluctivity of vacuum. Also, there is no electric current density in vacuum, i.e., $\sigma = 0$. In this study, the surroundings of the materials, usually a cryogenic liquid, are assumed to behave like vacuum. Here, it will be referred to as the air domain.

The materials considered here are normal conductors, superconductors, and ferromagnetic materials. Normal conductors are assumed to be characterized by a constant conductivity σ or resistivity ρ, and are usually assumed to be non-magnetic, i.e., they are described by $\mu = \mu_0$, or $\nu = \nu_0$. The constitutive laws associated with superconductors and ferromagnetic materials, as well as a brief description of these materials, are the topics of the next two sections.

1.2 Superconducting materials

Superconductivity was first discovered by Kamerlingh Onnes on mercury (Hg) in 1911 [1]. It is a physical property that some materials display at low temperature, below a critical temperature,

---

[1] Since the redefinition of SI units in 2019, the permeability of vacuum is an experimentally determined constant, $\mu_0 = 1.256\,637\,062\,12(19) \times 10^{-6}$ H/m, with a relative uncertainty about 1.5×10^{-10} [68]. The value chosen in this work is $\mu_0 = 4\pi \times 10^{-7}$ H/m $= 1.256\,637\,061\,43 \times 10^{-6}$ H/m.

denoted by T_c [69]. Superconductivity confers a unique magnetic behavior to those materials and allows them to carry current with zero electrical resistance [70]. Materials that exhibit superconductivity are called superconducting materials, or superconductors.

Superconductivity arises below a critical surface in the $(T, \boldsymbol{h}, \boldsymbol{j})$-space, with T standing for the temperature. For isotropic superconductors, the critical surface is only a function of the norms h and j of vectors $\boldsymbol{h}$ and $\boldsymbol{j}$. Fig. 1.1(a) illustrates a representative critical surface.

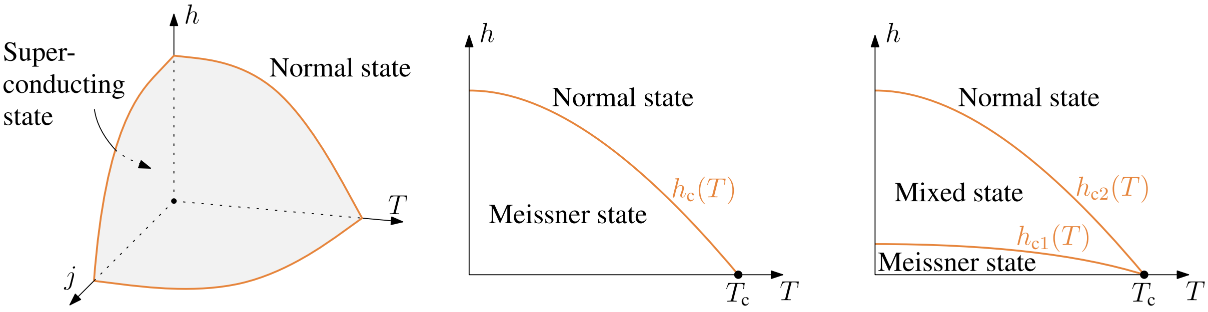

(a) Critical surface. (b) Type-I superconductors. (c) Type-II superconductors.

Figure 1.1: Illustration of the different states in isotropic superconducting materials, as a function of T, h, and j, the temperature, the norm of the magnetic field, and the norm of the current density, respectively. Diagrams in (b) and (c) are in the (T, h)-plane, i.e., for $j = 0$.

The class of superconducting materials is decomposed in two sub-classes: type-I and type-II superconductors [70]. Type-I superconductors are characterized by a single phase transition defining two states: the normal state and the Meissner state [2]. At a given temperature T with a given current density j, the transition occurs at a critical field $h_\mathrm{c} = h_\mathrm{c}(T, j)$. This is illustrated in Fig. 1.1(b) in the (T, h)-plane. Type-II superconductors demonstrate two phase transitions, with an intermediate state referred to as the mixed state or the vortex state [3]. Transitions are described by two critical fields h_c1 and h_c2, as depicted in Fig. 1.1(c). In the normal state, superconductors behave as normal conductors with non-negligible electrical resistance.

Type-II superconductors are further classified into low-temperature superconductors (LTS) and high-temperature superconductors (HTS) [10, 12, 11], depending on whether their critical temperature T_c is respectively below or above 77 K, the boiling temperature of liquid nitrogen [13]. The majority of HTS are ceramic materials, like rare-earth barium copper oxides (“ReBCO”), e.g., yttrium barium copper oxide (“YBCO”, $T_\mathrm{c} = 92$ K) [11], whereas common LTS are metallic alloys such as niobium titanium (Nb-Ti, $T_\mathrm{c} = 10$ K) or intermetallic compounds such as niobium tin ($\mathrm{Nb_3Sn}$, $T_\mathrm{c} = 18.3$ K) [71].

1.2.1 Meissner state

In the Meissner state [2], the material behaves in many ways like a perfect conductor. Any change in an external applied field is counterbalanced by macroscopic supercurrents, flowing in the material without electrical resistance. Moreover, at the phase transition to the Meissner state, any existing magnetic flux density is expelled from the bulk material. It only penetrates to a characteristic depth, referred to as the London penetration depth λ, which is temperature-dependent. Typically, at 0 K, λ is in the range 30-100 nm for type-I superconductors [72]. This magnetic flux expulsion is achieved by supercurrents that spontaneously appear at the material surface. Supercurrents are carried by superelectrons, that consist of pairs of electrons, referred to as Cooper pairs [73].

The properties of the Meissner state are described by the first and second London constitutive laws, that respectively read [74]:

$$\boldsymbol{e} = \partial_t(\Lambda \boldsymbol{j}), \qquad \textbf{curl}\,(\Lambda \boldsymbol{j}) = -\boldsymbol{b}, \tag{1.7}$$

with $\Lambda = \mu_0 \lambda^2$. The first London law describes perfect conductivity: it replaces the scalar relation $\boldsymbol{j} = \sigma \boldsymbol{e}$ in Eq. (1.6) and expresses that no loss is associated with the supercurrents. Instead, they store kinetic energy. The second London law expresses the magnetic flux expulsion.

The Meissner state is not considered further in this work.

1.2.2 Mixed or vortex state

The intermediate state that arises in type-II superconductors is a mixed state containing both normal and Meissner phases. Magnetic flux density can penetrate the material in the form of magnetic vortices [3]. A vortex can be viewed as a core of normal phase of radius ξ, the coherence length, typically in the $[1, 1000]$ nm range [9], surrounded by supercurrents flowing in the superconducting region. It is found experimentally that vortices hold a magnetic flux equal to the flux quantum $\phi_0 \approx 2.07 \times 10^{-15}$ Wb [75], so that the magnetic flux threading a superconductor is quantized.

When an external field is applied, vortices penetrate gradually in the material from its surface. If vortices are free to move inside the material, the material is said to be a reversible type-II superconductor [9]. In that case, the density of vortices follows reversibly the applied magnetic field, i.e., without hysteresis. Vortices repel each other and experiments show that they arrange in a triangular array.

Imperfections in the material, like dislocations, grain boundaries, and impurities, can create pinning centers that trap vortices. Intentionally introducing defects in the material can further increase this pinning effect. A force needs to be applied to unpin a vortex, and as a consequence, materials with pinning centers demonstrate a hysteretic behavior. In particular, they can trap magnetic flux permanently. Such materials are said to be irreversible, or hard, type-II superconductors [9]. Irreversible type-II superconductors are used in numerous applications. This is the only class of materials that is considered in this work.

When a current density $\boldsymbol{j}$ flows in a type-II superconductor, vortices are subjected to a Lorentz-like force density $\boldsymbol{f}_{\mathrm{L}} = \boldsymbol{j} \times \boldsymbol{b}$, where $\|\boldsymbol{b}\| = n_{\mathrm{v}}\phi_0$ with n_{v} the vortex density and ϕ_0 the flux quantum. Thus, in reversible materials, any current gives rise to a motion of vortices, or flux flow. Because the flux flow involves the motion of normal cores, losses take place in the material, see Fig. 1.2(a). The resulting flux flow resistivity is larger than that of classical metallic conductors at the same temperature. As a consequence, reversible superconductors have no practical interest for transporting current.

In irreversible superconductors, vortices move only if the Lorentz-like force exceeds the

(a) Reversible superconductors.

(b) Irreversible superconductors.

Figure 1.2: Schematics of the j-e relation in type-II superconductors.

pinning force. This defines a critical current density, or depinning current density, j_c, below which there is no flux flow and thus no losses. This is illustrated in Fig. 1.2(b). In general, the critical current density is a function of the local temperature and magnetic flux density. Above j_c, superconductivity is kept but the material exhibits losses. If Joule heating raises the temperature above the critical temperature, the material leaves the superconducting state.

The vortex physics is well described by the Ginzburg-Landau theory [76, 77, 78]. The associated microscopic description, at the scale of individual vortices, is however not suited for modeling macroscopic superconducting samples (≈ 1 cm^3), as it would involve a prohibitive amount of numerical resources [79]. Instead, we are interested in a macroscopic description of the response of irreversible type-II superconductors via a continuous electrodynamic model, with phenomenological constitutive laws. Below, we introduce two such models: the Bean model and the power law model.

Bean model

The Bean model [80], or critical state model (CST), is applicable in the case of strong pinning. It consists in assuming that an induced current density of norm j_c, the critical current density, is generated in every region that sees a local magnetic flux density variation. As long as the local magnetic flux density varies in the same direction or remains constant, the current density stays constant. If the local magnetic flux density variation changes direction, the current density also changes direction, keeping its norm of j_c. Only regions that have never been subjected to a magnetic flux density variation are free of current. Consequently, in the Bean model, the norm of the current density can only take the two values, 0 or j_c.

In the Bean model, the magnetic flux density distribution is therefore assumed to be independent of the rate of applied field, or sweep rate. The vortex dynamics is neglected and vortices are assumed to rearrange themselves instantaneously upon a change of the applied field.

Moreover, the model assumes that $h_{c1} \to 0$ and $h_{c2} \to \infty$, i.e., that the material is always in the vortex state. Finally, in the simplest form of this model, j_c is assumed to be independent of the magnetic flux density. This model is valid on a macroscopic scale only, as it actually averages quantities over a large number of vortices and does not describe them individually [81].

As an illustration of the solution obtained with this model, an infinitely long superconducting cylinder subjected to a parallel external applied field $\boldsymbol{h}_\mathrm{s}$ is considered. For an initially flux-free cylinder (zero-field cooled) and a vertical applied field of increasing amplitude, a flux variation is first produced near the sides of the cylinder, where an azimuthal current density appears and generates a reaction field that shields the inner region in the cylinder, as illustrated by situation 1 in Fig. 1.3(a).

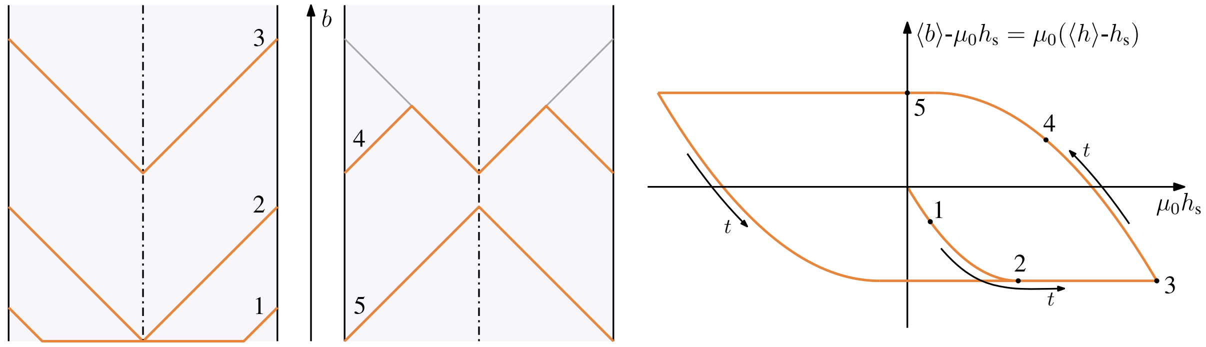

(a) Increasing applied fields. (b) Decreasing applied fields. (c) Magnetization curve.

Figure 1.3: Illustration of the magnetic flux density distribution in a infinitely long superconducting cylinder and the related magnetization curve, in the framework of the Bean model. Situations 1 to 5 are in chronological order (increasing t). The dash-dotted line in schematics (a) and (b) is the cylinder axis. The notation $\langle\cdot\rangle$ corresponds to a volume average.

The fact that the current density cannot exceed j_c limits the level of magnetic shielding; it only allows a decrease of magnetic field per unit length of j_c (A/m^2). If $\boldsymbol{h}_\mathrm{s}$ keeps increasing in amplitude, the magnetic flux progressively penetrates the cylinder, until full penetration, as depicted by situation 2 in Fig. 1.3(a). After full penetration, a constant azimuthal current flows in the cylinder and the shielding cannot be improved, the magnetic field inside the cylinder therefore keeps increasing with the external field, as shown by situation 3 in Fig. 1.3(a). When the applied field stops increasing and starts decreasing in amplitude, as in situations 4 and 5 of Fig. 1.3(b), the variation of magnetic flux also penetrates gradually.

The magnetic flux density distribution is thus history-dependent. In situation 5 in Fig. 1.3(b), permanent currents flow in the cylinder, it is said to be magnetized. The evolution of the volume average magnetic flux density $\langle\boldsymbol{b}\rangle = \mu_0\langle\boldsymbol{h}\rangle$ with respect to a cycling external applied field $\boldsymbol{h}_\mathrm{s}$ is hysteretic, as illustrated in the magnetization curve in Fig. 1.3(c).

Power law model

In practice, at finite temperature, thermal excitations allow some vortices to leave their pinning centers for current densities under the critical current density value, i.e., for $\|\boldsymbol{j}\| < j_\mathrm{c}$; this phenomenon is called flux creep. As a result, losses may be occuring for $\|\boldsymbol{j}\| < j_\mathrm{c}$ and the transition from flux pinning to flux flow is smoothed out. At a macroscopic scale, this smooth transition can be modelled by a power law [72, 82, 83],

$$\boldsymbol{j} = \frac{j_\mathrm{c}}{e_\mathrm{c}}\left(\frac{\|\boldsymbol{e}\|}{e_\mathrm{c}}\right)^{(1-n)/n}\boldsymbol{e} \qquad \text{or} \qquad \boldsymbol{e} = \frac{e_\mathrm{c}}{j_\mathrm{c}}\left(\frac{\|\boldsymbol{j}\|}{j_\mathrm{c}}\right)^{n-1}\boldsymbol{j}, \tag{1.8}$$

with e_c (V/m) a threshold electric field defining the current density j_c. By convention, e_c is often chosen to be 10^{-4} V/m. The exponent $n = U_0/k_B T$ describes the sharpness of the transition to flux flow, and compares the pinning energy barrier in the absence of current U_0 (J) to the thermal energy $k_B T$, where $k_B = 1.38 \times 10^{-23}$ J/K is the Boltzmann constant [84, 85, 86].

Typical values of the power law exponent n in LTS are between 40 and 100 [87, 13], and between 25 and 50 for HTS [88, 13]. In the limit $n \to \infty$, the power law model degenerates to the Bean model. Note that the power law model is only valid before the flux flow regime [81].

In the rest of this work, the power law is the model we consider. It is illustrated in Fig. 1.4. We will use the notation T2S for irreversible type-II superconductors described by this law. The notation T2S include both LTS and HTS materials.

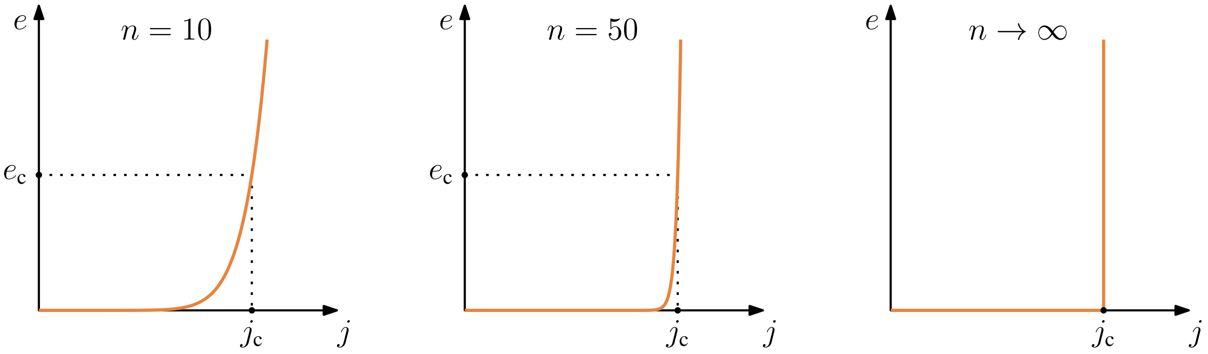

Figure 1.4: Power law for increasing values of the exponent n.

Magnetic constitutive law

Several choices are possible to model the magnetic behavior of T2S in the mixed state. In this work, the supercurrents are treated as eddy currents, and are described by the power law. These macroscopic currents generate a magnetic field via Ampère's law, and the magnetic constitutive law is taken as $\boldsymbol{b} = \mu_0 \boldsymbol{h}$, i.e., the superconductor is in the mixed state with $h_{c1} \ll \|\boldsymbol{h}\| \ll h_{c2}$.

1.3 Ferromagnetic materials

Ferromagnetic materials, or ferromagnets, are materials that exhibit a strong magnetic response to external magnetic fields [89]. A general h-b relationship is illustrated in Fig. 1.5 in a one-dimensional case. The general relation between the magnetic field and the magnetic flux density is highly nonlinear. Moreover, it is not a one-to-one relation and the materials usually exhibit a hysteretic behavior, which is not necessarily isotropic [90].

In this work, we consider isotropic and anhysteretic ferromagnetic materials, that we denote as SFM (for soft ferromagnetic materials). This amounts to considering materials for which the area enclosed by the h-b curve tends to zero and for which the curve is independent of the direction of the applied field. The associated magnetic constitutive law is a one-to-one relation-

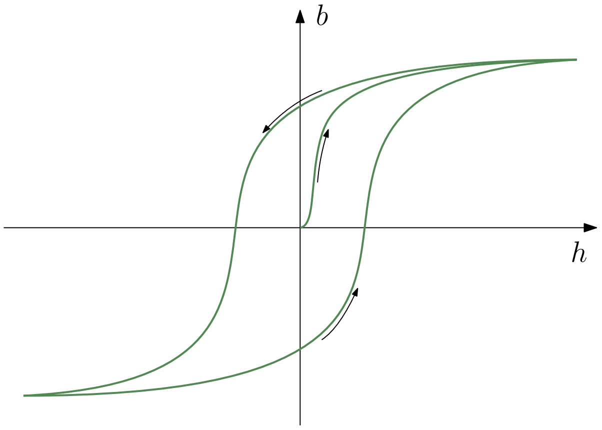

Figure 1.5: General hysteresis curve (major loop) in a ferromagnetic material. Black arrows indicate the direction of evolution, starting from a flux-free material.

ship, and vectors $\boldsymbol{b}$ and $\boldsymbol{h}$ are collinear. Under these assumptions, the relative permeability μ_r, defined such that $\boldsymbol{b} = \mu_0\mu_\text{r}\boldsymbol{h}$, is a function of the magnetic field that only depends on its norm.

A simple model [91] is proposed for describing $\mu_\text{r}(h)$, which consists of a rational expression of first order polynomials, written as

$$\boldsymbol{b} = \mu_0 \left(1 + \left(\frac{1}{\mu_{\text{r},0} - 1} + \frac{\|\boldsymbol{h}\|}{m_0}\right)^{-1}\right) \boldsymbol{h}, \tag{1.9}$$

with $\mu_{\text{r},0}$ (-) the relative permeability at the origin and m_0 (A/m) the saturation magnetic field. A graphical representation of this law is given in Fig. 1.6. The law can be inverted, to express the magnetic field as a function of the magnetic flux density, *i.e.*, so as to involve the reluctivity $\nu(b)$. The inverted expression is given in Eq. (B.31) in Appendix B.3. To give an idea, let us consider a supra50 FeNi alloy, for which typical values fitted to experimental measurements [92] are $\mu_{\text{r},0} = 1700$ and $\mu_0 m_0 = 1.31$ T.

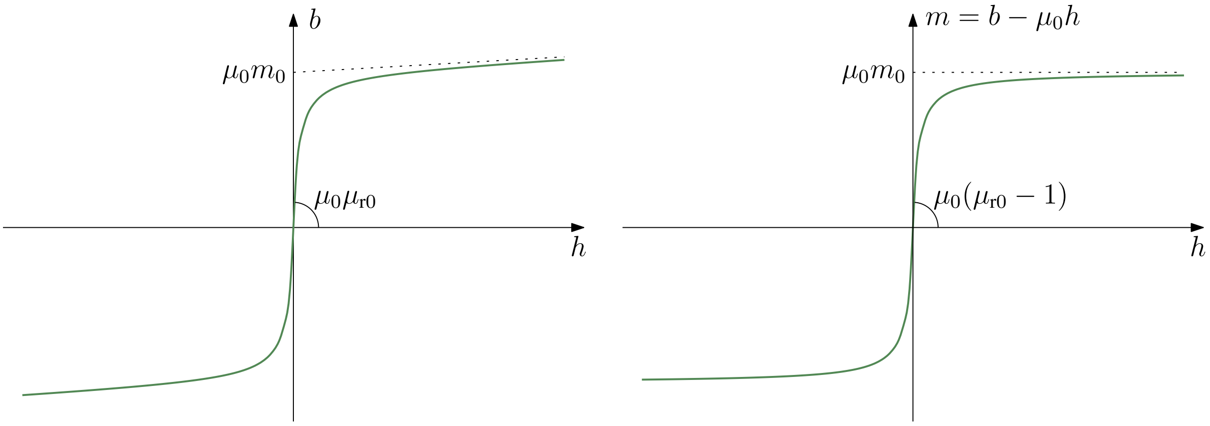

(a) Magnetic flux density.

(b) Magnetization.

Figure 1.6: Ferromagnetic constitutive law and representation of the physical parameters.

The model of Eq. (1.9) is convenient for two reasons. First, it provides the simplest description of the nonlinear anhysteretic ferromagnetic behavior that allows to obtain non-trivial conclusions during the numerical analysis. Second, the constitutive law can be analytically inverted, which is useful for comparing numerical results obtained with different formulations involving either the permeability or the reluctivity. In addition to this simple model, similar but alternative descriptions of the nonlinear permeability will be used in Sections 4.5 and 5.2, based on experimental measurements.

In this work, the electrical conductivity of SFM is neglected. They are treated as non-conducting materials, in which $\boldsymbol{j} = \boldsymbol{0}$.

1.4 Numerical modeling of type-II superconductors

Analytical solutions of the nonlinear equations describing the macroscopic magnetodynamic response of T2S are only available for simple geometrical configurations [26], such as thin strips or disks in a perpendicular magnetic field [93, 94], or infinite slabs in a parallel magnetic field [95]. An overview of analytical methods is proposed in [96]. Most practical and realistic problems do not benefit from analytical solutions and require numerical techniques to be described, which provides approximate solutions to the equations.

Different numerical techniques exist and have been applied to the modeling of T2S [26, 97, 49, 98], including integral methods based on a sand-pile model and Biot-Savart equations [99, 100], methods based on Fast Fourier Transforms (FFT) [101, 102, 103, 104], spectral methods [105], minimization techniques [106], such as the Minimum Electro-Magnetic Entropy Production (MEMEP) method [107, 108, 109, 110], or methods based on equivalent circuits with lumped elements [47]. The most commonly used method is the Finite Element Method (FEM). It is a versatile, popular, and general method allowing to tackle complicated geometries with relative ease.

The FEM has been widely used for classical electromagnetic modeling for decades [31, 111], as well as in the context of superconductors, for bulk magnetization modeling [23] or AC loss computation [81] in a large number of applications [29]. It is the method we consider in this work.

The finite element method does not treat directly the differential problem, referred to as the strong form of the problem. Instead, it is based on a variational form of the problem, known as a weak form. Transforming the strong form into a weak form can be done in a number of different ways, and each of them defines what we call a finite element *formulation*.

A large number of different finite element formulations exist [112, 113, 114]. They are written in terms of different physical fields and/or potentials [115]. Each formulation has its own particularities, advantages, and drawbacks. In particular, in the context of T2S modeling, the power law Eq. (1.8) can be written in two ways, involving either the conductivity, or the resistivity. The power law being strongly nonlinear, formulations written in terms of the conductivity present in fact entirely different numerical behaviors, efficiency and robustness, than formulations written in terms of the resistivity [36]. Selecting an appropriate formulation for a given problem is therefore an important aspect of superconductor modeling.

One of the most commonly used formulation is the h-formulation [116, 6]. It introduces a spurious resistivity in non-conducting regions, so that the whole domain is considered to be conducting, and solved for $\boldsymbol{h}$ everywhere. This allows to avoid the use of a scalar magnetic potential ϕ, and hence eases the implementation compared to its more efficient counterpart, the h-ϕ-formulation [117, 118, 79], which presents a smaller number of degrees of freedom. Recently, a version of the h-ϕ-formulation with a thin-shell approximation suited for nonlinear material modeling has been proposed [119, 120]. Another well-known variation of the h-ϕ-formulation is the t-ω-formulation [121, 122]. The original form of all these formulations involves the resistivity, which will be shown in the next chapters to be the optimal choice for T2S in most cases, in terms of numerical performance.

The dual a-formulation, or a-v-formulation [123, 124, 125, 61], involving the conductivity in their classical forms have also been advantageously used, as they offer the possibility of using large time steps for time integration [126].

In addition to these classical formulations, a number of mixed formulations have been recently proposed. Mixed formulations are defined as weak forms that involve more than one field, and that couple them in the volume or on interfaces [57].

The t-a-formulation [127, 50] is a mixed formulation that incudes a thin-shell approximation. It is mainly based on the a-formulation, but it handles the power law in thin superconducting regions in terms of the resistivity via a current vector potential. Extensions of the t-a-formulation involving homogenization techniques [52] or coupling with a third field in a t-a-h-formulation [128] have also been recently proposed. Other examples of mixed formulations are the a-v-j-formulation [129] or a-j-formulation [57], that also advantageously involve the power law resistivity instead of the conductivity. The e-h-formulation [130] is another example, it allows for accurate evaluations of the electric field and current density separately. Finally, the surface-coupled h-a-formulation [54, 56, 131] and h-ϕ-a-formulation [36, 57] are convenient and efficient choices for modelling rotating machines and systems with both T2S and SFM.

In Chapter 2, we present the h-ϕ-formulation and the a-formulation, as well as their space and time discretization for an implementation in a finite element solver. Mixed formulations are then presented and analyzed in Chapter 3. All formulations will finally be compared and exploited in Chapters 4 and 5 on a number of different problems of increasing complexity.

Chapter 2

Standard finite element formulations

In this chapter, we introduce two classical finite element formulations for magnetodynamic problems, and their applications to systems with irreversible type-II superconductors (T2S) and anhysteretic ferromagnetic materials (SFM). These formulations, the h-ϕ-formulation and the a-formulation, will serve as a basis for building mixed formulations in Chapter 3.

After defining the problem framework in Section 2.1, we derive the h-ϕ-formulation and the a-formulation in the continuous setting in Sections 2.2 and 2.3, respectively. We then discuss the space and time discretizations in Sections 2.4 and 2.5. Finally, in the last two sections, we analyze the treatment of T2S and SFM nonlinearities and we motivate the exploration of mixed formulations.

2.1 Problem definition

2.1.1 Magnetodynamic equations

We define a bounded domain Ω with a piecewise smooth boundary $\partial\Omega = \Gamma$. Inside Ω, we look for solutions to Maxwell's equations in the magnetodynamic approximation:

$$\operatorname{div} \boldsymbol{b} = 0, \tag{2.1}$$

$$\textbf{curl}\, \boldsymbol{h} = \boldsymbol{j}, \tag{2.2}$$

$$\textbf{curl}\, \boldsymbol{e} = -\partial_t \boldsymbol{b}, \tag{2.3}$$

as introduced in Chapter 1. Fields $\boldsymbol{b}$ and $\boldsymbol{h}$ are related by a magnetic constitutive law, which is material dependent and defined in the whole domain Ω,

$$\boldsymbol{b} = \mu \boldsymbol{h}, \quad \text{or} \quad \boldsymbol{h} = \nu \boldsymbol{b}. \tag{2.4}$$

In magnetic materials, μ (resp. ν) is a function of $\boldsymbol{h}$ (resp. $\boldsymbol{b}$), making the problem nonlinear.

For the electric constitutive law, the domain Ω is decomposed into two complementary domains: Ω_c, containing the conducting materials, and $\Omega_c^C = \Omega\backslash\Omega_c$, containing the remaining non-conducting materials. In $\Omega_{\rm c}$, the current density $\boldsymbol{j}$ and the electric field $\boldsymbol{e}$ are related by

$$\boldsymbol{e} = \rho \boldsymbol{j}, \quad \text{or} \quad \boldsymbol{j} = \sigma \boldsymbol{e}. \tag{2.5}$$

In normal conductors, such as copper, ρ and σ are considered to be constant in this work. By contrast, for T2S in the mixed state, ρ (resp. σ) is a strongly nonlinear function of $\boldsymbol{j}$ (resp. $\boldsymbol{e}$), as introduced in Section 1.2. Note that relations (2.5) will be slightly modified in Section 2.1.3 to account for external current or voltage sources.

In the non-conducting domain $\Omega_{\rm c}^{\rm C}$, the current density is strictly identical to zero, and no longer related to the electric field $\boldsymbol{e}$. We have

$$\boldsymbol{j} = \boldsymbol{0}. \tag{2.6}$$

The magnetodynamic equations do not allow to determine more than the curl of $\boldsymbol{e}$ in $\Omega_{\rm c}^{\rm C}$. Any gradient part in $\boldsymbol{e}$ in $\Omega_{\rm c}^{\rm C}$ lets the equations unchanged, and is therefore unknown [132]. This fundamental difference between the conducting and non-conducting domains will be reflected in the finite element formulations, where function space definitions will treat differently the subdomains $\Omega_{\rm c}$ and $\Omega_{\rm c}^{\rm C}$.

Models for stranded conductors, e.g., coils in which the current density is assumed uniform, are not discussed in this chapter. We refer to previous works [132, 133, 134], and to Section 4.5.1, where source fields will be briefly presented in the context of a 3D problem.

2.1.2 Initial and boundary conditions

The differential problem (2.1)-(2.3) is time-dependent and defines a diffusion problem. For well-posedness, information about the initial state, i.e., an initial condition, is required. In particular, the initial magnetic flux density $\boldsymbol{b}$ should be divergence-free, according to Eq. (2.1) [135].

To complement the differential problem defined by the magnetodynamic equations in Ω and the initial condition, boundary conditions have to be imposed on $\partial\Omega = \Gamma$. The boundary Γ is decomposed into two complementary domains: Γ_h and Γ_e, where the tangential components of $\boldsymbol{h}$ and $\boldsymbol{e}$ are prescribed, respectively. The boundary conditions read:

$$\boldsymbol{h} \times \boldsymbol{n}|_{\Gamma_h} = \bar{\boldsymbol{h}} \times \boldsymbol{n}|_{\Gamma_h}, \tag{2.7}$$

$$\boldsymbol{e} \times \boldsymbol{n}|_{\Gamma_e} = \bar{\boldsymbol{e}} \times \boldsymbol{n}|_{\Gamma_e}, \tag{2.8}$$

for $\bar{\boldsymbol{h}}$ and $\bar{\boldsymbol{e}}$ given functions and with $\boldsymbol{n}$ the external unit normal vector defined on Γ.

The particular case of homogeneous boundary conditions is often encountered and reads

$$\boldsymbol{h} \times \boldsymbol{n}|_{\Gamma_h} = \boldsymbol{0}, \tag{2.9}$$

$$\boldsymbol{e} \times \boldsymbol{n}|_{\Gamma_e} = \boldsymbol{0}. \tag{2.10}$$

In particular, Eq. (2.9) implies that $\boldsymbol{j} \cdot \boldsymbol{n}|_{\Gamma_h} = 0$, from Ampère's law (2.2). Similarly, Eq. (2.10) implies that $\partial_t \boldsymbol{b} \cdot \boldsymbol{n}|_{\Gamma_e} = 0$, from Faraday's law (2.3). If the initial condition satisfies $\boldsymbol{b} \cdot \boldsymbol{n}|_{\Gamma_e} = 0$, so does the solution for all t.

2.1.3 Global constraints on voltage and current

In addition to boundary conditions, global conditions must be prescribed on conducting regions that can carry a net current intensity. Let Ω_{c_i}, $i = 1, \ldots, N$, be the N connected regions of Ω_{c}. We define the subset C of indices i whose associated domains Ω_{c_i} make $\Omega_{\mathrm{c}}^{\mathrm{C}}$ multiply connected. Fig. 2.1 illustrates a typical situation for a 3D problem.

To simplify the formalism, we only consider the simple cases where the Ω_{c_i} with $i \in C$ have only one associated net current in this section. This excludes, for example, geometries as double tori (the shape of an “8”, with two “holes”), where two net currents can be defined. The extension to such topologies does not introduce any difficulty and is briefly discussed in Section A.1.3.

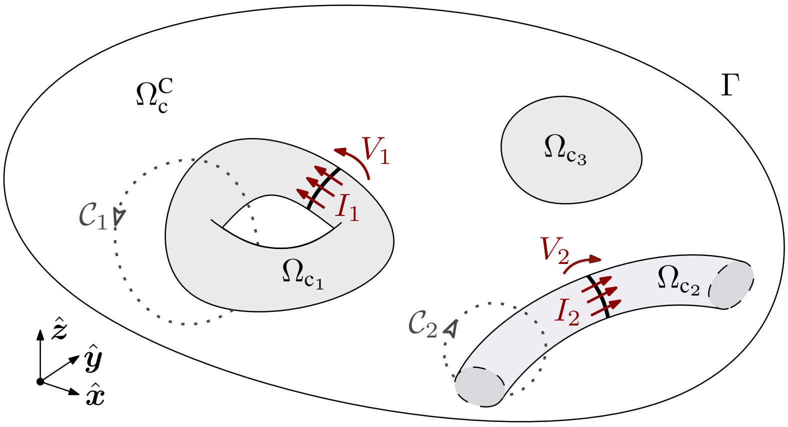

Figure 2.1: Example of a multiply connected $\Omega_{\mathrm{c}}^{\mathrm{C}}$ domain. Domain Ω_{c_1} is a torus contained inside Ω. Domain Ω_{c_2} is a wire crossing the domain boundary Γ at its terminals. Domain Ω_{c_3} is a bulk volume inside Ω. Only Ω_{c_1} and Ω_{c_2} make $\Omega_{\mathrm{c}}^{\mathrm{C}}$ multiply connected: curves $\mathcal{C}_1$ and $\mathcal{C}_2$ cannot be reduced to a point with a continuous deformation in $\Omega_{\mathrm{c}}^{\mathrm{C}}$. We have $C = \{1, 2\}$ and currents and voltages are associated with Ω_{c_1} and Ω_{c_2}. By contrast, there is no global current or voltage associated with Ω_{c_3}.

To each subdomain Ω_{c_i}, with $i \in C$, we associate its net current I_i, which is defined as

$$I_i = \oint_{\mathcal{C}_i} \boldsymbol{h} \cdot \boldsymbol{d\ell}, \tag{2.11}$$

with $\mathcal{C}_i$ a closed oriented curve contained in $\Omega_{\mathrm{c}}^{\mathrm{C}}$ that winds once around Ω_{c_i}.

We also associate with the current the net voltage V_i, that would be applied or measured across the terminals of an external current or voltage generator. To model this voltage, in each subdomain Ω_{c_i}, with $i \in C$, we define a source electric field $\boldsymbol{e}_{\mathrm{a},i}$, satisfying **curl** $\boldsymbol{e}_{\mathrm{a},i} = \boldsymbol{0}$ (in weak sense if $\boldsymbol{e}_{\mathrm{a},i}$ is discontinuous), such that

$$\oint_{\mathcal{C}_i^\star} \boldsymbol{e}_{\mathrm{a},i} \cdot \boldsymbol{d\ell} = -V_i \tag{2.12}$$

along any closed curve $\mathcal{C}_i^\star$ contained in Ω_{c_i} that winds once around Ω_{c_i}, positively with respect to I_i, as illustrated in Fig. 2.2. We can express the source field as $\boldsymbol{e}_{\mathrm{a}} = -\textbf{grad}\ v_{\mathrm{a}}$ (in weak

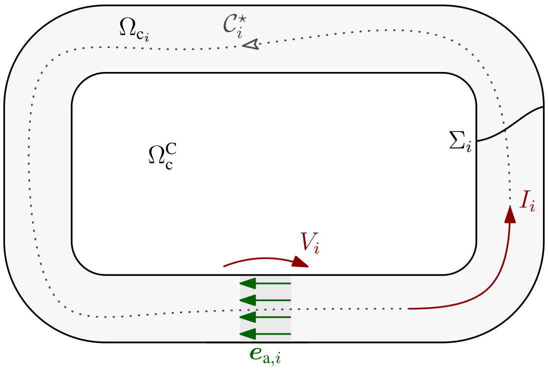

Figure 2.2: Source electric field $\boldsymbol{e}_{a,i}$ reproducing the effect of a voltage generator in a conducting domain Ω_{c_i}. Global variables are the total current I_i flowing in the domain, and the applied voltage V_i imposed by the generator.

sense), with v_a a discontinuous scalar potential. The discontinuity of v_a is equal to V_i across an arbitrary cut Σ_i that makes Ω_{c_i} simply connected.

For domains Ω_{c_i} with $i \in C$, that are simply connected in Ω but with terminals on Γ (such as Ω_{c_2} in Fig. 2.1), we can link each corresponding terminals to create closed loops $\mathcal{C}_i^\star$. In practice, this makes sense because such domains are modelled as fractions of symmetric or periodic domains via the boundary conditions.

Let us denote by $\boldsymbol{e}_a$ the sum of all $\boldsymbol{e}_{a,i}$ for $i \in C$, i.e.,

$$\boldsymbol{e}_a = \sum_{i \in C} \boldsymbol{e}_{a,i}, \tag{2.13}$$

to account for the source field, the electric constitutive law Eq. (2.5) is modified as follows [136, 132]

$$\boldsymbol{e} = \rho \boldsymbol{j} + \boldsymbol{e}_a. \tag{2.14}$$

This modification allows to generate currents that are not eddy currents, e.g., direct currents, without needing to model explicitly current or voltage generators. Consider the steady-state situation resulting from a constant voltage V_i applied on a resistive conductor loop as in Fig. 2.2, without any other external excitation. In a steady state, we have $\textbf{curl}\, \boldsymbol{e} = -\partial_t \boldsymbol{b} = \boldsymbol{0}$, so that, in particular, $\oint_{\mathcal{C}_i^\star} \boldsymbol{e} \cdot d\boldsymbol{\ell} = 0$. Because we have a net current flowing along the conducting loop, we also have $\oint_{\mathcal{C}_i^\star} \rho \boldsymbol{j} \cdot d\boldsymbol{\ell} \neq 0$. The simple law $\boldsymbol{e} = \rho \boldsymbol{j}$ would not allow for such a situation, and adding a source field is therefore necessary, so that $\oint_{\mathcal{C}_i^\star} \rho \boldsymbol{j} \cdot d\boldsymbol{\ell} = -\oint_{\mathcal{C}_i^\star} \boldsymbol{e}_a \cdot d\boldsymbol{\ell} = V_i$.

The source electric field $\boldsymbol{e}_a$ models the global effect of the generator. We can choose to define it on single cross-sections only, using Dirac distributions. However, in practice, depending on the formulation, it can be convenient to consider a larger support. As long as we consider the quantity $\boldsymbol{e}_r = \boldsymbol{e} - \boldsymbol{e}_a$ as the actual electric field, that drives the electrons in the conductors, the support of $\boldsymbol{e}_a$ is arbitrary and does not influence the solution. In particular, for T2S in the mixed state, the power law conductivity is written as a function of $\boldsymbol{e}_r$, i.e., $\sigma = \sigma(\boldsymbol{e}_r)$.

Note also that there are other possibilities to model current or voltage generators. One alternative approach is to remove them from the modelled domain Ω and to treat their influence through boundary conditions [137], which leads to equivalent formulations. Another approach involves voltage distribution functions [138], via a similar modification of the constitutive law.

For simplicity, in this work, we do not consider circuit coupling. We assume that, for every $i \in C$, either the current or the voltage is imposed. We denote by C_I the subset of C for which I_i is imposed to be equal to $\bar{I}_i$, and by C_V the complementary subset, for which V_i is imposed to be equal to $\bar{V}_i$. The global conditions read:

$$I_i = \bar{I}_i, \quad \text{for } i \in C_I, \tag{2.15}$$

$$V_i = \bar{V}_i, \quad \text{for } i \in C_V. \tag{2.16}$$

2.1.4 Strong form of the magnetodynamic problem

All the equations and conditions presented in this section fully define the magnetodynamic problem. They are summarized below, and are referred to as the *strong form* of the problem.

Magnetodynamic problem

Magnetodynamic equations:

$$\operatorname{div} \boldsymbol{b} = 0, \tag{2.17}$$

$$\mathbf{curl}\, \boldsymbol{h} = \boldsymbol{j}, \tag{2.18}$$

$$\mathbf{curl}\, \boldsymbol{e} = -\partial_t \boldsymbol{b}. \tag{2.19}$$

Constitutive laws:

$$\boldsymbol{b} = \mu \boldsymbol{h} \text{ (or } \boldsymbol{h} = \nu \boldsymbol{b}), \text{ in } \Omega, \tag{2.20}$$

$$\boldsymbol{e} = \rho \boldsymbol{j} + \boldsymbol{e}_{\mathrm{a}} \text{ (or } \boldsymbol{j} = \sigma(\boldsymbol{e} - \boldsymbol{e}_{\mathrm{a}})), \text{ in } \Omega_{\mathrm{c}}, \tag{2.21}$$

$$\boldsymbol{j} = \boldsymbol{0}, \text{ in } \Omega_{\mathrm{c}}^{\mathrm{C}}. \tag{2.22}$$

Boundary conditions:

$$\boldsymbol{h} \times \boldsymbol{n}|_{\Gamma_h} = \bar{\boldsymbol{h}} \times \boldsymbol{n}|_{\Gamma_h}, \tag{2.23}$$

$$\boldsymbol{e} \times \boldsymbol{n}|_{\Gamma_e} = \bar{\boldsymbol{e}} \times \boldsymbol{n}|_{\Gamma_e}. \tag{2.24}$$

Global conditions:

$$I_i = \bar{I}_i, \quad \text{for } i \in C_I, \tag{2.25}$$

$$V_i = \bar{V}_i, \quad \text{for } i \in C_V. \tag{2.26}$$

+ Initial condition.

2.2 Magnetic field formulation (h-ϕ-formulation)

The h-ϕ-formulation is expressed in terms of the magnetic field $\boldsymbol{h}$. The magnetic field is an element of the space $\mathcal{H}(\Omega)$, defined as

$$\begin{aligned}\mathcal{H}(\Omega) = \big\{\boldsymbol{h} \in H(\mathbf{curl};\Omega) \mid \mathbf{curl}\, \boldsymbol{h} = \boldsymbol{0} \text{ in } \Omega_{\mathrm{c}}^{\mathrm{C}},\\ (\boldsymbol{h} - \bar{\boldsymbol{h}}) \times \boldsymbol{n} = \boldsymbol{0} \text{ on } \Gamma_h, \mathcal{I}_i(\boldsymbol{h}) = \bar{I}_i \text{ for } i \in C_I\big\},\end{aligned} \tag{2.27}$$

with, as defined in Section A.1.2,

$$H(\mathbf{curl};\Omega) = \left\{\boldsymbol{h} \in \boldsymbol{L}^2(\Omega) : \mathbf{curl}\, \boldsymbol{h} \in \boldsymbol{L}^2(\Omega)\right\}. \tag{2.28}$$

The functional $\mathcal{I}_i(\boldsymbol{h})$ in Eq. (2.27) denotes the net current I_i flowing in conductor Ω_{c_i} for a given function $\boldsymbol{h}$. By Ampère's law, it is therefore given as the circulation of $\boldsymbol{h}$ along a closed loop $\mathcal{C}_i$ around that conductor:

$$\mathcal{I}_i(\boldsymbol{h}) = \oint_{\mathcal{C}_i} \boldsymbol{h} \cdot \boldsymbol{d\ell} = I_i. \tag{2.29}$$

Because they are included in the function space definition, boundary and global conditions Eqn. (2.23) and (2.25) are said to be *strongly* imposed and are referred to as *essential* conditions. By contrast, boundary and global conditions Eqn. (2.24) and (2.26) will be *weakly* enforced by the weak formulation and are referred to as *natural* (boundary and global) conditions.

We denote by $\mathcal{H}_0(\Omega)$ the same space but with homogeneous essential boundary and global conditions, i.e., with $\bar{\boldsymbol{h}} \times \boldsymbol{n} = \boldsymbol{0}$ on Γ_h and $\bar{I}_i = 0$ for $i \in C_I$.

The h-ϕ-formulation is a weak form of Faraday's law. Eq. (2.19) is multiplied by a test function $\boldsymbol{h}' \in \mathcal{H}_0(\Omega)$ and then integrated over the whole domain Ω. Using the curl-curl Green's identity (A.26), and the fact that $\textbf{curl}\, \boldsymbol{h}' = \boldsymbol{0}$ in Ω_c^C and $\boldsymbol{h}' \times \boldsymbol{n} = \boldsymbol{0}$ on Γ_h, we have, for any $\boldsymbol{h}' \in \mathcal{H}_0(\Omega)$,

$$\begin{aligned}
&\left(\partial_t(\mu\, \boldsymbol{h}) \,, \boldsymbol{h}'\right)_\Omega + \left(\textbf{curl}\, \boldsymbol{e} \,, \boldsymbol{h}'\right)_\Omega = 0 && (2.30)\\
\Leftrightarrow\ &\left(\partial_t(\mu\, \boldsymbol{h}) \,, \boldsymbol{h}'\right)_\Omega + \left(\boldsymbol{e} \,, \textbf{curl}\, \boldsymbol{h}'\right)_\Omega - \langle \boldsymbol{e} \times \boldsymbol{n} \,, \boldsymbol{h}' \rangle_\Gamma = 0, && (2.31)\\
\Leftrightarrow\ &\left(\partial_t(\mu\, \boldsymbol{h}) \,, \boldsymbol{h}'\right)_\Omega + \left(\boldsymbol{e} \,, \textbf{curl}\, \boldsymbol{h}'\right)_{\Omega_\text{c}} - \langle \bar{\boldsymbol{e}} \times \boldsymbol{n} \,, \boldsymbol{h}' \rangle_{\Gamma_e} = 0. && (2.32)
\end{aligned}$$

These expressions introduce notations for volume and surface integration that are used throughout the work. For any vector (resp. scalar) fields $\boldsymbol{f}$ and $\boldsymbol{g}$, we note

$$(\boldsymbol{f} \,, \boldsymbol{g})_\Omega = \int_\Omega \boldsymbol{f} \cdot \boldsymbol{g} \, d\Omega, \qquad \text{and} \qquad \langle \boldsymbol{f} \,, \boldsymbol{g} \rangle_\Gamma = \int_\Gamma \boldsymbol{f} \cdot \boldsymbol{g} \, d\Gamma, \tag{2.33}$$

where $\cdot$ is the dot product (resp. scalar multiplication).

To proceed, we need to express the electric field $\boldsymbol{e}$ in terms of the magnetic field $\boldsymbol{h}$ in Ω_c. Accounting for current or voltage generators in Ω_{c_i} with $i \in C$, we have from Eq. (2.21):

$$\boldsymbol{e} = \rho\, \textbf{curl}\, \boldsymbol{h} + \sum_{i \in C} \boldsymbol{e}_{\text{a},i}. \tag{2.34}$$

Introducing this expression in Eq. (2.32) yields

$$\left(\partial_t(\mu\, \boldsymbol{h}) \,, \boldsymbol{h}'\right)_\Omega + \left(\rho\, \textbf{curl}\, \boldsymbol{h} \,, \textbf{curl}\, \boldsymbol{h}'\right)_{\Omega_\text{c}} - \langle \bar{\boldsymbol{e}} \times \boldsymbol{n} \,, \boldsymbol{h}' \rangle_{\Gamma_e} + \sum_{i \in C} \left(\boldsymbol{e}_{\text{a},i} \,, \textbf{curl}\, \boldsymbol{h}'\right)_{\Omega_\text{c}} = 0. \tag{2.35}$$

We now show that the last term can be rewritten in terms of the global variables V_i and I_i. For $i \in C$, let us consider the integral

$$\left(\boldsymbol{e}_{\text{a},i} \,, \textbf{curl}\, \boldsymbol{h}\right)_{\Omega_{\text{c}_i}}. \tag{2.36}$$

By construction, we have $\textbf{curl}\, \boldsymbol{e}_{\text{a},i} = \boldsymbol{0}$. If Ω_{c_i} is made simply connected by introducing one cut Σ_i, as illustrated in Fig. 2.3, there exists a scalar field $v_{\text{a},i}$ such that $\boldsymbol{e}_{\text{a},i} = -\textbf{grad}\, v_{\text{a},i}$ in $\Omega_{\text{c}_i} \backslash \Sigma_i$. Across Σ_i, the scalar field $v_{\text{a},i}$ exhibit a discontinuity

$$v_{\text{a},i}|_{\Sigma_i^-} - v_{\text{a},i}|_{\Sigma_i^+} = V_i, \tag{2.37}$$

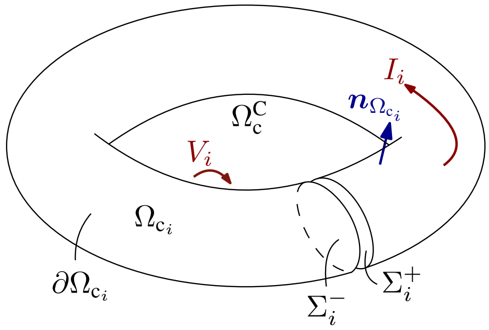

Figure 2.3: Truncated domain $\Omega_{c_i}\backslash\Sigma_i$ and its boundaries. The arrow for the voltage V_i represents the effect of the source field $\boldsymbol{e}_{a,i}$ imposed by the generator (and not the discontinuity of v_a across the cut Σ_i).

which satisfies the condition Eq. (2.12) for $\boldsymbol{e}_{a,i}$.

Using the grad-div Green's identity (A.25), we have

$$\begin{aligned}\left(\boldsymbol{e}_{a,i}\,,\mathbf{curl}\,\boldsymbol{h}\right)_{\Omega_{c_i}} &= -\left(\mathbf{grad}\,v_{a,i}\,,\mathbf{curl}\,\boldsymbol{h}\right)_{\Omega_{c_i}\backslash\Sigma_i}\\ &= -\left\langle\mathbf{curl}\,\boldsymbol{h}\cdot\boldsymbol{n}\,,v_{a,i}\right\rangle_{\partial(\Omega_{c_i}\backslash\Sigma_i)} + \left(\operatorname{div}\left(\mathbf{curl}\,\boldsymbol{h}\right),v_{a,i}\right)_{\Omega_{c_i}\backslash\Sigma_i},\end{aligned} \tag{2.38}$$

with $\partial(\Omega_{c_i}\backslash\Sigma_i) = \partial\Omega_{c_i}\cup\Sigma_i^-\cup\Sigma_i^+$. The first term of Eq. (2.38) vanishes on $\partial\Omega_{c_i}$ since we have $\mathbf{curl}\,\boldsymbol{h}\cdot\boldsymbol{n}_{\Omega_{c_i}} = \boldsymbol{j}\cdot\boldsymbol{n}_{\Omega_{c_i}} = 0$, and only remains nonzero on Σ_i^- and Σ_i^+. We also have $\operatorname{div}\left(\mathbf{curl}\,\cdot\right) = 0$ so that the second term of Eq. (2.38) is equal to zero. Therefore, we have,

$$\left(\boldsymbol{e}_{a,i}\,,\mathbf{curl}\,\boldsymbol{h}\right)_{\Omega_{c_i}} = -\left\langle\mathbf{curl}\,\boldsymbol{h}\cdot\boldsymbol{n}\,,v_{a,i}\right\rangle_{\Sigma_i^-\cup\Sigma_i^+}. \tag{2.39}$$

The normal component of $\mathbf{curl}\,\boldsymbol{h} = \boldsymbol{j}$ is continuous, and $\boldsymbol{n}_{\Sigma_i^+} = -\boldsymbol{n}_{\Sigma_i^-}$, so that

$$\begin{aligned}-\left\langle\mathbf{curl}\,\boldsymbol{h}\cdot\boldsymbol{n}\,,v_{a,i}\right\rangle_{\Sigma_i^-\cup\Sigma_i^+} &= -\left\langle\mathbf{curl}\,\boldsymbol{h}\cdot\boldsymbol{n}_{\Sigma_i^+}\,,\left(v_{a,i}|_{\Sigma_i^+} - v_{a,i}|_{\Sigma_i^-}\right)\right\rangle_{\Sigma_i^+},\\ &= V_i\left\langle\mathbf{curl}\,\boldsymbol{h}\cdot\boldsymbol{n}_{\Sigma_i^+}\,,1\right\rangle_{\Sigma_i^+},\\ &= -V_iI_i.\end{aligned} \tag{2.40}$$

Therefore, we obtain the link between the integral in Eq. (2.36) and the global variables:

$$\left(\boldsymbol{e}_{a,i}\,,\mathbf{curl}\,\boldsymbol{h}\right)_{\Omega_{c_i}} = -V_iI_i. \tag{2.41}$$

Using Eq. (2.41) in Eq. (2.35), with $\boldsymbol{h}'\in\mathcal{H}_0(\Omega)$ and introducing condition (2.26), as well as the notation for the functional $\mathcal{I}_i(\boldsymbol{h})$ defined in Eq. (2.29), this gives

$$\left(\partial_t(\mu\,\boldsymbol{h})\,,\boldsymbol{h}'\right)_\Omega + \left(\rho\,\mathbf{curl}\,\boldsymbol{h}\,,\mathbf{curl}\,\boldsymbol{h}'\right)_{\Omega_c} - \left\langle\bar{e}\times\boldsymbol{n}\,,\boldsymbol{h}'\right\rangle_{\Gamma_e} = \sum_{i\in C_V}\bar{V}_i\mathcal{I}_i(\boldsymbol{h}'). \tag{2.42}$$

We finally obtain the weak formulation by imposing that Eq. (2.42) holds for all $\boldsymbol{h}'\in\mathcal{H}_0(\Omega)$.

h-ϕ-formulation

From an initial solution at $t=0$, find $\boldsymbol{h} \in \mathcal{H}(\Omega)$ such that, for $t>0$ and $\forall \boldsymbol{h}' \in \mathcal{H}_0(\Omega)$,

$$(\partial_t(\mu\, \boldsymbol{h})\, , \boldsymbol{h}')_{\Omega} + (\rho\, \mathbf{curl}\, \boldsymbol{h}\, , \mathbf{curl}\, \boldsymbol{h}')_{\Omega_{\mathrm{c}}} - \langle \bar{\boldsymbol{e}} \times \boldsymbol{n}\, , \boldsymbol{h}' \rangle_{\Gamma_e} = \sum_{i \in C_V} \bar{V}_i \mathcal{I}_i(\boldsymbol{h}').$$

Even if the scalar potential ϕ does not appear explicitly in the weak formulation, by contrast with other variations of this formulation, as in [139], we still call it the h-ϕ-formulation, to stress the strong curl-free property of $\boldsymbol{h}$ in $\Omega_{\mathrm{c}}^{\mathrm{C}}$, which is a key point of the formulation.

The magnetic Gauss law (2.17) has not been explicitly introduced in the construction of the formulation, but we can retrieve it by taking $\boldsymbol{h}' = \mathbf{grad}\, \phi'$ as a test function in Eq. (2.31) [132]. This is developed in Section B.1 in Appendix.

2.3 Vector potential formulation (a-formulation)

For the a-formulation, we introduce two potentials: the magnetic vector potential $\boldsymbol{a}$, defined in the whole domain Ω, such that $\mathbf{curl}\, \boldsymbol{a} = \boldsymbol{b}$, and the electric scalar potential v, defined in Ω_{c} only, which is such that $\boldsymbol{e} = -\partial_t \boldsymbol{a} - \mathbf{grad}\, v$ in Ω_{c}. With these potentials, the magnetic Gauss law (2.17) and Faraday's law (2.19) are strongly satisfied. The fields $\boldsymbol{a}$ and v are not unique, as for any scalar field q, the substitution

$$\boldsymbol{a}^\star = \boldsymbol{a} + \int_0^t \mathbf{grad}\, q\, dt, \tag{2.43}$$

$$v^\star = v - q \quad \text{in } \Omega_{\mathrm{c}}, \tag{2.44}$$

lets the physical fields $\boldsymbol{b}$ and $\boldsymbol{e}$ unchanged. In this work, we choose q such that $q = v$ in Ω_{c}. As a consequence, $v^\star = 0$ and $\boldsymbol{e} = -\partial_t \boldsymbol{a}^\star$ in Ω_{c}, so that $\boldsymbol{a}^\star$ is a primitive of the electric field; it is called the *modified vector potential* [140]. This makes $\boldsymbol{a}^\star$ unique in Ω_{c} up to a gradient field, constant in time. In the following, we drop the $\cdot^\star$ superscript for conciseness.

In $\Omega_{\mathrm{c}}^{\mathrm{C}}$, the vector potential $\boldsymbol{a}$ is still not unique (only the curl of $\boldsymbol{e}$ is known in $\Omega_{\mathrm{c}}^{\mathrm{C}}$). Making $\boldsymbol{a}$ unique in $\Omega_{\mathrm{c}}^{\mathrm{C}}$ amounts to choosing a gauge. We will address the gauging question explicitly at the discretization step, in Section 2.4.2. For now, we assume that we have chosen a gauge.

We choose $\boldsymbol{a}$ in the following space

$$\mathcal{A}(\Omega) = \big\{ \boldsymbol{a} \in H(\mathbf{curl}; \Omega) \mid \boldsymbol{a} \text{ is gauged in } \Omega_{\mathrm{c}}^{\mathrm{C}}, (\boldsymbol{a} - \bar{\boldsymbol{a}}) \times \boldsymbol{n} = \mathbf{0} \text{ on } \Gamma_e \big\}, \tag{2.45}$$

where the essential boundary condition on Γ_e can be expressed from Eq. (2.24) because $\boldsymbol{a}$ is a primitive of $\boldsymbol{e}$. We denote by $\mathcal{A}_0(\Omega)$ the same space but with a homogeneous essential boundary condition, i.e., with $\bar{\boldsymbol{a}} \times \boldsymbol{n} = \mathbf{0}$ on Γ_e.

To account for external voltage or current sources, we introduce an additional unit source field $\boldsymbol{e}_{\mathrm{a1},i} \in H(\mathbf{curl};\Omega_{\mathrm{c}_i})$ in each Ω_{c_i}, with $i \in C$, such that $\mathbf{curl}\,\boldsymbol{e}_{\mathrm{a1},i} = \mathbf{0}$ and

$$\oint_{\mathcal{C}_i^\star} \boldsymbol{e}_{\mathrm{a1},i} \cdot d\boldsymbol{\ell} = -1. \tag{2.46}$$

We then generate the space

$$\mathcal{U}(\Omega_\mathrm{c}) = \left\{ \boldsymbol{e}_\mathrm{a} = \sum_{i\in C} V_i \boldsymbol{e}_{\mathrm{a1},i}\ ,\ V_i \in \mathbb{R} \;\middle|\; V_i = \bar{V}_i \text{ for } i \in C_V \right\} \tag{2.47}$$

for the total field $\boldsymbol{e}_\mathrm{a}$ introduced in Section 2.1.3. The unit source fields $\boldsymbol{e}_{\mathrm{a1},i}$ will be defined explicitly in the discrete setting, in Section 2.4.2. Again, we denote by $\mathcal{U}_0(\Omega_\mathrm{c})$ the same space but with homogeneous essential global conditions, i.e., with $\bar{V}_i = 0$ for $i \in C_V$.

The a-formulation is a weak form of Ampère's law. For the first set of equations, Eq. (2.18) is multiplied by a test function $\boldsymbol{a}' \in \mathcal{A}_0(\Omega)$ and integrated over Ω. Using the curl-curl Green's identity (A.26) and the function space definition, we have, for any $\boldsymbol{a}' \in \mathcal{A}_0(\Omega)$,

$$(\mathbf{curl}\,\boldsymbol{h}\ ,\boldsymbol{a}')_\Omega - (\boldsymbol{j}\ ,\boldsymbol{a}')_\Omega = 0, \tag{2.48}$$

$$\Leftrightarrow\ (\nu\,\mathbf{curl}\,\boldsymbol{a}\ ,\mathbf{curl}\,\boldsymbol{a}')_\Omega - \langle \boldsymbol{h}\times\boldsymbol{n}\ ,\boldsymbol{a}'\rangle_\Gamma + (\sigma\,\partial_t\boldsymbol{a}\ ,\boldsymbol{a}')_{\Omega_\mathrm{c}} + (\sigma\,\boldsymbol{e}_\mathrm{a}\ ,\boldsymbol{a}')_{\Omega_\mathrm{c}} = 0, \tag{2.49}$$

$$\Leftrightarrow\ (\nu\,\mathbf{curl}\,\boldsymbol{a}\ ,\mathbf{curl}\,\boldsymbol{a}')_\Omega - \left\langle \bar{\boldsymbol{h}}\times\boldsymbol{n}\ ,\boldsymbol{a}'\right\rangle_{\Gamma_h} + (\sigma\,\partial_t\boldsymbol{a}\ ,\boldsymbol{a}')_{\Omega_\mathrm{c}} + (\sigma\,\boldsymbol{e}_\mathrm{a}\ ,\boldsymbol{a}')_{\Omega_\mathrm{c}} = 0. \tag{2.50}$$

For the second set of equations, Ampère's law (2.18) is multiplied by a test function $\boldsymbol{e}_\mathrm{a}'$ with $\boldsymbol{e}_\mathrm{a}' \in \mathcal{U}_0(\Omega_\mathrm{c})$ and integrated over Ω_c:

$$(\mathbf{curl}\,\boldsymbol{h}\ ,\boldsymbol{e}_\mathrm{a}')_{\Omega_\mathrm{c}} - (\boldsymbol{j}\ ,\boldsymbol{e}_\mathrm{a}')_{\Omega_\mathrm{c}} = 0, \tag{2.51}$$

$$\Leftrightarrow\ (\mathbf{curl}\,\boldsymbol{h}\ ,\boldsymbol{e}_\mathrm{a}')_{\Omega_\mathrm{c}} + (\sigma\,\partial_t\boldsymbol{a}\ ,\boldsymbol{e}_\mathrm{a}')_{\Omega_\mathrm{c}} + (\sigma\,\boldsymbol{e}_\mathrm{a}\ ,\boldsymbol{e}_\mathrm{a}')_{\Omega_\mathrm{c}} = 0. \tag{2.52}$$

Using Eq. (2.41), the first term of Eq. (2.52) can be rewritten as

$$(\mathbf{curl}\,\boldsymbol{h}\ ,\boldsymbol{e}_\mathrm{a}')_{\Omega_\mathrm{c}} = -\sum_{i\in C} V_i' I_i = -\sum_{i\in C} \mathcal{V}_i(\boldsymbol{e}_\mathrm{a}') I_i, \tag{2.53}$$

where the functional $\mathcal{V}_i(\boldsymbol{e}_\mathrm{a})$ denotes the net voltage V_i applied on conductor Ω_{c_i}, as defined in Eq. (2.12), for a given function $\boldsymbol{e}_\mathrm{a}$. This yields

$$(\sigma\,\partial_t\boldsymbol{a}\ ,\boldsymbol{e}_\mathrm{a}')_{\Omega_\mathrm{c}} + (\sigma\,\boldsymbol{e}_\mathrm{a}\ ,\boldsymbol{e}_\mathrm{a}')_{\Omega_\mathrm{c}} = \sum_{i\in C_I} \bar{I}_i \mathcal{V}_i(\boldsymbol{e}_\mathrm{a}'). \tag{2.54}$$

We finally obtain the weak formulation by imposing that Eqn. (2.50) and (2.54) hold for all $\boldsymbol{a}' \in \mathcal{A}_0(\Omega)$ and $\boldsymbol{e}_\mathrm{a}' \in \mathcal{U}_0(\Omega_\mathrm{c})$.

a-formulation

From an initial solution at time $t = 0$, find $\boldsymbol{a} \in \mathcal{A}(\Omega)$ and $\boldsymbol{e}_\mathrm{a} \in \mathcal{U}(\Omega_\mathrm{c})$ such that, for $t > 0$, $\forall \boldsymbol{a}' \in \mathcal{A}_0(\Omega)$ and $\forall \boldsymbol{e}_\mathrm{a}' \in \mathcal{U}_0(\Omega_\mathrm{c})$,

$$(\nu\,\mathbf{curl}\,\boldsymbol{a}\ ,\mathbf{curl}\,\boldsymbol{a}')_\Omega - \left\langle \bar{\boldsymbol{h}}\times\boldsymbol{n}\ ,\boldsymbol{a}'\right\rangle_{\Gamma_h} + (\sigma\,\partial_t\boldsymbol{a}\ ,\boldsymbol{a}')_{\Omega_\mathrm{c}} + (\sigma\,\boldsymbol{e}_\mathrm{a}\ ,\boldsymbol{a}')_{\Omega_\mathrm{c}} = 0,$$

$$(\sigma\,\partial_t\boldsymbol{a}\ ,\boldsymbol{e}_\mathrm{a}')_{\Omega_\mathrm{c}} + (\sigma\,\boldsymbol{e}_\mathrm{a}\ ,\boldsymbol{e}_\mathrm{a}')_{\Omega_\mathrm{c}} = \sum_{i\in C_I} \bar{I}_i \mathcal{V}_i(\boldsymbol{e}_\mathrm{a}').$$

2.4 Space discretization

No approximation has been introduced for deriving the weak h-ϕ- and a-formulations. They are not yet suited for numerical implementation because of the infinite dimension of the function spaces $\mathcal{H}$ and $\mathcal{A}$. The next step is therefore to choose finite dimensional sub-spaces of $\mathcal{H}$ and $\mathcal{A}$, in which approximate solutions of the weak formulations will be sought.

To define finite dimensional function bases, the geometry of the problem is first discretized by a mesh, which is a subdivision of the continuous geometry into simple geometrical shapes, referred to as elements. In a one-dimensional space, the subdivision is made up of line segments. In a two-dimensional space, it is usually made up of triangles or quadrangles. And in a three-dimensional space, tetrahedra, pyramids, hexahedra or triangular prisms are usually used.

In this work, we consider meshes of degree one, in which every element is defined by straight lines, so curved geometries are inevitably approximated. The continuous domain Ω and its discretized approximation Ω^δ are therefore not identical. For conciseness, we however keep the notations of the continuous domain and its sub-domains for their discretized versions. It should be clear with the context whether we refer to domains of the continuous setting or to those of the discrete setting. The same comment holds for the physical fields, we also choose to keep the notations $\boldsymbol{h}$ and $\boldsymbol{a}$ for their discretized versions.

After discretizing the geometry, we introduce *shape functions*, that constitute the building blocks of the finite dimensional function bases. Electromagnetic problems are advantageously handled with discrete differential forms[1] as shape functions [141]. Among them, Whitney shape functions are forms of the lowest order and are associated with elementary entities of the mesh: nodes, edges, facets or volumes [141]. These are the main shape functions we will consider in this work. They are briefly introduced in Section A.2, and are directly applied for the discretization of the fields in the h-ϕ and a-formulations in the following sections.

In the following, we denote by $\mathcal{N}(\Omega_i)$, $\mathcal{E}(\Omega_i)$, $\mathcal{F}(\Omega_i)$, and $\mathcal{V}(\Omega_i)$ the set of nodes, edges, facets, and volumes of the mesh of a given domain Ω_i, respectively, including entities on the boundaries of Ω_i.

2.4.1 Discretization of *h* the h-ϕ-formulation

The unknown field in the h-ϕ-formulation is the magnetic field $\boldsymbol{h}$. In the continuous setting, $\boldsymbol{h}$ is sought in $\mathcal{H}(\Omega) \subset H(\textbf{curl};\Omega)$, defined in Eq. (2.27). In the discrete setting, we define a discrete function space $\mathcal{H}^{\delta,1}(\Omega) \subset W^1(\Omega) \subset H(\textbf{curl};\Omega)$, where $W^1(\Omega)$ is the space spanned by edge functions on a mesh of Ω. In general, any element $\boldsymbol{h} \in W^1(\Omega)$ can be written as

$$\boldsymbol{h} = \sum_{e\in\mathcal{E}(\Omega)} h_e \, \boldsymbol{w}_e, \tag{2.55}$$

---

[1] See Section A.1.2 for a definition of differential forms.

with the components h_e of $\boldsymbol{h}$ in the basis of the edge functions $\boldsymbol{w}_e$, i.e., the degrees of freedom for $\boldsymbol{h}$. The value of h_e is the circulation of $\boldsymbol{h}$ along edge e, $\forall e \in \mathcal{E}(\Omega)$,

$$h_e = \int_e \boldsymbol{h} \cdot d\boldsymbol{\ell}. \tag{2.56}$$

The $\cdot^{\delta,1}$ superscript in the notation $\mathcal{H}^{\delta,1}(\Omega)$ indicates that only lowest-order shape functions are considered. Higher-order shape functions will be investigated in the next chapter, when treating mixed formulations.

For the magnetic field $\boldsymbol{h}$ to be in $\mathcal{H}^{\delta,1}(\Omega)$, it must be curl-free in $\Omega_{\mathrm{c}}^{\mathrm{C}}$, which is not necessarily the case with the general expansion Eq. (2.55). To ensure $\mathbf{curl}\, \boldsymbol{h} = \mathbf{0}$ in $\Omega_{\mathrm{c}}^{\mathrm{C}}$, we only consider certain combinations of the degrees of freedom h_e. It can be shown that the kernel of the curl operator applied on elements of $W^1(\Omega_{\mathrm{c}}^{\mathrm{C}})$, denoted as $\mathcal{NS}(\mathbf{curl}, \Omega_{\mathrm{c}}^{\mathrm{C}})$, can be spanned by gradients of node functions, and by one independent cohomology function for every $i \in C$ [137, 142]. The decomposition reads as follows:

$$\boldsymbol{h} = \sum_{e \in \mathcal{E}(\Omega_{\mathrm{c}} \setminus \partial\Omega_{\mathrm{c}})} h_e\, \boldsymbol{w}_e + \sum_{n \in \mathcal{N}(\Omega_{\mathrm{c}}^{\mathrm{C}})} \phi_n\, \mathbf{grad}\, w_n + \sum_{i \in C} I_i\, \boldsymbol{c}_i, \tag{2.57}$$

where the h_e, ϕ_n and I_i are the degrees of freedom of the magnetic field $\boldsymbol{h} \in \mathcal{H}^{\delta,1}(\Omega)$. The $\boldsymbol{c}_i$'s are the cohomology functions that we define below. A representation of this decomposition in a 2D geometry is given in Fig. 2.4.

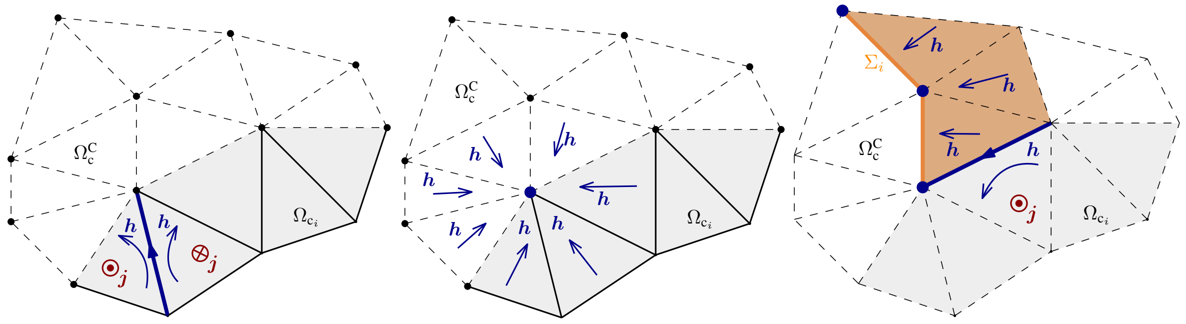

(a) Classical edge function $\boldsymbol{w}_e$. (b) Gradient of node functions w_n. (c) Cut function $\boldsymbol{c}_i$. Net current $\neq 0$.

Figure 2.4: Shape functions for $\boldsymbol{h}$ in the h-ϕ-formulation. The associated current density $\boldsymbol{j} = \mathbf{curl}\, \boldsymbol{h}$ is also represented, it is constant per element. The gray region is the conducting domain Ω_{c_i}. Only the cut function generates a non-zero net current. The orange elements in (c) represent its support, or the transition layer in $\Omega_{\mathrm{c}}^{\mathrm{C}}$, where it is a gradient.

In the conducting domain Ω_{c}, edge functions associated with edges on the boundary $\partial\Omega_{\mathrm{c}}$ are not considered because they are not curl-free in $\Omega_{\mathrm{c}}^{\mathrm{C}}$, and are therefore not associated with independent degrees of freedom.

In the non-conducting domain $\Omega_{\mathrm{c}}^{\mathrm{C}}$, the $\mathbf{grad}\, w_n$ functions are combinations of edge functions (see the first equation of Eqn. (A.22) in Appendix) ensuring that $\mathbf{curl}\, \boldsymbol{h} = \mathbf{0}$. We consider every node inside $\Omega_{\mathrm{c}}^{\mathrm{C}}$, including those on its boundary. The kernel $\mathcal{NS}(\mathbf{curl}, \Omega_{\mathrm{c}}^{\mathrm{C}})$ is completed by a number of $\mathrm{card}(C)$ (cardinal of C) linearly independent elements $\boldsymbol{c}_i$, $i \in C$, of the equivalence classes of the first de Rham cohomology space $\mathcal{H}^1_{\mathrm{dR}}(\Omega_{\mathrm{c}}^{\mathrm{C}})$, defined in Eq. (A.10). These elements are equivalent up to a gradient, so there is still freedom to fix them. The only constraint, for the degree of freedom I_i to make sense as the net current in loop $\mathcal{C}_i^\star$ in regard to Eq. (2.29), is that

$$\oint_{\mathcal{C}_i} \boldsymbol{c}_i \cdot d\boldsymbol{\ell} = 1, \quad \forall i \in C. \tag{2.58}$$

In this work, as in [132], we choose the $\boldsymbol{c}_i$'s as gradients of node functions with a support limited in a transition layer on one side of a cut[2] $\Sigma_i \subset \Omega_{\mathrm{c}}^{\mathrm{C}}$ with $\partial\Sigma_i \subset \partial\Omega_{\mathrm{c}}^{\mathrm{C}}$ associated with the curve $\mathcal{C}_i$, that it intersects once. This choice is illustrated in Figs. 2.4(c) and 2.5. We refer to these $\boldsymbol{c}_i$'s as the *cut functions*, they are global shape functions. They are the only shape functions in Eq. (5.11) that are associated with a non-zero current in Ω_{c_i}. The support of the c_i's are sometimes called "thick cuts" [143, 144].

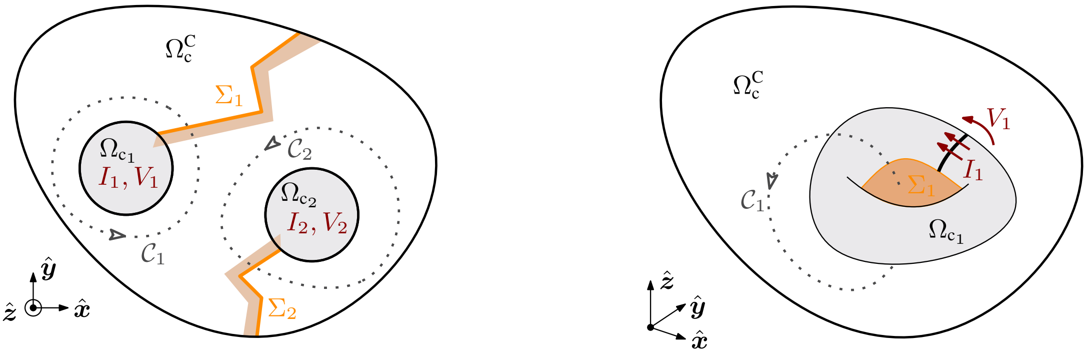

Figure 2.5: Cuts as supports for building cut functions $\boldsymbol{c}_i$ in the h-ϕ-formulation. (Left) 2D geometry with two conducting domains. The two cuts are represented by the dark orange lines and the transition layer is hinted by the light orange regions. Note that its support extends to one element inside the Ω_{c_i}'s, too. (Right) 3D case with one conducting domain. The cut is represented by the orange surface. The transition layer (not represented) is a layer of one elements below the cut and in $\Omega_{\mathrm{c}}^{\mathrm{C}}$.

To complete the construction of $\mathcal{H}^{\delta,1}(\Omega)$, the magnetic field $\boldsymbol{h}$ still has to verify the essential boundary conditions $(\boldsymbol{h} - \bar{\boldsymbol{h}}) \times \boldsymbol{n} = \boldsymbol{0}$ on Γ_h, $\mathcal{I}_i(\boldsymbol{h}) = \bar{I}_i$ for $i \in C_I$. If possible, this is done by constraints on the degrees of freedom $\boldsymbol{h}_e$, ϕ_n, and I_i. The latter is enforced by fixing $I_i = \bar{I}_i$ for $i \in C_I$, whereas for the former, this is only possible for the simplest forms of $\bar{\boldsymbol{h}}$ on Γ_h, e.g., when $\bar{\boldsymbol{h}}$ is constant on Γ_h. Otherwise, the constraint $(\boldsymbol{h} - \bar{\boldsymbol{h}}) \times \boldsymbol{n} = \boldsymbol{0}$ on Γ_h can be imposed weakly via additional equations, e.g., Lagrange multipliers [145].

As mentioned before, $\boldsymbol{h}$ and ϕ are not introduced as two separate fields. The scalar potential arises from combinations of edge functions, and is therefore automatically strongly coupled with the $\boldsymbol{h}$ field in Ω_{c}. This approach is that of [132] and differs from the implementation in [139], where $\boldsymbol{h}$ and ϕ are considered as two separate fields that are weakly coupled via additional continuity conditions. We however keep the notation h-ϕ to highlight the fact that curl-free functions are used in $\Omega_{\mathrm{c}}^{\mathrm{C}}$, by contrast with what is done in the "full h-formulation" [6], that involves edge functions in the whole domain Ω, as well as a spurious resistivity in $\Omega_{\mathrm{c}}^{\mathrm{C}}$. Even if it produces reliable numerical results, this "full h" approach involves a larger number of degrees of freedom, and hence requires a higher computational time in practice.

---

[2] Note that, in practice, with the cohomology solver [142] of Gmsh [60], no cut is explicitly introduced. Instead, the $\boldsymbol{c}_i$'s are directly defined as sums of edge functions (resulting in a gradient). The resulting shape function is completely equivalent.

2.4.2 Discretization of $\boldsymbol{a}$ and $\boldsymbol{e}_{\mathrm{a}}$ in the a-formulation

The unknown fields in the a-formulation are the magnetic vector potential $\boldsymbol{a}$ and the source electric field $\boldsymbol{e}_{\mathrm{a}}$. We describe their discretization separately.

Magnetic vector potential a

In the continuous setting, $\boldsymbol{a}$ is sought in $\mathcal{A}(\Omega) \subset H(\mathbf{curl};\Omega)$, defined in Eq. (2.45). For the discrete setting, we distinguish 3D and 2D models. In 3D, we define a discrete function space $\mathcal{A}^{\delta,1}(\Omega) \subset W^1(\Omega)$, built on a mesh of Ω. In general, if $\boldsymbol{a} \in W^1(\Omega)$, we can write

$$\boldsymbol{a} = \sum_{e\in\mathcal{E}(\Omega)} a_e \boldsymbol{w}_e, \tag{2.59}$$

with the components a_e of $\boldsymbol{a}$ in the basis of the edge functions $\boldsymbol{w}_e$. The $\cdot^{\delta,1}$ superscript in the notation $\mathcal{A}^{\delta,1}(\Omega)$ indicates that only lowest-order shape functions are considered.

The vector potential $\boldsymbol{a}$ is interpreted as a primitive of the electric field in the conducting domain Ω_{c}, which makes it unique up to a constant, whereas in the non-conducting domain $\Omega_{\mathrm{c}}^{\mathrm{C}}$, adding a gradient to $\boldsymbol{a}$ lets the only relevant physical field $\boldsymbol{b} = \mathbf{curl}\ \boldsymbol{a}$ unchanged. A gauge is therefore necessary in $\Omega_{\mathrm{c}}^{\mathrm{C}}$ to make the solution unique.

One valid gauge is the co-tree gauge [146], which is illustrated in Fig. 2.6. It consists in building a spanning tree[3] on the mesh of $\Omega_{\mathrm{c}}^{\mathrm{C}}$ (and its boundary), starting with a complete spanning tree on $(\partial\Omega_{\mathrm{c}}\cap\partial\Omega_{\mathrm{c}}^{\mathrm{C}})\cup\Gamma_e$, and fixing $a_e = 0$ on every edge e of that tree in $\Omega_{\mathrm{c}}^{\mathrm{C}}\backslash\partial\Omega_{\mathrm{c}}$, leaving only the edges of the co-tree as unknowns. One can show that the co-tree gauge reduces the number of degrees of freedom from one per edge to one per facet in $\Omega_{\mathrm{c}}^{\mathrm{C}}$ [132]. No condition is imposed on $\partial\Omega_{\mathrm{c}}$ because $\boldsymbol{a}$ is unique in the conducting domain Ω_{c}, and by continuity (of the tangential component), so is $\boldsymbol{a}$ on $\partial\Omega_{\mathrm{c}}$ [137]. The tree on Γ_e must be complete so that the remaining degrees of freedom are independent for imposing the essential boundary condition $(\boldsymbol{a}-\bar{\boldsymbol{a}})\times\boldsymbol{n} = \mathbf{0}$ on Γ_e [137]. Particular cases in which Γ_e is not topologically trivial are treated in [146]. Note that the essential boundary condition on Γ_e can be directly applied for simple forms of $\bar{\boldsymbol{a}}$ only, e.g., a zero magnetic flux on Γ_e. In this work, we assume that this is the case. Otherwise, other methods exist, e.g., with Lagrange multipliers [145].

As a result, after a co-tree gauge, the vector potential is expressed as

$$\boldsymbol{a} = \sum_{e\in\mathcal{E}(\Omega_{\mathrm{c}}\cup\text{co-tree}(\Omega_{\mathrm{c}}^{\mathrm{C}}))} a_e \boldsymbol{w}_e, \tag{2.60}$$

where the a_e for $e \in \mathcal{E}(\Gamma_e)$ are fixed by the essential boundary condition.

In 2D, two situations can happen. Either the magnetic flux density $\boldsymbol{b}$ is perpendicular to the 2D plane, or it is parallel to it. In the first case, $\boldsymbol{a}$ is therefore parallel to the plane and the situation is exactly the same as in 3D, with the co-tree gauge performed on the 2D mesh, as in Fig. 2.6.

---

[3] A spanning tree in a given domain is a connected set of edges that visits all nodes of that domain, and that does not contain any closed loop.

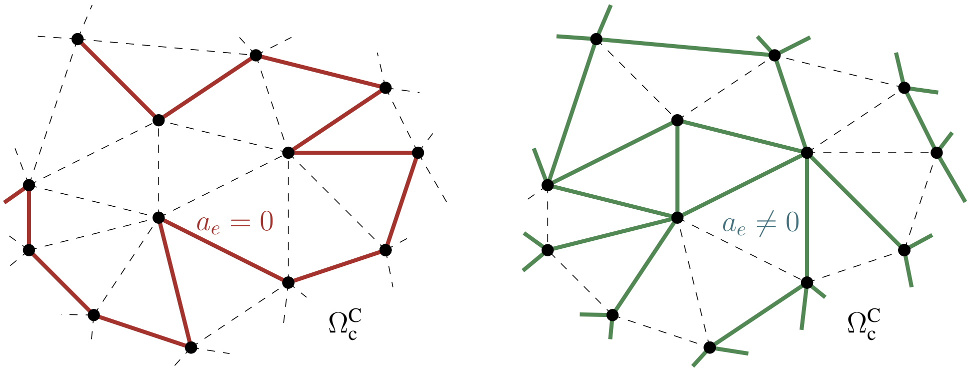

Figure 2.6: Illustration of the co-tree gauge on a 2D mesh. (Left) A portion of a tree in Ω_c^C, visiting all nodes of the domain without any cycle. All the degrees of freedom associated with the edges of that tree are fixed to zero. (Right) The associated co-tree, containing all edges that are not in the tree, for which the associated degrees of freedom are kept.

In the latter case, which is usually more interesting for T2S applications, the vector potential is perpendicular to the 2D plane. It is expressed as a linear combination of *perpendicular edge functions* $\boldsymbol{w}_n$, associated to every node n of the mesh. The only non-zero component of a perpendicular edge function $\boldsymbol{w}_n$ is associated with the normal direction to the plane, defined as $\hat{\boldsymbol{e}}_z$, and is equal to the node function w_n, i.e., $\boldsymbol{w}_n = w_n \hat{\boldsymbol{e}}_z$. The $\boldsymbol{w}_n$ functions can be seen as edge functions of fictitious edges e_n of unit length perpendicular to the plane, supported by the nodes.

We keep the notation $\mathcal{A}^{\delta,1}(\Omega)$ for the resulting space. Whether it refers to a 3D or a 2D case depends on the context. Here, elements $\boldsymbol{a} \in \mathcal{A}^{\delta,1}(\Omega)$ have the following decomposition:

$$\boldsymbol{a} = \sum_{n \in \mathcal{N}(\Omega)} a_n \boldsymbol{w}_n, \tag{2.61}$$

where coefficients a_n are the degrees of freedom, with those associated with nodes $n \in \mathcal{N}(\Gamma_e)$ fixed by the essential boundary condition. The circulation of $\boldsymbol{a}$ along the fictitious perpendicular edge e_n supported by node n is equal to a_n, $\forall n \in \mathcal{N}(\Omega)$,

$$a_n = \int_{e_n} \boldsymbol{a} \cdot d\boldsymbol{\ell}. \tag{2.62}$$

An illustration of the perpendicular edge functions associated with a reference triangle is proposed in Fig. 2.7. By construction, Eq. (2.61) implies div $\boldsymbol{a} = 0$, whatever the values of the degrees of freedom. Therefore, it satisfies an implicit Coulomb gauge, and the magnetic vector potential is unique up to a constant [146].

The curl of these functions is meant to represent contributions for the magnetic flux density $\boldsymbol{b} = \textbf{curl}\, \boldsymbol{a}$. As shown in Fig. 2.7, it is such that its flux across edges incident to the related node is equal to one (in absolute value) and equal to zero across all other edges[4]. Thus, the degree of freedom a_n contributes to the flux of $\boldsymbol{b}$ across edges incident to node n. From the top of the plane, a positive a_n induces a counter-clockwise rotation for $\boldsymbol{b}$ around node n.

---

[4] This flux across the edges in the two-dimensional geometry is equal to the physical flux across the perpendicular facets supported by the perpendicular edges in the three-dimensional extruded geometry with unit thickness.

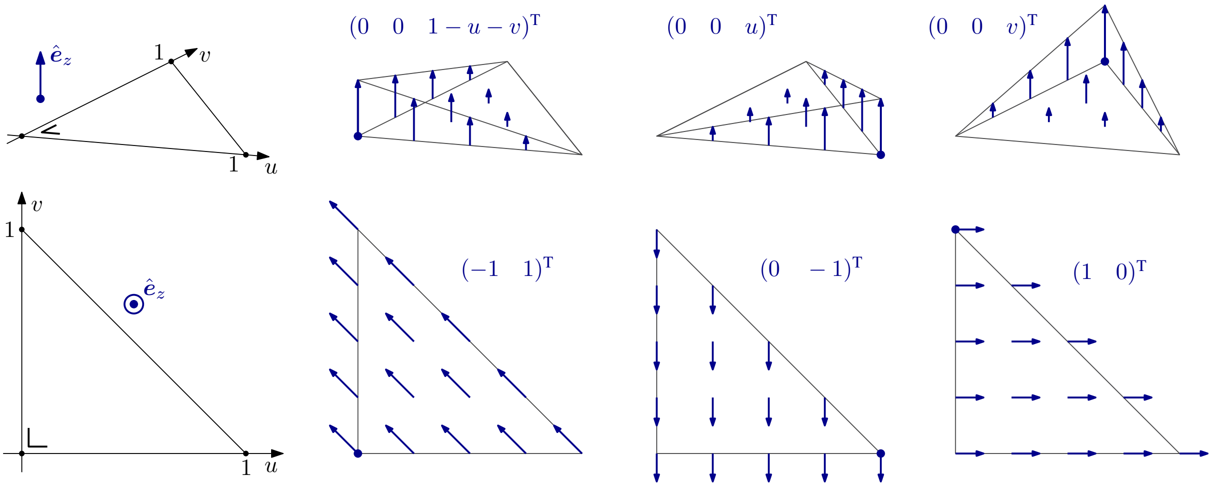

Figure 2.7: (Up) "Perpendicular edge functions" $\boldsymbol{w}_n$ in a reference triangle in 2D. These functions are curl-conform: their tangential component is continuous between different elements. (Down) Curl of perpendicular edge functions in the plane, which are div-conform: their normal component is continuous between elements. Note that the **curl** $\boldsymbol{w}_n$ functions are actually the gradients of node functions, **grad** w_n, with a clockwise rotation of $\pi/2$, i.e., **curl** $\boldsymbol{w}_n = \hat{\boldsymbol{e}}_z \times$ **grad** w_n.

Source electric field $\boldsymbol{e}_\mathrm{a}$

The source electric field defined in Eq. (2.47) is a linear combination of unit source fields $\boldsymbol{e}_{\mathrm{a}1,i}$ with degrees of freedom V_i. For $i \in C_V$, they are fixed to $\bar{V}_i$. The unit source fields are such that **curl** $\boldsymbol{e}_{\mathrm{a}1,i} = \mathbf{0}$ and

$$\oint_{\mathcal{C}_i^\star} \boldsymbol{e}_{\mathrm{a}1,i} \cdot d\boldsymbol{\ell} = -1. \tag{2.63}$$

When $\mathcal{C}_i^\star$ is included in $\Omega\backslash\Gamma$, $\boldsymbol{e}_{\mathrm{a}1,i}$ is an element of the first de Rham cohomology space $\mathcal{H}^1_{\mathrm{dR}}(\Omega_\mathrm{c})$. Conducting domains with terminals on Γ are treated as before. As with the magnetic vector potential, we distinguish 2D and 3D models. In both cases, we denote the associated function spaces by $\mathcal{U}^{\delta,1}(\Omega_\mathrm{c})$.

In 3D, we have freedom on the choice of the $\boldsymbol{e}_{\mathrm{a}1,i}$'s. As in [137], we define them on a one-element-thick transition layer on one side of a cut $\Sigma_i^\star$ in Ω_{c_i} as a sum of edge functions in Ω_{c_i}, similarly to the cut function $\boldsymbol{c}_i$ in $\Omega_\mathrm{c}^\mathrm{C}$ for the h-ϕ-formulation. In the transition layer, $\boldsymbol{e}_{\mathrm{a}1,i}$ is a gradient. In 2D with a perpendicular magnetic flux density $\boldsymbol{b}$, the situation is the same as in 3D, but on a 2D mesh. The unit source electric field is represented in Fig. 2.8 in this case.

In 2D with in-plane magnetic flux density, the electric field is perpendicular to the plane. To ensure **curl** $\boldsymbol{e}_{\mathrm{a}1,i} = \mathbf{0}$, the source field must be constant in each Ω_{c_i}. It can be interpreted as a source field per unit length in the third dimension.

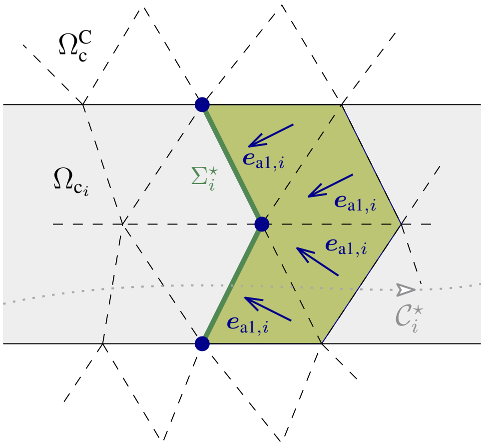

Figure 2.8: Unit source voltage function $e_{a1,i}$ in a 2D example (with in-plane current). One can show that $e_{a1,i}$ satisfies Eq. (2.63) for any $\mathcal{C}_i^\star$, because $e_{a1,i}$ is a gradient in the transition layer (green elements).

2.5 Time integration

After space discretization, the unknown fields involved in a finite element formulation are fully determined by a finite number $N \in \mathbb{N}$ of degrees of freedom, that are unknown functions of time. A system of N nonlinear ordinary differential equations for these degrees of freedom can be obtained by imposing that the weak formulation holds for N linearly independent test functions, e.g., the individual shape functions generating the discrete function space. The resulting differential problem is semi-discrete (still continuous in time) and first-order in time. It reads:

$$\mathbf{M}(\boldsymbol{x}, t)\frac{d\boldsymbol{x}}{dt}(t) + \mathbf{K}(\boldsymbol{x}, t)\boldsymbol{x}(t) = \boldsymbol{g}(t), \tag{2.64}$$

with $\boldsymbol{x} \in \mathbb{R}^N$ the unknown vector, containing the degrees of freedom, $\boldsymbol{g} \in \mathbb{R}^N$ the right-hand side vector, and $\mathbf{K}, \mathbf{M} \in \mathbb{R}^{N\times N}$ two system matrices that depend on $\boldsymbol{x}$ in case of nonlinear problems and whose entries are evaluated by numerical integration of the terms of the weak form. To obtain a fully discrete system that can be solved numerically, time must also be discretized [147]. From the initial solution $x(t_0) = x_0$ at time $t = t_0$, the solution is successively sought at discrete time instants t_n, $\boldsymbol{n} \in \mathbb{N}_0$, not necessarily equidistant.

A large number of time integration methods exists [147, 148], of various levels of complexity and orders of accuracy. In this work, we choose a backward Euler method for time integration [147, 149], which is a simple implicit method: in the equation for time t_n, $n \in \mathbb{N}_0$, all terms are evaluated at t_n, with the time derivative of $\boldsymbol{x}$ at time t_n being approximated by the finite difference

$$\left.\frac{d\boldsymbol{x}}{dt}\right|_{t_n} \approx \frac{\boldsymbol{x}(t_n) - \boldsymbol{x}(t_{n-1})}{t_n - t_{n-1}}, \tag{2.65}$$

where $\boldsymbol{x}(t_{n-1})$ is the known solution at the previous time instant t_{n-1}. It transforms the problem (2.64) into the following system of N nonlinear algebraic equations for the N degrees of freedom, that has to be solved after each time step:

$$\mathbf{A}(\boldsymbol{x}; t_n)\boldsymbol{x}(t_n) = \boldsymbol{b}(\boldsymbol{x}; t_n), \tag{2.66}$$

with, using the notation $\Delta t_n = t_n - t_{n-1}$ for the current time step,

$$\mathbf{A}(\boldsymbol{x}; t_n) = \Delta t_n^{-1}\, \mathbf{M}(\boldsymbol{x}, t_n) + \mathbf{K}(\boldsymbol{x}, t_n), \tag{2.67}$$

$$\boldsymbol{b}(\boldsymbol{x}; t_n) = \boldsymbol{g}(t_n) + \Delta t_n^{-1}\, \mathbf{M}(\boldsymbol{x}, t_n)\boldsymbol{x}(t_{n-1}). \tag{2.68}$$

For conciseness, we drop the explicit time dependence notation $\cdot(\cdot; t_n)$ for $\mathbf{A}$, $\boldsymbol{x}$, and $\boldsymbol{b}$ in the following.

Quadratic post-processing quantities with time derivatives

With the implicit Euler method, one should be careful when evaluating quadratic quantities with time derivatives, especially when we want to integrate them in time. For example, the instantaneous electromagnetic power $\mathcal{P}$ is defined as

$$\mathcal{P} = \big(\partial_t \boldsymbol{b}\,, \boldsymbol{h}\big)_{\Omega} + \big(\boldsymbol{j}\,, \boldsymbol{e}\big)_{\Omega_c}. \tag{2.69}$$

Integrating this quantity over one period in an AC regime gives an estimate of the power loss. For anhysteretic materials, the first term does not contribute to losses and can be dropped out immediately. But still, if we want an accurate evaluation of this term, one should consider the remark in Section B.2, and evaluate the first term of Eq. (2.69) at mid-step as follows:

$$\partial_t \boldsymbol{b} \cdot \boldsymbol{h}|_{n-1/2} \approx \frac{\boldsymbol{b}_n - \boldsymbol{b}_{n-1}}{\Delta t} \cdot \frac{\boldsymbol{h}_{n-1} + \boldsymbol{h}_n}{2}. \tag{2.70}$$

2.6 Linearization

At each time instant, after space and time discretizations, the original problem takes the form of a system of nonlinear algebraic equations. System (2.66) is given as the matrix form

$$\mathbf{A}(\boldsymbol{x})\boldsymbol{x} = \boldsymbol{b}(\boldsymbol{x}), \tag{2.71}$$

with $\boldsymbol{x}$ the vector of degrees of freedom. The system matrix $\mathbf{A}$ and the right-hand side vector $\boldsymbol{b}$ may depend on the unknown vector $\boldsymbol{x}$, which makes the system nonlinear.

In general, the nonlinear system given by Eq. (2.71) cannot be solved directly and iterative techniques are necessary. They consist in successively solving linear systems to approach the solution of the nonlinear system. The existing techniques are plentiful but they all present common features. We present them in the following paragraphs.

In this work, we consider two main iterative methods and combinations of them. The first method consists of a zeroth-order fixed point iteration, and is referred to as the Picard method [150, 151, 152]. The second one is the so-called Newton-Raphson method [153, 154]. We present them after the common features of iterative methods.

Methods for choosing the initial estimate

At each time step, iterations must start with an *initial estimate* of the solution. Initial estimates that are "close" to the exact solution usually help to reduce the number of iterations required to reach a given accuracy. Moreover, some methods may not converge if the initial estimate is "too far" from the exact solution.

The simplest possibility for choosing the initial estimate, or initial iterate, is to take the solution at the previous time step. This method is referred to as the *zeroth-order extrapolation method*. Several previous solutions can also be extrapolated. A *first-order extrapolation method* extrapolates the last two solutions with a linear polynomial. A *second-order extrapolation method* extrapolates the last three solution with a quadratic polynomial. The application of these three methods on a given degree of freedom x is represented in Fig. 2.9. These are the possibilities we will investigate in this work.

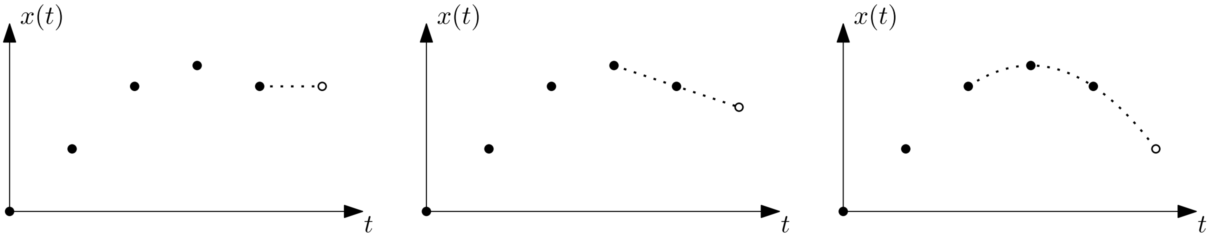

(a) Zeroth-order extrapolation. (b) First-order extrapolation. (c) Second-order extrapolation.

Figure 2.9: Application of the three techniques for choosing the initial estimate for a given degree of freedom x. Filled nodes represent previous solutions and the hollow node in each case is the initial estimate based on these previous solutions.

Convergence criterion

Then, a *convergence criterion* must be defined. Based on a given quantity, evaluated at each iteration, the convergence criterion indicates whether the current solution is considered accurate enough to step forward to the next time step. For example, for an approximate solution $\boldsymbol{x}_i$ at iteration i, the convergence criterion can be a condition on the residual $\boldsymbol{r}_i$ of the system, defined by [35]

$$\boldsymbol{r}_i = \boldsymbol{b}(\boldsymbol{x}_i) - \mathrm{A}(\boldsymbol{x}_i)\boldsymbol{x}_i. \tag{2.72}$$

If $\boldsymbol{x}_i$ is the exact solution to the nonlinear system, the residual is identical to zero. A possibility for the convergence criterion is an absolute tolerance on the 2-norm of the residual, *i.e.*, the accuracy is considered satisfying if $||\boldsymbol{r}_i|| \leq \varepsilon_{\text{abs}}$, with a given absolute tolerance ε_{abs}. A convergence criterion based on a relative tolerance can also be considered, for example, $||\boldsymbol{r}_i||/||\boldsymbol{r}_1|| \leq \varepsilon_{\text{rel}}$, with $\boldsymbol{r}_1$ the residual after the first iteration and a given relative tolerance ε_{rel}.

These choices are actually not easy to apply when comparing different methods, involving quantities with difference orders of magnitude, as is the case here, especially for mixed formulations. In this work, instead of considering the residual, we base the convergence criterion on the power estimate. To recall, at time t_n, it is defined as

$$\mathcal{P}_n = \big(\partial_t \boldsymbol{b}\,, \boldsymbol{h}\big)_{\Omega} + \big(\boldsymbol{j}\,, \boldsymbol{e}\big)_{\Omega_\text{c}}, \tag{2.73}$$

with the first term evaluated as proposed by Eq. (2.70). For a given relative tolerance ε_rel, we consider that the iterations have converged when

$$\frac{\mathcal{P}_n - \mathcal{P}_{n-1}}{\mathcal{P}_{n-1}} \leq \varepsilon_\text{rel}. \tag{2.74}$$

This choice does not provide an absolute proof of convergence as the system residual would do, but we have observed that it is a reliable and convenient indicator, e.g., see Section 4.1.1.

Handling convergence failure: adaptive time-stepping

In some situations, the iterative methods diverge or do not converge in a reasonable number of iterations. To treat these issues automatically, we use an adaptive time step procedure, which does not use fixed time steps Δt_n, but changes them adaptively depending on the dynamics of the problem. This will be crucial for efficient resolutions with Newton-Raphson iterations: small time steps are typically necessary during the first penetration of magnetic flux but one can afford larger steps once the sample is saturated. The heuristic procedure is defined as follows (taken from [155]):

- if the number of iterations exceeds i_max with a time step Δt or if the iterations diverge, the current time integration step restarts with a smaller time step equal to $\gamma\Delta t$, with $\gamma < 1$;
- if a step with time step Δt converges in less than i_fast iterations, the next time step is chosen equal to $\min(\beta\Delta t, \Delta t_\text{max})$, with $\beta > 1$ and a fixed Δt_max.

Values for γ, i_max, β, and Δt_max are up to the user and may depend on the application and the linearization technique. For example, the Picard method described below will typically require more iterations than the Newton-Raphson method for reaching a given accuracy.

2.6.1 The Picard iteration

The Picard iteration [150, 151, 152] is one of the simplest techniques for handling the nonlinearity. From an iterate $\boldsymbol{x}_i$ at iteration i, the next iterate $\boldsymbol{x}_{i+1}$ is sought by fixing the value of matrix $\mathbf{A}$ and vector $\boldsymbol{b}$ at the iterate $\boldsymbol{x}_i$, and looking for the $\boldsymbol{x}_{i+1}$ that satisfies the following linear system,

$$\mathbf{A}(\boldsymbol{x}_i)\boldsymbol{x}_{i+1} = \boldsymbol{b}(\boldsymbol{x}_i). \tag{2.75}$$

In general, this method does not exhibit a high convergence rate. It is usually a robust method in the sense that it usually converges for a wide range of initial iterates. An illustration of one iteration of this method in the case of a single unknown is given in Fig. 2.10(a). A common acceleration technique associated with fixed point methods is the Aitken's delta-squared process, which consists in a clever extrapolation of the last iterates [156, 157].

Note that in some cases, the iterates resulting from Picard iterations may enter cycles and fail to converge. This will be illustrated later in this chapter, e.g., in Fig. 2.18(a).

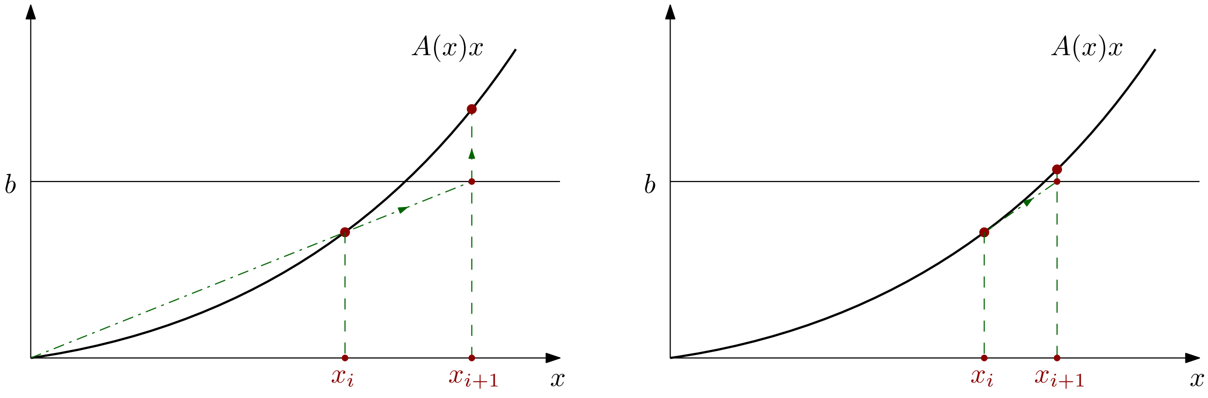

(a) Picard iteration. (b) Newton-Raphson iteration.

Figure 2.10: One iteration of the Picard and Newton-Raphson iterative techniques for the case of a single degree of freedom, for the equation $A(x)x = b$.

2.6.2 The Newton-Raphson iteration

The Newton-Raphson method [153] consists in approximating the nonlinear terms $\mathbf{A}(\boldsymbol{x})\boldsymbol{x}$ and $\boldsymbol{b}(\boldsymbol{x})$ to first order with a Taylor limited development, yielding a linear system. From an iterate $\boldsymbol{x}_i$, the next iterate $\boldsymbol{x}_{i+1}$ is computed by solving the following linear system,

$$\mathbf{A}(\boldsymbol{x}_i)\boldsymbol{x}_i + \mathbf{J}(\boldsymbol{x}_i)(\boldsymbol{x}_{i+1} - \boldsymbol{x}_i) = \boldsymbol{b}(\boldsymbol{x}_i), \tag{2.76}$$

with $\mathbf{J}$ the Jacobian matrix defined by

$$\mathbf{J}(\boldsymbol{x}) = \frac{\partial}{\partial \boldsymbol{x}}\big(\mathbf{A}(\boldsymbol{x})\boldsymbol{x} - \boldsymbol{b}(\boldsymbol{x})\big). \tag{2.77}$$

An example of one iteration of this method in the case of a single unknown is proposed in Fig. 2.10(b).

When the initial iterate is "sufficiently close" to the solution, and under other conditions, the convergence can be very fast, demonstrating a quadratic rate of convergence [158]. However, the Newton-Raphson method is usually less robust than the Picard technique in the sense that, if the initial iterate is not sufficiently close to the solution, the method may diverge. As will be illustrated later, e.g. in Fig. 2.18(b), iterates may also enter cycles that prevent the method to converge.

If the analytical expression of the Jacobian matrix Eq. (2.77) is not known, it can be evaluated numerically, which slightly lowers the convergence rate. In that case, this is referred to as a quasi-Newton-Raphson method, of which a popular example is the BFGS method [159]. In this work, if we do not have access to the exact Jacobian expression, e.g., when the constitutive laws are interpolated on experimental measurements, we evaluate the Jacobian with a finite difference approximation.

We can introduce a relaxation factor γ that multiplies the solution increment given by system (2.76) to define a new solution x_{i+1}^{relax} as follows:

$$x_{i+1} \leftarrow x_{i+1}^{\text{relax}} = x_i + \gamma\,(x_{i+1} - x_i). \tag{2.78}$$

The relaxation factor γ can be fixed a priori, or dynamically adapted. In some cases, relaxation factors help avoiding divergence or cycles in the iterations, but they may also reduce the convergence rate [90].

In general, the Newton-Raphson method offers efficient resolutions thanks to its quadratic rate of the convergence. When it can be used without convergence issues, it is usually preferred to the Picard method.

2.6.3 Hybrid iterations

Different combinations and variations of the Picard and Newton-Raphson methods can be investigated. For example, one method can be used on one nonlinear term of the equations while the other one is used on another nonlinear term. Also, it is possible to switch from one method to the other after a given number of iterations. We will consider these hybrid techniques in the following.

2.7 Analysis of the treatment of material nonlinearities

When applying the Newton-Raphson method on the power law for T2S, we quickly observe convergence issues with the a-formulation. Similarly, when applying the Newton-Raphson method on the saturation law for SFM, we observe convergence issues with the h-ϕ-formulation. In most cases, the iterations obtained from Eq. (2.76) do not converge towards a single solution. Instead, they enter cycles as represented in Figs. 2.11 and 2.12. Conversely, we also observe that when using the alternative formulation in the same situation, i.e., the h-ϕ-formulation for T2S, or the a-formulation for SFM, these cycles no longer appear and the Newton-Raphson iterations easily converge.

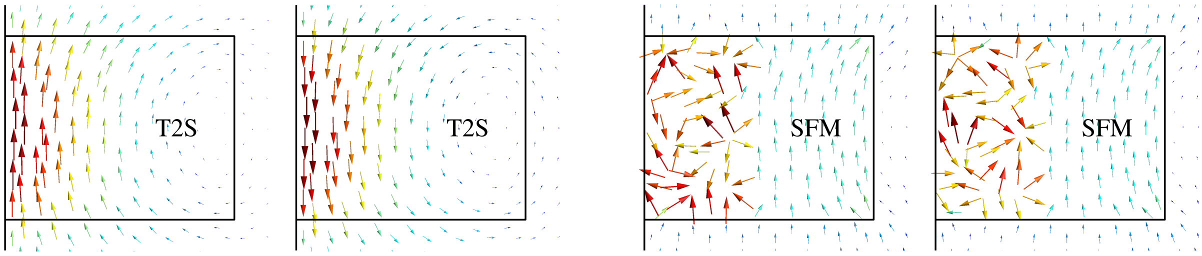

(a) a-formulation, T2S.

(b) h-ϕ-formulation, SFM.

Figure 2.11: Two successive Newton-Raphson iterations for (a) a T2S material and the a-formulation, and (b) a SFM material and the h-ϕ-formulation. The model represents a T2S or a SFM cylindrical pellet subjected to an external magnetic field. It is a 2D-axisymmetric model. The arrows represent the magnetic flux density. This is an illustration of non-converging behaviors: the Newton-Raphson iterations cycle between two wrong solutions.

Because taking the alternative formulation helps to circumvent the convergence issues, the observations do not cause much issues in situations where only one material, T2S or SFM, is involved. However, difficulties naturally arise when we want to combine the two materials in a

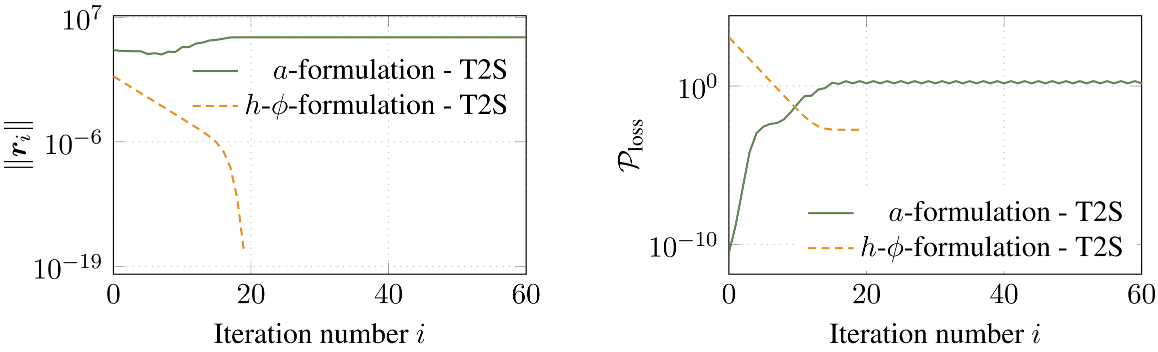

Figure 2.12: Iteration cycles observed on a T2S material with the a-formulation and the Newton-Raphson method. Same setting as in Fig. 2.11. The situation with the h-ϕ-formulation is also given for illustration, it converges without cycles. (Left) Evolution of the norm of the residual $\boldsymbol{r}_i = \boldsymbol{b}(\boldsymbol{x}_i) - \mathbf{A}(\boldsymbol{x}_i)\boldsymbol{x}_i$ with the iterations. (Right) Evolution of the power loss estimate $\mathcal{P}_{\text{loss}} = (\boldsymbol{j}\ , \boldsymbol{e})_{\Omega_c}$.

single model. Handling such situations is the subject of the next chapter, in which we consider mixed finite element formulations. But before moving on, we will analyze the cycling behavior in more detail in this section.

In Section 2.7.1, we introduce basic elements of fixed point theory. In Section 2.7.2, we propose two simplified nonlinear models with a single degree of freedom reproducing the convergence issues that we observe with finite element models (1D, 2D, or 3D), for both T2S and SFM materials. In Sections 2.7.3 and 2.7.4, we analyze the treatment of the simplified nonlinear models by different iterative techniques, in the light of the fixed point theory. In particular, we investigate the relevance of using relaxation factors or hybrid iterative techniques to prevent iteration cycles to appear.

2.7.1 Fixed points

Let us consider a convex subset $X \subset \mathbb{R}^N$ and a function $\boldsymbol{f} : X \mapsto X$. For simplicity, we assume that $\boldsymbol{f}$ is a continuously differentiable function. The point $\bar{\boldsymbol{x}} \in X$ is said to be a fixed point of $\boldsymbol{f}$ if

$$\boldsymbol{f}(\bar{\boldsymbol{x}}) = \bar{\boldsymbol{x}}, \tag{2.79}$$

i.e., it has its value unchanged under the transformation $\boldsymbol{f}$ [160].

In numerical analysis, a fixed point iteration is a method for finding fixed points of a function. Starting from an initial value $\boldsymbol{x}_0$, it consists in the following iteration:

$$\boldsymbol{x}_{i+1} = \boldsymbol{f}(\boldsymbol{x}_i), \quad i \in \mathbb{N}, \tag{2.80}$$

hoping that the sequence of the $\boldsymbol{x}_i$'s converges towards a fixed value $\bar{\boldsymbol{x}}$, one fixed point of $\boldsymbol{f}$.

If $\boldsymbol{f}$ is strictly contractive in X, that is, if there exists a constant $k < 1$ such that

$$\|\boldsymbol{f}(\boldsymbol{x}) - \boldsymbol{f}(\boldsymbol{y})\| \leq k\|\boldsymbol{x} - \boldsymbol{y}\|, \quad \forall \boldsymbol{x}, \boldsymbol{y} \in X, \tag{2.81}$$

then, the sequence of the $\boldsymbol{x}_i$'s computed from Eq. (2.80) converges strongly in $\mathbb{R}^N$ for any $\boldsymbol{x}_0 \in X$. Moreover, its limit $\lim_{i\to\infty} \boldsymbol{x}_i = \bar{\boldsymbol{x}}$ is the unique fixed point of $\boldsymbol{f}$ in X and the convergence is at least linear, i.e., there exists a constant $m < 1$ such that, $\forall i \in \mathbb{N}$,

$$\frac{\|\boldsymbol{x}_{i+1} - \bar{\boldsymbol{x}}\|}{\|\boldsymbol{x}_i - \bar{\boldsymbol{x}}\|} = \rho_i \leq m. \tag{2.82}$$

In this expression, we refer to ρ_i as the convergence factor [151, 157].

It may happen that the iterations do not converge, but approach cycles between two distinct values instead [161, 162]. In these cases, the values are said to be fixed points of period two, i.e., fixed points of the function $\boldsymbol{f} \circ \boldsymbol{f}$. They satisfy

$$\boldsymbol{f}\big(\boldsymbol{f}(\boldsymbol{x})\big) = \boldsymbol{x}, \tag{2.83}$$

without satisfying $\boldsymbol{f}(\boldsymbol{x}) = \boldsymbol{x}$. Fixed points of any higher period can also exist. In some cases, these "periodic" fixed points completely prevent the method from converging towards the sought solution. As observed above, this is the case for the T2S and SFM nonlinearities in the a-formulation and h-ϕ-formulation, respectively.

Particular case: $X \subset \mathbb{R}$. If $|f'(x)| < 1, \forall x \in X \subset \mathbb{R}$, it is strictly contractive in X, and fixed point iterations will converge to the unique fixed point $\bar{x}$ for any $x_0 \in X$. This condition on the derivative is a sufficient, but not necessary, condition for convergence. Moreover, when the iterates become sufficiently close to $\bar{x}$ (for some $i \geq i_0$, $i_0 \in \mathbb{N}$), we have $\rho_i \approx |f'(\bar{x})|$. The value of $|f'(\bar{x})|$ can be referred to as the asymptotic convergence factor; the smaller it is, the faster the convergence near the fixed point. One can show that $|f'(\bar{x})| \leq 1$ is also a *necessary* condition for the iterations to converge to $\bar{x}$ as an infinite sequence[5]. In the particular case $|f'(\bar{x})| = 0$, the convergence rate can be higher than linear. The nature of the convergence depends on the higher derivatives of f in the vicinity of $\bar{x}$ [157]. When $|f'(\bar{x})| \leq 1$, the fixed point $\bar{x}$ is said to be attractive. Otherwise, it is said to be repulsive. See Fig. 2.13.

By extension, if $\tilde{x}$ is a fixed point of period two, and hence not a fixed point of f, if $|g'(\tilde{x})| \leq 1$, with $g = f \circ f$, the fixed point of period two is said to be attractive. We can also say that the *cycle* containing $\tilde{x}$ is attracting. In general, this is no good news, because the point $\tilde{x}$ will therefore attract the iterates towards a cycle between two wrong solutions for a range of initial estimate values x_0, preventing convergence towards the solution $\bar{x}$.

Picard iteration. The Picard iteration (2.75) can be seen as a fixed point iteration for the function

$$\boldsymbol{f}_{\text{Pi}}(\boldsymbol{x}) = \mathbf{A}^{-1}(\boldsymbol{x})\boldsymbol{b}(\boldsymbol{x}), \tag{2.84}$$

so that evaluating $\boldsymbol{f}_{\text{Pi}}(\boldsymbol{x})$ involves solving a linear system at each iteration. Of course, the matrix $\mathbf{A}(\boldsymbol{x})$ must be nonsingular.

---

[5] Unlikely choices may offer convergence in a *finite* number of steps, such as $x_0 = \bar{x}$, in the case $|f'(\bar{x})| < 1$.

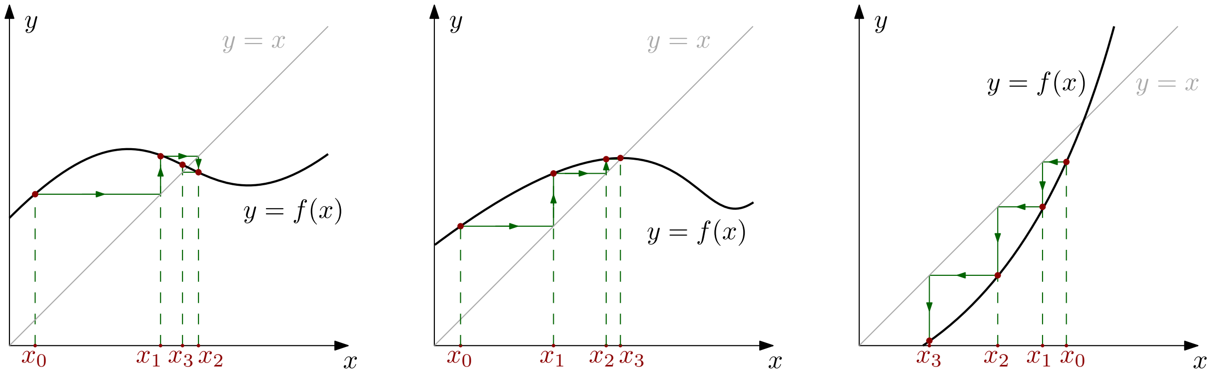

(a) Linear convergence. (b) Quadratic convergence. (c) Non-convergence.

Figure 2.13: Fixed point iteration in three distinct situations for the particular case $X \subset \mathbb{R}$. (a) The function f is strictly contractive and converges for any x_0 in the illustrated interval. (b) In addition to being strictly contractive, the function f is stationary at the fixed point, and the iterations converge quadratically once they are close enough to the fixed point. (c) The function is non-contractive, and the iterates diverge. For cases (a) and (b), the fixed point is said to be attractive. For case (c), it is repulsive.

Newton-Raphson iteration. Similarly, the Newton-Raphson iteration (2.76) can be rewritten as a fixed point iteration for the function

$$\boldsymbol{f}_{\mathrm{NR}}(\boldsymbol{x}) = \boldsymbol{x} + \mathbf{J}^{-1}(\boldsymbol{x})(\boldsymbol{b}(\boldsymbol{x}) - \mathbf{A}(\boldsymbol{x})\boldsymbol{x}), \tag{2.85}$$

provided that $\mathbf{J}(\boldsymbol{x})$ is nonsingular. It is interesting to notice that at a fixed point $\bar{\boldsymbol{x}}$, which is a solution of the problem (2.71), we have

$$\boldsymbol{f}'_{\mathrm{NR}}(\bar{\boldsymbol{x}}) = \mathbf{I} + \frac{\partial}{\partial \boldsymbol{x}}\left(\mathbf{J}^{-1}(\bar{\boldsymbol{x}})\right)\underbrace{\left(\boldsymbol{b}(\bar{\boldsymbol{x}}) - \mathbf{A}(\bar{\boldsymbol{x}})\bar{\boldsymbol{x}}\right)}_{=\,\mathbf{0}} + \underbrace{\mathbf{J}^{-1}(\bar{\boldsymbol{x}})\left(\mathbf{0} - \mathbf{J}(\bar{\boldsymbol{x}})\right)}_{=\,-\mathbf{I}} = \mathbf{0}. \tag{2.86}$$

If $\mathbf{J} : X \mapsto \mathbb{R}^{N\times N}$ is Lipschitz continuous, one can show that the local convergence is quadratic [158]. That is, if $\boldsymbol{x}_0$ is sufficiently close to the solution $\bar{\boldsymbol{x}}$, there exists a constant $k < 1$ such that, $\forall i \in \mathbb{N}$,

$$\frac{\|\boldsymbol{x}_{i+1} - \bar{\boldsymbol{x}}\|}{\|\boldsymbol{x}_i - \bar{\boldsymbol{x}}\|^2} \leq k. \tag{2.87}$$

In most cases, if the computational cost of one iteration is comparable, a method with a quadratic convergence rate is preferable to a method with a linear convergence rate [158].

In general, choosing an initial iterate x_0 that is sufficiently close to the solution to guarantee a fast convergence is not an easy task. However, in our case, we benefit from the time discretization and the knowledge of previous solutions. They help to provide initial estimates of good quality, especially when the time steps are small.

2.7.2 Simple models for T2S and SFM nonlinearities

To analyze the behavior of iterative techniques on the T2S and SFM nonlinearities, we simplify the finite element models to the simplest possible problems that still exhibit convergence issues. As we will see, single degree of freedom equations involving similar nonlinearities share the same features as more complicated finite element models.

Simple T2S model

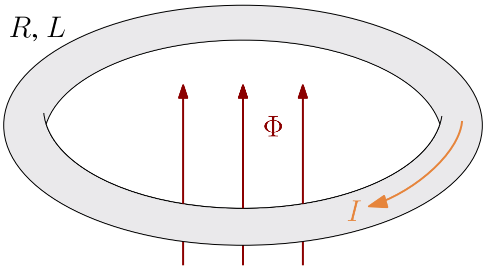

Figure 2.14: T2S ring for the single degree of freedom equation.

Consider a T2S ring subjected to a time-varying external magnetic flux Φ, and carrying a current intensity I, as illustrated in Fig. 2.14. The time derivative of Φ is denoted as $\dot{\Phi}$. The ring can be modelled by lumped elements: a nonlinear resistor $R = V_c/I_c(|I|/I_c)^{n-1}$, that mimics the electrical resistivity of the power law, with V_c, I_c and n fixed, in series with a linear inductor L, yielding $R(I)I + L\dot{I} = \dot{\Phi}$. After time discretization, solving the problem for the current intensity I flowing inside the ring gives rise to an equation of the form

$$f(x) = |x|^{n-1}x + \lambda x - b = 0, \tag{2.88}$$

to be solved at each time step, with λ and b two real parameters. By contrast, solving for the voltage across the resistor gives rise to an equation of the form

$$g(x) = |x|^{(1-n)/n}x + \lambda^{-1}x - c = 0, \tag{2.89}$$

with c another real parameter. The shapes of f and g are depicted in Fig. 2.15. The first case is analogous to the h-ϕ-formulation with T2S because it involves a resistivity-like nonlinearity whereas the second one is analogous to the a-formulation with T2S because it involves a conductivity-like nonlinearity.

Note that these analogues can also be obtained from a dimensional analysis of the h-ϕ and a-formulation. For f, we have

$$(\rho\, \textbf{curl}\, \boldsymbol{h}\ , \textbf{curl}\, \boldsymbol{h}')_{\Omega_c} + (\partial_t(\mu \boldsymbol{h})\ , \boldsymbol{h}')_{\Omega} - \text{source} = 0, \tag{2.90}$$

where the first term is nonlinear with the power law applied on the unknown, $|x|^{n-1}x$, whereas the second one is linear, λx. The parameter λ is a scaling parameter and b gathers the sources and the previous solution from the backward Euler approximation. Similarly, for g,

$$(\sigma\, \partial_t \boldsymbol{a}\ , \boldsymbol{a}')_{\Omega_c} + (\nu\, \textbf{curl}\, \boldsymbol{a}\ , \textbf{curl}\, \boldsymbol{a}')_{\Omega} - \text{source} = 0 \tag{2.91}$$

can be reduced to a nonlinear term, $|x|^{(1-n)/n}x$, a linear one, $\lambda^{-1}x$ with a scaling parameter, λ^{-1}, and a constant term, c.

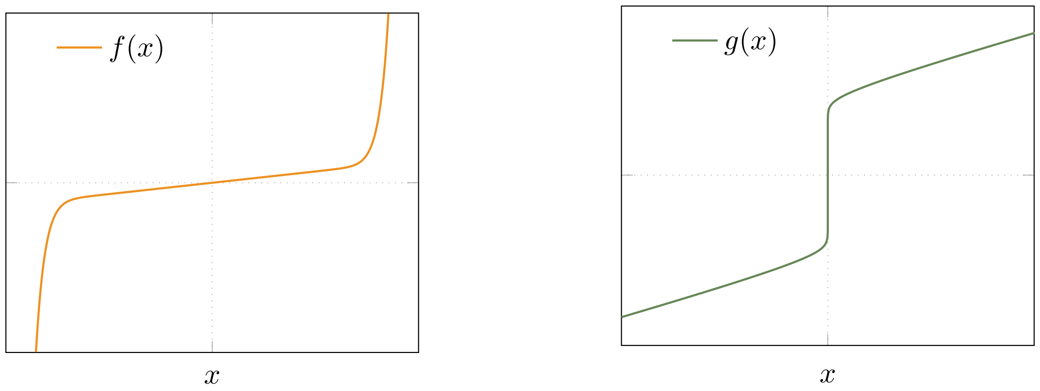

(a) $f(x) = |x|^{n-1}x + \lambda x - b$ (h-ϕ-formulation). (b) $g(x) = |x|^{(1-n)/n}x + \lambda^{-1}x - c$ (a-formulation).

Figure 2.15: Typical shapes of the nonlinear functions involved in (a) the h-ϕ-formulation, and (b) the a-formulation, for a T2S material modelled with the power law ($n = 20$, $\lambda = 1$) and for $b = c = 0$. Note that f and g are not inverse of each other, and that the slope of g diverges for $x \to 0$.

Simple SFM model

The simplest model involving the nonlinear saturation law of SFM consists in the numerical inversion of the saturation law. For an h-ϕ-formulation analogue, we consider the function

$$\bar{g}(x) = \mu_{\mathrm{r}}(x)x - c = 0, \tag{2.92}$$

where $\mu_{\mathrm{r}}(\cdot) = \mu(\cdot)/\mu_0$ is a saturation law, rescaled for easier analysis, and c is a real parameter. Here, for $\mu(\cdot)$, we use Eq. (1.9). This law has the analytical inverse given by Eq. (B.31) in Appendix for $\nu_{\mathrm{r}}(\cdot) = \mu_0\nu(\cdot)$, that is used to build the a-formulation analogue,

$$\bar{f}(x) = \nu_{\mathrm{r}}(x)x - b = 0, \tag{2.93}$$

where b is another real parameter. The shapes of $\bar{g}$ and $\bar{f}$ are depicted in Fig. 2.16. These functions are single degree of freedom versions a magnetostatic problem with the h-ϕ or a-formulation, respectively, i.e., a nonlinear term and a source term:

$$(\mu \boldsymbol{h}\ , \boldsymbol{h}')_{\Omega} - \text{source} = 0, \tag{2.94}$$
$$(\nu\ \textbf{curl}\ \boldsymbol{a}\ , \textbf{curl}\ \boldsymbol{a}')_{\Omega} - \text{source} = 0. \tag{2.95}$$

2.7.3 Iterations on the simple models for the T2S nonlinearity

We now investigate how different iterative techniques behave when applied on the simplified equations, $f(x) = 0$ and $g(x) = 0$, given by Eqn. (2.88) and (2.89), analogous to the h-ϕ and a-formulations with T2S, respectively.

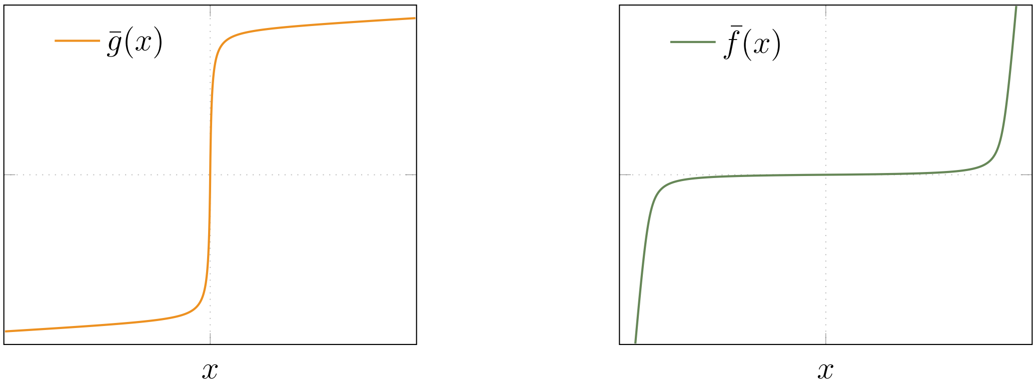

(a) $\bar{g}(x) = \mu_{\mathrm{r}}(x)x - c$ (h-ϕ-formulation).

(b) $\bar{f}(x) = \nu_{\mathrm{r}}(x)x - b$ (a-formulation).

Figure 2.16: Typical shapes of the nonlinear functions involved in (a) the h-ϕ-formulation, and (b) the a-formulation, for a SFM modelled with the saturation law given in Eq. (B.29) in Appendix, with $\mu_{\mathrm{r},0} = 1600$ and $m_0 = 10^6$ A/m, and for $c = b = 0$.

Analogue to the h-ϕ-formulation

The simplified equation chosen to simulate the power law nonlinearity in the h-ϕ-formulation where the resistivity ρ consists in finding the solution to Eq. (2.88):

$$f(x) = |x|^{n-1}x + \lambda x - b = 0, \tag{2.96}$$

for a given value of b, with n and λ two real parameters.

The Picard iteration function reads $x_{i+1} = f_{\text{Pi}}(x_i)$, with

$$f_{\text{Pi}}(x) = \frac{b}{|x|^{n-1} + \lambda}, \tag{2.97}$$

and the Newton-Raphson iteration reads $x_{i+1} = f_{\text{NR}}(x_i)$, with

$$f_{\text{NR}}(x) = x - \frac{|x|^{n-1}x + \lambda x - b}{n|x|^{n-1} + \lambda}. \tag{2.98}$$

These functions are illustrated in Fig. 2.17 for $n = 20$, $\lambda = 1$ and for various values of b. The successive iterations in this figure can be deduced as was shown in Fig. 2.13 on three examples. By inspection, one can see that Newton-Raphson iterations will converge for any initial iterate x_0 in all cases. By contrast, for $b = 1$ and $b = 1.5$, the Picard iteration function $f_{\text{Pi}}(x)$ presents a slope higher than one at the fixed point, so that it is repulsive. Instead, the iterates are attracted by fixed points of period 2, i.e., fixed points of the function $f_{\text{Pi}}(f_{\text{Pi}}(x))$. These points are not solutions of the original equation $f(x) = 0$ and, as they are attractive, they will therefore cause issues for convergence, as illustrated by the resulting cycle in Fig. 2.18(a).

To investigate the behavior of the iterative methods in more detail, we look at the number of iterations required to reach a given accuracy for a range of initial iterates x_0 and values of b. We iterate from x_0 and we stop at an iteration i only when $|f(x_i)| < \varepsilon_{\text{abs}}$, with $\varepsilon_{\text{abs}} = 10^{-8}$, or when i exceeds $i_{\max} = 300$. In the first case, we conclude that the method has converged, and

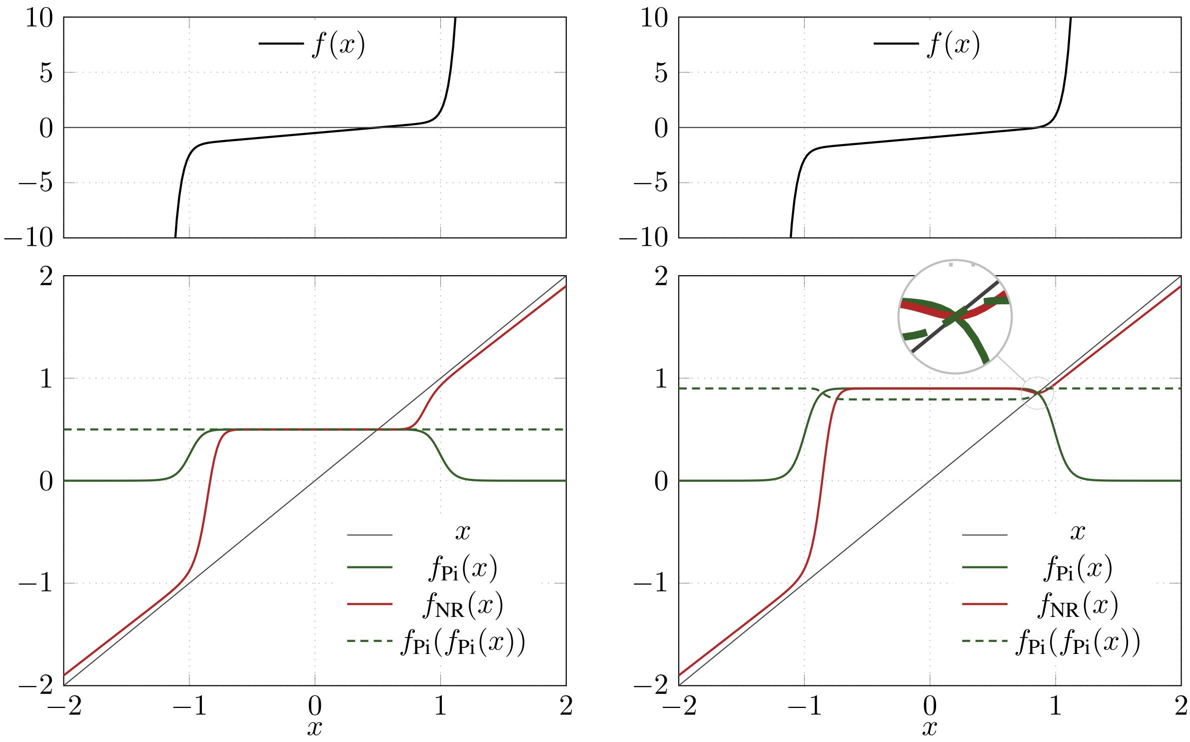

(a) $b = 0.5$. (b) $b = 0.9$.

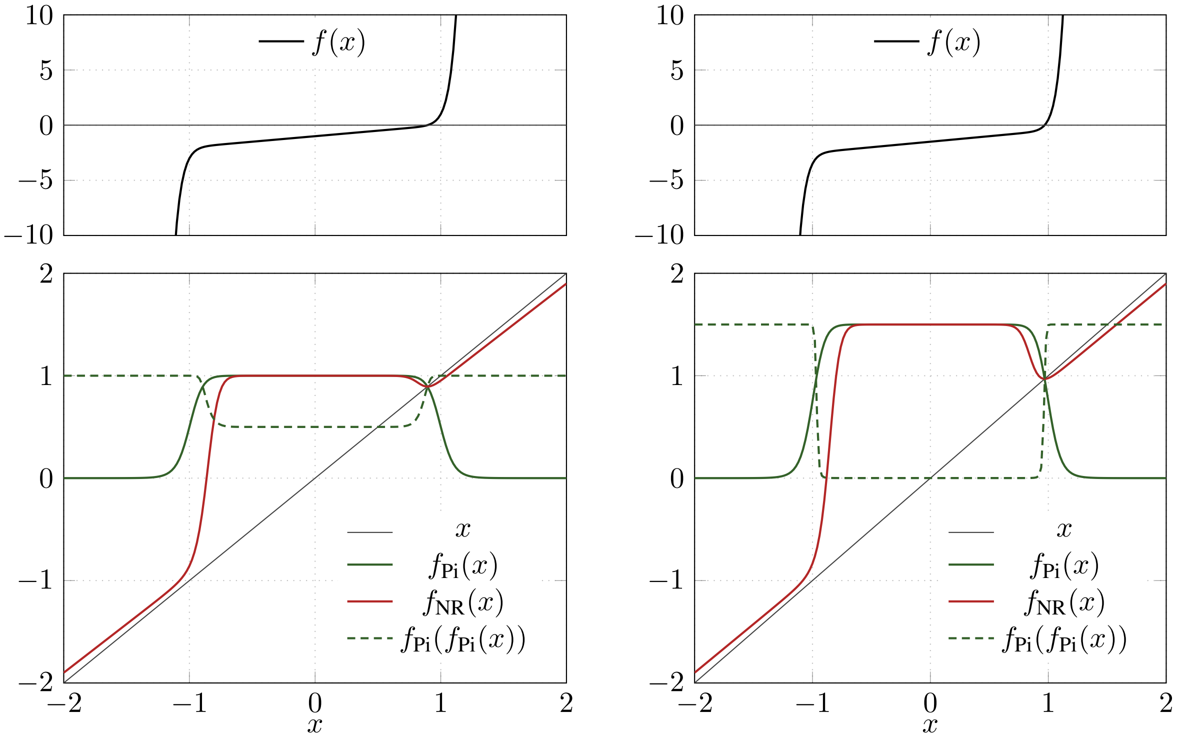

(c) $b = 1$. (d) $b = 1.5$.

Figure 2.17: Picard and Newton-Raphson iterations viewed as fixed point iterations for the single degree of freedom equation analogous to the T2S nonlinearity in h-ϕ-formulation, with $n = 20$ and $\lambda = 1$. In every case, $f_{\mathrm{NR}}(x)$ has a unique attractive fixed point. However, for $b = 1$ and $b = 1.5$, $f_{\mathrm{Pi}}(x)$ has a repulsive fixed point and presents attractive cycles of period 2.

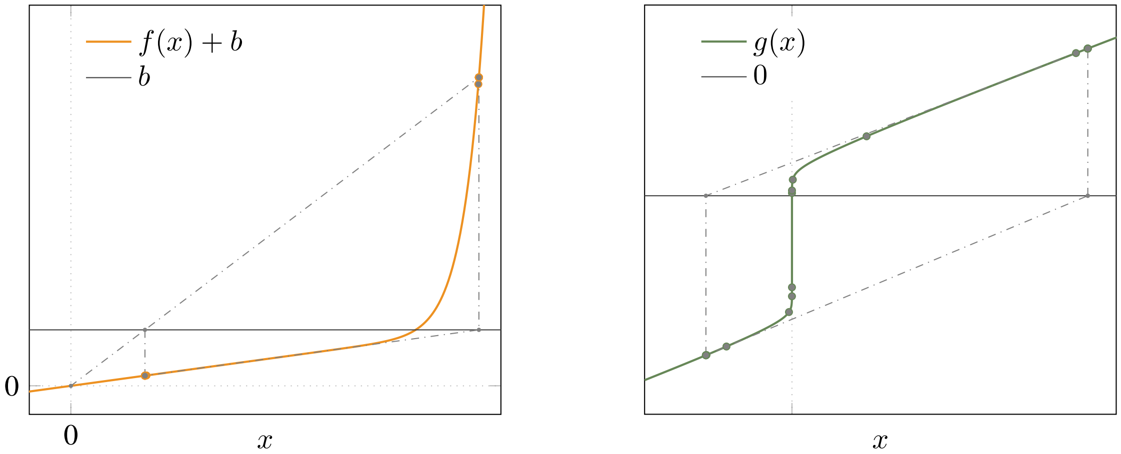

(a) Picard on $f(x)$ (h-ϕ-formulation). (b) Newton-Raphson on $g(x)$ (a-formulation).

Figure 2.18: Illustration of attracting iteration cycles on the single degree of freedom equation analogous to the T2S nonlinearity. (a) $f(x)$ with Picard iterations, $b = 1.1$. (b) $g(x)$ with Newton-Raphson iterations, $c = 0.6$. Highlighted dots represent the successive iterates and dash-dotted lines connect two successive cycling iterations.

we color the point (x_0, b) according to the iteration number i. In the latter case, iterates have either entered cycles or diverged, and the iterative technique has failed. Results are presented in Fig. 2.19.

We observe that the Newton-Raphson iterations converge in the whole x_0-b-domain. When x_0 is sufficiently close to the exact solution (the black curve in the figure), the number of iterations is small ($\lesssim 10$). This fast attraction basin gets however narrower as n increases. For $|b| \lesssim 1$, the number of iterations is small over a wide range of initial iterates, where the function $f(x)$ is well approximated by an affine function[6]. Overall, when x_0 moves further away from the solution, the number of iterations gets higher, and it increases with n as well.

The Picard iterations rarely converge. For $|b| \gtrsim 1$, convergence is only achieved with lucky (but isolated) choices of x_0, as those highlighted by the blue circles in the figure. Everywhere else, iterates enter cycles of period 2, as was illustrated in Figs. 2.17 and 2.18(a), and therefore do not converge. Using the Picard method in this situation is therefore impractical.

The general observations remain identical when λ is changed: the Newton-Raphson method converges in all situations whereas the Picard method fails for a wide range of b values. Moreover, the Newton-Raphson method converges very quickly towards the exact solution provided that the initial estimate is not too far from it.

---

[6] For a purely affine function, the exact solution is obtained after only one Newton-Raphson iteration whatever the initial iterate.

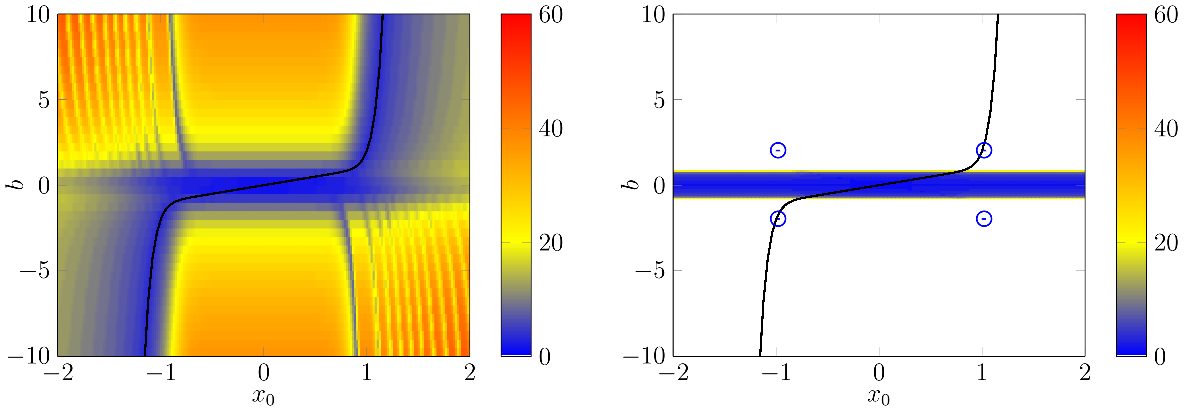

(a) Newton-Raphson, $n = 15$.

(b) Picard, $n = 15$.

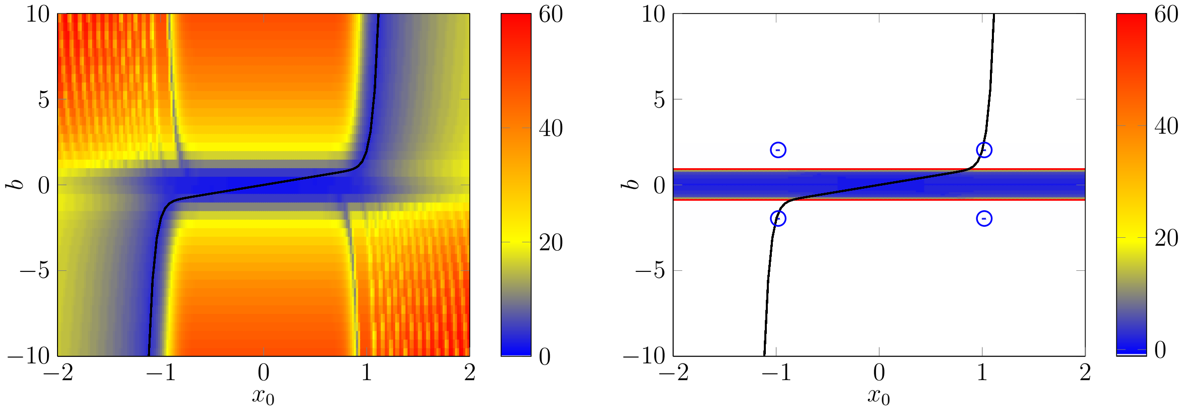

(c) Newton-Raphson, $n = 20$.

(d) Picard, $n = 20$.

Figure 2.19: Iteration number i at which $|f(x_i)| < \varepsilon_{\text{abs}}$ as a function of the initial iterate x_0 and the value of b, with $\lambda = 1$, and for two values of n. The black curves give the exact solution as a function of b. With the Newton-Raphson method, convergence is obtained in the whole domain. White regions associated with the Picard iterations are those where the maximum number of iterations $i_{\text{max}} = 300$ is reached without convergence, i.e., where the method has failed. In this case, all points in white regions enter cycles of period 2.

Analogue to the a-formulation

For the a-formulation, the analogous equation Eq. (2.89) reads

$$g(x) = |x|^{(1-n)/n} x + \lambda^{-1} x - c = 0, \tag{2.99}$$

with λ and c two real parameters. This function has a diverging slope at $x = 0$. Both for the Picard and Newton-Raphson methods, this will lead to issues for iterates that are close to zero. Therefore, we regularize the function as follows (and we keep the name g for simplicity):

$$g(x) = \frac{x}{\varepsilon + |x|^{(n-1)/n}} + \lambda^{-1} x - c, \tag{2.100}$$

with ε a strictly positive parameter, chosen as small as possible. Note that this parameter is also necessary in the finite element models, and represents a non-zero resistivity for $\|\boldsymbol{j}\| \to 0$ in T2S, which may not be desirable. In practice, ε can however be chosen small enough for its influence to be negligible in the solution, this will be discussed in Chapter 4.

The Picard iteration function reads $x_{i+1} = g_{\text{Pi}}(x_i)$, with

$$g_{\text{Pi}}(x) = \frac{c}{(\varepsilon + |x|^{(n-1)/n})^{-1} + \lambda^{-1}}, \tag{2.101}$$

and the Newton-Raphson iteration reads $x_{i+1} = g_{\text{NR}}(x_i)$, with

$$g_{\text{NR}}(x) = x - \frac{g(x)}{g'(x)}, \quad \text{with} \quad g'(x) = \frac{1}{\varepsilon + |x|^{(n-1)/n}} - \frac{n-1}{n} \frac{|x|^{(n-1)/n}}{(\varepsilon + |x|^{(n-1)/n})^2} + \lambda. \tag{2.102}$$

These functions are illustrated in Fig. 2.20 for $n = 20$, $\lambda = 1$ and for various values of c. Note that $g_{\text{Pi}}(0) \approx \varepsilon c$ and $g_{\text{NR}}(0) \approx \varepsilon c$. Consequently, if $\varepsilon > 0$ and $c \neq 0$, $g_{\text{Pi}}(0)$ and $g_{\text{NR}}(0)$ are not equal to zero, so that the point $x = 0$ is never a fixed point of g_{Pi} or g_{NR} for $c \neq 0$. The $g_{\text{Pi}}(x)$ and $g_{\text{NR}}(x)$ curves have a unique fixed point $\bar{x}$ each, for every value of c.

The situation is the opposite to that observed with the h-ϕ-formulation analogue. For the Picard method, the fixed points are always attractive, as $|g'_{\text{Pi}}(\bar{x})| < 1$. By inspection, one can see that the iterations will converge to them for any initial iterate x_0, whatever the value of c. For the Newton-Raphson method, this is not the case. The function g_{NR} always presents an attraction basin close to the solution, but it becomes narrower and narrower as c decreases. For $c = 1$ and $c = 1.5$, this is not an issue, any choice of x_0 will eventually lead to the solution. However, for $c = 0.6$ and $c = 0.9$, fixed points of period 2 appear, i.e., fixed points of the function $g_{\text{NR}}(g_{\text{NR}}(x))$. Two of them are attractive, and iterations end up in cycles as in Fig. 2.18(b).

As with the h-ϕ-formulation analogue, we look at the number of iterations required to reach a satisfying accuracy as a function of the initial estimate x_0 and the value of c. Starting from x_0, we stop at iteration i when $|g(x_i)| < \varepsilon_{\text{abs}}$, or when i exceeds i_{max}. We keep $\varepsilon_{\text{abs}} = 10^{-8}$ and $i_{\text{max}} = 300$. Results are presented in Fig. 2.21 for the two methods and two values of n.

For the Newton-Raphson method, there are large regions in the x_0-c-domain where convergence is not achieved. In these regions, iterations enter cycles similar to those that appear in Figs. 2.20 and 2.18(b). For $|c| \lesssim 1$, only initial iterates x_0 that are extremely close to the exact solution will eventually converge towards it, and the width of the attraction basin decreases when n increases[7]. On the other hand, for $|c| \gtrsim 1$, convergence is obtained after a small number of iterations.

The Picard method demonstrates a completely different behavior. All initial iterates x_0 converge towards the solution whatever the value of c. The number of iterations is however sometimes very high, especially in two bands of c values, and it increases with n.

It is also interesting to notice that the number of iterations for the Picard method barely depends on the initial iterate x_0. Most of the iterations are indeed spent during the last phase of the convergence, close to the solution, where the asymptotic convergence factor $|g'_{\text{Pi}}(\bar{x})|$ can be very close to 1, as shown in Fig. 2.20, so that the linear convergence is very slow.

---

[7] This is not visible in the graph due to the limited number of sampling points ($\approx 100 \times 100$).

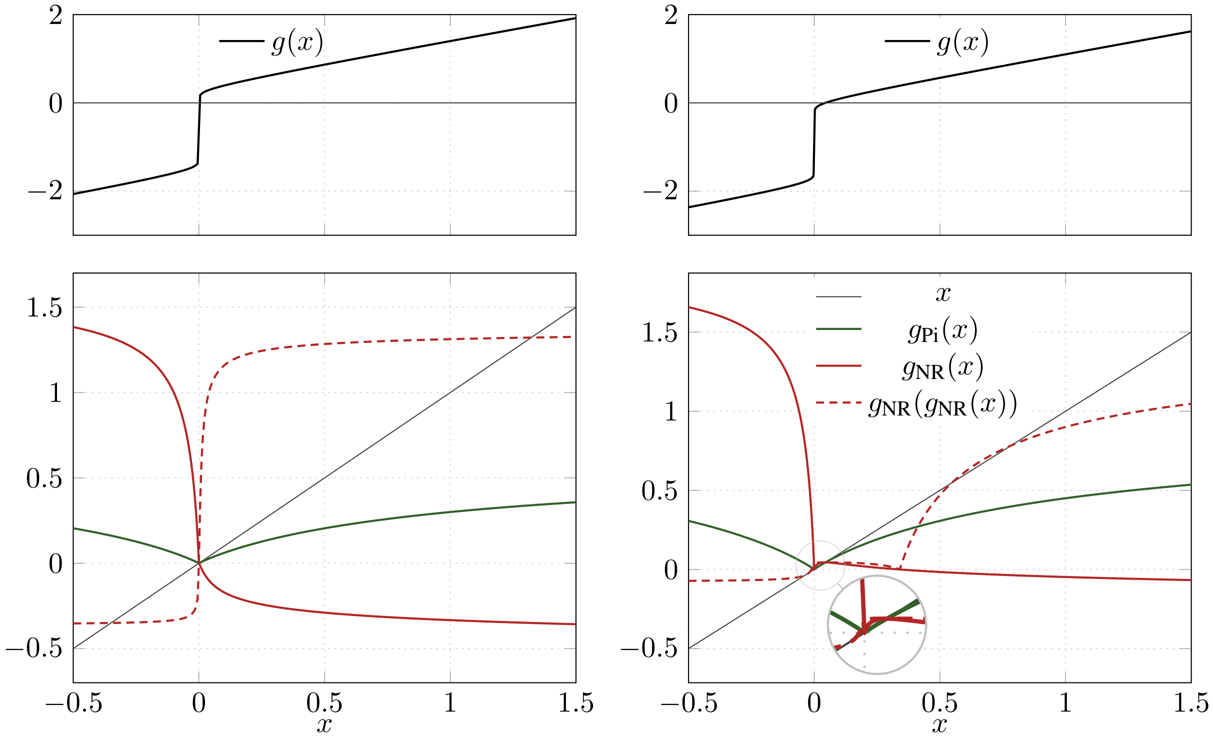

(a) $c = 0.6$. (b) $c = 0.9$.

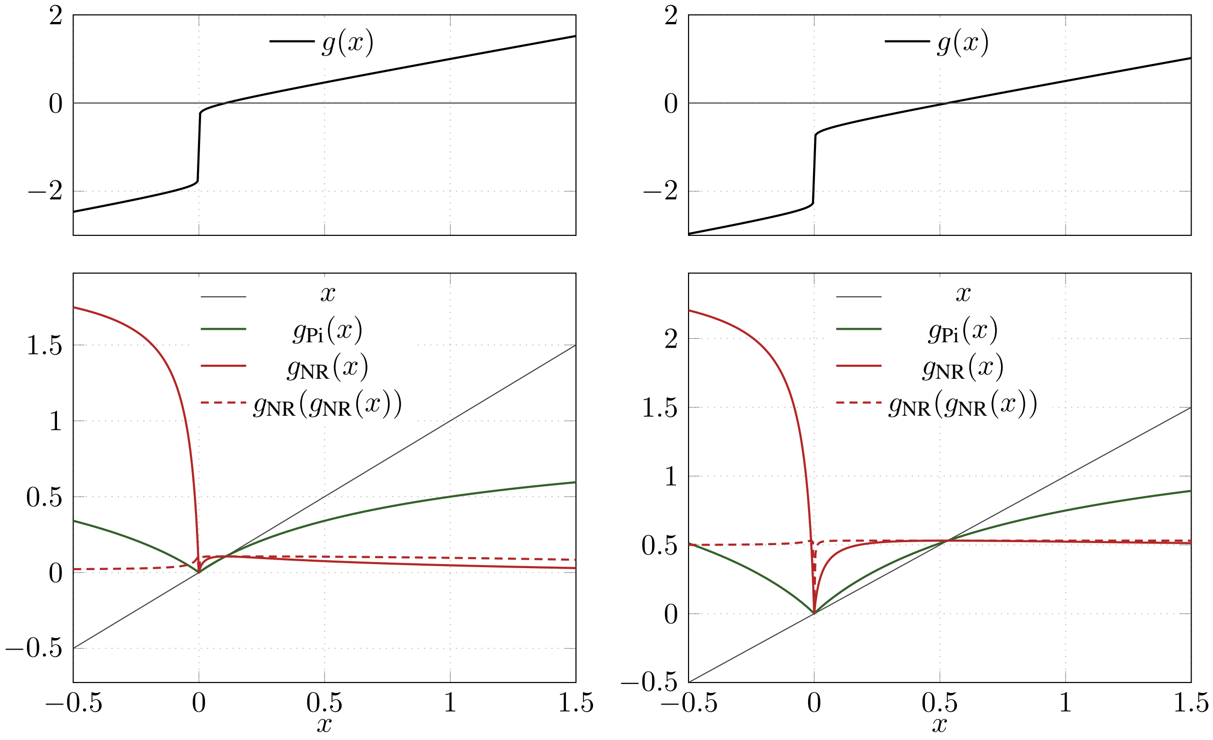

(c) $c = 1$. (d) $c = 1.5$.

Figure 2.20: Picard and Newton-Raphson iterations viewed as fixed point iterations for the single degree of freedom equation analogous to the T2S nonlinearity in a-formulation, with $n = 20$, $\lambda = 1$ and $\varepsilon = 10^{-5}$. In each case, $g_{\mathrm{Pi}}(x)$ has a unique attractive fixed point. However, for $c = 0.6$ and $c = 0.9$, $f_{\mathrm{Pi}}(x)$ presents attractive cycles of period 2 and the correct solution has a very small attraction basin. Note that $g_{\mathrm{Pi}}(0)$ and $g_{\mathrm{NR}}(0)$ are very small ($\approx \varepsilon c$) but not identical to zero (for $\varepsilon > 0$). The legend in (a) is the same as in the other plots.

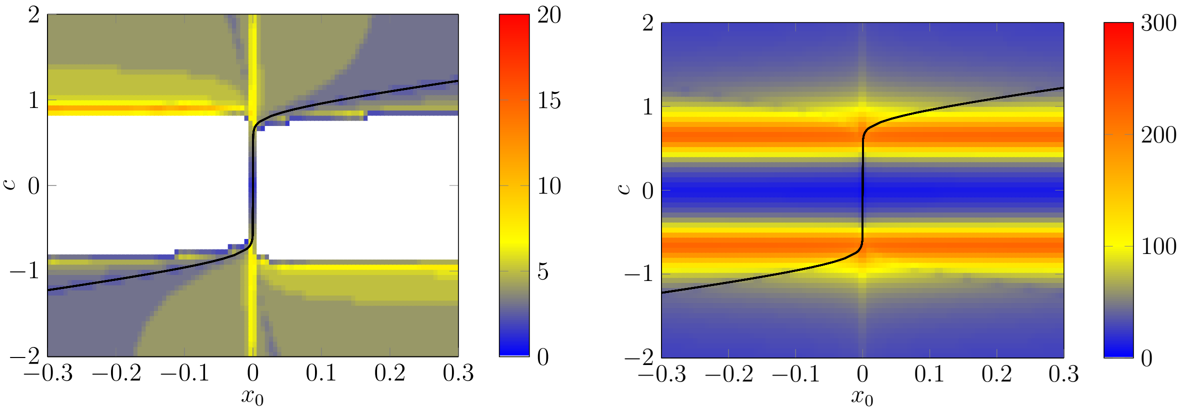

(a) Newton-Raphson, $n = 15$. (b) Picard, $n = 15$.

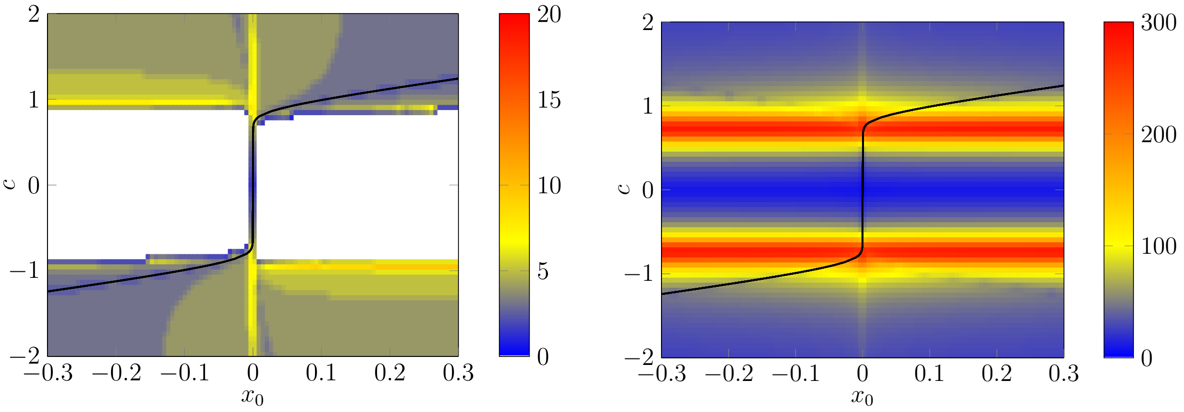

(c) Newton-Raphson, $n = 20$. (d) Picard, $n = 20$.

Figure 2.21: Iteration number i at which $|g(x_i)| < \varepsilon_{\text{abs}}$ as a function of the initial iterate x_0 and the value of c, with $\lambda = 1$ and two values of n. The black curves give the exact solution as a function of c. With the Picard method, convergence is obtained in the whole domain, but at the price of a large number of iterations. White regions associated with the Newton-Raphson iterations are those where the maximum number of iterations $i_{\text{max}} = 300$ is reached without convergence, i.e., where the method has failed. Here, all points in white regions enter cycles of period 2.

As with $f(x)$, the behavior of the iterative techniques on $g(x)$ is not significantly different when λ is increased or decreased: the Newton-Raphson method is impractical because it exhibits an extremely thin convergence domain for a significant range of c values, and the Picard method converges in all cases but demands a large number of iterations. One can infer that, if we only consider these two simple iterative methods, function $g(x)$ is more expensive to solve than function$f(x)$. This observation is maintained in more complicated finite element models involving the power law nonlinearity, as was mentioned earlier in this section.

To improve the performance of the iterative methods on $g(x)$, one can investigate several possibilities. For the Picard method, a common acceleration technique is the Aitken's delta-squared process [156, 157]. It can be seen as an extrapolation of the last three iterates. In our simple case, it consists in looking at the sequence of $x_{A,i}$ defined by

$$x_{A,i} = x_i - \frac{(\Delta x_i)^2}{\Delta^2 x_i}, \quad \text{with} \quad \begin{cases} \Delta x_i = x_{i+1} - x_i, \\ \Delta^2 x_i = x_i - 2x_{i+1} + x_{i+2}, \end{cases} \tag{2.103}$$

where the x_i's are obtained by Picard iterations. Provided that $\Delta^2 x$ does not approach zero, the sequence of the $x_{A,i}$'s can be proven to converge faster than that of the x_i's [157]. As can be seen in Fig. 2.22, this is indeed the case. Compared to the simple Picard method without Aikten's acceleration, the number of iterations is nearly divided by two in the whole x_0-c-domain.

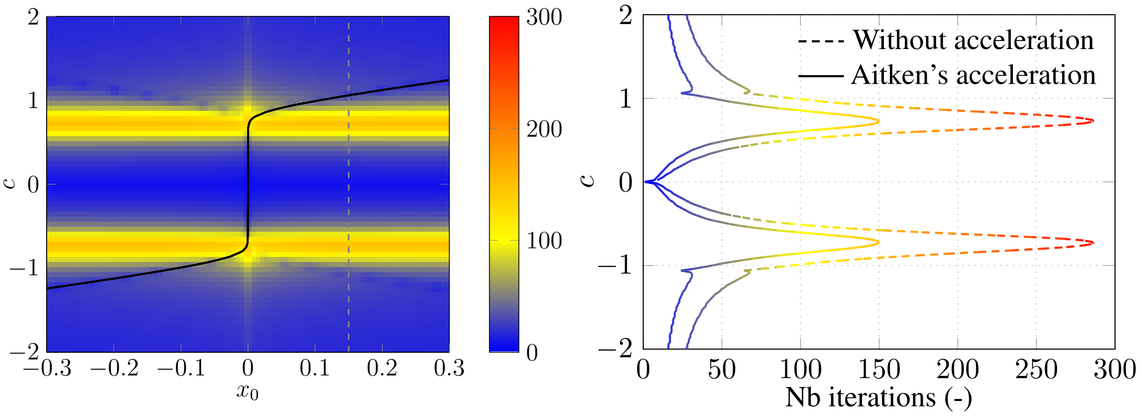

(a) Picard, $n = 20$, Aitken acceleration.

(b) Comparison for $x_0 = 0.15$.

Figure 2.22: (a) Iteration number i at which $|g(Ax_i)| < \varepsilon_{\text{abs}}$ as a function of the initial iterate x_0 and the value of c, with $\lambda = 1$, $n = 20$, and the Picard method with Aitken's acceleration technique. The black curve gives the exact solution as a function of c. The dashed gray line hints what is represented in the subfigure (b) on the right. (b) Number of iterations as a function of c for $x_0 = 0.15$; comparison between the simple Picard method (data from Fig. 2.21(d)) and the accelerated version with Aitken's technique. The number of iterations is nearly divided by two on the whole domain.

Another idea to accelerate the convergence of the Picard method while trying to avoid the iteration cycles of the Newton-Raphson method is to start with a given number i_{switch} of Picard iterations, and then switch to Newton-Raphson iterations. The results are shown in Fig. 2.23(a), with $i_{\text{switch}} = 10$. Because of the very narrow attraction basin of the Newton-Raphson method, 10 iterations are not always enough to approach the solution sufficiently and cycles still appear. We could consider more complicated algorithms to accelerate the convergence, but it is unlikely that they would generalize to real problems (1D, 2D, or 3D).

One idea to circumvent the cycles of period 2 arising in the Newton-Raphson method is to use relaxation factors [90]. This approach consists in multiplying the correction by a multiplier $\gamma > 0$ as follows:

$$g_{\text{NR}}(x) = x - \gamma \, \frac{g(x)}{g'(x)}. \tag{2.104}$$

Cycling iterates oscillate around the solution so we have to consider $\gamma < 1$ to get closer to it, which corresponds to an under-relaxation, which also slows down the convergence. The resulting convergence domain is illustrated in Fig. 2.23(b) for the particular choice $\gamma = 0.5$. The convergence domain is larger than that without relaxation factor of Fig. 2.21(c), but it is still not large enough: for $|c| \lesssim 0.5$ iterates still almost always cycle. Moreover, the number of iterations is increased in regions with $|c| \gtrsim 1$. Taking a smaller value of γ widens further the convergence region but at the same time also increases the number of iterations even more. The situation quickly becomes worse than with the Picard method, in terms of iterations needed.

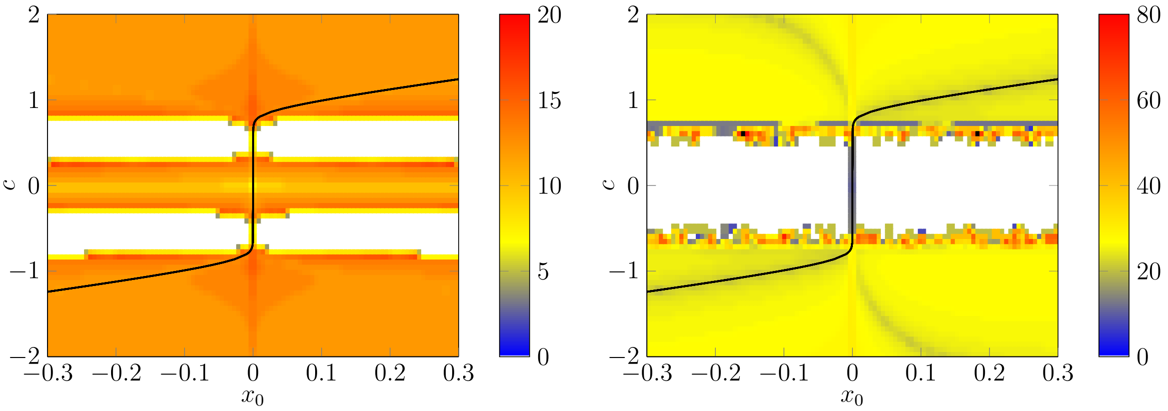

(a) Hybrid: switching at $i_{\text{switch}} = 10$. (b) Relaxation factor $\gamma = 0.5$.

Figure 2.23: Two ideas for improving the convergence of the Newton-Raphson method. Iteration number i at which $|g(x_i)| < \varepsilon_{\text{abs}}$ as a function of the initial iterate x_0 and the value of c, with $\lambda = 1$, $n = 20$. (a) Hybrid method, starting by i_{switch} Picard iterations and then switching to the Newton-Raphson method. (b) Relaxation factor. The convergence domain is increased compared to that of Fig. 2.21(c).

A simple relaxation technique is therefore not a good candidate for improving the Newton-Raphson method in this case. Dynamic adaptations of the relaxation factors are possible [90], but we have not found any robust solution.

The last two ideas are not conclusive for the equation $g(x) = 0$. As we will see now, the hybrid technique will however be interesting for the SFM nonlinearity, whose behavior for small values of x is less pathological.

2.7.4 Iterations on the simple models for the SFM nonlinearity

We conduct a similar analysis for $\bar{g}(x)$, from Eq. (2.92), and $\bar{f}(x)$, from Eq. (2.93). We fixed the parameters $\mu_{\text{r},0} = 1600$ and $m_0 = 10^6$ A/m. As shown in Fig. 2.24, results are comparable to those for $g(x)$ and $f(x)$.

Solving $\bar{f}(x)$ with the Newton-Raphson method is very efficient, see Fig. 2.24(a), whereas Picard iterations on the same function almost never converge, see Fig. 2.24(b). Convergence with Newton-Raphson is achieved for any initial estimate and the number of iterations is small. One can infer that modeling the SFM saturation law in terms of the reluctivity, e.g., with the a-formulation, and the Newton-Raphson method is therefore a suitable choice.

On the contrary, the function $\bar{g}(x)$, e.g., as it appears in the h-ϕ-formulation, is hard to solve with the standard Newton-Raphson method. Fig. 2.24(c) presents wide non-convergence regions for $|c| \lesssim 1$. Nevertheless, the situation is less desperate than with $g(x)$, i.e., the power law as in the a-formulation, as the attraction basin close to the exact solution is not so narrow in this case with the permeability. This is related to the fact that, for realistic materials, $|\bar{g}'(0)| = \mu_{\text{r},0}$ is much smaller than $|g'(0)| = 1/\varepsilon$.

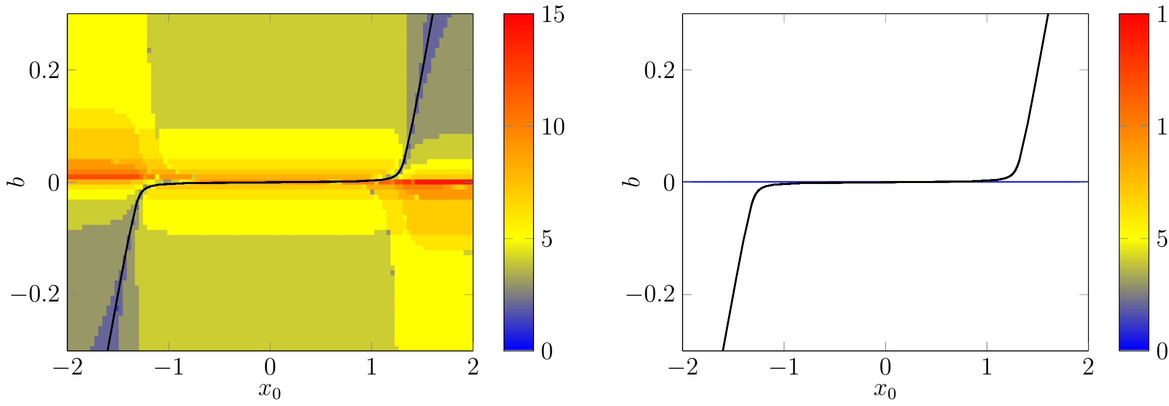

(a) Newton-Raphson on $\bar{f}(x)$, a-formulation. (b) Picard on $\bar{f}(x)$, a-formulation.

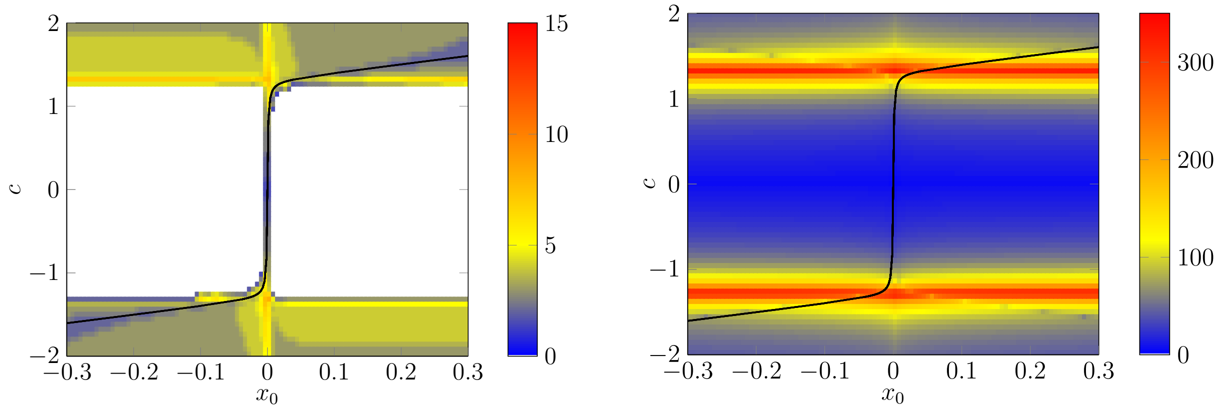

(c) Newton-Raphson on $\bar{g}(x)$, h-ϕ-formulation. (d) Picard on $\bar{g}(x)$, h-ϕ-formulation.

Figure 2.24: Iteration number i at which (a-b) $|\bar{f}(x_i)|$, or (c-d) $|\bar{g}(x_i)|$, become smaller than $\varepsilon_{\text{abs}} = 10^{-8}$ as a function of the initial iterate x_0 and the value of c or b. The black curves give the exact solution as a function of c or b. White regions associated with the Newton-Raphson iterations are those where the maximum number of iterations i_{switch} is reached without convergence, i.e., where the method has failed. Here, all points in white regions enter cycles of period 2. (a) The Newton-Raphson iterations on $\bar{f}(x)$ converge quickly in all cases. (b) The Picard iterations on $\bar{f}(x)$ hardly converge. (c) The Newton-Raphson iterations on $\bar{g}(x)$ fail to converge for a wide range of values of c, and (d) the Picard iterations on $\bar{g}(x)$ converge, but slowly.

As for the Picard iterations applied on $\bar{g}(x)$, Fig. 2.24(d) shows that they converge in the whole x_0-c-domain, but at the cost of a large number of iterations, irrespective of x_0, except when the initial solution is close to the solution.

Solving the saturation law with the permeability, e.g., with the h-ϕ-formulation, is therefore not optimal with the simple Newton-Raphson or Picard iterations. It is however possible to improve the situation by using a hybrid technique. When we start by Picard iterations and then switch to Newton-Raphson iterations for $i > i_{\text{switch}}$, we obtain the results of Fig. 2.25. By contrast with the situation for the power law (Fig. 2.23(a)), the smaller slope $|\bar{g}'(0)|$ provides a wider convergence basin in the whole range of c values.

In practice, choosing the value of i_{switch} in the hybrid technique is a trade-off between efficiency and robustness. Even if we do not guarantee the convergence with the hybrid method, if we can choose x_0 sufficiently close to the solution, i.e., if we have good predictors or small

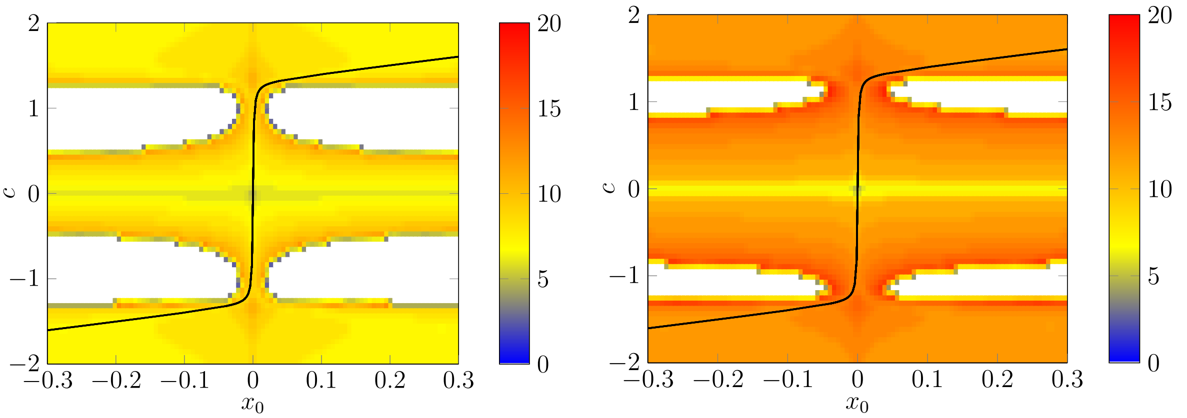

(a) Hybrid, h-ϕ-formulation, $i_{\text{switch}} = 5$.

(b) Hybrid, h-ϕ-formulation, $i_{\text{switch}} = 10$.

Figure 2.25: Iteration number i at which $|\bar{g}(x_i)|$ becomes smaller than $\varepsilon_{\text{abs}} = 10^{-8}$ as a function of the initial iterate x_0 and the constant c. The method is a hybrid iterative scheme, starting by i_{switch} Picard iterations, and then switching to Newton-Raphson iterations. The black curves give the exact solution as a function of c. All points in white regions enter cycles of period 2.

time steps, the hybrid approach is worth considering.

As for relaxation factors, we have observed that they are not easy to use efficiently. They quickly lead to a large number of iterations in regions where the method would have otherwise converged without problems. Dynamic choices of relaxation factors have also been considered, but they require parameters to be fixed by a trial and error procedure, which does not necessarily generalize to several problems or field regimes.

2.8 Summary and motivation for mixed formulations

The main conclusions of the analysis of the previous section generalize to models of higher dimensions. For 1D, 2D, or 3D finite element problems, we observe the same behaviors when dealing with the power law involved in T2S, or the saturation law in SFM. We summarize the main observations here, as this serves as a motivation for the next chapter, but these observations will be further illustrated in Chapter 4.

The power law of T2S is more efficiently and more robustly handled when written in terms of the resistivity, rather than in terms of the conductivity [36, 13, 163], even when it is regularized. If we have the choice among the two standard formulations presented in this chapter, the h-ϕ-formulation should therefore be preferred over the a-formulation for T2S modeling.

The addition of spatial dimensions in finite element models also brings some new difficulties that further complexify the problem resolution. For example, while the Newton-Raphson iterations converged in the whole parameter domain for the simple function $f(x)$, this is no longer the case in higher dimensions with the h-ϕ-formulation: if the time steps are too large for the initial estimates to be sufficiently close to the exact solutions, we observe diverging iterates and non-convergence behaviors. With T2S, magnetic flux fronts typically penetrate gradually inside the material; a sufficient number of time steps is necessary to follow their penetration with the Newton-Raphson method.

By contrast, for the Picard iteration and the a-formulation, non-convergent behaviors are not observed and the number of iterations is still largely independent of the initial estimate in the finite element models. As will be discussed in Chapter 4, this observation can be exploited to perform large time steps and get quick results with a reasonable accuracy.

For the saturation law of SFM, the situation is dual to that for the power law. The a-formulation leads to better performance than the h-ϕ-formulation. For the h-ϕ-formulation, using a hybrid Picard-Newton-Raphson technique remains a valid option, but its efficiency usually relies on preliminary tests by trial and error, and it is still less efficient than using the a-formulation directly.

For models that involve one of the two materials individually, T2S or SFM, we can choose the optimal option, h-ϕ-formulation or a-formulation, respectively. However, questions arise when both materials enter the same finite element models. This is the subject of the next chapter, in which we propose mixed formulations that involve the T2S and SFM nonlinear constitutive laws in their best possible form.

Chapter 3

Mixed finite element formulations

In the previous chapter, we introduced two standard formulations, the h-ϕ-formulation and the a-formulation, as well as the main difficulties arising when modeling the non-linear magnetic response of irreversible type-II superconductors (T2S) or anhysteretic ferromagnetic materials (SFM). In particular, we observed that problems involving the power law in terms of the resistivity were much easier to solve than problems involving the power law in terms of the conductivity. This is the main reason why the h-ϕ-formulation is an interesting choice for T2S modeling.

However, the h-ϕ-formulation is not always the optimal choice. For example, when both T2S and SFM are combined in the same problem, the nonlinear permeability of the SFM may induce convergence difficulties with the h-ϕ-formulation [36, 57]. Moreover, the h-ϕ-formulation may not always be the most convenient choice. Complicated geometries made up of thin T2S tapes are advantageously modeled with dedicated thin-shell formulations [127, 51]. Similarly, rotating parts of T2S motors are more easily handled with a magnetic vector potential [54].

These observations have recently been motivations for considering formulations that couple different fields in different regions of the problem. They are referred to as mixed formulations. Some of them have already been widely studied for magnetostatic and magnetodynamic problems in the past [164, 165, 114]. Recently, they proved to be relevant in systems with T2S [129, 54, 56, 127, 55, 131].

Mixed formulations are interesting alternatives to standard formulations but they also introduce new difficulties. To be well-posed, the function spaces involved in mixed formulations must satisfy well-known stability conditions [166, 167]. If these conditions are not satisfied, numerical instabilities may arise, which can strongly deteriorate the quality of the numerical solution.

In this chapter, we present four formulations that enter the framework of mixed formulations and perturbed saddle-point problems. The first one is the h-ϕ-a-formulation, involving both standard formulations in different regions, coupled via a common surface. It is discussed in Section 3.1. The second one is the t-a-formulation, which is dedicated to T2S tapes, featuring a thin-shell approximation. It is presented in Section 3.2. The last two are variations of the standard formulations with auxiliary fields, coupled via volume integrals, and derived in

Section 3.3.

In Section 3.4, we describe the space discretization of the mixed formulations and we illustrate the stability issues that may arise when choosing function spaces that do not satisfy the stability conditions, mainly for the h-ϕ-a and t-a-formulations. With the motivation to avoid the observed stability issues, we then present the basics of stability analysis in Section 3.5. In particular, we present the so-called inf-sup condition, and its numerical evaluation with an inf-sup test. At last, in Section 3.6, we apply the theory of mixed formulation to the different formulations so as to justify the choices of function spaces.

3.1 Surface-coupled h-ϕ-a-formulation

When a system contains both T2S and SFM, classical formulations such as the h-ϕ-formulation or the a-formulation face convergence issues. As was shown in the previous chapter, the power law in T2S is more efficiently handled with a Newton-Raphson method in the h-ϕ-formulation, which involves the electrical resistivity. Conversely, the a-formulation is more efficient than the h-ϕ-formulation to deal with the typical saturation law describing the permeability of SFM [36]. Combining the h-ϕ and a-formulations into a coupled h-ϕ-a-formulation allows one to choose the best suited formulation in each region and has proved to be an efficient method for modeling systems with both materials [36, 131].

Similar mixed formulations have been considered in a number of other situations. In [54], a 2D model of rotating machines with superconducting windings involves an h-a-formulation[1], with the motivation that the continuity conditions between the fixed and rotating parts of the motor are more easily written in terms of the scalar-like vector potential $\boldsymbol{a}$ of the a-formulation in 2D, whereas the T2S power law is best handled with an h-formulation. This coupled formulation may also be a useful alternative to the “full-h-formulation” [6], that involves a spurious resistivity in air [56], as the number of degrees of freedom is reduced in the non-conducting regions.

We now derive this surface-coupled formulation. The system is modeled in a domain Ω. Boundary conditions are applied on its external boundary $\partial\Omega = \Gamma$, which is decomposed into two complementary domains: Γ_e, where the normal component of $\boldsymbol{b}$ or the tangential component of $\boldsymbol{e}$ is imposed, and Γ_h, where the tangential component of $\boldsymbol{h}$ is imposed. The problem definition is the same as in Chapter 2.

The domain Ω is decomposed into two parts: Ω_h, containing the T2S domain, and Ω_a, containing the nonlinear SFM domain, which is assumed to have a negligible electrical conductivity. Parts of Ω where constitutive laws are linear can be put in either Ω_h or Ω_a. The optimal choice depends on the situation, and will be discussed later. For simplicity, we assume that Ω_a is entirely non-conducting. The generalization to conducting domains in Ω_a is straightforward.

Inside Ω_h, the conducting domain is denoted by $\Omega_{h,\mathrm{c}}$ and the non-conducting domain is denoted by $\Omega_{h,\mathrm{c}}^{\mathrm{C}}$, with $\Omega_h = \Omega_{h,\mathrm{c}} \cup \Omega_{h,\mathrm{c}}^{\mathrm{C}}$. The common boundary of Ω_h and Ω_a is denoted by Γ_{m}.

---

[1] No magnetic scalar potential ϕ is introduced in [54].

Coupling operates via this common interface. We also introduce the outer normal vectors $\boldsymbol{n}_{\Omega_h}$ and $\boldsymbol{n}_{\Omega_a}$. Choices of domain decomposition are illustrated in Fig. 3.1 for 2D and 3D simple geometries.

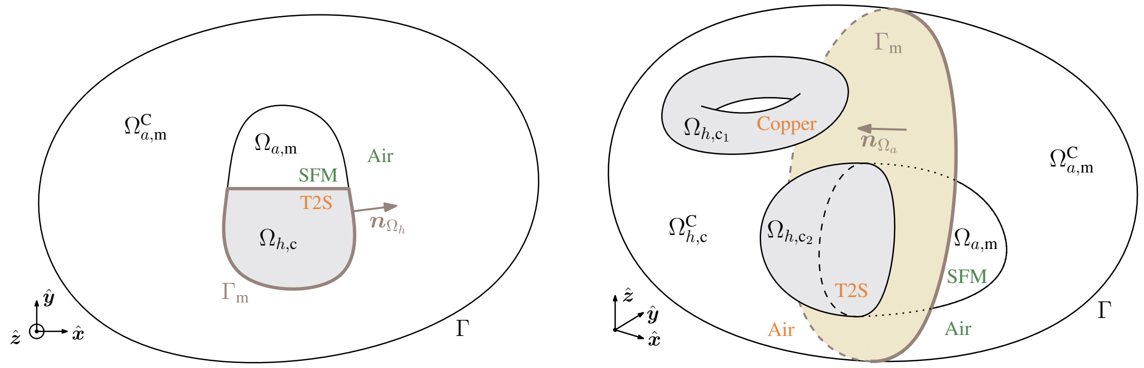

(a) 2D geometry. (b) 3D geometry.

Figure 3.1: Simple geometries illustrating the domain decomposition for the h-ϕ-a-formulation. The gray regions are the conducting domains (linear or nonlinear), that are all chosen to be put in Ω_h. The domain $\Omega_{a,\mathrm{m}}$ is the nonlinear SFM domain, put in Ω_a, and $\Omega^{\mathrm{C}}_{a,\mathrm{m}}$ refers to its complementary in Ω_a. (a) 2D example with a nonlinear SFM domain $\Omega_{a,\mathrm{m}}$ on top of a nonlinear T2S domain $\Omega_{h,\mathrm{c}}$, surrounded by an air domain $\Omega^{\mathrm{C}}_{a,\mathrm{m}}$. With the illustrated choice for domain decomposition, the coupling boundary Γ_{m} is equal to $\partial\Omega_h = \partial\Omega_{\mathrm{c}} = \partial\Omega_{h,\mathrm{c}}$. (b) 3D example with two connected conducting domains Ω_{h,c_1} (copper) and Ω_{h,c_2} (T2S), a nonlinear SFM domain $\Omega_{a,\mathrm{m}}$, surrounded by an air domain $\Omega^{\mathrm{C}}_{h,\mathrm{c}} \cup \Omega^{\mathrm{C}}_{a,\mathrm{m}}$.

We now write the two standard formulations in Ω_a and Ω_h and couple them to obtain the h-ϕ-a-formulation. The classical a-formulation is a weak form of Ampère's law where the magnetic flux density $\boldsymbol{b}$ is expressed via a vector potential $\boldsymbol{a}$ as $\boldsymbol{b} = \operatorname{\mathbf{curl}} \boldsymbol{a}$. Here, it is introduced in Ω_a only. We choose $\boldsymbol{a} \in \mathcal{A}(\Omega_a)$ with

$$\mathcal{A}(\Omega_a) = \big\{\boldsymbol{a} \in H(\mathbf{curl};\Omega_a) \mid (\boldsymbol{a} - \bar{\boldsymbol{a}}) \times \boldsymbol{n}_{\Omega_a} = \mathbf{0} \text{ on } \Gamma_e \cap \partial\Omega_a\big\}, \tag{3.1}$$

with $\bar{\boldsymbol{a}} \times \boldsymbol{n}_{\Omega_a}$ a fixed trace on $\Gamma_e \cap \partial\Omega_a$. Because we placed all conducting materials in Ω_h, Ampère's law reads $\operatorname{\mathbf{curl}} \boldsymbol{h} = \mathbf{0}$ in Ω_a. We multiply this equation by a test function $\boldsymbol{a}'$ in the space $\mathcal{A}_0(\Omega_a)$ with the homogeneous essential boundary condition $\boldsymbol{a} \times \boldsymbol{n}_{\Omega_a} = \mathbf{0}$ on $\Gamma_e \cap \partial\Omega_a$, and integrate the product over the whole domain Ω_a. We obtain

$$(\operatorname{\mathbf{curl}} \boldsymbol{h}\,, \boldsymbol{a}')_{\Omega_a} = 0 \tag{3.2}$$

$$\Leftrightarrow\ (\boldsymbol{h}\,, \operatorname{\mathbf{curl}} \boldsymbol{a}')_{\Omega_a} - \langle \boldsymbol{h} \times \boldsymbol{n}_{\Omega_a}\,, \boldsymbol{a}' \rangle_{(\Gamma_h \cap \partial\Omega_a) \cup \Gamma_{\mathrm{m}}} = 0, \tag{3.3}$$

using the curl-curl Green's identity (A.26). Prescribing the value of $\boldsymbol{h} \times \boldsymbol{n}_{\Omega_a}$ on $\Gamma_h \cap \partial\Omega_a$ constitutes a natural boundary condition for the a-formulation. For conciseness, we consider homogeneous natural boundary conditions on $\Gamma_h \cap \partial\Omega_a$. Therefore, after introducing the vector potential $\boldsymbol{a}$, the formulation amounts to finding $\boldsymbol{a} \in \mathcal{A}(\Omega_a)$ such that $\forall \boldsymbol{a}' \in \mathcal{A}_0(\Omega_a)$,

$$(\nu \operatorname{\mathbf{curl}} \boldsymbol{a}\,, \operatorname{\mathbf{curl}} \boldsymbol{a}')_{\Omega_a} - \langle \boldsymbol{h} \times \boldsymbol{n}_{\Omega_a}\,, \boldsymbol{a}' \rangle_{\Gamma_{\mathrm{m}}} = 0, \tag{3.4}$$

with the reluctivity $\nu = \mu^{-1}$. On Γ_{m}, the tangential magnetic field is still unknown. It will be coupled with the formulation in Ω_h that we derive below.

In the complementary domain Ω_h, we use the h-ϕ-formulation. This is a weak form of Faraday's law. In the h-formulation, the magnetic field $\boldsymbol{h}$ is sought in $\mathcal{H}(\Omega_h)$ defined as

$$\begin{aligned}\mathcal{H}(\Omega_h) = \big\{\boldsymbol{h} \in H(\mathbf{curl};\Omega_h) \mid \mathbf{curl}\,\boldsymbol{h} = \mathbf{0} \text{ in } \Omega_{h,\mathrm{c}}^{\mathrm{C}}, \\ (\boldsymbol{h} - \bar{\boldsymbol{h}}) \times \boldsymbol{n}_{\Omega_h} = \mathbf{0} \text{ on } \Gamma_h \cap \partial\Omega_h,\ \mathcal{I}_i(\boldsymbol{h}) = \bar{I}_i \text{ for } i \in C_I\big\}.\end{aligned} \tag{3.5}$$

Only curl-free functions are considered in the non-conducting domain $\Omega_{h,\mathrm{c}}^{\mathrm{C}}$, so that the current density $\boldsymbol{j} = \mathbf{curl}\,\boldsymbol{h}$ is exactly zero in $\Omega_{h,\mathrm{c}}^{\mathrm{C}}$, by construction. Cohomology basis functions are used in addition to gradients to span the kernel $\mathcal{NS}(\mathbf{curl}, \Omega_{h,\mathrm{c}}^{\mathrm{C}})$ of the curl operator in $\Omega_{h,\mathrm{c}}^{\mathrm{C}}$, when $\Omega_{h,\mathrm{c}}^{\mathrm{C}}$ is not simply connected.

Note that, in this context, $\partial\Omega_{h,\mathrm{c}}$ has to be considered as a part of $\Omega_{h,\mathrm{c}}^{\mathrm{C}}$. Indeed, if $\boldsymbol{h} \in \mathcal{H}(\Omega_h)$, the quantity $\mathbf{curl}\,\boldsymbol{h} \cdot \boldsymbol{n}$ is continuous across any interface; therefore, on the interface $\partial\Omega_{h,\mathrm{c}}$, across which no current flows, we have $\mathbf{curl}\,\boldsymbol{h} \cdot \boldsymbol{n}|_{\partial\Omega_{h,\mathrm{c}}} = \mathbf{0}$, and $\boldsymbol{h}$ is (locally) the gradient of a scalar function. This is illustrated in the discrete setting by the fact that edge functions are not considered on $\partial\Omega_{h,\mathrm{c}}$ because they would otherwise induce a non-zero current density in $\Omega_{h,\mathrm{c}}^{\mathrm{C}}$ (see Section 2.4.1). Consequently, even in the example of Fig. 3.1(a) where $\Gamma_{\mathrm{m}} = \partial\Omega_{h,\mathrm{c}}$, the boundary $\partial\Omega_{h,\mathrm{c}}$ formally constitutes the domain $\Omega_{h,\mathrm{c}}^{\mathrm{C}}$, which is not simply connected. In addition to gradients, a cohomology basis function has to be introduced. This allows us to treat global conditions as was done in the standard h-ϕ-formulation.

The weak form is obtained by projecting Faraday's law on test functions $\boldsymbol{h}' \in \mathcal{H}_0(\Omega_h)$:

$$(\partial_t(\mu\,\boldsymbol{h})\,,\boldsymbol{h}')_{\Omega_h} + (\mathbf{curl}\,\boldsymbol{e}\,,\boldsymbol{h}')_{\Omega_h} = 0 \tag{3.6}$$

$$\Leftrightarrow\ (\partial_t(\mu\,\boldsymbol{h})\,,\boldsymbol{h}')_{\Omega_h} + (\boldsymbol{e}\,,\mathbf{curl}\,\boldsymbol{h}')_{\Omega_h} - \langle \boldsymbol{e} \times \boldsymbol{n}_{\Omega_h}\,,\boldsymbol{h}'\rangle_{(\Gamma_e \cap \partial\Omega_h)\cup\Gamma_{\mathrm{m}}} = 0. \tag{3.7}$$

The space $\mathcal{H}_0(\Omega_h)$ for test functions is the space defined in Eq. (3.5) but with homogeneous essential boundary conditions, $\bar{\boldsymbol{h}} \times \boldsymbol{n}_{\Omega_h} = \mathbf{0}$ on $\Gamma_h \cap \partial\Omega_h$ and $\bar{I}_i = 0$ for $i \in C_I$.

In $\Omega_{h,\mathrm{c}}^{\mathrm{C}}$, we have $\mathbf{curl}\,\boldsymbol{h}' = \mathbf{0}$, and in $\Omega_{h,\mathrm{c}}$, we have $\boldsymbol{e} = \rho\,\mathbf{curl}\,\boldsymbol{h} + \boldsymbol{e}_{\mathrm{a}}$. For conciseness again, we consider homogeneous natural boundary conditions on $\Gamma_e \cap \partial\Omega_h$. Following the same procedure as in Section 2.2 for the treatment of the source electric field $\boldsymbol{e}_{\mathrm{a}}$, the formulation (3.7) then becomes

$$(\partial_t(\mu\,\boldsymbol{h})\,,\boldsymbol{h}')_{\Omega_h} + (\rho\,\mathbf{curl}\,\boldsymbol{h}\,,\mathbf{curl}\,\boldsymbol{h}')_{\Omega_{h,\mathrm{c}}} - \langle \boldsymbol{e} \times \boldsymbol{n}_{\Omega_h}\,,\boldsymbol{h}'\rangle_{\Gamma_{\mathrm{m}}} = \sum_{i\in C_V} \bar{V}_i \mathcal{I}_i(\boldsymbol{h}'), \tag{3.8}$$

with the $\bar{V}_i$'s being the imposed voltages in the natural global conditions for $i \in C_V$.

On the remaining boundary Γ_{m}, the tangential electric field $\boldsymbol{e}$ is still unknown. It has to be coupled with that of the a-formulation in Ω_a. Thus, the final step of the derivation consists in coupling the two separate formulations (3.4) and (3.8) in Ω_a and Ω_h. The tangential trace of the magnetic field on Γ_{m} in (3.4) can be directly expressed in terms of the magnetic field $\boldsymbol{h}$ of (3.8). Similarly, the tangential trace of the electric field on Γ_{m} in (3.8) can be expressed in terms of the vector potential $\boldsymbol{a}$ of (3.4), with $\boldsymbol{e} = -\partial_t \boldsymbol{a}$ (modified magnetic vector potential).

The immediate natural coupling is a consequence of the use of two complementary formulations in Ω_h and Ω_a. No Lagrange multiplier needs to be introduced.

The h-ϕ-a-formulation is obtained by imposing that the final coupled equations hold $\forall \boldsymbol{h}' \in \mathcal{H}_0(\Omega_h)$, $\forall\, \boldsymbol{a}' \in \mathcal{A}_0(\Omega_a)$.

h-ϕ-a-formulation

From an initial solution at time $t = 0$, find $\boldsymbol{h} \in \mathcal{H}(\Omega_h)$ and $\boldsymbol{a} \in \mathcal{A}(\Omega_a)$ such that, for $t > 0$, and $\forall \boldsymbol{h}' \in \mathcal{H}_0(\Omega_h)$, $\forall \boldsymbol{a}' \in \mathcal{A}_0(\Omega_a)$,

$$\big(\partial_t(\mu\, \boldsymbol{h})\, , \boldsymbol{h}'\big)_{\Omega_h} + \big(\rho\, \mathbf{curl}\, \boldsymbol{h}\, , \mathbf{curl}\, \boldsymbol{h}'\big)_{\Omega_{h,\mathrm{c}}} + \langle \partial_t \boldsymbol{a} \times \boldsymbol{n}_{\Omega_h}\, , \boldsymbol{h}' \rangle_{\Gamma_\mathrm{m}} = \sum_{i \in C_V} \bar{V}_i \mathcal{I}_i(\boldsymbol{h}'),$$

$$\langle \boldsymbol{h} \times \boldsymbol{n}_{\Omega_a}\, , \boldsymbol{a}' \rangle_{\Gamma_\mathrm{m}} - (\nu\, \mathbf{curl}\, \boldsymbol{a}\, , \mathbf{curl}\, \boldsymbol{a}')_{\Omega_a} = 0.$$

3.2 Thin-shell t-a-formulation

The second mixed formulation we consider is the so-called t-a-formulation for modeling thin superconducting tapes [127, 168, 50]. In this formulation, the tape is modeled as a line in 2D, or a surface in 3D. The current density inside the tape is described via a current vector potential whereas the external magnetic flux density is expressed as the curl of a magnetic vector potential, naturally allowing discontinuous tangential components of the magnetic field across the tape. This t-a-formulation can be viewed as a geometric limiting case of the h-ϕ-a-formulation for thin geometries [56].

The t-a-formulation has been applied to problems of increasing complexity, such as Roebel cables [42], or CORC® cables [169, 45]. It has also been extended to thick T2S racetrack coils [52], with a homogenization approach. In this chapter, we present its basic formulation.

In [56], this formulation is derived from the h-ϕ-a-formulation with a thin-sheet approximation. Circuit coupling is then performed with winding functions [138]. Here, we present a version of the t-a-formulation following a different approach for circuit coupling. With the same philosophy as in [170], in each tape, either we strongly impose the current intensity, directly in the function space, or we weakly impose the voltage, with a circuit equation contained in the formulation. The formulation derived below is valid for 2D and 3D geometries.

The t-a-formulation applies to situations with thin conducting domains. Let us consider a conducting domain $\Gamma_w \subset \Omega_a$ of constant thickness w, as in Fig. 3.2. We start from the classical a-formulation in the whole domain Ω_a, with homogeneous natural boundary conditions for conciseness: find $\boldsymbol{a} \in \mathcal{A}(\Omega_a)$ such that $\forall \boldsymbol{a}' \in \mathcal{A}_0(\Omega_a)$,

$$(\nu\, \mathbf{curl}\, \boldsymbol{a}\, , \mathbf{curl}\, \boldsymbol{a}')_{\Omega_a} - (\boldsymbol{j}\, , \boldsymbol{a}')_{\Gamma_w} = 0, \tag{3.9}$$

with a given current density $\boldsymbol{j}$ (A/m^2) in Γ_w. Instead of modeling the tape Γ_w as a volume, we collapse it into a surface and replace $\boldsymbol{j}$ by a surface current density $\boldsymbol{k} = w\boldsymbol{j}$ (A/m), perpendicular to the normal vector $\boldsymbol{n}$. This constitutes the main approximation of the formulation: the thickness is not represented in the geometry but introduced inside the equation. Possible variations of $\boldsymbol{j}$ across the thickness are therefore chosen not to be modeled.

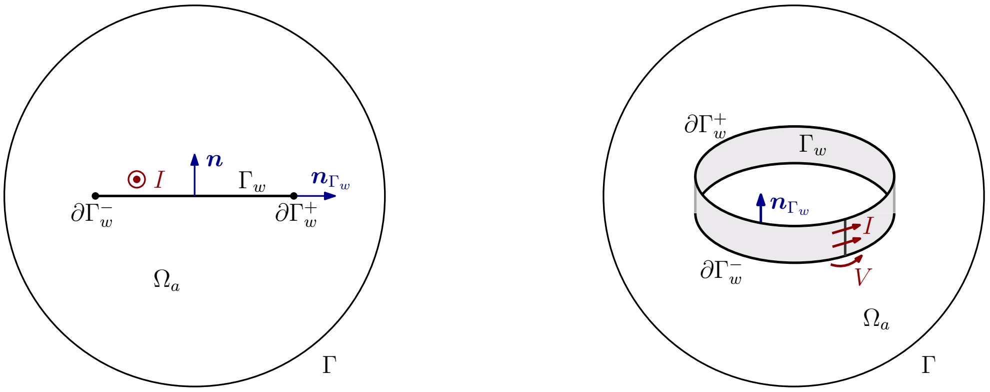

(a) 2D problem.

(b) 3D problem.

Figure 3.2: Conventions for the t-a-formulation derivation. (a) 2D case with a tape with current density perpendicular to the modeled plane. Note the distinction between $\boldsymbol{n}$ and $\boldsymbol{n}_{\Gamma_w}$. (b) 3D case with a tape loop, e.g., a racetrack coil. In 3D, the effect of an external voltage/current source is modeled on an arbitrary cross-section.

Definition (3.1) implies that the tangential component of the vector potential $\boldsymbol{a} \in \mathcal{A}(\Omega_a)$ is continuous across Γ_w, but allows for $\boldsymbol{h} \times \boldsymbol{n} = \nu \,\textbf{curl}\, \boldsymbol{a} \times \boldsymbol{n}$ to be discontinuous. Actually, we can show that the relation $(\boldsymbol{h}_1 - \boldsymbol{h}_2) \times \boldsymbol{n} = \boldsymbol{k}$ is weakly satisfied, with an upward normal, $\boldsymbol{h}_1$ the field on the top of the tape and $\boldsymbol{h}_2$ the field below.

If the current density were known, the problem would be closed. But here, as we want to represent eddy currents, an equation for the distribution of $\boldsymbol{k}$ is required. Since the current density is divergence-free in the magnetodynamic regime, we can express $\boldsymbol{j}$ via a current vector potential $\boldsymbol{t}$, defined up to a gradient, such that

$$\boldsymbol{j} = \textbf{curl}\, \boldsymbol{t}. \tag{3.10}$$

Adding any gradient to $\boldsymbol{t}$ lets the current density unchanged, so $\boldsymbol{t}$ is not unique. To gauge $\boldsymbol{t}$, we choose it along the normal to the tape, i.e., $\boldsymbol{t} = t\boldsymbol{n}$ [127].

The tape boundary $\partial\Gamma_w$ is decomposed into two disjoint parts[2], $\partial\Gamma_w^-$ and $\partial\Gamma_w^+$, as represented in Fig. 3.2. We model a possible power source on an arbitrary cross-section of the tape that imposes either a current intensity I or a voltage V. On lateral boundaries $\partial\Gamma_w^-$ and $\partial\Gamma_w^+$, we have $\boldsymbol{j} \cdot \boldsymbol{n}_{\Gamma_w} = 0$, so t is constant. We strongly fix it to 0 on $\partial\Gamma_w^-$ and let its value, denoted by T, remain free on the other lateral boundary $\partial\Gamma_w^+$. The value of T is related to the total injected current intensity I. Indeed, on any cross-section S of the tape, using Stokes' theorem, we have

$$I = \int_S \boldsymbol{j} \cdot d\boldsymbol{S} = \int_S \textbf{curl}\, \boldsymbol{t} \cdot d\boldsymbol{S} = \oint_{\partial S} \boldsymbol{t} \cdot d\boldsymbol{\ell}_{\partial S} = w(t|_{\partial\Gamma_w^+} - t|_{\partial\Gamma_w^-}) = wT. \tag{3.11}$$

In terms of the current vector potential $\boldsymbol{t}$, Eq. (3.9) reads

$$(\nu \,\textbf{curl}\, \boldsymbol{a} \,, \textbf{curl}\, \boldsymbol{a}')_{\Omega_a} - \langle w \,\textbf{curl}\, \boldsymbol{t} \,, \boldsymbol{a}' \rangle_{\Gamma_w} = 0. \tag{3.12}$$

---

[2] For simplicity, in 3D, we restrict ourselves to closed current loops, and we do not consider technical difficulties such as non-orientable surfaces.

To close the problem, this equation must be complemented by a second one. On the tape surface Γ_w, we weakly impose the equality $\partial_t \boldsymbol{a} = -\boldsymbol{e}$, with the electric field $\boldsymbol{e}$ being expressed in terms of the current vector potential $\boldsymbol{t}$ and the source electric field $\boldsymbol{e}_\text{a}$, using Eq. (2.21), i.e., $\boldsymbol{e} = \rho\, \textbf{curl}\, \boldsymbol{t} + \boldsymbol{e}_\text{a}$. Multiplying the equation by a test function, and integrating over the tape surface Γ_w yields the following weak form: find $\boldsymbol{t} \in \mathcal{T}(\Gamma_w)$, such that $\forall \boldsymbol{t}' \in \mathcal{T}_0(\Gamma_w)$, with $\mathcal{T}$ and $\mathcal{T}_0$ to be defined later,

$$0 = \langle \partial_t \boldsymbol{a} \,, \textbf{curl}\, \boldsymbol{t}' \rangle_{\Gamma_w} + \langle \boldsymbol{e} \,, \textbf{curl}\, \boldsymbol{t}' \rangle_{\Gamma_w} \tag{3.13}$$

$$\Leftrightarrow 0 = \langle \partial_t \boldsymbol{a} \,, \textbf{curl}\, \boldsymbol{t}' \rangle_{\Gamma_w} + \langle \rho\, \textbf{curl}\, \boldsymbol{t} \,, \textbf{curl}\, \boldsymbol{t}' \rangle_{\Gamma_w} + \langle \boldsymbol{e}_\text{a} \,, \textbf{curl}\, \boldsymbol{t}' \rangle_{\Gamma_w} . \tag{3.14}$$

Note that $\partial_t \cdot$ is a shorthand for the time derivative, it is not related to the current vector potential. From the context, there should be no confusion for the time variable t and the current vector potential $\boldsymbol{t}$, or its component t along $\boldsymbol{n}$.

The third term in Eq. (3.14) is linked to global quantities. We can recognize the similarity with the integral (2.36) appearing in the standard formulation derivations. Here, it is a surface integral. Let us consider the integral

$$\langle \boldsymbol{e}_\text{a} \,, \textbf{curl}\, \boldsymbol{t} \rangle_{\Gamma_w} . \tag{3.15}$$

By construction, we have $\textbf{curl}\, \boldsymbol{e}_\text{a} = \boldsymbol{0}$. If Γ_w is made simply connected by introducing one cut Σ, as illustrated in Fig. 3.3, then, there exists a scalar field v_a such that $\boldsymbol{e}_\text{a} = -\textbf{grad}\, v_\text{a}$ in $\Gamma_w \backslash \Sigma$. Across Σ, the scalar field v_a exhibits a discontinuity equal to

$$v_\text{a}|_{\Sigma^+} - v_\text{a}|_{\Sigma^-} = V, \tag{3.16}$$

which satisfies the condition Eq. (2.12) for $\boldsymbol{e}_\text{a}$.

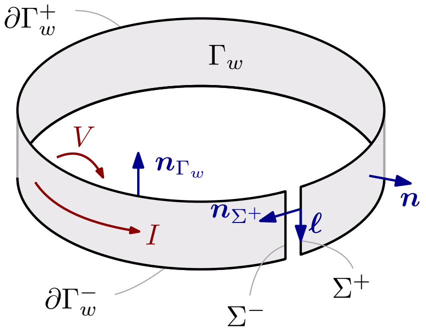

Figure 3.3: Truncated domain $\Gamma_w \backslash \Sigma$ and its boundaries. Note the different notations for $\boldsymbol{n}$, the normal to the tape, perpendicular to the surface of the tape, which is the direction of the vector potential $\boldsymbol{t}$, and for $\boldsymbol{n}_{\Gamma_w}$, the normal to the boundary of the tape, parallel to the tape, which arises when applying Green's identities on the surface Γ_w. The arrow for the voltage V represents the effect of the source field $\boldsymbol{e}_\text{a}$, with the convention of Section 2.1.

Using the grad-div Green's identity (A.25), we have

$$\begin{aligned} \langle \boldsymbol{e}_\text{a} \,, \textbf{curl}\, \boldsymbol{t} \rangle_{\Gamma_w} &= -\langle \textbf{grad}\, v_\text{a} \,, \textbf{curl}\, \boldsymbol{t} \rangle_{\Gamma_w \backslash \Sigma} \\ &= -\left\langle \textbf{curl}\, \boldsymbol{t} \cdot \boldsymbol{n}_{\Gamma_w \backslash \Sigma} \,, v_\text{a} \right\rangle_{\partial(\Gamma_w \backslash \Sigma)} + \langle \text{div}\, (\textbf{curl}\, \boldsymbol{t}) \,, v_\text{a} \rangle_{\Gamma_w \backslash \Sigma} , \end{aligned} \tag{3.17}$$

with $\partial(\Gamma_w \backslash \Sigma) = \partial\Gamma_w \cup \Sigma^- \cup \Sigma^+$ (closed curve). The first term of Eq. (3.17) vanishes on $\partial\Gamma_w$ since $\mathbf{curl}\, \boldsymbol{t} \cdot \boldsymbol{n}_{\Gamma_w} = \boldsymbol{j} \cdot \boldsymbol{n}_{\Gamma_w} = 0$, and only remains nonzero on Σ^- and Σ^+. We also have div $(\mathbf{curl}\, \cdot) = 0$ so that the second term of Eq. (3.17) is equal to zero. Therefore, we have,

$$\langle \boldsymbol{e}_\mathrm{a} \,, \mathbf{curl}\, \boldsymbol{t} \rangle_{\Gamma_w} = - \int_{\Sigma^- \cup \Sigma^+} v_\mathrm{a}\, \mathbf{curl}\, \boldsymbol{t} \cdot \boldsymbol{n}_{\Gamma_w \backslash \Sigma}\, d\ell. \tag{3.18}$$

The normal component of $\mathbf{curl}\, \boldsymbol{t} = \boldsymbol{j}$ is continuous, and $\boldsymbol{n}_{\Sigma^+} = -\boldsymbol{n}_{\Sigma^-}$, so that

$$\begin{aligned} - \int_{\Sigma^- \cup \Sigma^+} v_\mathrm{a}\, \mathbf{curl}\, \boldsymbol{t} \cdot \boldsymbol{n}_{\Sigma^- \cup \Sigma^+}\, d\ell &= - \int_{\Sigma^+} (v_\mathrm{a}|_{\Sigma^+} - v_\mathrm{a}|_{\Sigma^-})\, \mathbf{curl}\, \boldsymbol{t} \cdot \boldsymbol{n}_{\Sigma^+}\, d\ell \\ &= V \int_{\Sigma^+} \mathbf{curl}\, \boldsymbol{t} \cdot \boldsymbol{n}_{\Sigma^+}\, d\ell \\ &= -VI/w. \end{aligned} \tag{3.19}$$

For the last integral, the current vector potential along $\boldsymbol{n}$, i.e., $\boldsymbol{t} = t\boldsymbol{n}$, so that we have,

$$\mathbf{curl}\, \boldsymbol{t} = \mathbf{grad}\, t \times \boldsymbol{n} + t\, \mathbf{curl}\, \boldsymbol{n} = \mathbf{grad}\, t \times \boldsymbol{n}, \tag{3.20}$$

because $\mathbf{curl}\, \boldsymbol{n} = \mathbf{0}$. We can write

$$\begin{aligned} \int_{\Sigma^+} \mathbf{curl}\, \boldsymbol{t} \cdot \boldsymbol{n}_{\Sigma^+}\, d\ell &= \int_{\Sigma^+} (\mathbf{grad}\, t \times \boldsymbol{n}) \cdot \boldsymbol{n}_{\Sigma^+}\, d\ell \\ &= \int_{\Sigma^+} (\boldsymbol{n} \times \boldsymbol{n}_{\Sigma^+}) \cdot \mathbf{grad}\, t\, d\ell \\ &= \int_{\Sigma^+} \mathbf{grad}\, t \cdot d\boldsymbol{\ell} \\ &= t|_{\partial\Gamma_w^-} - t|_{\partial\Gamma_w^+} \\ &= -I/w, \end{aligned} \tag{3.21}$$

using Eq. (3.11).

Gathering the results, we can rewrite the third term of Eq. (3.14) as follows:

$$w\, \langle \boldsymbol{e}_\mathrm{a} \,, \mathbf{curl}\, \boldsymbol{t}' \rangle_{\Gamma_w} = -V\mathcal{I}(\boldsymbol{t}'), \tag{3.22}$$

with $\mathcal{I}(\boldsymbol{t}') = wT' = I'$ being the net current flowing in the tape for the potential $\boldsymbol{t}'$. Combining Eqn. (3.14) and (3.22) yields

$$\langle w\, \partial_t \boldsymbol{a} \,, \mathbf{curl}\, \boldsymbol{t}' \rangle_{\Gamma_w} + \langle w\, \rho\, \mathbf{curl}\, \boldsymbol{t} \,, \mathbf{curl}\, \boldsymbol{t}' \rangle_{\Gamma_w} = V\mathcal{I}(\boldsymbol{t}'). \tag{3.23}$$

We now generalize to N distinct tapes $\Gamma_{w,i}$ with $i \in C = \{1, 2, \dots, N\}$. The union of these tapes is Γ_w. The thickness w_i of one tape $\Gamma_{w,i}$ is constant, but may differ from one tape to another. We denote by w the general thickness on Γ_w, with $w|_{\Gamma_{w,i}} = w_i$. The total current I_i is imposed on a subset C_I of C whereas the voltage V_i is imposed on the complementary set C_V. Assuming homogeneous natural boundary conditions on Γ_h for conciseness, the t-a-formulation reads as follows.

t-a-formulation

From an initial solution, find $\boldsymbol{a} \in \mathcal{A}(\Omega_a)$ and $\boldsymbol{t} \in \mathcal{T}(\Gamma_w)$, such that for all time instants and $\forall \boldsymbol{a}' \in \mathcal{A}_0(\Omega_a)$, $\forall \boldsymbol{t}' \in \mathcal{T}_0(\Gamma_w)$,

$$\begin{aligned}(\nu\, \mathbf{curl}\, \boldsymbol{a}\,, \mathbf{curl}\, \boldsymbol{a}')_{\Omega_a} - \langle w\, \mathbf{curl}\, \boldsymbol{t}\,, \boldsymbol{a}'\rangle_{\Gamma_w} &= 0,\\ \langle w\, \partial_t \boldsymbol{a}\,, \mathbf{curl}\, \boldsymbol{t}'\rangle_{\Gamma_w} + \langle w\, \rho\, \mathbf{curl}\, \boldsymbol{t}\,, \mathbf{curl}\, \boldsymbol{t}'\rangle_{\Gamma_w} &= \sum_{i\in C_V} \bar{V}_i \mathcal{I}_i(\boldsymbol{t}').\end{aligned}$$

The notation $\mathcal{I}_i(\boldsymbol{t}') = w_i T_i' = I_i'$ denotes the net current flowing in tape i for the potential $\boldsymbol{t}'$. The space $\mathcal{T}(\Gamma_w)$ is the set of functions $\boldsymbol{t} = t\boldsymbol{n}$ such that **curl** $\boldsymbol{t}$ is in the dual space of the relevant trace space on Γ_w of functions in $\mathcal{A}(\Omega_a)$, with $\boldsymbol{t} = \mathbf{0}$ on $\partial\Gamma_w^-$, and $\boldsymbol{t} = (I_i/w_i)\boldsymbol{n}$ on $\partial\Gamma_{w,i}^+$ for $i \in C_I$. The space $\mathcal{T}_0(\Gamma_w)$ is the same space but with homogeneous essential conditions, i.e., $\boldsymbol{t} = \mathbf{0}$ on $\partial\Gamma_{w,i}^+$ for $i \in C_I$. The function spaces will be made explicit in the space discretization step.

As with the h-ϕ-a-formulation, if the current I_i is imposed, then $\boldsymbol{t}' = \mathbf{0}$ on $\partial\Gamma_{w,i}^+$, and the global term (3.22) does not enter the problem. It can however be used as a circuit equation to compute the voltage V_i associated with the imposed current I_i, as a post-processing quantity. Conversely, if the voltage V_i is imposed, then I_i is a degree of freedom and the global term enters the system of equations.

In 2D, the vector potential $\boldsymbol{a}$ is chosen to have only one out-of-plane component (Coulomb gauge, such as with perpendicular edge functions in the discrete setting). In that case, $\mathcal{A}(\Omega_a)$ can be identified with the Sobolev space $H^1(\Omega_a)$ (see chapter 2 of Ref. [167]). With $\boldsymbol{z}$ being the direction of the current density, perpendicular to the 2D plane, if $\Gamma_w \cap \Gamma_e = \emptyset$ [171], we can choose $\boldsymbol{t}$ in

$$\begin{aligned}\mathcal{T}(\Gamma_w) = \big\{\boldsymbol{t} = t\boldsymbol{n} \,\big|\, &(\boldsymbol{z}\cdot \mathbf{curl}\, \boldsymbol{t}) \in H^{-1/2}(\Gamma_w),\\ &t = 0 \text{ on } \partial\Gamma_w^-\,, t = I_i/w_i \text{ on } \partial\Gamma_{w,i}^+ \text{ for } i \in C_I\big\}.\end{aligned} \tag{3.24}$$

3.3 Volume-coupled formulations

In Section 3.1, we presented a coupled formulation suited to systems containing both T2S and SFM, described by strongly nonlinear constitutive laws. The objective was to involve these nonlinearities in their most efficient form, i.e., with ρ and ν instead of σ and μ. For the h-ϕ-a-formulation, this was done via a surface coupling of two standard formulations.

We present in this section an alternative coupling and propose two volume-coupled formulations. They are modified versions of the h-ϕ and a-formulations in which an auxiliary field is introduced to invert one of the constitutive laws.

3.3.1 Volume-coupled h-ϕ-b-formulation

The first volume-coupled formulation is based on the h-ϕ-formulation, whose weak form reads: find $\boldsymbol{h} \in \mathcal{H}(\Omega)$, such that, $\forall \boldsymbol{h}' \in \mathcal{H}_0(\Omega)$,

$$\left(\partial_t(\mu\,\boldsymbol{h})\,,\boldsymbol{h}'\right)_\Omega + \left(\rho\,\mathbf{curl}\,\boldsymbol{h}\,,\mathbf{curl}\,\boldsymbol{h}'\right)_{\Omega_\text{c}} - \langle \bar{\boldsymbol{e}} \times \boldsymbol{n}\,,\boldsymbol{h}'\rangle_{\Gamma_e} = \sum_{i\in C_V} \bar{V}_i \mathcal{I}_i(\boldsymbol{h}'). \tag{3.25}$$

We separate Ω in two regions: Ω_m, containing the nonlinear SFM, and Ω_m^C, its complementary domain, containing only materials with a linear magnetic constitutive law. In Ω_m, to avoid using the permeability μ that sometimes leads to convergence issues, we introduce the magnetic flux density $\boldsymbol{b}$ as an auxiliary field in Ω_m, such that [114]

$$\nu\,\boldsymbol{b} = \boldsymbol{h}, \tag{3.26}$$

and we rewrite the first term of Eq. (3.25) as

$$\left(\partial_t(\mu\,\boldsymbol{h})\,,\boldsymbol{h}'\right)_\Omega = \left(\mu_0\,\partial_t\boldsymbol{h}\,,\boldsymbol{h}'\right)_{\Omega_\text{m}^\text{C}} + \left(\partial_t\boldsymbol{b}\,,\boldsymbol{h}'\right)_{\Omega_\text{m}}, \tag{3.27}$$

where we assumed that $\mu = \mu_0$ in Ω_m^C, for simplicity. The field $\boldsymbol{b}$ is chosen in a given function space $\mathcal{B}(\Omega_\text{m})$ that will be made explicit in the space discretization step. Finally, the condition Eq. (3.26) is weakly enforced by imposing that

$$\left(\nu\,\boldsymbol{b}\,,\boldsymbol{b}'\right)_{\Omega_\text{m}} - \left(\boldsymbol{h}\,,\boldsymbol{b}'\right)_{\Omega_\text{m}} = 0, \tag{3.28}$$

for all test functions $\boldsymbol{b}' \in \mathcal{B}_0(\Omega_\text{m})$.

For conciseness, we assume a homogeneous natural boundary condition $\bar{\boldsymbol{e}} \times \boldsymbol{n}|_{\Gamma_e} = \boldsymbol{0}$. The final formulation reads as follows.

h-ϕ-b-formulation

From an initial solution at time $t = 0$, find $\boldsymbol{h} \in \mathcal{H}(\Omega)$ and $\boldsymbol{b} \in \mathcal{B}(\Omega_\text{m})$ such that, for $t > 0$, $\forall \boldsymbol{h}' \in \mathcal{H}_0(\Omega)$ and $\forall \boldsymbol{b}' \in \mathcal{B}_0(\Omega_\text{m})$,

$$\begin{aligned}
\left(\mu_0\,\partial_t\boldsymbol{h}\,,\boldsymbol{h}'\right)_{\Omega_\text{m}^\text{C}} + \left(\rho\,\mathbf{curl}\,\boldsymbol{h}\,,\mathbf{curl}\,\boldsymbol{h}'\right)_{\Omega_\text{c}} + \left(\partial_t\boldsymbol{b}\,,\boldsymbol{h}'\right)_{\Omega_\text{m}} &= \sum_{i\in C_V} \bar{V}_i \mathcal{I}_i(\boldsymbol{h}'),\\
\left(\boldsymbol{h}\,,\boldsymbol{b}'\right)_{\Omega_\text{m}} - \left(\nu\,\boldsymbol{b}\,,\boldsymbol{b}'\right)_{\Omega_\text{m}} &= 0.
\end{aligned}$$

3.3.2 Volume-coupled a-j-formulation

The second volume-coupled formulation is based on the a-formulation, and has been proposed in 2D in [129]. We start with its standard weak form: find $\boldsymbol{a} \in \mathcal{A}(\Omega)$ and $\boldsymbol{e}_\text{a} \in \mathcal{U}(\Omega_\text{c})$ such that, $\forall \boldsymbol{a}' \in \mathcal{A}_0(\Omega)$ and $\forall \boldsymbol{e}_\text{a}' \in \mathcal{U}_0(\Omega_\text{c})$,

$$\left(\nu\,\mathbf{curl}\,\boldsymbol{a}\,,\mathbf{curl}\,\boldsymbol{a}'\right)_\Omega - \left\langle \bar{\boldsymbol{h}} \times \boldsymbol{n}\,,\boldsymbol{a}'\right\rangle_{\Gamma_h} + \left(\sigma\,\partial_t\boldsymbol{a}\,,\boldsymbol{a}'\right)_{\Omega_\text{c}} + \left(\sigma\,\boldsymbol{e}_\text{a}\,,\boldsymbol{a}'\right)_{\Omega_\text{c}} = 0, \tag{3.29}$$

$$\left(\sigma\,\partial_t\boldsymbol{a}\,,\boldsymbol{e}_\text{a}'\right)_{\Omega_\text{c}} + \left(\sigma\,\boldsymbol{e}_\text{a}\,,\boldsymbol{e}_\text{a}'\right)_{\Omega_\text{c}} = \sum_{i\in C_I} \bar{I}_i \mathcal{V}_i(\boldsymbol{e}_\text{a}'). \tag{3.30}$$

We introduce the current density $\boldsymbol{j}$ as an auxiliary field on the conducting region Ω_c, such that

$$\rho\,\boldsymbol{j} = -\partial_t \boldsymbol{a} - \boldsymbol{e}_\mathrm{a}, \tag{3.31}$$

for $\boldsymbol{j}$ chosen in a function space $\mathcal{J}(\Omega_\mathrm{c})$, that will be defined explicitly in the space discretization step. This equation is weakly enforced by ensuring that

$$(\rho\boldsymbol{j}\,,\boldsymbol{j}')_{\Omega_\mathrm{c}} + (\partial_t\boldsymbol{a}\,,\boldsymbol{j}')_{\Omega_\mathrm{c}} + (\boldsymbol{e}_\mathrm{a}\,,\boldsymbol{j}')_{\Omega_\mathrm{c}} = 0 \tag{3.32}$$

holds for all test functions $\boldsymbol{j}' \in \mathcal{J}_0(\Omega_\mathrm{c})$.

For conciseness, we assume a homogeneous natural boundary condition $\bar{\boldsymbol{h}} \times \boldsymbol{n}|_{\Gamma_h} = \boldsymbol{0}$. Introducing the auxiliary field $\boldsymbol{j}$ in Eqn. (3.29)-(3.30), and combining with Eq. (3.32) yields the following formulation.

a-j-formulation

From an initial solution at time $t = 0$, find $\boldsymbol{a} \in \mathcal{A}(\Omega)$, $\boldsymbol{j} \in \mathcal{J}(\Omega_\mathrm{c})$ and $\boldsymbol{e}_\mathrm{a} \in \mathcal{U}(\Omega_\mathrm{c})$ such that, for $t > 0$, $\forall \boldsymbol{a}' \in \mathcal{A}_0(\Omega)$, $\boldsymbol{j}' \in \mathcal{J}_0(\Omega_\mathrm{c})$ and $\forall \boldsymbol{e}'_\mathrm{a} \in \mathcal{U}_0(\Omega_\mathrm{c})$,

$$\begin{aligned}
(\nu\,\mathbf{curl}\,\boldsymbol{a}\,,\mathbf{curl}\,\boldsymbol{a}')_{\Omega} - (\boldsymbol{j}\,,\boldsymbol{a}')_{\Omega_\mathrm{c}} &= 0,\\
-(\boldsymbol{j}\,,\boldsymbol{e}'_\mathrm{a})_{\Omega_\mathrm{c}} &= \sum_{i\in C_I} \bar{I}_i \mathcal{V}_i(\boldsymbol{e}'_\mathrm{a}),\\
(\partial_t\boldsymbol{a}\,,\boldsymbol{j}')_{\Omega_\mathrm{c}} + (\boldsymbol{e}_\mathrm{a}\,,\boldsymbol{j}')_{\Omega_\mathrm{c}} + (\rho\boldsymbol{j}\,,\boldsymbol{j}')_{\Omega_\mathrm{c}} &= 0.
\end{aligned}$$

3.4 Space discretization and numerical oscillations

As for the standard formulations in the previous chapter, for a practical resolution of the weak formulations, the unknown fields are sought in finite-dimensional function spaces, built on a mesh of the original geometry. We consider Whitney shape functions, associated with elementary entities of the mesh.

In mixed formulations in particular, function spaces must be chosen carefully. As will be shown below, choosing only the lowest-order Whitney shape functions may lead to spurious and unphysical oscillations in the numerical solutions for the h-ϕ-a and t-a-fomulations.

In order to stabilize the problems, we investigate function spaces with local enrichment. This solution is inspired by well-known results in mixed formulations in mechanics, such as Stokes' (nearly) incompressible flow problems [166, 172]. Fields in these problems are however coupled inside the domain (volume coupling), whereas here, we couple the fields via boundaries of domains (surface coupling). Surface coupling is common with Mortar methods, coupling spectral and finite element methods [173, 174, 175], or with the extended finite element method "X-FEM" [171].

In this section, we introduce the different function spaces that we consider for obtaining stable results, and we discuss the stability issues that may result from different choices. We will later analyze the validity of the possible choices in Section 3.6 in the light of saddle-point theory, that we will recall in Section 3.5.

As in Chapter 2, we keep the same notations for domains and fields in the continuous and discrete setting, for readability. We keep in mind that domains and fields here are discretized versions of those in the continuous setting.

3.4.1 Surface-coupled h-ϕ-a-formulation

Lowest order function spaces $\mathcal{H}^{\delta,1}(\Omega_h)$ and $\mathcal{A}^{\delta,1}(\Omega_a)$

The simplest choice for $\boldsymbol{h}$ and $\boldsymbol{a}$ in the h-ϕ-a-formulation is to keep the same function spaces as those proposed for the h-ϕ and a-formulations in Chapter 2, restricted in Ω_h and Ω_a, respectively. We refer to these spaces as $\mathcal{H}^{\delta,1}(\Omega_h)$ and $\mathcal{A}^{\delta,1}(\Omega_a)$, with the superscript $\cdot^{\cdot,1}$ refering to the fact that these are the lowest-order spaces.

Similarly to Eq. (5.11), the space $\mathcal{H}^{\delta,1}(\Omega_h)$ is spanned by elements $\boldsymbol{h}$ written as

$$\boldsymbol{h} = \sum_{e\in\mathcal{E}(\Omega_{h,\mathrm{c}}\backslash\partial\Omega_{h,\mathrm{c}})} h_e\, \boldsymbol{w}_e + \sum_{n\in\mathcal{N}(\Omega_{h,\mathrm{c}}^{\mathrm{C}})} \phi_n\, \textbf{grad}\, w_n + \sum_{i\in C} I_i\, \boldsymbol{c}_i, \tag{3.33}$$

with degrees of freedom h_e, ϕ_n and I_i. The basis is made of edge functions or combinations of them. We remind the fact that $\partial\Omega_{h,\mathrm{c}}$ is considered to be a part of $\Omega_{h,\mathrm{c}}^{\mathrm{C}}$. Because we assume that all conducting domains are put in Ω_h, there is no degrees of freedom solely associated with edges on Γ_{m}, as this coupling surface at most intersects $\partial\Omega_{\mathrm{c}}$, and is not inside Ω_{c}. As a consequence, only traces of gradients of node functions, $\textbf{grad}\, w_n$, and traces of cut functions, $\boldsymbol{c}_i$, are considered on Γ_{m}.

The space $\mathcal{A}^{\delta,1}(\Omega_a)$ is also identical to those for the a-formulation but now restricted to Ω_a. Two distinct situations can happen, but we keep the same notation, $\mathcal{A}^{\delta,1}(\Omega_a)$, for both. First, following Eq. (2.60) for 3D problems, or 2D problems with in-plane current density, we have for $\boldsymbol{a} \in \mathcal{A}^{\delta,1}(\Omega_a)$ the decomposition

$$\boldsymbol{a} = \sum_{e\in\mathcal{E}((\partial\Omega_{\mathrm{c}}\cap\Omega_a)\cup\text{co-tree}(\Omega_a))} a_e \boldsymbol{w}_e, \tag{3.34}$$

where the a_e are the degrees of freedom of $\boldsymbol{a}$, associated with all edges on $\partial\Omega_{\mathrm{c}} \cap \Omega_a$, and with edges of a co-tree built in the whole domain Ω_a, which is non-conducting, starting with a complete tree on $(\partial\Omega_{\mathrm{c}} \cup \Gamma_e) \cap \Omega_a$. Second, for 2D problems with in-plane magnetic field, following Eq. (2.61), we have the following decomposition, with "perpendicular edge" functions:

$$\boldsymbol{a} = \sum_{n\in\mathcal{N}(\Omega_a)} a_n \boldsymbol{w}_n. \tag{3.35}$$

The support entities for the lowest order function spaces are illustrated in Fig. 3.4 for a 2D problem with in-plane magnetic field. As with standard formulations, when possible, essential boundary conditions are directly imposed by fixing the corresponding degrees of freedom.

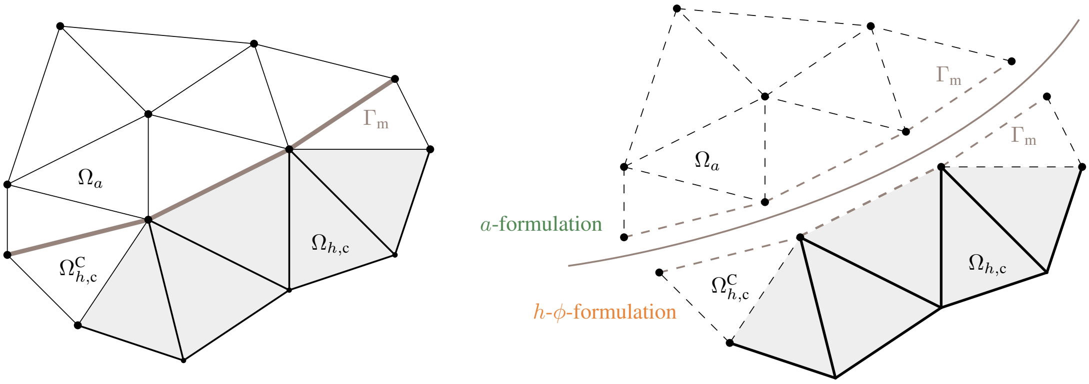

Figure 3.4: Support entities for lowest-order shape functions for $\boldsymbol{h} \in \mathcal{H}^{\delta,1}(\Omega_h)$ and $\boldsymbol{a} \in \mathcal{A}^{\delta,1}(\Omega_a)$ in a 2D geometry with in-plane magnetic field. (Left) Mesh of a part of the domain, with the coupling boundary Γ_m represented by the brown line. The gray region represents the conducting domain. (Right) Domain decomposed into Ω_a and Ω_h. The solid, and not dashed, edges represent supports for edge functions in Ω_h; the nodes represent supports for gradients of node functions in Ω_h, and support for perpendicular edge functions in Ω_a. The support of a possible cut function in Ω_h is not represented.

Enriched spaces with hierarchical shape functions $\mathcal{H}^{\delta,2}(\Omega_h)$ and $\mathcal{A}^{\delta,2}(\Omega_a)$

Enriching the spaces can be done globally on the whole Ω_h or Ω_a domains, or locally in some parts of them only. In our case, global enrichment will not be necessary for stabilization and we therefore choose hierarchical functions to be able to combine functions of different orders consistently in different regions of the problem [176, 137]. The alternative choice is however valid, too.

We introduce hierarchical conform functions, i.e., continuous functions, that we formally associate with edges. Let m and n be the nodes defining an edge $e = \{m, n\}$. We define the associated hierarchical basis function $w_{2,e}$ as $w_{2,e} = w_m w_n$, which is the product of the two node functions w_m and w_n. The new function $w_{2,e}$ vanishes on all nodes and can be referred to as a bubble function. The associated functions and their gradients on the reference triangle in 2D are represented in Fig. 3.5. On simplices, these functions are second-order polynomials.

To obtain stable formulations, we will show that it is sufficient to introduce these functions on the coupling surface Γ_m only. We introduce two enriched spaces: one for $\boldsymbol{h}$ in Ω_h, and one for $\boldsymbol{a}$ in Ω_a.

An enriched space for the magnetic field $\boldsymbol{h}$ in Ω_h is defined by the expansion Eq. (3.33) with an additional term:

$$\boldsymbol{h} = \sum_{e\in\mathcal{E}(\Omega_{h,\mathrm{c}}\setminus\partial\Omega_{h,\mathrm{c}})} h_e\,\boldsymbol{w}_e + \sum_{n\in\mathcal{N}(\Omega^\mathrm{C}_{h,\mathrm{c}})} \phi_n\,\mathbf{grad}\,w_n + \sum_{i\in C} I_i\,\boldsymbol{c}_i + \sum_{e\in\mathcal{E}(\Gamma_\mathrm{m})} \phi_{2,e}\,\mathbf{grad}\,w_{2,e}, \qquad (3.36)$$

with the new degrees of freedom $\phi_{2,e}$, associated with edges on the coupling surface Γ_m only. Note that the new term is curl-free and does not contribute to the current density, and that the circulation of **grad** $w_{2,e}$ along every edge is equal to zero. We denote the resulting function space by $\mathcal{H}^{\delta,2}(\Omega_h)$. Elements in this function space are curl-conform.

For the magnetic vector potential $\boldsymbol{a}$ in Ω_a, in 2D problems with in-plane magnetic field, we

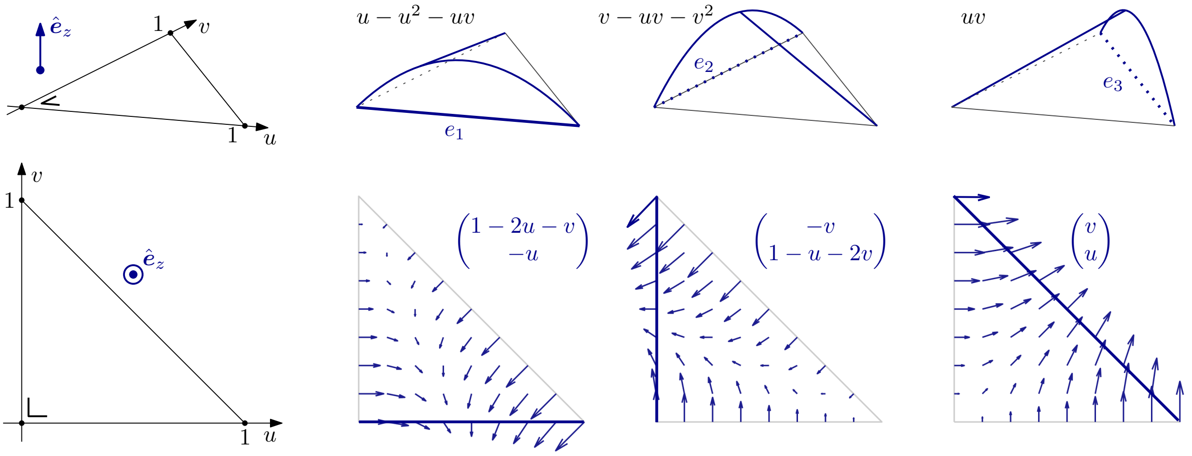

Figure 3.5: (Up) Second-order bubble functions $w_{2,e}$ in the reference triangle in perspective view. These functions are conform: they are continuous between elements. (Down) Gradient of second-order bubble functions in the plane. These gradients are curl-conform: their tangential component is continuous between different elements.

introduce new “perpendicular edge functions” $\boldsymbol{w}_{2,e}$, perpendicular to the plane with the only non-zero component equal to $w_{2,e}$. To the decomposition Eq. (3.35), we add a new term:

$$\boldsymbol{a} = \sum_{n \in \mathcal{N}(\Omega_a)} a_n \boldsymbol{w}_n + \sum_{e \in \mathcal{E}(\Gamma_\mathrm{m})} a_{2,e}\, \boldsymbol{w}_{2,e}, \tag{3.37}$$

with the new degrees of freedom $a_{2,e}$, associated with edges on Γ_m only. The associated function space is denoted by $\mathcal{A}^{\delta,2}(\Omega_a)$. Elements in this function space are curl-conform. The flux of **curl** $\boldsymbol{w}_{2,e}$ across every facet is equal to zero, see Fig. 3.6.

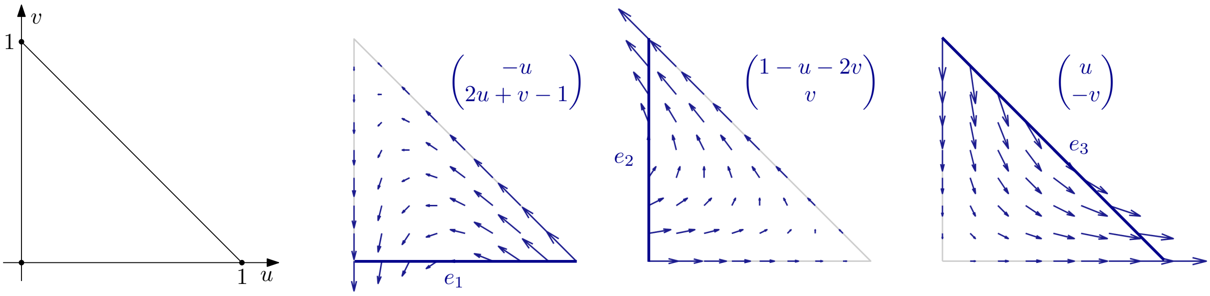

Figure 3.6: Curl of second-order perpendicular bubble edge functions $\boldsymbol{w}_{2,e}$ in the plane. They are div-conform: their normal component is continuous between different elements.

For 3D problems or 2D problems with in-plane current density, we can also add specific hierarchical shape functions on Γ_m for $\boldsymbol{a}$. We do not describe these functions explicitly here, see [177, 178, 179] for more details. We denote by $\mathcal{A}^{\delta,2}(\Omega_a)$ the resulting function space. The additional shape functions contribute to linear variations of **curl** $\boldsymbol{a} = \boldsymbol{b}$ inside the elements adjacent to Γ_m, whereas with $\boldsymbol{a} \in \mathcal{A}^{\delta,1}(\Omega_a)$, $\boldsymbol{b} =$ **curl** $\boldsymbol{a}$ is constant in elements.

Tangential traces of $\boldsymbol{h}$ and $\boldsymbol{a}$ on Γ_{m} in 2D

For simplicity, we consider a 2D problem with an in-plane magnetic field. In the h-ϕ-a-formulation, the only fields that are exchanged between the h-ϕ and a-formulations are the tangential traces of $\boldsymbol{h}$ and $\boldsymbol{a}$ on the coupling boundary Γ_{m}. As will be shown later, the range spaces of these traces are important because they will determine the stability of the coupled formulation.

The tangential trace $\boldsymbol{n} \times (\boldsymbol{h} \times \boldsymbol{n})|_{\Gamma_{\mathrm{m}}}$ of functions $\boldsymbol{h} \in \mathcal{H}^{\delta,1}(\Omega_h)$ on the coupling curve Γ_{m} is piecewise constant along Γ_{m}, and possibly discontinuous between adjacent edges of Γ_{m}. For $\boldsymbol{h} \in \mathcal{H}^{\delta,2}(\Omega_h)$, it is still possibly discontinuous between adjacent edges, but becomes piecewise affine along Γ_{m}.

For a magnetic vector potential $\boldsymbol{a} \in \mathcal{A}^{\delta,1}(\Omega_a)$, the tangential trace $\boldsymbol{n} \times (\boldsymbol{a} \times \boldsymbol{n})|_{\Gamma_{\mathrm{m}}}$ is perpendicular to the plane and its non-zero component is piecewise affine along Γ_{m}, and continuous between adjacent edges. For $\boldsymbol{a} \in \mathcal{A}^{\delta,2}(\Omega_a)$, it is still continuous but becomes piecewise quadratic along Γ_{m}.

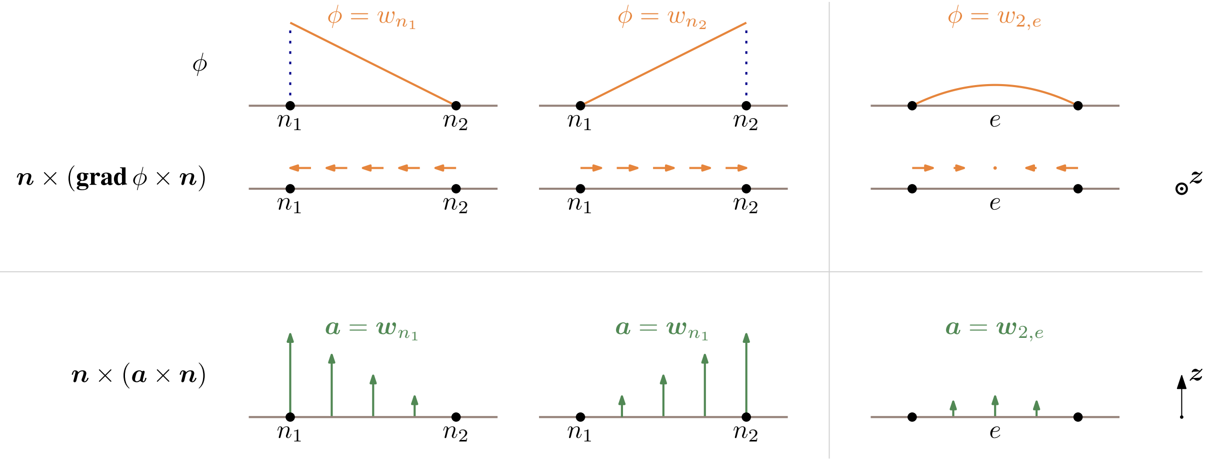

Figure 3.7: Tangential traces of shape functions for $\boldsymbol{h}$ and $\boldsymbol{a}$ on an edge of Γ_{m} for 2D problems with in-plane magnetic field. Traces are independent of the direction of the normal $\boldsymbol{n}$.

Observations

Let us consider a simple 2D geometry made of two stacked bars, surrounded by air, and subjected to an external magnetic field. The bottom bar is a T2S ($n = 20$, $j_{\mathrm{c}} = 3 \times 10^8$ A/m^2) and defines Ω_h, whereas the top bar is a linear ferromagnet ($\mu_{\mathrm{r}} = 1000$, $\sigma = 0$). The air and ferromagnetic domains constitute Ω_a. This geometry is represented in Fig. 3.8.

Using lowest order Whitney elements for both fields, i.e., $\boldsymbol{h} \in \mathcal{H}^{\delta,1}(\Omega_h)$ and $\boldsymbol{a} \in \mathcal{A}^{\delta,1}(\Omega_a)$, results in non-physical oscillations where the coupling interface Γ_{m} separates two regions of different permeabilities. This is illustrated in Figs. 3.9(a) and 3.10(a). By adjusting the numerical values of the permeability, we observe that the oscillation amplitude decreases when the permeability of the ferromagnet is lowered.

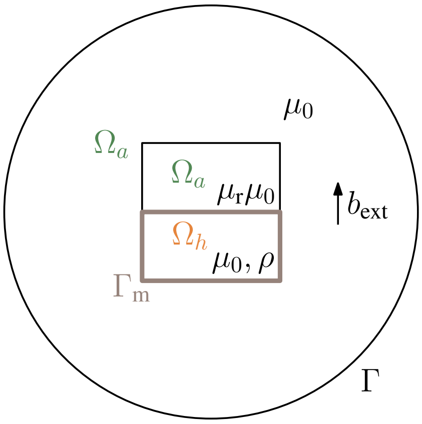

Figure 3.8: Simple 2D geometry for the h-ϕ-a-formulation. Stack of two bars: a T2S bar with $n = 20$, $j_c = 3 \times 10^8$ A/m^2 and $\mu = \mu_0$ (bottom bar) and a ferromagnetic bar $\sigma = 0$ and $\mu_r = 1000$ (top bar), surrounded by air. Bar width: 20 mm. Bar height: 10 mm. The system is subjected to a vertical applied field. The brown curve is Γ_m.

When choosing $\boldsymbol{h} \in \mathcal{H}^{\delta,2}(\Omega_h)$ and $\boldsymbol{a} \in \mathcal{A}^{\delta,1}(\Omega_a)$, as shown in Figs. 3.9(b) and 3.10(b), the oscillations no longer appear, whatever the value of the permeability jump across Γ_m. Likewise, choosing $\boldsymbol{h} \in \mathcal{H}^{\delta,1}(\Omega_h)$ and $\boldsymbol{a} \in \mathcal{A}^{\delta,2}(\Omega_a)$, also stabilizes the problem.

Enriching both spaces by choosing $\boldsymbol{h} \in \mathcal{H}^{\delta,2}(\Omega_h)$ and $\boldsymbol{a} \in \mathcal{A}^{\delta,2}(\Omega_a)$ is no longer a valid option and oscillations appear again in the numerical solution.

It is important to emphasize that oscillations are not a consequence of the nonlinearity of the equations. If the T2S is replaced by a linear conductor, or even by air, stability issues remain. The nonlinearities of the materials are the motivation behind the use of mixed formulations, but are not the cause of the oscillations. Note also that because oscillations are less important for lower permeability jumps across Γ_m, they can easily be missed in case of nonlinear SFM, that saturate quickly at the large fields involved in many superconducting systems.

We will show in Section 3.6 that these observations on the 2D problem can be justified by the theory of perturbed saddle-point problems. In particular, we will show that the choices $\{\mathcal{H}^{\delta,1}(\Omega_h), \mathcal{A}^{\delta,1}(\Omega_a)\}$ and $\{\mathcal{H}^{\delta,2}(\Omega_h), \mathcal{A}^{\delta,2}(\Omega_a)\}$ fail to satisfy an important stability condition, known as the inf-sup condition.

The stability analysis will only be conducted for 2D problems, with in-plane magnetic field, but observations in 3D are found to be exactly similar: one has to enrich exactly one of the two fields $\boldsymbol{h}$ or $\boldsymbol{a}$ to get rid of spurious oscillations in the numerical solution.

3.4.2 Thin-shell t-a-formulation

Function spaces for $\boldsymbol{a}$

The magnetic vector potential $\boldsymbol{a}$ in the t-a-formulation can be discretized exactly as in the a-formulation, that is, with perpendicular edge functions in 2D, or with edge functions and a

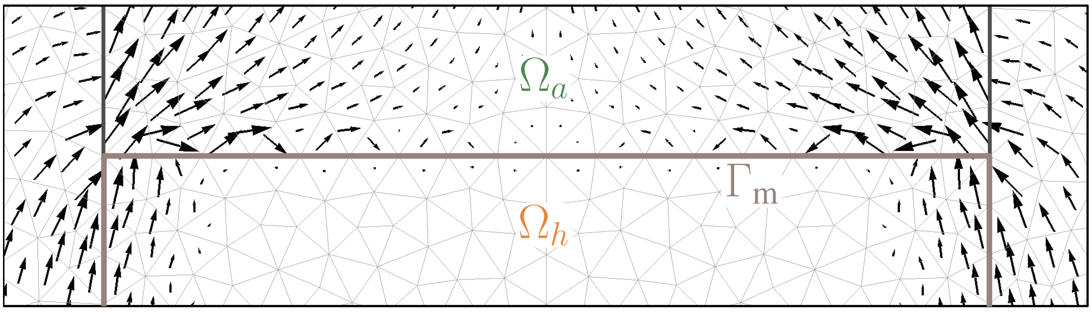

(a) $\boldsymbol{h} \in \mathcal{H}^{\delta,1}(\Omega_h)$ and $\boldsymbol{a} \in \mathcal{A}^{\delta,1}(\Omega_a)$.

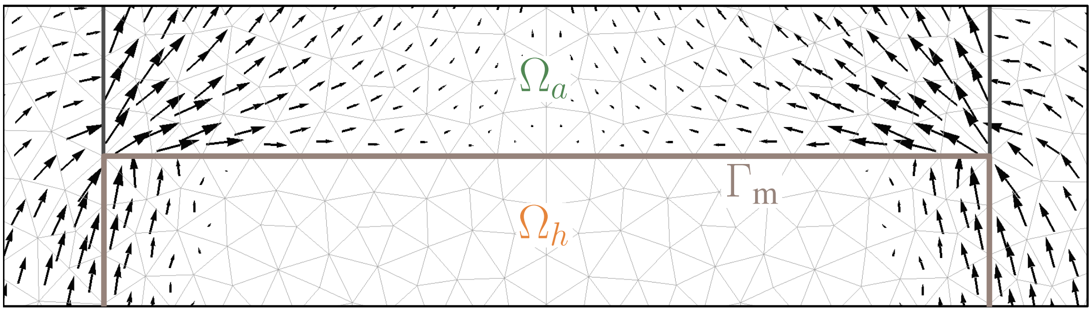

(b) $\boldsymbol{h} \in \mathcal{H}^{\delta,2}(\Omega_h)$ and $\boldsymbol{a} \in \mathcal{A}^{\delta,1}(\Omega_a)$.

Figure 3.9: Details of two solutions for the stacked bar problem, magnetic flux density near the material interface (arrows represent the average value in each element). (a) Unstable choice of function spaces, resulting in non-physical oscillations on Γ_m. (b) Example of a stabilized problem with hierarchical basis functions for $\boldsymbol{h}$, on Γ_m only.

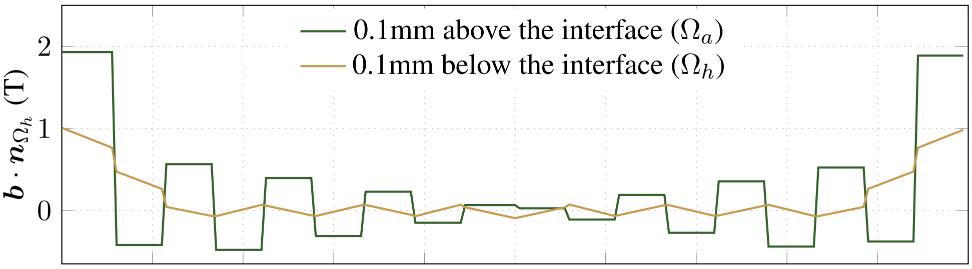

(a) $\boldsymbol{h} \in \mathcal{H}^{\delta,1}(\Omega_h)$ and $\boldsymbol{a} \in \mathcal{A}^{\delta,1}(\Omega_a)$.

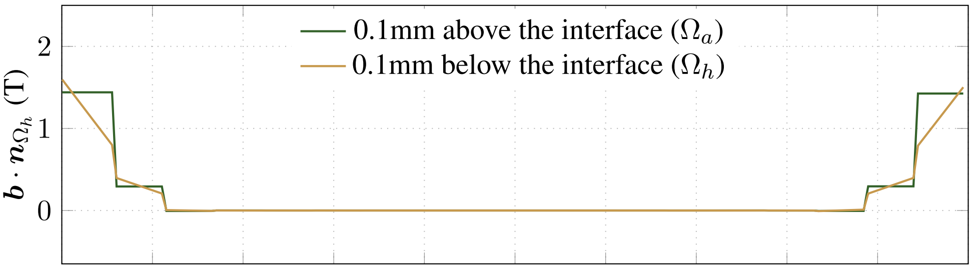

(b) $\boldsymbol{h} \in \mathcal{H}^{\delta,2}(\Omega_h)$ and $\boldsymbol{a} \in \mathcal{A}^{\delta,1}(\Omega_a)$.

Figure 3.10: Normal magnetic flux density distribution (horizontal position in abscissa) just above and just below the material interface for the stacked bar problem, in correspondence with Fig. 3.9. (a) Unstable choice of function spaces, such that strong spurious oscillations take place. (b) Stabilized solution, with higher order hierarchical basis functions for $\boldsymbol{h}$, on Γ_m only.

co-tree gauge in 3D. Note that 2D problems with an in-plane current density do not make sense for the t-a-formulation and are therefore not considered.

At the tape surface, the tangential component of the magnetic field $\boldsymbol{h} = \nu \boldsymbol{b}$ has to be discontinuous to account for a surface current density in the tape. Discretizing the field $\boldsymbol{a}$ as a 1-form implies that the magnetic flux density $\boldsymbol{b} = \textbf{curl}\, \boldsymbol{a}$ is a 2-form, so that it is b-conform. The lack of h-conformity naturally allows for the tangential component of $\boldsymbol{h} = \nu \boldsymbol{b}$ to be discontinuous at the boundary between two adjacent elements and no particular treatment is necessary compared to the usual function space for $\boldsymbol{a}$, as introduced in Section 2.4.2. For example, this is not the case for thin-shell formulations based on the h-ϕ-formulation, such as in [119], where degrees of freedom on the tape surface need to be duplicated to allow for a discontinuous magnetic field.

In 2D, with lowest-order Whitney elements, the vector potential $\boldsymbol{a}$ is discretized as

$$\boldsymbol{a} = \sum_{n \in \mathcal{N}(\Omega_a)} a_n \boldsymbol{w}_n. \tag{3.38}$$

We denote the resulting space by $\mathcal{A}^{\delta,1}(\Omega_a)$, as before. As will be shown, choosing lowest-order shape functions for $\boldsymbol{a}$ and $\boldsymbol{t}$ results in spurious oscillations in the numerical solution. We will show that one possibility to circumvent this issue is to enrich the function space of $\boldsymbol{a}$ with hierarchical shape functions, associated with edges of the tapes Γ_w only. This yields

$$\boldsymbol{a} = \sum_{n \in \mathcal{N}(\Omega_a)} a_n \boldsymbol{w}_n + \sum_{e \in \mathcal{E}(\Gamma_w)} a_{2,e}\, \boldsymbol{w}_{2,e}, \tag{3.39}$$

which defines the space $\mathcal{A}^{\delta,2}(\Omega_a)$.

In 3D, we also choose the same spaces as for the h-ϕ-a-formulation. The lowest-order shape functions are accompanied by a co-tree gauge in the whole domain minus the tapes, where all edges are kept. The space $\mathcal{A}^{\delta,1}(\Omega_a)$ is described by

$$\boldsymbol{a} = \sum_{e \in \mathcal{E}(\Gamma_w \cup \text{co-tree}(\Omega_a))} a_e \boldsymbol{w}_e. \tag{3.40}$$

As in 2D, this space can be enriched to get rid of nonphysical oscillations. We use the same functions as for the h-ϕ-a-formulation to define the resulting space $\mathcal{A}^{\delta,2}(\Omega_a)$.

Function spaces for $\boldsymbol{t}$

The current vector potential $\boldsymbol{t}$ satisfies $\textbf{curl}\, \boldsymbol{t} = \boldsymbol{j} = \textbf{curl}\, \boldsymbol{h}$, so that it differs from the magnetic field $\boldsymbol{h}$ up to a gradient. In formulations without the thin-shell approximation, it can be discretized as a 1-form and chosen to belong to a gauged subspace of $H(\textbf{curl}; \Omega_\text{c})$. With the thin-shell approximation, it is no longer defined in the conducting volume Ω_c, but rather on the surface tapes Γ_w. It is gauged by being defined along the normal $\boldsymbol{n}$ of the tapes.

For $\boldsymbol{t}$ along $\boldsymbol{n}$, we write $\boldsymbol{t} = t\boldsymbol{n}$, and we describe the scalar field t with node functions. Starting with lowest-order node functions, we have the general decomposition

$$t = \sum_{n \in \mathcal{N}(\Gamma_w)} t_n w_n, \tag{3.41}$$

where the w_n's are the node functions on the tape, defined on Γ_w only, i.e., on a 1D curve in a 2D problem, or on a 2D surface in a 3D problem. Correspondingly, for the vector $\boldsymbol{t}$, we introduce the "perpendicular function" $\boldsymbol{w}_n = w_n \boldsymbol{n}$.

The decomposition Eq. (3.41) is too general. As said in Section 3.2, the scalar t must be constant on the lateral boundaries $\partial\Gamma_w^+$ and $\partial\Gamma_w^-$ to enforce $\boldsymbol{j} \cdot \boldsymbol{n}_{\Gamma_w} = 0$ (notice the distinction between $\boldsymbol{n}$ and $\boldsymbol{n}_{\Gamma_w}$[3]). Moreover, the difference $t|_{\partial\Gamma_{w,i}^+} - t|_{\partial\Gamma_{w,i}^-}$ was shown in Eq. (3.11) to be related to the total current I_i flowing in tape $\Gamma_{w,i}$:

$$T_i = t|_{\partial\Gamma_{w,i}^+} - t|_{\partial\Gamma_{w,i}^-} = I_i/w_i. \tag{3.42}$$

Without loss of generality, we can therefore choose $t|_{\partial\Gamma_{w,i}^-} = 0$, and introduce a global shape function ℓ_i defined as the sum of all node functions of nodes on $\partial\Gamma_{w,i}^+$:

$$\ell_i = \sum_{n \in \mathcal{N}(\partial\Gamma_{w,i}^+)} w_n. \tag{3.43}$$

Again, ℓ_i is restricted to the tape region and is not defined outside of it. Its support is limited to a layer of one element adjacent to $\partial\Gamma_{w,i}^+$. We denote by $\boldsymbol{\ell}_i = \ell_i \boldsymbol{n}$ the corresponding global shape function for the vector $\boldsymbol{t}$. Note that in 2D, the sum in Eq. (3.43) contains only one term.

The resulting function space reads

$$\boldsymbol{t} = \sum_{n \in \mathcal{N}(\Gamma_w \setminus (\partial\Gamma_w^- \cup \partial\Gamma_w^+))} t_n \, \boldsymbol{w}_n + \sum_{i \in C} T_i \, \boldsymbol{\ell}_i, \tag{3.44}$$

where the t_n's and T_i's are the degrees of freedom. For $i \in C_I$, we apply the essential global condition $T_i = \bar{I}_i/w_i$. We denote by $\mathcal{T}^{\delta,1}(\Gamma_w)$ the space generated by these functions. It is illustrated in Fig. 3.11.

We will also consider an enriched function space for $\boldsymbol{t}$ as a possibility to stabilize the mixed formulation. To edges e of Γ_w minus the boundaries $\partial\Gamma_w^+$ and $\partial\Gamma_w^-$, we associate hierarchical node functions $w_{2,e}$, and "perpendicular functions" $\boldsymbol{w}_{2,e} = w_{2,e}\boldsymbol{n}$ identical to those of Fig. 3.6. This defines the space $\mathcal{T}^{\delta,2}(\Gamma_w)$, with the current vector potential $\boldsymbol{t}$ decomposed as

$$\boldsymbol{t} = \sum_{n \in \mathcal{N}(\Gamma_w \setminus (\partial\Gamma_w^- \cup \partial\Gamma_w^+))} t_n \, \boldsymbol{w}_n + \sum_{i \in C} T_i \, \boldsymbol{\ell}_i + \sum_{e \in \mathcal{E}(\Gamma_w \setminus (\partial\Gamma_w^- \cup \partial\Gamma_w^+))} t_{2,e} \boldsymbol{w}_{2,e}. \tag{3.45}$$

Observations

A representative example is obtained with the simple geometry of Fig. 3.13(a), illustrating a single straight T2S tape (thickness: 1 μm, width: 10 mm, $n = 20$, $j_\mathrm{c} = 2.5 \times 10^8$ A/m^2), modelled in 2D, with an imposed current intensity. For the lowest-order function spaces $\mathcal{A}^{\delta,1}(\Omega_a)$ and $\mathcal{T}^{\delta,1}(\Gamma_w)$, results are shown in Figs. 3.13(b) and 3.12. The magnetic flux density distribution

---

[3] The normal $\boldsymbol{n}$ is the normal to the tape and is defined on the whole Γ_w, whereas the normal $\boldsymbol{n}_{\Gamma_w}$ is in the local plane tangent to Γ_w and normal to the boundaries $\partial\Gamma_w^+$ and $\partial\Gamma_w^-$, and is defined only on those boundaries. See Fig. 3.2(b).

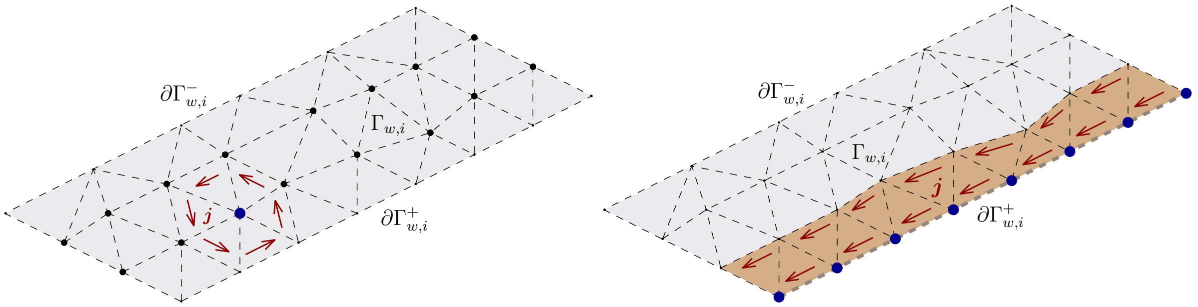

(a) Support of $\boldsymbol{w}_n$ and associated current density. (b) Support of $\boldsymbol{\ell}_i$ and associated current density.

Figure 3.11: Support of the shape functions for $\boldsymbol{t} \in \mathcal{T}^{\delta,1}(\Gamma_w)$ in the t-a-formulation in a 3D problem and their associated current density $\boldsymbol{j} = \textbf{curl}\, \boldsymbol{t}$ (in red). For clarity, the domain and mesh outside the tape $\Gamma_{w,i}$ are not represented. (a) "Perpendicular function" $\boldsymbol{w}_n$ on the tape. Degrees of freedom are only associated with nodes inside $\Gamma_{w,i}$, and not on its boundaries. (b) Global shape function $\boldsymbol{\ell}_i$ for the total current in the tape.

does not exhibit problematic oscillations, but the current density is clearly nonphysical. Such oscillations also appear with linear (ohmic) materials, and are not a consequence of the nonlinearity of the T2S response. The oscillation amplitude however decreases when the resistivity increases, so the stability issues are more important with T2S.

As with the h-ϕ-a-formulation, oscillations no longer appear if the function space for $\boldsymbol{a}$ is enriched with hierarchical elements on Γ_w. With the choice $\boldsymbol{a} \in \mathcal{A}^{\delta,2}(\Omega_a)$ and $\boldsymbol{t} \in \mathcal{T}^{\delta,1}(\Gamma_w)$, we obtain the green curve in Fig. 3.12. Increasing the order for $\boldsymbol{t}$ instead of $\boldsymbol{a}$, i.e., choosing $\boldsymbol{a} \in \mathcal{A}^{\delta,1}(\Omega_a)$ and $\boldsymbol{t} \in \mathcal{T}^{\delta,2}(\Gamma_w)$, leads to similar stabilized results with linear (ohmic) materials but induces convergence issues with the Newton-Raphson iterations for T2S materials. Replacing Newton-Raphson iterations by Picard ones does not help either.

Observations in 3D are exactly similar to those in 2D: one has to enrich exactly one of the two fields $\boldsymbol{a}$ or $\boldsymbol{t}$ to get rid of spurious oscillations in the numerical solution. And for nonlinear materials such as T2S, enriching $\boldsymbol{a}$ is the only valid option, because enriching $\boldsymbol{t}$ leads to convergence troubles with the iterative techniques. The stabilization with $\boldsymbol{a} \in \mathcal{A}^{\delta,2}(\Omega_a)$ is illustrated in Fig. 3.14, for a 3D geometry that consists in a flat annulus T2S tape with an applied current, placed in air.

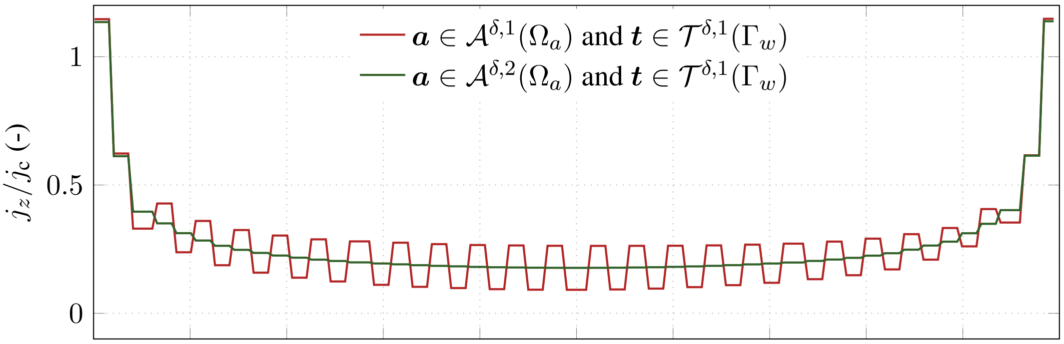

Figure 3.12: Current density for the simple tape problem. Nonphysical oscillations appear when using lowest-order elements for both fields. Enriching the space for $\boldsymbol{a}$ on Γ_w stabilizes the problem.

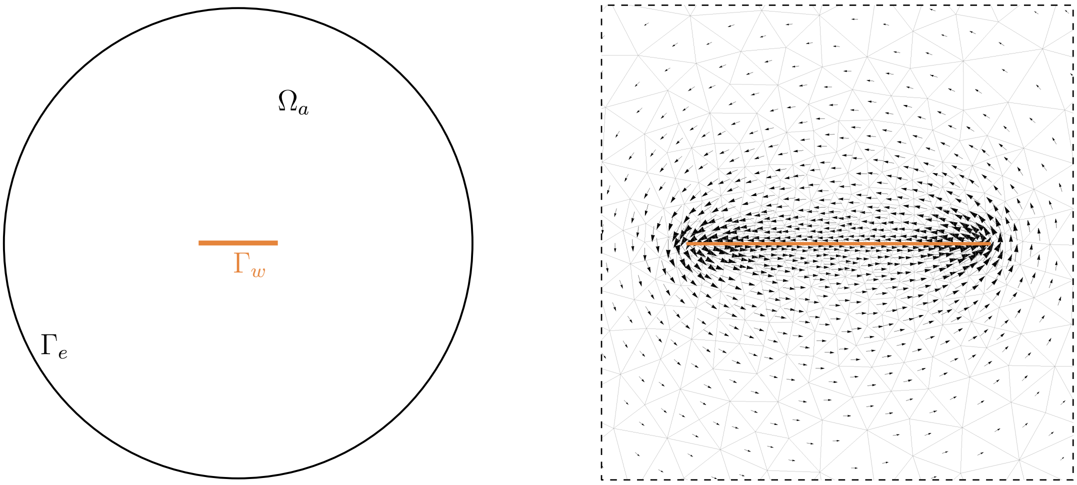

(a) Problem geometry.

(b) Magn. flux density (zoom).

Figure 3.13: Simple problem for the t-a-formulation: a superconducting tape in air, with an imposed total current intensity. (a) The problem geometry and domains. (b) Magnetic flux density near the tape, solution with first-order basis functions, $\boldsymbol{a} \in \mathcal{A}^{\delta,1}(\Omega_a)$ and $\boldsymbol{t} \in \mathcal{T}^{\delta,1}(\Gamma_w)$. Oscillations are not visible when looking at $\boldsymbol{b}$ only.

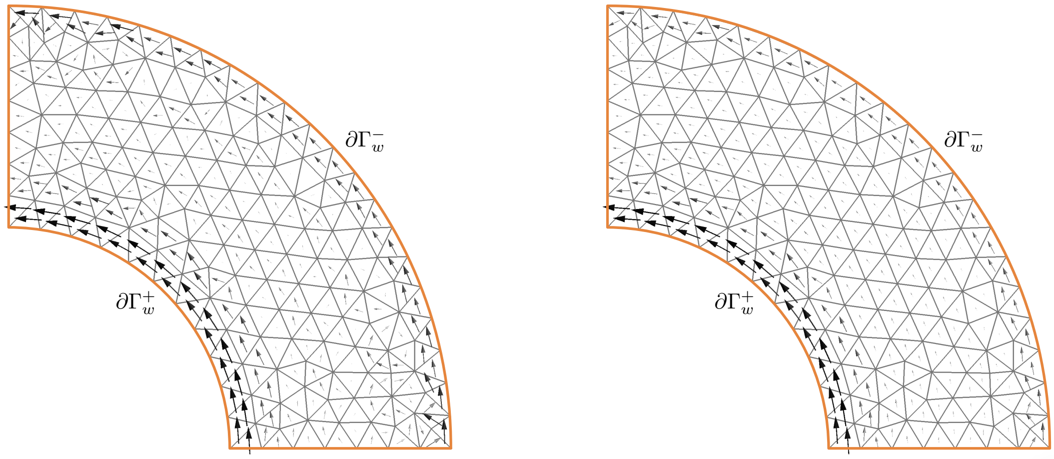

(a) $\boldsymbol{a} \in \mathcal{A}^{\delta,1}(\Omega_a)$ and $\boldsymbol{t} \in \mathcal{T}^{\delta,1}(\Gamma_w)$.

(b) $\boldsymbol{a} \in \mathcal{A}^{\delta,2}(\Omega_a)$ and $\boldsymbol{t} \in \mathcal{T}^{\delta,1}(\Gamma_w)$.

Figure 3.14: Current density for the annulus geometry. Flat annulus T2S tape with an applied current, only one quarter of the full annulus is modelled, and placed in air. In this 3D problem, conclusions are identical to those for 2D cases: one has to enrich the space for $\boldsymbol{a}$ on Γ_w to stabilize the problem. The solution in (a) presents nonphysical oscillations, which is not the case for the solution in (b).

3.4.3 Volume-coupled h-ϕ-b-formulation

Function space for $\boldsymbol{h}$

For the magnetic field $\boldsymbol{h}$, we keep the same function space as for the h-ϕ-formulation, with $\boldsymbol{h}$ defined in the whole domain Ω and described by edge functions or combinations of them:

gradients and cohomology basis functions. We have, as in Eq. (5.11),

$$\boldsymbol{h} = \sum_{e\in\mathcal{E}(\Omega_\mathrm{c}\setminus\partial\Omega_\mathrm{c})} h_e\,\boldsymbol{w}_e + \sum_{n\in\mathcal{N}(\Omega_\mathrm{c}^\mathrm{C})} \phi_n\,\textbf{grad}\,w_n + \sum_{i\in C} I_i\,\boldsymbol{c}_i, \tag{3.46}$$

where the h_e, ϕ_n and I_i coefficients are the degrees of freedom for the magnetic field $\boldsymbol{h}$ in the discrete function space $\mathcal{H}^{\delta,1}(\Omega)$.

Function space for $\boldsymbol{b}$

The main motivation for the h-ϕ-b-formulation is to invert the magnetic constitutive law, not to introduce new continuity conditions. A simple possibility to discretize the auxiliary field $\boldsymbol{b}$ in the magnetic domain Ω_m is to consider classical edge functions, to be able to match exactly the magnetic field $\boldsymbol{h}$. We define $\mathcal{B}^{\delta,1}(\Omega_\mathrm{m})$ as the space of fields $\boldsymbol{b}$ that are expressed as

$$\boldsymbol{b} = \sum_{e\in\mathcal{E}(\Omega_\mathrm{m})} b_e\boldsymbol{w}_e. \tag{3.47}$$

Together with $\boldsymbol{h} \in \mathcal{H}^{\delta,1}(\Omega)$, this choice is observed to produce reliable results in 2D, whether Ω_m is conducting or not. It does not introduce any additional continuity constraint with respect to the standard h-ϕ-formulation. The magnetic field $\boldsymbol{h}$ is still strongly curl-conform, but the auxiliary magnetic flux density $\boldsymbol{b}$ (made of 1-forms) is not forced to be div-conform. The zero divergence of $\boldsymbol{b}$ in Ω_m and $\mu\boldsymbol{h}$ in $\Omega_\mathrm{m}^\mathrm{C}$ is only enforced weakly in the formulation.

Note that when Ω_m is non-conducting, the local space for $\boldsymbol{h}$ is curl-free. One could be tempted to modify the space described by Eq. (3.47) to make it curl-free as well. However, in the case of nonlinear magnetic materials, this is not correct. In $\Omega_\mathrm{m} \cap \Omega_\mathrm{c}^\mathrm{C}$, we have

$$\textbf{curl}\,\boldsymbol{b} = \textbf{curl}\,(\nu^{-1}\boldsymbol{h}) = \textbf{grad}\,\nu^{-1} \times \boldsymbol{h}, \tag{3.48}$$

which is therefore not necessarily equal to zero. In practice, even if choosing only curl-free functions for $\boldsymbol{b}$ can be shown to satisfy the stability conditions, it results in non-physical solutions for nonlinear materials.

In 3D problems with non-conducting Ω_m, we observed that another choice provides better convergence properties. We define the alternative space $\mathcal{B}^{\delta,1}_\mathrm{cst}(\Omega_\mathrm{m})$ as the space of fields $\boldsymbol{b}$ that are expressed as

$$\boldsymbol{b} = \sum_{v\in\mathcal{V}(\Omega_\mathrm{m})} (b_{v,x}\,\hat{\boldsymbol{e}}_x + b_{v,y}\,\hat{\boldsymbol{e}}_y + b_{v,z}\,\hat{\boldsymbol{e}}_z)1_{K_v} \tag{3.49}$$

with $b_{v,x}$, $b_{v,y}$, and $b_{v,z}$ the degrees of freedom, $K(v)$ the element associated with volume v, and 1_{K_v} the indicator function of element K_v, which is equal to one inside K_v and to zero outside of it. Fields in this space are constant vectors within each element, but may be discontinuous between them. This choice also yields valid results in 2D for non-conducting Ω_m, but involves more degrees of freedom than $\mathcal{B}^{\delta,1}(\Omega_\mathrm{m})$.

No stability issues have been observed with $\boldsymbol{h} \in \mathcal{H}^{\delta,1}(\Omega)$ and $\boldsymbol{b} \in \mathcal{B}^{\delta,1}(\Omega_\mathrm{m})$ or $\mathcal{B}^{\delta,1}_\mathrm{cst}(\Omega_\mathrm{m})$.

3.4.4 Volume-coupled a-j-formulation

Function spaces for $\boldsymbol{a}$ and $\boldsymbol{e}_\mathrm{a}$

For the magnetic vector potential $\boldsymbol{a}$, we keep the same function space as for the a-formulation. It is defined in the whole domain Ω and described by perpendicular edge functions in 2D with in-plane magnetic field,

$$\boldsymbol{a} = \sum_{n\in\mathcal{N}(\Omega)} a_n \boldsymbol{w}_n, \tag{3.50}$$

or by classical edge functions with a co-tree gauge otherwise,

$$\boldsymbol{a} = \sum_{e\in\mathcal{E}(\Omega_\mathrm{c}\cup\text{co-tree}(\Omega_\mathrm{c}^\mathrm{C}))} a_e \boldsymbol{w}_e. \tag{3.51}$$

As before, we denote these spaces by $\mathcal{A}^{\delta,1}(\Omega)$.

The source electric field is also defined exactly as in the standard a-formulation: constant per connected conducting region in 2D with in-plane magnetic field, or defined as a sum of edge functions on a transition layer otherwise. We denote these function spaces by $\mathcal{U}^{\delta,1}(\Omega_\mathrm{c})$, as was defined in Section 2.4.2.

Function space for $\boldsymbol{j}$

A simple choice for the auxiliary field $\boldsymbol{j}$ in the conducting domain Ω_c is to keep the same function space as for $\boldsymbol{a}$. We define $\mathcal{J}^{\delta,1}(\Omega_\mathrm{c})$ as the space of fields $\boldsymbol{j}$ that are expressed as

$$\boldsymbol{j} = \sum_{n\in\mathcal{N}(\Omega_\mathrm{c})} j_n \boldsymbol{w}_n, \tag{3.52}$$

in 2D problems with in-plane magnetic field, as in [129], or expressed as

$$\boldsymbol{j} = \sum_{e\in\mathcal{E}(\Omega_\mathrm{c})} j_e \boldsymbol{w}_e, \tag{3.53}$$

in 3D problems, or 2D problems with in-plane current density.

In practice, no stability issue is observed with the choices $\boldsymbol{a} \in \mathcal{A}^{\delta,1}(\Omega)$, $\boldsymbol{e}_\mathrm{a} \in \mathcal{U}^{\delta,1}(\Omega_\mathrm{c})$ and $\boldsymbol{j} \in \mathcal{J}^{\delta,1}(\Omega_\mathrm{c})$. However, as will be discussed in the next chapter, some discrete problems involving source electric fields $\boldsymbol{e}_\mathrm{a}$ appear to be ill-conditioned.

3.5 Basics of stability analysis of saddle-point problems

Mixed finite element formulations face numerical stability issues if function spaces for their unknowns are not chosen consistently. Typically, spurious oscillations in the numerical solution may arise and affect the accuracy of the method, as illustrated in the previous section for the h-ϕ-a and t-a-formuations. The theory of mixed finite element formulations provides compatibility conditions on spaces to ensure the numerical stability of the problem [167].

The formulations introduced in this chapter fit into the classical framework of perturbed saddle-point problems. In this section, we present the stability conditions relevant to this class of problems, following closely Brezzi's classical treatment [167]. We also describe the *inf-sup test* [180], a numerical test which is used for checking the compatibility of specific functions spaces in the discrete setting. In the next section, we apply the theoretical results to analyze the four mixed formulations.

3.5.1 Spaces, norms and operators

We consider two Hilbert spaces V and Q, and their dual spaces V' and Q', respectively, containing all linear functionals $V \to \mathbb{R}$ and $Q \to \mathbb{R}$, respectively. On these spaces, we build perturbed saddle-point problems of the following form.

Perturbed saddle-point problem

For given $f \in V'$ and $g \in Q'$, find $u \in V$ and $p \in Q$ such that

$$a(u,v) + b(v,p) = \langle f, v\rangle, \quad \forall v \in V, \tag{3.54}$$
$$b(u,q) - c(p,q) = \langle g, q\rangle, \quad \forall q \in Q, \tag{3.55}$$

with $a(\cdot,\cdot)$, $b(\cdot,\cdot)$, and $c(\cdot,\cdot)$ continuous bilinear forms on $V \times V$, $V \times Q$, and $Q \times Q$, respectively, and where $\langle f, v\rangle$ (resp. $\langle g, q\rangle$) denotes the value of the functional f (resp. g) at v (resp. q). We also denote by A, B, and C the linear continuous operators associated with $a(\cdot,\cdot)$, $b(\cdot,\cdot)$, and $c(\cdot,\cdot)$, verifying

$$a(u,v) = \langle Au\ , v\rangle\,, \quad b(u,q) = \langle Bu\ , q\rangle\,, \quad c(p,q) = \langle Cp\ , q\rangle\,, \tag{3.56}$$

as well as their adjoint operators A^{T}, B^{T}, and C^{T}, verifying

$$a(u,v) = \left\langle u\ , A^{\mathrm{T}}v\right\rangle, \quad b(u,q) = \left\langle u\ , B^{\mathrm{T}}q\right\rangle, \quad c(p,q) = \left\langle p\ , C^{\mathrm{T}}q\right\rangle. \tag{3.57}$$

The term $-c(p,q)$ in Eq. (3.55) is considered to be the perturbation to the classical (unperturbed) saddle-point problem defined as follows. For given $f \in V'$ and $g \in Q'$, find $u \in V$ and $p \in Q$ such that

$$a(u,v) + b(v,p) = \langle f, v\rangle, \quad \forall v \in V, \tag{3.58}$$
$$b(u,q) \qquad\qquad = \langle g, q\rangle, \quad \forall q \in Q. \tag{3.59}$$

We refer to the problems above as those in the *continuous setting*, considering Hilbert spaces V and Q of infinite dimension.

In practice, we solve a discretized version of the (perturbed) saddle-point problems and we look for elements u^δ and p^δ in finite-dimensional spaces $V^\delta \subseteq V$ and $Q^\delta \subseteq Q$, respectively, i.e., the finite element spaces, with operators $a^\delta(\cdot,\cdot)$, $b^\delta(\cdot,\cdot)$, and $c^\delta(\cdot,\cdot)$ defined on these discrete spaces, as well as with the linear operators A^δ, B^δ, C^δ and their adjoint. We refer to the associated problem as the problem in the *discrete setting*.

The superscript $\cdot^\delta$ refers to a mesh of characteristic size δ. For conciseness, we drop the superscript for elements of V^δ and Q^δ, for elements of their dual spaces $(V^\delta)'$ and $(Q^\delta)'$, as well as for the bilinear operators. We keep the superscript for function spaces and linear operators.

Spaces V^δ and Q^δ are equipped with appropriate norms $\|\cdot\|_{V^\delta}$ and $\|\cdot\|_{Q^\delta}$. Dual norms are used for elements in the dual spaces $V^{\delta\prime}$ and $Q^{\delta\prime}$, they are defined as

$$\|f\|_{V^{\delta\prime}} = \sup_{v\in V^\delta} \frac{\langle f, v\rangle}{\|v\|_{V^\delta}} \quad \text{and} \quad \|g\|_{Q^{\delta\prime}} = \sup_{q\in Q^\delta} \frac{\langle g, q\rangle}{\|q\|_{Q^\delta}}. \tag{3.60}$$

Norms are also associated with the bilinear operators, they are denoted and defined as follows:

$$\|a^\delta\| = \sup_{u,v\in V^\delta} \frac{a(u,v)}{\|u\|_{V^\delta}\|v\|_{V^\delta}}, \tag{3.61}$$

$$\|b^\delta\| = \sup_{u\in V^\delta, q\in Q^\delta} \frac{b(u,q)}{\|u\|_{V^\delta}\|q\|_{Q^\delta}}, \tag{3.62}$$

$$\|c^\delta\| = \sup_{p,q\in Q^\delta} \frac{c(p,q)}{\|p\|_{Q^\delta}\|q\|_{Q^\delta}}. \tag{3.63}$$

The bilinear operators are assumed continuous, so their norm is finite [167].

We finally define two kernels associated with the coupling bilinear operator $b(\cdot,\cdot)$ of the (perturbed) saddle-point problem, that will play an important role in stability conditions:

$$K^\delta = \{v \in V^\delta : b(v,q) = 0, \forall q \in Q^\delta\} = \ker B^\delta, \tag{3.64}$$

$$H^\delta = \{q \in Q^\delta : b(v,q) = 0, \forall v \in V^\delta\} = \ker(B^\delta)^{\mathrm{T}}. \tag{3.65}$$

3.5.2 Solvability and stability of unperturbed saddle-point problems

Theorem 4.2.3. in [167] states that the unperturbed saddle-point problem (3.58)-(3.59) in the discrete setting has a unique solution $(u,p) \in V^\delta \times Q^\delta$ for every $f \in (V^\delta)'$ and $g \in (Q^\delta)'$ if $\operatorname{im} B^\delta = (Q^\delta)'$ and if $a(\cdot,\cdot)$ is coercive on K^δ, i.e.,

$$\exists \alpha^\delta > 0 \quad : \quad a(v,v) \geq \alpha^\delta \|v\|^2_{V^\delta}, \quad \forall v \in K^\delta. \tag{3.66}$$

Moreover, if

$$\exists \beta^\delta > 0 \quad : \quad \inf_{q\in Q^\delta} \sup_{v\in V^\delta} \frac{b(v,q)}{\|q\|_{Q^\delta}\|v\|_{V^\delta}} = \beta^\delta > 0, \tag{3.67}$$

then the unique solution (u,p) satisfies

$$\|u\|_{V^\delta} \leq \frac{1}{\alpha^\delta}\,\|f\|_{(V^\delta)'} + \frac{2\|a^\delta\|}{\alpha^\delta\beta^\delta}\,\|g\|_{(Q^\delta)'}, \tag{3.68}$$

$$\|p\|_{Q^\delta} \leq \frac{2\|a^\delta\|}{\alpha^\delta\beta^\delta}\,\|f\|_{(V^\delta)'} + \frac{2\|a^\delta\|^2}{\alpha^\delta(\beta^\delta)^2}\,\|g\|_{(Q^\delta)'}. \tag{3.69}$$

Condition (3.67) is the so-called inf-sup condition, or the Babuška-Brezzi condition [145, 181]. When the values $\|a^\delta\|$, α^δ, and β^δ can be chosen independent of the mesh, the problem is said to be stable, in the sense that the solution is bounded in terms of the right-hand side functional norms.

Note that conditions (3.66) and (3.67) are sufficient, but not necessary. Also, the bounds provided by Eqn. (3.68) and (3.69) can be improved when more restrictive conditions are met. For example, when $a(\cdot,\cdot)$ is a symmetric operator, which is often the case in practice, the unique solution (u,p) satisfies

$$\|u\|_{V^\delta} \leq \frac{1}{\alpha^\delta}\,\|f\|_{(V^\delta)'} + \frac{2\|a^\delta\|^{1/2}}{(\alpha^\delta)^{1/2}\beta^\delta}\,\|g\|_{(Q^\delta)'}, \tag{3.70}$$

$$\|p\|_{Q^\delta} \leq \frac{2\|a^\delta\|^{1/2}}{(\alpha^\delta)^{1/2}\beta^\delta}\,\|f\|_{(V^\delta)'} + \frac{\|a^\delta\|}{(\beta^\delta)^2}\,\|g\|_{(Q^\delta)'}. \tag{3.71}$$

If the coupling linear operator B^δ is not surjective, a solution exists only if $g \in \operatorname{im} B^\delta$. When this is the case, p is defined up to an element of the kernel H^δ, so that the solution is not unique. We however retrieve unicity and stability if we look for elements of Q^δ in the kernel orthogonal complement $(H^\delta)^\perp$ only, i.e., if we replace Q^δ by $(H^\delta)^\perp$ in the expressions above. The stability bounds therefore no longer hold for the whole space Q^δ, but only on $(H^\delta)^\perp$.

The comment above is particularly important in this work for studying the perturbed saddle-point problems associated with the mixed finite element formulations. In other applications, the stability analysis can usually be first conducted on the unperturbed problem before introducing perturbations [167]. In our case, we will have to treat the perturbed problems directly, as their unperturbed versions are not necessarily well-posed.

3.5.3 Solvability and stability of perturbed saddle-point problems

For the perturbed saddle point-problem (3.54)-(3.55) in the discrete setting, we present two distinct results. First, if $a(\cdot,\cdot)$ and $c(\cdot,\cdot)$ are coercive on their whole spaces, i.e., if

$$\exists \alpha^\delta > 0 \ : \ a(v,v) \geq \alpha^\delta \|v\|^2_{V^\delta}, \quad \forall v \in V^\delta, \tag{3.72}$$

$$\exists \gamma^\delta > 0 \ : \ c(q,q) \geq \gamma^\delta \|q\|^2_{Q^\delta}, \quad \forall q \in Q^\delta, \tag{3.73}$$

then, for every $f \in (V^\delta)'$ and $g \in (Q^\delta)'$, the perturbed problem has a unique solution (u,p) satisfying (proposition 4.3.1. of [167])

$$\frac{\alpha^\delta}{2}\|u\|^2_{V^\delta} + \frac{\gamma^\delta}{2}\|p\|^2_{Q^\delta} \leq \frac{1}{2\alpha^\delta}\|f\|^2_{(V^\delta)'} + \frac{1}{2\gamma^\delta}\|g\|^2_{(Q^\delta)'}, \tag{3.74}$$

which follows from Lax-Milgram theorem [182, 183]. This result provides bounds for the solution irrespective of whether the coupling operator $b(\cdot,\cdot)$ satisfies an inf-sup condition or not. However, the provided bounds are often unsatisfactory [167]. Indeed, in many application cases, the perturbation $-c(\cdot,\cdot)$ is such that γ^δ can be very small, and we would like a better bound for vanishing (but non-zero) perturbations.

The second result involves an inf-sup condition on the coupling operator, and lifts the whole space coercivity conditions. For simplicity, because this will be the case in practice for our problems, we directly assume that both $a(\cdot,\cdot)$ and $c(\cdot,\cdot)$ are symmetric and positive semi-definite bilinear operators. If $a(\cdot,\cdot)$ is coercive on K^δ and $c(\cdot,\cdot)$ is coercive on H^δ, i.e., if

$$\exists\alpha^\delta > 0 \ : \ a(v,v) \geq \alpha^\delta \|v\|^2_{V^\delta}, \quad \forall v \in K^\delta, \tag{3.75}$$

$$\exists\gamma^\delta > 0 \ : \ c(q,q) \geq \gamma^\delta \|q\|^2_{Q^\delta}, \quad \forall q \in H^\delta, \tag{3.76}$$

and if

$$\exists\beta^\delta > 0 \ : \ \inf_{q\in(H^\delta)^\perp} \sup_{v\in(K^\delta)^\perp} \frac{b(v,q)}{\|q\|_{Q^\delta}\|v\|_{V^\delta}} = \beta^\delta > 0, \tag{3.77}$$

then, the perturbed problem has a unique solution (u,p) satisfying (theorem 4.3.1. in [167])

$$\|u\|_{V^\delta} + \|p\|_{Q^\delta} \leq k^\delta \left(\|f\|_{(V^\delta)'} + \|g\|_{(Q^\delta)'}\right), \tag{3.78}$$

with k^δ a constant depending only on the stability constants, α^δ, β^δ, and γ^δ, and continuity constants $\|a^\delta\|$ and $\|c^\delta\|$. Note that the inf-sup condition (3.77) has to hold on the orthogonal complements $\cdot^\perp$ of H^δ and K^δ only. The dependence on the stability and continuity constants is now more interesting than that of Eq. (3.74) (see [167]).

In the particular case often encountered in practice where

$$c(p,q) = \lambda \ (p,q)_{Q^\delta}, \quad \lambda \geq 0, \tag{3.79}$$

where $(\cdot,\cdot)_{Q^\delta}$ is the inner product in Q^δ, so that $\gamma^\delta = \|c^\delta\| = \lambda$, under the same conditions, the bounds are given by (theorem 4.3.2. in [167])

$$\|u\|_{V^\delta} \leq \frac{(\beta^\delta)^2 + 4\lambda\|a^\delta\|}{\alpha^\delta(\beta^\delta)^2} \|f\|_{(V^\delta)'} + \frac{2\|a^\delta\|^{1/2}}{(\alpha^\delta)^{1/2}\beta^\delta} \|g\|_{(Q^\delta)'} \tag{3.80}$$

$$\|p\|_{Q^\delta} \leq \frac{2\|a^\delta\|^{1/2}}{(\alpha^\delta)^{1/2}\beta^\delta} \|f\|_{(V^\delta)'} + \frac{4\|a^\delta\|}{\lambda\|a^\delta\| + 2(\beta^\delta)^2} \|g\|_{(Q^\delta)'}. \tag{3.81}$$

With these bounds, we clearly see the improvement compared to Eq. (3.74): when $\lambda \to 0$, they do not diverge. Note that for $\lambda = 0$, we almost recover Eqn. (3.70) and (3.71), but as we mentioned before, we only want to represent small but non-zero λ values, as our problems with $\lambda = 0$ are not necessarily well-posed.

Link with the solution in the continuous setting

For simplicity, we still assume that $a(\cdot,\cdot)$ and $c(\cdot,\cdot)$ are symmetric, positive semi-definite continuous bilinear operators, which will be the case in the applications. Let $(\bar{u},\bar{p}) \in V \times Q$ be the exact solution of the perturbed saddle point-problem (3.54)-(3.55) in the continuous setting. In the discrete setting, with finite-dimensional spaces $V^\delta \subseteq V$ and $Q^\delta \subseteq Q$, if conditions (3.75), (3.76), and (3.77) hold, the perturbed saddle point-problem (3.54)-(3.55) in the discrete setting admits a unique solution $(u, p) \in V^\delta \times Q^\delta$ that satisfies (proposition 5.5.2. in [167])

$$\|u - \bar{u}\|_{V^\delta} + \|p - \bar{p}\|_{Q^\delta} \leq \bar{k}^\delta \left(\inf_{v \in V^\delta} \|v - \bar{u}\|_{V^\delta} + \inf_{q \in Q^\delta} \|q - \bar{p}\|_{Q^\delta} \right), \tag{3.82}$$

with a constant $\bar{k}^\delta$ depending only on the stability constants, α^δ, β^δ, γ^δ, and continuity constants, $\|a^\delta\|$, $\|b^\delta\|$, $\|c^\delta\|$. Note the addition of $\|b^\delta\|$ compared to previous bounds. If all these values can be chosen independent of the mesh, $\bar{k}^\delta$ is bounded with mesh refinement and the problem is said to be stable.

3.5.4 Numerical inf-sup test

In many practical cases, the inf-sup value β^δ cannot be evaluated analytically. Instead, it can be estimated with a numerical inf-sup test [167, 180]. On a given mesh, unknown fields $u \in V^\delta$ and $p \in Q^\delta$ are described by vectors $\boldsymbol{u}^\delta$ and $\boldsymbol{p}^\delta$ containing the degrees of freedom for the two fields. The size of these vectors depends on the discretization. We introduce orthogonal matrices $\mathbf{N}^\delta_{V^\delta}$ and $\mathbf{N}^\delta_{Q^\delta}$ such that

$$\|u\|^2_{V^\delta} = \left(\boldsymbol{u}^\delta\right)^{\mathrm{T}} \mathbf{N}^\delta_{V^\delta} \boldsymbol{u}^\delta \quad \text{and} \quad \|p\|^2_{Q^\delta} = \left(\boldsymbol{p}^\delta\right)^{\mathrm{T}} \mathbf{N}^\delta_{Q^\delta} \boldsymbol{p}^\delta. \tag{3.83}$$

These "norm matrices" can be obtained in practice from the finite element assembly of the following dummy formulations:

$$\text{find } u \in V^\delta \ : \ (u, v)_{V^\delta} = 0, \quad \forall v \in V^\delta, \tag{3.84}$$

$$\text{and find } p \in Q^\delta \ : \ (p, q)_{Q^\delta} = 0, \quad \forall q \in Q^\delta, \tag{3.85}$$

with $(\cdot, \cdot)_{V^\delta}$ and $(\cdot, \cdot)_{Q^\delta}$ the inner products in V^δ and Q^δ. The resulting system matrices are $\mathbf{N}^\delta_{V^\delta}$ and $\mathbf{N}^\delta_{Q^\delta}$ for the given mesh, respectively.

Then, we introduce the coupling matrix $\mathbf{B}^\delta$, satisfying $b(u, p) = \left(\boldsymbol{p}^\delta\right)^{\mathrm{T}} \mathbf{B}^\delta \boldsymbol{u}^\delta$, and which is the lower off-diagonal block of the global matrix system associated with the finite element assembly of the perturbed saddle-point problem (3.54)-(3.55), written on the considered mesh:

$$\begin{pmatrix} \mathbf{A}^\delta & (\mathbf{B}^\delta)^{\mathrm{T}} \\ \mathbf{B}^\delta & -\mathbf{C}^\delta \end{pmatrix} \begin{pmatrix} \boldsymbol{u}^\delta \\ \boldsymbol{p}^\delta \end{pmatrix} = \begin{pmatrix} \boldsymbol{f}^\delta \\ \boldsymbol{g}^\delta \end{pmatrix}, \tag{3.86}$$

with the right-hand side vectors $\boldsymbol{f}^\delta$ and $\boldsymbol{g}^\delta$, and diagonal blocks $\mathbf{A}^\delta$ and $\mathbf{C}^\delta$.

In terms of these norm and coupling matrices, Eq. (3.77) expressed in matrix form reads

$$\inf_{\boldsymbol{q}^\delta \in (H^\delta)^\perp} \sup_{\boldsymbol{v}^\delta \in (K^\delta)^\perp} \frac{\left(\boldsymbol{q}^\delta\right)^{\mathrm{T}} \mathbf{B}^\delta \boldsymbol{v}^\delta}{\left(\left(\boldsymbol{q}^\delta\right)^{\mathrm{T}} \mathbf{N}^\delta_{Q^\delta} \boldsymbol{q}^\delta\right) \left(\left(\boldsymbol{v}^\delta\right)^{\mathrm{T}} \mathbf{N}^\delta_{V^\delta} \boldsymbol{v}^\delta\right)} = \beta^\delta. \tag{3.87}$$

This expression is still not easy to evaluate *as is*, but the inf-sup value β^δ in Eq. (3.87) can be shown to be equal to the square root of the smallest *non-zero* eigenvalue of the following generalized eigenvalue problem [184]:

$$\left(\mathbf{B}^\delta\left(\mathbf{N}^\delta_{V^\delta}\right)^{-1}\left(\mathbf{B}^\delta\right)^{\mathrm{T}}\right)\boldsymbol{q}^\delta = \lambda^\delta\,\mathbf{N}^\delta_{Q^\delta}\boldsymbol{q}^\delta. \tag{3.88}$$

Note that we disregard zero eigenvalues because they are associated with eigenvectors defining elements in H^δ that are not involved in the inf-sup condition. Note also that the norm $\|b^\delta\|$ is the square root of the largest eigenvalue of the generalized eigenvalue problem Eq. (3.88).

Equivalently, β^δ and $\|b^\delta\|$ can also be obtained by the converse generalized eigenvalue problem written for $\boldsymbol{v}^\delta$:

$$\left(\left(\mathbf{B}^\delta\right)^{\mathrm{T}}\left(\mathbf{N}^\delta_{Q^\delta}\right)^{-1}\mathbf{B}^\delta\right)\boldsymbol{v}^\delta = \mu^\delta\,\mathbf{N}^\delta_{V^\delta}\boldsymbol{v}^\delta. \tag{3.89}$$

Zero eigenvalues are associated with eigenvectors defining elements in K^δ and are therefore disregarded as well. Depending on the sizes of vectors $\boldsymbol{v}^\delta$ and $\boldsymbol{q}^\delta$, i.e., on the number of degrees of freedom for each field, solving Eq. (3.88) or Eq. (3.89) might not have the same computational cost, and one of them might be more interesting to consider in practice.

The inf-sup test consists in computing β^δ values for a sequence of progressively refined meshes, i.e., with decreasing mesh size δ. If the values appear to be bounded from below by a positive value independent of mesh size, and if the other conditions (coercivity and continuity) are met, then the problem has high chances to be stable. On the other hand, if β^δ tends to zero, we expect stability issues, because the inf-sup condition then fails to be satisfied with a $\beta^\delta > 0$ independent of the mesh size. The numerical test does not provide a formal proof of stability, but experience shows that it is a reliable indicator [180, 185] in a wide range of applications [186, 187, 171].

3.6 Stability analysis

In this section we apply the stability results presented in the previous section on the four mixed formulations introduced earlier in this chapter: the h-ϕ-a, t-a, h-ϕ-b, and a-j-formulations.

We restrict the analysis to 2D problems with in-plane magnetic field, we will only mention when conclusions also extend to 3D problems. Moreover, we do not address the technical difficulties brought by the power law nonlinearity for T2S materials. These difficulties are not restricted to mixed formulations, are not the direct cause for the oscillations, and are outside the scope of this work. See [188, 189] for a rigorous treatment of them. In practice, we observe that all conclusions on stability are the same whether we consider linear materials or not, which justifies to let them aside for this work.

In addition to stability results, we also take a deeper look into the results of the inf-sup tests for the h-ϕ-a and h-ϕ-b-formulations, from which instructive interpretations can be extracted.

3.6.1 Surface-coupled h-ϕ-a-formulation

Linear equations

We start the analysis with a linear problem. We consider materials with constant resistivity and reluctivity values, but not necessarily homogeneous in space.

Using the implicit Euler method, at a given time step n, the solution $(\boldsymbol{a}, \boldsymbol{h}) = (\boldsymbol{a}_n, \boldsymbol{h}_n)$ depends on the solution at the previous time step $(\cdot)_{n-1}$. If we multiply the first equation of the h-ϕ-a-formulation by the time step Δt, we obtain the system

$$\big(\mu\, \boldsymbol{h}\,, \boldsymbol{h}'\big)_{\Omega_h} + (\Delta t\, \rho\, \mathbf{curl}\, \boldsymbol{h}\,, \mathbf{curl}\, \boldsymbol{h}')_{\Omega_{h,\mathrm{c}}} + \langle \boldsymbol{a} \times \boldsymbol{n}_{\Omega_h}\,, \boldsymbol{h}' \rangle_{\Gamma_\mathrm{m}} = \langle \boldsymbol{s}, \boldsymbol{h}' \rangle, \tag{3.90}$$

$$\langle \boldsymbol{h} \times \boldsymbol{n}_{\Omega_a}\,, \boldsymbol{a}' \rangle_{\Gamma_\mathrm{m}} - (\nu\, \mathbf{curl}\, \boldsymbol{a}\,, \mathbf{curl}\, \boldsymbol{a}')_{\Omega_a} = 0, \tag{3.91}$$

with the right-hand side functional defined by

$$\langle \boldsymbol{s}, \boldsymbol{h}' \rangle = \langle \boldsymbol{a}_{n-1} \times \boldsymbol{n}_{\Omega_h}\,, \boldsymbol{h}' \rangle_{\Gamma_\mathrm{m}} + \big((\mu\, \boldsymbol{h})_{n-1}\,, \boldsymbol{h}'\big)_{\Omega_h} + \Delta t \sum_{i \in C_V} \bar{V}_i \mathcal{I}_i(\boldsymbol{h}'). \tag{3.92}$$

System (3.90)-(3.91) can be rewritten as

$$\big(\mu\, \boldsymbol{h}\,, \boldsymbol{h}'\big)_{\Omega_h} + (\Delta t\, \rho\, \mathbf{curl}\, \boldsymbol{h}\,, \mathbf{curl}\, \boldsymbol{h}')_{\Omega_{h,\mathrm{c}}} + \langle \boldsymbol{a} \times \boldsymbol{n}_{\Omega_h}\,, \boldsymbol{h}' \rangle_{\Gamma_\mathrm{m}} = \langle \boldsymbol{s}, \boldsymbol{h}' \rangle, \tag{3.93}$$

$$\langle \boldsymbol{a}' \times \boldsymbol{n}_{\Omega_h}\,, \boldsymbol{h} \rangle_{\Gamma_\mathrm{m}} - (\nu\, \mathbf{curl}\, \boldsymbol{a}\,, \mathbf{curl}\, \boldsymbol{a}')_{\Omega_a} = 0, \tag{3.94}$$

using $\boldsymbol{n}_{\Omega_a} = -\boldsymbol{n}_{\Omega_h}$. For conciseness, we consider homogeneous essential boundary conditions. Problem (3.93)-(3.94) can therefore be cast into the form of the perturbed saddle point problem (3.54)-(3.55), with identical function spaces for unknown functions and test functions.

The case of non-homogeneous essential boundary conditions can be easily treated by removing the associated degrees of freedom from the function spaces and introducing them separately in the formulation, so that they enter directly the right-hand side as sources; the following analysis is unchanged, and conclusions are identical [167].

After discretization, we obtain a system of linear equations in a matrix form. The formulation will be considered stable if a sequence of problems on progressively refined meshes satisfies conditions (3.61) to (3.63) and (3.75) to (3.77), with constants α^δ, β^δ, γ^δ, $\|a^\delta\|$, $\|b^\delta\|$, and $\|c^\delta\|$ independent of mesh size.

In the following, the notation $\mathcal{H}_0^\delta(\Omega_h)$ refers to either $\mathcal{H}_0^{\delta,1}(\Omega_h)$ or $\mathcal{H}_0^{\delta,2}(\Omega_h)$, and the notation $\mathcal{A}_0^\delta(\Omega_a)$ refers to either $\mathcal{A}_0^{\delta,1}(\Omega_a)$ or $\mathcal{A}_0^{\delta,2}(\Omega_a)$. We will consider the different cases in the inf-sup test. In $\mathcal{H}_0^\delta(\Omega_h)$ and $\mathcal{A}_0^\delta(\Omega_a)$, we define the norms

$$\|\boldsymbol{h}\|^2_{\mathcal{H}_0^\delta} = (\mu_0\, \boldsymbol{h}\,, \boldsymbol{h})_{\Omega_h} + (\Delta t_0\, \rho_0\, \mathbf{curl}\, \boldsymbol{h}\,, \mathbf{curl}\, \boldsymbol{h})_{\Omega_{h,\mathrm{c}}}\,, \tag{3.95}$$

$$\|\boldsymbol{a}\|^2_{\mathcal{A}_0^\delta} = (\nu_0\, \mathbf{curl}\, \boldsymbol{a}\,, \mathbf{curl}\, \boldsymbol{a})_{\Omega_a}\,, \tag{3.96}$$

with ρ_0 being a characteristic resistivity and Δt_0 a characteristic time step.

With these norms, whatever the discretization, $\forall \boldsymbol{h} \in \mathcal{H}_0^\delta(\Omega_h)$ and $\forall \boldsymbol{a} \in \mathcal{A}_0^\delta(\Omega_a)$, we have

$$\begin{aligned} a(\boldsymbol{h},\boldsymbol{h}) &= \big(\mu\,\boldsymbol{h}\,,\boldsymbol{h}\big)_{\Omega_h} + (\Delta t\,\rho\,\mathbf{curl}\,\boldsymbol{h}\,,\mathbf{curl}\,\boldsymbol{h})_{\Omega_{h,\mathrm{c}}} && (3.97)\\ &\geq \inf(\mu/\mu_0, \Delta t/\Delta t_0\cdot\rho/\rho_0)\,\|\boldsymbol{h}\|^2_{\mathcal{H}_0^\delta}, && (3.98)\\ c(\boldsymbol{a},\boldsymbol{a}) &= (\nu\,\mathbf{curl}\,\boldsymbol{a}\,,\mathbf{curl}\,\boldsymbol{a})_{\Omega_a} && (3.99)\\ &\geq \inf(\nu/\nu_0)\,\|\boldsymbol{a}\|^2_{\mathcal{A}_0^\delta}, && (3.100)\end{aligned}$$

which proves the coercivity properties (3.75) and (3.76), with values independent on the mesh size: $\alpha^\delta = \inf(\mu/\mu_0, \Delta t/\Delta t_0\cdot\rho/\rho_0) > 0$, and $\gamma^\delta = \inf(\nu/\nu_0) > 0$.

Similarly, for the continuity constants, we have

$$\begin{aligned} a(\boldsymbol{h},\boldsymbol{h}) &= \big(\mu\,\boldsymbol{h}\,,\boldsymbol{h}\big)_{\Omega_h} + (\Delta t\,\rho\,\mathbf{curl}\,\boldsymbol{h}\,,\mathbf{curl}\,\boldsymbol{h})_{\Omega_{h,\mathrm{c}}} && (3.101)\\ &\leq \sup(\mu/\mu_0, \Delta t/\Delta t_0\cdot\rho/\rho_0)\,\|\boldsymbol{h}\|^2_{\mathcal{H}_0^\delta}, && (3.102)\\ c(\boldsymbol{a},\boldsymbol{a}) &= (\nu\,\mathbf{curl}\,\boldsymbol{a}\,,\mathbf{curl}\,\boldsymbol{a})_{\Omega_a} && (3.103)\\ &\leq \sup(\nu/\nu_0)\,\|\boldsymbol{a}\|^2_{\mathcal{A}_0^\delta}. && (3.104)\end{aligned}$$

As $a(\cdot,\cdot)$ and $c(\cdot,\cdot)$ are symmetric and positive-definite bilinear operators, they satisfy [167]

$$\begin{aligned} (a(\boldsymbol{h}_1,\boldsymbol{h}_2))^2 &\leq a(\boldsymbol{h}_1,\boldsymbol{h}_1)\,a(\boldsymbol{h}_2,\boldsymbol{h}_2), \quad \forall \boldsymbol{h}_1,\boldsymbol{h}_2 \in \mathcal{H}_0^\delta(\Omega_h), && (3.105)\\ (c(\boldsymbol{a}_1,\boldsymbol{a}_2))^2 &\leq c(\boldsymbol{a}_1,\boldsymbol{a}_1)\,c(\boldsymbol{a}_2,\boldsymbol{a}_2), \quad \forall \boldsymbol{a}_1,\boldsymbol{a}_2 \in \mathcal{A}_0^\delta(\Omega_a). && (3.106)\end{aligned}$$

Consequently, the norms from (3.61) and (3.63) are finite and satisfy $\|a^\delta\| \leq \sup(\mu/\mu_0, \Delta t/\Delta t_0\cdot\rho/\rho_0) < \infty$, and $\|c^\delta\| \leq \sup(\nu/\nu_0) < \infty$, which are also independent on the mesh size.

The remaining conditions for stability are the inf-sup condition and the continuity of $b(\cdot,\cdot)$: there must exist a $\beta > 0$ independent of mesh size that fulfils,

$$\inf_{\boldsymbol{a}\in(H^\delta)^\perp}\ \sup_{\boldsymbol{h}\in(K^\delta)^\perp} \frac{\langle \boldsymbol{a}\times\boldsymbol{n}_{\Omega_h}\,,\boldsymbol{h}\rangle_{\Gamma_\mathrm{m}}}{\|\boldsymbol{a}\|_{\mathcal{A}_0^\delta}\|\boldsymbol{h}\|_{\mathcal{H}_0^\delta}} = \beta^\delta \geq \beta, \qquad (3.107)$$

and $\|b^\delta\|$ must be bounded from above. To check these two conditions, we perform a numerical inf-sup test on a characteristic problem involving the h-ϕ-a-formulation.

We consider the stacked bar geometry represented in Fig. 3.15, with linear homogeneous materials: a linear conductor with $\rho = 1.6\times10^{-8}$ Ωm, and a linear non-conducting ferromagnet with $\mu_\mathrm{r} = 1000$, surrounded by air. We analyze the behavior of the values of β^δ and $\|b^\delta\|$, obtained from the generalized eigenvalue problem Eq. (3.88), or Eq. (3.89), considering different discretization levels. Four cases are considered: $\boldsymbol{h} \in \mathcal{H}_0^{\delta,i}(\Omega_h)$ and $\boldsymbol{a} \in \mathcal{A}_0^{\delta,j}(\Omega_a)$, for $(i,j) \in \{1,2\}\times\{1,2\}$, with function spaces defined in Section 3.4.1. Results are shown in Fig. 3.16.

First, the norm $\|b^\delta\|$ of the coupling operator can clearly be bounded from above independent of the function spaces, as deduced from the values in the upper part of Fig. 3.16. However, the evolution of the inf-sup value follows two distinct behaviors. When exactly one of the two fields $\boldsymbol{h}$ and $\boldsymbol{a}$ is enriched with hierarchical elements, the inf-sup value β^δ does not decrease, so that the inf-sup condition is likely to be satisfied, in which case Eq. (3.82) ensures the stability

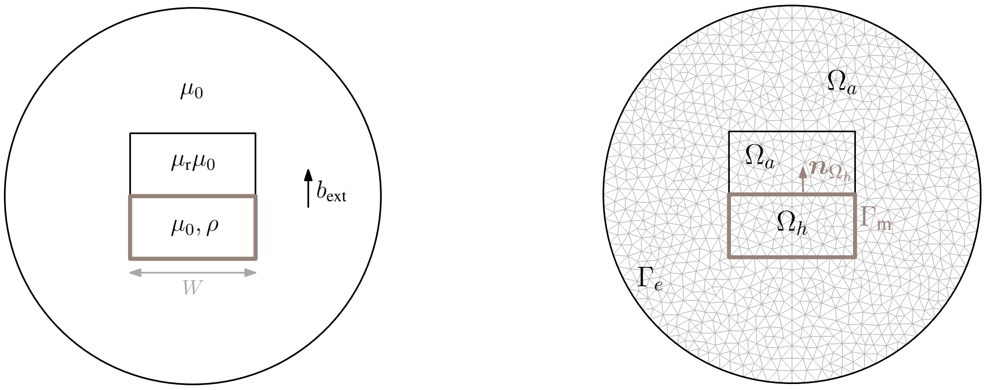

(a) Problem geometry.

(b) Domain definition and mesh.

Figure 3.15: Simple 2D geometry for the inf-sup test on the h-ϕ-a-formulation. Stack of a conducting bar with $\rho = 1.6 \times 10^{-8}$ Ωm and $\mu = \mu_0$ (below) and a ferromagnetic bar $\sigma = 0$ and $\mu_r = 1000$ (above), of common width W, surrounded by air. The system is subjected to a vertical applied field. The thick curve is Γ_m.

of the associated problem. On the other cases, if none of the fields is enriched with hierachical elements, or if both of them are, the inf-sup value β^δ decreases as $\beta^\delta \sim \delta$ and stability issues, i.e., oscillations in the numerical solution, are not a surprise.

In practice, when choosing $\boldsymbol{h} \in \mathcal{H}_0^{\delta,1}(\Omega_h)$ and $\boldsymbol{a} \in \mathcal{A}_0^{\delta,1}(\Omega_a)$, or $\boldsymbol{h} \in \mathcal{H}_0^{\delta,2}(\Omega_h)$ and $\boldsymbol{a} \in \mathcal{A}_0^{\delta,2}(\Omega_a)$, we do indeed observe oscillations in the numerical solution. This was illustrated in Figs. 3.9(a) and 3.10(a) with a T2S. However, these oscillations only appear at interfaces between regions with large permeability jumps across Γ_m. By contrast, when no ferromagnetic material is present in the geometry, the numerical results are satisfying. These behaviors can be explained by Eq. (3.74) (Proposition 4.3.1 of [167]), that follows from the Lax-Milgram theorem. Because $a(\cdot,\cdot)$ and $c(\cdot,\cdot)$ are coercive on their whole space, the problem has a unique solution $(\boldsymbol{a}, \boldsymbol{h})$ and we have the following inequality:

$$\frac{\alpha^\delta}{2}\|\boldsymbol{a}\|^2_{\mathcal{A}_0^\delta} + \frac{\gamma^\delta}{2}\|\boldsymbol{h}\|^2_{\mathcal{H}_0^\delta} \leq \frac{1}{2\alpha^\delta}\|\boldsymbol{s_a}\|^2_{(\mathcal{A}_0^\delta)'} + \frac{1}{2\gamma^\delta}\|\boldsymbol{s_h}\|^2_{(\mathcal{H}_0^\delta)'}, \tag{3.108}$$

with $\boldsymbol{s_a}$ and $\boldsymbol{s_h}$ the right-hand sides of the final system (after treating non-homogeneous essential boundary conditions). This bound is valid irrespective of whether the coupling operator satisfies the inf-sup condition or not. Consequently, the problem is actually always stable in the sense of Eq. (3.108). However, the provided bound deteriorates when either α^δ or γ^δ decreases, which is the case when considering a ferromagnetic material in Ω_a, in particular. Indeed, when $1/\nu \to \infty$ in Ω_a, we have $\gamma^\delta \to 0$. With practical mesh resolutions and ferromagnetic materials, the bound in Eq. (3.108) appears to be too loose. This explains why stability issues still arise for choices that fail to satisfy the inf-sup condition.

As said above, we can extend to spaces with non-homogeneous essential boundary conditions, and hence to non-homogeneous function spaces. In practice, when dealing with ferromagnetic materials adjacent to Γ_m, it is therefore recommended to choose either $\boldsymbol{h} \in \mathcal{H}^{\delta,1}(\Omega_h)$ and $\boldsymbol{a} \in \mathcal{A}^{\delta,2}(\Omega_a)$, or $\boldsymbol{h} \in \mathcal{H}^{\delta,2}(\Omega_h)$ and $\boldsymbol{a} \in \mathcal{A}^{\delta,1}(\Omega_a)$, to guarantee stability.

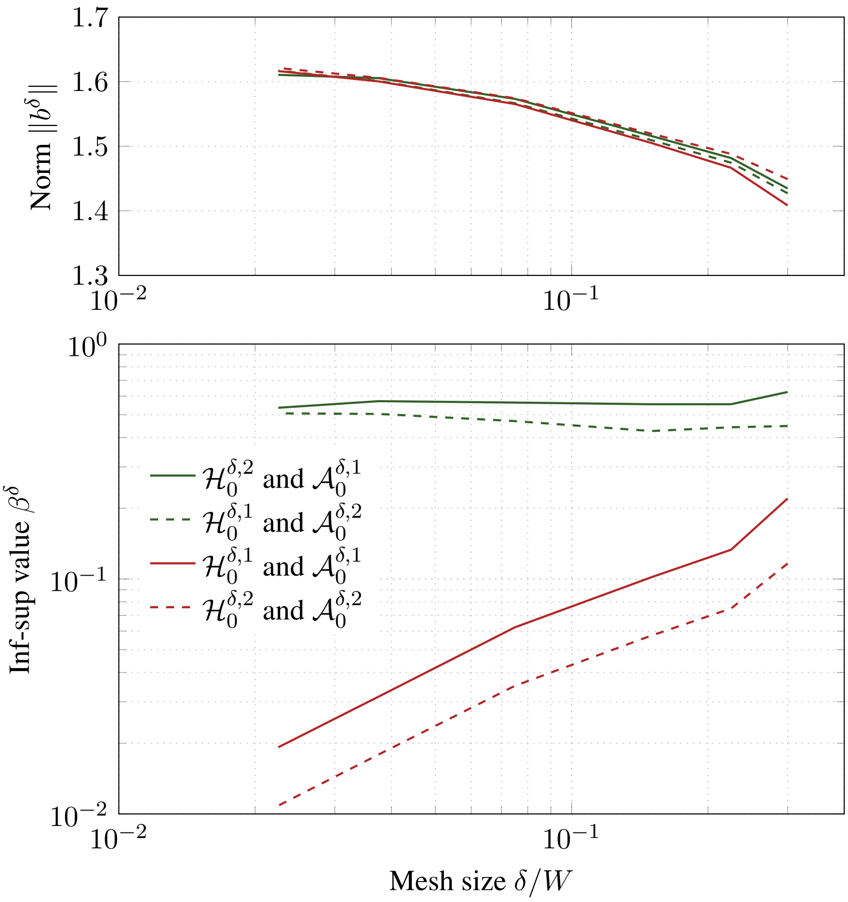

Figure 3.16: Evolution of the inf-sup constant β^δ from Eq. (3.107) and the norm $\|b\|$ with mesh refinement ($\delta/W \to 0$) on the stacked bar linear problem shown in Fig. 3.15. Four cases are considered: $\boldsymbol{h} \in \mathcal{H}_0^{\delta,i}(\Omega_h)$ and $\boldsymbol{a} \in \mathcal{A}_0^{\delta,j}(\Omega_a)$, for $(i,j) \in \{1,2\} \times \{1,2\}$. We can only conclude on stability when $i \neq j$, i.e., when exactly one space is enriched with respect to Whitney elements (green lines). The legend is the same for both graphs.

Interpretation

To illustrate the link between the eigenvalue problem and the spurious oscillations, we investigate the solution of the generalized eigenvalue problem arising in the inf-sup test, defined by Eq. (3.88). We apply it on the same stacked-bar problem as before, still with linear materials.

For the stability analysis, we are only interested in the non-zero eigenvalues, whose associated eigenvectors form a basis of the orthogonal complement $(H^\delta)^\perp$ of the kernel H^δ, for a given mesh. These eigenvalues are represented in Fig. 3.17 for both stable and unstable choices of function spaces, at two different discretization levels. The same conclusions as from Fig. 3.16 can be drawn, by looking only at the smallest (and highest) eigenvalue(s). In particular, with the choice $\boldsymbol{h} \in \mathcal{H}^{\delta,1}(\Omega_h)$ and $\boldsymbol{a} \in \mathcal{A}^{\delta,1}(\Omega_a)$, the problem is unstable because it contains modes of smaller and smaller eigenvalues as the mesh is refined. The eigenvector associated with the smallest eigenvalue of the fine mesh is represented in Fig. 3.18(a). Clearly, such a mode (among others) is also activated in the unstable solution of Fig. 3.9(a) with nonlinear materials. To give an idea, the 40th mode is shown in Fig. 3.18(b).

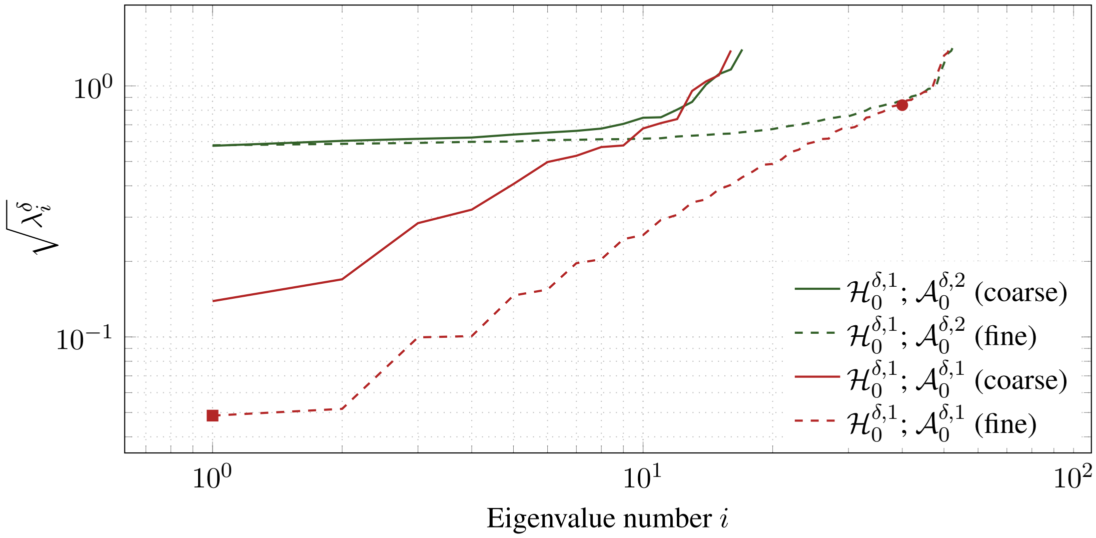

Figure 3.17: Distribution of the square root of the non-zero eigenvalues computed from Eq. (3.88) on the stacked-bar geometry with linear materials. The smallest values are the inf-sup values β^δ, the largest are the norms $\|b^\delta\|$. Eigenvectors associated with the square and circle points are represented in Fig. 3.18.

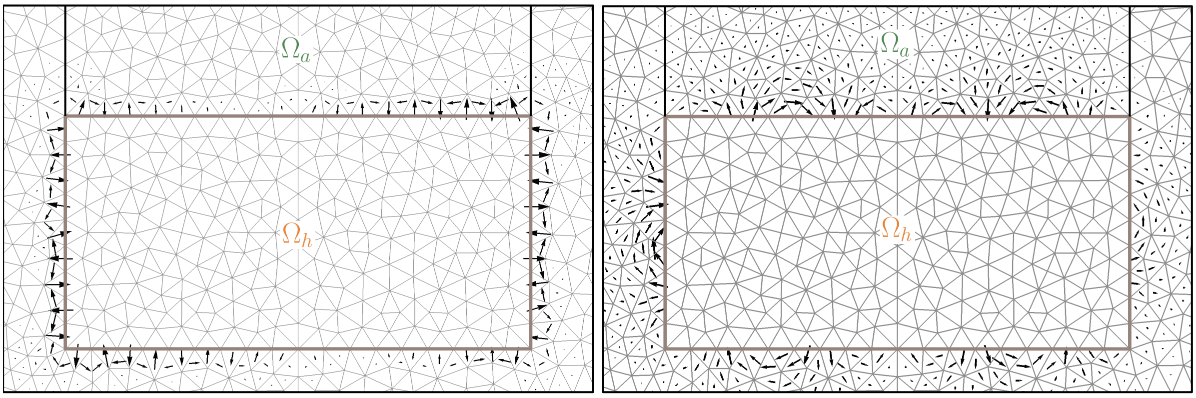

(a) Square in Fig. 3.17, smallest eigenvalue.

(b) Circle in Fig. 3.17.

Figure 3.18: Eigenvectors associated with the two dots in Fig. 3.17, for the (unstable) choice $\boldsymbol{h} \in \mathcal{H}^{\delta,1}(\Omega_h)$ and $\boldsymbol{a} \in \mathcal{A}^{\delta,1}(\Omega_a)$ and the same mesh as in Fig. 3.9. The brown curve is Γ_m.

Of course, similar highly oscillating modes still exist in the $(H^\delta)^\perp$ basis for the stable choice $\boldsymbol{h} \in \mathcal{H}^{\delta,1}(\Omega_h)$ and $\boldsymbol{a} \in \mathcal{A}^{\delta,2}(\Omega_a)$, but their eigenvalues are levelled up and the new modes appearing with mesh refinement do no longer introduce smaller and smaller eigenvalues.

Intuitively, one can understand how adding bubble shape functions for either $\boldsymbol{h}$ or $\boldsymbol{a}$ helps increasing the inf-sup value. Let us consider the fraction in the inf-sup equation Eq. (3.107),

$$\frac{\langle \boldsymbol{a} \times \boldsymbol{n}_{\Omega_h}, \boldsymbol{h} \rangle_{\Gamma_\mathrm{m}}}{\|\boldsymbol{a}\|_{\mathcal{A}_0^\delta} \|\boldsymbol{h}\|_{\mathcal{H}_0^\delta}}, \tag{3.109}$$

and a vector potential $\boldsymbol{a}$ whose trace exhibits symmetric oscillations on a part of Γ_m, as depicted in Fig. 3.19. Such a function is close to what constitutes the infimum argument of Eq. (3.107), as can be seen in Fig. 3.18(a).

If we have only access to magnetic fields $\boldsymbol{h} \in \mathcal{H}^{\delta,1}(\Omega_h)$, generated by gradient of lowest-order node functions w_n and w_{n+1} on Γ_m, the integral $\langle \boldsymbol{a} \times \boldsymbol{n}_{\Omega_h}\,, \textbf{grad}\, w_i \rangle_{\Gamma_\mathrm{m}}$ in the numerator of the fraction (3.109) is equal to zero by considering the node n_i. This is true for the node n_{i+1} as well. Of course, one should be careful not to conclude too quickly, as the function $\boldsymbol{a}$ has to belong to $(H^\delta)^\perp$. It cannot be chosen so that it vanishes for all $\boldsymbol{h}$, but the fact that highly oscillating functions yield small values of the fraction (3.109) can still be understood intuitively.

By contrast, the introduction of bubble functions for $\boldsymbol{h} \in \mathcal{H}^{\delta,2}(\Omega_h)$ and the possibility of considering them as component of the argument of the supremum of Eq. (3.107) directly makes the oscillating vector potential $\boldsymbol{a}$ less problematic, as the integral $\langle \boldsymbol{a} \times \boldsymbol{n}_{\Omega_h}\,, \textbf{grad}\, w_{2,e_i} \rangle_{\Gamma_\mathrm{m}}$ no longer vanishes with the bubble function w_{2,e_i}, whereas the norms in the denominator remain comparable. Again, this does not imply directly that the inf-sup condition is verified, but it provides an element to understand why highly oscillating functions are no longer associated with small values of the fraction (3.109).

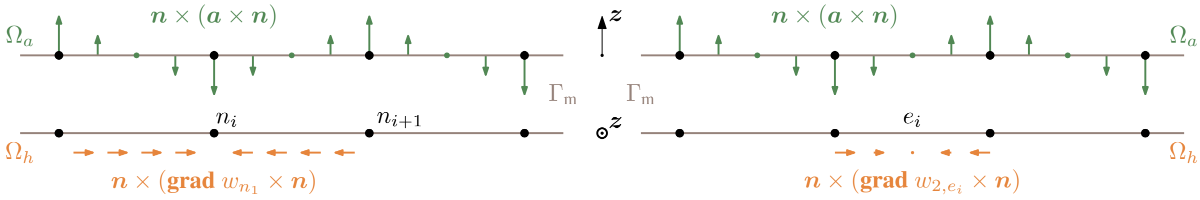

(a) Lowest-order shape function for $\boldsymbol{h} \in \mathcal{H}^{\delta,1}(\Omega_h)$. (b) Bubble shape function for $\boldsymbol{h} \in \mathcal{H}^{\delta,2}(\Omega_h)$.

Figure 3.19: Situation on the coupling boundary Γ_m for a symmetrically oscillating vector potential $\boldsymbol{a}$ at the material interface, and illustration of why choosing $\boldsymbol{h} \in \mathcal{H}^{\delta,2}(\Omega_h)$ and $\boldsymbol{a} \in \mathcal{A}^{\delta,1}(\Omega_a)$ stabilizes the problem. (a) Gradients of node functions bring a zero contribution to the coupling integral. (b) The integral involving bubble functions does no longer vanish.

Nonlinear equations

We consider SFM in Ω_a, characterized by a saturation law for the permeability, and T2S in Ω_h, whose resistivity is described by a power law. The associated system of equations after time discretization is as in Eqn. (3.90)-(3.91), but with solution-dependent coefficients ρ and ν. With a Newton-Raphson linearization, we obtain a problem that is iteratively solved. The solution $(\boldsymbol{h}, \boldsymbol{a}) = (\boldsymbol{h}_n^k, \boldsymbol{a}_n^k)$ at time step n and iteration k depends on the solutions at the previous time step $(\cdot)_{n-1}$ and previous iteration $(\cdot)^{k-1}$. Using, $\boldsymbol{n}_{\Omega_a} = -\boldsymbol{n}_{\Omega_h}$, we obtain the linear system

$$\left(\mu_0\, \boldsymbol{h}\,, \boldsymbol{h}'\right)_{\Omega_h} + \left(\Delta t\, (\partial \boldsymbol{e}/\partial \boldsymbol{j})^{k-1}\ \textbf{curl}\, \boldsymbol{h}\,, \textbf{curl}\, \boldsymbol{h}'\right)_{\Omega_{h,\mathrm{c}}} + \langle \boldsymbol{a} \times \boldsymbol{n}_{\Omega_h}\,, \boldsymbol{h}' \rangle_{\Gamma_\mathrm{m}} = \langle \tilde{\boldsymbol{s}}_{\boldsymbol{h}}, \boldsymbol{h}' \rangle, \tag{3.110}$$

$$\langle \boldsymbol{a}' \times \boldsymbol{n}_{\Omega_h}\,, \boldsymbol{h} \rangle_{\Gamma_\mathrm{m}} - \left((\partial \boldsymbol{h}/\partial \boldsymbol{b})^{k-1}\, \textbf{curl}\, \boldsymbol{a}\,, \textbf{curl}\, \boldsymbol{a}'\right)_{\Omega_a} = \langle \tilde{\boldsymbol{s}}_{\boldsymbol{a}}, \boldsymbol{a}' \rangle, \tag{3.111}$$

with right-hand side functionals $\tilde{\boldsymbol{s}}_{\boldsymbol{h}}$ and $\tilde{\boldsymbol{s}}_{\boldsymbol{a}}$ defined by

$$
\begin{aligned}
\langle \tilde{\boldsymbol{s}}_{\boldsymbol{h}}, \boldsymbol{h}' \rangle =& \langle \boldsymbol{a}_{n-1} \times \boldsymbol{n}_{\Omega_h}, \boldsymbol{h}' \rangle_{\Gamma_{\mathrm{m}}} + \left((\mu\, \boldsymbol{h})_{n-1}, \boldsymbol{h}' \right)_{\Omega_h} \\
&- \left(\Delta t \left((\rho \mathbf{I} - \partial \boldsymbol{e}/\partial \boldsymbol{j})\, \mathbf{curl}\, \boldsymbol{h} \right)^{k-1}, \mathbf{curl}\, \boldsymbol{h}' \right)_{\Omega_{h,\mathrm{c}}} + \Delta t \sum_{i \in C_V} \bar{V}_i \mathcal{I}_i(\boldsymbol{h}'), \qquad (3.112)\\
\langle \tilde{\boldsymbol{s}}_{\boldsymbol{a}}, \boldsymbol{a}' \rangle =& - \left(\left((\nu \mathbf{I} - \partial \boldsymbol{h}/\partial \boldsymbol{b})\, \mathbf{curl}\, \boldsymbol{a} \right)^{k-1}, \mathbf{curl}\, \boldsymbol{a}' \right)_{\Omega_a}, \qquad (3.113)
\end{aligned}
$$

with $\mathbf{I}$ being the identity matrix. The structure is similar to that of system (3.93)-(3.94). Coercivity and continuity of diagonal operators $a(\cdot,\cdot)$ and $c(\cdot,\cdot)$, in the sense of the norms (3.95) and (3.96) are only satisfied if the eigenvalues of matrices $(\partial \boldsymbol{e}/\partial \boldsymbol{j})^{k-1}$ and $(\partial \boldsymbol{h}/\partial \boldsymbol{b})^{k-1}$ are bounded away from zero and infinity, independently of the mesh. This is the case for the differential reluctivity with classical saturation laws. However, with the power law, the differential resistivity tends to zero for small current densities, so that we cannot verify the coercivity condition with norm (3.95), and tends to infinity to large current densities, so that continuity is not satisfied either.

To avoid the technical difficulty due to the power law, we could use a regularized version, such as

$$
\rho = \min \left(\rho_0 + \frac{e_{\mathrm{c}}}{j_{\mathrm{c}}} \left(\frac{\|\boldsymbol{j}\|}{j_{\mathrm{c}}} \right)^{n-1},\ \rho_{\mathrm{M}} \right), \qquad (3.114)
$$

with two limiting resistivity values ρ_0 and ρ_{M}. If the residual resistivity ρ_0 is small enough compared to $e_{\mathrm{c}}/j_{\mathrm{c}}$, the effect on the numerical solution can be neglected. The upper bound ρ_{M} can be chosen to model flux flow. In practice, we observe that introducing limiting resistivities is not required for obtaining reliable results. We therefore choose not to address this technical detail here, as the resistivity does not play such an important role as the permeability. Stability issues are not observed to depend on its value.

Note that we would also have to tackle this difficulty in standard formulations to discuss their well-posedness in a formal mathematical framework. We refer to others works for a rigorous treatment of the power law in simpler formulations [188, 189]. We keep in mind that, by contrast to the linear case, in this work, we therefore do not establish a formal proof of stability for nonlinear materials, due to this particular operator $a(\cdot,\cdot)$.

Conducting an inf-sup test provides results that are exactly similar to those in Fig. 3.16, and we observe that in practice, the conclusions obtained for the linear case remain and lead to the same recommendations. When choosing $\boldsymbol{h} \in \mathcal{H}^{\delta,1}(\Omega_h)$ and $\boldsymbol{a} \in \mathcal{A}^{\delta,2}(\Omega_a)$, or $\boldsymbol{h} \in \mathcal{H}^{\delta,2}(\Omega_h)$ and $\boldsymbol{a} \in \mathcal{A}^{\delta,1}(\Omega_a)$, we obtain stable results, whereas the other combinations lead to spurious oscillations. As with linear materials, the larger the permeability jump across the coupling interface Γ_{m}, the larger the oscillation amplitude. Also, as already mentioned before, in the large fields involved in T2S system, the (nonlinear) SFM usually saturate rapidly, so that the oscillation amplitude rapidly decreases in practical simulations, even with unstable choices of function spaces.

Generalization to 3D problems

In practice, we observe the same conclusions on 3D problems: enriching one of the two fields gives results that do no present any oscillations.

3.6.2 Thin-shell t-a-formulation

We directly consider a nonlinear material in Γ_w, e.g., a superconducting tape. Including a nonlinear SFM in Ω_a does not raise any additional difficulty. We restrict the analysis to 2D problems with an in-plane magnetic field. With the same procedure as for the h-ϕ-a-formulation, for every iteration k at time step n, we obtain the following discrete linear system for the unknowns $\boldsymbol{t} \in \mathcal{T}_0^\delta(\Gamma_w)$ and $\boldsymbol{a} \in \mathcal{A}_0^\delta(\Omega_a)$,

$$\left(\nu\, \mathbf{curl}\, \boldsymbol{a} \,, \mathbf{curl}\, \boldsymbol{a}'\right)_{\Omega_a} - \left\langle w\, \mathbf{curl}\, \boldsymbol{t} \,, \boldsymbol{a}'\right\rangle_{\Gamma_w} = 0, \tag{3.115}$$

$$-\left\langle w\, \mathbf{curl}\, \boldsymbol{t}' \,, \boldsymbol{a}\right\rangle_{\Gamma_w} - \left\langle \Delta t\, w\, (\partial \boldsymbol{e}/\partial \boldsymbol{j})^{k-1}\, \mathbf{curl}\, \boldsymbol{t} \,, \mathbf{curl}\, \boldsymbol{t}'\right\rangle_{\Gamma_w} = \langle \tilde{\boldsymbol{s}}_{\boldsymbol{t}}, \boldsymbol{t}'\rangle, \tag{3.116}$$

$\forall \boldsymbol{t}' \in \mathcal{T}_0^\delta(\Gamma_w)$ and $\forall \boldsymbol{a}' \in \mathcal{A}_0^\delta(\Omega_a)$, with a right-hand side functional $\tilde{\boldsymbol{s}}_{\boldsymbol{t}}$ defined by,

$$\begin{aligned}\langle \tilde{\boldsymbol{s}}_{\boldsymbol{t}}, \boldsymbol{t}'\rangle = &- \left\langle w\, \boldsymbol{a}_{n-1} \,, \mathbf{curl}\, \boldsymbol{t}'\right\rangle_{\Gamma_w} - \Delta t \sum_{i \in C_V} \bar{V}_i \mathcal{I}_i(\boldsymbol{t}') \\ &+ \left\langle \Delta t\, w\, \left((\rho \mathbf{I} - \partial \boldsymbol{e}/\partial \boldsymbol{j})\, \mathbf{curl}\, \boldsymbol{t}\right)^{k-1} \,, \mathbf{curl}\, \boldsymbol{t}'\right\rangle_{\Gamma_w},\end{aligned} \tag{3.117}$$

$\forall \boldsymbol{t}' \in \mathcal{T}_0^\delta(\Gamma_w)$. As before, the function space notations refer either to the lowest-order spaces or to the enriched spaces.

In $\mathcal{A}_0^\delta(\Omega_a)$, we use the same norm as for the h-ϕ-a-formulation,

$$\|\boldsymbol{a}\|^2_{\mathcal{A}_0^\delta} = \left(\nu_0\, \mathbf{curl}\, \boldsymbol{a} \,, \mathbf{curl}\, \boldsymbol{a}\right)_{\Omega_a}, \tag{3.118}$$

so that we can choose $\alpha^\delta = \inf(\nu/\nu_0) > 0$, and we have $\|a^\delta\| \leq \sup(\nu/\nu_0) < \infty$, whatever the mesh. Therefore, the first diagonal block is coercive and continuous on the whole space.

The inf-sup condition requires to find a $\beta > 0$ independent of the mesh size that fulfils

$$\inf_{\boldsymbol{t} \in (H^\delta)^\perp} \sup_{\boldsymbol{a} \in (K^\delta)^\perp} \frac{\left\langle w\, \mathbf{curl}\, \boldsymbol{t} \,, \boldsymbol{a}\right\rangle_{\Gamma_w}}{\|\boldsymbol{t}\|_{\mathcal{T}_0^\delta} \|\boldsymbol{a}\|_{\mathcal{A}_0^\delta}} = \beta^\delta \geq \beta. \tag{3.119}$$

To evaluate this condition in the discrete setting, it remains to choose a norm for $\boldsymbol{t} \in \mathcal{T}_0^\delta(\Gamma_w)$, as defined in Eq. (3.24). To avoid the evaluation of the fractional $H^{-1/2}(\Gamma_w)$-norm for the field $\boldsymbol{t}$ defined on the surface Γ_w, we use a mesh-dependent norm, as is common in the discrete setting [171]. We assume a uniform mesh on Γ_w, for which there exists a δ and two finite non-zero constants c_1 and c_2 such that $c_1 \delta \leq \delta_e \leq c_2 \delta$, $\forall e \in \mathcal{E}(\Gamma_w)$, where δ_e is the length of edge e. For a given mesh length δ, we define

$$\|\boldsymbol{t}\|^2_{\mathcal{T}_0^\delta} = \delta \left\langle w\, \Delta t_0\, \rho_0\, \mathbf{curl}\, \boldsymbol{t} \,, \mathbf{curl}\, \boldsymbol{t}\right\rangle_{\Gamma_w}, \tag{3.120}$$

with Δt_0 and ρ_0 being characteristic time step and resistivity values. The inverse inequality [190]

$$\|\mu\|_{H^{-1/2}(\Gamma)} \geq c\sqrt{\delta}\|\mu\|_{L^2(\Gamma)}, \quad \forall \mu \in H^{-1/2}(\Gamma), \tag{3.121}$$

with a finite constant c, implies that satisfying the inf-sup condition with norm (3.120) is a necessary condition for stability in terms of the norm $\|\cdot\|_{H^{-1/2}(\Gamma_w)}$. In [191], the condition is also shown to be sufficient.

Fig. 3.20 gives the evolution of the inf-sup constant for a sequence of progressively refined meshes, for four choices of function spaces. Analogously to the h-ϕ-a-formulation, it is only when exactly one approximation space is enriched with hierarchical elements that the inf-sup constant is uniformly bounded from below. These choices are good candidates if we want a stable formulation. On the other hand, when choosing $\boldsymbol{t} \in \mathcal{T}_0^{\delta,1}(\Gamma_w)$ and $\boldsymbol{a} \in \mathcal{A}_0^{\delta,1}(\Omega_a)$, or $\boldsymbol{t} \in \mathcal{T}_0^{\delta,2}(\Gamma_w)$ and $\boldsymbol{a} \in \mathcal{A}_0^{\delta,2}(\Omega_a)$, the test suggests that stability issues may arise. In practice, this is indeed the case, see Fig. 3.12.

We observed that with the choice $\boldsymbol{t} \in \mathcal{T}_0^{\delta,2}(\Gamma_w)$ and $\boldsymbol{a} \in \mathcal{A}_0^{\delta,1}(\Omega_a)$, the Newton-Raphson procedure faces convergence issues. Using a fixed point method does not help either, and no satisfying numerical solution has been found in the nonlinear case. On the other hand, when considering a linear conductor, no particular issue is encountered and oscillations disappear, as expected from the inf-sup test. We therefore believe that the issue for nonlinear materials is related to the iterative technique rather than to the structure of the saddle-point problem. Investigating this phenomenon would constitute an instructive further work.

By contrast, the choice $\boldsymbol{t} \in \mathcal{T}_0^{\delta,1}(\Gamma_w)$ and $\boldsymbol{a} \in \mathcal{A}_0^{\delta,2}(\Omega_a)$ provides good results and no issue has been observed. Our results match the observations in [192], where the function space for $\boldsymbol{a}$ is however enriched in the whole Ω_a domain, instead of only in the vicinity of Γ_w. This is more expensive in terms of computational work for a given mesh, but also offers a more accurate representation of the magnetic flux density in Ω_a.

To prove formally the stability of the choice $\boldsymbol{t} \in \mathcal{T}_0^{\delta,1}(\Gamma_w)$ and $\boldsymbol{a} \in \mathcal{A}_0^{\delta,2}(\Omega_a)$, we have to prove coercivity of $c(\cdot,\cdot)$ on the kernel H^δ, as well as continuity of bilinear operators $b(\cdot,\cdot)$ and $c(\cdot,\cdot)$. For the coercivity on the kernel H^δ, we note that with the particular choice $\boldsymbol{t} \in \mathcal{T}_0^{\delta,1}(\Gamma_w)$ and $\boldsymbol{a} \in \mathcal{A}_0^{\delta,2}(\Omega_a)$, H^δ reduces to 0, so the coercivity condition is trivially satisfied. A priori estimates for $\|b^\delta\|$ and $\|c^\delta\|$ cannot be obtained easily with the fractional norm $\|\cdot\|_{H^{-1/2}(\Gamma_w)}$. These properties are not investigated in this work.

To conclude, extending to spaces with non-homogeneous essential boundary conditions, we recommend choosing $\boldsymbol{t} \in \mathcal{T}^{\delta,1}(\Gamma_w)$ and $\boldsymbol{a} \in \mathcal{A}^{\delta,2}(\Omega_a)$. This choice ensures a bounded inf-sup value and does not exhibit any stability issues. We observe that this is also valid in 3D problems.

3.6.3 Volume-coupled h-ϕ-b-formulation

The volume-coupled h-ϕ-b-formulation does not exhibit any stability issues for the function spaces that have been introduced in Section 3.4.3. We analyze here the well-posedness of the formulation.

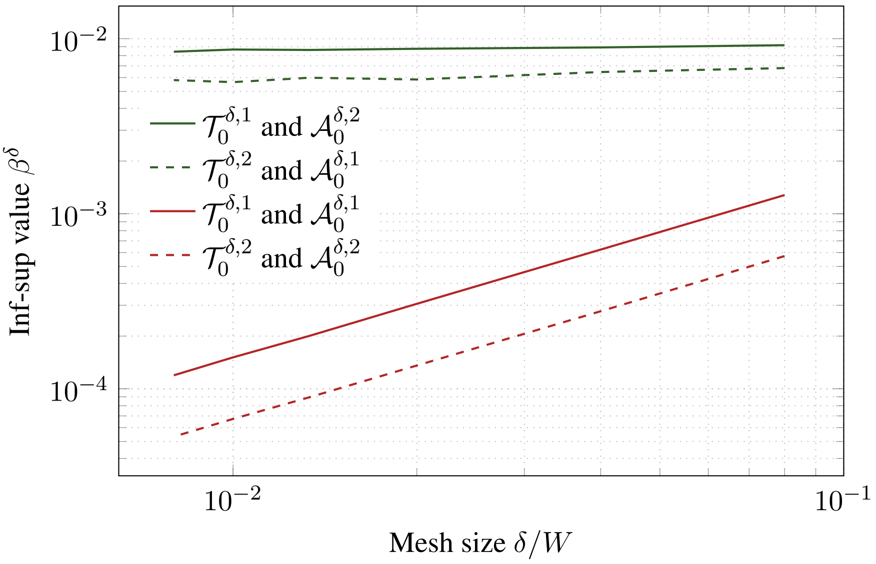

Figure 3.20: Evolution of the inf-sup constant with mesh refinement ($\delta \to 0$) on the simple tape problem ($n = 20$, $j_\text{c} = 2.5 \times 10^{10}$ A/m^2). Four cases are considered $\boldsymbol{t} \in \mathcal{T}_0^{\delta,i}(\Omega_h)$ and $\boldsymbol{a} \in \mathcal{A}_0^{\delta,j}(\Omega_a)$, for $(i,j) \in \{1,2\} \times \{1,2\}$. We observe instabilities when $i = j$. In practice, the usual Newton-Raphson scheme with $i = 2$, $j = 1$ does not converge. Only the case $i = 1$, $j = 2$ leads to satisfying results.

For simplicity and conciseness, we consider linear materials. As before, we also assume homogeneous essential boundary conditions in the developments, the generalization to the non-homogeneous case being immediate. At each time step n, the h-ϕ-b-formulation can be written as: find $\boldsymbol{h} \in \mathcal{H}_0^{\delta,1}(\Omega)$ and $\boldsymbol{b} \in \mathcal{B}_0^{\delta,1}(\Omega_\text{m})$ such that

$$(\mu_0\, \boldsymbol{h}\, , \boldsymbol{h}')_{\Omega_\text{m}^\text{C}} + (\Delta t\, \rho\, \textbf{curl}\, \boldsymbol{h}\, , \textbf{curl}\, \boldsymbol{h}')_{\Omega_\text{c}} + (\boldsymbol{b}\, , \boldsymbol{h}')_{\Omega_\text{m}} = \langle \boldsymbol{s}\, , \boldsymbol{h}' \rangle\, , \tag{3.122}$$

$$(\boldsymbol{h}\, , \boldsymbol{b}')_{\Omega_\text{m}} - (\nu\, \boldsymbol{b}\, , \boldsymbol{b}')_{\Omega_\text{m}} = 0, \tag{3.123}$$

$\boldsymbol{h}' \in \mathcal{H}_0^{\delta,1}(\Omega)$ and $\boldsymbol{b}' \in \mathcal{B}_0^{\delta,1}(\Omega_\text{m})$. The right-hand side functional $\boldsymbol{s}$ is defined by

$$\langle \boldsymbol{s}\, , \boldsymbol{h}' \rangle = (\mu_0\, \boldsymbol{h}_{n-1}\, , \boldsymbol{h}')_{\Omega_\text{m}^\text{C}} + (\boldsymbol{b}_{n-1}\, , \boldsymbol{h}')_{\Omega_\text{m}} + \Delta t \sum_{i \in C_V} \bar{V}_i \mathcal{I}_i(\boldsymbol{h}'), \tag{3.124}$$

$\boldsymbol{h}' \in \mathcal{H}_0^{\delta,1}(\Omega)$, with $\boldsymbol{h}_{n-1}$ and $\boldsymbol{b}_{n-1}$ being the solutions at the previous time step. This problem has the form of a perturbed saddle point problem (3.54)-(3.55).

In $\mathcal{H}_0^{\delta,1}(\Omega)$ and $\mathcal{B}_0^{\delta,1}(\Omega_\text{m})$, we define the norms

$$\|\boldsymbol{h}\|^2_{\mathcal{H}_0^{\delta,1}} = (\mu_0\, \boldsymbol{h}\, , \boldsymbol{h})_\Omega + (\Delta t_0\, \rho_0\, \textbf{curl}\, \boldsymbol{h}\, , \textbf{curl}\, \boldsymbol{h})_{\Omega_\text{c}}\, , \tag{3.125}$$

$$\|\boldsymbol{b}\|^2_{\mathcal{A}_0^{\delta,1}} = (\nu_0\, \boldsymbol{b}\, , \boldsymbol{b})_{\Omega_\text{m}}\, , \tag{3.126}$$

with Δt_0 and ρ_0 being characteristic time step and resistivity values. With these norm definitions, the lower diagonal bilinear operator $c(\boldsymbol{b}_1, \boldsymbol{b}_2) = (\nu\, \boldsymbol{b}_1\, , \boldsymbol{b}_2)_{\Omega_\text{m}}$ is trivially coercive and continuous, provided that $\nu > 0$. It is also symmetric and positive-definite. On the other hand, the upper diagonal $a(\boldsymbol{h}_1, \boldsymbol{h}_2) = (\mu_0\, \boldsymbol{h}_1\, , \boldsymbol{h}_2)_{\Omega_\text{m}^\text{C}} + (\Delta t\, \rho\, \textbf{curl}\, \boldsymbol{h}_1\, , \textbf{curl}\, \boldsymbol{h}_2)_{\Omega_\text{c}}$ is continuous but not coercive on the whole space $\mathcal{H}_0^{\delta,1}(\Omega)$. Indeed, for any curl-free field $\boldsymbol{h}$ whose support is on

Ω_m only, we have $a(\boldsymbol{h},\boldsymbol{h}) = 0$. Therefore, one cannot use directly the Lax-Milgram theorem for solvability, nor the bounds of Eq. (3.74) for stability.

Instead, we will verify the coercivity of $a(\cdot,\cdot)$ on the kernel K^δ and the inf-sup condition on the coupling operator $b(\cdot,\cdot)$.

By definition, the kernel K^δ is the set of elements $\boldsymbol{h}_0 \in \mathcal{H}_0^{\delta,1}(\Omega)$ that verify

$$(\boldsymbol{b}\,,\boldsymbol{h}_0)_{\Omega_\mathrm{m}} = 0, \quad \forall \boldsymbol{b} \in \mathcal{B}_0^{\delta,1}(\Omega_\mathrm{m}). \tag{3.127}$$

Because $\mathcal{B}_0^{\delta,1}(\Omega_\mathrm{m})$ contains the restriction of all individual elements in $\mathcal{H}_0^{\delta,1}(\Omega)$ to Ω_m, elements $\boldsymbol{h}_0$ in the kernel K^δ must be identically equal to zero in Ω_m. Therefore, the kernel expresses as

$$K^\delta = \{\boldsymbol{h}_0 \in \mathcal{H}_0^{\delta,1}(\Omega) \ : \ \boldsymbol{h}_0|_{\Omega_\mathrm{m}} = \boldsymbol{0}\}. \tag{3.128}$$

Consequently, $\forall \boldsymbol{h}_0 \in K^\delta$, we have

$$\begin{aligned} a(\boldsymbol{h}_0,\boldsymbol{h}_0) &= (\mu_0\,\boldsymbol{h}_0\,,\boldsymbol{h}_0)_{\Omega_\mathrm{m}^\mathrm{C}} + (\Delta t\,\rho\,\mathbf{curl}\,\boldsymbol{h}_0\,,\mathbf{curl}\,\boldsymbol{h}_0)_{\Omega_\mathrm{c}} \\ &= (\mu_0\,\boldsymbol{h}_0\,,\boldsymbol{h}_0)_{\Omega} + (\Delta t\,\rho\,\mathbf{curl}\,\boldsymbol{h}_0\,,\mathbf{curl}\,\boldsymbol{h}_0)_{\Omega_\mathrm{c}} \\ &= \|\boldsymbol{h}_0\|^2_{\mathcal{H}_0^{\delta,1}}, \end{aligned} \tag{3.129}$$

so that coercivity condition Eq. (3.75) is verified on K^δ.

The inf-sup expression reads

$$\inf_{\boldsymbol{h}\in(K^\delta)^\perp}\ \sup_{\boldsymbol{b}\in(H^\delta)^\perp} \frac{(\boldsymbol{h}\,,\boldsymbol{b})_{\Omega_\mathrm{m}}}{\|\boldsymbol{h}\|_{\mathcal{H}_0^{\delta,1}}\|\boldsymbol{b}\|_{\mathcal{B}_0^{\delta,1}}}. \tag{3.130}$$

To evaluate it, we carry out an inf-sup test on a simple 2D problem of a rectangular magnetic bar, placed in air, as represented in Fig. 3.21. The results are shown in Fig. 3.22 for four cases: triangular or quadrangular mesh, and conducting or non-conducting magnetic domain Ω_m.

When Ω_m is non-conducting, for both meshes, the inf-sup values β^δ are nearly constant and do not approach zero as the mesh is refined. The inf-sup test is successfully passed. This result is further strengthened by the absence of non-physical oscillations in the numerical solution. The spaces $\mathcal{H}_0^{\delta,1}(\Omega)$ and $\mathcal{B}_0^{\delta,1}(\Omega_\mathrm{m})$ can be confidently considered to be stable choices for the h-ϕ-b-formulation with a non-conducting magnetic domain.

When Ω_m is conducting, for both meshes, the inf-sup values β^δ decrease as $\beta^\delta \sim \delta$, and the inf-sup test fails. We have no guarantee that the choices $\mathcal{H}_0^{\delta,1}(\Omega)$ and $\mathcal{B}_0^{\delta,1}(\Omega_\mathrm{m})$ lead to a stable h-ϕ-b-formulation. In practice, however, no particular issue has been observed on the tested cases, and the numerical solution to the h-ϕ-b-formulation matches that of the standard formulations.

Interpretation in the non-conducting case

It can be instructive to work out the inf-sup expression (3.130) in the non-conducting case, i.e., when $\Omega_\mathrm{m} \subset \Omega_\mathrm{c}^\mathrm{C}$. For simplicity, let us also consider that the conducting domain Ω_c is empty so that $\boldsymbol{h}$ is described everywhere as a gradient.

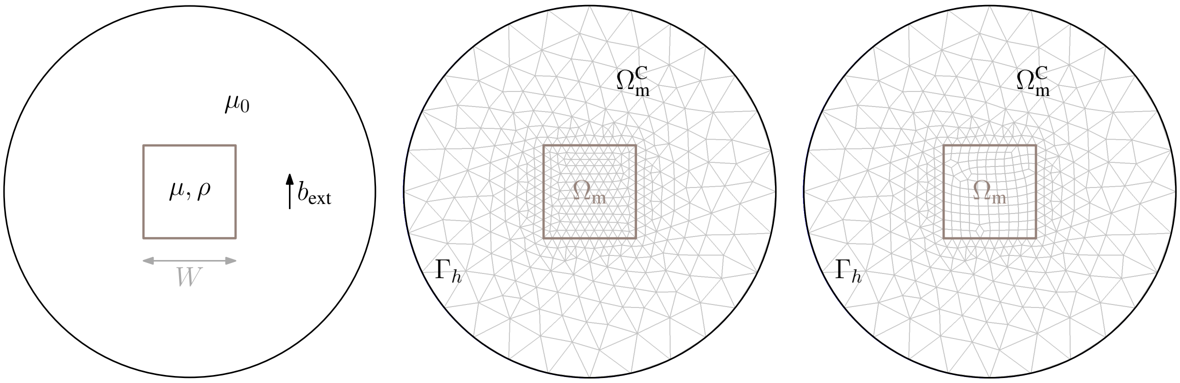

(a) Problem geometry. (b) Simplicial mesh. (c) Quadrangular mesh in Ω_{m}.

Figure 3.21: Simple 2D geometry for the inf-sup test on the h-ϕ-b-formulation. It consists of a magnetic bar with relative permeability $\mu_{\text{r}} = 10^3$ surrounded by air. If the magnetic bar is conducting, $\rho = 1.7 \times 10^{-8}$ Ωm. The cross-section of the bar is a square of side W. (a) The problem geometry and parameters. (b) A triangular mesh for the whole domain. (c) A hybrid mesh with triangles in $\Omega_{\text{m}}^{\text{C}}$ and quadrangles in Ω_{m}.

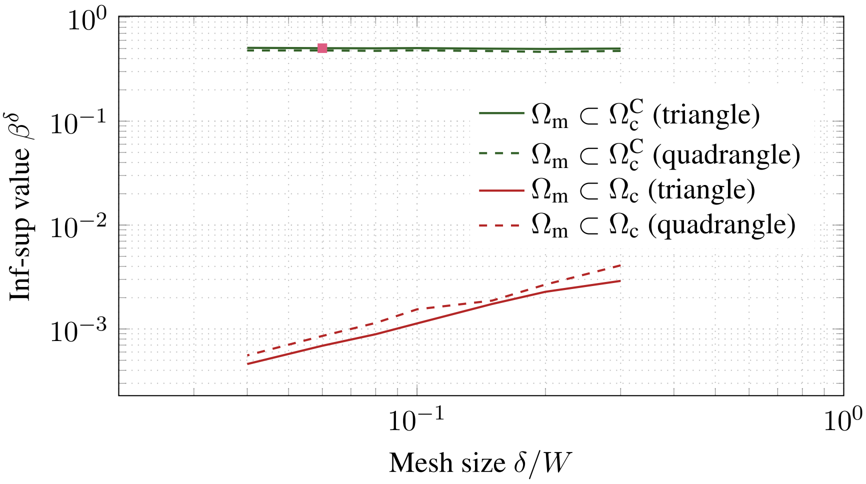

Figure 3.22: Evolution of the inf-sup values with mesh refinement ($\delta \to 0$) on the simple 2D magnetic bar problem ($\mu_{\text{r}} = 10^3$), for $\mathcal{H}_0^{\delta,1}(\Omega)$ and $\mathcal{B}_0^{\delta,1}(\Omega_{\text{m}})$. Four cases are considered: triangular or quadrangular mesh, and conducting ($\rho = 1.7 \times 10^{-8}$ Ωm) or non-conducting magnetic domain Ω_{m}. The inf-sup test fails in the conducting case, even if in practice, no stability issue is observed.

We notice that, for any $\boldsymbol{h} \in \mathcal{H}_0^{\delta,1}(\Omega)$, it is possible to choose a particular $\boldsymbol{b} \in \mathcal{B}_0^{\delta,1}(\Omega_{\text{m}})$ that is exactly equal to $\boldsymbol{h}$ everywhere in Ω_{m}, i.e., such that $\boldsymbol{b} = \mu_0 \boldsymbol{h}|_{\Omega_{\text{m}}}$. Hence, by choosing this magnetic flux density, we can rewrite the inf-sup expression as follows:

$$\begin{aligned}\inf_{\boldsymbol{h}\in(K^\delta)^\perp}\ \sup_{\boldsymbol{b}\in(H^\delta)^\perp} \frac{(\boldsymbol{h}\,,\boldsymbol{b})_{\Omega_\mathrm{m}}}{\|\boldsymbol{h}\|_{\mathcal{H}_0^{\delta,1}}\|\boldsymbol{b}\|_{\mathcal{B}_0^{\delta,1}}} &\geq \inf_{\boldsymbol{h}\in(K^\delta)^\perp} \frac{(\boldsymbol{h}\,,\mu_0\boldsymbol{h}|_{\Omega_\mathrm{m}})_{\Omega_\mathrm{m}}}{\|\boldsymbol{h}\|_{\mathcal{H}_0^{\delta,1}}\ \|\mu_0\boldsymbol{h}|_{\Omega_\mathrm{m}}\|_{\mathcal{B}_0^{\delta,1}}}\\ &= \inf_{\boldsymbol{h}\in(K^\delta)^\perp} \frac{(\boldsymbol{h}\,,\mu_0\boldsymbol{h}|_{\Omega_\mathrm{m}})_{\Omega_\mathrm{m}}}{\sqrt{(\mu_0\boldsymbol{h}\,,\boldsymbol{h})_\Omega}\sqrt{(\nu_0\mu_0\boldsymbol{h}|_{\Omega_\mathrm{m}}\,,\mu_0\boldsymbol{h}|_{\Omega_\mathrm{m}})_{\Omega_\mathrm{m}}}}\\ &= \inf_{\boldsymbol{h}\in(K^\delta)^\perp} \sqrt{\frac{(\mu_0\boldsymbol{h}\,,\boldsymbol{h})_{\Omega_\mathrm{m}}}{(\mu_0\boldsymbol{h}\,,\boldsymbol{h})_\Omega}},\end{aligned} \tag{3.131}$$

so that the inf-sup value cannot be smaller than the last infimum. If $\Omega_\mathrm{m} = \Omega$, the infimum is equal to one and this proves the stability. But in the general case, Ω_m does not cover Ω and computing the value of the infimum is not trivial, due to the fact that $\boldsymbol{h}$ is chosen in the orthogonal complement of the discrete kernel K^δ, given by Eq. (3.128). Of course, this is the reason why the numerical inf-sup test for evaluating the inf-sup expression (3.130) is helpful in practice. Here, we just want to look at the result of the generalized eigenvalue problem in the light of the simplification of Eq. (3.131).

For illustration, Fig. 3.23 gives the distribution of eigenvalues for the mesh size $\delta = 0.06W$, which corresponds to the square point in Fig. 3.22, and Fig. 3.24 shows the scalar potential of the eigenvectors associated with the three selected eigenvalues in Fig. 3.23. For comparison, eigenvalues for the conducting magnetic bar are also represented.

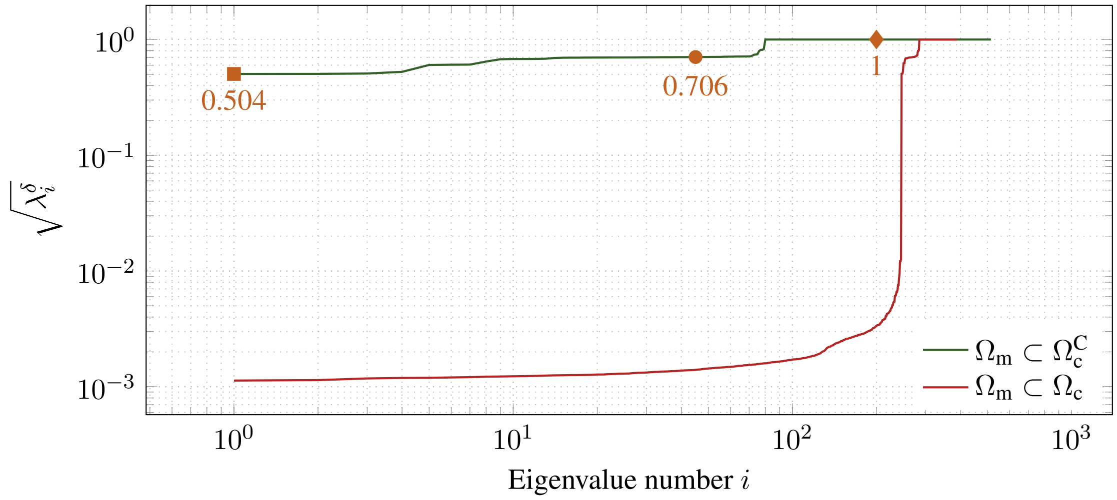

Figure 3.23: Distribution of the square root of the non-zero eigenvalues computed from Eq. (3.88) on the simple magnetic bar geometry for the h-ϕ-b-formulation and the choice $\boldsymbol{h} \in \mathcal{H}_0^{\delta,1}(\Omega)$ and $\boldsymbol{b} \in \mathcal{B}_0^{\delta,1}(\Omega_\mathrm{m})$ on a triangular mesh in two cases. The smallest values are the inf-sup value β^δ. Eigenvectors associated with the highlighted points are represented in Fig. 3.24. The mesh for the conducting and non-conducting cases were not the same.

For the eigenvectors illustrated in Fig. 3.24, one can approximate the expression

$$\sqrt{\frac{(\mu_0\boldsymbol{h}\,,\boldsymbol{h})_{\Omega_\mathrm{m}}}{(\mu_0\boldsymbol{h}\,,\boldsymbol{h})_\Omega}}, \tag{3.132}$$

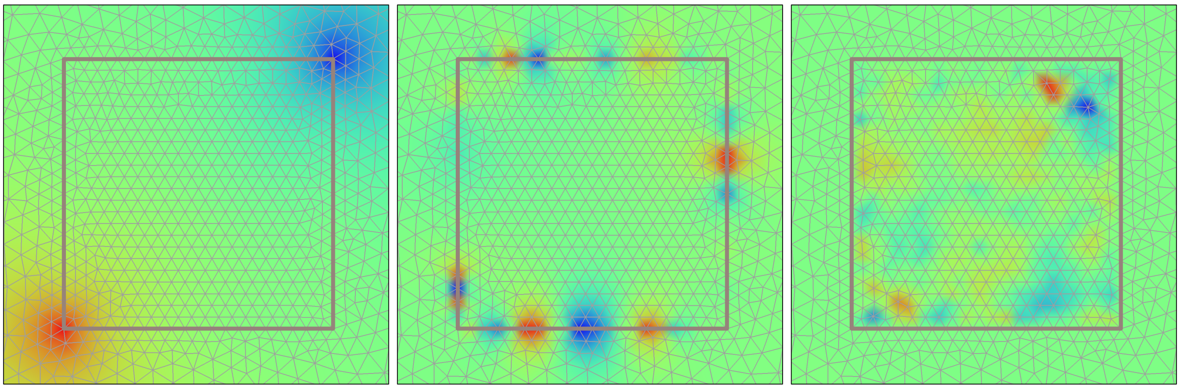

(a) $\phi_{\perp,1}$, $\sqrt{\lambda_1^\delta} \approx 1/2$. (b) $\phi_{\perp,45}$, $\sqrt{\lambda_{45}^\delta} \approx \sqrt{2}/2$. (c) $\phi_{\perp,200}$, $\sqrt{\lambda_{200}^\delta} = 1$.

Figure 3.24: Scalar potentials $\phi_{\perp,i}$ of the eigenvectors $\boldsymbol{h}_{\perp,i} = \mathbf{grad}\ \phi_{\perp,i}$ associated with the highlighted eigenvalues in Fig. 3.23 for a non-conducting magnetic material. The brown curves delimit Ω_m (inside) and $\Omega_\mathrm{m}^\mathrm{C}$ (outside). The colormap is: -1 (blue), 0 (green), +1 (red).

arising in the lower bound for the inf-sup constant in Eq. (3.131). For the first eigenvector, large gradients of the scalar potential $\phi_{\perp,1}$ are located in the vicinity of (two) right corners of the boundary $\partial\Omega_\mathrm{m}$ in this particular geometry, such that, in a first approximation,

$$(\mu_0\, \mathbf{grad}\ \phi_{\perp,1}\ , \mathbf{grad}\ \phi_{\perp,1})_{\Omega_\mathrm{m}} \approx 1/4\, (\mu_0\, \mathbf{grad}\ \phi_{\perp,1}\ , \mathbf{grad}\ \phi_{\perp,1})_{\Omega}\,, \tag{3.133}$$

so that having $\sqrt{\lambda_1^\delta} \approx 1/2$ is not surprising. Note that modes $\boldsymbol{h}_{\perp,i} \in (K^\delta)^\perp$ must be harmonic in $\Omega_\mathrm{m}^\mathrm{C}$ to be orthogonal to functions in K^δ, in particular[4]. For the 45th eigenvector, the field is almost symmetric on both sides of $\partial\Omega_\mathrm{m}$, so that

$$(\mu_0\, \mathbf{grad}\ \phi_{\perp,45}\ , \mathbf{grad}\ \phi_{\perp,45})_{\Omega_\mathrm{m}} \approx 1/2\, (\mu_0\, \mathbf{grad}\ \phi_{\perp,45}\ , \mathbf{grad}\ \phi_{\perp,45})_{\Omega}\,. \tag{3.134}$$

Such modes are associated with the plateau in Fig. 3.23 around level $\approx \sqrt{2}/2$. Finally, the 200th eigenvector is equal to zero in $\Omega_\mathrm{m}^\mathrm{C}$, so that

$$(\mu_0\, \mathbf{grad}\ \phi_{\perp,200}\ , \mathbf{grad}\ \phi_{\perp,200})_{\Omega_\mathrm{m}} = (\mu_0\, \mathbf{grad}\ \phi_{\perp,200}\ , \mathbf{grad}\ \phi_{\perp,200})_{\Omega}\,, \tag{3.135}$$

and Eq. (3.132) is equal to one. These last modes that are internal to Ω_m are associated with unit eigenvalues.

Interpretation in the conducting case

In the conducting case, the magnetic field can no longer be expressed as a gradient if the current density is non-zero. The inf-sup expression now involves a curl-curl term in the denominator:

$$\inf_{\boldsymbol{h}\in(K^\delta)^\perp} \sup_{\boldsymbol{b}\in(H^\delta)^\perp} \frac{(\boldsymbol{h}\ , \boldsymbol{b})_{\Omega_\mathrm{m}}}{\sqrt{(\mu_0\, \boldsymbol{h}\ , \boldsymbol{h})_\Omega + (\Delta t_0\, \rho_0\, \mathbf{curl}\ \boldsymbol{h}\ , \mathbf{curl}\ \boldsymbol{h})_{\Omega_\mathrm{c}}}\sqrt{(\nu_0\, \boldsymbol{b}\ , \boldsymbol{b})_{\Omega_\mathrm{m}}}}. \tag{3.136}$$

---

[4] The orthogonality condition for the elements $\boldsymbol{h}_\perp = \mathbf{grad}\ \phi_\perp$ of $(K^\delta)^\perp$ with respect to those in the kernel K^δ is the weak form of a Laplace problem for the scalar potential $\phi_\perp$ in $\Omega_\mathrm{m}^\mathrm{C}$, with a zero net flux across $\partial\Omega_\mathrm{m}$ as a boundary condition.

Fields $\boldsymbol{h} \in (K^\delta)^\perp$ with a large curl but a small support in Ω_m will contribute to small value of the fraction. As the mesh is refined, Fig. 3.22 shows that the values associated with these fields become smaller and smaller.

3.6.4 Volume-coupled a-j-formulation

The volume-coupled a-j-formulation does not exhibit any stability issue for the function spaces that have been introduced in Section 3.4.4. In practice, as already mentioned, problems involving a source electric field $\boldsymbol{e}_\mathrm{a}$ are however ill-conditioned and the resolution of the resulting linear systems is not an easy task. This will be further illustrated in the next chapter.

In this section, we briefly justify the well-posedness of the a-j-formulation. Let us first consider the situation without a source field $\boldsymbol{e}_\mathrm{a}$. In this case, the a-j-formulation reduces to

$$(\nu\, \mathbf{curl}\, \boldsymbol{a} \,, \mathbf{curl}\, \boldsymbol{a}')_\Omega - (\boldsymbol{j} \,, \boldsymbol{a}')_{\Omega_\mathrm{c}} = 0, \tag{3.137}$$

$$-(\boldsymbol{a} \,, \boldsymbol{j}')_{\Omega_\mathrm{c}} - (\Delta t \rho\, \boldsymbol{j} \,, \boldsymbol{j}')_{\Omega_\mathrm{c}} = -(\boldsymbol{a}_{n-1} \,, \boldsymbol{j}')_{\Omega_\mathrm{c}} \,. \tag{3.138}$$

As for the other mixed formulations, with homogeneous essential boundary conditions, this formulation has the structure of the perturbed saddle-point problem (3.54)-(3.55). In terms of the norms

$$\|\boldsymbol{a}\|^2_{\mathcal{A}_0^{\delta,1}} = (\nu_0\, \mathbf{curl}\, \boldsymbol{a} \,, \mathbf{curl}\, \boldsymbol{a})_\Omega \,, \tag{3.139}$$

$$\|\boldsymbol{j}\|^2_{\mathcal{J}_0^{\delta,1}} = (\Delta t_0\, \rho_0\, \boldsymbol{j} \,, \boldsymbol{j})_{\Omega_\mathrm{c}} \,, \tag{3.140}$$

the diagonal operators $a(\cdot,\cdot)$ and $c(\cdot,\cdot)$ are coercive and continuous. The Lax-Milgram theorem implies solvability, and Eq. (3.74) gives a bound on the solution. Because we have not observed any stability issue in the tested examples in this work, other than the difficulties with a source electric field, that we believe are not associated with the structure of the saddle-point problem, we do no pursue the analysis further.

Note that in the full formulation, the source electric field $\boldsymbol{e}_{\mathrm{a},i}$ can be seen as a Lagrange multiplier for imposing a given current intensity $\bar{I}_i$ in the conducting domain Ω_{c_i}, with $i \in C_I$:

$$(\nu\, \mathbf{curl}\, \boldsymbol{a} \,, \mathbf{curl}\, \boldsymbol{a}')_\Omega - (\boldsymbol{j} \,, \boldsymbol{a}')_{\Omega_\mathrm{c}} = 0, \tag{3.141}$$

$$(\partial_t \boldsymbol{a} \,, \boldsymbol{j}')_{\Omega_\mathrm{c}} + (\rho\, \boldsymbol{j} \,, \boldsymbol{j}')_{\Omega_\mathrm{c}} + (\boldsymbol{e}_\mathrm{a} \,, \boldsymbol{j}')_{\Omega_\mathrm{c}} = 0, \tag{3.142}$$

$$(\boldsymbol{j} \,, \boldsymbol{e}'_\mathrm{a})_{\Omega_\mathrm{c}} = -\sum_{i\in C_I} \bar{I}_i \mathcal{V}_i(\boldsymbol{e}'_\mathrm{a}). \tag{3.143}$$

3.7 Summary

In this chapter, we proposed four different mixed finite element formulations suited for modeling systems with T2S and SFM, or thin superconducting tapes. We also described their space discretization, taking care of verifying the stability conditions associated with the resulting perturbed saddle-point problems. In particular, the surface-coupled h-ϕ-a and t-a-formulations present numerical oscillations if the discrete function spaces are not chosen properly. Stability is obtained by a local enrichment of the function space of one of the two fields involved in these formulations.

The four mixed formulations introduced here in addition to the two standard formulations presented in Chapter 2 offer a large variety of possibilities for modeling systems with T2S. Mainly because of the nonlinearity of the equations, all choices are however not equivalent. It is the aim of the next chapter to compare the numerical performances of the different formulations, with the objective of determining general recommendations on which formulation to choose for different types of problems.

Chapter 4

Numerical performance of the formulations

In this chapter, we compare the performance of the standard and mixed formulations presented in the Chapters 2 and 3, on different test cases. The performance of a formulation is evaluated in terms of its *accuracy* and *efficiency*.

The *accuracy* of a formulation is its ability to produce accurate numerical results when applied on a discrete problem. A formulation is said to be accurate if the resulting numerical solution is *satisfyingly close* to the solution of the continuous equations. A direct comparison with analytical solutions is only possible when the said solutions are known; in the context of type-II superconductors (T2S), this is rarely the case. When this is not possible, we rather compare the solutions of different formulations with each other, for progressively refined meshes and time discretization levels. We then rely on the extensive literature on standard and mixed formulations, both for linear materials and T2S, to consider that these fine numerical solutions can be taken as reference solutions.

We refer to this approach as the verification of the formulations, by contrast with a validation of the models, that would involve comparing numerical results and experimental measurements.

The *efficiency* of a formulation is related to its abillity to provide accurate results in a small number of evaluations, or in a small amount of time. Problems with T2S are nonlinear, so a first indicator for efficiency is the total number of iterations that is needed to obtain an accurate solution. Moreover, as the spatial discretization for different formulations does not necessarily involve similar numbers of degrees of freedom, the size of the system to be solved at each iteration is not identical for all formulations. This is especially relevant in 3D problems [57]. In addition to the number of iterations, we therefore also compare the computational time associated with each resolution.

Note that the objective of this work is not to propose high-performance resolutions of systems with T2S, but rather to compare the relative performance of different approaches and formulations. As we implemented all the formulations in the same software, the open-source finite element solver GetDP [59], we believe this comparison is fair for obtaining relative performance indicators. We have not considered more recent and efficient finite element libraries such as Gmsh-Fem [193], that could be used to improve the absolute efficiency of the methods. Such a consideration would constitute an interesting further work. For example, the assembly step and the convergence criterion evaluation are, in the current implementation, two computationally expensive tasks that can be improved by parallelization.

In this work, all models and formulations are implemented in GetDP [59]. The geometry and mesh generation is performed by Gmsh [60]. Both GetDP and Gmsh are open-source software. Also, the models presented in this chapter constitute the main part of the open-source Life-HTS toolkit [194] and are available online[1].

In this chapter, we consider problems of increasing complexity. In Section 4.1, we illustrate the main features of the two standard formulations on a simple 1D problem with a T2S bar. In particular, we describe the consequences of the power law shape on the numerical performance. As will be shown later, most observations made in this 1D problem can be generalized to problems in higher dimensions.

In Section 4.2, we extend the conclusions to a 2D axisymmetric T2S system subjected to an applied field, and we test the a-j-formulation, that proves to be an efficient choice for T2S modelling in 2D. In Section 4.3, we consider the 2D problem of a single T2S tape with an imposed current intensity. In particular, we apply the t-a-formulation. In Sections 4.4 and 4.5 we consider 2D and 3D problems involving both T2S and anhysteretic ferromagnetic materials (SFM). We illustrate the advantages of using dedicated mixed formulations.

We summarize the observations and give practical recommendations in Section 4.6. As will be shown, no formulation performs better than all other ones in all test cases. The best formulation in terms of accuracy and efficiency is problem-dependent.

4.1 T2S slab (1D)

We start the analysis with a simple 1D problem. It consists of an infinite superconducting slab of width W, subjected to an applied magnetic flux density $\boldsymbol{b}_\text{s}$. The direction of the applied field is parallel to the slab. The geometry is infinite along the applied field direction, so there is no demagnetizing field. Consequently, only the magnetic field inside the slab is unknown and only the slab must be meshed.

A Cartesian coordinate system (x, y, z) is defined such that the symmetry plane at the half-width of the slab coincides with the (y, z)-plane, with the applied field along the z-direction as illustrated in Fig. 4.1. The magnetic field distribution inside the material only depends on x and the original problem reduces to a one-dimensional problem. As the problem is symmetric, we only model one half of the slab.

For this problem, we consider the two standard formulations: the h-ϕ and the a-formulations. The objective is to highlight the impact of using the power law in terms of the resistivity or in terms of the conductivity. Mixed formulations will be investigated later. For the h-ϕ-formulation, one layer of quadrangular elements is considered, as depicted in orange in Fig. 4.1,

---

[1] Available online at `www.life-hts.uliege.be`.

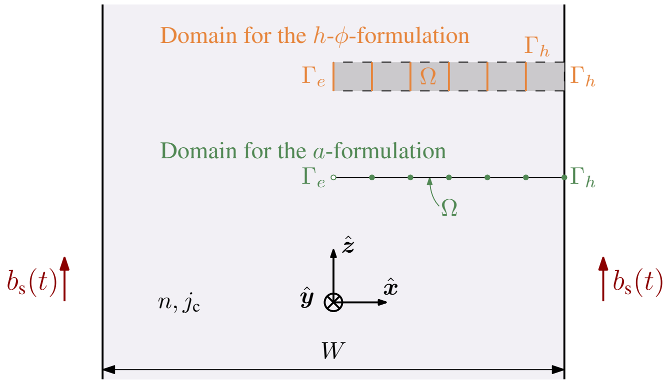

Figure 4.1: Superconducting slab problem and domain definition for the two standard formulations. Degrees of freedom for the h-ϕ-formulation are associated with the vertical edges, minus the rightmost one. Degrees of freedom for the a-formulation are associated with the nodes, minus the leftmost one.

to build a 1D-like problem on a rectangular domain $\Omega = \Omega_\mathrm{c}$. On the top and bottom boundaries of the domain, we have $\boldsymbol{h} \times \boldsymbol{n} = \boldsymbol{0}$, and degrees of freedom associated with edges on these boundaries are fixed to zero. On the rightmost edge, we impose the essential condition $\boldsymbol{h}\times\boldsymbol{n}|_{\Gamma_h} = \nu_0 \boldsymbol{b}_\mathrm{s}$. On the leftmost edge, we impose the natural symmetry condition $\boldsymbol{e}\times\boldsymbol{n}|_{\Gamma_e} = \boldsymbol{0}$.

For the a-formulation, a segment of line elements is considered as a 1D domain, as depicted in green in Fig. 4.1. The vector potential is supported by perpendicular edge functions associated with the nodes of the domain. On the leftmost node, we impose the essential symmetry condition $\boldsymbol{a} \times \boldsymbol{n}|_{\Gamma_e} = \boldsymbol{0}$. On the rightmost node, we impose the natural boundary condition $\boldsymbol{h} \times \boldsymbol{n}|_{\Gamma_h} = \nu_0 \boldsymbol{b}_\mathrm{s}$.

In this section, we first verify the implementation against an approximate analytical solution, and we compare the numerical results of both formulations in terms of accuracy. We then briefly discuss the possibility of using large time steps in some situations. Finally, we conclude by comparing the formulations in terms of their efficiency. We will see that we reproduce the results that were predicted in Section 2.7.2 by models with a single degree of freedom.

4.1.1 Verification with a scaling solution

The magnetic field in a zero-field cooled slab subjected to a linearly increasing applied field obeys a scaling equation. An approximate solution to this scaling equation is proposed in [95]. For information, it is presented in Section B.4 in Appendix. The validity of the approximate solution is limited to the first flux penetration and breaks down when the front reaches the symmetry line [95]. In this section, we verify the implementation of the two standard finite element formulations on this 1D problem.

The superconducting slab is described by a power law with the constant values $n = 40$ and $j_\mathrm{c} = 3 \times 10^8$ A/m^2. We apply a linear ramp of magnetic flux density from 0 to 10 T, with a rate of 5 T/s. The numerical domain is discretized with a number of elements N_e, describing the number of quadrangles for the h-ϕ-formulation and the number of nodes (minus one) in the a-formulation. The time step is denoted as Δt.

Numerical solution of the h-ϕ-formulation

With $\boldsymbol{h} \in \mathcal{H}^{\delta,1}(\Omega)$, the magnetic field is along $\hat{\boldsymbol{z}}$, piecewise linear and continuous in $\Omega = \Omega_\text{c}$. The current density is element-wise constant and not continuous.

We run a 1D-like finite element model with a relative tolerance of $\varepsilon_\text{rel} = 10^{-10}$ for the convergence criterion, based on the power estimate $\mathcal{P}$, and Newton-Raphson iterations for linearization. Fig. 4.2 compares the numerical solution and the approximate analytical solution for two different discretization levels.

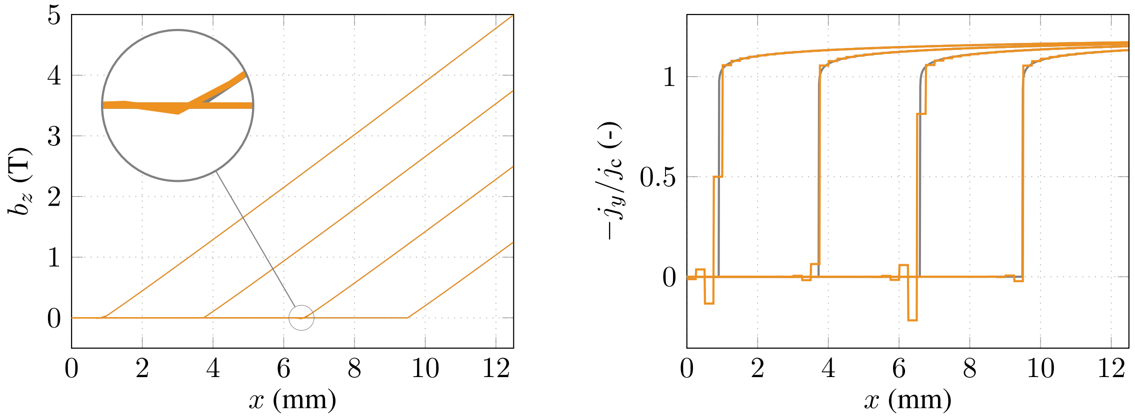

(a) Magnetic flux density, coarse mesh. (b) Current density, coarse mesh.

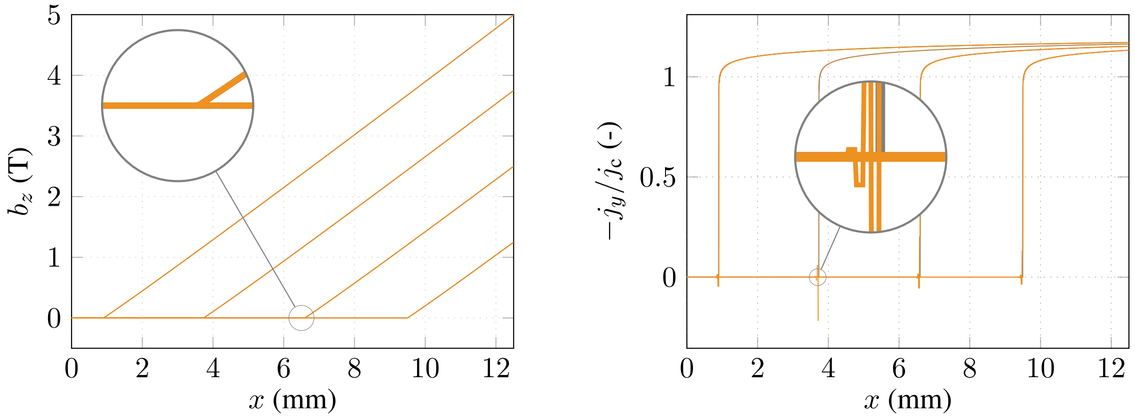

(c) Magnetic flux density, fine mesh. (d) Current density, fine mesh.

Figure 4.2: Comparison between the numerical solution of the h-ϕ-formulation (orange curves) and the approximate analytical solution (gray curves) of the scaling equation for $n = 40$ and $j_\text{c} = 3 \times 10^8$ A/m^2. Four time instants are considered: 0.25, 0.5, 0.75 and 1 s, and two different discretization levels are compared. Coarse mesh: $N_e = 50$ and $\Delta t = 0.01$ s. Fine mesh: $N_e = 500$ and $\Delta t = 0.001$ s.

The flux front position is accurately represented, as well as the shape of the magnetic flux density distribution. For the coarse mesh, a small oscillating pattern of $\boldsymbol{b}$ is visible over a few elements ahead of the front, see the zoom in Fig. 4.2(a). The largest difference with the approximate analytical solution is however only around 50 mT, which is small with respect to the average amplitude of the magnetic flux density in the slab. The current density is proportional to the spatial derivative of $\boldsymbol{h} = \nu_0 \boldsymbol{b}$ and these oscillations thus lead to non-negligible errors on the current density profile, ahead of the front. When the mesh is refined, the oscillations of $\boldsymbol{b}$

decrease in amplitude, but because the slope of these oscillations does not necessarily decrease, a similar error is still observed in the current density profile. However, because it is limited to a few elements, the spatial extent of this error decreases as the elements shrink with mesh refinement.

When the spatial and time discretization are refined, the numerical solution is observed to converge steadily towards the approximate solution of the scaling law. With $N_e = 5000$ and $\Delta t = 0.001$ s, the largest difference between the numerical and analytical magnetic flux density distributions is only 0.15 mT, and is still located at the front position.

For verification, the same problem is solved with Picard iterations. This method has been characterized in Chapter 2 as possibly leading to iteration cycles. This is indeed observed here. When the time step is not small enough, the iterations enter cycles that prevent the method from converging. The required time step for avoiding cycles is much smaller than the time step required for a convergence with the Newton-Raphson method. Combined with the fact that the Picard iterations exhibit a slower rate of convergence, this leads to very time-consuming simulations. Nevertheless, when it converges, the solution quality is identical to that obtained with the Newton-Raphson method.

In summary, for a given spatial and time discretization, when linearization methods do not cycle, they provide the same results. We consider the numerical results to be accurate because they rapidly converge towards the approximate analytical solution. The only noticeable error is observed ahead of the flux front and consists in small amplitude oscillations of $\boldsymbol{b}$, and oscillations of $\boldsymbol{j}$ of larger amplitude over a few elements. However, the importance of this error steadily decreases as the mesh is refined.

Numerical solution of the a-formulation

With $\boldsymbol{a} \in \mathcal{A}^{\delta,1}(\Omega)$, the vector potential is along $\hat{\boldsymbol{y}}$, piecewise linear and continuous in $\Omega = \Omega_{\text{c}}$. The magnetic flux density is along $\hat{\boldsymbol{z}}$, element-wise constant and discontinuous. The electric field is expressed as a finite difference approximation of the time derivative of the vector potential. It is thus also piecewise linear. The current density is obtained with the power law involving the nonlinear conductivity.

We run a 1D finite element model with a relative tolerance $\varepsilon_{\text{rel}} = 10^{-8}$ for the convergence criterion based on the power estimate $\mathcal{P}$ and Picard iterations for linearization. Fig. 4.3 compares the numerical solution and the approximate analytical solution for two different discretization levels.

With both coarse and fine meshes, the magnetic flux density and the flux front position are accurately represented. On the other hand, the current density profile suffers from large errors ahead of the flux front, especially on the coarse mesh. This is not surprising. Oscillations are observed in the vector potential over a few elements ahead of the flux front, as was the case for the magnetic field in the h-ϕ-formulation. The electric field, which is a time derivative of the vector potential, is thus also subject to those oscillations, and small values of the electric field are highly amplified by the power law when computing the current density. Due to the shape of the power law, this strong amplification of errors is restricted to small values of the electric

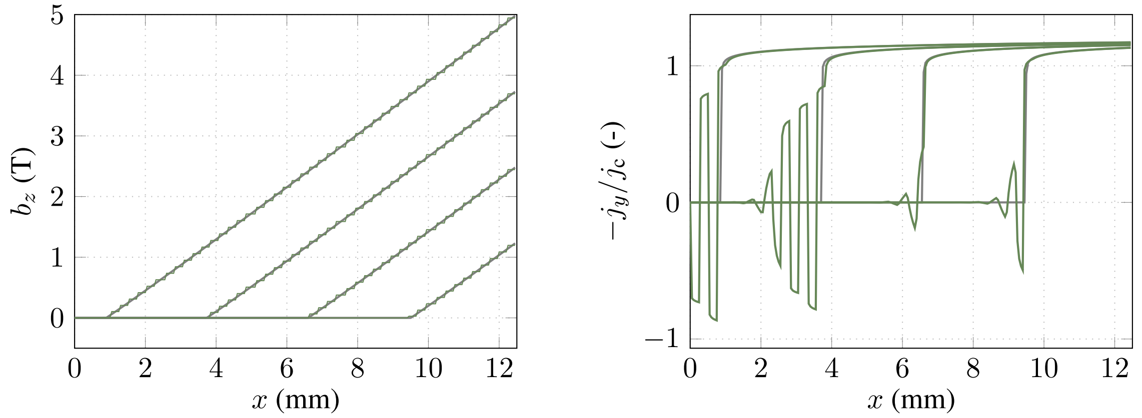

(a) Magnetic flux density, coarse mesh.

(b) Current density, coarse mesh.

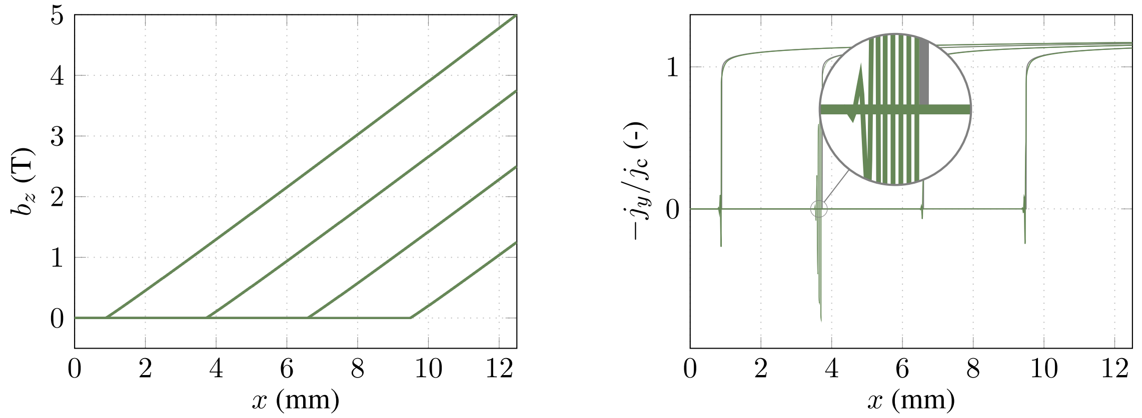

(c) Magnetic flux density, fine mesh.

(d) Current density, fine mesh.

Figure 4.3: Comparison between the numerical solution of the a-formulation (green curves) and the approximate analytical solution (gray curves) of the scaling equation for $n = 40$ and $j_c = 3 \times 10^8$ A/m^2. Four time instants are considered: 0.25, 0.5, 0.75 and 1 s, and two different discretization levels are compared. Coarse mesh: $N_e = 50$ and $\Delta t = 0.01$ s. Fine mesh: $N_e = 500$ and $\Delta t = 0.001$ s.

field. Consequently, this oscillating pattern is only observed in non-penetrated regions. When the mesh is refined, the error persists but, because it spreads over a few elements, its spatial extent is reduced.

When the time step is reduced together with the mesh refinement, the numerical solution converges steadily towards the approximate solution to the scaling law, similarly to the situation for the h-ϕ-formulation.

Oscillations also arise with second-order line elements. This is illustrated in Fig. 4.4, where we consider linear elements enriched on the whole line Ω with the hierarchical second-order perpendicular edge functions $\boldsymbol{w}_{2,e}$, as defined in Section 3.4.1. They allow to describe $\boldsymbol{b}$ with piecewise linear functions in each element, not necessarily continuous between elements. Oscillating patterns in the current density profile are still present. Since no improvement is brought by second-order elements, we keep linear elements in the following.

The same model is solved with the Newton-Raphson method as a linearization technique. It was observed in Chapter 2 that this situation was very likely to give rise to iteration cycles.

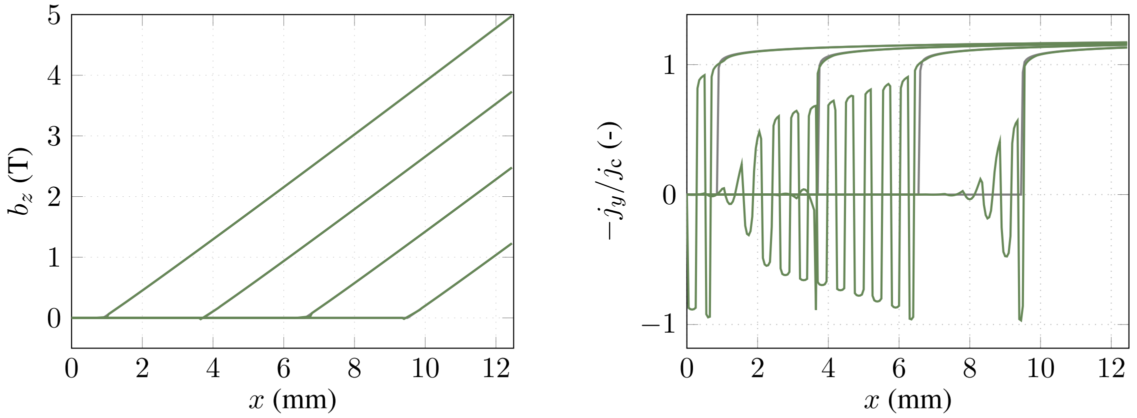

(a) Magnetic flux density, coarse.

(b) Current density, coarse.

Figure 4.4: Comparison between the numerical solution of the a-formulation with second-order elements (green curves) and the approximate analytical solution (gray curves) of the scaling equation for $n = 40$ and $j_c = 3 \times 10^8$ A/m^2. Four time instants are considered: 0.25, 0.5, 0.75 and 1 s. Coarse: $N_e = 50$ and $\Delta t = 0.01$ s.

This is observed here also. Without relaxation factors, the iterations do not converge, even for very small time steps, but instead follow a cycle far from equilibrium between two solutions. These cycles have the same origin as in models with a single unknown, as they are due to the shape of the power law.

To conclude, the a-formulation produces accurate results with Picard iterations. Oscillating patterns ahead of the flux front are more important than with the h-ϕ-formulation because of the shape of the power law, but the associated error decreases steadily with mesh refinement.

4.1.2 Possibility of using large time steps

In some situations, we observe that the iterative techniques converge even with very large time steps, while providing accurate magnetic flux density distributions. With the a-formulation and Picard iterations, it has even been observed that the larger the time step, the easier the convergence. A single-time-step method has already been discussed in [124, 72, 36]. To some extent, such an approach is also possible with the h-ϕ-formulation and Newton-Raphson iterations. This will be illustrated below. It can thus be tempting to use very large time steps to accelerate the simulations. This possibility should however be exploited with care as not all quantities are determined with accuracy when large time steps are used. In this section, we explore the validity of this approach.

To illustrate the results, we consider the 1D slab problem. The magnetic flux and current penetration profiles are compared for two time discretization levels: with a single time step, and with 100 time steps for a given final value of the applied field. Materials with $n = 10$ and $n = 100$ are chosen, still with the constant critical current density $j_c = 3 \times 10^8$ A/m^2. Fig. 4.5 compares the corresponding numerical solutions of the h-ϕ-formulation. Results from the a-formulation are similar.

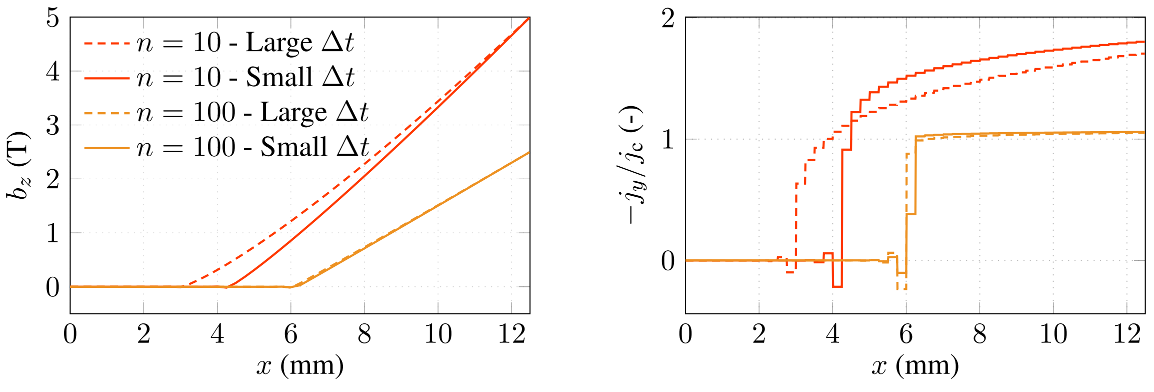

(a) Magnetic flux density.

(b) Current density.

Figure 4.5: Comparison between the numerical solutions of the h-ϕ-formulation on the 1D slab geometry for two time discretization levels for $n = 10$ and $n = 100$. Dashed curves correspond to the solution obtained with a single time step whereas solid curve are obtained after 100 time steps ($\Delta t = 0.01$ s for $n = 10$, and $\Delta t = 0.005$ s for $n = 100$). Solid curves coincide well with the approximated analytical solution from [95] (not represented in the figure). The legend is the same for both figures.

As can be seen in the figure, even if the method converges in the four cases, there is a large error on the magnetic flux density distribution and the current density profile for the low power exponent $n = 10$. Clearly, the single-time-step approach is not accurate in that case. However, with a larger value of n, both time discretization levels provide an accurate description of $\boldsymbol{b}$ and $\boldsymbol{j}$. Using large time steps in this case may be interesting to get fast results, especially with the a-formulation, which is particularly robust.

Results in Fig. 4.5 hint that the size of the time step has a limited influence on $\boldsymbol{b}$ and $\boldsymbol{j}$ for large values of the power law parameter n. As discussed in the following paragraphs, this is however not the case for all other quantities.

In the Bean model [80] limit ($n \to \infty$) and with a linear ramp of applied field, the magnetic flux density distribution is linear in space and the flux front propagates at constant speed. In the finite element model, time derivatives are estimated by a finite difference approximation (backward Euler method). This approximation amounts to replacing the instantaneous increase rate of the magnetic flux density by its average increase rate over the considered time step. This is illustrated in Fig. 4.6 in the extreme case of a single time step for the whole time interval from a virgin state. In this situation, the time derivative is underestimated almost everywhere in the material. If more time steps are considered, the underestimation error is localized near the front and its influence on the numerical solution is thus reduced. A power law model with a finite exponent n yields a different distribution but the finite difference still underestimates the time derivative. The error on the time derivative is, in a first approximation, equivalent for all values of n, up to the Bean model limit.

The error on time derivatives induces an error on the electric field $\boldsymbol{e}$: weakly via Faraday's law $\textbf{curl}\, \boldsymbol{e} = -\partial_t \boldsymbol{b}$ in the h-ϕ-formulation, and strongly via $\boldsymbol{e} = -\partial_t \boldsymbol{a}$ in the a-formulation. This is where the influence of n comes into play. For large values of n, the resulting error on the current density $\boldsymbol{j}$ is small because of the low differential conductivity in the power law for $\|\boldsymbol{j}\|$ close to j_c. But when the value of n decreases, the differential conductivity for $\|\boldsymbol{j}\|$ close

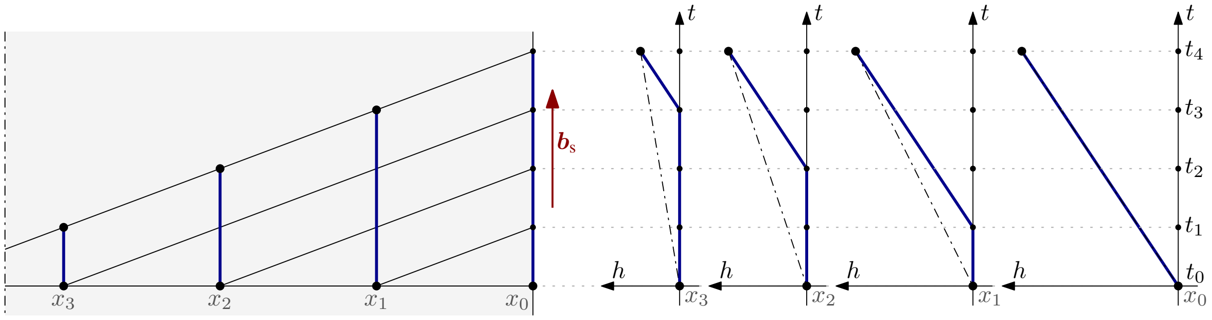

Figure 4.6: Illustration of the error induced by the finite difference approximation of the time derivative in the case of large time steps. Left: magnetic flux density distribution inside the superconductor at several time instants for a linearly increasing source field in the Bean model limit. Right: time evolution of the magnetic flux density at several spatial points (bold blue curves) and illustration of the finite difference approximation (dash-dotted lines) in the case of a single numerical time step. Time instants $t_0, \dots, t_4$ are equidistant.

to j_c increases, which in turn increases the error on $\boldsymbol{j}$. Moreover, because $\boldsymbol{e}$ is underestimated, $\boldsymbol{j}$ is also underestimated and this provokes the need for a larger penetration distance to reach $\boldsymbol{h} = \boldsymbol{h}_s$ at the material-air interface, as observed in Fig. 4.5.

As a consequence, even though the use of very large time steps provides accurate current and magnetic field distributions when n is large enough, time derivatives are badly approximated and lead to non-negligible errors on the electric field. Power quantities and losses rely on time derivatives and on the electric field, hence, they also suffer from important errors. This is illustrated in Fig. 4.7. A single time step may cause an error as high as 50% on the instantaneous power estimate $\mathcal{P} = \big(\partial_t \boldsymbol{b}\,, \boldsymbol{h}\big)_\Omega + \big(\boldsymbol{j}\,, \boldsymbol{e}\big)_{\Omega_c}$.

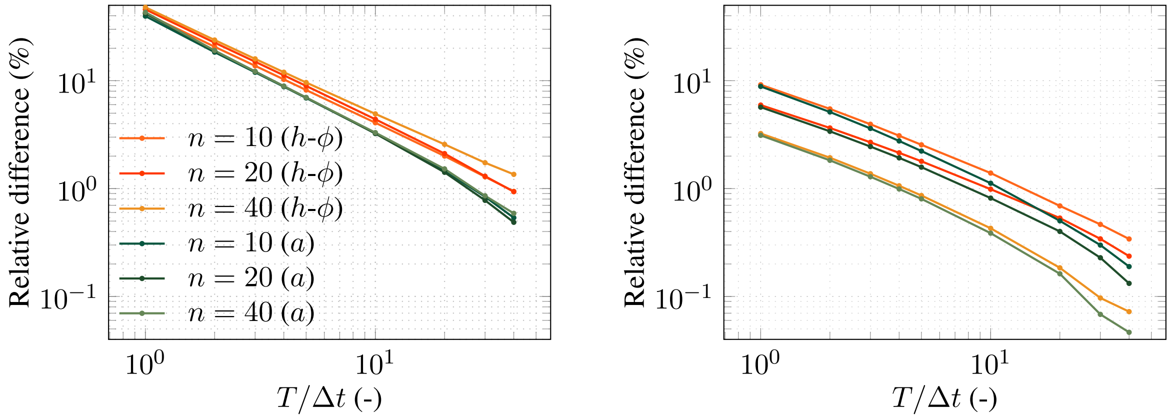

(a) Influence on the power estimate $\mathcal{P}$.

(b) Influence on the magnetic flux density.

Figure 4.7: Influence of the number of time steps on the solution accuracy for $n = 10, 20, 40$ for the h-ϕ and a-formulations. Starting from a virgin state at $t = 0$ s, a ramp of applied field with rate 2.5 T/s is applied during $T = 1$ s. Number of elements: $N_e = 50$. One reference solution is computed for each formulation, it is the numerical solution obtained with 1000 time steps. (a) Relative difference on the power estimate $\mathcal{P}$ compared to the associated reference solution at the end of the simulation. (b) Relative difference on the magnetic flux density: it is computed as the largest difference with the reference solution at the end of the simulation, normalized by 2.5T. The legend is the same as in (a).

4.1.3 Comments on the power law

Combining the observations of Sections 4.1.1 and 4.1.2, we can distinguish two distinct consequences of the nonlinearity of the power law on the numerical behavior of the finite element models. We propose in Fig. 4.8 to look at two main regions on the differential conductivity graph: *Region 1*, for which $dj/de \gg j_\mathrm{c}/e_\mathrm{c}$ and *Region 2*, for which $dj/de \ll j_\mathrm{c}/e_\mathrm{c}$.

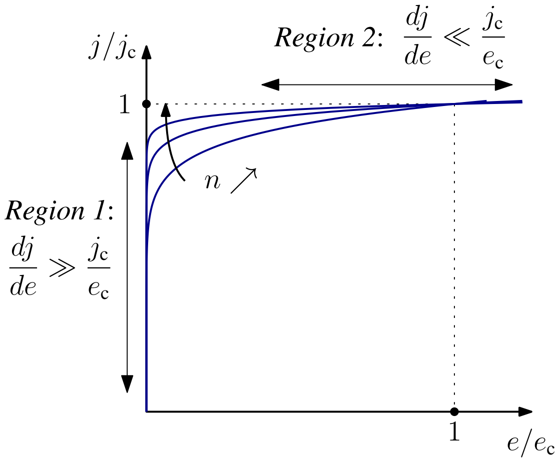

Figure 4.8: Representation of the power law for type-II superconductors and the two distinct regions for the associated differential conductivity dj/de. The high differential conductivity in *Region 1* is responsible for numerical oscillations of the current density in flux-free regions, especially for the a-formulation. The small differential conductivity in *Region 2* allows for large time steps to be used in order to get a good approximation of the current density and the magnetic field.

In *Region 1*, the current density is extremely sensitive to the electric field. The sensitivity increases with n. Notably, in the a-formulation, the current density $\boldsymbol{j}$ is calculated from $\boldsymbol{e} = -\partial_t \boldsymbol{a}$ and this high sensitivity induces large amplitude oscillations in the flux-free region of the superconductor, as was observed in Fig. 4.3. In the h-ϕ-formulation, this effect is much less important, as $\boldsymbol{j}$ is expressed as $\textbf{curl}\, \boldsymbol{h}$. The magnetic field also exhibits small oscillations after the flux front, but they are not strongly amplified by a nonlinear law.

In *Region 2*, the current density is much less sensitive to the electric field. The sensitivity decreases with n. The existence of this small differential conductivity allows for very large time steps to be used. In the a-formulation, a large error on $\boldsymbol{e} = -\partial_t \boldsymbol{a}$ does not induce a large error on $\boldsymbol{j}$, so that the resulting current density distribution remains accurate. Similarly, in the h-ϕ-formulation, a large error on $\textbf{curl}\, \boldsymbol{e} = -\partial_t \boldsymbol{b}$ does not translate into a large error on $\boldsymbol{j}$ in penetrated regions.

4.1.4 Efficiency of the formulations

In this section, we comment on the efficiency of the standard formulations applied on a simple 1D axisymmetric problem, with a cylinder of radius $R = 12.5$ mm. We compare the formulations on a similar spatial discretization, $N_e = 50$ quadrangles for the h-ϕ-formulation and $N_e = 50$ line segments for the a-formulation, and with identical time steps Δt. As an indicator of the efficiency, we consider the total number of iterations, equal to the number of solved linear systems, needed to model the response to a given external field. Because the number of degrees of freedom and the structure of the matrix are equivalent in both formulations, the number of iterations is proportional to the computational time for both formulations with direct linear solvers.

In the superconducting cylinder, we choose $n = 20$ and $j_\text{c} = 3 \times 10^8$ A/m^2. Three applied field functions are considered, as illustrated in Fig. 4.9: triangle and sinusoidal cycles with peak magnetic flux density of 10 T and a "creep" source that consists in two linear ramps followed by a zero applied field. These excitations fully penetrate the cylinder at some point (in the Bean model limit, the full penetration field is $\mu_0 R j_\text{c} = 4.71$ T). Time discretization is fixed using the results in Fig. 4.7: with $n = 20$, using 10 time steps for a ramp of applied field from 0 to 2.5 T yields errors on the power estimate smaller than 5% and maximum errors on the magnetic flux density distribution smaller than 1%, which is considered accurate enough. By extension, the time step here is fixed to 0.05 s, which also provides 10 steps for each 2.5 T change in the triangle source. The same time step is chosen for the other two sources.

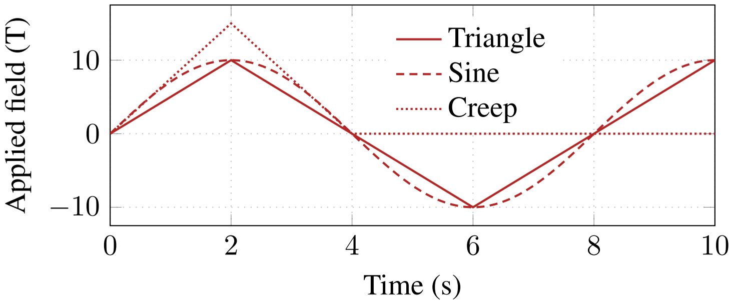

Figure 4.9: Time evolution of the three different applied source field functions.

For the h-ϕ-formulation, we iterate with a Newton-Raphson method, a relative tolerance $\varepsilon_\text{rel} = 10^{-8}$, and we consider three different possibilities for choosing the initial estimate: zeroth, first, and second-order extrapolations of the last solutions, as was proposed in Section 2.6. For the a-formulation, we iterate with a Picard method and we consider the same three possibilities for choosing the initial estimate. Convergence difficulties are observed with the Picard method if the relative tolerance is chosen smaller than $\varepsilon_\text{rel} = 10^{-5}$, so that we choose $\varepsilon_\text{rel} = 10^{-5}$ in the following. The choices for the initial iterates are illustrated in Fig. C.1 in Appendix for the case of a linear ramp of applied field.

The results are given in Table 4.1. The first observation is that the impact of the first estimate is significant, the best choice for each formulation leads to a strong reduction of the number of iterations in all cases, compared to other choices. With the h-ϕ-formulation, the first-order extrapolation is beneficial for the convergence whereas with the a-formulation, the second-order extrapolation appears to be more interesting.

The second observation is that the a-formulation requires many more iterations (and computational time) compared to the h-ϕ-formulation. This conclusion would be even more pronounced if identical tolerances were considered. This is related to the lower convergence rate of the Picard method with respect to the Newton-Raphson method. As an illustration, Fig. 4.10 shows the evolution of the norm of the system residual, Eq. (2.72), for three different time steps.

Formulation	h-ϕ-formulation			a-formulation		
Linearization	Newton-Raphson			Picard		
Extrapolation	0th	1st	2nd	0th	1st	2nd
Triangle	5 200	**2 580**	4 128	23 475	6 093	4 268
Sine	4 933	**2 830**	4 109	24 307	11 504	7 389
Creep	3 893	**2 556**	3 964	67 293	45 994	38 566

Table 4.1: Number of iterations for simulating the magnetic response to three source fields, with $N_e = 50$ and $\Delta t = 0.05$ s, for the two standard formulations and three different choices for the initial iterate. Note that the tolerance on the power estimate was $\varepsilon_{\text{rel}} = 10^{-8}$ for the h-ϕ-formulation and $\varepsilon_{\text{rel}} = 10^{-5}$ for the a-formulation. The bold numbers are the minima of each line.

When they converge, the Newton-Raphson iterations progressively approach the solution. The convergence rate is first linear, the residual is divided by a constant value at each iteration, and the flux propagates steadily. Fig. C.2 in Appendix illustrates how the front progressively propagates with the h-ϕ-formulation for two different extrapolation methods. Many iterations can be needed if the time step is large. Then, the convergence becomes quadratic and a few iterations are enough for reaching a very small residual.

Note that Fig. 4.10(a) shows cases for which the method converges. As already mentioned, using Newton-Raphson iterations with the h-ϕ-formulation and large time steps is not as robust as using Picard iterations with the a-formulation in the same situation. In some cases, the Newton-Raphson algorithm diverges and the iterations must then be started again using a smaller time step.

By contrast with Newton-Raphson iterations, Picard iterations do not exhibit a monotonous decrease of the residual. Fig. C.3 in Appendix shows the evolution of the magnetic flux density distribution with Picard iterations in two different cases. Picard iterations lead to less efficient resolutions than Newton-Raphson iterations. However, as said above, they offer a more robust behavior when using large time steps.

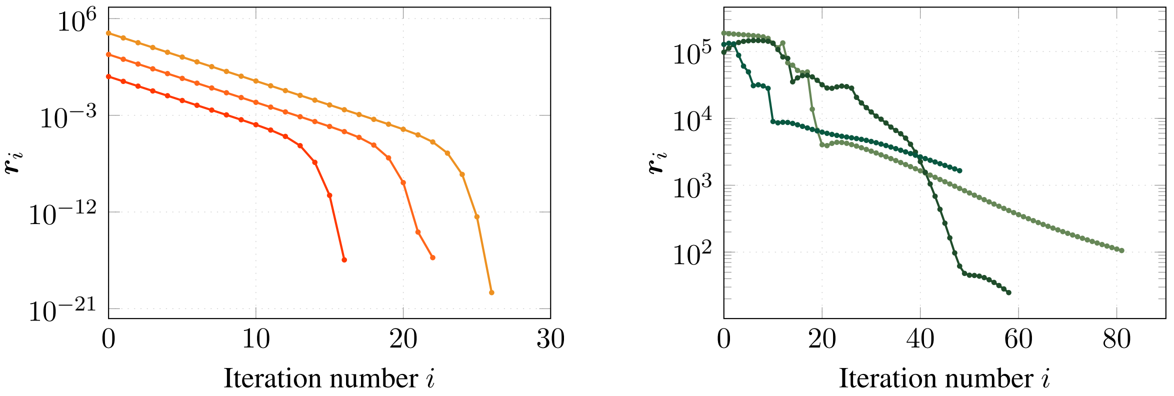

(a) Newton-Raphson, h-ϕ-formulation.

(b) Picard, a-formulation.

Figure 4.10: Evolution of the norm of the residual $\boldsymbol{r}_i = \boldsymbol{b} - \mathbf{A}(\boldsymbol{x}_i)\boldsymbol{x}_i$ with the iterations, for three representative examples of time integration steps and for the two linearization techniques. (a) Newton-Raphson iterations with the h-ϕ-formulation and the zeroth-order extrapolation. (b) Picard iterations with the a-formulation and the first-order extrapolation.

4.2 T2S cylinder (2D)

The next problem consists of a superconducting bulk cylinder subjected to an external applied field b_s, as illustrated in Fig. 4.11(a). This test case is comparable to benchmark 4 of the HTS modeling website [195]. The bulk superconductor has a radius $R = 12.5$ mm and a height $H = 10$ mm. The critical current density is constant and equal to $j_c = 3 \times 10^8$ A/m^2. The external field is applied parallel to its axis, the z-axis, so that the problem is 2D and axisymmetric. The time evolution of the applied field is illustrated in Fig. 4.11(b) with $b_{\text{max}} = 1$ T and t_1, t_2, and t_3 equal to 5, 10, and 15 s, respectively.

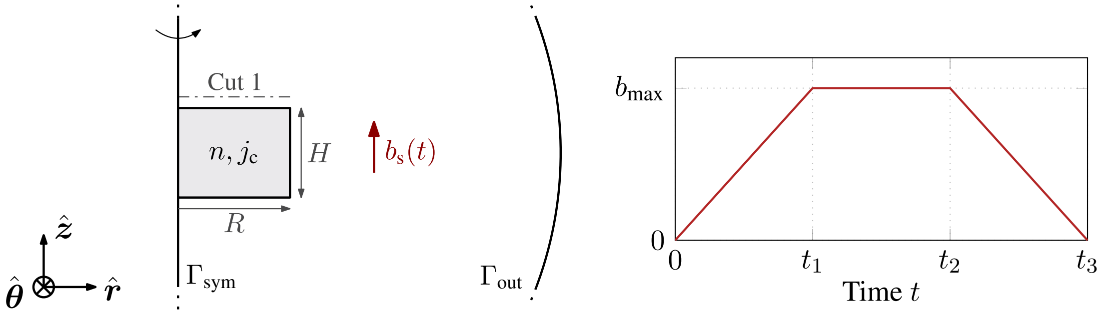

(a) Cylinder geometry. (b) External applied field $b_s(t)$.

Figure 4.11: Superconducting cylinder test case. An external applied field b_s is applied parallel to a T2S cylinder, the problem is axisymmetric and is solved in 2D. (a) Problem geometry. The dash-dotted gray segment is the cut along which the magnetic flux density is sampled for Fig. 4.12. Only a part of the meshed air domain is represented in the figure, but the full half-disk is modelled. (b) Time evolution of the applied field $b_s(t)$.

The outer boundary Γ_{out} is placed at a distance of 10 cm from the center of the cylinder. This is a bit less than 10 times the cylinder radius. Far from the cylinder, the magnetic field generated by currents flowing in the cylinder can be approximated by that generated by a magnetic dipole [196]. It decreases as $1/r^3$ [197] in the axisymmetric situation we consider here. The truncation error is therefore expected to be of the order of 0.1% of the main field close to the cylinder, in a first approximation. We consider this to be an acceptable error. Mapping the outer boundary to infinity helps to reduce the truncation error [198]. This method has been studied in detail in [199] in the context of T2S, but is not considered here.

4.2.1 Comparison of the solutions

We compare the numerical solution obtained with three formulations. We consider both standard formulations, h-ϕ and a, as well as the volume-coupled a-j-formulation. The other formulations, h-ϕ-a, t-a, and h-ϕ-b are not relevant in this case.

For the h-ϕ-formulation, the external boundary Γ_{out} is put in Γ_h and the essential boundary condition $(\boldsymbol{h} - \boldsymbol{h}_s) \times \boldsymbol{n}|_{\Gamma_{\text{out}}} = \boldsymbol{0}$ is imposed via a Dirichlet condition on the magnetic scalar potential ϕ. The symmetry boundary Γ_{sym} is put in Γ_e and the associated homogeneous natural boundary condition $\boldsymbol{b} \cdot \boldsymbol{n}|_{\Gamma_{\text{sym}}} = 0$ is implicitly imposed in the weak form.

For the a and a-j-formulations, the whole boundary $\Gamma_{\text{out}} \cup \Gamma_{\text{sym}}$ is put in Γ_e. The essential boundary conditions $\boldsymbol{b} \cdot \boldsymbol{n}|_{\Gamma_{\text{sym}}} = 0$ and $(\boldsymbol{b} - \boldsymbol{b}_{\text{s}}) \cdot \boldsymbol{n}|_{\Gamma_{\text{out}}} = 0$ are imposed via Dirichlet conditions on the magnetic vector potential $\boldsymbol{a}$, taking care of the axisymmetry of the problem. The additional Dirichlet condition $\boldsymbol{j} \times \boldsymbol{n}|_{\Gamma_{\text{sym}}} = 0$ is imposed for the a-j-formulation.

Note that the boundary conditions on Γ_{out} are not equivalent in the two cases. Because Γ_{out} is not at an infinite distance from the T2S cylinder, this introduces a systematic modelling difference between the formulations.

The azimuthal current density distributions obtained with the three formulations are represented in Fig. 4.13 at the three instants t_1, t_2, and t_3, with a rather fine mesh ($\approx 4 \times 10^4$ elements). As already observed with the 1D slab problem, the current density obtained from the a-formulation exhibits oscillations ahead of the sharp flux penetration front, because small oscillations in the unknown field $\boldsymbol{a}$ are strongly amplified by the power law. To a lesser extent, oscillations are also present with the a-j-formulation. By contrast, the h-ϕ-formulation produces a much cleaner front. This is further illustrated in Fig. 4.14, where the situation is worse with a coarser mesh. For the a-j-formulation on the coarse mesh, the transition between opposite current densities is badly described along the represented segment because $\boldsymbol{j}$ is forced to be element-wise linear and continuous.

As for the magnetic flux density, results from the three formulations nicely match each other, as shown in Fig. 4.12, where its z-component is sampled along a segment, 2 mm above the cylinder at times t_1, t_2, and t_3. The solutions inside the T2S cylinder also almost coincide (not represented in the figures). With mesh and time step refinement, the solutions of the three formulations are seen to approach each other (both globally and locally). The global convergence is illustrated in Fig. 4.15. Compared to the tape problem that will be presented in the next section, a very fine mesh is however necessary to get a difference smaller than 1%.

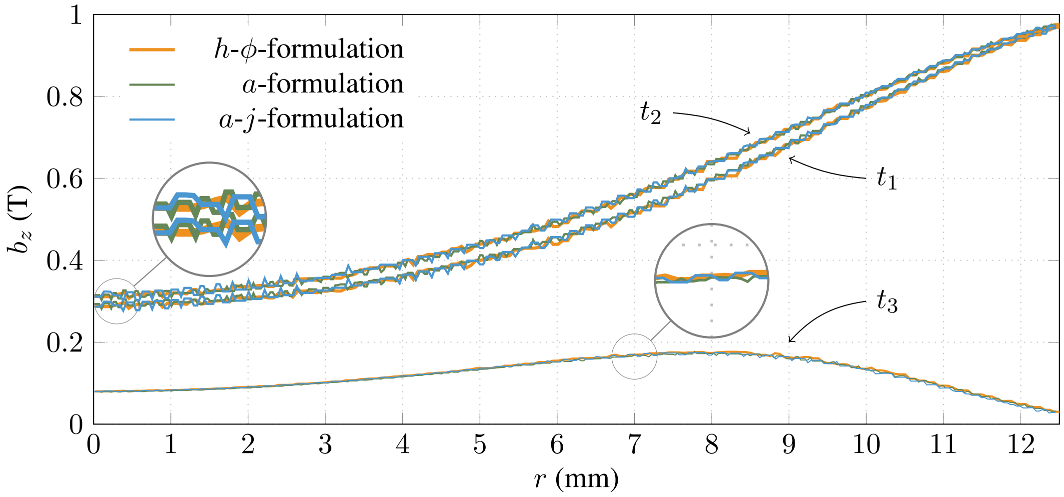

Figure 4.12: Distribution of the z-component of the magnetic flux density along the cut represented in Fig. 4.11(a), 2 mm above the cylinder, at the instants t_1, t_2 and t_3 for a maximum applied field $b_{\text{max}} = 1$ T, $n = 20$, and $j_{\text{c}} = 3 \times 10^8$ A/m^2. Time step: $\Delta t = t_1/50$. Fine mesh with $\approx 4 \times 10^4$ elements. The highlighted circles illustrate that the difference between the formulations are of the order of the inter-element variations of the solutions at the considered space discretization level.

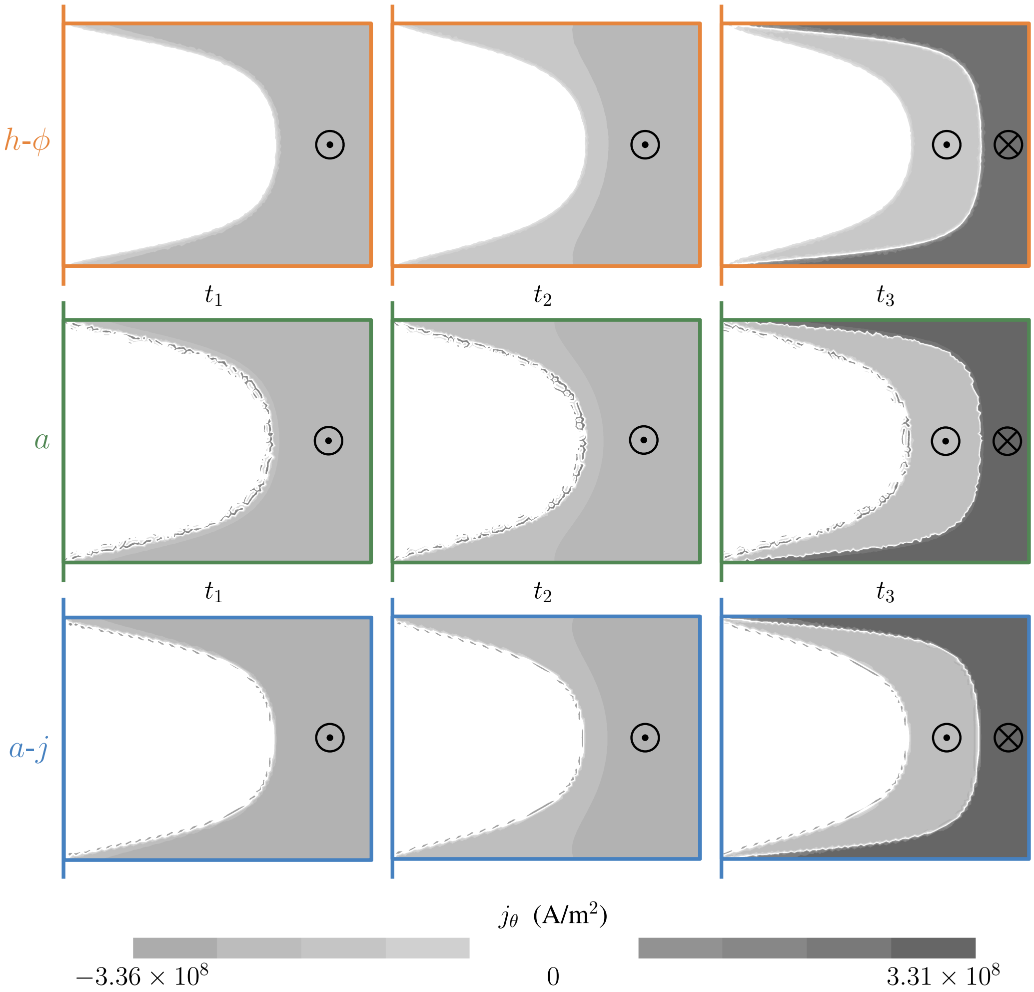

Figure 4.13: Current density distribution in a slice of the bulk cylindrical geometry at the instants t_1, t_2, and t_3 for a maximum applied field of 1 T, $n = 20$, and $j_c = 3 \times 10^8$ A/m^2. Time step: $\Delta t = t_1/50$. Fine mesh with $\approx 4 \times 10^4$ elements. White areas are free of current, light gray areas carry out-of-plane current densities and dark gray areas carry opposite current densities. Top row: h-ϕ-formulation. Middle row: a-formulation. Bottom row: a-j-formulation.

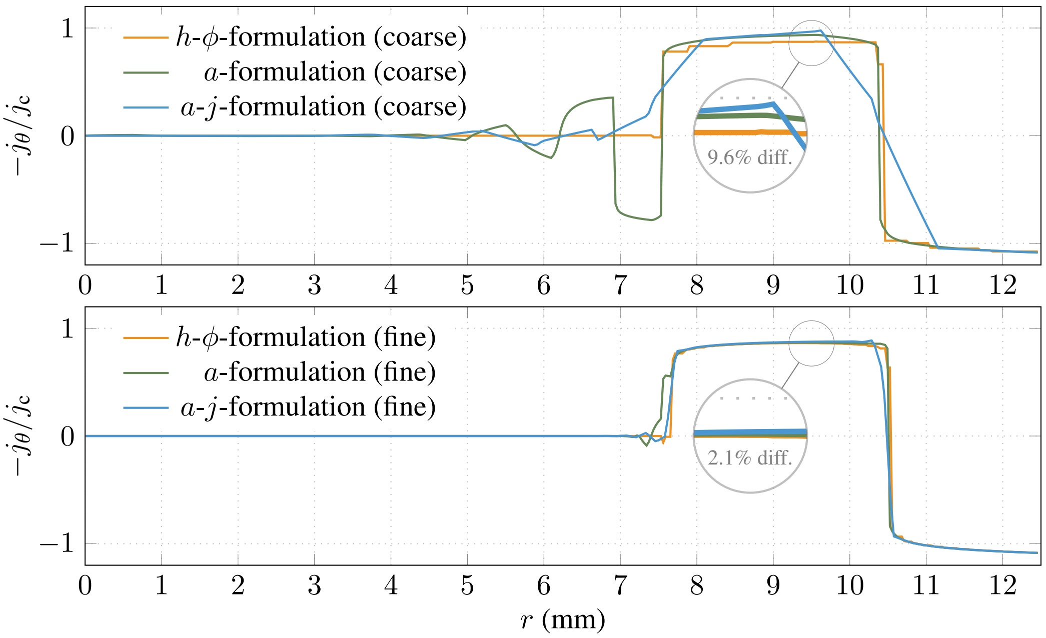

Figure 4.14: Current density profiles as a function of the distance r to the symmetry axis, at the mid-height of the cylinder, at time t_3 for a maximum applied field of 1 T, $n = 20$, and $j_c = 3 \times 10^8$ A/m^2. Upper figure: coarse mesh of $\approx$ 2000 nodes. Lower figure: finer mesh with $\approx 4 \times 10^4$ nodes. The percentages inside the highlighted circles are the local relative differences between the h-ϕ and a-j-formulations.

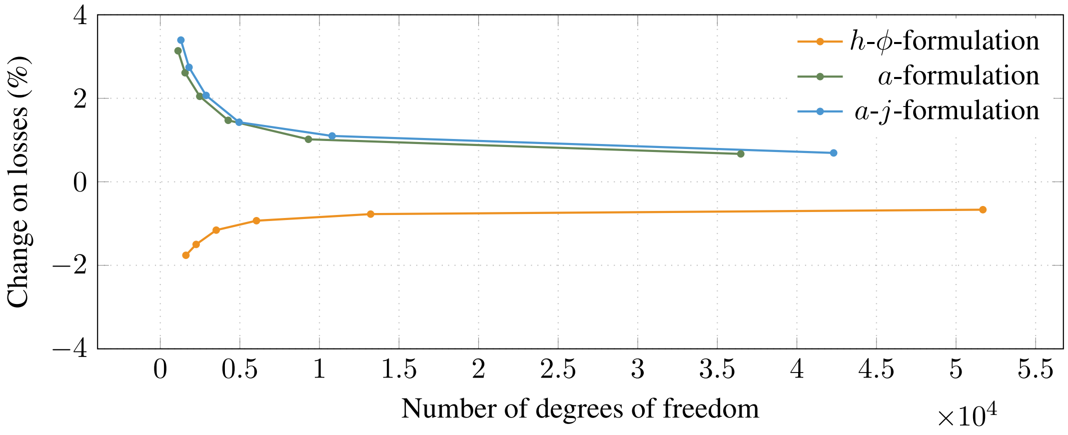

Figure 4.15: Change of AC losses $\int_0^{t_3} (\boldsymbol{j}\,,\boldsymbol{e})_{\Omega_c}\, dt$, relative to an accurate solution, for various numbers of degrees of freedom, for the two formulations, with a constant time step $\Delta t = t_1/50$, $n = 20$, and $j_c = 3 \times 10^8$ A/m^2. The reference value is determined as the average of the solutions obtained with the finest mesh for the h-ϕ and a-formulations.

4.2.2 Efficiency of the formulations

The convergence speeds of the different methods are not identical. Depending on the formulation, the linearization technique and the choice for the first iterate, the iterative techniques may require very different numbers of iterations to converge. Because the simulation time directly depends on the total number of iterations, this affects the calculation speed. As was done for the 1D slab problem, we now compare the three formulations in terms of their efficiency.

We consider three discretization levels: coarse, medium, and fine, defined by a multiplier α equal to 4, 2, and 1, respectively. The mesh size varies from 0.3α mm in the cylinder to 3α mm on the outer surface Γ_{out}. The number of time steps from 0 to t_3 is fixed to $300/\alpha$. The power law exponent is fixed to $n = 25$ and the critical current density is also kept constant and equal to $j_c = 3 \times 10^8$ A/m^2. The same convergence criterion is used for the three formulations, it is based on the power estimate, with a relative tolerance of $\varepsilon_{\text{rel}} = 10^{-6}$ on its change between two iterations.

Results are presented in Table 4.2 in terms of the total number of iterations for the full simulation. As for the 1D slab, the a-formulation suffers from the low convergence rate of the Picard method. Its associated mixed volume-coupled a-j-formulation demonstrates a much more efficient numerical behavior. As the introduction of the auxiliary field $\boldsymbol{j}$ allows for the resistivity to be involved instead of the conductivity, Newton-Raphson iterations can be used without leading to iteration cycles. It is observed that this leads to a number of iterations that is even smaller than with the h-ϕ-formulation.

Note also that if meshes are equivalent, the number of degrees of freedom are not identical for the different formulations. For the fine mesh, the h-ϕ, a, and a-j-formulations involve $14\,438$, $10\,916$, and $12\,624$ degrees of freedom, respectively.

As in the 1D bar problem, the choice for the first iteration has a non-negligible influence on the resolution efficiency. Both the h-ϕ and a-j-formulations perform better when the last solution is taken as a first estimate, whereas a second-order extrapolation is still the best choice for the a-formulation.

Formulation		h-ϕ-formulation			a-formulation			a-j-formulation		
Linearization		Newton-Raphson			Picard			Newton-Raphson		
Extrapolation		0th	1st	2nd	0th	1st	2nd	0th	1st	2nd
Cylinder	Coarse	570	612	824	16 382	10 905	9 182	**480**	549	608
	Medium	1 287	1 344	1 808	34 858	20 935	16 654	**904**	1 021	1 148
	Fine	2 671	2 751	3 780	74 929	41 467	27 006	**1 760**	1 989	2 235

Table 4.2: Total number of solved linear systems for the simulation from 0 to t_3 in the cylinder case, for three discretization levels ($\alpha = 4, 2, 1$), $n = 25$, three extrapolation techniques with the h-ϕ, a, and a-j-formulations. Relative tolerance for the convergence criterion: $\varepsilon_{\text{rel}} = 10^{-6}$. Bold numbers are the minima of each line. Simulation times for the fastest simulations of each line (bold numbers) are, on a single Intel Core i7 2.2 GHz CPU: 30” (coarse), 3’16” (medium), and 27’07” (fine).

4.3 T2S tape (2D)

The problem of this section consists of a superconducting tape with an imposed current. The tape has a large aspect ratio: its thickness is $w = 1$ μm and its width is $W = 12$ mm. The critical current density is chosen constant and equal to $j_\text{c} = 2.5 \times 10^{10}$ A/m^2. Cartesian coordinates are introduced with the x-axis along the width of the tape and the y-axis along its height. A sine-wave current intensity $I(t) = I_\text{max} \sin(2\pi f t)$ is imposed, with a frequency $f = 50$ Hz and an amplitude $I_\text{max} = F I_\text{c}$, where $I_\text{c} = W w j_\text{c}$ is the critical current intensity and $F \in [0, 1]$ is a constant. The outer boundary Γ_out is circular and placed at a distance of 6 cm from the center of the tape. This test case is comparable to benchmark 1 of the HTS modeling website [195].

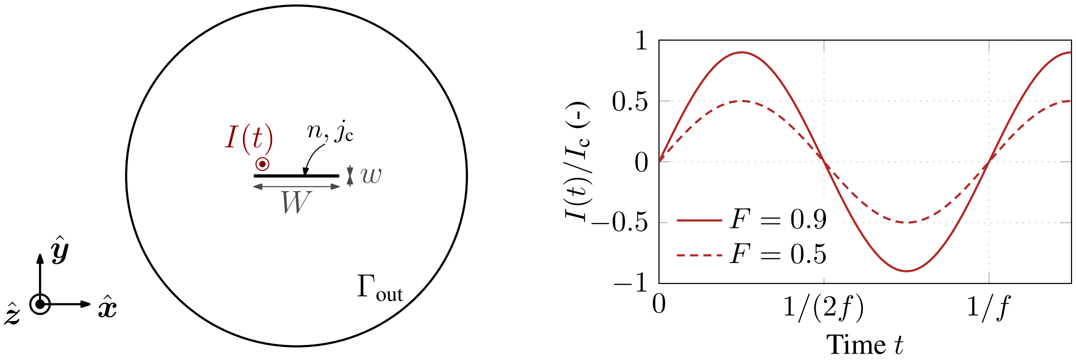

(a) Tape geometry.

(b) Imposed current intensity $I(t)$.

Figure 4.16: Simple tape test case (not to scale). A current intensity $I(t)$ is imposed in the tape. The problem is 2D. (a) Problem geometry. The plane symmetry is not exploited here. (b) Time evolution of the imposed current intensity.

4.3.1 Comparison of the solutions

As for the T2S cylinder problem, we first compare the numerical results obtained with different relevant formulations. For this problem, in addition to the standard formulations, we consider the t-a-formulation, featuring a thin-shell approximation. The a-j-formulation proved to be an efficient choice for modeling bulk T2S, we will show here that it suffers from bad conditioning.

For the standard formulations and the a-j-formulation, the tape is meshed with a single layer of first-order structured quadrangular elements. The tape can typically be described with a reasonable accuracy with $\approx$ 50-100 elements along its width [200], so the aspect ratio of quadrangles can be as high as $\approx$ 100-200. Discretizing the tape with a small number of elements across its thickness has been proven to produce accurate field distribution and power loss evaluation [200, 6], at least for simple cable configurations as is the case here [51]. With only one layer of elements, we only model an average current density over the thickness. This approximation is also the main assumption of the t-a-formulation, in which the tape is represented as a line segment and first-order line elements are used along its width. In all cases, we mesh the air with triangular elements. Extensions to more complex cable configurations that would require more element layers are investigated in [51], using an efficient h-ϕ-formulation with a thin-shell approximation.

In all formulations, Γ_{out} is put in Γ_e in order to impose (strongly or weakly) the homogeneous boundary condition $\boldsymbol{b} \cdot \boldsymbol{n}|_{\Gamma_{\text{out}}} = 0$. The total current $I = I(t)$ is imposed via (strong or weak) global conditions.

We run the four formulations on a relatively fine mesh of approximately 3000 elements. The a-j-formulation faces important numerical issues that we discuss in the next paragraph, but the results of the other three formulations nicely match each other. Fig. 4.17 shows the current density and magnetic flux density distributions inside the tape after one fourth of a period. With mesh and time refinement, the solutions of the h-ϕ, a, and t-a-formulations converge to each other and the solutions are considered accurate, see Fig. 4.18. Note that the current density profile is still very sensitive to errors in the $\boldsymbol{a}$ field with the a-formulation, especially with large n values. The convergence criterion must be strong enough if accurate current density profiles are sought with the a-formulation.

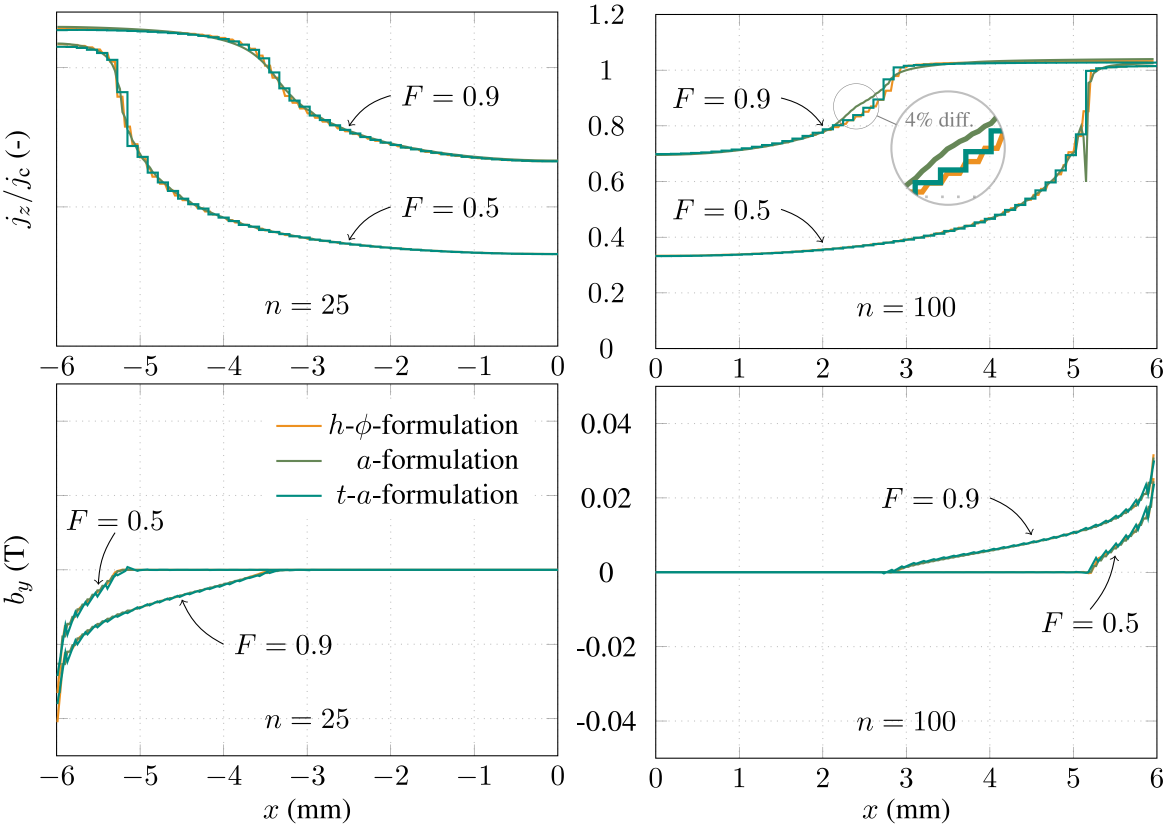

Figure 4.17: Current density (z-component, up) and magnetic flux density (y-component, down) distributions inside the tape at time instant $t = 1/(4f)$ for $n = 25$ (left) and $n = 100$ (right), $j_c = 2.5 \times 10^{10}$ A/m^2, and $F = 0.5$ or $F = 0.9$. Results from three formulations are presented, as the tested linear solvers did not manage to solve linear systems associated with the a-j-formulation. Only one half of the tape is represented in each case. The legend is the same for all figures. The percentage inside the highlighted circle is the local relative difference between the solutions of the h-ϕ and a-formulations.

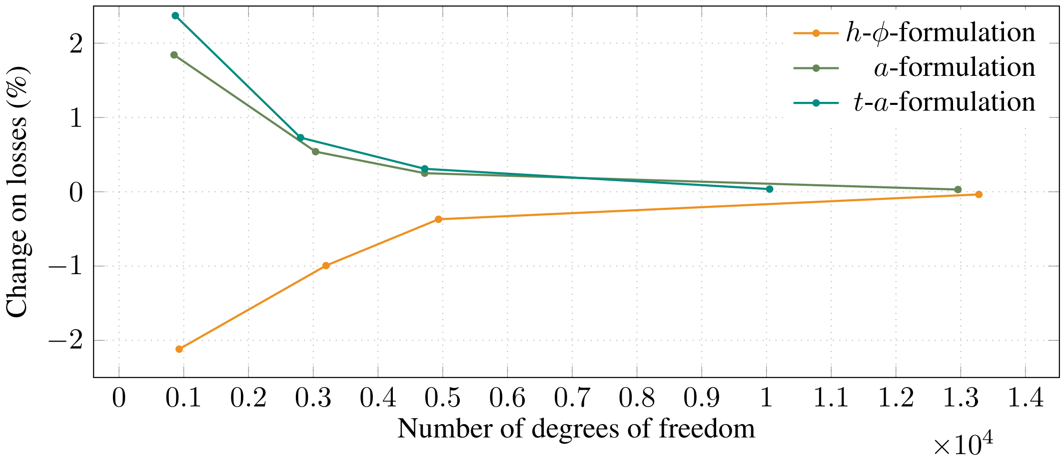

Figure 4.18: Change of AC losses $\int_0^{t_\text{f}} (\boldsymbol{j}\ , \boldsymbol{e})_{\Omega_\text{c}}\ dt$, with $t_\text{f} = 5/(4f)$, relative to an accurate solution, for various numbers of spatial degrees of freedom, for three formulations, with a constant time step $\Delta t = 1/(120f)$, $n = 25$, $j_\text{c} = 2.5 \times 10^{10}$ A/m^2, and $F = 0.9$. The accurate solution is the average of the values obtained with the h-ϕ and t-a-formulations on the finest mesh.

Failure of the linear solver on the a-j-formulation

The default direct sparse solver from MUMPS [201] fails to solve the linear system associated with the a-j-formulation. We observed that this is linked to the global condition on the current intensity. If we replace the applied current by an applied field, and remove the global conditions, which implicitly implies that $V = 0$ on the tape, no issue is encountered and the solver succeeds to solve the linear system, and performs well, as for the cylinder case in Section 4.2.

On very coarse meshes, i.e., with a small number of degrees of freedom and hence a small system matrix size, no issue is encountered. We also observed that a simple preconditioning consisting of multiplying the equation related to the global constraint by a small number, e.g., μ_0^2, allows for slightly finer meshes to be solved. This however does not suffice to circumvent the difficulty with a practical spatial discretization.

In [129], authors solved the same formulation with the Matlab differential algebraic equation solver `ode15s` [202, 203] and did not observe any solving difficulties. We also tried the default Matlab 2018a direct solver[2] [204] on systems that were observed to be problematic with MUMPS. This default solver tackles the linear systems without troubles.

Finally, it is interesting to note that on 3D problems, the solving issues do no longer appear. When modeling a straight tape in a 3D geometry, no difficulty is faced with the a-j-formulation, whether we introduce global constraints or not.

Because we had efficient alternative formulations for solving the tape problem in 2D, i.e., the h-ϕ and t-a-formulations, we have not investigated further the cause for these numerical difficulties. Analyzing deeper the matrix structure arising with global variables in 2D, as well as looking for efficient preconditioning methods are interesting further works.

---

[2] Called with the command `x = A\b`, for a matrix system `Ax = b`.

4.3.2 Efficiency of the formulations

As for the previous test cases, the convergence speed of the three formulations is not identical. Strong differences in terms of number of iterations are observed.

We consider three discretization levels: coarse, medium, and fine, defined by a multiplier α equal to 4, 2, and 1, respectively. A number of $200/\alpha$ elements are used in the tape, quadrangles for the h-ϕ and a-formulations, and lines for the t-a-formulation, and the mesh size progressively increases away from the tape up to a mesh size of 3α mm on Γ_{out}. The power exponent is fixed to $n = 25$. We model the magnetic response to the sinusoidal current defined in Fig. 4.16(b) with $F = 0.9$, from $t = 0$ to $t = 5/(4f)$, using a number of $300/\alpha$ time steps.

Results are gathered in Table 4.3. As already observed on the other problems, the Picard iterations that must be used for the a-formulation make this formulation much more computationally expensive than the others. The h-ϕ-formulation offers the most efficient resolution, with first or second-order extrapolations for the initial iterates, closely followed by the t-a-formulation, with second-order extrapolation. Note that the numbers of degrees of freedom associated with the three formulations are comparable, so that the h-ϕ-formulation is also the fastest choice in this case.

Formulation		h-ϕ-formulation			a-form.	t-a-formulation		
Linearization		Newton-Raphson			Picard	Newton-Raphson		
Extrapolation		0th	1st	2nd	2nd	0th	1st	2nd
Tape	Coarse	4 124	836	**455**	1 827	2 310	744	549
	Medium	8 558	983	**732**	4 222	4 734	1 259	832
	Fine	17 266	**867**	1 058	8 172	9 941	2 185	1 435

Table 4.3: Total number of solved linear systems for the simulation from 0 to $5/(4f)$ in the tape case, for three discretization levels ($\alpha = 4, 2, 1$), different extrapolation techniques with the h-ϕ, a, and the t-a-formulations. Relative tolerance for the convergence criterion: $\varepsilon_{\text{rel}} = 10^{-6}$, except for the a-formulation, for which $\varepsilon_{\text{rel}} = 10^{-4}$. Bold numbers are the minima of each line. Simulation times for the fastest simulations of each line (bold numbers) are, on a single Intel Xeon 2 GHz CPU: 20” (coarse), 2’50” (medium), and 14’ (fine).

4.4 T2S and SFM cylinders (2D)

The next problem is a hybrid structure made up of a T2S bulk cylinder placed below a SFM cylinder, subjected to an external applied field $b_{\text{s}}(t)$, as illustrated in Fig. 4.19(a). Interactions of T2S and SFM in such hybrid structures have been studied in [205, 206, 207, 92].

The cylinders have a common radius $R = 12.5$ mm and an identical height $H_{\text{T2S}} = H_{\text{SFM}} = 5$ mm. The external field is applied parallel to the cylinders axis, the z-axis, so that the problem is 2D and axisymmetric. The time evolution of the applied field is illustrated in Fig. 4.19(b) with $b_{\max} = 1.5$ T and $t_1 = 5$ s and $t_2 = 10$ s. The outer boundary Γ_{out} is a half-circle placed at a distance of 10 cm from the center of the T2S cylinder.

In the T2S, the critical current density is chosen constant and equal to $j_\mathrm{c} = 3 \times 10^8$ A/m^2, and the power exponent is fixed to $n = 20$. The SFM is assumed non-conducting and has a field-dependent permeability described by the simple form Eq. (1.9), with the parameter values $\mu_0 m_0 = 1.31$ T and $\mu_{\mathrm{r},0} = 1700$. This law has the analytical inverse given by Eq. (B.31) for the reluctivity.

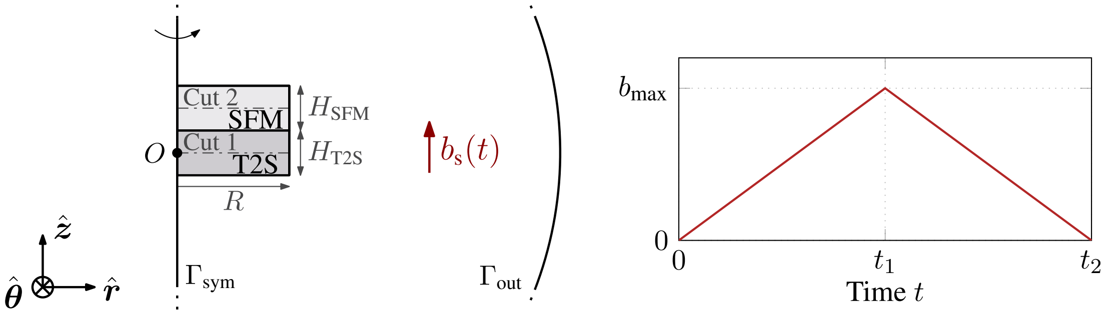

(a) Cylinders geometry.

(b) External applied field $b_\mathrm{s}(t)$.

Figure 4.19: Hybrid T2S-SFM test case. An external field b_s is applied parallel to an T2S-SFM hybrid structure. The problem is axisymmetric and is solved in 2D. (a) Problem geometry. The two dash-dotted lines are segments along which the numerical solution is compared. Only a part of the meshed air domain is represented, but the full half-disk is modelled. (b) Time evolution of the applied field $b_\mathrm{s}(t)$.

4.4.1 Comparison of the solutions

We compare the numerical solutions obtained with different relevant formulations. In addition to the two standard h-ϕ and a-formulations, we consider the three mixed formulations that were designed for handling models with both T2S and SFM: the h-ϕ-a, h-ϕ-b, and a-j-formulations.

For the h-ϕ-a-formulation, we place the air in the a-domain Ω_a and we choose $\boldsymbol{h} \in \mathcal{H}^{\delta,1}(\Omega_h)$ and $\boldsymbol{a} \in \mathcal{A}^{\delta,2}(\Omega_a)$ for stabilization. Placing the air in Ω_a or in Ω_h is nearly equivalent in terms of number of degrees of freedom, because both the $\boldsymbol{h}$ and $\boldsymbol{a}$ fields are discretized with one unknown per node in 2D. This is no longer the case in 3D, as will be illustrated in Section 4.5. For the h-ϕ-b-formulation, we take $\boldsymbol{b} \in \mathcal{B}^{\delta,1}(\Omega_\mathrm{m})$.

The boundary conditions are the same as for the single T2S cylinder of Section 4.2, with conditions for the h-ϕ-a and h-ϕ-b-formulations identical to those for the h-ϕ-formulation.

We run the five formulations from $t = 0$ to $t = t_2$. As for the other models, we observe that all methods provide numerical results that match each other. As an illustration, Fig. 4.20 shows the current density and magnetic flux density distributions along the mid-height horizontal segment in the T2S cylinder, denoted as “Cut 1” in Fig 4.19(a). Note the non-zero radial component, b_r, which is a result of the presence of the SFM cylinder, channelling flux lines on top of the T2S cylinder [92]. As already shown before, the current density obtained from the a and a-j-formulations exhibit stronger oscillations ahead of the flux front than the current density obtained via h-conform formulations. The spatial extent of these oscillations decreases when the mesh is refined. Fig. C.4 in Appendix shows the results obtained with a coarser mesh.

The magnetic flux density components along the mid-height horizontal segment in the SFM cylinder, denoted as "Cut 2" in Fig 4.19(a), is represented in Fig. 4.21. Again, all formulations provide comparable results, the difference between the different curves being of the order of the inter-element variations of b_r or b_z. The same results but on a coarser mesh are presented in Fig. C.5 in Appendix.

Global convergence is also checked. As an illustration, Fig. 4.22 shows the evolution of AC losses in the T2S cylinder with mesh refinement for a given time discretization, for the five considered formulations.

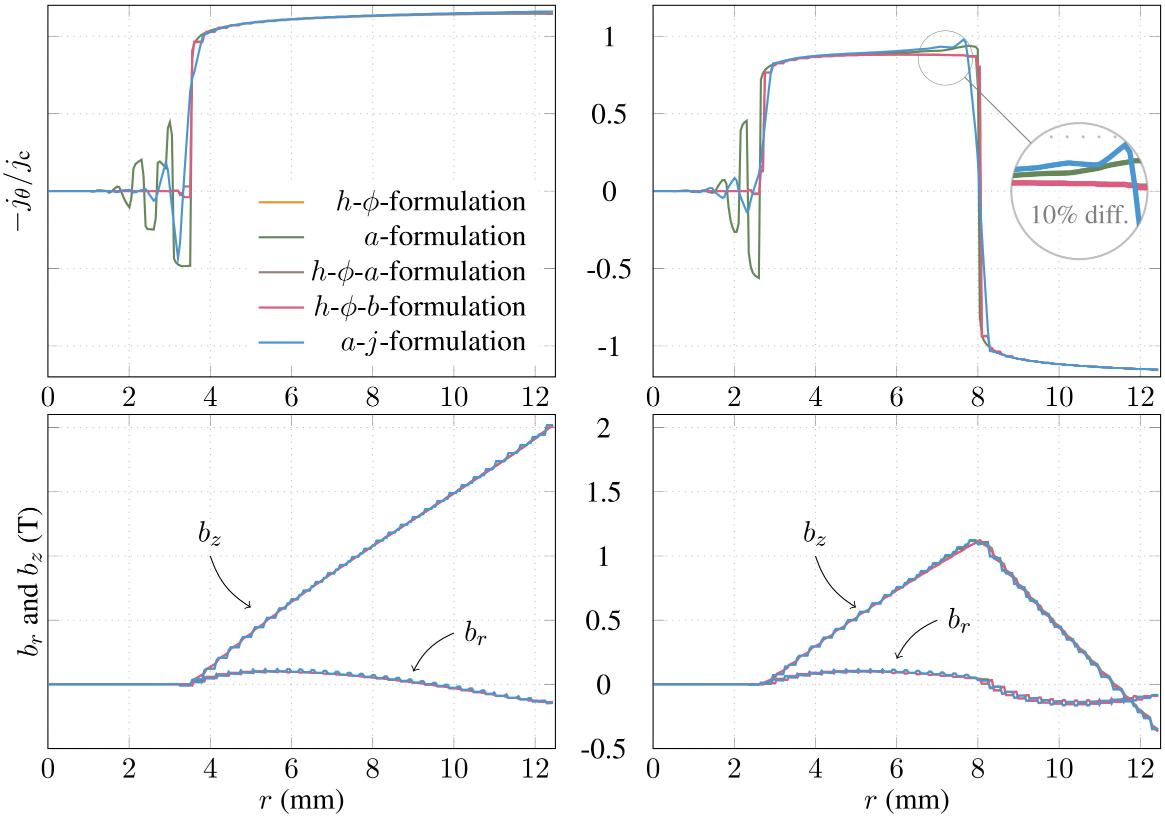

Figure 4.20: Azimuthal current density (up) and magnetic flux density r and z-components (down) along the mid-height horizontal segment in the T2S cylinder ("Cut 1" of Fig. 4.19(a)) at time $t = t_1$ (left) and $t = t_2$ (right). Results of five formulations are presented. Fine mesh resolution: $\alpha = 1$ (see Section 4.4.2). The legend is the same for all figures. The percentage inside the highlighted circle is the local relative difference between the solutions of the h-ϕ and a-j-formulations.

4.4.2 Efficiency of the formulations

The five tested formulations perform differently in terms of numerical efficiency. In this section, we compare the required number of iterations for a complete resolution, for the different formulations and for various levels of spatial and time discretization.

We define three discretization levels: coarse, medium, and fine, defined by a multiplier α equal to 4, 2, and 1, respectively. The mesh size varies from 0.3α mm in the cylinders to 3α mm on the outer surface. The initial time step is fixed to $\alpha\kappa t_2/240$, with $\kappa = 1$ or 2.

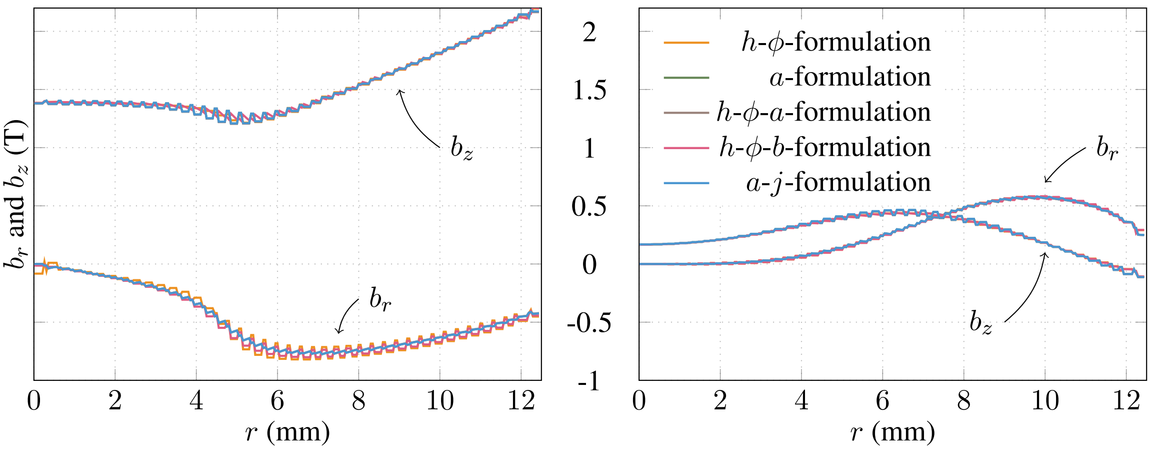

Figure 4.21: Magnetic flux density components along the mid-height horizontal segment in the SFM cylinder ("Cut 2" of Fig. 4.19(a)) at time $t = t_1$ (left) and $t = t_2$ (right). Results of five formulations are presented. Fine mesh resolution: $\alpha = 1$ (see Section 4.4.2). The legend is the same for both figures.

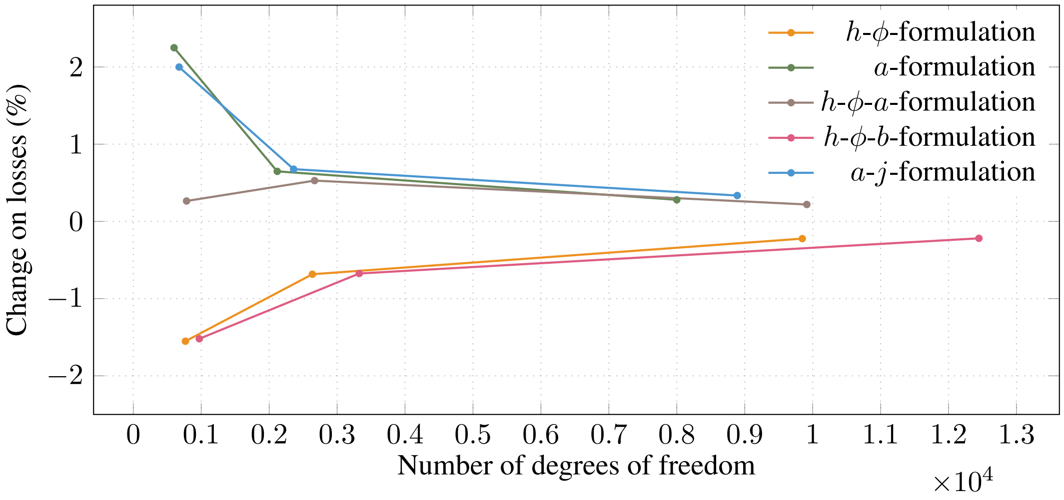

Figure 4.22: Change of AC losses $\int_0^{t_2} (\boldsymbol{j}\ , \boldsymbol{e})_{\Omega_c}\ dt$, relative to an accurate solution, for various numbers of spatial degrees of freedom, for five formulations, with constant time step $\Delta t = t_1/(60)$, $n = 20$, and $j_c = 3 \times 10^8$ A/m^2. The accurate solution is the average of the values obtained with the h-ϕ-b and a-j-formulations on the finest mesh.

An adaptive time-stepping algorithm is used to handle divergent or non-converging iterations. We use the procedure described in Section 2.6, with $\gamma = 1/2$, $\beta = 2$, Δt_{max} equal to the initial time step, $i_{\text{fast}} = i_{\text{max}}/4$. For the Newton-Raphson and Picard iterations, we choose $i_{\text{max}} = 50$ and $i_{\text{max}} = 500$, respectively. These are heuristic values.

Results are presented in Tables 4.4 and 4.5. In all cases, the a-j-formulation together with a zeroth-order extrapolation for the initial iterate demonstrates a better efficiency than the other methods. Because it also involves less degrees of freedom (DOFs) than the other mixed formulations, it is also the fastest in terms of computational time.

For coarse discretization levels especially, the h-ϕ-formulation encounters iterations cycles that deteriorate its efficiency. With smaller time steps or with a hybrid linearization technique for the SFM that consists in switching from Picard to Newton-Raphson after a number of $i_{\text{switch}} = 10$ iterations, the situation improves, but remains less efficient than the mixed formulations.

It is interesting to notice that the number of iterations does not scale linearly with the number of time steps. When it is multiplied by two from $\kappa = 2$ to $\kappa = 1$, the number of iterations is less than doubled. The fact that reducing the time step helps providing a good initial iterate is not a surprise, and was already hinted by iteration graphs in Section 2.7. For the a-formulation, the effect of the time step is less marked, as the number of Picard iterations is much less dependent on the initial iterate, as was shown in Section 2.7, too. The Picard method provides a very robust convergence, allowing for large time steps to be used, as mentioned in Section 4.1.2. In this example, a time step of $\Delta t = t_1 = t_2 - t_1$ already give a good first approximation of the magnetic field and current density at time instants t_1 and t_2.

Formulation		h-ϕ-form.		a-form.	h-a-form.		h-ϕ-b-form.		a-j-form.	
Linearization T2S		N-R		Picard	N-R		N-R		N-R	
Linearization SFM		N-R	Hybrid	N-R	N-R		N-R		N-R	
Extrapolation		1st	1st	2nd	0th	1st	0th	1st	0th	1st
Coarse	$\kappa = 2$	1 206	664	1 004	593	526	583	509	**464**	484
	$\kappa = 1$	946	1 068	1 823	649	713	643	680	**510**	567
Medium	$\kappa = 2$	1 492	1 153	1 671	1 124	1 030	1 130	1 016	**893**	921
	$\kappa = 1$	1 548	1 819	2 951	1 324	1 412	1 318	1403	**961**	1 121
Fine	$\kappa = 1$	3 468	3 606	3 987	2 892	3 084	2 833	2 855	**1 958**	2 350

Table 4.4: Total number of solved linear systems for the hybrid T2S-SFM model from $t = 0$ to $t = t_2$ for different discretization levels ($\alpha = 4, 2, 1$, $\kappa = 2, 1$), different extrapolation techniques, and five formulations. N-R stands for Newton-Raphson. For the hybrid method, $i_{\text{switch}} = 10$. Relative tolerance for the convergence criterion: $\varepsilon_{\text{rel}} = 10^{-6}$, except for the a-formulation, where $\varepsilon_{\text{rel}} = 10^{-4}$. Bold numbers are the minima of each line. Underlined numbers indicate that the resolution has encountered iteration cycles. Simulation times for the fastest simulations of each line (bold numbers) are, on a single Intel i7 2.2 GHz CPU, from top to bottom: 18”, 21”, 2’05”, 2’34”, and 22’14”.

Formulation	# DOFs	# iterations	Time/it.	Time/it./DOF	Total time
h-ϕ	9 847	3 468	633 ms	64.3 µs	38 m 05 s
a	8 000	3 987	618 ms	77.3 µs	41 m 03 s
h-ϕ-a	9 914	3 084	721 ms	72.7 µs	34 m 47 s
h-ϕ-b	12 447	2 833	773 ms	62.1 µs	36 m 30 s
a-j	8 890	1 958	681 ms	76.6 µs	22 m 14 s

Table 4.5: Comparison of the different formulations for the hybrid T2S-SFM model. Performance figures for the best choices with the five formulations and for $\alpha = \kappa = 1$, in correspondence with the last row of Table 4.4. CPU times are for a single Intel i7 2.2 GHz CPU.

In this particular test case, the gain obtained with the mixed formulations is not so high, compared to the standard h-ϕ-formulation. This does not generalize to every other case. In practice, there is no a priori guarantee to avoid cycles with the h-ϕ-formulation, even with reasonably small time steps. Getting an efficient resolution method based on the h-ϕ-formulation often relies on trial-and-error preliminary tests, as opposed to the situation with the mixed formulations, that always exhibit a good efficiency. This observation will be further illustrated in the next 3D problem.

4.5 T2S and SFM in a magnet motor pole (3D)

The last problem of this chapter is a hybrid T2S-SFM 3D structure. It consists of four T2S bulks placed on top of a SFM substrate. The T2S-SFM stack is then put in the bore of a magnetizing coil. The geometry is described in Fig. 4.23 and geometrical dimensions are given in Table 4.6(a) [40, 57]. Symmetry allows us to model one-eighth of the geometry, such that the finite element model in defined on the geometry of Fig. 4.23(b).

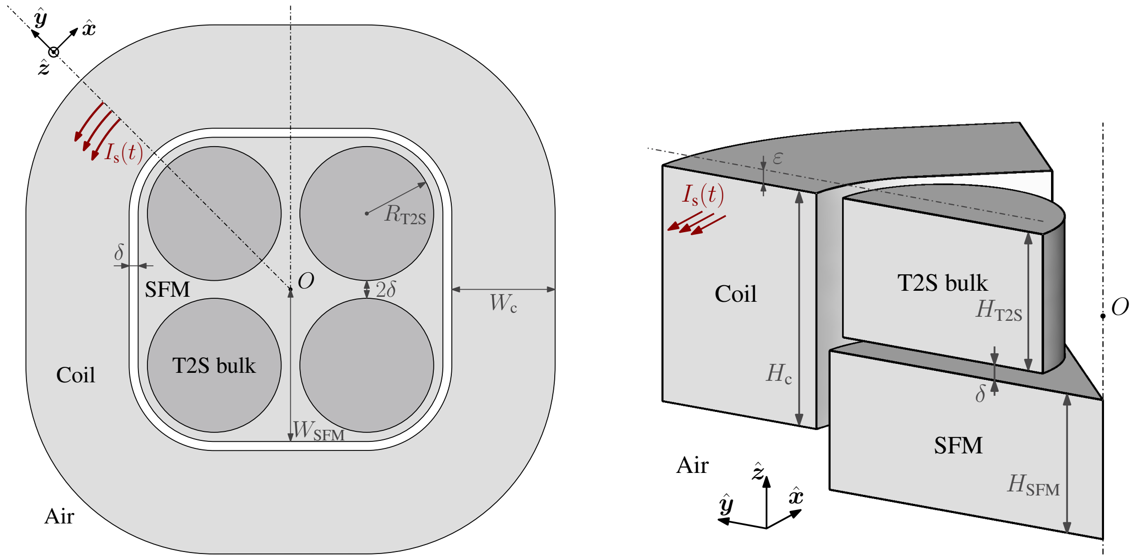

(a) Full geometry, seen from above.

(b) One-eighth of the geometry.

Figure 4.23: Geometry of the motor pole and its magnetizing coil. The problem exhibits four plane symmetries: $x = 0$, $y = 0$, $x = y$, and $x = -y$, with the axis origin O at the center of the bulks, so that one can model one-eighth of the problem. Curved boundaries of the SFM and coil domains are quarters of circles, whose centers coincide with those of the T2S bulks. The top surface of the T2S bulks and that of the coil are in the same plane. The dash-dotted gray line is where the magnetic flux density is sampled for Fig. 4.25, it is at $\varepsilon = 2$ mm above the T2S bulk and coil top surfaces, in the plane $x = 0$.

We model the magneto-quasistatic response of the T2S bulks and the SFM substrate to an applied current in the magnetizing coil. The coil is made up of $N_{\text{turns}} = 55.5$ turns of a winded T2S tape that carries a net current $I_s(t)$ defined by

$$I_s(t) = \begin{cases} I_{\max}\ \sin(\pi t/2T), & t < T, \\ I_{\max}\ e^{-(t-T)/\tau}, & t > T, \end{cases} \tag{4.1}$$

with $I_{\max} = 2$ kA, $T = 2$ ms, and $\tau = 10$ ms, see Fig. 4.24(a). Eddy currents in the coil are neglected, and the current density amplitude is assumed uniform inside it, and directed counter-clockwise along concentric circles in curved regions, or parallel to the boundaries in straight regions of the coil. We model the response of the system from a virgin state at $t = 0$ (zero-field cooled) to $t = 10\,T$.

The T2S bulks are described by the power law with field-dependent critical current density

$j_c(\boldsymbol{b})$ and power exponent $n(\boldsymbol{b})$ defined by

$$j_c(\boldsymbol{b}) = \frac{j_{c0}}{1 + \|\boldsymbol{b}\|/b_0}, \qquad n(\boldsymbol{b}) = n_1 + \frac{n_0 - n_1}{1 + \|\boldsymbol{b}\|/b_0}, \tag{4.2}$$

with $j_{c0} = 5 \times 10^8$ A/m^2, $b_0 = 0.5$ T, $n_0 = 21$, and $n_1 = 5$ [208]. These are representative values for YBCO pellets. The field-dependence is handled with a "fixed-point" approach for linearization: at a given iteration, the field from the previous iteration is used for $j_c(\boldsymbol{b})$ and $n(\boldsymbol{b})$. We did not observe any new difficulties with this approach, nor a significant impact on the total number of iteration with respect to problems with constant j_c and n values.

The SFM is assumed non-conducting and its permeability follows a saturation law based on experimental data for a Cobalt Steel VACOFLUX 50 material [209]. The saturation law is shown in Fig. 4.24(b). The saturation magnetization is around 2.2 T. In the finite element model, a linear interpolation is used on the discrete experimental data to get a continuous function $\mu(\boldsymbol{h})$, or $\nu(\boldsymbol{b})$, and the differential permeability, or differential reluctivity, required for Newton-Raphson iterations, is evaluated by a finite difference on $\mu(\boldsymbol{h})$, or $\nu(\boldsymbol{b})$, respectively.

Parameter		Value	
T2S radius	R_{T2S}	15.0	mm
T2S height	H_{T2S}	17.7	mm
SFM half-width	W_{SFM}	34.0	mm
SFM height	H_{SFM}	17.7	mm
Coil width	W_c	23.1	mm
Coil height	H_c	30.0	mm
Small gap	δ	2.0	mm
Air radius	R_{out}	270.0	mm

(a) Geometric parameters.

Parameter	Value	
j_{c0}	5×10^8	A/m^2
b_0	0.5	T
n_0	21	-
n_1	5	-
$I_{\max}$	2	kA
N_{turns}	55.5	-
T	2	ms
τ	10	ms

(b) T2S and coil parameter values.

Table 4.6: Geometric and parameter values for the magnet motor pole problem.

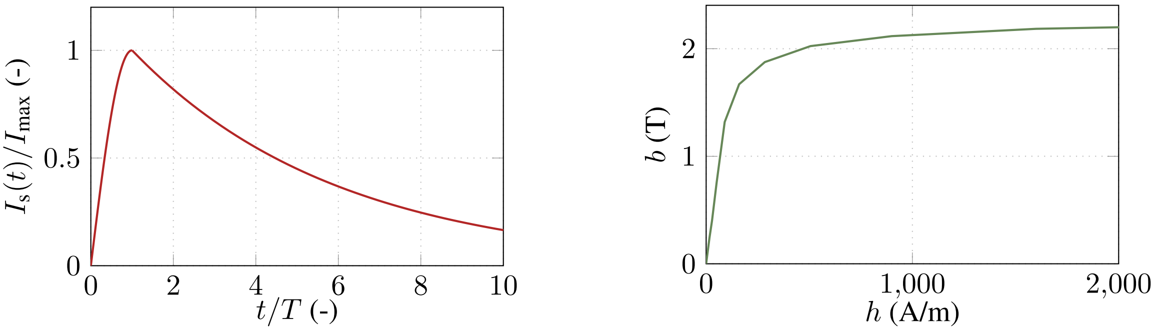

(a) Source current $I_s(t)$.

(b) SFM saturation curve.

Figure 4.24: Source current and SFM saturation curve for the magnet motor pole problem.

The modeled domain is denoted by Ω, and is decomposed into a conducting part, Ω_c, containing the T2S bulk, and a non-conducting part Ω_c^C, containing the air, the SFM, and the coil. In addition, the SFM domain is referred to as Ω_m, and its complementary domain is denoted by Ω_m^C. The coil is denoted by Ω_s. The domain boundary Γ consists of one-eighth of a sphere as an outer boundary Γ_{out}, placed at a distance R_{out} from the center O, and two half-disks as symmetry boundaries Γ_{sym} (in planes $x = 0$ and $x = y$).

4.5.1 Source fields

The inducting coil is handled as a stranded inductor, as proposed in [134]. Eddy currents are not modeled in Ω_s so that $\Omega_\text{s} \subset \Omega_\text{c}^\text{C}$, i.e., no electrical conductivity is defined in Ω_s. We distinguish two cases depending on the formulation: whether Ω_s is in a b-conform or in an h-conform region. The coil is in a b-conform region with the a and a-j-formulations, and with the h-ϕ-a-formulation if $\Omega_\text{s} \subset \Omega_a$. Conversely, it belongs to an h-conform region with the h-ϕ and h-ϕ-b-formulations, and with the h-ϕ-a-formulation if $\Omega_\text{s} \subset \Omega_h$.

Weak global constraint in b-conform formulations

In the first case, the source current density $\boldsymbol{j}_\text{s}$ is explicitly introduced in the formulation via an integral on Ω_s [134]. For the a-formulation, with $\boldsymbol{e}_\text{a} = \boldsymbol{0}$ because no global variable is associated with the T2S bulk, we write, with $\Omega_\text{s} \subset \Omega_\text{c}^\text{C}$,

$$(\nu\, \textbf{curl}\, \boldsymbol{a}\, , \textbf{curl}\, \boldsymbol{a}')_{\Omega} + (\sigma\, \partial_t \boldsymbol{a}\, , \boldsymbol{a}')_{\Omega_\text{c}} = (\boldsymbol{j}_\text{s}\, , \boldsymbol{a}')_{\Omega_\text{s}}\, . \tag{4.3}$$

This can be immediately generalized to the a-j and h-ϕ-a-formulations.

Strong global constraint in h-conform formulations

In the second case, a generalized unit source field $\boldsymbol{h}_\text{s1}$ associated with a unit source current of 1 A is computed before the main finite element resolution, and included in the function space of the total magnetic field $\boldsymbol{h}$ as a global shape function, i.e., a function spreading over several mesh elements and associated with a global degree of freedom. Keeping notations of Chapter 2, the total magnetic field is expressed as

$$\boldsymbol{h} = I_\text{s}\, \boldsymbol{h}_\text{s1} + \sum_{e \in \mathcal{E}(\Omega_\text{c} \setminus \partial\Omega_\text{c})} h_e\, \boldsymbol{w}_e + \sum_{n \in \mathcal{N}(\Omega_\text{c}^\text{C})} \phi_n\, \textbf{grad}\, w_n + \sum_{i \in C} I_i\, \boldsymbol{c}_i, \tag{4.4}$$

with the new degree of freedom I_s, fixed by the global essential[3] condition $I_\text{s} = I_\text{s}(t)$. For simplicity, let us keep the notation $\mathcal{H}^{\delta,1}(\Omega)$ for the generated function space. Note that in this motor pole problem, the T2S bulk is simply connected and is not associated with any global condition so that $C = \{\}$ and the last term of Eq. (4.4) drops out.

The resulting weak formulations are unchanged, the difference is only contained in the unknown field $\boldsymbol{h}$ function space, that explicitly involves the known field associated with the source current. The generalized unit source field $\boldsymbol{h}_\text{s1} \in \mathcal{H}_\text{s}^{\delta,1}(\Omega)$ generated by a current density $\boldsymbol{j}_\text{s1} = \boldsymbol{j}_\text{s}/I_\text{s}$ satisfies, in the coil region Ω_s,

$$(\textbf{curl}\, \boldsymbol{h}_\text{s1}\, , \textbf{curl}\, \boldsymbol{h}'_\text{s1})_{\Omega_\text{s}} = (\boldsymbol{j}_\text{s1}\, , \textbf{curl}\, \boldsymbol{h}'_\text{s1})_{\Omega_\text{s}}\, , \quad \forall \boldsymbol{h}_\text{s1} \in \mathcal{H}_\text{s0}^{\delta,1}(\Omega), \tag{4.5}$$

and is curl-free in the complementary domain Ω_s^C, with function spaces $\mathcal{H}_\text{s}^{\delta,1}(\Omega)$ and $\mathcal{H}_\text{s0}^{\delta,1}(\Omega)$ defined as described in [134]. In a nutshell, $\boldsymbol{h}_\text{s1}$ is generated by edge functions associated with edges of a co-tree defined in the interior of Ω_s, and by a cut function in the complementary domain Ω_s^C to account for the effect of the source current outside of the coil.

---

[3] We do not treat the associated voltage here, nor the possibility to impose it as a natural global condition.

4.5.2 Comparison of the solutions and efficiencies of the formulations

We now compare the performance levels of different formulations on the 3D problem. We run simulations on the same mesh, with characteristic lengths of 1.6 mm on the T2S bulk, 2.8 mm on the SFM substrate, and 4 mm on the magnetizing coil, that progressively increases up to 40 mm on the outer surface. The resulting mesh is made up of $5\,797$ nodes and contains only tetrahedra.

For time discretization, for all formulations, the time step is fixed to $\Delta t = T/80$ for $0 < t < T$, and is progressively increased afterwards, so that a total of 48 time steps are used from $t = T$ to $t = 10\,T$. In total, a number of 128 time steps is therefore obtained. They were chosen small enough so that the adaptive time-stepping algorithm was not triggered for any formulation.

The convergence criterion is based on the instantaneous power $\mathcal{P} = (\partial_t \boldsymbol{b}\,, \boldsymbol{h})_{\Omega} + (\boldsymbol{j}\,, \boldsymbol{e})_{\Omega_{\text{c}}}$. Iterations stop when the relative change of $\mathcal{P}$ is smaller than $\varepsilon_{\text{rel}} = 10^{-6}$ in each of the sub-domains, or $\varepsilon_{\text{rel}} = 10^{-5}$ when Picard iterations are used, that is, when either σ or μ is involved.

We consider eight different formulations or variations of them. They are presented in the paragraphs below, and summarized in Table 4.7.

	NL laws	Function space(s)	Number of degrees of freedom (DOFs)*
h	ρ, μ	$\boldsymbol{h} \in \mathcal{H}^{\delta,1}(\Omega)$ with $\Omega_{\text{c}} = \Omega$ and ρ_{s}	$35\,532 \approx N_{\mathcal{E}}$ in Ω
h-ϕ	ρ, μ	$\boldsymbol{h} \in \mathcal{H}^{\delta,1}(\Omega)$	$12\,172 \approx N_{\mathcal{E}}$ in Ω_{c} + $N_{\mathcal{N}}$ in $\Omega_{\text{c}}^{\text{C}}$
$\bar{a}$	σ, ν	$\boldsymbol{a} \in \mathcal{A}^{\delta,1}(\Omega)$ with $\Omega_{\text{c}} = \Omega$ and σ_{s}	$29\,010 \approx N_{\mathcal{E}}$ in Ω
a	σ, ν	$\boldsymbol{a} \in \mathcal{A}^{\delta,1}(\Omega)$	$26\,964 \approx N_{\mathcal{E}}$ in Ω_{c} + $N_{\mathcal{F}}$ in $\Omega_{\text{c}}^{\text{C}}$
h-a	ρ, ν	$\boldsymbol{h} \in \mathcal{H}^{\delta,1}(\Omega_{\text{c}})$, $\quad \boldsymbol{a} \in \mathcal{A}^{\delta,2}(\Omega_{\text{c}}^{\text{C}})$	$32\,045 \approx N_{\mathcal{E}}$ in Ω_{c} + $N_{\mathcal{F}}(\dagger)$ in $\Omega_{\text{c}}^{\text{C}}$
h-ϕ-a	ρ, ν	$\boldsymbol{h} \in \mathcal{H}^{\delta,2}(\Omega_{\text{m}}^{\text{C}})$, $\quad \boldsymbol{a} \in \mathcal{A}^{\delta,1}(\Omega_{\text{m}})$	$15\,776 \approx N_{\mathcal{E}}$ in $\Omega_{h,\text{c}}$ + $N_{\mathcal{N}}(\dagger)$ in $\Omega_{h,\text{c}}^{\text{C}}$ + $N_{\mathcal{F}}$ in Ω_{m}
h-ϕ-b	ρ, ν	$\boldsymbol{h} \in \mathcal{H}^{\delta,1}(\Omega)$, $\quad \boldsymbol{b} \in \mathcal{B}_{\text{cst}}^{\delta,1}(\Omega_{\text{m}})$	$20\,821 \approx N_{\mathcal{E}}$ in Ω_{c} + $N_{\mathcal{N}}$ in $\Omega_{\text{c}}^{\text{C}}$ + $N_{\mathcal{V}}$ (×3) in Ω_{m}
a-j	ρ, ν	$\boldsymbol{a} \in \mathcal{A}^{\delta,1}(\Omega)$, $\quad \boldsymbol{j} \in \mathcal{J}^{\delta,1}(\Omega_{\text{c}})$	$36\,019 \approx N_{\mathcal{E}}$ (×2) in Ω_{c} + $N_{\mathcal{F}}$ in $\Omega_{\text{c}}^{\text{C}}$

Table 4.7: Summary of the different formulations considered for the 3D magnet motor pole problem. NL stands for nonlinear. $N_{\mathcal{N}}$, $N_{\mathcal{E}}$, $N_{\mathcal{F}}$, and $N_{\mathcal{V}}$ are shortcuts for the number nodes, edges, facets, and volumes, respectively. ($\star$) The DOFs removed by the application of essential boundary conditions are not explicitly expressed, nor are the DOFs associated with global variables and function space enrichements for stability, hence the approximation sign "$\approx$" in the last column of the table. (†) For surface-coupled formulations, a local enrichment is necessary on the coupling boundary Γ_{m} to guarantee stability [55]. In 3D, this adds twice the number of facets on Γ_{m} to the number of DOFs if one wants to enrich $\mathcal{A}^{\delta,1}$, which is our choice for the h-a-formulation, or once the number of edges on Γ_{m} to the number of DOFs if one prefers to enrich $\mathcal{H}^{\delta,1}$, which is our choice for the h-ϕ-a-formulation.

First, we consider the standard h-ϕ-formulation. To illustrate the benefit of using curl-free functions in $\Omega_{\text{c}}^{\text{C}}$, we also consider the alternative "full h-formulation", in which the magnetic field is discretized with edge functions on the whole domain Ω, instead of in the conducting domain Ω_{c} only, hence introducing a spurious resistivity ρ_{s} in $\Omega_{\text{c}}^{\text{C}}$ [210]. This method leads to more unknowns in $\Omega_{\text{c}}^{\text{C}}$, one per edge instead of one per node with curl-free functions, and was shown to produce ill-conditioned matrices [211]. However, this approach is popular in proprietary software, e.g., COMSOL [209], because of the ease of its implementation. Note that a h-ϕ-formulation analogue has been recently implemented in COMSOL, where the field $\boldsymbol{h}$ and ϕ are weakly coupled via Lagrange multipliers [139, 212].

Then, we consider the standard a-formulation. In parallel with the "full h-formulation", we also consider a modified version of the a-formulation where we remove the co-tree gauge in $\Omega_{\mathrm{c}}^{\mathrm{C}}$ and instead introduce a spurious conductivity σ_{s} in $\Omega_{\mathrm{c}}^{\mathrm{C}}$. We refer to this modified formulation as the $\bar{a}$-formulation. It leads to more degrees of freedom in $\Omega_{\mathrm{c}}^{\mathrm{C}}$, one per edge instead of one per facet with the co-tree gauge. Actually, one can sometimes afford to have $\sigma_{\mathrm{s}} = 0$, hence making the matrix system singular, as some iterative linear solvers do not require uniqueness of the solution to converge.

For the h-formulation, the spurious resistivity in air is fixed to $\rho_{\mathrm{s}} = 10^{-3}$ Ωm. For the $\bar{a}$-formulation, the spurious conductivity is fixed to $\sigma_{\mathrm{s}} = 1$ S/m. Typical resistivity values observed in the T2S bulks are of the order of $e_{\mathrm{c}}/j_{\mathrm{c}}(\boldsymbol{b}) = 6 \times 10^{-13}$ Ωm for $\|\boldsymbol{b}\| = 1$ T, so that the chosen values of ρ_{s} and $1/\sigma_{\mathrm{s}}$ are much higher. We have not observed any significant impact of the spurious parameters on the numerical solution quality.

Next, we consider the surface-coupled h-ϕ-a-formulation. The main motivation of this formulation is to put the T2S bulk Ω_{c} in Ω_h, and the SFM substrate Ω_{m} in Ω_a, in order to use a Newton-Raphson method for both nonlinearities, without risking to encounter iteration cycles. We can choose to place the other subdomains, i.e., the coil Ω_{s} and the air, either in Ω_h, or Ω_a. We consider two distinct choices. In what we will denote as the h-a-formulation, we put the coil and the air in Ω_a (the absence of the scalar potential ϕ in the notation hints that $\Omega_h \subset \Omega_{\mathrm{c}}$). Conversely, we keep the notation h-ϕ-a-formulation for the alternative choice where we put the coil and the air in Ω_h.

Finally, we consider the two volume-coupled formulations: the h-ϕ-b-formulation and the a-j-formulation. We choose $\boldsymbol{b} \in \mathcal{B}_{\mathrm{cst}}^{\delta,1}(\Omega_{\mathrm{m}})$, as defined in Section 3.4.3.

We run the simulations with the eight formulations. Global and local solutions agree with each other. The total hysteresis loss in the T2S bulk is given in Table 4.8, the difference between the values is at most 1%. The norm of $\boldsymbol{b}$ along the dashed line of Fig. 4.23(b) is represented in Fig. 4.25 for the a and h-ϕ-formulations. All other formulations yield results that are visually indistinguishable from these two formulations. Results also nicely match inside the T2S bulk and SFM substrate. For illustration, the current density in the T2S bulk is represented in Fig. 4.26.

A good accuracy can be achieved with all formulations. However, as in all other test cases in this chapter, the computational cost associated with each of them is not equivalent. This is clearly demonstrated by the performance figures in Table 4.8. Firstly, in 3D, the number of DOFs is strongly affected by the choice of function spaces. When possible, is it always preferable to introduce a magnetic scalar potential ϕ, or to gauge the magnetic vector potential $\boldsymbol{a}$ in $\Omega_{\mathrm{c}}^{\mathrm{C}}$. Also, using the scalar potential ϕ in $\Omega_{\mathrm{c}}^{\mathrm{C}}$ instead of the vector potential $\boldsymbol{a}$ in the surface-coupled formulation leads to fewer DOFs.

Secondly, the number of iterations required to reach convergence strongly depends on the involved nonlinear laws. For the h and h-ϕ-formulations, the large number of iterations is due to the Picard iterations that are used for the permeability of the SFM. We observed that in some cases, a Newton-Raphson scheme (with or without relaxation factors) applied on the permeability works without difficulty, leading to a CPU time - still higher but - nearly similar to that obtained with coupled formulations. However, this is not guaranteed in general. Typically,

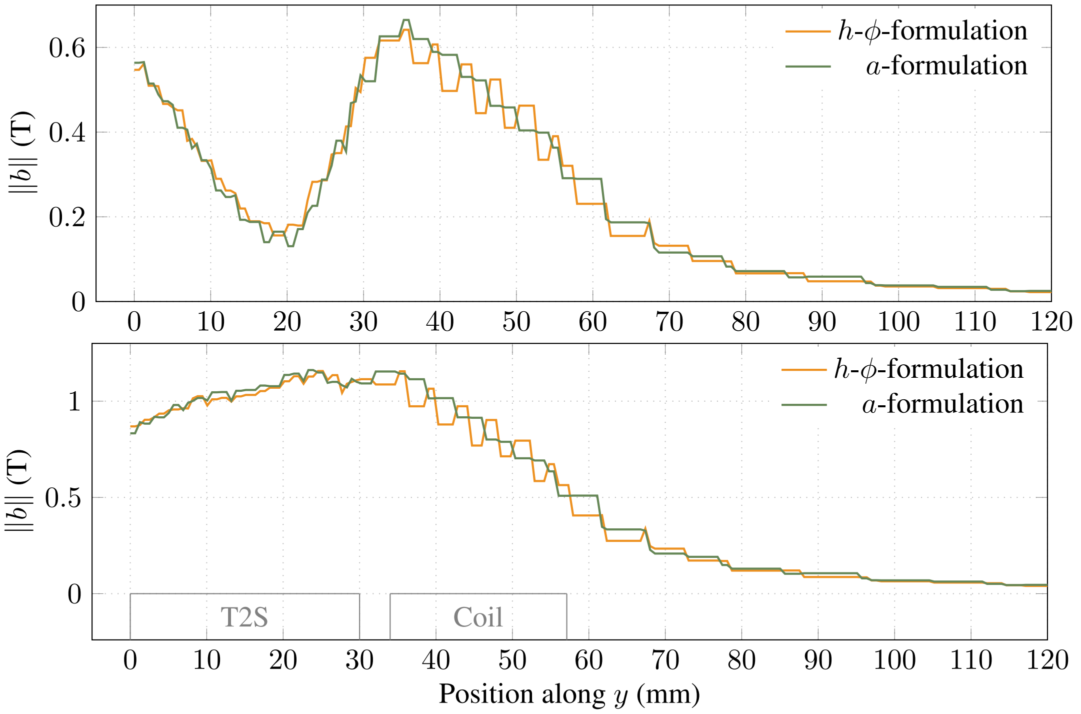

Figure 4.25: Norm of the magnetic flux density at $\varepsilon = 2$ mm above the system, along the dashed line represented in Fig. 4.23(b). The upper plot is at $t = 0.25\,T$ and the lower plot at $t = 3.5\,T$. Curves obtained with the h, h-ϕ-a, h-ϕ-b-formulations are visually indistinguishable from those resulting from the h-ϕ-formulation (h-conform field in air). The same is true for curves obtained with the $\bar{a}$, h-a, a-j-formulations in comparison to those resulting from the a-formulation (b-conform field in air).

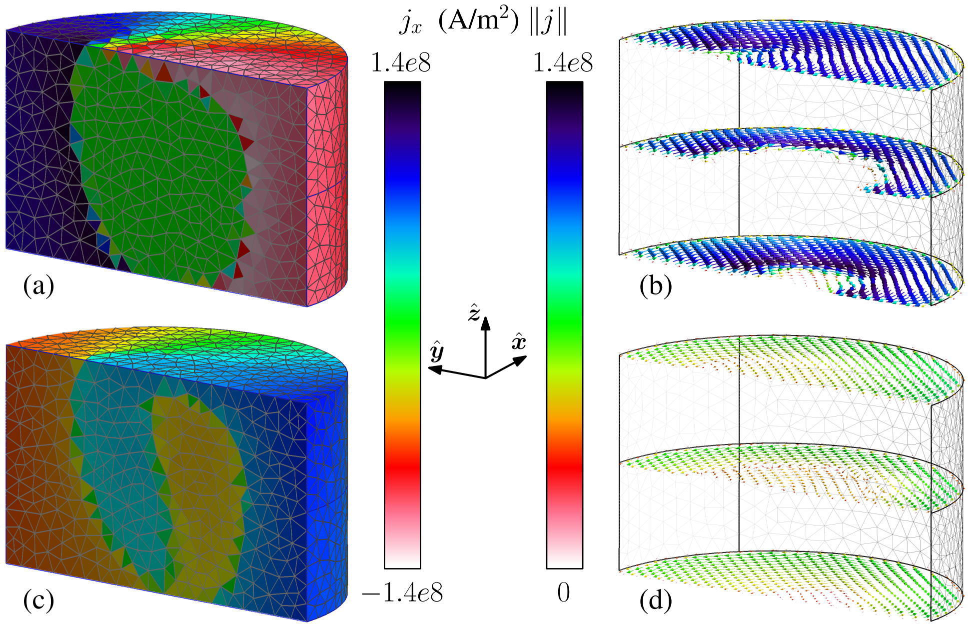

Figure 4.26: Current density obtained with the h-ϕ-a-formulation in the bulk during the magnetizing pulse: (a)-(b) at $t = 0.25\,T$, and (c)-(d) during relaxation at $t = 3.5\,T$. (a)-(c) x-component j_x in the bulk, and (b)-(d) full vector $\boldsymbol{j}$ in three planes.

with the discretization presented here, convergence issues are indeed observed. Circumventing these issues requires a numerical parameter tuning by a trial-and-error procedure if one wants to keep the standard formulations. For the $\bar{a}$ and a-formulations, the conductivity in T2S is even more difficult to handle efficiently and, as before, we only obtained convergence with Picard iterations.

For the coupled formulations, in surface and in volume, the number of iterations is directly reduced thanks to the shapes of the ρ and ν laws that naturally allow for an efficient use of Newton-Raphson iterations, without requiring any parameter tuning.

Surface-coupled formulations appear to be the best choices, especially the h-ϕ-a-formulation, that only involves the magnetic vector potential $\boldsymbol{a}$ in the SFM substrate. Volume-coupled formulations introduce more DOFs but may possibly be easier to implement, because the associated function spaces do not involve higher-order shape functions.

Interestingly, the CPU time per iteration does not scale directly with the number of DOFs in this 3D problem. The matrix structures associated with the formulations are different and this could influences the linear solver resolution. Note that in the 2D problem presented in the previous section, the difference was less marked, see Table 4.5.

The CPU times are given as an indication. In the considered implementation, a significant amount of time is spent in post-processing operations, including the evaluation of $\mathcal{P}$ as a volume integral at each iteration for the convergence criterion. The cost of this task could be strongly reduced with a more efficient approach. Additionally, the assembly step could be made much faster with a parallelization.

Formulation	T2S loss (J)	# DOFs	# iterations	Time/it.	Time/it./DOF	Total time
h	6.35	35 532	4 057	3.3 s	92 µs	3 h 42 m
h-ϕ	6.36	12 172	3 937	1.4 s	116 µs	1 h 33 m
$\bar{a}$	6.38	29 010	2 955	3.1 s	107 µs	2 h 33 m
a	6.39	26 964	3 147	2.1 s	76 µs	1 h 48 m
h-a	6.31	32 045	1 124	2.7 s	83 µs	50 m
h-ϕ-a	6.33	15 776	1 108	2.1 s	133 µs	39 m
h-ϕ-b	6.37	20 821	1 104	3.2 s	151 µs	58 m
a-j	6.34	36 019	2 225	3.6 s	101 µs	2 h 15 m

Table 4.8: Comparison of the different formulations. Performance figures for the 128 time steps of the eight formulations with lowest-order elements (except on the coupling boundary for coupled formulations where higher-order elements are used). T2S loss is the total hysteresis loss in the T2S bulk from $t = 0$ to $t = 10\,T$. Results differ by maximum 1%. Picard iterations were used for the first four formulations (for σ or μ), which explains the large associated number of iterations. When trying more efficient method such as Newton-Raphson iterations (with or without relaxation factors), we have not obtained robust behaviors. CPU times are for a single AMD EPYC Rome CPU at 2.9 GHz.

4.6 Summary and general recommendations

In this chapter, we compared the performance levels of standard and mixed formulations on various problems, from a 1D T2S bar to a 3D hybrid system containing both T2S and SFM. We observed that when space and time discretizations are chosen fine enough, all formulations produce accurate results in terms of local and global quantities, in the sense that they all tend towards each other. With coarse meshes, the only non-negligible source of error we noticed arises when the current density is expressed from the electric field via the power law, which is the case with the a-formulation. This results in large oscillations in the current density profile ahead of flux fronts in flux-free regions, over a few finite elements. With mesh refinement, however, the spatial extent of this error decreases.

All the presented formulations offer accurate solutions, but the computational resources they require for doing so are not equivalent. The efficiency of the resolution significantly depends on the chosen formulation. With T2S, formulations involving the resistivity instead of the conductivity perform notably better than the others, as we have not found any way to handle the power law conductivity with efficient linearization techniques. To a lesser extent, with SFM, formulations involving the reluctivity instead of the permeability are more convenient to consider, as they do not require any parameter tuning for avoiding iteration cycles. They directly allow for standard Newton-Raphson iterations to be used effectively. Hybrid problems involving both T2S and SFM were proven to be solved efficiently with the dedicated h-ϕ-a, h-ϕ-b, and a-j-formulations, in 2D and 3D problems.

In addition to the choice of the formulation, the choice of a first estimate for the iterative methods can have an important influence on the numerical performance. We considered three different possibilities for the first estimate, and the best choice was demonstrated to be formulation-dependent. In general, a first-order extrapolation of the last two solutions gives good results with the h-ϕ-formulation; a second-order extrapolation of the last three solutions appears to be a good choice for the a and t-a-formulations; and simply using the previous solution as a first estimate is usually preferable for the h-ϕ-a, h-ϕ-b, and a-j-formulations. When considering a new problem, it is however recommended to evaluate the different possibilities, as the optimal choice might depend on the situation.

We also discussed the possibility of using large time steps in some circumstances for problems with T2S. Large time steps provide good approximations of the magnetic flux density and current density distributions for values of the power exponent n that are large enough. The a-formulation together with Picard iterations on the conductivity were shown to be robust choices for the large-time-step approach. This was illustrated on a 1D problem, but conclusions hold on 2D and 3D problems [124, 36]. Provided that accurate evaluations of the electric field and the power loss are not sought, the large-time-step approach provides good results in a small amount of time.

Comparisons also highlighted that mixed formulations have an interest for problems with T2S only. For the 2D T2S cylinder problem, the a-j-formulation was observed to be the most efficient choice, even outperforming the standard h-ϕ-formulation. Thin-shell formulations such as the t-a-formulation also offer interesting properties. In particular, even though this has not been discussed in this chapter, complicated 3D geometries, such as Roebel cables [42, 120, 51], or twisted tapes in CORC® cables [45] are easier to handle using thin-shell approximations.

The numerical study of this chapter also demonstrated that an important point to take into consideration when choosing a formulation is the number of associated degrees of freedom (DOFs), which is especially relevant in 3D. The number of DOFs directly affects the computational work required for the numerical resolution. In particular, when possible, using a scalar potential instead of a gauged vector potential in the non-conducting domain $\Omega_{\text{c}}^{\text{C}}$ should be preferred.

Also, depending on whether the problem is 2D or 3D, different formulations do not compare equivalently. For example, the a-j-formulation usually involves less DOFs than the h-ϕ-a-formulation in 2D, but this is no longer necessarily the case in 3D, where the co-tree gauge for the vector potential $\boldsymbol{a}$ in $\Omega_{\text{c}}^{\text{C}}$ only reduces the number of DOFs to one per facet in $\Omega_{\text{c}}^{\text{C}}$, whereas the use of a scalar potential ϕ in $\Omega_{\text{c}}^{\text{C}}$ involves one DOF per node in $\Omega_{\text{c}}^{\text{C}}$.

We also observed that the number of DOFs does not solely determine the cost per iteration of a formulation. As was shown with the 3D magnet motor pole problem, the CPU time per DOF (and per iteration) is not constant. It can nearly be doubled from one formulation to another.

As a final conclusion, no formulation outperforms all the others in all situations. The most efficient choice is problem-dependent, which demonstrates the utility of considering different formulations when facing a new problem. In general, for problems with T2S only, we would recommend to first test the h-ϕ or a-j-formulations for 2D problems, and the h-ϕ-formulation for 3D problems. For hybrid T2S-SMF models, we would recommend in priority the a-j-formulation for 2D problems and the h-ϕ-a-formulation for 3D problems.

Chapter 5

Two applications with a non-trivial geometry

In the previous chapter, we applied different finite element formulations on problems with simple geometries. This allowed us to assess the advantages and drawbacks of each formulation and to extract general conclusions for their applications. In this chapter, we focus on two distinct applications that involve more complex geometries.

The first application, presented in Section 5.1, consists in the evaluation of AC losses in wires made up of twisted superconducting filaments with the h-ϕ-formulation. Implementing the associated 3D problem is already a non-trivial task, because it quickly gets extremely expensive in terms of computational work, while it also involves technical difficulties related to periodic boundary conditions and periodic cohomology functions. In addition to the 3D problem, we present a change of variables that allows a dimension reduction to 2D for geometries that are helicoidally symmetric, and we discuss how this approach can be applied to superconducting materials.

The second application, presented in Section 5.2, consists in the calculation of the shielding effectiveness associated with layered hollow structures made up of a stack of second generation (2G) superconducting tapes with a ferromagnetic substrate. As for the first application, the direct 3D problem has a high computational cost and we propose two simpler models that will be shown to reproduce the global magnetic behavior of the structures. In addition, we will validate the models against experimental measurements.

5.1 Problems with a helicoidal symmetry

AC losses in wires made up of superconducting filaments can be reduced by twisting the filaments [213, 69, 214]. The filaments are embedded in a conducting matrix and the electromagnetic response of the resulting system is not trivial. Numerical modeling is helpful to get a better understanding of the underlying physical behavior. However, with twisted filaments, the wire geometry is fully 3D in Cartesian coordinates. As shown in [215] for multi-filamentary MgB_2

wires, solving a full 3D model can be extremely expensive in terms of computational work. When possible, it is therefore highly interesting to exploit the symmetries in the problem.

In particular, when wires present a helicoidal symmetry, i.e., a combination of translation and rotation symmetries, it is possible to reduce the dimension from 3D to 2D, if one works in an appropriate coordinate system, referred to as the helicoidal coordinate system.

The method for expressing the original helicoidally symmetric 3D problem as a 2D mathematically equivalent problem has been introduced in optical waveguide applications [216, 217, 218]. In the following, it is referred to as the *helicoidal transformation method*. In addition to waveguide applications, this method has been applied to electrostatic problems [219, 220], linear magnetodynamic problems [58], and nonlinear magnetodynamic problems with superconduting filaments [221, 222, 223].

Approximate models have also been investigated, such as in [224, 225], where authors estimate leaking currents in the conducting matrix with a 2D finite element model, by introducing equivalent resistance values between the filaments, obtained via a preliminary 2D electrostatic resolution. Another model is proposed in [226], where authors investigate the use of a Frenet frame to simplify the 3D geometry definition and approximate the AC losses by considering a fraction of the pitch length of the wire in a 3D model, or a cross-section of the wire in a 2D model.

In this study, we consider the helicoidal transformation method. It offers the advantage of reducing the dimension from 3D to 2D without introducing any approximation in the continuous setting by transforming the differential forms using the metric tensor of the change of variables. In this section, we do not enter into the technical details describing general transformations of differential forms, we rather refer to the extensive literature about this topic. Useful references are, e.g., [227, 228]. Instead, we present the main results and directly apply them on our magnetodynamic problem, involving type-II superconductors (T2S).

In Section 5.1.1, we first introduce the change of variables. In Section 5.1.2, we derive the h-ϕ-formulation in helicoidal coordinates, and describe the associated practical implementation in a finite element code. In Section 5.1.3, we verify the implementation by comparing the numerical results of the proposed method with those of a 3D model written in the classical Cartesian coordinate system. Finally, in Section 5.1.4, we propose an extension of the method to problems whose boundary conditions are not helicoidally symmetric, such as problems involving the excitation of a twisted wire by a transverse field. Here, we only apply this extension to linear materials, and provide brief prospects for its application to nonlinear materials. Also, we only apply the helicoidal transformation method on a wire with round superconducting filaments, embedded in a conducting matrix, but the method directly applies to other types of helicoidally symmetric geometries as well, such as single-layer CORC® cables [45] or twisted stacked tape conductors [44].

A peculiarity of our approach is that we take care of maintaining the curl-free property of the magnetic field in the non-conducting domains. This allows us to benefit from the advantages of the standard h-ϕ-formulation in Cartesian coordinates. In addition, the extension to non-helicoidally symmetric boundary conditions constitutes a novelty compared to state-of-the-art models.

5.1.1 Helicoidal change of variables

Let us consider a Cartesian coordinate system (x, y, z), of origin O. We define the helicoidal change of variables $(x, y, z) \to (\xi_1, \xi_2, \xi_3)$ as the following transformation

$$\begin{cases} \xi_1 = x\cos(\alpha z) + y\sin(\alpha z), \\ \xi_2 = -x\sin(\alpha z) + y\cos(\alpha z), \\ \xi_3 = z, \end{cases} \quad \Leftrightarrow \quad \begin{cases} x = \xi_1\cos(\alpha\xi_3) - \xi_2\sin(\alpha\xi_3), \\ y = \xi_1\sin(\alpha\xi_3) + \xi_2\cos(\alpha\xi_3), \\ z = \xi_3, \end{cases} \tag{5.1}$$

with the new coordinate system (ξ_1, ξ_2, ξ_3) with the same origin O, and $\alpha \in \mathbb{R}$ the twisting parameter, which is the unique parameter of the transformation. We also define the pitch length p of the transformation, that is inversely proportional to the twisting parameter, $p = 2\pi/\alpha$.

With this transformation, helices in the (x, y, z)-space, $\Omega_{\boldsymbol{x}}$, with pitch length p and whose axis contains the origin O and is in the z-direction, are mapped into straight lines in the (ξ_1, ξ_2, ξ_3)-space, $\Omega_{\boldsymbol{\xi}}$. This is illustrated in Fig. 5.1 for two helices of pitch length $p = 1$. A geometry is said to be helicoidally symmetric, or to have a helicoidal symmetry if, for one value of α, its description in the (ξ_1, ξ_2, ξ_3)-space is independent of ξ_3. In that case, we also say that such a geometry is ξ_3-invariant.

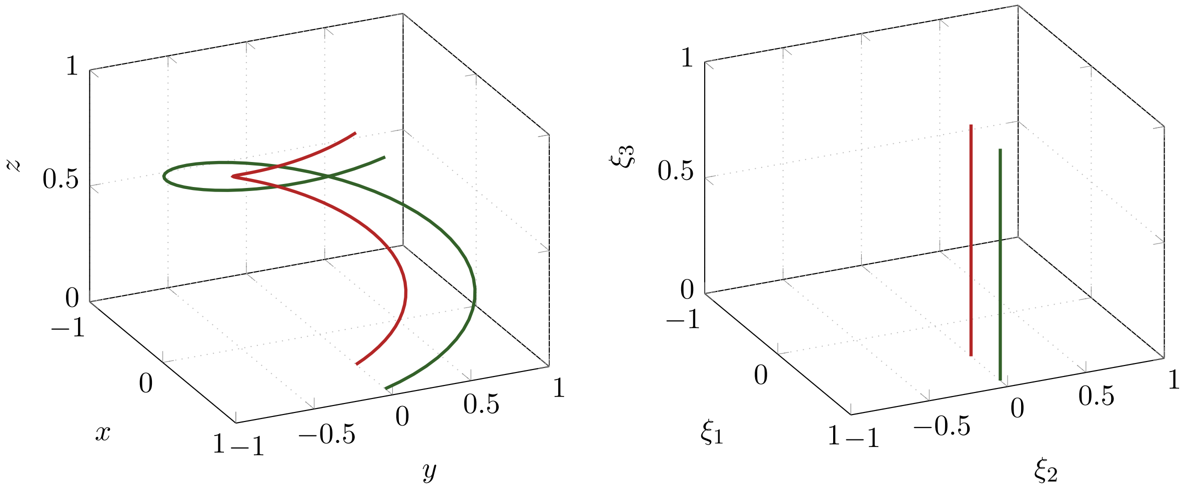

(a) In the (x, y, z)-space, $\Omega_{\boldsymbol{x}}$.

(b) In the (ξ_1, ξ_2, ξ_3)-space, $\Omega_{\boldsymbol{\xi}}$.

Figure 5.1: Transformation of two helicoidal curves with the change of variables Eq. (5.1) with $\alpha = 2\pi$.

The helicoidal change of variables Eq. (5.1) has the following Jacobian $\mathbf{J}$:

$$\mathbf{J} = \frac{\partial x_i}{\partial \xi_j} = \begin{pmatrix} \cos(\alpha\xi_3) & -\sin(\alpha\xi_3) & -\alpha\xi_1\sin(\alpha\xi_3) - \alpha\xi_2\cos(\alpha\xi_3) \\ \sin(\alpha\xi_3) & \cos(\alpha\xi_3) & \alpha\xi_1\cos(\alpha\xi_3) - \alpha\xi_2\sin(\alpha\xi_3) \\ 0 & 0 & 1 \end{pmatrix}, \tag{5.2}$$

and, conversely, the following inverse transposed Jacobian $\mathbf{J}^{-\mathrm{T}}$:

$$\mathbf{J}^{-\mathrm{T}} = \frac{\partial \xi_j}{\partial x_i} = \begin{pmatrix} \cos(\alpha\xi_3) & -\sin(\alpha\xi_3) & 0 \\ \sin(\alpha\xi_3) & \cos(\alpha\xi_3) & 0 \\ \alpha\xi_2 & -\alpha\xi_1 & 1 \end{pmatrix}, \tag{5.3}$$

written in terms of the (ξ_1, ξ_2, ξ_3)-variables.

The Jacobian matrix describes the mapping of vectors between the $\Omega_{\boldsymbol{x}}$ and $\Omega_{\boldsymbol{\xi}}$ spaces. One-forms, such as the magnetic field $\boldsymbol{h}$, follow the transformation [216, 229]

$$\boldsymbol{h}_{\boldsymbol{x}} = \mathbf{J}^{-\mathrm{T}}\, \boldsymbol{h}_{\boldsymbol{\xi}}, \tag{5.4}$$

where $\boldsymbol{h}_{\boldsymbol{x}}$ and $\boldsymbol{h}_{\boldsymbol{\xi}}$ denote the descriptions of the vector $\boldsymbol{h}$ via its components in $\Omega_{\boldsymbol{x}}$ and $\Omega_{\boldsymbol{\xi}}$, respectively. Two-forms, such as the current density $\boldsymbol{j}$, follow the transformation [216, 229]

$$\boldsymbol{j}_{\boldsymbol{x}} = \frac{\mathbf{J}}{\det \mathbf{J}}\, \boldsymbol{j}_{\boldsymbol{\xi}}, \tag{5.5}$$

where $\boldsymbol{j}_{\boldsymbol{x}}$ and $\boldsymbol{j}_{\boldsymbol{\xi}}$ denote the descriptions of the vector $\boldsymbol{j}$ via its components in $\Omega_{\boldsymbol{x}}$ and $\Omega_{\boldsymbol{\xi}}$, respectively. In the case of the helicoidal transformation, from Eq. (5.2), we have $\det \mathbf{J} = 1$.

We now turn to see the effect of the transformation on the weak form of the h-ϕ-formulation with homogeneous natural boundary conditions. In the Cartesian coordinate system $\Omega_{\boldsymbol{x}}$, it reads (see Section 2.2): find $\boldsymbol{h}_{\boldsymbol{x}} \in \mathcal{H}(\Omega_{\boldsymbol{x}})$ such that, $\forall \boldsymbol{h}'_{\boldsymbol{x}} \in \mathcal{H}_0(\Omega_{\boldsymbol{x}})$, we have

$$\left(\partial_t(\mu\, \boldsymbol{h}_{\boldsymbol{x}})\,, \boldsymbol{h}'_{\boldsymbol{x}}\right)_{\Omega_{\boldsymbol{x}}} + \left(\rho\, \textbf{curl}\, \boldsymbol{h}_{\boldsymbol{x}}\,, \textbf{curl}\, \boldsymbol{h}'_{\boldsymbol{x}}\right)_{\Omega_{\mathrm{c},\boldsymbol{x}}} = \sum_{i\in C_V} \bar{V}_i \mathcal{I}_i(\boldsymbol{h}'_{\boldsymbol{x}}), \tag{5.6}$$

where fields are expressed via their components in $\Omega_{\boldsymbol{x}}$.

To apply the helicoidal transformation on Eq. (5.6), we use Eqn. (5.4) and (5.5), we introduce a $\det \mathbf{J}$ factor in both integrals to account for the change of variables, and we use the fact that $\mathcal{I}_i(\boldsymbol{h}'_{\boldsymbol{\xi}}) = \mathcal{I}_i(\boldsymbol{h}'_{\boldsymbol{x}}), \forall i \in C$, because the circulation, which is a scalar quantity, is maintained by the change of variables. Consequently, in the helicoidal space $\Omega_{\boldsymbol{\xi}}$, the h-ϕ-formulation reads: find $\boldsymbol{h}_{\boldsymbol{\xi}} \in \mathcal{H}(\Omega_{\boldsymbol{\xi}})$ such that, $\forall \boldsymbol{h}'_{\boldsymbol{\xi}} \in \mathcal{H}_0(\Omega_{\boldsymbol{\xi}})$, we have

$$\big(\partial_t(\tilde{\boldsymbol{\mu}}\, \boldsymbol{h}_{\boldsymbol{\xi}})\,, \boldsymbol{h}'_{\boldsymbol{\xi}}\big)_{\Omega_{\boldsymbol{\xi}}} + \big(\tilde{\boldsymbol{\rho}}\, \textbf{curl}\, \boldsymbol{h}_{\boldsymbol{\xi}}\,, \textbf{curl}\, \boldsymbol{h}'_{\boldsymbol{\xi}}\big)_{\Omega_{\mathrm{c},\boldsymbol{\xi}}} = \sum_{i\in C_V} \bar{V}_i \mathcal{I}_i(\boldsymbol{h}'_{\boldsymbol{\xi}}), \tag{5.7}$$

where fields are expressed via their components in $\Omega_{\boldsymbol{\xi}}$, and with $\tilde{\boldsymbol{\mu}}$ and $\tilde{\boldsymbol{\rho}}$ two tensors that are defined below. In Eq. (5.7), the curl operator has to be regarded as a notation for the same operator as in Cartesian coordinates, but applied (blindly) on coordinates in the (ξ_1, ξ_2, ξ_3)-space. Explicitly, the (ξ_1, ξ_2, ξ_3)-components of $\textbf{curl}\, \boldsymbol{h}_{\boldsymbol{\xi}}$ are $\partial_{\xi_2} h_{\xi_3} - \partial_{\xi_3} h_{\xi_2}$, $\partial_{\xi_3} h_{\xi_1} - \partial_{\xi_1} h_{\xi_3}$, and $\partial_{\xi_1} h_{\xi_2} - \partial_{\xi_2} h_{\xi_1}$, respectively, with $\boldsymbol{h}_{\boldsymbol{\xi}} = (h_{\xi_1}, h_{\xi_2}, h_{\xi_3})$.

The effect of the change of variables can therefore be fully contained in the two "material parameter" tensors $\tilde{\boldsymbol{\mu}}$ and $\tilde{\boldsymbol{\rho}}$, defined as follows:

$$\tilde{\boldsymbol{\mu}} = \mu\, \mathbf{J}^{-1}\mathbf{J}^{-\mathrm{T}} \det(\mathbf{J}) = \mu \mathbf{T}^{-1} \qquad \text{and} \qquad \tilde{\boldsymbol{\rho}} = \rho\, \frac{1}{\det(\mathbf{J})}\, \mathbf{J}^{\mathrm{T}}\mathbf{J} = \rho \mathbf{T}, \tag{5.8}$$

with the metric tensor $\mathbf{T}$, defined as

$$\mathbf{T} = \frac{1}{\det(\mathbf{J})}\, \mathbf{J}^{\mathrm{T}}\mathbf{J} = \begin{pmatrix} 1 & 0 & -\alpha\xi_2 \\ 0 & 1 & \alpha\xi_1 \\ -\alpha\xi_2 & \alpha\xi_1 & 1+\alpha^2(\xi_1^2+\xi_2^2) \end{pmatrix}, \tag{5.9}$$

and its inverse $\mathbf{T}^{-1}$, that reads:

$$\mathbf{T}^{-1} = \det(\mathbf{J})\,\mathbf{J}^{-1}\mathbf{J}^{-\mathrm{T}} = \begin{pmatrix} 1+\alpha^2\xi_2^2 & \alpha^2\xi_1\xi_2 & \alpha\xi_2 \\ \alpha^2\xi_1\xi_2 & 1+\alpha^2\xi_1^2 & -\alpha\xi_1 \\ \alpha\xi_2 & -\alpha\xi_1 & 1 \end{pmatrix}. \tag{5.10}$$

Equations (5.6) and (5.7) are, up to now, in the continuous setting, two completely equivalent ways of writing the h-ϕ-formulation in the physical domain Ω, either described in terms of the $\boldsymbol{x}$-coordinates, or in terms of the $\boldsymbol{\xi}$-coordinates. Indeed, no approximation has been introduced and the change of variables is regular.

The advantage of Eq. (5.7) over Eq. (5.6) is that it consists of integrals over ξ_3-independent domains for helicoidally symmetric geometries (of course, provided that the twisting parameter α is chosen so that $p = 2\pi/\alpha$ is equal to the pitch length of the physical geometry).

In addition, and this is a key property of the metric tensor, $\mathbf{T}$ and $\mathbf{T}^{-1}$ are also ξ_3-independent, as shown in Eqn. (5.9) and (5.10). As a consequence, both the integrands and the domains of integrations in the weak formulation (5.7) are ξ_3-independent. If the boundary conditions of the original problem are also ξ_3-independent when expressed in helicoidal coordinates, the solution of Eq. (5.7), i.e., the magnetic field $\boldsymbol{h}_{\boldsymbol{\xi}}$, will be ξ_3-independent as well. In such a situation, the integration over ξ_3 is trivial, the problem dimension can be reduced from 3D to 2D. Numerically, the associated 2D problem is therefore significantly cheaper to solve than the original 3D problem.

In particular, boundary conditions are helicoidally symmetric in the case of an imposed current in a wire or an axial (in the z-direction) field excitation, or a combination of both. By contrast, a transverse field excitation, e.g., an applied field along $\hat{\boldsymbol{e}}_x$ or $\hat{\boldsymbol{e}}_y$ in the Cartesian coordinate system, does not transform into a ξ_3-independent field in the helicoidal space. The treatment of such excitations will be discussed in Section 5.1.4.

In the next section, we describe how the associated 2D problem can be discretized and implemented, assuming helicoidally symmetric boundary conditions. We then verify the implementation in Section 5.1.3.

5.1.2 Practical implementation of a full h-ϕ-formulation in 2D

From now on, for conciseness, we refer to the (x, y, z) and (ξ_1, ξ_2, ξ_3)-spaces as the $\boldsymbol{x}$ and $\boldsymbol{\xi}$-spaces, respectively. Also, as we mainly work in the helicoidal coordinate system, we denote the magnetic field $\boldsymbol{h}_{\boldsymbol{\xi}}$ and the current density $\boldsymbol{j}_{\boldsymbol{\xi}}$ expressed via their components in the $\boldsymbol{\xi}$-space as $\boldsymbol{h}$ and $\boldsymbol{j}$ directly, for conciseness. We also drop the subscript $\cdot_{\xi}$ for domains $\Omega_{\boldsymbol{\xi}}$, $\Omega_{\mathrm{c},\boldsymbol{\xi}}$, and $\Omega^{\mathrm{C}}_{\mathrm{c},\boldsymbol{\xi}}$. When we refer to quantities in the $\boldsymbol{x}$-space instead, this will be expressed explicitly.

We consider a general helicoidally symmetric system, made up of (twisted) conducting wires, that constitute the conducting domain Ω_{c}, surrounded by a non-conducting domain $\Omega_{\mathrm{c}}^{\mathrm{C}}$, with an external boundary Γ_{out}. The system is subjected to a given axial field $\boldsymbol{h}_{\mathrm{axial}}$, and a current intensity (or an applied voltage) is imposed on each conducting wire. An example of such a geometry is represented in Fig. 5.2.

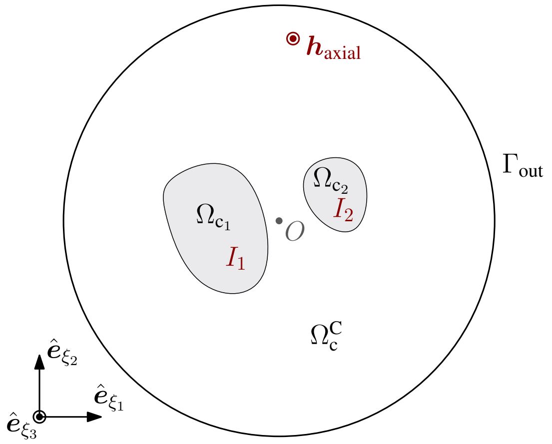

Figure 5.2: General 2D problem, ξ_3-invariant, in the helicoidal coordinate system of center O. Helicoidally symmetric boundary or global conditions are represented in red: an axial field $\boldsymbol{h}_{\text{axial}}$ in $\Omega_{\text{c}}^{\text{C}}$, and applied current intensities I_1 and I_2 on the conducting domains Ω_{c_1} and Ω_{c_2}. The physical 3D system is generated by a rotated extrusion of the represented geometry.

One could be tempted to implement Eq. (5.7) directly as a classical 2D problem with in-plane magnetic field, with the only difference of having anisotropic tensors instead of scalar material parameters. But this would not be correct: the fact that the problem is ξ_3-independent does not imply that the involved magnetic field only has two components in the $\boldsymbol{\xi}$-space. One has to consider three independent components for the magnetic field $\boldsymbol{h}$ in Eq. (5.7).

Decomposition of the magnetic field

To benefit from existing implementations of the h-ϕ-formulation, we decompose the magnetic field $\boldsymbol{h}$ into two parts: a "parallel component" $\boldsymbol{h}_{\parallel}$, containing the ξ_1 and ξ_2-components of $\boldsymbol{h}$, and a "perpendicular component" $\boldsymbol{h}_{\perp}$, containing only the ξ_3-component. We write

$$\boldsymbol{h}(\xi_1,\xi_2) = \boldsymbol{h}_{\parallel}(\xi_1,\xi_2) + \boldsymbol{h}_{\perp}(\xi_1,\xi_2), \tag{5.11}$$

or, in terms of their explicit components,

$$\begin{pmatrix} h_{\xi_1}(\xi_1,\xi_2) \\ h_{\xi_2}(\xi_1,\xi_2) \\ h_{\xi_3}(\xi_1,\xi_2) \end{pmatrix} = \begin{pmatrix} h_{\xi_1}(\xi_1,\xi_2) \\ h_{\xi_2}(\xi_1,\xi_2) \\ 0 \end{pmatrix} + \begin{pmatrix} 0 \\ 0 \\ h_{\xi_3}(\xi_1,\xi_2) \end{pmatrix}, \tag{5.12}$$

where $\boldsymbol{h} = \boldsymbol{h}(\xi_1,\xi_2)$ because the solution is ξ_3-independent. Note that the vectors $\boldsymbol{h}_{\parallel}$ and $\boldsymbol{h}_{\perp}$ are not orthogonal in the $\boldsymbol{x}$-space.

In the $\boldsymbol{\xi}$-space, the curl-free condition for the magnetic field in the non-conducting domain $\Omega_{\text{c}}^{\text{C}}$ is expressed as $(\det \mathbf{J})^{-1}\mathbf{J}\,\textbf{curl}\,\boldsymbol{h} = \mathbf{0}$. Because the Jacobian is non-singular, it results in a curl-free condition on the field $\boldsymbol{h}$ in the $\boldsymbol{\xi}$-space as well (with the curl operator defined as before). The fact that $\partial_{\xi_3}\cdot = 0$ implies, in $\Omega_{\text{c}}^{\text{C}}$,

$$\textbf{curl}\,\boldsymbol{h} = \begin{pmatrix} \partial_{\xi_2} h_{\xi_3} \\ -\partial_{\xi_1} h_{\xi_3} \\ \partial_{\xi_1} h_{\xi_2} - \partial_{\xi_2} h_{\xi_1} \end{pmatrix} = \mathbf{0}. \tag{5.13}$$

With the decomposition defined by Eq. (5.11), the third component of Eq. (5.13) implies that $\textbf{curl}\,\boldsymbol{h}_{\|} = \boldsymbol{0}$, which it the same condition as for a classical 2D formulation, where a two-component magnetic field is considered. Also, for the first two components of the curl to be equal to zero in Eq. (5.13), the perpendicular field $\boldsymbol{h}_{\perp}$ must be constant within each connected region of $\Omega_{\mathrm{c}}^{\mathrm{C}}$. These conditions are introduced in the function space definitions, i.e., they are strongly enforced. They will be made explicit at the space discretization step.

With the decomposition $\boldsymbol{h} = \boldsymbol{h}_{\|} + \boldsymbol{h}_{\perp}$, the h-ϕ-formulation reads explicitly as follows. From an initial solution at time $t = 0$, find $\boldsymbol{h}_{\|} \in \mathcal{H}_{\|}(\Omega)$ and $\boldsymbol{h}_{\perp} \in \mathcal{H}_{\perp}(\Omega)$ such that, for $t > 0$, $\boldsymbol{h}'_{\|} \in \mathcal{H}_{\|,0}(\Omega)$ and $\boldsymbol{h}'_{\perp} \in \mathcal{H}_{\perp,0}(\Omega)$,

$$\left(\partial_t(\tilde{\boldsymbol{\mu}}\,(\boldsymbol{h}_{\|} + \boldsymbol{h}_{\perp}))\,, \boldsymbol{h}'_{\|}\right)_{\Omega} + \left(\tilde{\boldsymbol{\rho}}\,\textbf{curl}\,(\boldsymbol{h}_{\|} + \boldsymbol{h}_{\perp})\,, \textbf{curl}\,\boldsymbol{h}'_{\|}\right)_{\Omega_{\mathrm{c}}} = \sum_{i \in C_V} \bar{V}_i \mathcal{I}_i(\boldsymbol{h}'_{\|}), \tag{5.14}$$

$$\left(\partial_t(\tilde{\boldsymbol{\mu}}\,(\boldsymbol{h}_{\|} + \boldsymbol{h}_{\perp}))\,, \boldsymbol{h}'_{\perp}\right)_{\Omega} + \left(\tilde{\boldsymbol{\rho}}\,\textbf{curl}\,(\boldsymbol{h}_{\|} + \boldsymbol{h}_{\perp})\,, \textbf{curl}\,\boldsymbol{h}'_{\perp}\right)_{\Omega_{\mathrm{c}}} = 0, \tag{5.15}$$

where the products between $\boldsymbol{h}_{\|}$ and $\boldsymbol{h}_{\perp}$ or their curl do not vanish because of the coupling induced by tensors $\tilde{\boldsymbol{\mu}}$ and $\tilde{\boldsymbol{\rho}}$. Note that $\mathcal{I}_i(\boldsymbol{h}'_{\perp}) = 0$. The function spaces $\mathcal{H}_{\|}(\Omega)$ and $\mathcal{H}_{\perp}(\Omega)$ are defined explicitly in the space discretization step.

For the nonlinear resistivity of T2S, the current density entering the power law $\rho = \rho(\boldsymbol{j})$ involves the vector norm of $\boldsymbol{j}$, which is not invariant under the helicoidal transformation. Using the fact that $\det \mathbf{J} = 1$, we have, from Eq. (5.5),

$$\tilde{\boldsymbol{\rho}} = \rho(\boldsymbol{j}_{\boldsymbol{x}})\,\mathbf{T} = \rho(\mathbf{J}\,\textbf{curl}\,(\boldsymbol{h}_{\|} + \boldsymbol{h}_{\perp}))\,\mathbf{T}. \tag{5.16}$$

Note that the presence of the Jacobian matrix in Eq. (5.16) introduces a ξ_3-dependence. This is not an issue when the power law only involves the norm of $\boldsymbol{j}_{\boldsymbol{x}}$, because we have $\|\boldsymbol{j}_{\boldsymbol{x}}\|^2 = \boldsymbol{j}_{\boldsymbol{x}}^{\mathrm{T}}\boldsymbol{j}_{\boldsymbol{x}} = \boldsymbol{j}^{\mathrm{T}}\mathbf{J}^{\mathrm{T}}\mathbf{J}\boldsymbol{j} = \boldsymbol{j}^{\mathrm{T}}\mathbf{T}\boldsymbol{j}$, which is ξ_3-independent. For simplicity, we can therefore choose $\xi_3 = 0$ in Eq. (5.16) in that case, and work with

$$\mathbf{J}|_{\xi_3=0} = \begin{pmatrix} 1 & 0 & -\alpha\xi_2 \\ 0 & 1 & \alpha\xi_1 \\ 0 & 0 & 1 \end{pmatrix}. \tag{5.17}$$

More complex constitutive laws that treat differently distinct components of $\boldsymbol{j}$, e.g., anisotropic critical current densities, may not necessarily be treated directly with this approach, and may need to be considered with more caution. Here, we stay in the simple situation of an isotropic power law.

Space discretization

In practice, we can discretize the parallel field $\boldsymbol{h}_{\|}$ exactly as the two-component field in a classical 2D h-ϕ-formulation with in-plane magnetic field, i.e., with gradient of node functions and cohomology functions in $\Omega_{\mathrm{c}}^{\mathrm{C}}$, and with edge functions in Ω_{c} (see Section 2.4.1). This defines the function space $\mathcal{H}_{\|}^{\delta,1}(\Omega)$.

We choose to discretize the perpendicular field $\boldsymbol{h}_{\perp}$ with perpendicular edge functions. To account for the fact that $\boldsymbol{h}_{\perp}$ must be constant in each connected region of $\Omega_{\mathrm{c}}^{\mathrm{C}}$, we introduce global functions. Let K be the number of such connected regions, we describe the perpendicular field by the expansion

$$\boldsymbol{h}_\perp = \sum_{n\in\mathcal{N}(\Omega_\mathrm{c}\backslash\partial\Omega_\mathrm{c})} h_{\perp,n}\, \boldsymbol{w}_n + \sum_{i=1}^{K} C_i\, \boldsymbol{p}_i, \tag{5.18}$$

with $\boldsymbol{w}_n$ the perpendicular edge function associated with node n (see Section 2.4.2), and $\boldsymbol{p}_i$ a global shape function defined as the sum of all perpendicular edge functions associated with nodes in the i^th connected region of $\Omega_\mathrm{c}^\mathrm{C}$, including those on its boundary, for $i \in \{1, \dots, K\}$. The support of the shape function $\boldsymbol{p}_i$ is not restricted to $\Omega_\mathrm{c}^\mathrm{C}$: it is non-zero on a layer of one element adjacent to $\partial\Omega_\mathrm{c}$ in Ω_c. This defines the function space $\mathcal{H}_\perp^{\delta,1}(\Omega)$. Both $\boldsymbol{h}_\parallel$ and $\boldsymbol{h}_\perp$ are described as discrete 1-forms, and so is their sum, $\boldsymbol{h}$.

For simplicity, and because this is the only situation that we will consider in the illustrative examples below, from now on, we assume that there is only one connected non-conducting region $\Omega_\mathrm{c}^\mathrm{C}$, such that $K = 1$, and we rename $C_1 = C$.

Global constraints and boundary conditions

For the global constraints, the current intensity flowing in a conducting domain is a scalar and its value is therefore independent of the system of coordinates. It can be imposed exactly as in a classical 2D problem with in-plane magnetic field, i.e., strongly via the degree of freedom associated with the cut function for the corresponding conducting domain. Alternatively, an applied voltage can be imposed weakly as in the classical formulation.

For the boundary conditions, we consider a circular external boundary Γ_out, placed in $\Omega_\mathrm{c}^\mathrm{C}$ and sufficiently far from the conductors such that we can assume $\boldsymbol{b}\cdot\boldsymbol{n}|_{\Gamma_\mathrm{out}} = 0$, as represented in Fig. 5.2. This condition is imposed for $\boldsymbol{h}_\parallel$ via a homogeneous natural boundary condition on Γ_out. This lets the out-of-plane component of the magnetic field, h_z, undetermined on Γ_out. It corresponds to the applied axial field, that we can freely impose. We derive below how to translate this condition on $\boldsymbol{h}_\perp|_{\Gamma_\mathrm{out}}$.

Let us first consider the situation with a zero axial field. At a distance R far from conductors carrying a net current intensity I, the magnetic field tends to be purely azimuthal and axisymmetric. We have $\boldsymbol{h}_{\boldsymbol{x}} = \frac{I}{2\pi R}(-\sin\theta \quad \cos\theta \quad 0)^\mathrm{T}$, with θ the cylindrical azimuthal coordinate. In terms of helicoidal coordinates, on the plane $\xi_3 = 0$, it reads

$$\boldsymbol{h} = \mathbf{J}^\mathrm{T}|_{\xi_3=0}\, \boldsymbol{h}_{\boldsymbol{x}} = \frac{I}{2\pi R}\begin{pmatrix} -\sin\theta \\ \cos\theta \\ \alpha\xi_2\sin\theta + \alpha\xi_1\cos\theta \end{pmatrix} = \frac{I}{2\pi R}\begin{pmatrix} -\sin\theta \\ \cos\theta \\ \alpha R \end{pmatrix}, \tag{5.19}$$

using $\xi_2 = R\sin\theta$ and $\xi_1 = R\cos\theta$ for $\xi_3 = 0$. Consequently, to guarantee $h_z|_{\Gamma_\mathrm{out}} = 0$, one has to impose that $h_{\xi_3}|_{\Gamma_\mathrm{out}} = I\alpha/2\pi$, i.e., one has to fix the degree of freedom C associated with the non-conducting domain to the value $C = I\alpha/2\pi$.

By superposition, if one wants to impose a non-zero axial field h_axial on the external boundary

Γ_{out} in addition to a net current intensity, we therefore have the following essential condition:

$$C = \frac{I\alpha}{2\pi} + h_{\text{axial}}, \tag{5.20}$$

because the axial field $\boldsymbol{h_x} = (0 \quad 0 \quad h_{\text{axial}})^{\mathrm{T}}$ transforms into $\boldsymbol{h} = \mathbf{J}^{\mathrm{T}}\,\boldsymbol{h_x} = (0 \quad 0 \quad h_{\text{axial}})^{\mathrm{T}}$ in the $\boldsymbol{\xi}$-space.

5.1.3 Verification against a 3D model

To verify the implementation, we compare the solution of our 2D model in helicoidal coordinates to the solution of a standard 3D model of the same problem. This will also quantify the computational gain offered by reducing the dimension from 3D to 2D.

We consider a cylindrical wire, made up of six identical Nb-Ti superconducting filaments, twisted and embedded into a copper matrix, as illustrated in Figs. 5.3 and 5.4. In order to simplify the geometry, the cross-sections of the filaments are assumed to be circles, and the 3D geometry is generated by a helicoidal extrusion of the 2D cross-section. This is of course an approximation of a realistic geometry. If needed, cross-sections of round twisted filaments can be computed accurately using envelope theory [230, 231, 58] or computer-aided-design tools [60].

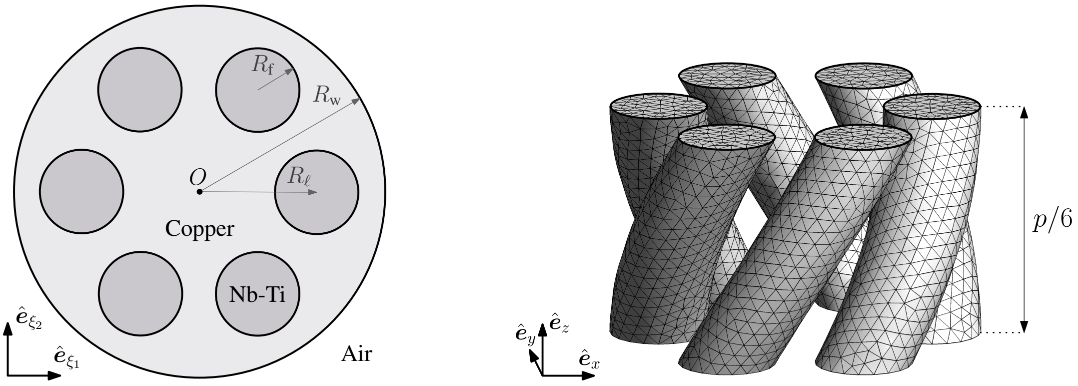

(a) Wire geometry in 2D, on the $z = \xi_3 = 0$ plane.

(b) Twisted filaments in 3D.

Figure 5.3: Geometries for the verification of the helicoidal problem. Six twisted Nb-Ti filaments embedded in a copper matrix. The boundary of the air region outside the matrix is not represented (but is part of the model, too). (a) Geometry in the (ξ_1, ξ_2)-plane. (b) One-sixth of a pitch length represented in the $\boldsymbol{x}$-space. The copper matrix is not represented, for clarity purposes.

The filament radius is $R_{\text{f}} = 35\ \mu$m, their centers are at a distance $R_{\ell} = 98\ \mu$m from the center of the wire, and the matrix radius is $R_{\text{w}} = 155\ \mu$m. The pitch length is fixed to $p = 1000\ \mu$m, and air is modelled outside the wire up to a distance $R_{\text{out}} = 500\ \mu$m.

We assume that the Nb-Ti filaments are characterized by $j_{\text{c}} = 7 \times 10^9$ A/m^2 and $n = 50$, and the copper resistivity is fixed to $\rho = 1.81 \times 10^{-10}\ \Omega$m. A total current $I(t) = 0.5\, I_{\text{c}}\, \sin(2\pi t/T)$ is imposed in the whole wire, with a period $T = 0.1$ s and $I_{\text{c}} = 162$ A, which is an approximate value for the critical current for the six filaments, that are not round but helicoidal extrusions of circles. We also impose a zero axial field along $\hat{\boldsymbol{e}}_z$.

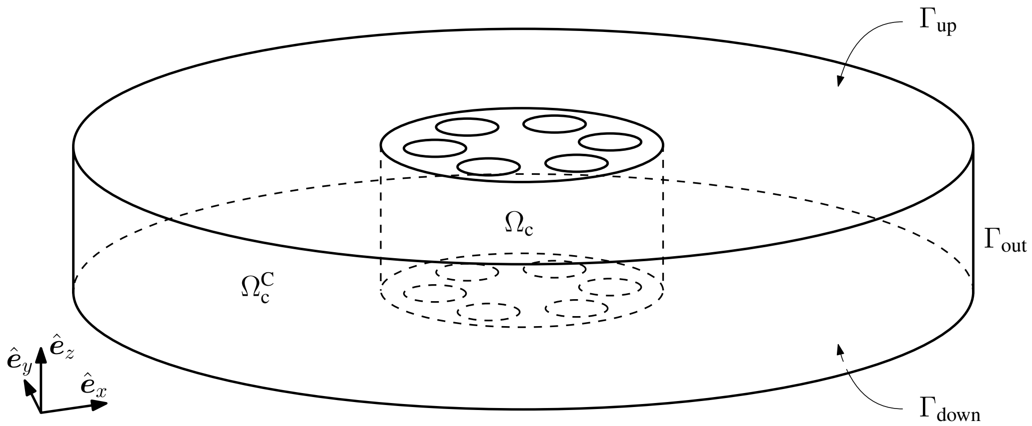

Figure 5.4: Filament 3D geometry and its boundaries. For clarity purposes, the twisted filaments inside the copper matrix are not represented.

3D verification model

We consider the 3D geometry represented in Figs. 5.3(b) and 5.4. It represents a periodic cell of one-sixth of a whole pitch length p. Building and meshing the 3D model represented in Fig. 5.3(b) is not a trivial task. To account for the periodicity of the problem, the mesh must be identical on the top and bottom boundaries $\Gamma_{\rm up}$ and $\Gamma_{\rm down}$. As an h-ϕ-formulation will be used, cohomology basis functions must also be periodic. The quality of the mesh inside the filaments plays an important role for the accuracy of the resulting numerical solution. Typically, better results are obtained with a structured mesh inside the filaments. Implementing all these constraints is permitted by the open-source finite element mesh generator Gmsh [60], and periodic cuts and cohomology basis functions are generated as described in [142, 51].

For the h-ϕ-formulation, we set a homogeneous natural boundary condition on the external boundary $\Gamma_{\rm out}$, so that $\boldsymbol{b} \cdot \boldsymbol{n}|_{\Gamma_{\rm out}} = 0$ is weakly enforced. For the top and bottom boundaries $\Gamma_{\rm up}$ and $\Gamma_{\rm down}$, which are are topologically identical, the periodic condition $\boldsymbol{h} \times \boldsymbol{n}|_{\Gamma_{\rm up}} = -\boldsymbol{h} \times \boldsymbol{n}|_{\Gamma_{\rm down}}$ is imposed by linking the degrees of freedom for the magnetic field $\boldsymbol{h}$ associated with edges on $\partial\Omega_{\rm c} \cap (\Gamma_{\rm up} \cup \Gamma_{\rm down})$. On non-conducting boundaries $\partial\Omega_{\rm c}^{\rm C} \cap (\Gamma_{\rm up} \cup \Gamma_{\rm down})$, the periodic constraint is expressed in terms of the magnetic scalar potential, we fix $\phi|_{\Gamma_{\rm up}} = \phi|_{\Gamma_{\rm down}}$. The case of an axial applied field is treated by a cut function, as described later.

The total current intensity flowing in the conducting domain made up of the filaments and matrix is imposed via a cohomology basis function, as represented in Fig. 5.5(a). For information, we illustrate in Fig. 5.5(b) the cut that would be used in the case of a non-conducting matrix. Because of the periodicity, each filament is linked to the next one so that there is topologically only one strand of filament. In a different situation where distinct current intensities are imposed in distinct filaments, the problem loses its $p/6$-periodicity, but still exhibits a p-periodicity (at least). In that case, the 3D model should therefore represent a whole pitch length.

Note that the periodicity makes the domain Ω topologically equivalent to a torus. For the non-conducting domain, we have $\beta^1(\Omega_{\rm c}^{\rm C}) = 2$, and this introduces an additional cut for the magnetic scalar potential, as represented in Fig. 5.6. The cohomology basis function associated

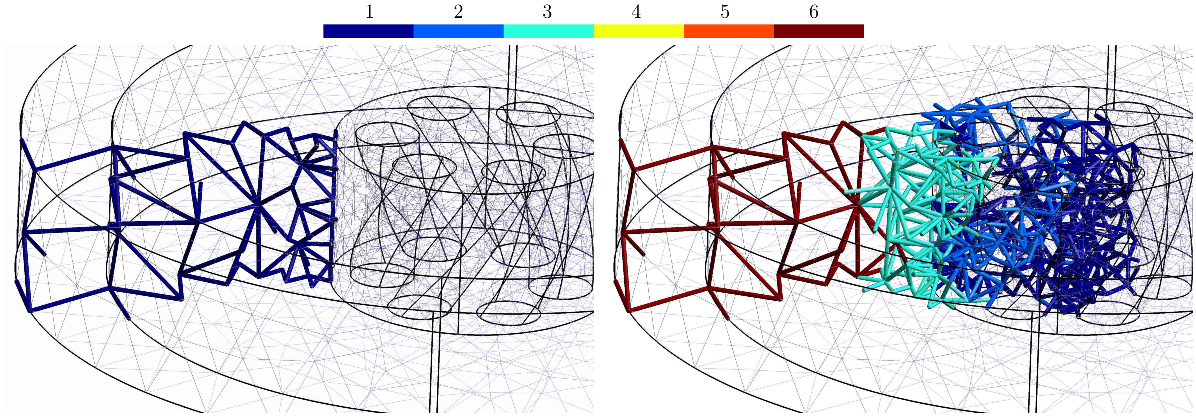

(a) Conducting matrix.

(b) Non-conducting matrix.

Figure 5.5: Periodic supports for the cut functions (cohomology basis functions), to impose a total current $I(t)$ in the conducting domain, and multiplicity of the associated edges (legend in the color bar). (a) Conducting matrix, the non-conducting domain Ω_c^C is the exterior the matrix and filaments, $I(t)$ is the total current. (b) Alternative case of a non-conducting matrix, where only the filaments belong to Ω_c. The periodicity is such that there is only one strand of twisted filament: the same current must flow inside each of the six parts. The support for the single cut function involves edges with multiplicity up to 6, as $I(t)$ is the current flowing in one filament.

with this cut is responsible for fixing an axial field h_{axial} along $\hat{\boldsymbol{e}}_z$. The degree of freedom associated with this cut function is equal to the circulation $h_{\text{axial}}\, p/6$ of the axial field h_{axial} along the total height $p/6$ of the model. In our problem, we impose $h_{\text{axial}} = 0$.

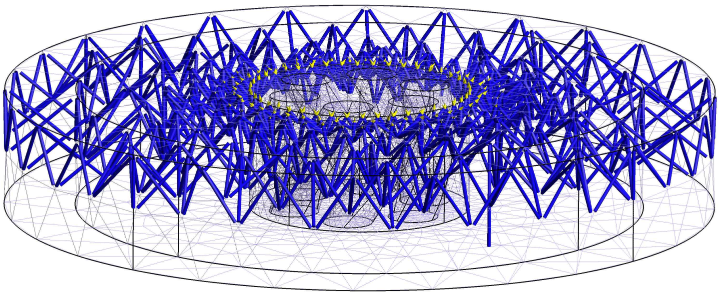

Figure 5.6: Support for the "axial cut function", used to impose an axial field (conducting matrix case).

Before comparing the results, we first verify that the 3D model correctly outputs a helicoidally symmetric solution. From the numerical solution in the $\boldsymbol{x}$-space, we extract the magnetic flux density $\boldsymbol{b}$ and the current density $\boldsymbol{j}$ along the helicoidal fiber of pitch length p passing at point $\boldsymbol{x} = \big(r\cos(\theta), r\sin(\theta), 0\big)$, with $r = R_\ell + 0.7R_{\text{f}}$ and $\theta = \pi/50$, from $z = 0$ to $z = p$. We exploit the periodicity of the problem to obtain values for $z > p/6$. The components of vectors $\boldsymbol{b}$ and $\boldsymbol{j}$ in the $\boldsymbol{x}$ and $\boldsymbol{\xi}$-spaces are represented in Fig. 5.7 for a relatively fine tetrahedral mesh ($144\,840$ DOFs), at time $t = T/4$. The same result but on a coarser mesh ($16\,556$ DOFs) is given in Fig. C.6 in Appendix. Vector components in the $\boldsymbol{\xi}$-space are obtained using the one and two-forms transformation relations, Eqn. (5.4) and (5.5).

The oscillations along the fiber represent inter-element variations, that decrease in amplitude with mesh refinement. Up to these inter-element variations, the 3D solution correctly presents

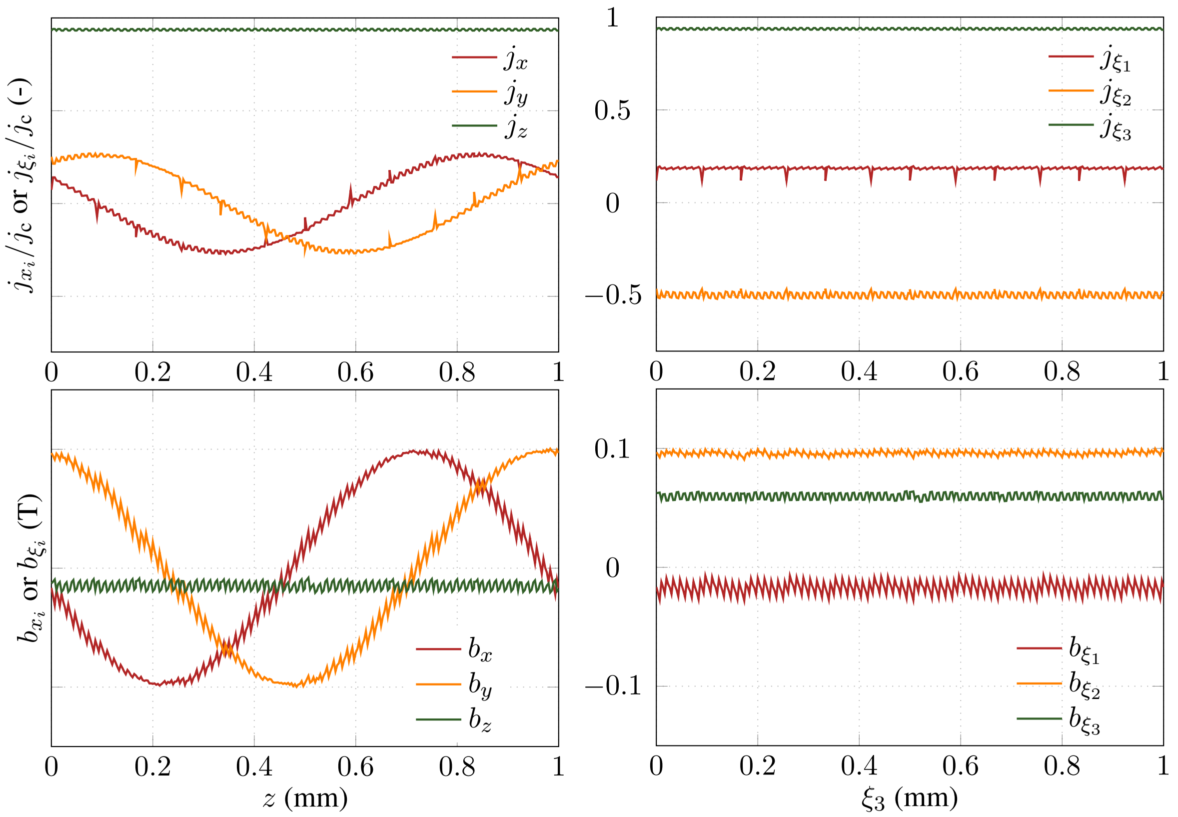

Figure 5.7: Current density (up) and magnetic flux density (down) along the helicoidal fiber of pitch length p passing at point $\boldsymbol{x} = \big(r\cos(\theta), r\sin(\theta), 0\big)$, with $r = R_\ell + 0.7R_\text{f}$ and $\theta = \pi/50$, from $z = 0$ to $z = p$. (Left) Three components of the vectors in the $\boldsymbol{x}$-space. (Right) Three components of the vectors in the $\boldsymbol{\xi}$-space. Solution of the 3D model with the h-ϕ-formulation on a fine tetrahedral mesh involving 144 840 DOFs, solution at $t = T/4$.

a helicoidal symmetry. It is interesting to notice that the current density $\boldsymbol{j}_{\boldsymbol{\xi}}$ is not purely along the ξ_3-direction, but has non-zero ξ_1 and ξ_2-components, too. Similarly, b_{ξ_3} is not equal to zero. This is an illustration of the necessity to consider a three-component magnetic field in the 2D model written in the helicoidal space.

Comparison of the results from the 3D and 2D models

We now compare the results of the 2D problem in helicoidal coordinates with the reference 3D problem described above, in order to verify the implementation. Note that for the 2D model, in this particular case, we could further exploit the symmetry and model only one-sixth of the circular region depicted in Fig. 5.3(a), using periodic boundary conditions on the symmetric boundaries as well as adapted cohomology functions in Ω_c^C, hence reducing the computational cost even more. We however choose to stay general and we model the full 2D cross-section.

The solution of the 2D model on a relatively coarse mesh (4 700 DOFs), is represented in Fig. 5.8, in the $\boldsymbol{x}$-space. The current mostly flows in the superconducting filaments, as shown by the different scales for the middle and right subfigures. The current flow along the filaments induces a non-zero perpendicular magnetic flux density b_z at the center of the wire. The current density is represented in Fig. 5.9 in both the $\boldsymbol{\xi}$ and $\boldsymbol{x}$-spaces. As with the 3D model, this figure clearly demonstrates the necessity of considering a three-component magnetic field $\boldsymbol{h}$ in the $\boldsymbol{\xi}$-space, because the current density is not necessarily purely along $\hat{\boldsymbol{e}}_{\xi_3}$.

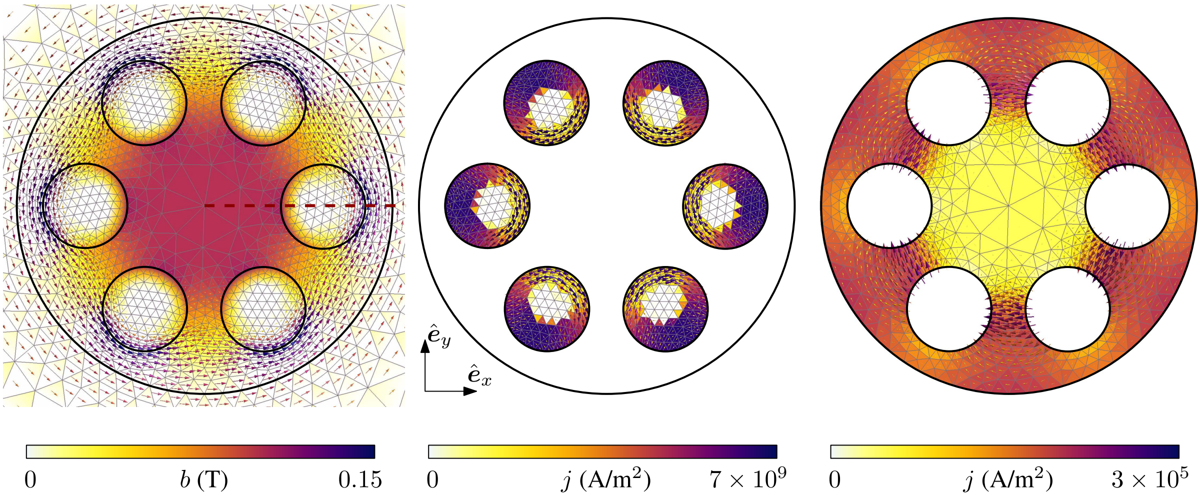

Figure 5.8: Magnetic flux density (left), current density in the filaments (middle), and current density in the matrix (right) at time $t = T/4$ for the 2D problem solved in the helicoidal $\boldsymbol{\xi}$-space, but represented in the $\boldsymbol{x}$-space. The arrows represent the in-plane x and y-components of $\boldsymbol{b}$ and $\boldsymbol{j}$, whereas the triangular elements are colored as a function of the perpendicular z-component of $\boldsymbol{b}$ and $\boldsymbol{j}$. The dashed red line in the left figure is the cut along which is magnetic flux density is represented in Fig. 5.10.

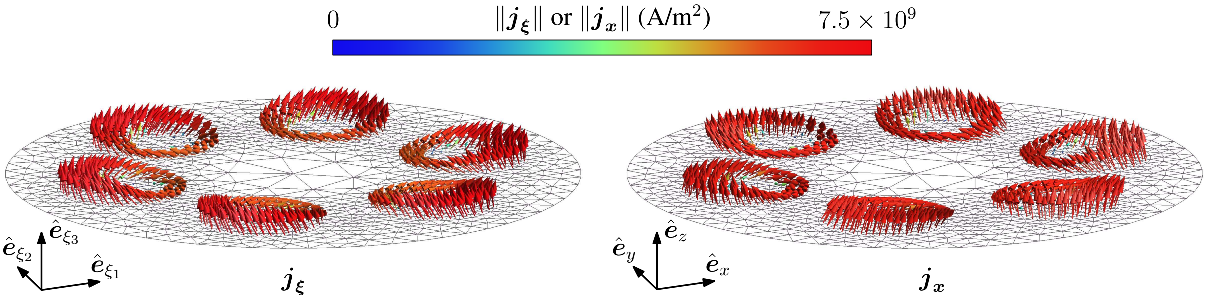

Figure 5.9: Current density in both the $\boldsymbol{\xi}$ and $\boldsymbol{x}$-spaces at time $t = T/4$ for the 2D problem solved in the helicoidal $\boldsymbol{\xi}$-space. One can verify that $\boldsymbol{j}_{\boldsymbol{x}}$ is (almost) parallel to the filament boundary (a small portion of current goes into the copper matrix).

A comparison of the local field distribution of the 2D model with that of the reference 3D model is shown in Fig. 5.10, along the dashed red line highlighted in Fig. 5.8, for two mesh resolutions. The solution of the 3D model is taken on the plane $\xi_3 = 0$, but this choice is arbitrary: as was shown in Fig. 5.7, up to the inter-element variation, the solution of the 3D model is also ξ_3-independent. Solutions of the 2D and 3D models match locally. We verified that this was also the case for the current density (not represented in the figures).

A comparison of a global quantity is proposed in Fig. 5.11, where the AC losses per unit length along $\hat{\boldsymbol{e}}_z$ in both the superconducting filaments and the conducting matrix are compared for the two models, and for two mesh resolutions. For the 2D model, the AC loss is computed as $(\tilde{\boldsymbol{\rho}}\, \boldsymbol{j}\ , \boldsymbol{j})_{\Omega_{\mathrm{c}}}$, where Ω_{c} is either restricted to the filaments, or to the matrix. For the 3D model,

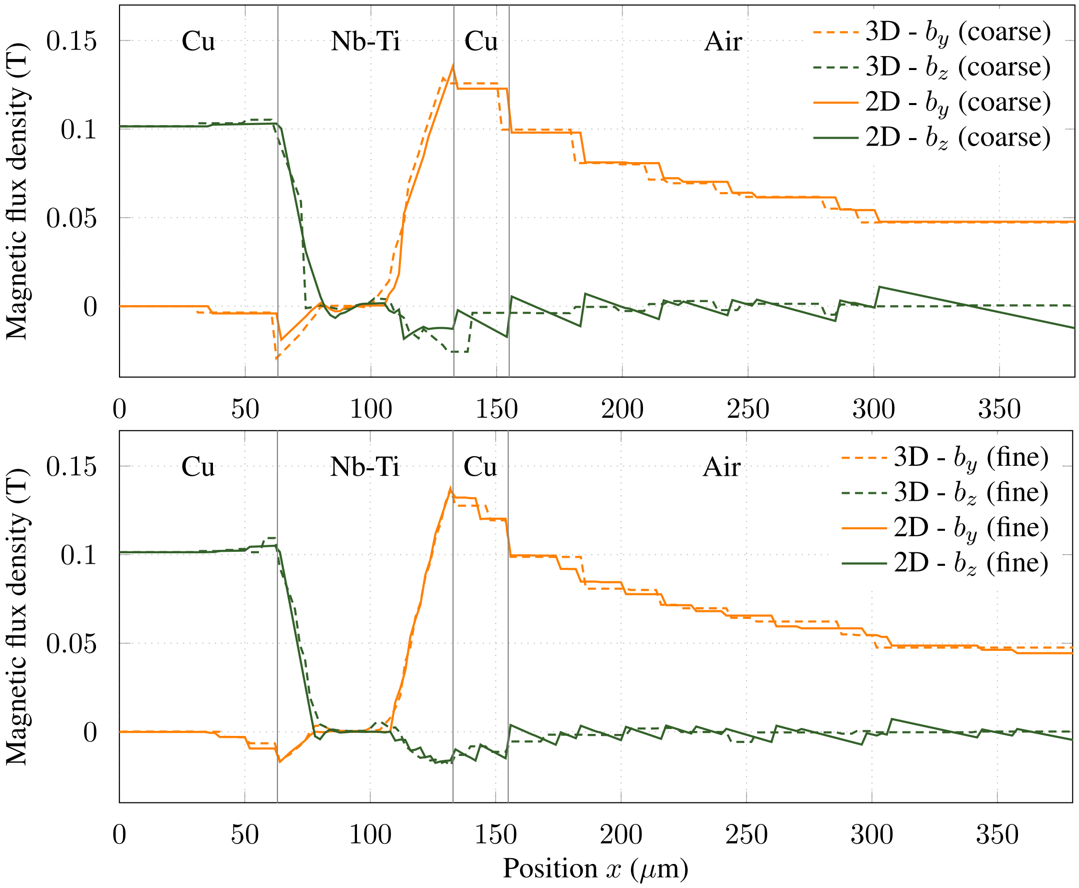

Figure 5.10: Magnetic flux density along the dashed red line represented in Fig. 5.8, for the 3D and 2D models, at time $t = T/4$, with coarse (up) and fine (down) mesh resolutions.

the integral $(\rho\, \boldsymbol{j}_{\boldsymbol{x}}\, , \boldsymbol{j}_{\boldsymbol{x}})_{\Omega_{c,\boldsymbol{x}}}$ is computed over the 3D domain in the $\boldsymbol{x}$-space, and the result is divided by $p/6$, to obtain the AC loss per unit length as well.

Meshes for the coarse resolution in the $z = \xi_3 = 0$ plane are similar for the 2D and 3D models, as well as meshes for the fine resolution. However, the 2D solution is less sensitive to the mesh resolution. This is due to the inter-element variations between the different tetrahedra in the 3D mesh, that require to be significantly lowered to get an accurate evaluation of the quadratic quantity representing the AC losses. Meshes with prisms, i.e., extruded triangles, were also tested. They give slightly better results, but also increase the complexity of the meshing step, as pyramids must be used as transition elements between prisms and tetrahedra.

The local and global quantity agreement justifies the validity of the 2D model in helicoidal coordinates. The main motivation is the dimension reduction, which allows for tremendously more efficient simulations in terms of computational resources. This is demonstrated by Table 5.1, that compares the performance figures of the 2D and 3D models on meshes with similar characteristic length for the finite elements (triangles in 2D and tetrahedra in 3D).

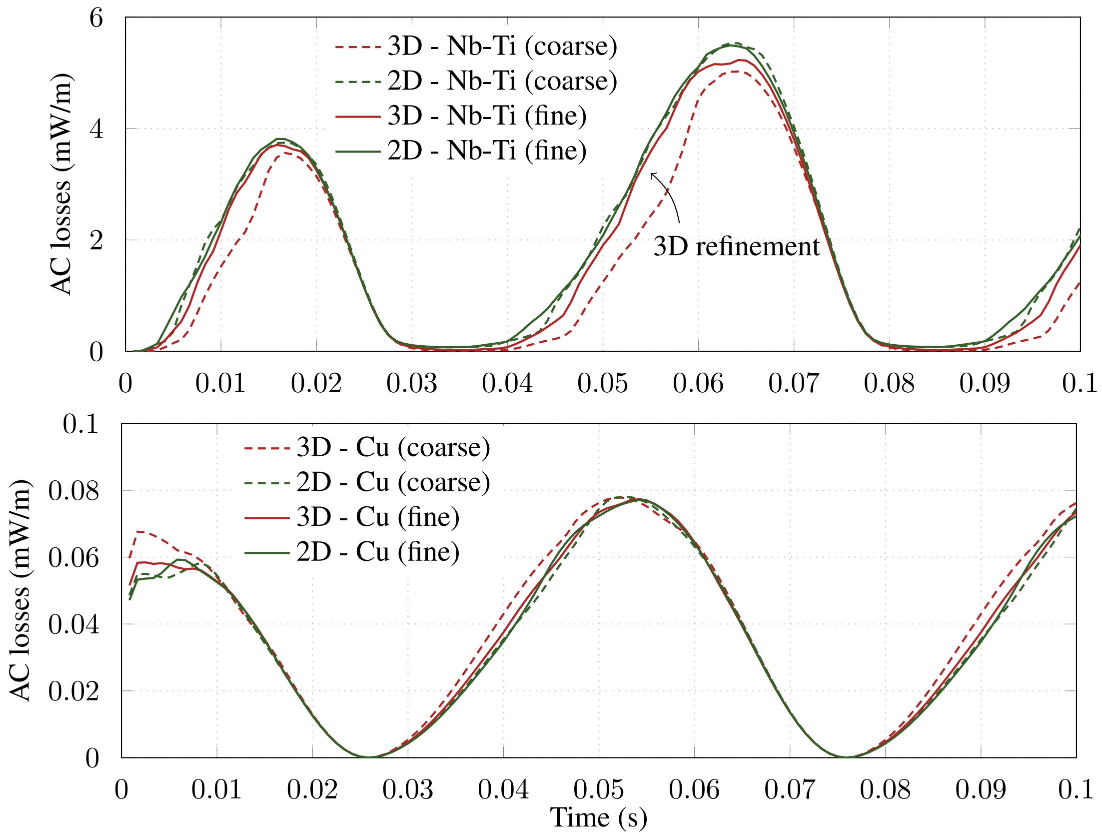

Figure 5.11: AC losses in the superconducting filaments (up) and in the conducting matrix (down) for an imposed current $I(t) = 0.5\ I_\mathrm{c}\ \sin(2\pi t/T)$, as a function of time, for two mesh resolutions, with the 2D model in helicoidal coordinates and the 3D verification model.

Model and mesh		# DOFs	# iterations	Time/it.	Time/it./DOF	Total time
3D model	Coarse	16 556	1 645	1.82 s	110 µs	50 m
	Medium	85 605	2 893	22.26 s	260 µs	17 h 53 m
	Fine	144 870	3 255	45.77 s	315 µs	41 h 23 m
2D model	Coarse	1 797	1 299	0.13 s	72 µs	3 m
	Medium	4 481	1 948	0.32 s	71 µs	10 m
	Fine	6 002	2 258	0.46 s	76 µs	17 m

Table 5.1: Performance figures for the 3D and 2D models of the twisted superconducting filaments with imposed current and no axial field, computed with 150 time steps from $t = 0$ to $t = 5T/4$. Elements in the 2D coarse, medium, and fine resolutions have similar characteristic lengths to those in the 3D meshes, respectively. The dimension reduction allows for a tremendous acceleration of the resolution.

5.1.4 Extension to non-helicoidally-invariant boundary conditions

An interesting external excitation to consider on twisted conductors is a transverse field, applied perpendicular to the wire axis. For a constant field in the y-direction, we have

$$\boldsymbol{h}_x = \begin{pmatrix} 0 \\ 1 \\ 0 \end{pmatrix} \quad \Rightarrow \quad \boldsymbol{h}_\xi = \mathrm{J}^\mathrm{T}\ \boldsymbol{h_x} = \begin{pmatrix} \sin \alpha\xi_3 \\ \cos \alpha\xi_3 \\ \alpha\xi_1 \cos \alpha\xi_3 - \alpha\xi_2 \sin \alpha\xi_3 \end{pmatrix}. \tag{5.21}$$

The expression of the transverse field in the $\boldsymbol{\xi}$-space is therefore not ξ_3-independent, as illustrated in Fig. 5.12. As a consequence, the solution of the magnetodynamic problem will not be ξ_3-independent either. We can however exploit the periodic structure of the problem by expressing the solution as a series of periodic functions with respect to ξ_3.

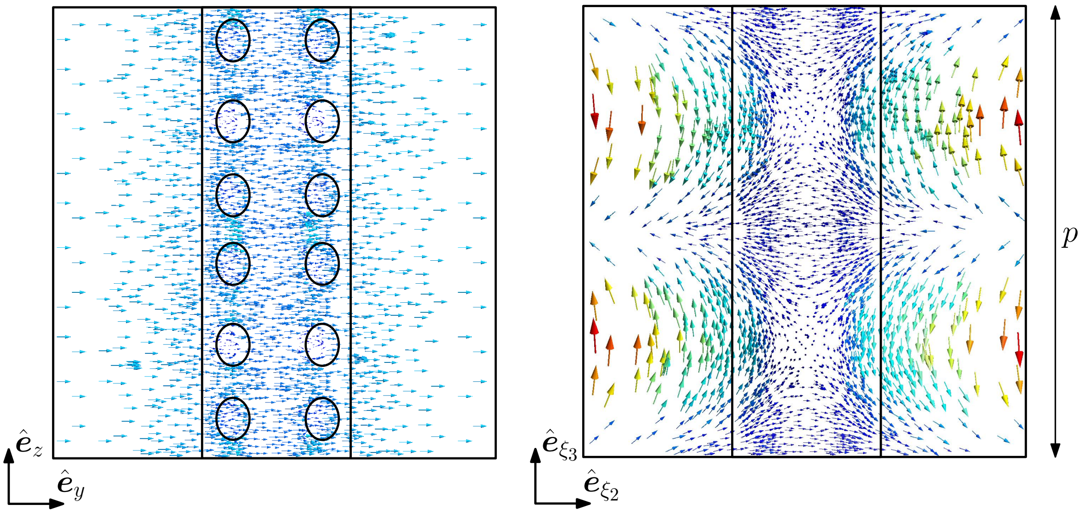

Figure 5.12: Constant applied field along $\hat{\boldsymbol{e}}_y$ for the six twisted filament geometry. (Left) Representation in the $\boldsymbol{x}$-space on the plane $x = 0$. (Right) Representation in the $\boldsymbol{\xi}$-space on the plane $\xi_1 = 0$. See Eq. (5.21).

In all generality, given the p-periodicity with respect to ξ_3, by separation of variables, we can express the magnetic field $\boldsymbol{h} = \boldsymbol{h}(\xi_1, \xi_2, \xi_3)$ as the following series:

$$\boldsymbol{h}(\xi_1, \xi_2, \xi_3) = \sum_{k=-\infty}^{\infty} \boldsymbol{h}_k(\xi_1, \xi_2) f_k(\xi_3), \tag{5.22}$$

with the modes $f_k = f_k(\xi_3)$ that are functions of ξ_3 only and that are defined as

$$f_k(\xi_3) = \begin{cases} \sqrt{2}\cos(\alpha k \xi_3), & k < 0, \\ 1, & k = 0, \\ \sqrt{2}\sin(\alpha k \xi_3), & k > 0, \end{cases} \tag{5.23}$$

and with the associated mode coefficients $\boldsymbol{h}_k = \boldsymbol{h}_k(\xi_1, \xi_2)$ that are general three-component vector functions of ξ_1 and ξ_2.

The modes f_k are orthogonal and have a unit norm, denoted as $\|f_k\| = 1$, in the sense of following the inner product:

$$\langle f_{k_1}, f_{k_2} \rangle = \frac{1}{p} \int_0^p f_{k_1} f_{k_2} \, d\xi_3 = \delta_{k_1 k_2}, \quad \forall k_1, k_2 \in \mathbb{Z}. \tag{5.24}$$

They also satisfy the following property:

$$\frac{\partial f_k}{\partial \xi_3} = \alpha k f_{-k}(\xi_3), \quad \forall k \in \mathbb{Z}. \tag{5.25}$$

Introducing a similar decomposition of the magnetic field into its in-plane and perpendicular components as in the helicoidally symmetric case for each mode coefficient $\boldsymbol{h}_k$, we can rewrite Eq. (5.22) as

$$\boldsymbol{h}(\xi_1,\xi_2,\xi_3) = \sum_{k=-\infty}^{\infty} \big(\boldsymbol{h}_{\|,k}(\xi_1,\xi_2) + \boldsymbol{h}_{\perp,k}(\xi_1,\xi_2)\big)\, f_k(\xi_3), \tag{5.26}$$

with the $\boldsymbol{h}_{\|,k}$ containing the ξ_1 and ξ_2-components of $\boldsymbol{h}_k$, and the $\boldsymbol{h}_{\perp,k}$ containing its ξ_3-component. Equation (5.26) generalizes the decomposition in Eq. (5.11) for the case of helicoidally symmetry boundary conditions. In the symmetric case, the only mode that is involved is $f_0(\xi_3) = 1$, with coefficients $\boldsymbol{h}_{\|,0} = \boldsymbol{h}_{\|}$ and $\boldsymbol{h}_{\perp,0} = \boldsymbol{h}_{\perp}$, whereas the coefficients of the other modes, $\boldsymbol{h}_{\|,k}$ and $\boldsymbol{h}_{\perp,k}$, $\forall k \in \mathbb{Z}_0$, are all equal to zero.

The curl of decomposition (5.26) reads

$$\begin{aligned}\textbf{curl}\, \boldsymbol{h}(\xi_1,\xi_2,\xi_3) &= \sum_{k=-\infty}^{\infty} \left(f_k(\xi_3)\, \textbf{curl}\, \boldsymbol{h}_{\|,k}(\xi_1,\xi_2) + \frac{\partial f_k}{\partial \xi_3} \hat{\boldsymbol{e}}_{\xi_3} \times \boldsymbol{h}_{\|,k}(\xi_1,\xi_2) \right) \\ &\quad + \sum_{k=-\infty}^{\infty} f_k(\xi_3)\, \textbf{curl}\, \boldsymbol{h}_{\perp,k}(\xi_1,\xi_2),\end{aligned} \tag{5.27}$$

where $\hat{\boldsymbol{e}}_{\xi_3}$ is the unit vector in the ξ_3-direction.

Space discretization

As the only term in Eq. (5.27) contributing to the ξ_3-component of the curl involves the curl of $\boldsymbol{h}_{\|,k}$, we can keep the same discrete function space for the $\boldsymbol{h}_{\|,k}$ as for $\boldsymbol{h}_{\|}$ in Section 5.1.2, however without the cohomology functions for $k \neq 0$, as net currents cannot be ξ_3-dependent in a magnetodynamic regime. The net currents are handled by cut functions involved in the coefficient $\boldsymbol{h}_{\|,0}$ of the constant mode $f_0(\xi_3) = 1$.

As in the ξ_3-independent case, we express the perpendicular field $\boldsymbol{h}_{\perp,k}$ as a sum of perpendicular edge functions. As the $\boldsymbol{h}_{\|,k}$ functions also contribute to the ξ_1 and ξ_2-components of the curl of $\boldsymbol{h}$ for $k \neq 0$ in Eq. (5.27) via the cross product term, the curl-free condition in $\Omega_{\mathrm{c}}^{\mathrm{C}}$ does no longer result in a constant perpendicular field in $\Omega_{\mathrm{c}}^{\mathrm{C}}$, for $k \neq 0$. Instead, as is shown below, the curl-free condition induces a coupling between the parallel and perpendicular fields in $\Omega_{\mathrm{c}}^{\mathrm{C}}$. For simplicity, and as was done before, we assume that there is only one connected non-conducting region $\Omega_{\mathrm{c}}^{\mathrm{C}}$.

Using curl-free $\boldsymbol{h}_{\|,k}$ functions in $\Omega_{\mathrm{c}}^{\mathrm{C}}$ and Eq. (5.27), the curl-free condition on $\boldsymbol{h}$ in $\Omega_{\mathrm{c}}^{\mathrm{C}}$ reads

$$\textbf{curl}\, \boldsymbol{h}(\xi_1,\xi_2,\xi_3) = \sum_{k=-\infty}^{\infty} \left(\frac{\partial f_k}{\partial \xi_3} \hat{\boldsymbol{e}}_{\xi_3} \times \boldsymbol{h}_{\|,k}(\xi_1,\xi_2) + f_k(\xi_3)\, \textbf{curl}\, \boldsymbol{h}_{\perp,k}(\xi_1,\xi_2) \right) = \boldsymbol{0}. \tag{5.28}$$

Using the mode property Eq. (5.25), this yields

$$\sum_{k=-\infty}^{\infty} \big(\alpha k f_{-k}(\xi_3)\hat{\boldsymbol{e}}_{\xi_3} \times \boldsymbol{h}_{\|,k}(\xi_1,\xi_2) + f_k(\xi_3)\,\mathbf{curl}\,\boldsymbol{h}_{\perp,k}(\xi_1,\xi_2)\big) = \mathbf{0}, \tag{5.29}$$

$$\Leftrightarrow \sum_{k=-\infty}^{\infty} \big(-\alpha k f_{k}(\xi_3)\hat{\boldsymbol{e}}_{\xi_3} \times \boldsymbol{h}_{\|,-k}(\xi_1,\xi_2) + f_k(\xi_3)\,\mathbf{curl}\,\boldsymbol{h}_{\perp,k}(\xi_1,\xi_2)\big) = \mathbf{0}, \tag{5.30}$$

$$\Leftrightarrow \sum_{k=-\infty}^{\infty} f_k(\xi_3)\big(\mathbf{curl}\,\boldsymbol{h}_{\perp,k}(\xi_1,\xi_2) - \alpha k\hat{\boldsymbol{e}}_{\xi_3} \times \boldsymbol{h}_{\|,-k}(\xi_1,\xi_2)\big) = \mathbf{0}, \tag{5.31}$$

which results in the following condition, $\forall k \in \mathbb{Z}$:

$$\mathbf{curl}\,\boldsymbol{h}_{\perp,k}(\xi_1,\xi_2) - \alpha k\hat{\boldsymbol{e}}_{\xi_3} \times \boldsymbol{h}_{\|,-k}(\xi_1,\xi_2) = \mathbf{0}. \tag{5.32}$$

For $k = 0$, we retrieve the same condition as in the helicoidally symmetric problem, that is, $\boldsymbol{h}_{\perp,0}$ must be constant in Ω_c^C, with a value given by Eq. (5.20). For $k \neq 0$, the condition can be enforced via the independent degrees of freedom of the parallel and perpendicular field mode components. Indeed, in Ω_c^C, we have the expansions

$$\boldsymbol{h}_{\perp,k}(\xi_1,\xi_2) = \sum_{n\in\mathcal{N}(\Omega_c)} h_{\perp,n,k}\, w_n\hat{\boldsymbol{e}}_{\xi_3}, \quad \text{and} \quad \boldsymbol{h}_{\|,-k}(\xi_1,\xi_2) = \sum_{n\in\mathcal{N}(\Omega_c^C)} \phi_{\|,n,-k}\,\mathbf{grad}\, w_n \tag{5.33}$$

where $w_n\hat{\boldsymbol{e}}_{\xi_3} = \boldsymbol{w}_n$ is the usual perpendicular edge function. In terms of the individual degrees of freedom, Eq. (5.32) reads

$$\sum_{n\in\mathcal{N}(\Omega_c^C)} h_{\perp,n,k}\begin{pmatrix}\partial_{\xi_2} w_n\\ -\partial_{\xi_1} w_n\\ 0\end{pmatrix} - \alpha k\;\phi_{\|,n,-k}\begin{pmatrix}-\partial_{\xi_2} w_n\\ \partial_{\xi_1} w_n\\ 0\end{pmatrix} = \mathbf{0}, \tag{5.34}$$

$$\Leftrightarrow \sum_{n\in\mathcal{N}(\Omega_c^C)} \big(h_{\perp,n,k} + \alpha k\;\phi_{\|,n,-k}\big)\begin{pmatrix}\partial_{\xi_2} w_n\\ -\partial_{\xi_1} w_n\\ 0\end{pmatrix} = \mathbf{0}. \tag{5.35}$$

The last equation is valid over the whole span of Ω_c^C if and only if the first parenthesis is constant, i.e., if

$$h_{\perp,n,k} + \alpha k\;\phi_{\|,n,-k} = C_k, \quad C_k \in \mathbb{R}, \quad \forall n \in \mathcal{N}(\Omega_c^C). \tag{5.36}$$

That is, to ensure a curl-free magnetic field in Ω_c^C, the degrees of freedom of the mode $\boldsymbol{h}_{\perp,k}$ must be linked directly to those of the mode $\boldsymbol{h}_{\|,-k}$ in Ω_c^C. Still for $k \neq 0$, the constants C_k can be arbitrarily fixed to zero, as adding any constant to $\phi_{\|,-k}$ lets the physical fields unchanged. Note that this link between the degrees of freedom induces a non-negligible reduction of the number of unknowns.

Boundary conditions for a transverse field

The transverse field defined in Eq. (5.21) applied as a boundary condition on Γ_{out} only involves the modes f_{-1} and f_1. We have

$$\boldsymbol{h}_{\parallel,-1}(\xi_1,\xi_2) = \frac{\sqrt{2}}{2}\begin{pmatrix}0\\1\\0\end{pmatrix}, \qquad \boldsymbol{h}_{\parallel,+1}(\xi_1,\xi_2) = \frac{\sqrt{2}}{2}\begin{pmatrix}1\\0\\0\end{pmatrix}, \tag{5.37}$$

$$\boldsymbol{h}_{\perp,-1}(\xi_1,\xi_2) = \frac{\sqrt{2}}{2}\begin{pmatrix}0\\0\\\alpha\xi_1\end{pmatrix}, \qquad \boldsymbol{h}_{\perp,+1}(\xi_1,\xi_2) = \frac{\sqrt{2}}{2}\begin{pmatrix}0\\0\\-\alpha\xi_2\end{pmatrix}. \tag{5.38}$$

Expressing the functions for $\boldsymbol{h}_{\parallel,-1}$ and $\boldsymbol{h}_{\parallel,+1}$ in terms of a scalar potential, we can verify that it satisfies Eq. (5.36).

Results on linear materials

For linear materials, the orthogonality between the modes allows us to treat different modes independently. The full 3D weak formulation Eq. (5.7) can be integrated along ξ_3 for every mode, giving rise to a "quasi-3D" model. We derive the resulting formulation in Section B.5 in Appendix. To verify the validity of this approach, we compare the obtained results with those from a classical 3D model. We consider the same geometry as in Section 5.1.3, but with linear materials, and with an applied transverse field instead of an imposed current intensity.

For verification, we fix the following model parameters. The filaments have a constant resistivity $\rho = 1.81 \times 10^{-12}$ Ωm, and the matrix has a constant resistivity $\rho = 10^{-8}$ Ωm (dummy values chosen for verification only). The system is subjected to a transverse field ramp along y, from $b_y = 0$ T at $t = 0$ to $b_y = 0.1$ T at $t = 0.1$ ms (these are dummy values, chosen such that the diffusion skin depth is smaller than the filament radius).

Boundary conditions for the quasi-3D model are imposed on Γ_{out} so as to satisfy Eqn. (5.37) and (5.38). Only modes $f_{-1}(\xi_3) = \sqrt{2}\cos\alpha\xi_3$ and $f_{+1}(\xi_3) = \sqrt{2}\sin\alpha\xi_3$ are activated, so that the problem amounts to find the associated parallel and perpendicular magnetic field coefficient functions in the (ξ_1,ξ_2)-plane, the full field reading

$$\begin{aligned}\boldsymbol{h}(\xi_1,\xi_2,\xi_3) = &\big(\boldsymbol{h}_{\parallel,-1}(\xi_1,\xi_2) + \boldsymbol{h}_{\perp,-1}(\xi_1,\xi_2)\big)\, f_{-1}(\xi_3)\\ &+ \big(\boldsymbol{h}_{\parallel,+1}(\xi_1,\xi_2) + \boldsymbol{h}_{\perp,+1}(\xi_1,\xi_2)\big)\, f_{+1}(\xi_3).\end{aligned} \tag{5.39}$$

The result of the linear quasi-3D model is illustrated in Fig. 5.13 in the $\boldsymbol{x}$-space.

Comparisons with the solution of the 3D problem are given in Figs. 5.14 and 5.15, along a characteristic line in the $z = \xi_3 = 0$ plane and along a helicoidal fiber of pitch length p, passing at point $\boldsymbol{x} = \big(r,0,0\big)$, with $r = R_\ell + 0.8R_{\text{f}}$, from $z = 0$ to $z = p$, respectively. Both models agree with each other.

As in the helicoidally-invariant boundary condition case, exploiting the geometrical symmetry allows for a strong reduction of the computational work. It should however be mentioned that, in this case, the quasi-3D model involves twice the number of degrees of freedom compared to the pure 2D model in an applied current case, as two modes are involved.

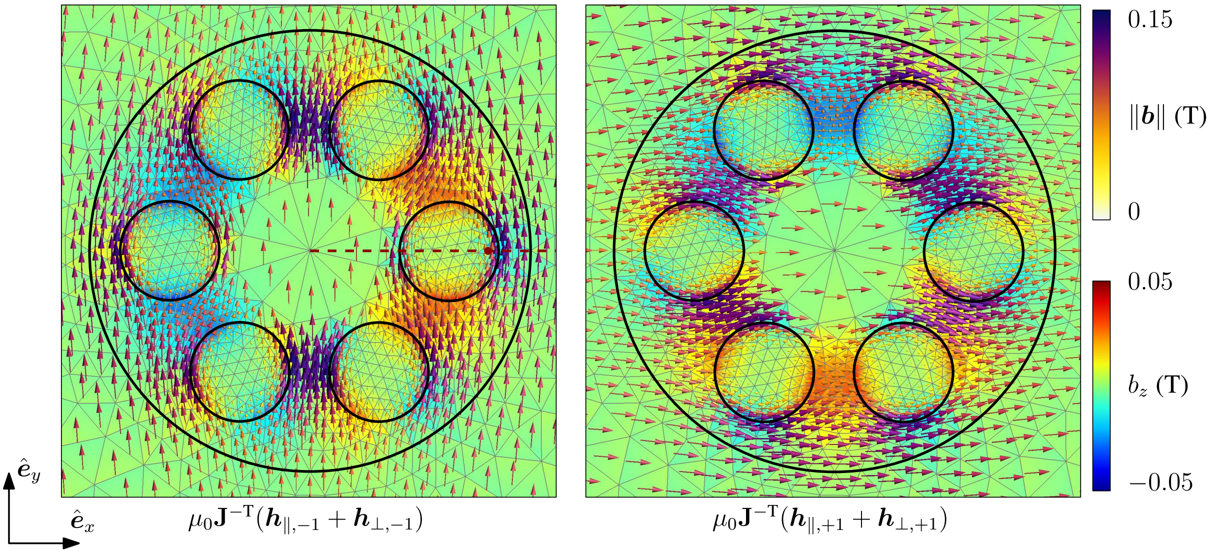

$\mu_0 \mathbf{J}^{-\mathrm{T}}(\boldsymbol{h}_{\|,-1} + \boldsymbol{h}_{\perp,-1})$ $\mu_0 \mathbf{J}^{-\mathrm{T}}(\boldsymbol{h}_{\|,+1} + \boldsymbol{h}_{\perp,+1})$

Figure 5.13: Solution of the quasi-3D model with linear materials subjected to a transverse field, represented on the $z = 0$ plane in the $\boldsymbol{x}$-space. The arrows represent the magnetic flux density and are colored as a function of its norm, using the upper color map on the right, and the triangular elements are colored as a function of the z-component of the magnetic flux density, using the lower color map on the right. The dashed red line is where the field is taken for Fig. 5.14, and the red dot along that line represents the intersection with the plane $z = 0$ of the helicoidal fiber along which the field is taken for Fig. 5.15. (Left) Field function for the even mode $f_{-1}(\xi_3) = \sqrt{2}\cos\alpha\xi_3$. (Right) Field function for the odd mode $f_{+1}(\xi_3) = \sqrt{2}\sin\alpha\xi_3$.

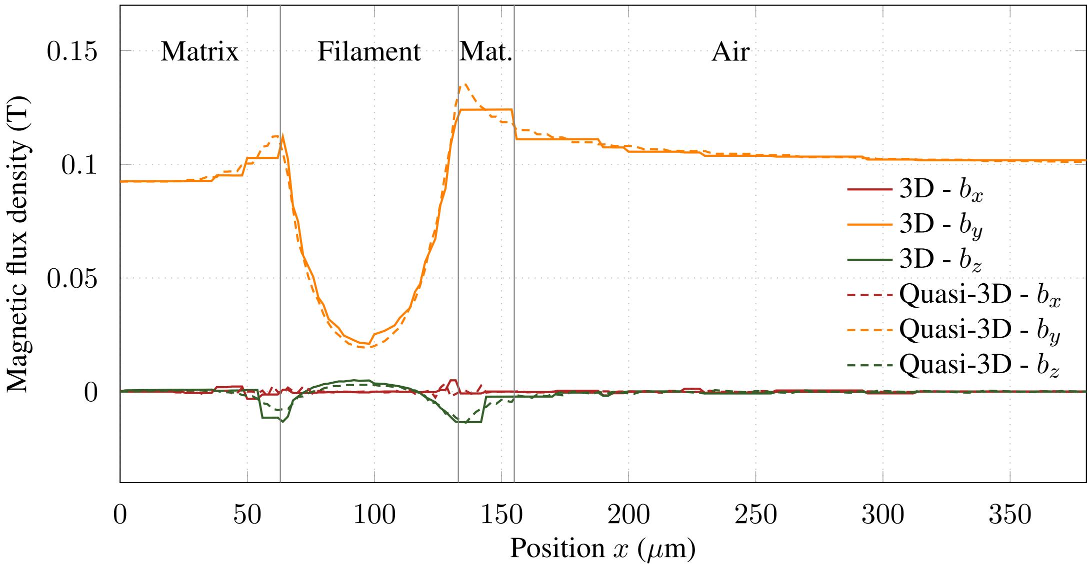

Figure 5.14: Magnetic flux density components along the dashed red line represented in Fig. 5.13, at $z = 0$, for the 3D and Quasi-3D models with a fine mesh resolution.

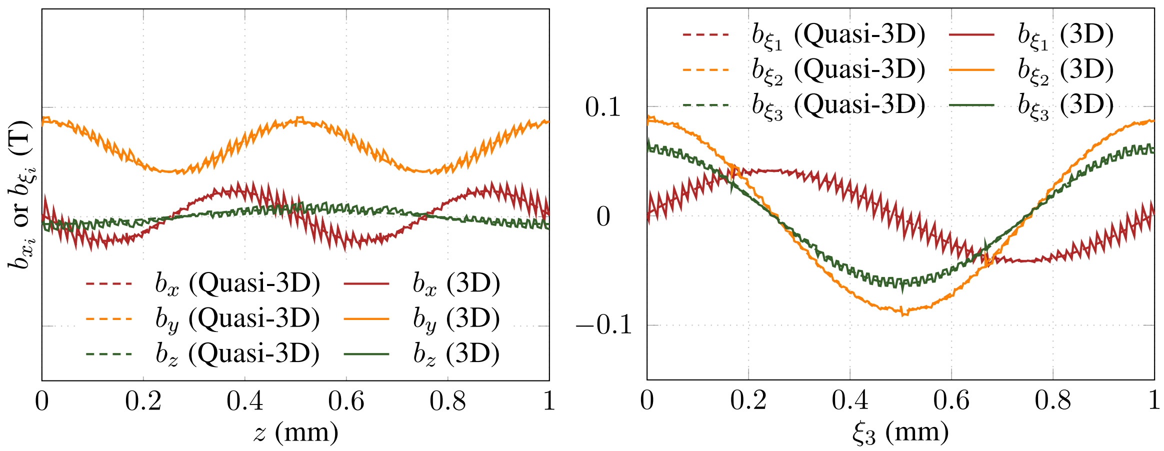

Figure 5.15: Magnetic flux density along the helicoidal fiber of pitch length p, passing at point $\boldsymbol{x} = (r, 0, 0)$, with $r = R_\ell + 0.8R_\mathrm{f}$ (represented by the red dot in Fig. 5.13), from $z = 0$ to $z = p$, for the 3D and Quasi-3D models. (Left) Three components of the vectors in the $\boldsymbol{x}$-space. (Right) Three components of the vectors in the $\boldsymbol{\xi}$-space.

Comments for nonlinear materials

If part of the geometry contains nonlinear materials, such as superconducting filaments, a mode decoupling is no longer possible. Let us consider the h-ϕ-formulation in helicoidal coordinates, Eq. (5.7), expressed in terms of the spectral decomposition of the magnetic field, Eq. (5.26). As derived in Section B.5 in Appendix, the eddy current term of the formulation expands as a double sum on $k, k' \in \mathbb{Z}$ of the terms given by Eq. (B.49).

Each term in Eq. (B.49) involves the tensor $\tilde{\boldsymbol{\rho}}$, which, for a superconducting filament, depends on the full local current density (as well as the full magnetic flux density, for a field-dependent critical current density). First, as the argument of the power law involves the full current density, all modes are directly coupled via the resistivity tensor $\tilde{\boldsymbol{\rho}}$. Second, this also implies that we can no longer exploit the orthogonality of the modes, as the integrals along ξ_3 now involve ξ_3-dependent coefficients, so that the inner product does no longer appear.

An infinite number of modes involved in the expansion Eq. (5.26) are likely to be excited. As one cannot aim for an exact solution along the ξ_3-direction with the numerical model, the expansion must therefore be truncated. Observations on the 3D solution suggest that considering only two modes for the response to a transverse field might already provide a good first evaluation of the solution. This is illustrated by Figs. 5.16 and 5.17, with the evolution of $\boldsymbol{h}$ along one helicoidal fiber.

Note that we have however no a priori guarantee for the number of modes to consider on a new problem. Also, the complexity of the formulation, due to the mode coupling, quickly increases with the number of considered modes. The investigation has not been pursed in this work, but writing the problem for one or two modes would constitute an interesting further work.

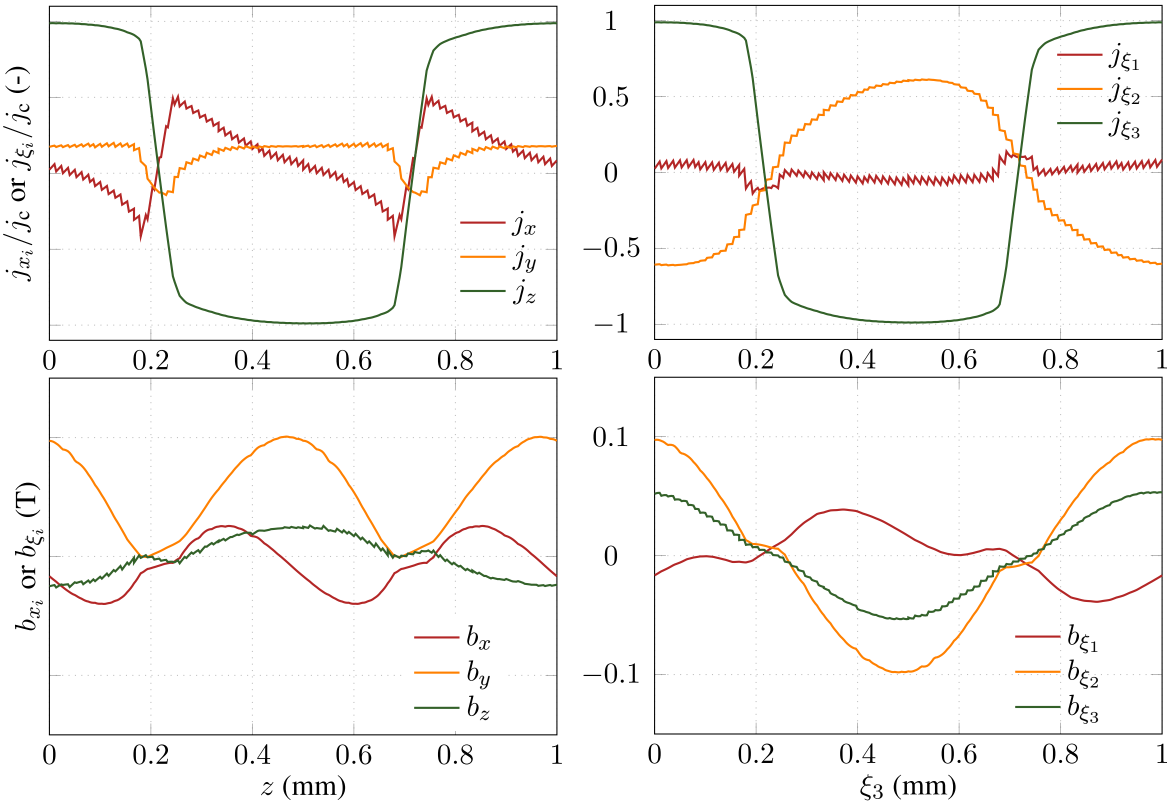

Figure 5.16: Current density (up) and magnetic flux density (down) along the helicoidal fiber of pitch length p, passing through point $\boldsymbol{x} = \big(r, 0, 0\big)$, with $r = R_\ell + 0.8R_\text{f}$ from $z = 0$ to p, for a transverse applied field along $\hat{\boldsymbol{e}}_y$ and Nb-Ti filaments. (Left) Three components of the vectors in the $\boldsymbol{x}$-space. (Right) Three components of the vectors in the $\boldsymbol{\xi}$-space. Solution of the 3D model on a fine prism mesh.

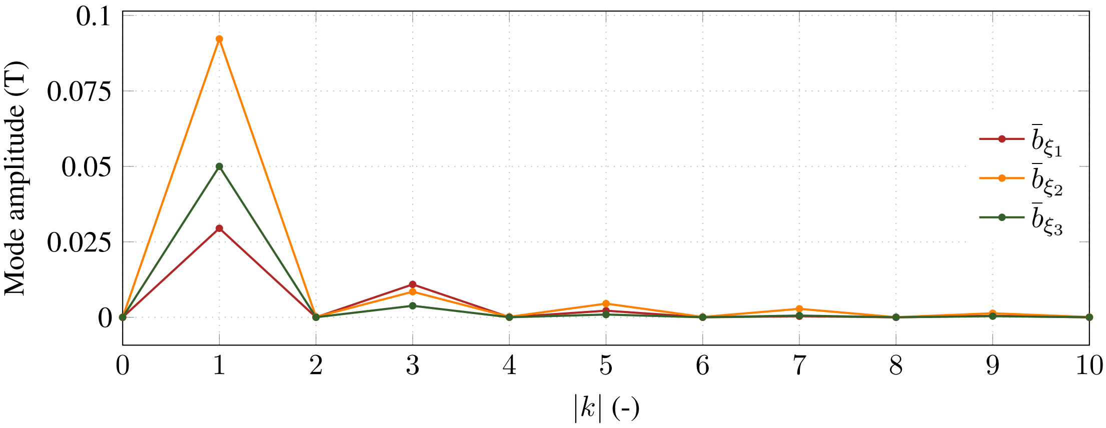

Figure 5.17: Amplitudes of the mode contributions for the evolution of the three components of $\boldsymbol{b}$ in the $\boldsymbol{\xi}$-space, along the same helicoidal fiber as in Fig. 5.16. Modes for even numbers of k are not excited by a transverse field. The mode amplitude for $|k| = 5$ is less than 5% of the one for $|k| = 1$.

5.2 Stacked-tape magnetic shield

Due to their ability to sustain large current densities without losses, superconducting materials can be used as efficient passive magnetic shields at low frequency [53, 232, 233]. Compared to conventional shields made up of ferromagnetic materials, superconducting shields are not limited by a saturation magnetization and can therefore operate at much higher flux densities [233, 234, 235, 236].

Superconducting shielding can be achieved by low-temperature supeconductors (LTS) [234, 235] or high-temperature superconductors (HTS). For HTS, bulk materials [27, 237, 238, 239] or coated conductors can be used, such as eye-shaped loops [240, 241] or stacks of tapes [48].

In this work, we focus on the last category: stacks of HTS tapes. We consider magnetic shields made up of stacks of YBCO tape annuli, as illustrated in Fig. 5.18. More specifically, we consider the finite element modelling of their magnetic response at 77 K. As a significant volume fraction of the tapes consists in the ferromagnetic substrate (SFM), assumed anhysteretic, the whole structure is a HTS-SFM hybrid. As was discussed in the previous chapter, numerical modelling of these hybrid structures is not a trivial task, and different approaches may result in completely different numerical behaviors.

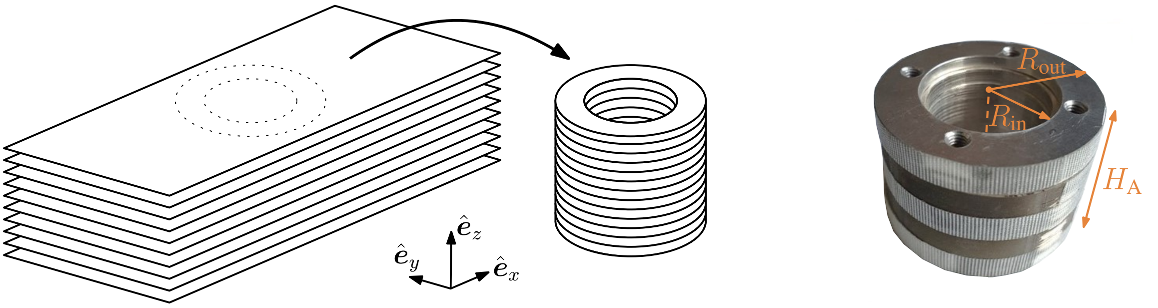

(a) Illustration of the fabrication process. (b) Sample A [242].

Figure 5.18: Fabrication process and picture of a stacked-tape magnetic shield (sample A). Each tape consists mainly of a ferromagnetic substrate, coated by a thin layer of HTS.

Numerical modelling of the magnetic shields is relevant to understand and quantify the influence of the material parameters on the overall magnetic shielding. For example, once the models are validated against experimental measurements, they can be exploited to explore the influence of the permeability of the ferromagnetic substrate on the shielding properties, or the effect of a field-dependent critical current density. Such discussions are conducted in [53]. Here, we focus on the numerical aspect of the modelling.

We first define the problem in Section 5.2.1. In Sections 5.2.2 and 5.2.3, we propose two different models suited for a finite element analysis. The first model is a simplification of the layered structure in which we consider a limited number of tapes in the stack. The second model follows a homogenization approach [243], that amounts to replacing the layered stack of tapes by a fictitious homogeneous material with anisotropic properties.

We then assess the accuracy and efficiency of both models for different finite element formulations. In Section 5.2.4, we consider the shielding with respect to an axial external field, that can be modelled as a 2D axisymmetric problem, and in Section 5.2.5, we analyze a transverse applied field configuration, that requires a 3D model.

We will show that obtaining accurate results is challenging and that it can be computationally expensive. The objective of our analysis is to provide recommendations on how to model hybrid HTS-SFM layered structures. The two models we propose must be seen as first investigations. They offer general observations on the main difficulties associated with the stacked-tape magnetic shield problem.

5.2.1 Problem definition and experimental measurements

The magnetic shields consist of stacks of YBCO tape annuli, extracted from a 46 mm-wide coated conductor [242, 53], as illustrated in Figure 5.18. The superconducting tape is based on a rolling assisted biaxially textured substrate (RABiTS) [32], made up of Ni-5at.%W, which is approximately 75 μm thick. The filling volume fraction of the ferromagnetic substrate (SFM) in the tape, and hence also in the whole stack, is equal to $f = 0.92$. Annuli have an inner radius $R_{\text{in}} = 13$ mm and an outer radius $R_{\text{out}} = 22.5$ mm. Three samples, A, B, and C, of different height $H_{(\cdot)}$ and number of tapes $N_{(\cdot)}$ are considered. We have $H_{\text{A}} = 24$ mm, $H_{\text{B}} = 14.9$ mm, and $H_{\text{C}} = 9.9$ mm, with $N_{\text{A}} = 294$, $N_{\text{B}} = 182$, and $N_{\text{C}} = 121$. The fabrication process of the system is described in [244, 245].

The first magnetization curve [90] of the ferromagnetic substrate has been measured in [246] at room temperature, 293 K, and in liquid nitrogen at a temperature of 77 K. Experimental measurements (up to 0.2 T) are interpolated to obtain the continuous saturation curves illustrated in Fig. 5.19 that will be used in the numerical simulations to describe the magnetic constitutive law. Above 0.2 T, the measurements are smoothly extrapolated to approach the saturation permeability of μ_0. At both 293 K and 77 K, the relative permeability first increases, up to values of $\mu_{\text{r}} = 330$ and $\mu_{\text{r}} = 365$, respectively, and then progressively decreases down to $\mu_{\text{r}} = 1$ for high field values.

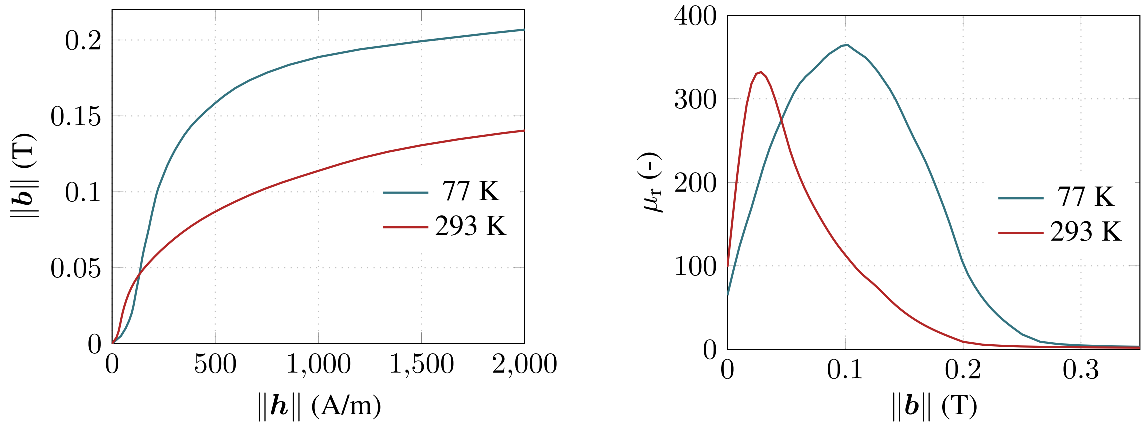

(a) Saturation curves.

(b) Magnetic permeability.

Figure 5.19: Saturation law and magnetic permeability of the ferromagnetic substrate at both 293 K and 77 K. Curves are obtained by interpolation of experimental measurements [246] below 0.2 T, and smooth extrapolation of them above 0.2 T.

A volume fraction $f = 0.92$ of the stack of tapes is therefore characterized by the field-dependent permeability mentioned above. For the complementary volume fraction, $1 - f$, containing the superconducting layer as well as buffer layers, we assume that $\mu = \mu_0$.

The ferromagnetic substrate is considered non-conducting. Only the superconducting layer is modelled as a conducting material. We neglect the conductivity of other layers, and we assume that the HTS fills a volume fraction of $(1 - f)$ of the whole stack. The HTS layer is described by the power law, with $n = 20$ and a field-dependent critical current density $j_{\mathrm{c}}(\boldsymbol{b})$ that follows Kim's law [88]:

$$j_{\mathrm{c}}(\boldsymbol{b}) = \frac{j_{\mathrm{c}0}}{1 + \|\boldsymbol{b}\|/b_0}, \tag{5.40}$$

with $j_{\mathrm{c}0} = 7 \times 10^9$ A/m^2 and $b_0 = 0.1$ T, two constant parameters that were found to faithfully reproduce the experimental measurements. We refer to [242] for a more detailed discussion about the parameter identification. For simplicity, we assume that $j_{\mathrm{c}}(\boldsymbol{b})$ only depends on the norm $\|\boldsymbol{b}\|$ of the magnetic flux density. In reality, tapes are more sensitive to fields perpendicular to their surface than to parallel fields [247, 35, 248], but we neglect anisotropic effects here. We already obtain a satisfying agreement between the models and the measurements with this assumption [242].

We study the magnetic response of the shield to an external applied field $\boldsymbol{b}_{\mathrm{s}}$ in two configurations: axial and transverse. In the axial configuration, the field $\boldsymbol{b}_{\mathrm{s}}$ is applied parallel to the stacked-tape cylinder axis, i.e., in the z-direction. In the transverse configuration, the field is applied perpendicular to the cylinder axis, e.g., in the x-direction. See Fig. 5.20. To quantify the shielding properties of the stacked tape, we define the shielding factor SF as follows:

$$\mathrm{SF} = \frac{\|\boldsymbol{b}_{\mathrm{s}}\|}{\|\boldsymbol{b}_{\mathrm{in}}\|}, \tag{5.41}$$

where $\boldsymbol{b}_{\mathrm{in}}$ is the magnetic flux density at the center of the stack. This quantity is related to a local measurement. It is the main indicator that we will compare during the numerical analysis.

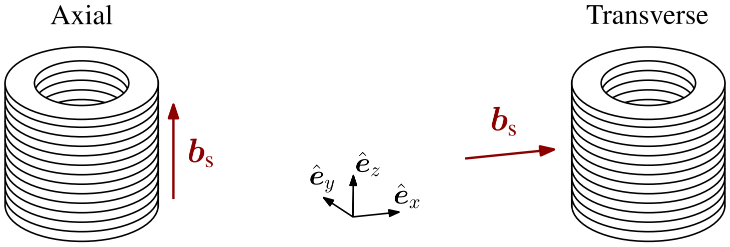

Figure 5.20: Axial and transverse configurations.

At room temperature, the YBCO layers are not in a superconducting state and behave like a normal conductor. As a result, only the ferromagnetic substrate significantly contributes to the magnetic shielding. The shielding is much more effective in the transverse configuration, due to the layered structure of the stack that does not offer paths of low reluctance for vertical field lines in the axial configuration. At 77 K, the HTS layers are superconducting, and this offers strong shielding properties in the axial configuration due to the appearance of screening currents in response to a time-varying magnetic flux.

The shielding factors have been measured experimentally in [242] on the three samples, at both room temperature and 77 K, in both axial and transverse configurations, for a linear ramp of applied field up to 60 mT, with a rate of 0.75 mT/s. The measurements are given in Fig. C.7 in Appendix. A second set of measurements has been conducted at 77 K, with an axial field up to 670 mT at a rate of 5 mT/s on the three samples. The associated shielding factors are illustrated in Fig. C.8 in Appendix.

5.2.2 Simple model

Modelling the detailed stacks of $N_{(\cdot)} > 120$ tapes is expensive in terms of computational resources, but may not be necessary for reproducing the global shielding behavior of the overall stack. For the first approach, we propose to model the stacked-tape magnetic shield with a limited number of tapes $N_\text{s} < N_{(\cdot)}$, with a fictitious thickness $w_\text{s} = H_{(\cdot)}/N_\text{s}$, in order to reproduce the total height $H_{(\cdot)}$ of the stack. As a first step in the numerical analysis, we will assess the influence of N_s on the obtained shielding factors to verify the validity of this approach.

As already mentioned, we assume that each tape consists in the superposition of a SFM layer of thickness fw_s and a HTS layer of thickness $(1-f)w_\text{s}$. We do not model other material layers in the coated conductor, neglecting their role in the shielding properties.

In the axial configuration, the problem is axisymmetric and can be described by a 2D model, as represented in Fig. 5.21(a). In the transverse configuration, a 3D model is necessary. By symmetry, only a quarter of the domain can be modelled, as illustrated in Fig. 5.21(b).

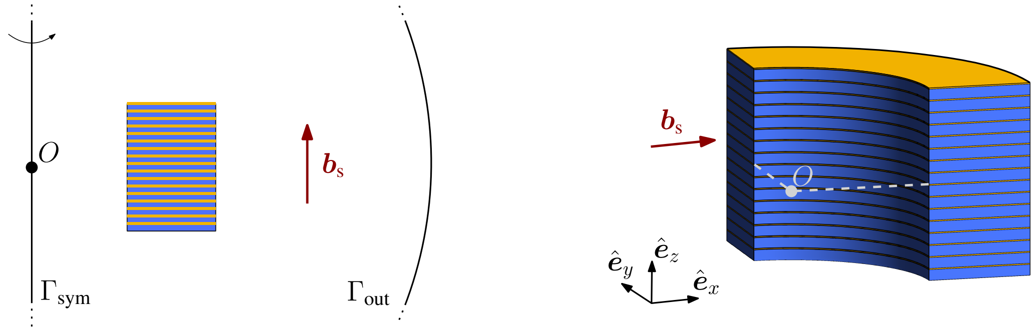

(a) Axial configuration. (b) Transverse configuration.

Figure 5.21: Axial and transverse configurations for the simple model. Yellow regions represent the HTS layers and blue regions represent the SFM layers. The point O is the coordinate system center, where the magnetic flux density $\boldsymbol{b}_\text{in}$ is taken for computing the shielding factor. (a) Axial configuration, the scale is not respected for the external boundary and HTS layer thickness, for clarity. (b) Transverse configuration, the domain boundary is not represented.

The external field is imposed via an essential boundary condition on the circular or spherical external surface Γ_out, placed at a distance $R = 100$ mm from the center O, whereas symmetry conditions are imposed on the symmetry surface(s) Γ_sym, strongly or weakly, depending on the formulation. A global condition is also associated with each tape Ω_{c_i}, $i \in \{1,\dots,N_\text{s}\}$. In the axial configuration, screening currents are free to appear and no external voltage is imposed, so that we have $\bar{V}_i = 0$, $\forall i \in \{1,\dots,N_\text{s}\}$. In the transverse configuration, both the total current and the voltage are equal to zero by symmetry in each tape. This is enforced by strong global conditions, either on the current, or on the voltage.

5.2.3 Homogeneous model

As a second method, we propose to replace the layered structure by a homogeneous material with anisotropic properties [243, 249, 46]. The homogeneous material has both superconducting and ferromagnetic properties, and the problem is written in terms of the local average fields $\boldsymbol{h}$, $\boldsymbol{b}$, $\boldsymbol{e}$, and $\boldsymbol{j}$, also referred to as the macroscale fields [250], assuming that each finite element in the homogeneous model covers a sufficiently high number of tapes in the z-direction. The problem geometry is illustrated in Fig. 5.22. Note that a plane symmetry with respect to $z = 0$ can be introduced to reduce the computational domain by half.

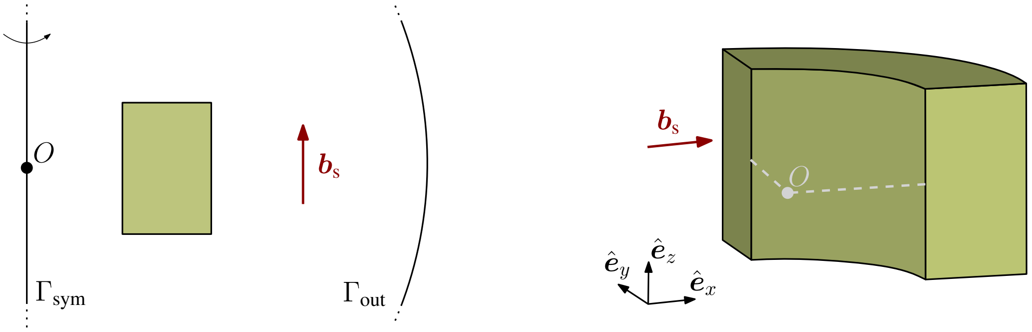

(a) Axial configuration. (b) Transverse configuration.

Figure 5.22: Axial and transverse configurations for the homogeneous model. The green region represents the hybrid HTS-SFM material with anisotropic material properties. The point O is the coordinate system center, where the magnetic flux density $\boldsymbol{b}_\mathrm{in}$ is taken for computing the shielding factor. (a) Axial configuration, the scale is not respected for the external boundaries and HTS layer thickness, for clarity. (b) Transverse configuration, the external domain boundaries are not represented.

Boundary conditions are identical to those in the simplified detailed model, but global conditions only involve one conducting domain. In the axial configuration, a zero applied voltage is imposed, strongly or weakly, depending on the formulation. In the transverse configuration, either a zero applied voltage or a zero current intensity is strongly imposed.

Anisotropic permeability and reluctivity

The homogeneous material is anisotropic and its magnetic permeability takes the form of a diagonal tensor, defined as follows [243]:

$$\tilde{\boldsymbol{\mu}}(\boldsymbol{h}) = \begin{pmatrix} \bar{\mu}(\boldsymbol{h}^\mathrm{F}) & 0 & 0 \\ 0 & \bar{\mu}(\boldsymbol{h}^\mathrm{F}) & 0 \\ 0 & 0 & \bar{\bar{\mu}}(\boldsymbol{h}^\mathrm{F}) \end{pmatrix} \quad \text{with} \quad \begin{cases} \bar{\mu}(\boldsymbol{h}^\mathrm{F}) = f\mu(\boldsymbol{h}^\mathrm{F}) + (1-f)\mu_0, \\ \bar{\bar{\mu}}(\boldsymbol{h}^\mathrm{F}) = \big(f/\mu(\boldsymbol{h}^\mathrm{F}) + (1-f)/\mu_0\big)^{-1}, \end{cases} \tag{5.42}$$

where $\boldsymbol{h}^{\mathrm{F}}$ denotes the local magnetic field in the SFM, which is the relevant quantity to be used as an argument for the field-dependent permeability. This quantity, however, is not the main unknown of the homogeneous model. Instead, the model is written in terms of the average magnetic field $\boldsymbol{h}$. To use Eq. (5.42), one must therefore express $\boldsymbol{h}^{\mathrm{F}}$ in terms of $\boldsymbol{h}$.

The volume average field $\boldsymbol{h}$ is defined as $\boldsymbol{h} = f\boldsymbol{h}^{\mathrm{F}} + (1-f)\boldsymbol{h}^{\mathrm{S}}$, where $\boldsymbol{h}^{\mathrm{S}}$ is the local field in the HTS material. By continuity of the tangential component of the magnetic field and of the normal component of the magnetic flux density, we have

$$h_x^{\mathrm{F}} = h_x^{\mathrm{S}}, \qquad h_y^{\mathrm{F}} = h_y^{\mathrm{S}}, \qquad \mu(\boldsymbol{h}^{\mathrm{F}})h_z^{\mathrm{F}} = \mu_0 h_z^{\mathrm{S}}, \tag{5.43}$$

with $(h_x^{\mathrm{F}}, h_y^{\mathrm{F}}, h_z^{\mathrm{F}})$ and $(h_x^{\mathrm{S}}, h_y^{\mathrm{S}}, h_z^{\mathrm{S}})$ the components of $\boldsymbol{h}^{\mathrm{F}}$ and $\boldsymbol{h}^{\mathrm{S}}$ in the Cartesian coordinate system represented in Fig. 5.22. Consequently, the relation between the components (h_x, h_y, h_z) of the average magnetic field, $\boldsymbol{h}$, and the components of the magnetic field in the SFM, $\boldsymbol{h}^{\mathrm{F}}$, can be written as

$$\begin{pmatrix} h_x^{\mathrm{F}} \\ h_y^{\mathrm{F}} \\ h_z^{\mathrm{F}} \end{pmatrix} = \begin{pmatrix} h_x \\ h_y \\ \mu_0 h_z / \big(f\mu_0 + (1-f)\mu(\boldsymbol{h}^{\mathrm{F}})\big) \end{pmatrix}. \tag{5.44}$$

Because of the nonlinear permeability $\mu(\boldsymbol{h}^{\mathrm{F}})$, interpolated from experimental measurements, expressing $\boldsymbol{h}^{\mathrm{F}}$ in terms of $\boldsymbol{h}$ therefore requires to solve an implicit equation for h_z^{F} at each point where the permeability value is needed. We solve this equation using a quasi-Newton method, which is a variation of the Newton-Raphson method in which the Jacobian is approximated by a finite difference.

Conversely, for formulations that involve the magnetic flux density as a primal unknown, the magnetic reluctivity takes the form of a diagonal tensor as well, defined as follows:

$$\tilde{\boldsymbol{\nu}}(\boldsymbol{b}) = \begin{pmatrix} \bar{\nu}(\boldsymbol{b}^{\mathrm{F}}) & 0 & 0 \\ 0 & \bar{\nu}(\boldsymbol{b}^{\mathrm{F}}) & 0 \\ 0 & 0 & \bar{\bar{\nu}}(\boldsymbol{b}^{\mathrm{F}}) \end{pmatrix} \quad \text{with} \quad \begin{cases} \bar{\nu}(\boldsymbol{b}^{\mathrm{F}}) = \big(f/\nu(\boldsymbol{b}^{\mathrm{F}}) + (1-f)/\nu_0\big)^{-1}, \\ \bar{\bar{\nu}}(\boldsymbol{b}^{\mathrm{F}}) = f\nu(\boldsymbol{b}^{\mathrm{F}}) + (1-f)\nu_0, \end{cases} \tag{5.45}$$

where the non-constant reluctivity in the SFM depends on the local magnetic flux density $\boldsymbol{b}^{\mathrm{F}}$ in the SFM. Following similar steps as for the magnetic field, we can express the relation between the Cartesian components (b_x, b_y, b_z) of the average magnetic flux density, $\boldsymbol{b}$, and the Cartesian components $(b_x^{\mathrm{F}}, b_y^{\mathrm{F}}, b_z^{\mathrm{F}})$ of the field in the SFM, $\boldsymbol{b}^{\mathrm{F}}$, as follows:

$$\begin{pmatrix} b_x^{\mathrm{F}} \\ b_y^{\mathrm{F}} \\ b_z^{\mathrm{F}} \end{pmatrix} = \begin{pmatrix} \nu_0 b_x / \big(f\nu_0 + (1-f)\nu(\boldsymbol{b}^{\mathrm{F}})\big) \\ \nu_0 b_y / \big(f\nu_0 + (1-f)\nu(\boldsymbol{b}^{\mathrm{F}})\big) \\ b_z \end{pmatrix}. \tag{5.46}$$

This also involves an implicit equation for the x and y-components (that can be solved at once). We also use a quasi-Newton method.

This averaging approach is a simple form of general homogenization techniques involving multi-scale resolutions [250]. Here, the microscale problem is fully contained in the implicit equation Eq. (5.44) or Eq. (5.46).

Anisotropic resistivity

The current density can only flow in the (x, y)-plane. To prevent current from flowing in the z-direction, we introduce a large resistivity ρ_∞ in that direction [46]. In practice, we found that $\rho_\infty = 0.01\ \Omega\mathrm{m}$ gives satisfying results for the considered problems and material parameters. In the Cartesian coordinate system represented in Fig. 5.22, the resistivity takes the form of a diagonal tensor, defined as follows:

$$\tilde{\boldsymbol{\rho}}(\boldsymbol{j};\boldsymbol{b}) = \frac{1}{1-f}\begin{pmatrix} \rho(\boldsymbol{j}^{\mathrm{S}};\boldsymbol{b}^{\mathrm{S}}) & 0 & 0 \\ 0 & \rho(\boldsymbol{j}^{\mathrm{S}};\boldsymbol{b}^{\mathrm{S}}) & 0 \\ 0 & 0 & \rho_\infty \end{pmatrix}, \tag{5.47}$$

where the power law resistivity depends on the local current density $\boldsymbol{j}^{\mathrm{S}}$ and magnetic flux density $\boldsymbol{b}^{\mathrm{S}}$ in the HTS layer. As the SFM is assumed non-conducting, it does not carry any current density and the relation between the average current density $\boldsymbol{j}$ and $\boldsymbol{j}^{\mathrm{S}}$ is straightforward. We have $\boldsymbol{j}^{\mathrm{S}} = \boldsymbol{j}/(1-f)$, still assuming that $(1-f)$ is the filling factor of the HTS. The local magnetic flux density $\boldsymbol{b}^{\mathrm{S}}$ that is involved in the field-dependent critical current density $j_{\mathrm{c}} = j_{\mathrm{c}}(\boldsymbol{b}^{\mathrm{S}})$ can be derived from $\boldsymbol{b}$ and $\boldsymbol{b}^{\mathrm{F}}$, computed from Eq. (5.44) or Eq. (5.46), depending on the formulation.

As handling the power law in terms of the conductivity has been ruled out as an efficient technique in the previous chapter, we do not consider the conductivity tensor here. Note that using the conductivity may still be useful in the case of large time step calculations [126, 239].

Note that in the axial configuration, as the current density is azimuthal by construction, there is no need to introduce an anisotropic resistivity tensor. The usual (isotropic) constitutive law can be used *as is*.

5.2.4 Model comparison in axial field (2D-axi)

In this section, we compare the numerical results and performance of the two approaches with different formulations on the 2D axisymmetric model reproducing the experimental axial configuration at 77 K for an applied field up to 670 mT, for sample B. For both models, we consider three formulations: the h-ϕ, h-ϕ-b, and a-j-formulations. For the h-ϕ-b-formulation, we take $\boldsymbol{b} \in \mathcal{B}^{\delta,1}(\Omega_{\mathrm{m}})$, as defined in Eq. (3.47).

The space discretization is performed using triangular elements, except in the HTS layers of the simple model, where one layer of quadrangular elements is used. The characteristic mesh size is fixed to 0.4α mm in the tapes, to 1.5α mm in the vicinity of the center O, and to 6α mm on the outer surface Γ_{out}, with α equal to 4, 2, 1, and 0.5 for the coarse, medium, fine, and finer discretization levels, respectively. For the homogeneous model, the mesh size is allowed to increase up to 1.6α mm in the center of the stack. The coarse meshes associated with $\alpha = 4$ for both models are illustrated in Fig. 5.23.

For the time discretization, we model the response from $t = 0$ to $t = 135$ s with a minimum of 40 time steps. In case of non-convergence, the time step is reduced using the adaptive time-stepping procedure described in Section 4.4.2, with $i_{\max} = 180$.

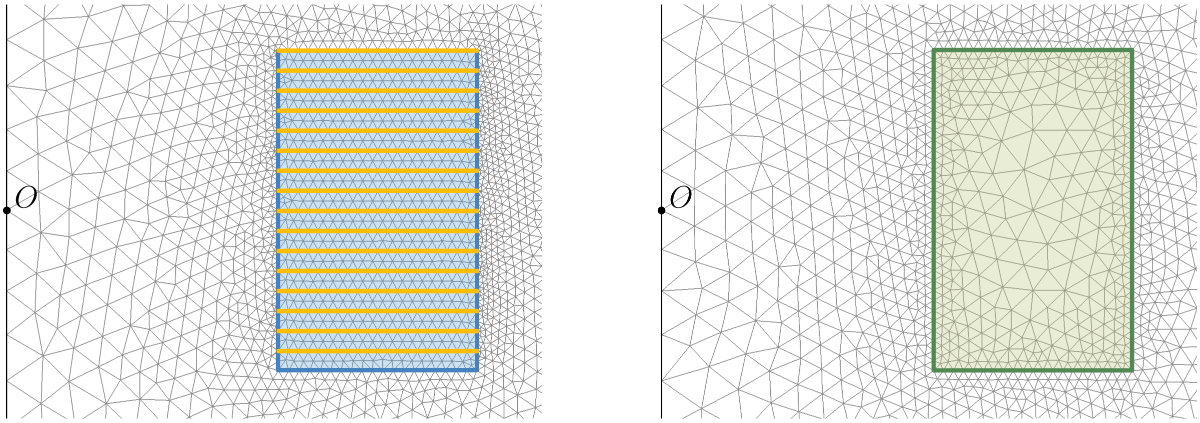

(a) Simple model. (b) Homogeneous model.

Figure 5.23: Coarse meshes ($\alpha = 4$) for the simple and homogeneous models in the axial configuration for sample B. (a) Simple model with $N_\mathrm{s} = 16$, the yellow lines represent the HTS layers, meshed with quadrangles whose size can be inferred from adjacent triangles. (b) Homogeneous model with coarser mesh size at the center of the stack, as the solution is less sensitive to the mesh resolution in that region.

Influence of N_s in the simple model

We first evaluate the influence of the mesh resolution on the numerical solution. The results of the h-ϕ-formulation are illustrated in Fig. 5.24. Especially at low fields and for a large number of tapes, noticeable changes are still observed in the SF values when refining from $\alpha = 1$ to $\alpha = 0.5$, with the largest variation being of the order of 6%. In the small field regime, the current density only circulates over a small portion of the HTS layers. This is shown in the upper-left part of Fig. 5.29, and helps to understand why a fine discretization is required to get an accurate description of the overall magnetic response.

The influence of the number of tapes N_s on the SF values is illustrated in Fig. 5.25, with the three considered formulations. All three formulations give comparable results. Note that the numerical results qualitatively match with the experimental measurements, especially at large field values.

At a fine mesh resolution and with different formulations, the chosen value of N_s is seen to have a significant influence on the SF, especially at low fields. In the axial configuration, most of the shielding is generated by screening currents in the HTS layers, and the height over which these layers are distributed influences the shielding effectiveness, as shown by the measurements in Fig. C.8 in Appendix. Because the simple model is built using a SFM layer at the bottom of the stack, taking smaller values of N_s reduces the overall height covered by HTS layers, and hence reduces the obtained SF.

To further investigate the influence of N_s on the numerical solution, we consider a modified version of the simple model in which we introduce a symmetry with respect to the (x, y)-plane, by considering that the tapes are stacked upside-down below the plane, i.e., for $z > 0$. In this symmetric variation of the simple model, the HTS layers cover the entire height of the physical sample. We compare the obtained SF values to the one obtained with the asymmetric model in Fig. 5.26, using the h-ϕ-formulation. As can be expected, the difference between both approaches reduces as the number of tapes is increased. The SF values from the symmetric

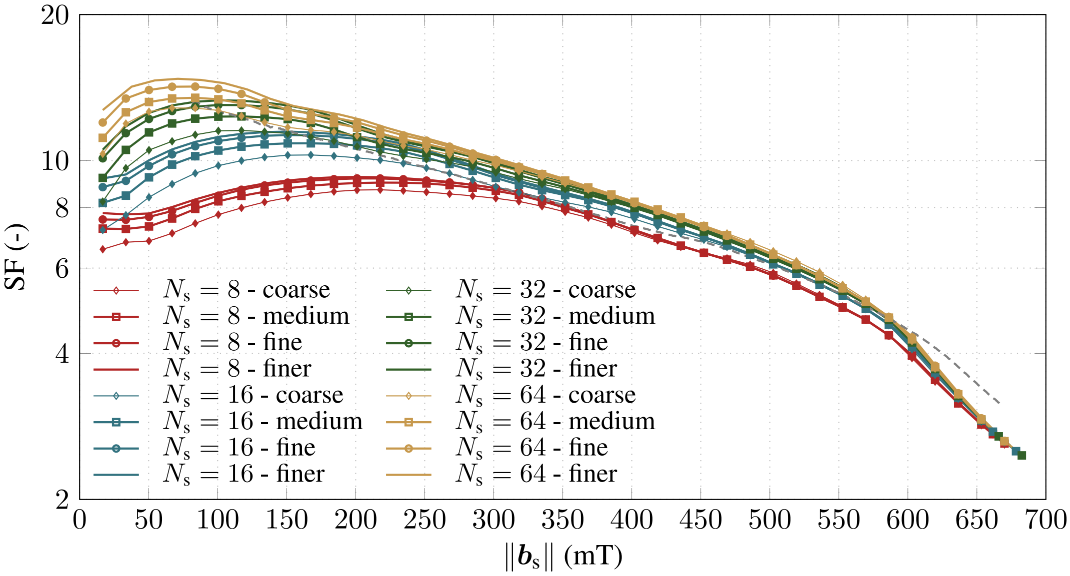

Figure 5.24: Shielding factors of sample B in the axial configuration from the h-ϕ-formulation, for four different numbers of tapes N_s with the simple model (asymmetric case), and four different discretization levels. The dashed gray curve corresponds to the experimental measurements.

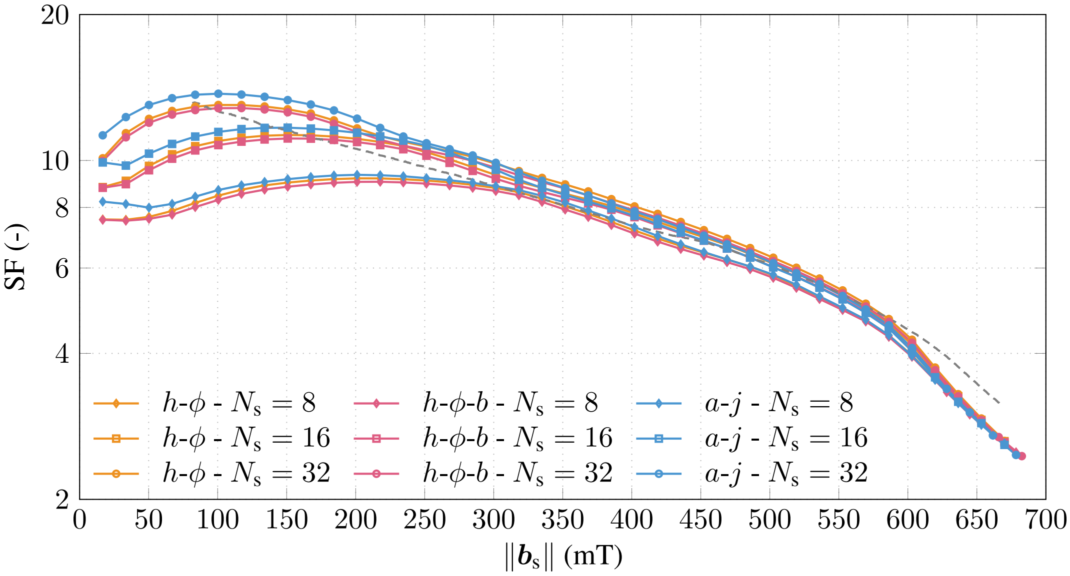

Figure 5.25: Shielding factors of sample B in the axial configuration from the h-ϕ, h-ϕ-b, and a-j-formulations on the simple model in the axial configuration, for different numbers of tapes N_s (asymmetric case). Results are obtained on a fine mesh ($\alpha = 1$). The dashed gray curve corresponds to the experimental measurements.

approach demonstrates a lower dependence on N_s.

The reduced equivalent HTS height is one piece of explanation for the influence of N_s on the SF values, but ending the stack with a SFM or a HTS layer also has an influence on the field lines in the vicinity of the materials. Ferromagnetic materials attract them, whereas screening current in HTS have the opposite effect. As the SF value is sensitive to the field lines distribution, it is not surprising to obtain qualitatively different curves in the symmetric and asymmetric cases.

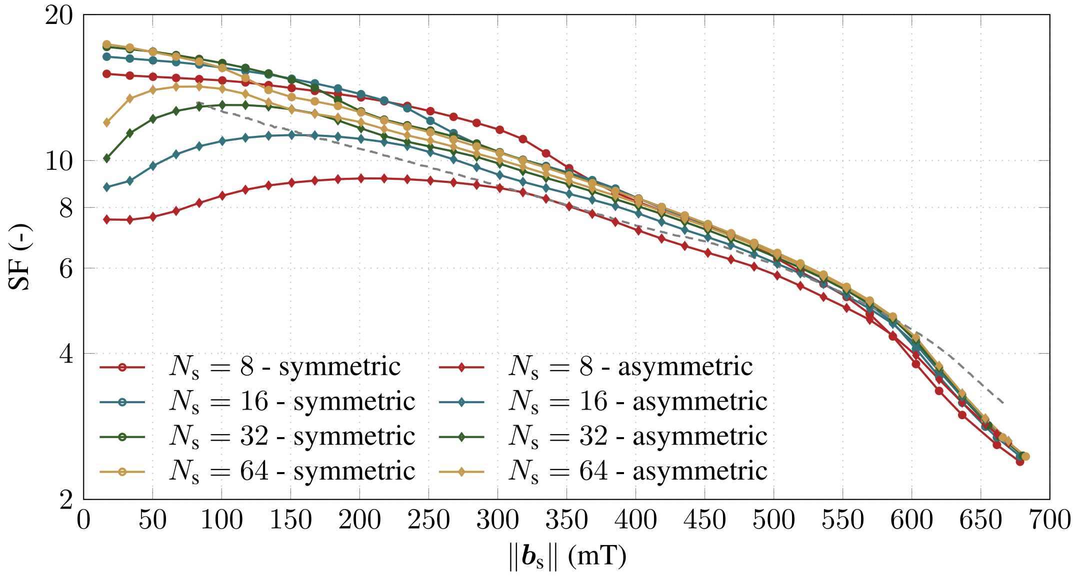

Figure 5.26: Influence of the number of tapes N_s in the simple model on the shielding factor of sample B in the axial configuration. Results are obtained on a fine mesh ($\alpha = 1$) with the h-ϕ-formulation. The asymmetric case is what is represented in Fig. 5.21, whereas in the symmetric case there is a HTS layer at the bottom of the stack. The dashed gray curve corresponds to the experimental measurements.

To faithfully reproduce the overall behavior of the stack of tapes in the axial configuration, the number of modelled tapes must therefore be large enough. In the following, we choose $N_s = 64$. This however gives rise to a very detailed geometry description. Simplifying the geometry, at the cost of introducing anisotropic material properties and handling a HTS-SFM hybrid fictitious material is the idea of the second model, that we now consider.

Comparison with the homogeneous model

Results from simulations with the three formulations on the homogeneous model are given in Fig. 5.27. As with the simple model, the mesh size significantly influences the SF values at low fields. As is illustrated in the bottom-left part of Fig. 5.29, in that field regime, the magnetic flux density only penetrates the hybrid material over a small depth. It is expected that an accurate description of the magnetic response can only be obtained with sufficiently fine space discretization in that region.

As shown in Figs. 5.28 and 5.29, both models provide similar results, in good agreement with the experimental measurements. Results obtained with the three formulations are of comparable accuracy. As discussed in the next paragraphs, the different approaches however do not perform identically in terms of computational work.

Comments on the numerical efficiency

In the homogeneous approach, the geometry definition is simplified, but the whole stack of tapes becomes both conducting and magnetic. For an identical mesh, the number of degrees of

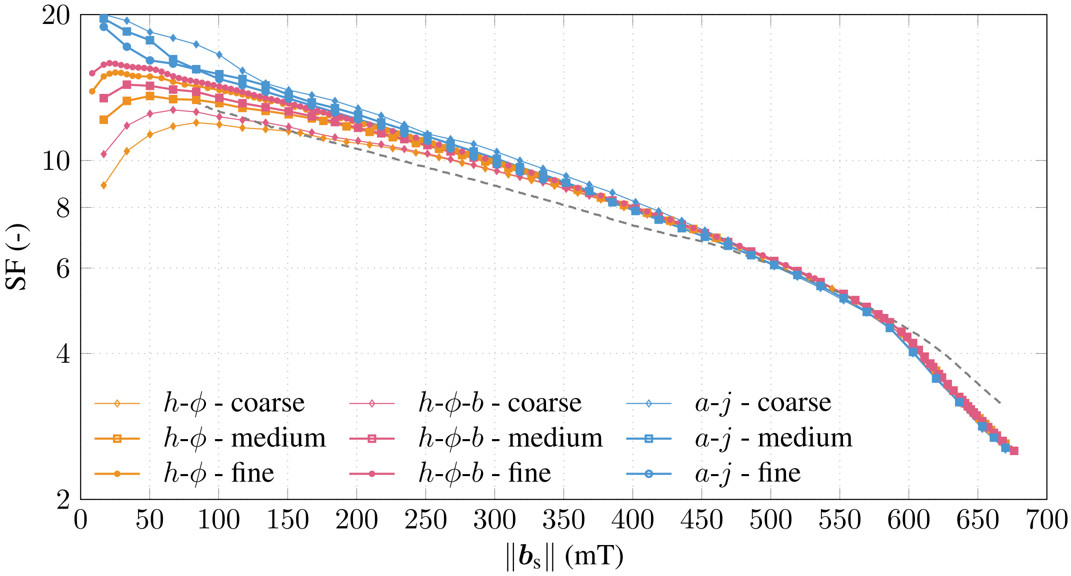

Figure 5.27: Shielding factors of sample B from the h-ϕ, h-ϕ-b, and a-j-formulations on the homogeneous model in the axial configuration, for three different discretization levels ($\alpha = 4$, 2, and 1). The dashed gray curve corresponds to the experimental measurements.

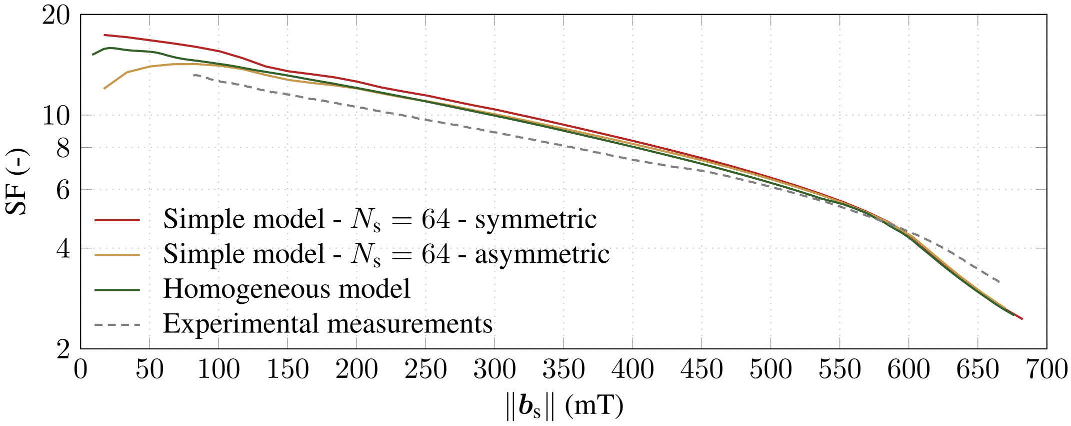

Figure 5.28: Shielding factors of sample B from the h-ϕ-formulation on the simple and homogeneous models in the axial configuration on a fine mesh ($\alpha = 1$). The dashed gray curve corresponds to the experimental measurements.

freedom (DOFs) is therefore affected. In particular, with the h-ϕ and h-ϕ-b-formulations, edge functions are used in the whole homogeneous material, instead of in the HTS layers only; and with the a-j-formulation, DOFs for the auxiliary $\boldsymbol{j}$ field are associated with every node in the hybrid material, compared to those in the HTS layers only in the simple model. The anisotropy of material parameters is also expected to have an influence on the convergence of the iterative techniques. Furthermore, the implicit equation included in the material parameter law introduces an additional cost compared to the explicit material law in the simple model. For all these reasons, it is difficult to know a priori which of the two models, simple or homogeneous, will be the most efficient. We compare the performance figures of the different approaches in Table 5.2, for the fine mesh resolution.

A Newton-Raphson method is used in all cases, except for the magnetic nonlinearity in the

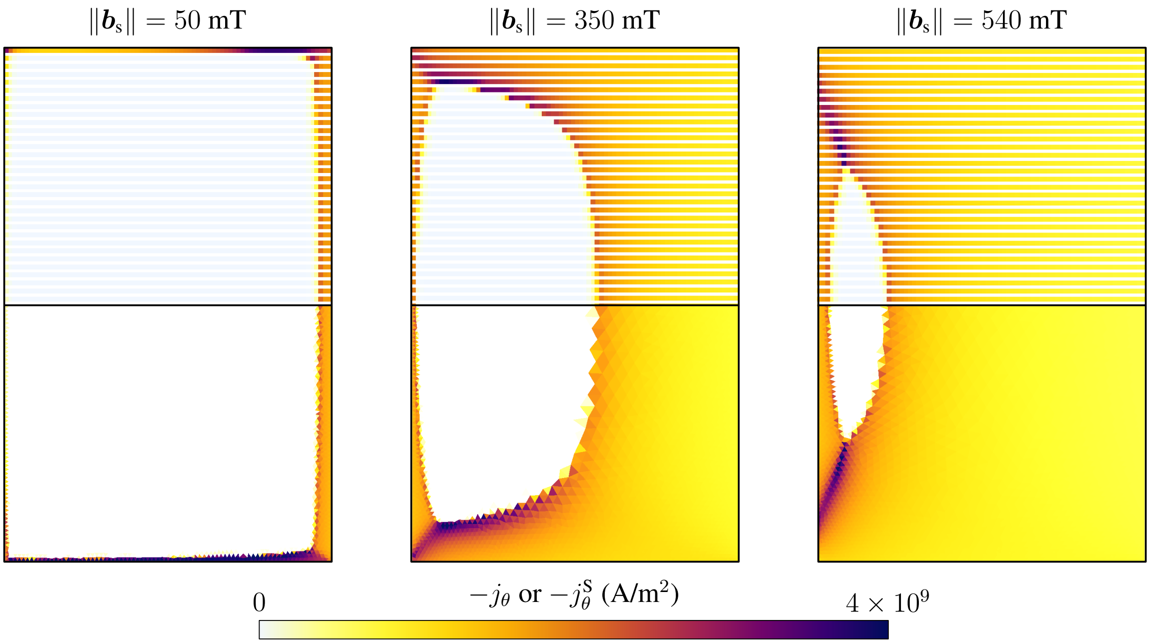

Figure 5.29: Comparison of the azimuthal current density obtained with the simple and homogeneous models in the axial configuration, with the fine mesh resolution ($\alpha = 1$) for three values of the applied field. (Up) Simple model with $N_\text{s} = 64$ and the h-ϕ-formulation. The HTS layer have been thickened in the representation for clarity purposes. (Down) Homogeneous model with the h-ϕ-b-formulation.

h-ϕ-formulation, for which a hybrid method is the only choice that offers satisfying results among the possibilities presented in Chapter 2. In the hybrid method, we switch from Picard to Newton-Raphson after $i_\text{switch} = 10$ iterations. No iteration cycle has been observed with this choice.

During the resolution, some time steps have to be temporarily reduced due to divergent iterates, especially at the end of the simulation. This is handled by the adaptive time-stepping procedure. We also observed that the field-dependent critical current density and the treatment of the saturation law obtained from experimental measurements were particularly demanding in terms of number of iterations. As observed in the previous chapter, reducing the time step is an easy solution for improving the situation.

Table 5.2 shows that the a-j-formulation is the most efficient formulation in terms of computational time. For $N_\text{s} = 64$, note that it only converges for the finer mesh level. The default linear solver from MUMPS [201] fails to solve the linear systems when using coarser meshes. The a-j-formulation involves a limited number of DOFs compared to the h-ϕ-b-formulation, and almost always converges with the maximum prescribed time step. By contrast, the h-ϕ and h-ϕ-b-formulations require smaller and smaller time steps for increasing values of N_s in the simple model, and are even more restrictive with the homogeneous model.

The increased number of DOFs in the h-ϕ-b-formulation compared to the h-ϕ-formulation induces an extra CPU time per iteration, that is not compensated by the decreased number of iterations obtained by the mixed formulation. In this situation, the permeability law is efficiently treated by the hybrid iterative technique and moving to the mixed h-ϕ-b-formulation for involving the reluctivity is not worth it.

Model	Formul.	# DOFs	# iterations (# t.s.)	Time/it.	Time/it./DOF	Total time
Simple $N_\mathrm{s} = 8$	h-ϕ	41 351	1 247 (45)	1.9 s	45.8 µs	39 m
	h-ϕ-b	74 172	1 057 (40)	2.5 s	30.4 µs	44 m
	a-j	41 801	1 214 (40)	1.7 s	41.8 µs	35 m
Simple $N_\mathrm{s} = 16$	h-ϕ	44 516	1 538 (57)	2.0 s	45.4 µs	51 m
	h-ϕ-b	78 298	1 100 (42)	2.7 s	30.6 µs	49 m
	a-j	45 622	1 233 (40)	1.9 s	41.0 µs	38 m
Simple $N_\mathrm{s} = 32$	h-ϕ	51 261	1 599 (64)	2.5 s	46.9 µs	1 h 05 m
	h-ϕ-b	85 237	1 431 (57)	3.0 s	35.8 µs	1 h 12 m
	a-j	53 679	1 361 (43)	2.3 s	42.2 µs	51 m
Simple $N_\mathrm{s} = 64$	h-ϕ	55 925	2 536 (112)	2.6 s	47.1 µs	1 h 51 m
	h-ϕ-b	92 290	2 491 (106)	3.4 s	37.1 µs	2 h 22 m
	a-j	60 967	Not converged	/	/	/
	a-j (finer)	192 916	2 419 (54)	8.9 s	46.2 µs	6 h 59 m
Homogeneous	h-ϕ	49 068	2 522 (95)	2.4 s	49.7 µs	1 h 42 m
	h-ϕ-b	62 807	1 828 (124)	2.7 s	43.6 µs	2 h 09 m
	a-j	44 498	1 176 (40)	2.5 s	55.8 µs	48 m

Table 5.2: Comparison of the performance figures obtained with the different approaches and formulations, on the fine mesh resolution ($\alpha = 1$), except for the a-j-formulation with $N_\mathrm{s} = 64$, for which $\alpha = 0.5$. Simulation up to $\|\boldsymbol{b}_\mathrm{s}\| = 670$ mT in the axial configuration, with a minimum of 40 time steps. The actual number of time steps resulting from the adaptive time-stepping procedure is given within parenthesis in the table. The CPU times are for a single AMD EPYC Rome CPU at 2.9 GHz.

For the medium and coarse space discretization levels, the general observations on the simple model are similar to the ones presented in Table 5.2, except for the a-j-formulation, that faces solving difficulties for $N_\mathrm{s} = 8$ and 16 tapes, similar to the ones observed with $N_\mathrm{s} = 64$ and the fine mesh. For the homogeneous model, the a-j-formulation is still the most efficient formulation with coarse and medium meshes, but the difference with the other two formulations is less marked.

The performance figures are seen to be very sensitive to numerical parameters. For example, as was shown in Chapter 4, the choice of the first iterate has a significant influence on the overall efficiency. Here, a first-order extrapolation of the last two solutions was found to be the most efficient option. The numerical parameters involved in the adaptive time-stepping algorithm also have a strong influence on the overall efficiency.

Both in terms of accuracy and efficiency, none of the two models, simple or homogeneous, significantly outperforms the other in the axial configuration. The computational cost associated with the implicit equation resolution in the homogeneous model only accounts for approximately 6% of the total cost of the simulation, and does not disqualify the approach. Depending on the finite element software, one of the two models may be easier to implement, and this could be the criterion for choosing one approach or the other.

Note that variations of the proposed models could be investigated, as well as other methods and formulations. For example, the layers (and mesh size) in the simple model could be coarsened in the center of the stack. Other existing methods such as the homogeneous t-a-formulation [52] or thin-shell h-ϕ-formulation [119] are relevant possibilities to consider.

5.2.5 Model comparison in transverse field (3D)

We now consider the different approaches applied on the 3D model reproducing the experimental transverse configuration for sample B at 77 K, for an applied field up to 60 mT. We consider the same three formulations as in the axial configuration: the h-ϕ, h-ϕ-b, and a-j-formulations. For the h-ϕ-b-formulation, we take $\boldsymbol{b} \in \mathcal{B}^{\delta,1}(\Omega_\text{m})$, as defined in Eq. (3.47).

We consider a structured mesh in the stack of tapes, and an unstructured mesh outside of it. We define three discretization levels: coarse, medium, and fine, associated with a multiplier α equal to 4, 2, and 1, respectively. The characteristic mesh size is fixed to 0.7α mm in the vicinity of the center O and to 10α mm on the outer surface Γ_out. The characteristic length of elements in the stack of tapes along the x and y-directions is around 0.7α mm. For the simple model, a single layer of tetrahedral elements is considered for the HTS part of each tape, and a number of $32/N_\text{s} \times 4/\alpha$ tetrahedral layers are considered for the SFM part of each tape. For the homogeneous model, $88/\alpha$ layers of hexahedral elements are generated over the whole height H_B of the sample, which corresponds to thicker elements than for the simple model. Even with such a coarsening, we will see that the homogeneous model is already computationally demanding. The coarse meshes for both models are represented in Fig. 5.30, only one-eighth of the full problem is represented.

We model the magnetic response of the system from $t = 0$ to $t = 80$ s, with a minimum of 40 time steps. An adaptive time-stepping procedure is used as for the 2D model in the axial configuration, with identical numerical parameters.

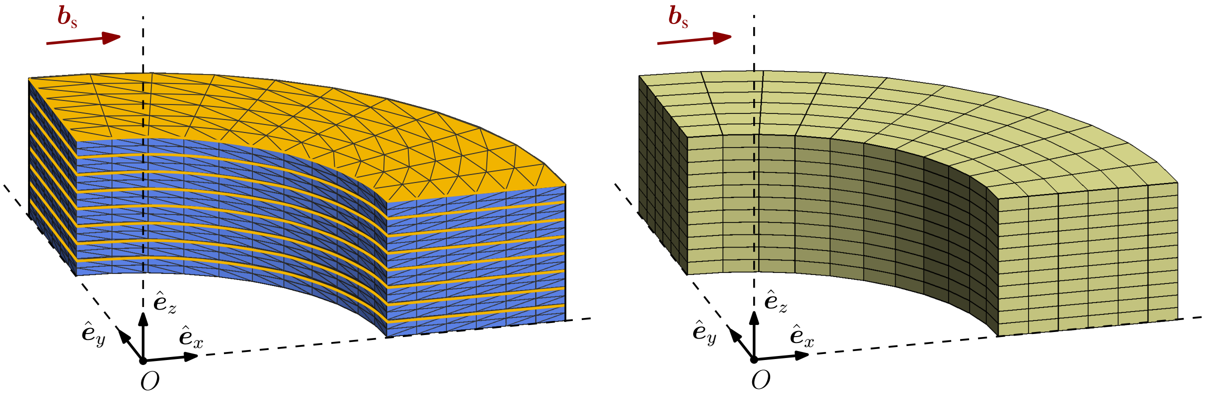

(a) Simple model. (b) Homogeneous model.

Figure 5.30: Coarse meshes ($\alpha = 4$) in the stack of tapes for the simple and homogeneous models in the transverse configuration for sample B. One-eighth of the full stack is represented. (a) Simple model with $N_\text{s} = 16$, symmetric model. (b) Homogeneous model with hexahedra in the stack of tapes.

Influence of the space discretization in the simple model

We first estimate the mesh influence on the numerical solution. We fix the number of tapes to $N_\text{s} = 16$. The SF values obtained with the three discretization levels and the three formulations are presented in Fig. 5.31. Note that the a-j-formulation with the fine level did not converge in a reasonable amount of time: it was stopped after 30 hours of computation, after reaching an applied field of $\|\boldsymbol{b}_\mathrm{s}\| = 7.5$ mT only.

The solutions approach each other, but convergence is not yet achieved with the fine mesh, as is suggested by the difference between the successive curves for $\alpha = 2$ and $\alpha = 1$. The fine simulations are however already very expensive in terms of computational resources. In this case, as will be discussed later, the h-ϕ-formulation is the fastest choice, with an associated CPU time of more than 7 hours for $\alpha = 1$. The SF is however a local indicator, and it is sensitive to the solution accuracy. As illustrated in Fig. 5.32, a small difference in absolute value results in a large relative difference close to the center O.

This observation highlights the difficulty of evaluating accurately the shielding effectiveness, especially in 3D. The geometry is non-trivial and the material response is highly nonlinear.

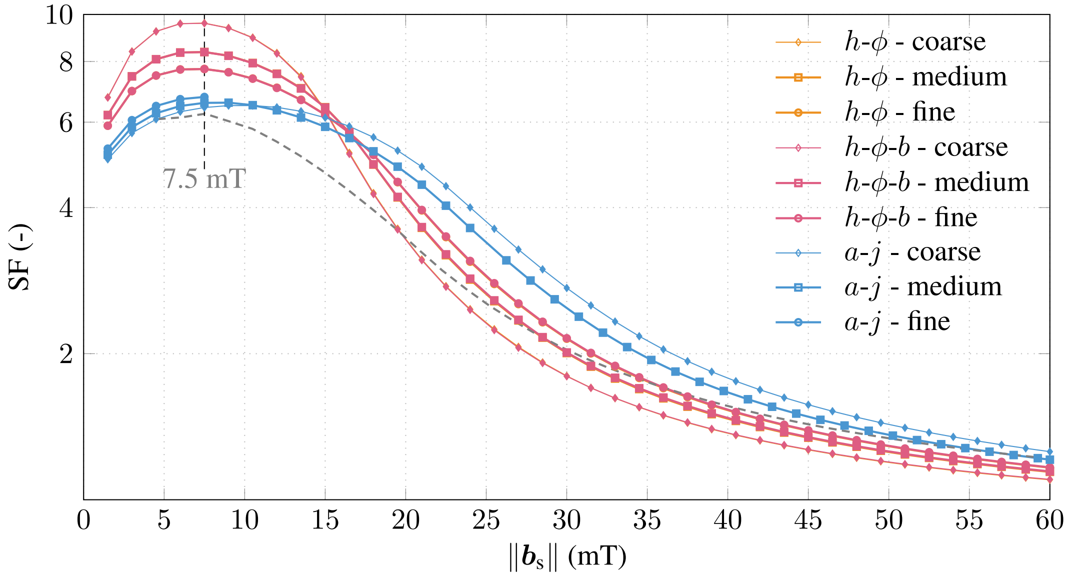

Figure 5.31: Shielding factors of sample B from the h-ϕ, h-ϕ-b, and a-j-formulations on the simple model ($N_\mathrm{s} = 16$) in the transverse configuration, for three discretization levels ($\alpha = 4$,2, and 1). Curves for the h-ϕ and h-ϕ-b-formulations are visually indistinguishable. The fine curve for the a-j-formulation stops at 7.5 mT, after 30 hours of CPU time. The dashed black line at that field value is related to what is plotted in Fig. 5.32. The dashed gray curve corresponds to the experimental measurements.

Influence of the ending tape in the simple model

As for the axial configuration, we assess the influence of the number of tapes N_s on SF values. In addition to the asymmetric model pictured in Fig. 5.21(b), we consider the symmetric variation in which the tapes are stacked upside-down for $z < 0$. Results on a fine mesh are presented in Fig. 5.26 for N_s equal to 8, 16, and 32.

Compared to the axial configuration, the influence of N_s is very limited. In this case, it is smaller than the difference between the formulations observed in Fig. 5.31. Physically, in the transverse configuration, most of the shielding is achieved by the high permeability of the SFM, and the field lines are mostly parallel to the SFM layers. Changing the value of N_s does not

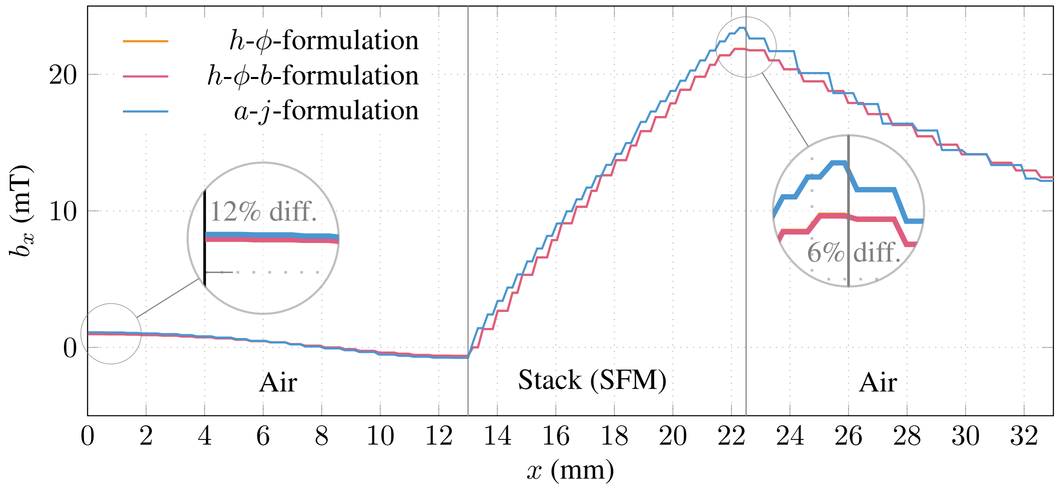

Figure 5.32: Distribution of the x-component of the magnetic flux density along the x-axis (see Fig. 5.30) for sample B in the transverse configuration in the simple model ($N_\mathrm{s} = 16$) with three formulations and the fine mesh resolution ($\alpha = 1$), for an applied field $\|\boldsymbol{b}_\mathrm{s}\| = 7.5$ mT, as indicated in Fig. 5.31. The curves for the h-ϕ and h-ϕ-b-formulations are visually indistinguishable. The percentages inside the highlighted circles correspond to the relative difference between the local values from the h-ϕ and a-j-formulations.

qualitatively change the SFM height seen by the horizontal field lines. Starting the stack with either a SFM or a HTS layer either attracts or repels the field lines nearby, but this is observed to only slightly influence the SF value.

In the following, we consider the symmetric version of the stack, because it allows to model only one-half of its height, which is also the case for the homogeneous model that is symmetric by construction. We also choose $N_\mathrm{s} = 16$.

Comparison with the homogeneous model

We now compare the solutions with the homogeneous model. Simulations are much slower than with the simple model: not all tests converge in a reasonable amount of time. We will discuss the numerical performance after comparing the results.

The SF values obtained with the different cases are presented in Fig. 5.34, together with two curves from the simple model for comparison. The magnetic flux density distributions and relative permeability maps are compared in Figs. 5.35 and 5.36. Even though local differences may be significant, e.g., on the top of the stack of tapes for the relative permeability, the homogeneous model correctly reproduces the results of the simple model. The current density distributions (not represented in the figures) are also comparable.

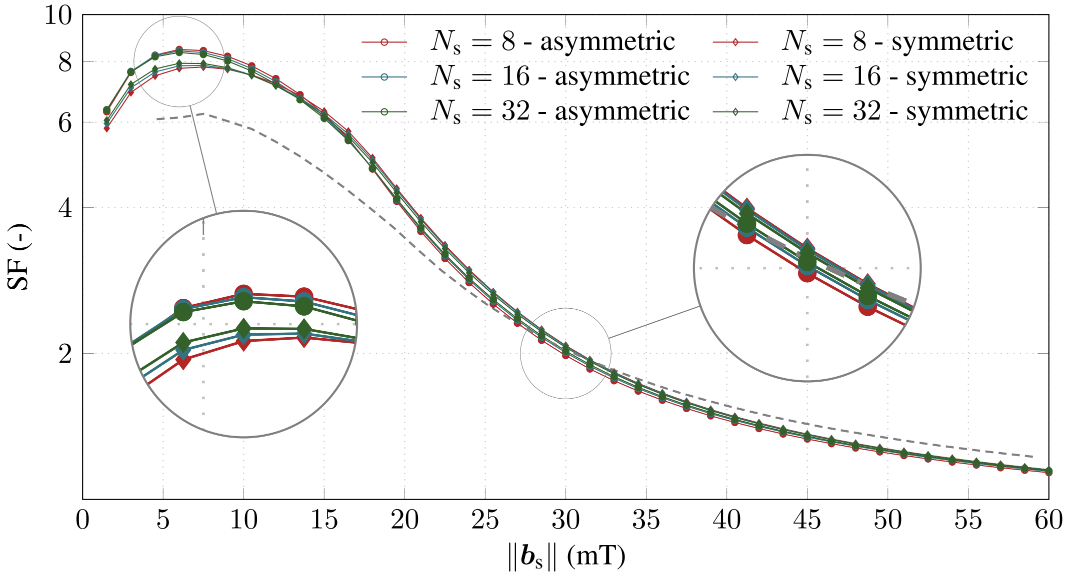

Figure 5.33: Influence of the number of tapes N_s in the simple model on the shielding factor of sample B in the transverse configuration. Results are obtained on a fine mesh ($\alpha = 1$) with the h-ϕ-formulation. The asymmetric case is what is represented in Fig. 5.21, whereas in the symmetric case the tapes are stacked upside-down for $z < 0$. The dashed gray curve corresponds to the experimental measurements.

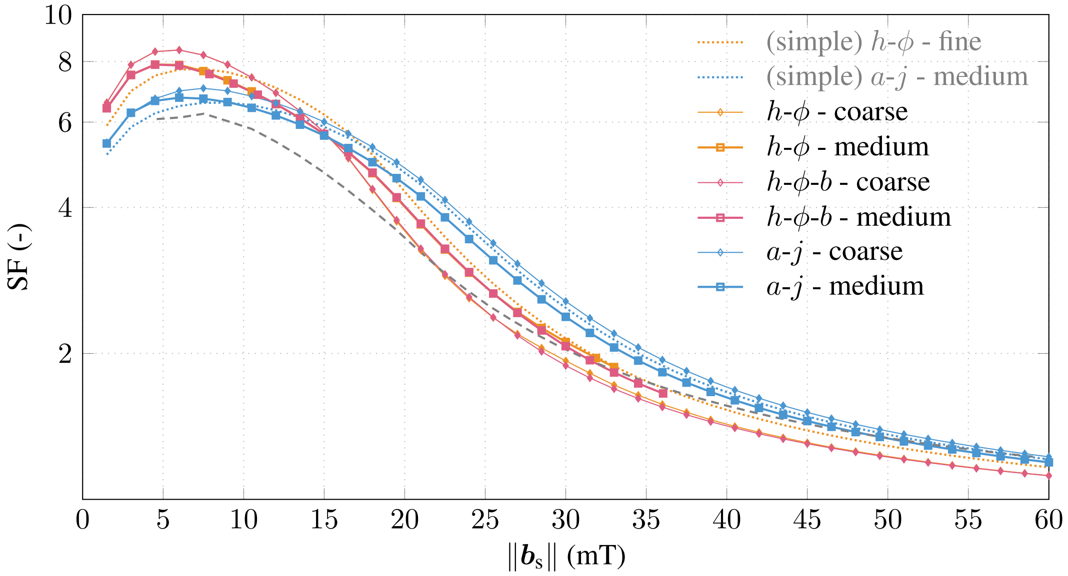

Figure 5.34: Shielding factors of sample B from the h-ϕ, h-ϕ-b, and a-j-formulations on the homogeneous model in the transverse configuration, for different discretization levels. The dotted curves are given for comparison with the simple model. The dashed gray curve corresponds to the experimental measurements.

Comments on the numerical efficiency

Both models give results of comparable accuracy, but the associated computational work is not the same. Even more than in the axial configuration, significant differences in efficiency are observed. A Newton-Raphson method is used in all cases, except for the magnetic nonlinearity

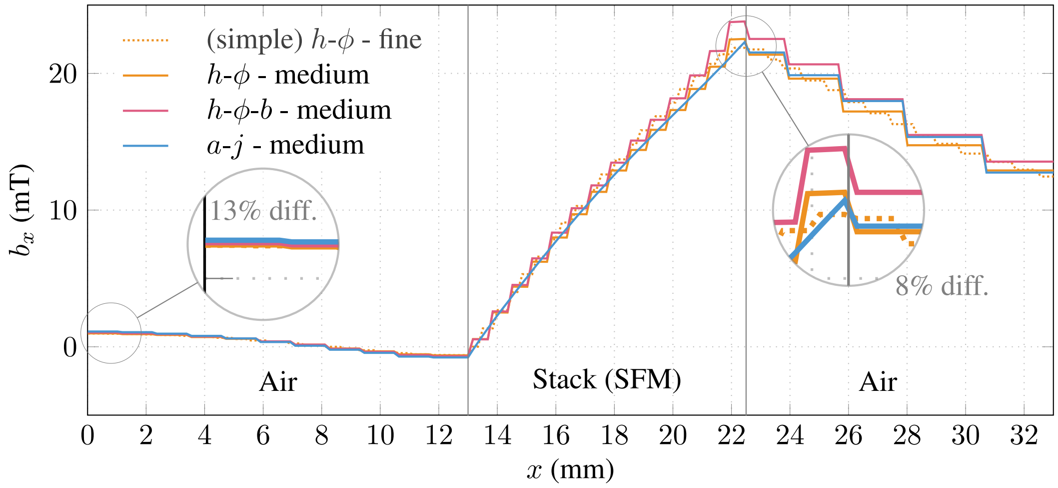

Figure 5.35: Distribution of the x-component of the magnetic flux density along the x-axis (see Fig. 5.30) for sample B in the transverse configuration in the homogeneous model with three formulations and the medium mesh resolution ($\alpha = 2$), for an applied field $\|\boldsymbol{b}_\text{s}\| = 7.5$ mT. The result of the simple model with the h-ϕ-formulation and $\alpha = 1$ is given for comparison. The percentages associated with the highlighted circles correspond to the largest local relative difference between the values from the simple and homogeneous models.

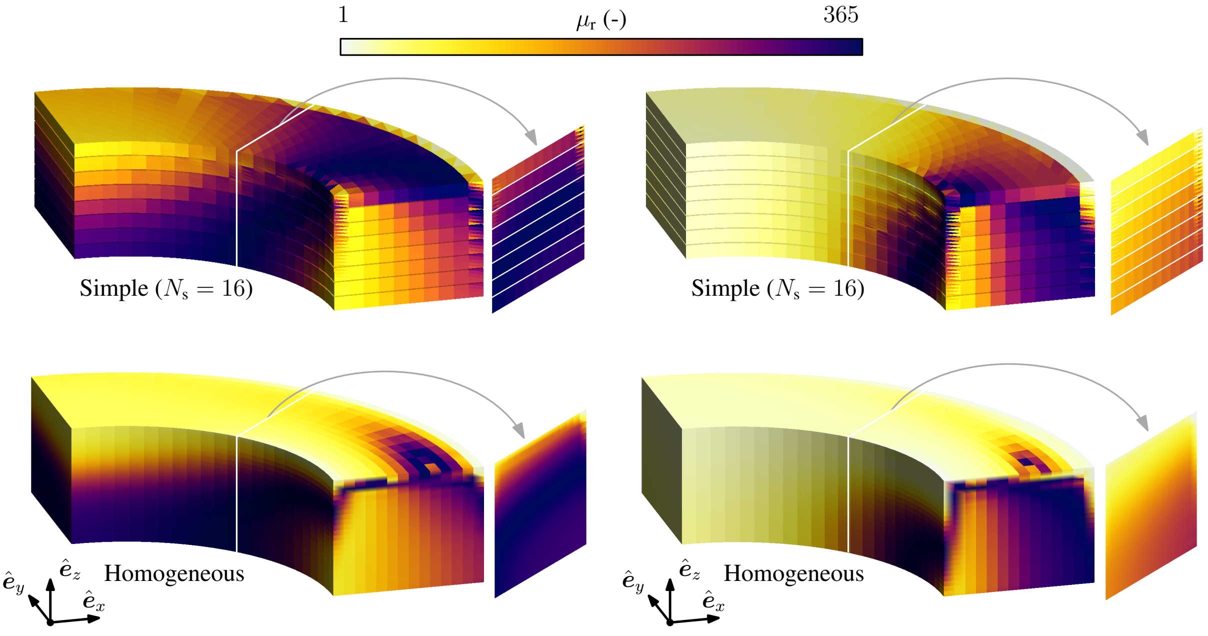

(a) $\|\boldsymbol{b}_\text{s}\| = 12$ mT.

(b) $\|\boldsymbol{b}_\text{s}\| = 24$ mT.

Figure 5.36: Comparison of the relative permeability obtained with the simple and homogeneous models in the transverse configuration and the h-ϕ-formulation, with the medium mesh resolution ($\alpha = 2$) for two values of applied field: (a) 12 mT, and (b) 24 mT. The solution in the plane $x = y$ is also represented, and indicated by the gray arrows. (Up) Simple model with $N_\text{s} = 16$. (Down) Homogeneous model, the represented permeability is the scalar value $\mu_\text{r}(\boldsymbol{h}^\text{F})$.

in the h-ϕ-formulation, for which a hybrid method with $i_\text{switch} = 10$ is considered. Performance figures are gathered in Table 5.3, with simulation times for a single AMD EPYC Rome CPU at

2.9 GHz.

For the simple model, the h-ϕ-b-formulation converges in a smaller number of iterations than the h-ϕ-formulation. This is directly related to the fact that the reluctivity is more efficiently handled than the permeability. However, the number of degrees of freedom (DOFs) involved with the h-ϕ-b-formulation is much higher. As a consequence, with the default direct sparse solver from MUMPS [201], the CPU time associated with the h-ϕ-b-formulation becomes higher for the fine mesh resolution.

Model	Formul.	# DOFs	# it. (# t.s.)	Time/it.	Time/it./DOF	Total time
Simple - Coarse	h-ϕ	3 579	413 (40)	0.5 s	153 μs	3 m 46
	h-ϕ-b	10 419	165 (40)	1.0 s	91 μs	1 m 37
	a-j	18 224	172 (40)	1.3 s	73 μs	3 m 50
Simple - Medium	h-ϕ	23 511	471 (40)	4.6 s	195 μs	35 m 50
	h-ϕ-b	84 015	222 (40)	9.4 s	111 μs	34 m 40
	a-j	120 716	765 (43)	18.0 s	149 μs	3 h 49 m
Simple - Fine	h-ϕ	151 676	524 (40)	50.8 s	335 μs	7 h 23 m
	h-ϕ-b	631 204	278 (40)	178.2 s	282 μs	13 h 46 m
	a-j	823 073	120 (6)	900.0 s	1 093 μs	>30 h (7.5 mT)
Homog. - Coarse	h-ϕ	3 406	560 (40)	0.5 s	153 μs	4 m 57
	h-ϕ-b	6 118	295 (40)	0.9 s	142 μs	4 m 17
	a-j	11 960	196 (40)	1.0 s	84 μs	3 m 36
Homog. - Medium	h-ϕ	28 636	3 383 (38)	6.3 s	219 μs	> 6 h (33 mT)
	h-ϕ-b	53 260	4 822 (252)	35.8 s	672 μs	>48 h (36 mT)
	a-j	84 938	307 (40)	41.2 s	485 μs	3 h 31 m

Table 5.3: Comparison of the performance figures obtained with the different approaches and formulations. Simulation up to $\|\boldsymbol{b}_\text{s}\| = 60$ mT in the transverse configuration, with a minimum of 40 time steps. The actual number of time steps resulting from the adaptive time-stepping procedure is given within parenthesis in the fourth column of the table. Gray values are associated with simulations that did not end properly: either because of exceedingly slow convergence (a-j and h-ϕ-b), or because of iteration cycles (h-ϕ). The field values within parenthesis in the last column indicates where the simulation was stopped, if it was not at 60 mT. The CPU times are for a single AMD EPYC Rome CPU at 2.9 GHz.

For the simple model, the performance of the a-j-formulation deteriorates with mesh refinement. The number of DOFs is higher than for the other formulations in this 3D problem, and the number of iterations significantly increases from the coarse to medium discretization levels. At the fine level, for $\alpha = 1$, we decided to stop the simulation after 30 hours of CPU time, when the simulation only reaches a field of 7.5 mT, as depicted in Fig. 5.31. This is almost five times the total duration of the h-ϕ-formulation for the complete simulation on the same mesh.

For the homogeneous model, mixed formulations perform better than the h-ϕ-formulation at the coarse discretization level, thanks to the significant gain in number of iterations obtained by handling the reluctivity instead of the permeability.

At the medium discretization level, the a-j-formulation is the only formulation that converges with only 40 time steps. By contrast, the h-ϕ-formulation enters iteration cycles at an applied field of 33 mT: the hybrid iterative technique with $i_\text{switch} = 10$ is not robust enough. Reducing the time step with the adaptive procedure does not help to avoid these cycles in this case and convergence fails. Note that below 33 mT, no cycle is encountered, but the time step still has to be temporarily reduced due to divergent iterates, several times during the simulation.

For the h-ϕ-b-formulation and $\alpha = 2$, the simulation does not end within 48 hours of CPU time, at which point the simulation only reaches an applied field of 36 mT, whereas for the simple model at a comparable discretization level, the complete simulation is achieved after less than an hour. Contrary to the situation with the h-ϕ-formulation, no iteration cycle is observed, but very small time steps are necessary to avoid divergence of the Newton-Raphson iterations. The combination of anisotropic materials properties with strongly nonlinear constitutive laws, in a hybrid magnetic-conducting region together with a mixed formulation makes the problem non-trivial, and might explain the small time step requirement.

For the fine discretization level on the homogeneous model (not represented in the table), the h-ϕ and h-ϕ-b-formulations face the same difficulties as in the medium level, and the a-j-formulation becomes extremely slow, as is the case in the simple model at the fine level.

The performance figures in Table 5.3 lead to the conclusion that the simple model should be preferred to the proposed implementations of the homogeneous model. The computational cost of the latter model rapidly increases with mesh refinement and convergence difficulties are encountered with the h-ϕ and h-ϕ-b-formulations, whereas in the simple model, these two formulations lead to robust and more efficient resolutions.

5.2.6 Summary

The numerical performance analysis for the axial (2D-axi) and the transverse (3D) configuration do not lead to the same conclusions. In the axial case, the simple and homogeneous models lead to comparable performance. Among the tested formulations, the a-j-formulation is the most efficient. It is the formulation we would recommend in this configuration.

In the transverse case, the homogeneous model is observed to be particularly slow compared to the simple model. The h-ϕ-formulation faces iteration cycles that are not easy to avoid, and the h-ϕ-b-formulation requires very small time steps to converge with the tested implementation. On the contrary, the simple model is observed to produce efficient resolutions, with the h-ϕ-b-formulation for coarse discretization levels, and with the h-ϕ-formulation for finer ones. The a-j-formulation does not compete with the other formulations, it leads to significantly slower resolutions, which matches with the conclusions obtained in Section 4.5 with the 3D magnet motor pole problem.

Conclusions

In this thesis, we studied different finite element formulations applied to systems containing nonlinear materials such as type-II superconductors or ferromagnetic materials, or combinations of them. We observed that they may perform very differently. Thus, implementing robust and efficient numerical models for problems involving these materials requires carefully designed formulations. The main objective of this dissertation was to contribute to the development of such formulations.

We first presented the standard h-ϕ and a-formulations. A key difference between these two formulations is that the power law and saturation law, i.e., the electric and magnetic nonlinear laws respectively associated with type-II superconductors and ferromagnetic materials, are involved in inverse manners. In the light of fixed point theory, we proposed a qualitative and quantitative analysis of the treatment of these nonlinearities by different linearization techniques. As a general conclusion, among the tested methods, the most efficient and robust resolutions were shown to be obtained when the power law is written in terms of the resistivity and when the saturation law is written in terms of the reluctivity, i.e., the inverse of the permeability.

These results, combined with the fact that neither of the standard formulations involves both nonlinearities in their optimal form, is a motivation for looking for alternative formulations. We proposed and gathered from the literature four mixed formulations that directly involve the resistivity and the reluctivity: the h-ϕ-a (or h-a), t-a, h-ϕ-b, and a-j-formulations. Each of these mixed formulations is written in terms of two main unknown fields and takes the form of a perturbed saddle-point problem. Hence, the function spaces associated with the unknown fields need to satisfy particular stability conditions, including the so-called inf-sup condition, in order to avoid mathematical instabilities that may manifest themselves as spurious oscillations in the numerical solution. We conducted inf-sup tests to assess the validity of different choices of function spaces in the discrete setting. For the surface-coupled h-ϕ-a and t-a-formulations, stability can be achieved via a local enrichment of the function space of one of the two fields on the coupling surface, with respect to the lowest-order function spaces. For the volume-coupled h-ϕ-b and a-j-formulations, lowest-order function spaces for both fields were shown to provide stable numerical problems.

After the presentation of the six finite element formulations and the discussion of their spatial discretization, we compared their numerical performance levels by applying them on a collection of relatively simple problems involving type-II superconductors, with geometries ranging from 1D to 3D, possibly coupled with ferromagnetic materials. We highlighted significant differences in terms of numerical efficiency between the formulations. However, we showed that none of the six formulations outperforms all the other ones in all situations: the best formulation is problem-dependent. In particular, the a-j-formulation demonstrates good performances on 2D problems but it is usually less efficient than the h-ϕ or h-ϕ-a-formulation on 3D problems.

We finally applied the formulations on two distinct applications exhibiting non-trivial geometries. The first application consisted in the computation of AC losses in cables made up of twisted superconducting filaments. Tackling directly the associated 3D problem is computationally expensive, but when the cables present a helicoidal symmetry, the problem dimension can be reduced from 3D to 2D via an adequate change of variables, which drastically reduces the computational work for a given simulation. We presented this approach and applied it on a superconducting cable. We also extended the method to problems with non-helicoidally symmetric boundary conditions. We only applied this extension to linear materials.

The second and last application on a more complex geometry was the evaluation of the shielding effectiveness of magnetic shields made up of a stack of a large number of superconducting tape annuli. Two simplified approaches were proposed for modeling the resulting layered superconducting-ferromagnetic hybrid structure, in axial (2D) and transverse (3D) configurations: (i) representing the structure with a limited number of tapes with an increased thickness, and (ii) replacing the whole structure by a fictitious anisotropic hybrid material. Both were successfully validated against experimental measurements.

Perspectives

As listed below, the results presented in this dissertation have led to specific questions that can be investigated in future works. The first question concerns the stability of mixed formulations for 3D problems. In this work, the stability analysis was formally conducted on 2D problems only. In practice, the conclusions were observed to be valid for 3D problems as well, but extensions of the stability analysis to these problems, including the analysis of various types of elements such as prisms, pyramids, or hexahedra, would strengthen the observations. Additionally, an interesting study would be to compare our stability results to well-studied stable dual bases of elements such as Buffa-Christiansen elements [251].

The next question is related to the discretization of the t-a-formulation. Using lowest-order function spaces for $\boldsymbol{t}$ and $\boldsymbol{a}$ results in spurious oscillations in the numerical solution, and numerical inf-sup tests indicate that enriching one of the two function spaces may lead to a stable discrete formulation. Indeed, enriching the function space for $\boldsymbol{a}$ produces stable results, free of spurious oscillations, for both linear and nonlinear materials. However, with an enrichment of the function space for $\boldsymbol{t}$, convergence issues are observed with nonlinear materials, the Newton-Raphson algorithm always diverges, whereas the situation with linear materials does not present complications. A deeper look into the associated matrix structure might provide a better understanding of these observations.

The third unanswered question relates to the failure of the tested linear solvers on the volume-coupled a-j-formulation, in the case where it is coupled with global conditions on voltage or current. The a-j-formulation was shown to offer very efficient resolutions for 2D problems with type-II superconductors, irrespective of whether they contain ferromagnetic materials or not, but the difficulties linear solvers encounter currently prevent us to fully exploit this formulation. Investigating alternative choices for imposing the global conditions such as voltage distribution functions [138] may possibly help to circumvent the issue.

The different formulations and models presented in this work also open the way to several possibilities of extensions. First, the mode decomposition approach for helicoidally symmetric geometries with non-symmetric boundary conditions was only applied to linear materials. A natural extension consists in implementing the method for nonlinear materials, by considering a small number of modes, directly coupled via the weak formulation.

Next, in addition to the simple and fully homogeneous models, other approaches could be considered for the stacked-tape magnetic shields. The thin-shell h-ϕ-formulation accounting for permeability jumps [51], or alternative homogeneous models based on the t-a-formulation [252] are interesting starting points for other approaches.

Also, the focus in this thesis was to compare the relative performance of different formulations within the same finite element framework. Therefore, optimizing the implementation to improve their absolute performance has not been the priority. Considering high-performance computing, e.g., by including state-of-the-art parallelization techniques for the assembly and post-processing steps or by investigating preconditioning methods for the resolution step, may strongly improve the performance of the current implementation.

Finally, as all the models presented in this work were purely magnetic, a relevant next step is to consider a coupling with thermal equations, e.g., in order to describe multiphysics phenomena like quenches. The progressive approach we followed in this dissertation for designing mixed formulations, starting by a detailed analysis of the separate nonlinear laws, could be applied to the large number of nonlinear parameters appearing in magneto-thermal equations, and help to handle them.

Appendix A

Mathematical framework

A.1 Elements of algebraic topology and function spaces

We introduce below a few basic elements of algrebraic topology, directly applied in the context of our problem. Most elements are adapted from [253]. The section below is not meant to be a complete introduction to chains and cochains, it is just a collection of several definitions, results and interpretations, that we considered to be useful in the context of this work.

A.1.1 Chains and homology

In a 3-dimensional region Ω, we define as $C_p(\Omega)$ the vector space of all p-dimensional objects over which a p-fold integration[1] can be performed [253]. Elements of $C_p(\Omega)$ are called p-chains. For example, a point is a 0-chain, an oriented curve is a 1-chain, an oriented surface is a 2-chain, and a volume is a 3-chain. The addition of two p-chains and the multiplication of p-chain by a real number are two operations defined on elements of the vector space $C_p(\Omega)$.

We also introduce the boundary operators ∂_p, defined as

$$\partial_p \ : \ C_p(\Omega) \rightarrow C_{p-1}(\Omega), \quad p = 1, 2, 3, \tag{A.1}$$

with the classical conventions for orientation. We have

$$(\partial_1 \partial_2)s = 0, \quad \forall s \in C_2(\Omega) \qquad \text{and} \qquad (\partial_2 \partial_3)v = 0, \quad \forall v \in C_3(\Omega), \tag{A.2}$$

so that the spaces $C_0(\Omega)$, $C_1(\Omega)$, $C_2(\Omega)$, and $C_3(\Omega)$ form a complex:

$$C_0(\Omega) \xleftarrow{\partial_1} C_1(\Omega) \xleftarrow{\partial_2} C_2(\Omega) \xleftarrow{\partial_3} C_3(\Omega). \tag{A.3}$$

It is called a complex because the composition of any two successive morphisms (boundary operators) vanishes, i.e., the image of one morphism is contained inside the kernel of the next

---

[1] A 0-fold integration has to be understood as the sum of the values of a function at a finite set of points [253].

one. We say that a complex is *exact* if the image of one morphism is *equal to* (and not only contained in) the kernel of the next morphism in the sequence [51].

In general, the complex (A.3) is not exact. There might exist 1-chains in Ω with a zero boundary, e.g., closed curves, that are not boundaries of a 2-chain in Ω, e.g, a surface. This is the case when the domain Ω is not simply connected. Consider the curve c in Fig. A.1 for the domain $\Omega_\mathrm{c}^\mathrm{C}$. Also, there might exist 2-chains in Ω with a zero boundary, e.g., closed surfaces, that are not boundaries of a 3-chain in Ω, e.g., a volume. This is the case when the domain Ω has cavities in it. The first and second homology spaces, that we define below, give measures of the extent by which the complex fails to be exact [253].

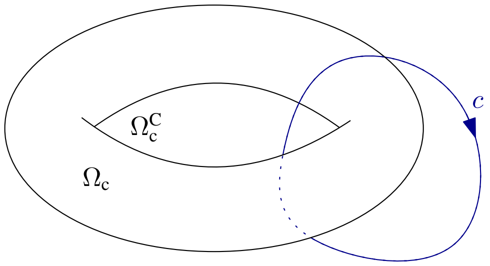

Figure A.1: Torus Ω_c and its complementary domain $\Omega_\mathrm{c}^\mathrm{C}$. The closed curve c is an example of 1-chain that belongs to $\mathcal{NS}(\partial_1, \Omega_\mathrm{c}^\mathrm{C})$ but not to $\mathcal{R}(\partial_2, \Omega_\mathrm{c}^\mathrm{C})$. Indeed, there is no surface *contained in* $\Omega_\mathrm{c}^\mathrm{C}$ whose boundary is c.

The first and second homology spaces are the vector spaces defined as the following quotient spaces:

$$\mathcal{H}_1(\Omega) = \mathcal{NS}(\partial_1, \Omega) \,/\, \mathcal{R}(\partial_2, \Omega), \tag{A.4}$$

$$\mathcal{H}_2(\Omega) = \mathcal{NS}(\partial_2, \Omega) \,/\, \mathcal{R}(\partial_3, \Omega), \tag{A.5}$$

with $\mathcal{NS}(\partial_p, \Omega)$ and $\mathcal{R}(\partial_p, \Omega)$ respectively the kernel and the range of the boundary operator ∂_p applied on elements of $C_p(\Omega)$. That is, $\mathcal{H}_1(\Omega)$ is the set of equivalence classes $[\boldsymbol{c}]$ of 1-chains in $C_1(\Omega)$, where $\boldsymbol{c}_1$ and $\boldsymbol{c}_2$ belong to the same equivalence class if $\boldsymbol{c}_1 - \boldsymbol{c}_2 \in \mathcal{R}(\partial_2, \Omega)$, i.e., if the difference of $\boldsymbol{c}_1$ and $\boldsymbol{c}_2$ is the boundary of a 2-chain in $C_2(\Omega)$, in which case we say that $\boldsymbol{c}_1$ and $\boldsymbol{c}_2$ are homologous. We also define the first Betti number: $\beta_1(\Omega) = \dim(\mathcal{H}_1(\Omega))$.

The first homology space is particularly useful for the h-ϕ-formulation, in the non-conducting domain $\Omega_\mathrm{c}^\mathrm{C}$, where $\beta_1(\Omega_\mathrm{c}^\mathrm{C}) = \dim(\mathcal{H}_1(\Omega_\mathrm{c}^\mathrm{C}))$ is equal to the number of cuts that need to be introduced to define a magnetic scalar potential in $\Omega_\mathrm{c}^\mathrm{C}$ [253].

The second homology space $\mathcal{H}_2(\Omega)$ is not used in this work.

A.1.2 Cochains and cohomology

We define the spaces

$$H^1(\Omega) = \left\{u \in L^2(\Omega) : \textbf{grad}\, u \in \boldsymbol{L}^2(\Omega)\right\}, \tag{A.6}$$

$$H(\textbf{curl}; \Omega) = \left\{\boldsymbol{u} \in \boldsymbol{L}^2(\Omega) : \textbf{curl}\, \boldsymbol{u} \in \boldsymbol{L}^2(\Omega)\right\}, \tag{A.7}$$

$$H(\mathrm{div}; \Omega) = \left\{\boldsymbol{u} \in \boldsymbol{L}^2(\Omega) : \mathrm{div}\, \boldsymbol{u} \in L^2(\Omega)\right\}, \tag{A.8}$$

where the gradient, curl and divergence operator have to be understood in the sense of distribution [141], and where $L^2(\Omega)$, and $\boldsymbol{L}^2(\Omega)$, are the vector spaces of square integrable scalar fields on Ω and vector fields on Ω, respectively[2].

Elements of $H^1(\Omega)$, $H(\mathbf{curl};\Omega)$, $H(\mathrm{div};\Omega)$ and $L^2(\Omega)$ are also called p-cochains, or p-forms, with $p = 0, 1, 2, 3$, respectively, in the sense that they can be considered as integrands of p-fold integrals over p-chains. There is a duality between p-chains and p-cochains under integration.

By construction, and because $\mathbf{curl}\ \mathbf{grad} \cdot = \mathbf{0}$ and $\mathrm{div}\ \mathbf{curl} \cdot = 0$, we have the following inclusions: $\mathbf{grad}\ H^1(\Omega) \subset H(\mathbf{curl};\Omega)$, $\mathbf{curl}\ H(\mathbf{curl};\Omega) \subset H(\mathrm{div};\Omega)$, and $\mathrm{div}\ H(\mathrm{div};\Omega) \subset L^2(\Omega)$. Spaces $H^1(\Omega)$, $H(\mathbf{curl};\Omega)$, $H(\mathrm{div};\Omega)$ and $L^2(\Omega)$ form a complex:

$$H^1(\Omega) \xrightarrow{\mathbf{grad}} H(\mathbf{curl};\Omega) \xrightarrow{\mathbf{curl}} H(\mathrm{div};\Omega) \xrightarrow{\mathrm{div}} L^2(\Omega). \tag{A.9}$$

As mentioned in the previous section, it is called a complex because the composition of any two successive morphisms (differential operators) vanishes, i.e., the image of one morphism is contained inside the kernel of the next morphism. We say that a complex is *exact* if the image of one morphism is *equal to* (and not only contained in) the kernel of the next morphism in the sequence [51].

In general, the complex (A.9) is not exact. That is, there might exist functions in $H(\mathbf{curl};\Omega)$ with a zero curl that are not gradients of functions in $H^1(\Omega)$, and there might exist functions in $H(\mathrm{div};\Omega)$ with a zero divergence that are not curls of functions in $H(\mathbf{curl};\Omega)$.

We denote by $\mathcal{R}(\mathbf{grad},\Omega)$ the range of the gradient operator applied on elements of $H^1(\Omega)$, and by $\mathcal{NS}(\mathbf{curl},\Omega)$ the kernel of the curl operator applied on elements of $H(\mathbf{curl};\Omega)$. The first de Rham cohomology space is the vector space defined as the following quotient space

$$\mathcal{H}^1_{\mathrm{dR}}(\Omega) = \mathcal{NS}(\mathbf{curl},\Omega) \,/\, \mathcal{R}(\mathbf{grad},\Omega), \tag{A.10}$$

that is, the set of equivalence classes $[\boldsymbol{w}]$, where $\boldsymbol{w}_1 \sim \boldsymbol{w}_2$ (we read "$\boldsymbol{w}_1$ is cohomologous to $\boldsymbol{w}_2$") if $\boldsymbol{w}_1 - \boldsymbol{w}_2 \in \mathcal{R}(\mathbf{grad},\Omega)$, i.e., if $\boldsymbol{w}_1 - \boldsymbol{w}_2$ is the gradient of a function in $H^1(\Omega)$. If $\mathcal{NS}(\mathbf{curl},\Omega) = \mathcal{R}(\mathbf{grad},\Omega)$, which is the case when Ω is simply connected, then $\mathcal{H}^1_{\mathrm{dR}}(\Omega) = 0$.

We introduce $\beta^1 = \dim(\mathcal{H}^1_{\mathrm{dR}}(\Omega))$. A cohomology basis of $\mathcal{H}^1_{\mathrm{dR}}(\Omega)$ is made up of β^1 linearly independent equivalence classes of $\mathcal{H}^1_{\mathrm{dR}}(\Omega)$. To generate $\mathcal{NS}(\mathbf{curl},\Omega)$, one has to add to elements of $\mathcal{R}(\mathbf{grad},\Omega)$ one element from each of the β^1 linearly independent equivalence classes of $\mathcal{H}^1_{\mathrm{dR}}(\Omega)$. Note also that $\beta^1 = \beta_1$ [253].

Although it is not used in this work, we also define the second de Rham cohomology space:

$$\mathcal{H}^2_{\mathrm{dR}} = \mathcal{NS}(\mathrm{div},\Omega) \,/\, \mathcal{R}(\mathbf{curl},\Omega). \tag{A.11}$$

---

[2] To avoid confusion, note that $H^1(\Omega)$ refers to the Sobolev space defined in Eq. (A.6), and not to the first cohomology space as the notation with superscript might suggest. In this work, we denote (co)-homology spaces with the round letter $\mathcal{H}$. Note that $\mathcal{H}$ will also refers to the space for the magnetic field $\boldsymbol{h}$ in the finite element formulations. With the context, there should not be any confusion.

A.1.3 Global currents and voltages associated with general geometries

In Section 2.1.3, we have only considered cases in which a single current and voltage is associated with each connected conducting sub-domain Ω_{c_i} with $i \in C$. There might be cases for which this is no longer true. For example, a double torus has two holes, and two distinct net currents and voltages can be defined.

Using notations of the paragraphs above for the homology spaces, we can generalize the definitions introduced in Section 2.1.3 for the global variables. Let β_1 be the first Betti number of $\Omega_{\mathrm{c}}^{\mathrm{C}}$. We can define β_1 curves $\mathcal{C}_i$ in $\Omega_{\mathrm{c}}^{\mathrm{C}}$ that generate $\mathcal{H}_1(\Omega_{\mathrm{c}}^{\mathrm{C}})$. We can also define β_1 curves $\mathcal{C}_j^\star$ in Ω_{c}. In particular, conducting domains with terminals on the domain boundary Γ are treated by linking their terminals to close the curves.

Defining the linking number of two curves as the number of times each curve winds around the other, accounting for orientation with the usual right-hand sign convention, we can choose the curves $\mathcal{C}_i$ and $\mathcal{C}_j^\star$ so that the matrix formed by their linking numbers is the identity matrix, i.e., Link$(\mathcal{C}_i, \mathcal{C}_j^\star) = \delta_{ij}$ [253]. To each $(\mathcal{C}_i, \mathcal{C}_i^\star)$ pair, we can associate the current-voltage pair, (I_i, V_i), with $i \in 1, \dots, \beta_1$.

A.2 Whitney forms

Whitney forms are associated with simplicial entities: node, lines, triangles, and tetrahedra, or 0-, 1-, 2-, and 3-simplices, respectively [141]. See Fig. A.2. For extensions of Whitney forms to non-simplicial entities, such as quadrangles, pyramids, prisms or hexahedra, we refer to the literature [254, 177].

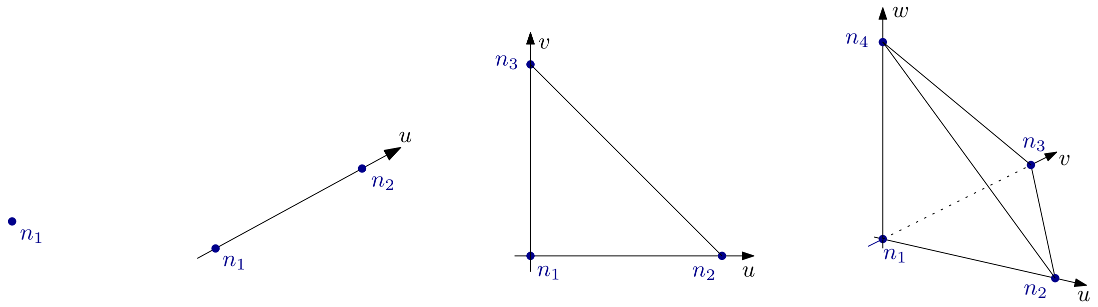

Figure A.2: Reference 0-, 1-, 2-, and 3-simplices (from left to right) and the node numbering convention. Lengths along the axes are equal to one. Coordinate for the line is u, with $n_1 = (0)$ and $n_2 = (1)$. Coordinates for the triangle are (u, v) with $n_1 = (0, 0)$, $n_2 = (1, 0)$, and $n_3 = (0, 1)$. Coordinates for the tetrahedron are (u, v, w) with $n_1 = (0, 0, 0)$, $n_2 = (1, 0, 0)$, $n_3 = (0, 1, 0)$, and $n_3 = (0, 0, 1)$.

In the following, we denote by $\mathcal{N}(\Omega_i)$, $\mathcal{E}(\Omega_i)$, $\mathcal{F}(\Omega_i)$, and $\mathcal{V}(\Omega_i)$ the set of nodes, edges, facets, and volumes of the mesh of a given domain Ω_i, respectively, including entities on the boundaries of Ω_i.

A.2.1 Node functions (0-forms)

The node function w_n of a node $n \in \mathcal{N}(K)$ in a simplicial element K is the barycentric coordinate function associated to that node in K, that is, the unique affine function in K whose value at node n is one and zero at others nodes. Barycentric functions constitute the main building blocks for Whitney forms [177]. The support of w_n extends to every simplicial element that contains n. This node function is a 0-form associated with a 0-simplex. Functions generated by combinations of node functions are *conform*, in the sense that they are continuous.

The node functions in the reference triangle are illustrated in Fig. A.3. In the reference simplices, with conventions and coordinates from Fig. A.2, and the notation $w_i = w_{n_i}$, we have

$$\begin{aligned} &\text{Node} && w_1 = 1, && \text{(A.12)}\\ &\text{Line} && w_1 = 1-u, \quad w_2 = u, && \text{(A.13)}\\ &\text{Triangle} && w_1 = 1-u-v, \quad w_2 = u, \quad w_3 = v, && \text{(A.14)}\\ &\text{Tetrahedra} && w_1 = 1-u-v-w, \quad w_2 = u, \quad w_3 = v, \quad w_4 = w. && \text{(A.15)} \end{aligned}$$

We denote by $W^0(K)$ the function space spanned by node functions in an element K.

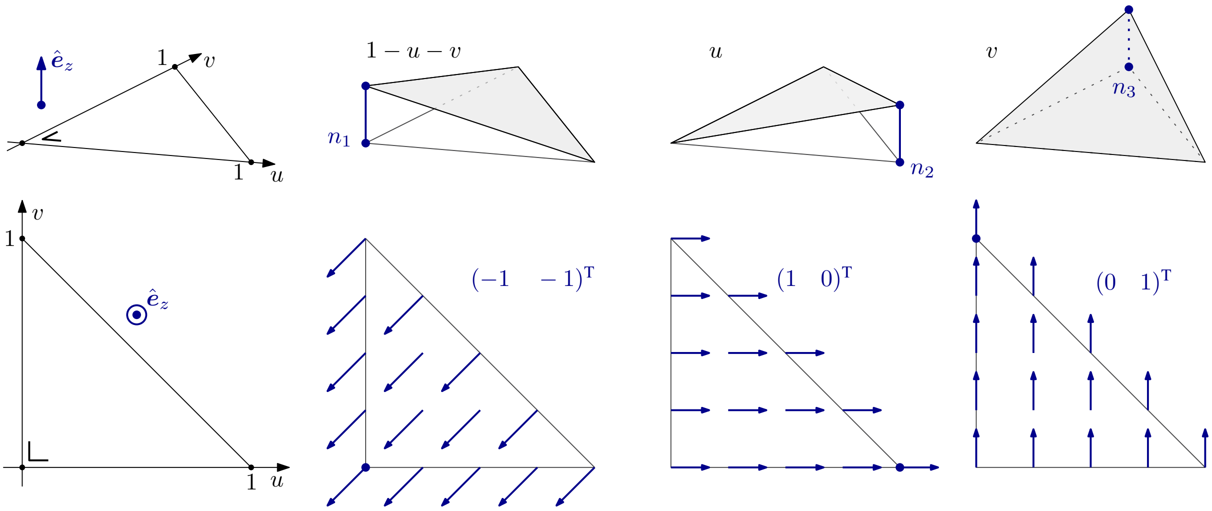

Figure A.3: (Up) Node functions w_n in the reference triangle in perspective view. Node functions are conform: they are continuous between elements. (Down) Gradient of node functions in the plane. These gradients are curl-conform: their tangential component is continuous between different elements.

A.2.2 Edge functions (1-forms)

An edge $e \in \mathcal{E}(K)$ is the oriented segment between two nodes $m, n \in \mathcal{N}(K)$. We note $e = \{m, n\}$. The edge function $\boldsymbol{w}_e$ associated with edge $e = \{m, n\}$ is defined as [31]

$$\boldsymbol{w}_e = w_m \, \mathbf{grad} \, w_n - w_n \, \mathbf{grad} \, w_m. \tag{A.16}$$

Therefore, its support extends to every simplicial element that contains e [141]. Edge functions for the reference triangle are illustrated in Fig. A.4. The circulation of $\boldsymbol{w}_e$ along edge e is one, and zero along every other edges. It is a 1-form. Functions $\boldsymbol{u}$ generated by a linear combination of edge functions are *curl-conform*, in the sense that their "tangential" trace[3] $\boldsymbol{u}\times\boldsymbol{n}$ is continuous across any interface of normal $\boldsymbol{n}$.

We denote by $W^1(K)$ the function space spanned by edge functions in an element K.

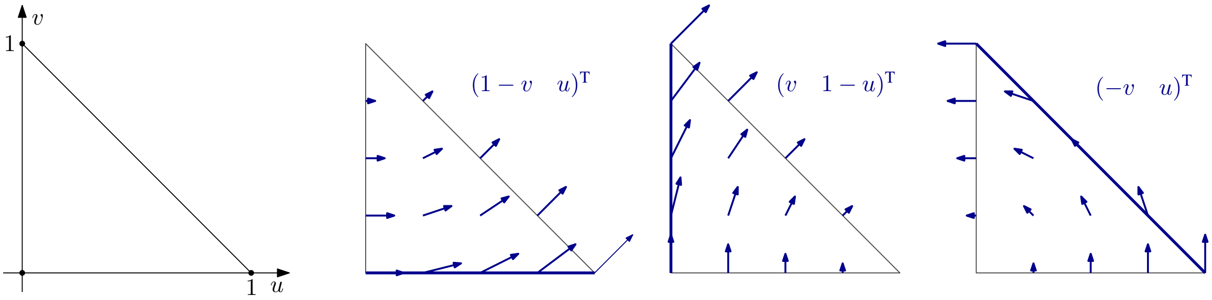

Figure A.4: Edge functions $\boldsymbol{w}_e$ in the reference triangle. The circulation of $\boldsymbol{w}_e$ along the corresponding edge is equal to one, whereas it is equal to zero along any other edges. Functions $\boldsymbol{w}_e$ are curl-conform: their tangential component is continuous between different elements.

A.2.3 Facet functions (2-forms)

A facet $f \in \mathcal{F}(K)$ is the oriented triangle defined by three nodes $m, n, k \in \mathcal{N}(K)$, or three edges $c = \{m, n\}, d = \{n, k\}, e = \{k, m\} \in \mathcal{E}(K)$. We note $f = \{m, n, k\} = \{\{m, n\}, \{n, k\}, \{k, m\}\}$. The orientation of the normal to the facet follows the right-hand rule for the sense of circulation of nodes m, n, k around the triangle. The facet function $\boldsymbol{w}_f$ associated with facet f is defined as [31]

$$\boldsymbol{w}_f = 2\big(w_m \,\mathbf{grad}\, w_n \times \mathbf{grad}\, w_k + w_k \,\mathbf{grad}\, w_m \times \mathbf{grad}\, w_n + w_n \,\mathbf{grad}\, w_k \times \mathbf{grad}\, w_m\big). \tag{A.17}$$

The support of $\boldsymbol{w}_f$ also extends to every volume that contains f, i.e., to only one volume if f is on the boundary of the mesh, to two volumes otherwise. The flux of $\boldsymbol{w}_f$ across facet f is one, and zero across every other facet. Functions $\boldsymbol{u}$ generated by a linear combination of facet functions are *div-conform*, in the sense that their normal trace $\boldsymbol{u} \cdot \boldsymbol{n}$ is continuous across any interface of normal $\boldsymbol{n}$.

We denote by $W^2(K)$ the function space spanned by facet functions in an element K.

A.2.4 Volume functions (3-forms)

A volume $v \in \mathcal{V}$ is a tetrahedron defined by four facets, oriented with their normal pointing outwards with respect to the tetrahedron. The volume function w_v is constant and equal to $1/\mathrm{vol}(v)$ in v, where $\mathrm{vol}(v)$ is the volume of v. It is non-zero in v only, and is discontinuous across different volumes [31].

---

[3] The quantity $\boldsymbol{u} \times \boldsymbol{n}$ is not the actual tangential component of $\boldsymbol{u}$ along an interface of normal $\boldsymbol{n}$: it is perpendicular to it. The tangential component is $\boldsymbol{n} \times (\boldsymbol{u} \times \boldsymbol{n})$.

We denote by $W^3(K)$ the function space spanned by volume functions in an element K.

A.2.5 Sequence of discrete function spaces

From the local spaces $W^p(K)$, for $p = 0, 1, 2$, or 3, on an element K, we construct the global spaces $W^p(\Omega)$, for $p = 0, 1, 2$, or 3, on the mesh of a domain Ω, by considering every node, edge, facet, or volume, of Ω, respectively. We have the following inclusions in the continuous function spaces

$$W^0(\Omega) \subset H^1(\Omega), \tag{A.18}$$

$$W^1(\Omega) \subset H(\mathbf{curl}; \Omega), \tag{A.19}$$

$$W^2(\Omega) \subset H(\mathrm{div}; \Omega), \tag{A.20}$$

$$W^3(\Omega) \subset L^2(\Omega). \tag{A.21}$$

See Section A.1 for definitions of the continuous function spaces.

Similarly to the continuous function spaces, the discrete function spaces $W^p(\Omega)$ also form a complex. To see why, we first need to introduce the notion of *incidence*. We denote by $\mathrm{i}(n, e)$ the incidence of node n and edge e, which is equal to 1 if $e = \{\cdot, n\}$, to -1 if $e = \{n, \cdot\}$, and to 0 otherwise. Next, the incidence $\mathrm{i}(e, f)$ of edge e and facet f is equal to 1 if e belongs to f and circulates positively around it, accordingly to the right-hand rule, to -1 if it circulates in the opposite direction, and to 0 if e does not belong to f. Finally, the incidence $\mathrm{i}(f, v)$ of facet f and volume v is equal to 1 if f belongs to v and has an outward normal with respect to v, to -1 if it has an inward normal, and to 0 if f does not belong to v.

We can show that, $\forall n \in \mathcal{N}(\Omega)$, $\forall e \in \mathcal{E}(\Omega)$, and $\forall f \in \mathcal{F}(\Omega)$, respectively, we have [141]

$$\sum_{e \in \mathcal{E}(\Omega)} \mathrm{i}(n, e)\, \boldsymbol{w}_e = \mathbf{grad}\, w_n, \qquad \sum_{f \in \mathcal{F}(\Omega)} \mathrm{i}(e, f)\, \boldsymbol{w}_f = \mathbf{curl}\, \boldsymbol{w}_e, \qquad \sum_{v \in \mathcal{V}(\Omega)} \mathrm{i}(f, v)\, w_v = \mathrm{div}\, \boldsymbol{w}_f. \tag{A.22}$$

The first equation is particularly useful in this work. It states that the gradient of any node function can be expressed as a sum of edge functions.

Eqn. (A.22) induce the inclusions **grad** $W^0(\Omega) \subset W^1(\Omega)$, **curl** $W^1(\Omega) \subset W^2(\Omega)$, and div $W^2(\Omega) \subset W^3(\Omega)$, and explicitly show that the discrete functions spaces form the complex

$$W^0(\Omega) \xrightarrow{\mathbf{grad}} W^1(\Omega) \xrightarrow{\mathbf{curl}} W^2(\Omega) \xrightarrow{\mathrm{div}} W^3(\Omega). \tag{A.23}$$

In the case where the domain Ω is topologically trivial, this complex is exact. This complex is the discrete counterpart of the de Rham complex, described by Eq. (A.9).

A.2.6 Higher order functions

Whitney shape functions are shape functions of the lowest order. To improve the accuracy of approximations, p-forms of higher polynomial order can be introduced [137]. They are however no longer be associated with p-simplices, but they keep the same continuity properties as Whitney functions.

A.3 Green's identities

Let $\boldsymbol{G}$ be a continuously differentiable vector field defined on a compact subset Ω of $\mathbb{R}^n$ with piecewise smooth boundary $\partial\Omega$. The divergence theorem states that

$$\int_{\Omega} \operatorname{div} \boldsymbol{G}\, d\Omega = \oint_{\partial\Omega} \boldsymbol{G} \cdot \boldsymbol{n}\, d\Gamma, \tag{A.24}$$

with $\boldsymbol{n}$ the unit normal vector field, pointing outwards. Considering the particular cases $\boldsymbol{G} = \boldsymbol{u}\, v$ and $\boldsymbol{G} = \boldsymbol{u} \times \boldsymbol{v}$ yields two useful identities, referred to as Green's identities [255]. These identities are of utmost importance in the construction of weak forms. The *grad-div Green's identity* writes

$$(\boldsymbol{u}\,, \mathbf{grad}\; v)_{\Omega} + (\operatorname{div} \boldsymbol{u}\,, v)_{\Omega} = \langle \boldsymbol{u} \cdot \boldsymbol{n}\,, v \rangle_{\partial\Omega} \tag{A.25}$$

and the *curl-curl Green's identity* writes

$$(\boldsymbol{u}\,, \mathbf{curl}\; \boldsymbol{v})_{\Omega} - (\mathbf{curl}\; \boldsymbol{u}\,, \boldsymbol{v})_{\Omega} = \langle \boldsymbol{u} \times \boldsymbol{n}\,, \boldsymbol{v} \rangle_{\partial\Omega} = \langle \boldsymbol{v} \times \boldsymbol{u}\,, \boldsymbol{n} \rangle_{\partial\Omega} = - \langle \boldsymbol{v} \times \boldsymbol{n}\,, \boldsymbol{u} \rangle_{\partial\Omega} \,. \tag{A.26}$$

Appendix B

Additional developments

B.1 Magnetic Gauss law

The magnetic Gauss law (2.17) has not been explicitly introduced in the derivation of the h-ϕ-formulation, but we can retrieve it by taking $\boldsymbol{h}' = \textbf{grad}\,\phi'$ as a test function in (2.31). We have

$$\begin{aligned}
& \left(\partial_t(\mu\,\boldsymbol{h})\,,\textbf{grad}\,\phi'\right)_\Omega + \left(\boldsymbol{e}\,,\textbf{curl}\,(\textbf{grad}\,\phi')\right)_\Omega - \langle \boldsymbol{e}\times\boldsymbol{n}\,,\textbf{grad}\,\phi'\rangle_\Gamma = 0, && \text{(B.1)}\\
\Leftrightarrow\quad & -\big(\text{div}\,\big(\partial_t(\mu\,\boldsymbol{h})\big)\,,\phi'\big)_\Omega + \langle \partial_t(\mu\boldsymbol{h})\cdot\boldsymbol{n}\,,\phi'\rangle_\Gamma - \langle \boldsymbol{e}\times\boldsymbol{n}\,,\textbf{grad}\,\phi'\rangle_\Gamma = 0, && \text{(B.2)}
\end{aligned}$$

where we used $\textbf{curl}\,(\textbf{grad}\,\cdot) = \boldsymbol{0}$, and the grad-div Green's identity (A.25). The second term of Eq. (B.2) can be worked out as follows (assuming a smoothed boundary Γ):

$$\begin{aligned}
\langle \partial_t(\mu\boldsymbol{h})\cdot\boldsymbol{n}\,,\phi'\rangle_\Gamma &= -\,\langle \textbf{curl}\,\boldsymbol{e}\cdot\boldsymbol{n}\,,\phi'\rangle_\Gamma && \text{(B.3)}\\
&= -\,\langle \text{div}\,(\boldsymbol{e}\times\boldsymbol{n})\,,\phi'\rangle_\Gamma - \langle \boldsymbol{e}\cdot\textbf{curl}\,\boldsymbol{n}\,,\phi'\rangle_\Gamma && \text{(B.4)}\\
&= -\,\langle \text{div}\,(\boldsymbol{e}\times\boldsymbol{n})\,,\phi'\rangle_\Gamma && \text{(B.5)}\\
&= \quad \langle \boldsymbol{e}\times\boldsymbol{n}\,,\textbf{grad}\,\phi'\rangle_\Gamma - \int_\Gamma \text{div}\,\big((\boldsymbol{e}\times\boldsymbol{n})\phi'\big)\,d\Gamma && \text{(B.6)}
\end{aligned}$$

where the last term is equal to zero because Γ is closed. Therefore, for $\boldsymbol{h}' = \textbf{grad}\,\phi'$, the formulation reads

$$\begin{aligned}
& \big(\text{div}\,\big(\partial_t(\mu\,\boldsymbol{h})\big)\,,\phi'\big)_\Omega = 0, && \text{(B.7)}\\
\Leftrightarrow\quad & \partial_t\big(\,(\text{div}\,(\mu\,\boldsymbol{h})\,,\phi')_\Omega\,\big) = 0, && \text{(B.8)}\\
\Leftrightarrow\quad & (\text{div}\,(\mu\,\boldsymbol{h})\,,\phi')_\Omega = \text{constant}. && \text{(B.9)}
\end{aligned}$$

If the initial condition is such that the constant is equal to zero, this is the weak form of the magnetic Gauss law.

B.2 Centered finite difference approximations of order two

We consider a smooth function of time $u = u(t)$, and its truncated Taylor development around time $t = t_n$:

$$u_{n-1} = u_n - \Delta t \dot{u}_n + \frac{\Delta t^2}{2} \ddot{u}_n + \mathcal{O}(\Delta t^3), \tag{B.10}$$

with $\Delta t = t_n - t_{n-1}$, $u_n = u(t_n)$, and the dot notation for time derivatives. We have

$$\dot{u}_n = \frac{u_n - u_{n-1}}{\Delta t} + \frac{\Delta t}{2} \ddot{u}_n + \mathcal{O}(\Delta t^2) \quad \Rightarrow \quad \dot{u}_n \approx \frac{u_n - u_{n-1}}{\Delta t}, \tag{B.11}$$

that is, the backward Euler approximation has a truncation error $\mathcal{O}(\Delta t)$, i.e., of the order of Δt. The first approach for evaluating the quadratic quantity $u\dot{u}$ at time $t = t_n$ is the following

$$\begin{aligned} (u\dot{u})_n &= u_n (\dot{u})_n && \text{(B.12)} \\ &= u_n \left(\frac{u_n - u_{n-1}}{\Delta t} + \frac{\Delta t}{2} \ddot{u}_n + \mathcal{O}(\Delta t^2) \right) && \text{(B.13)} \\ &= u_n \frac{u_n - u_{n-1}}{\Delta t} + \frac{\Delta t}{2} u_n \ddot{u}_n + \mathcal{O}(\Delta t^2). && \text{(B.14)} \end{aligned}$$

The associated approximation is

$$(u\dot{u})_n \approx u_n \frac{u_n - u_{n-1}}{\Delta t}, \tag{B.15}$$

which has a truncation error $\mathcal{O}(\Delta t)$ equal to $u_n \ddot{u}_n \; \Delta t/2$. Problems arise in particular when u is a sinusoidal-like function. In that case, the product $u_n \ddot{u}_n$ has a constant (negative) sign for all t_n so that the error also has a constant sign. If we integrate $u\dot{u}$ in time over one period, errors therefore accumulate. In practice, we observe that a non-negligible error is associated with this approach.

A much more accurate evaluation of the quantity $u\dot{u}$ reads, at mid-time step,

$$(u\dot{u})_{n-\frac{1}{2}} \approx \frac{u_n + u_{n-1}}{2} \frac{u_n - u_{n-1}}{\Delta t}. \tag{B.16}$$

This expression involves two centered differences rather than one backward difference as in Eq. (B.15). As we show below, the associated truncation error is $\mathcal{O}(\Delta t^2)$.

Let us consider a smooth scalar function of time $u = u(t)$, and two time instants t_{n-1} and t_n. Using Taylor's theorem around t_{n-1} and t_n, we have

$$u_{n-\frac{1}{2}} = u_{n-1} + \frac{\Delta t}{2} \dot{u}_{n-1} + \frac{\Delta t^2}{8} \ddot{u}_{n-1} + \frac{\Delta t^3}{48} \dddot{u}_{n-1} + \mathcal{O}(\Delta t^4), \tag{B.17}$$

$$u_{n-\frac{1}{2}} = u_n - \frac{\Delta t}{2} \dot{u}_n + \frac{\Delta t^2}{8} \ddot{u}_n - \frac{\Delta t^3}{48} \dddot{u}_n + \mathcal{O}(\Delta t^4), \tag{B.18}$$

with $u_n = u(t_n)$, $u_{n-\frac{1}{2}} = u(t_n - \Delta t/2)$, $\Delta t = t_n - t_{n-1}$, and the dot notation for time derivatives. From these equations, we can build two approximations of order two:

$$u_{n-\frac{1}{2}} = \frac{u_n + u_{n-1}}{2} + \frac{\Delta t^2}{16} (\ddot{u}_{n-1} + \ddot{u}_n) + \mathcal{O}(\Delta t^4) \quad \Rightarrow \quad u_{n-\frac{1}{2}} \approx \frac{u_n + u_{n-1}}{2}, \tag{B.19}$$

$$\dot{u}_{n-\frac{1}{2}} = \frac{u_n - u_{n-1}}{\Delta t} + \frac{\Delta t^2}{24} \dddot{u}_{n-\frac{1}{2}} + \mathcal{O}(\Delta t^4) \quad \Rightarrow \quad \dot{u}_{n-\frac{1}{2}} \approx \frac{u_n - u_{n-1}}{\Delta t}. \tag{B.20}$$

The first one is obtained with the sum of Eqn. (B.17) and (B.18), and the second one by their difference, with the substitutions $n \to n' + \frac{1}{2}$, and $n \to n' - \frac{1}{2}$, respectively.

For the quadratic quantity $u\dot{u}$ evaluated at $t_{n-1/2}$, we have

$$(u\dot{u})_{n-\frac{1}{2}} = \left(\frac{u_n + u_{n-1}}{2} + \mathcal{O}(\Delta t^2)\right)\left(\frac{u_n - u_{n-1}}{\Delta t} + \mathcal{O}(\Delta t^2)\right) \tag{B.21}$$

$$= \frac{u_n + u_{n-1}}{2}\frac{u_n - u_{n-1}}{\Delta t} + \mathcal{O}(\Delta t^2), \tag{B.22}$$

such that the approximation

$$(u\dot{u})_{n-\frac{1}{2}} \approx \frac{u_n + u_{n-1}}{2}\frac{u_n - u_{n-1}}{\Delta t} \tag{B.23}$$

has an error $\mathcal{O}(\Delta t^2)$. Moreover, we can show that the error is not of constant sign in case of a sinusoidal function.

For the electromagnetic power $\mathcal{P}$, we therefore choose to approximate the integrand of the first term of Eq. (2.69) at mid-time step $n - 1/2$ as

$$\partial_t \boldsymbol{b} \cdot \boldsymbol{h}|_{n-1/2} \approx \frac{\boldsymbol{b}_n - \boldsymbol{b}_{n-1}}{\Delta t} \cdot \frac{\boldsymbol{h}_{n-1} + \boldsymbol{h}_n}{2}. \tag{B.24}$$

It should be clear that the backward Euler method used for time discretization still introduces an error $\mathcal{O}(\Delta t)$, which we are satisfied with. We do not improve this order of accuracy with correction (B.24). However, with the correction, we avoid to introduce an additional error on post-processing integration of power estimates, which turns out to be significant with the naive approach, especially for situations with important inductive behaviors, such as with T2S.

B.3 Jacobian derivations

The linearization of the system matrix by the Newton-Raphson technique requires the expressions of the derivatives of the nonlinear constitutive laws. As these laws are vector relations, the derivatives are second-order tensor expressions. In the following expressions, we use the index notation.

The power law, given by

$$\boldsymbol{e} = \frac{e_{\mathrm{c}}}{j_{\mathrm{c}}}\left(\frac{\|\boldsymbol{j}\|}{j_{\mathrm{c}}}\right)^{n-1} \boldsymbol{j} = \rho(\|\boldsymbol{j}\|)\boldsymbol{j}, \tag{B.25}$$

with e_{c} (V/m), j_{c} (A/m^2) and n (-) three parameters, gives

$$\frac{\partial e_i}{\partial j_j} = \rho(\|\boldsymbol{j}\|)\delta_{ij} + (n-1)\frac{\rho(\|\boldsymbol{j}\|)}{\|\boldsymbol{j}\|^2}\, j_i j_j. \tag{B.26}$$

Conversely, the power law conductivity diverges for $\|\boldsymbol{e}\| \to 0$. In this work, the constitutive law has been regularized as follows,

$$\boldsymbol{j} = \frac{j_{\mathrm{c}}}{e_{\mathrm{c}}}\frac{1}{\varepsilon_\sigma + (\|\boldsymbol{e}\|/e_{\mathrm{c}})^{(n-1)/n}}\, \boldsymbol{e} = \sigma(\|\boldsymbol{e}\|)\boldsymbol{e}, \tag{B.27}$$

with the regularization parameter $\varepsilon_\sigma = 10^{-8}$. Its tensor derivative is given by

$$\frac{\partial j_i}{\partial e_j} = \sigma(\|\boldsymbol{e}\|)\,\delta_{ij} - \frac{n-1}{n}\frac{\big(\sigma(\|\boldsymbol{e}\|)\big)^2}{j_\mathrm{c} e_\mathrm{c}}\left(\frac{e_\mathrm{c}}{\|\boldsymbol{e}\|}\right)^{(n+1)/n} e_i e_j. \tag{B.28}$$

An invertible saturation law for ferromagnetic materials reads as follows,

$$\boldsymbol{b} = \mu_0\left(1+\left(\frac{1}{\mu_{\mathrm{r},0}-1}+\frac{\|\boldsymbol{h}\|}{m_0}\right)^{-1}\right)\boldsymbol{h} = \mu(\|\boldsymbol{h}\|)\boldsymbol{h}, \tag{B.29}$$

with $\mu_{\mathrm{r},0}$ (-) and m_0 (A/m) two parameters. The tensor derivative yields

$$\frac{\partial b_i}{\partial h_j} = \mu(\|\boldsymbol{h}\|)\delta_{ij} - \frac{\mu_0}{m_0}\left(\frac{1}{\mu_{\mathrm{r},0}-1}+\frac{\|\boldsymbol{h}\|}{m_0}\right)^{-2}\frac{h_i h_j}{\|\boldsymbol{h}\|}. \tag{B.30}$$

Conversely, the inverse law, given by

$$\boldsymbol{h} = \frac{1}{2}\left(\frac{\|\boldsymbol{b}\|}{\mu_0} - \frac{\mu_{\mathrm{r},0}m_0}{\mu_{\mathrm{r},0}-1} + s(\|\boldsymbol{b}\|)\right)\frac{\boldsymbol{b}}{\|\boldsymbol{b}\|} = \nu(\|\boldsymbol{b}\|)\boldsymbol{b}, \tag{B.31}$$

with

$$s(\|\boldsymbol{b}\|) = \sqrt{\left(\frac{\mu_{\mathrm{r},0}m_0}{\mu_{\mathrm{r},0}-1} - \frac{\|\boldsymbol{b}\|}{\mu_0}\right)^2 + \frac{4m_0}{\mu_{\mathrm{r},0}-1}\frac{\|\boldsymbol{b}\|}{\mu_0}}, \tag{B.32}$$

gives

$$\begin{aligned}\frac{\partial h_i}{\partial b_j} = \nu(\|\boldsymbol{b}\|)\delta_{ij} + \frac{1}{2}\Bigg(&\frac{\mu_{\mathrm{r},0}m_0}{(\mu_{\mathrm{r},0}-1)\|\boldsymbol{b}\|^3} - \frac{1}{\|\boldsymbol{b}\|^3}s(\|\boldsymbol{b}\|)\\ &+ \big(s(\|\boldsymbol{b}\|)\big)^{-1}\left(\frac{2-\mu_{\mathrm{r},0}}{\mu_{\mathrm{r},0}-1}m_0 + \frac{\|\boldsymbol{b}\|}{\mu_0}\right)\frac{1}{\mu_0\|\boldsymbol{b}\|^2}\Bigg)b_i b_j.\end{aligned} \tag{B.33}$$

B.4 Approached solution for first-flux penetration

The one-dimensional problem of first flux penetration in a zero-field cooled superconducting semi-infinite volume, $\{(x,y,z)\in\mathbb{R}^3 | x \geq 0\}$ is studied in [95]. The applied field is in the z-direction and increases linearly with a rate of $\dot{b}_\mathrm{s}$ (T/s). The geometry is illustrated in Fig. B.1.

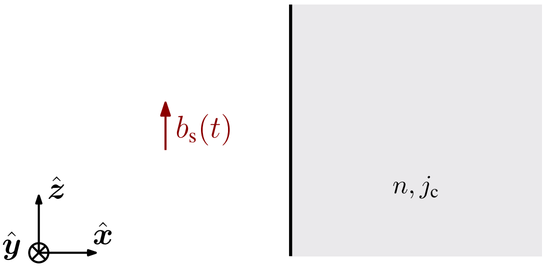

Figure B.1: Semi-infinite superconducting slab (gray region) subjected to an external field.

By symmetry, the magnetic flux density inside the superconductor is parallel to $\hat{\boldsymbol{z}}$ and varies spatially with x only. The current density is directed along $\hat{\boldsymbol{y}}$ and varies spatially with x only as well. Thus, we have $\boldsymbol{b} = b(x,t)\hat{\boldsymbol{z}}$ and $\boldsymbol{j} = j(x,t)\hat{\boldsymbol{y}}$. For a power law model $e = e_\mathrm{c}|j/j_\mathrm{c}|^n \operatorname{sign}(j)$, the governing equations reduce to the following nonlinear diffusion equation, for $x > 0$,

$$\frac{\partial b}{\partial t} = \frac{e_\mathrm{c}}{(\mu_0 j_\mathrm{c})^n} \frac{\partial}{\partial x} \left(\left| \frac{\partial b}{\partial x} \right|^{n-1} \frac{\partial b}{\partial x} \right), \tag{B.34}$$

with the initial condition $b(x,0) = 0$, $x \geq 0$ (zero-field cooled) and the boundary condition $b(0,t) = \dot{b}_\mathrm{s}\, t$, $t > 0$ (continuity of the tangential component of the magnetic field).

The problem is simplified by introducing a scaling variable ξ and a function f such that

$$b(x,t) = \dot{b}_\mathrm{s}\, t\, f(\xi(x,t)), \quad \xi(x,t) = \frac{\dot{b}_\mathrm{s}\, x}{e_\mathrm{c}} \left(\frac{t}{\tau} \right)^{-n/(1+n)}, \tag{B.35}$$

with τ a characteristic time $\tau = \mu_0 j_\mathrm{c} e_\mathrm{c} / \dot{b}_\mathrm{s}^2$, so that the initial condition is automatically satisfied and the boundary condition becomes $f(0) = 1$. The function f is then injected into Eq. (B.34), that reduces to a nonlinear ordinary differential equation for the function f of the scaling variable ξ,

$$f - \frac{n}{1+n}\, \xi f' = \left(|f'|^n \right)', \quad \text{with} \quad f(0) = 1. \tag{B.36}$$

We also introduce an unknown value ξ_0 at which the scaling function is forced to vanish, i.e., such that $f(\xi_0) = 0$. This serves as a second boundary condition. This parameter expresses the finite speed of propagation of the flux front (for $n > 1$) and describes its evolution. In terms of ξ_0, the flux front position x_0 at time t is then given by

$$x_0(t) = \frac{e_\mathrm{c} \xi_0}{\dot{b}_\mathrm{s}} \left(\frac{t}{\tau} \right)^{n/(1+n)}. \tag{B.37}$$

Equation (B.36) cannot be solved analytically, but is well approximated by the following expression [95]:

$$f(\xi) = \left(1 - \frac{\xi}{\xi_0} \right)^{n/(n-1)} (1 + a\xi) \quad \text{for} \quad \xi \in [0, \xi_0], \tag{B.38}$$

with the two parameters a and ξ_0 given by

$$a = \frac{1}{2n(2n-1)(n-1)} \qquad \text{and} \qquad \xi_0 = \left(\frac{n+1}{(n-1)^n} \big(n(1+a) \big)^{n-1} \right)^{1/(n+1)}. \tag{B.39}$$

The associated current density profile is given by

$$j(x,t) = j_\mathrm{c} \left(\frac{t}{\tau} \right)^{1/(1+n)} |f'(\xi(x,t))|. \tag{B.40}$$

Note that in the limit $n \to \infty$, we have $\xi_0 \to 1$, so that $x_0(t) = \dot{b}_\mathrm{s} t / \mu_0 j_\mathrm{c}$, which induces that the flux front advances at the constant velocity $\dot{b}_\mathrm{s} / \mu_0 j_\mathrm{c}$. This is consistent with the Bean model.

B.5 Quasi-3D h-ϕ-formulation in helicoidal coordinates

In this section, we expand the full h-ϕ-formulation expressed in helicoidal coordinates,

$$\left(\partial_t(\tilde{\boldsymbol{\mu}}\,\boldsymbol{h})\,,\boldsymbol{h}'\right)_{\Omega_{\text{3D}}} + \left(\tilde{\boldsymbol{\rho}}\,\textbf{curl}\,\boldsymbol{h}\,,\textbf{curl}\,\boldsymbol{h}'\right)_{\Omega_{\text{c,3D}}} = \sum_{i\in C_V} \bar{V}_i\mathcal{I}_i(\boldsymbol{h}'), \tag{B.41}$$

written in the 3D domain Ω_{3D}, in terms of a magnetic field $\boldsymbol{h}(\xi_1,\xi_2,\xi_3)$ decomposed as in Section 5.1.4):

$$\boldsymbol{h}(\xi_1,\xi_2,\xi_3) = \sum_{k=-\infty}^{\infty} \left(\boldsymbol{h}_{\parallel,k}(\xi_1,\xi_2) + \boldsymbol{h}_{\perp,k}(\xi_1,\xi_2)\right) f_k(\xi_3), \tag{B.42}$$

with the modes $f_k(\xi_3)$ defined as

$$f_k(\xi_3) = \begin{cases} \sqrt{2}\cos(\alpha k\xi_3), & k<0,\\ 1, & k=0,\\ \sqrt{2}\sin(\alpha k\xi_3), & k>0. \end{cases} \tag{B.43}$$

We remind that these modes are orthogonal and have a unit norm, i.e.,

$$\langle f_{k_1}, f_{k_2}\rangle = \frac{1}{p}\int_0^p f_{k_1}f_{k_2}\,d\xi_3 = \delta_{k_1k_2}, \quad \forall k_1,k_2\in\mathbb{Z}. \tag{B.44}$$

We denote by $\|f_k\|$ the norm of the mode f_k $(=1)$. We also have

$$\frac{\partial f_k}{\partial \xi_3} = \alpha k f_{-k}(\xi_3), \quad \forall k\in\mathbb{Z}. \tag{B.45}$$

Flux variation term

The first term of Eq. (B.41), $\left(\partial_t(\tilde{\boldsymbol{\mu}}\,\boldsymbol{h})\,,\boldsymbol{h}'\right)_{\Omega_{\text{3D}}}$ expands as the following double sum

$$\begin{aligned}\sum_{k=-\infty}^{\infty}\sum_{k'=-\infty}^{\infty} &\left(\partial_t(\tilde{\boldsymbol{\mu}}\,\boldsymbol{h}_{\parallel,k}f_k)\,,\boldsymbol{h}_{\parallel,k'}f_{k'}\right)_{\Omega_{\text{3D}}} + \left(\partial_t(\tilde{\boldsymbol{\mu}}\,\boldsymbol{h}_{\perp,k}f_k)\,,\boldsymbol{h}_{\parallel,k'}f_{k'}\right)_{\Omega_{\text{3D}}}\\ &+ \left(\partial_t(\tilde{\boldsymbol{\mu}}\,\boldsymbol{h}_{\parallel,k}f_k)\,,\boldsymbol{h}_{\perp,k'}f_{k'}\right)_{\Omega_{\text{3D}}} + \left(\partial_t(\tilde{\boldsymbol{\mu}}\,\boldsymbol{h}_{\perp,k}f_k)\,,\boldsymbol{h}_{\perp,k'}f_{k'}\right)_{\Omega_{\text{3D}}}.\end{aligned} \tag{B.46}$$

Because the decomposition in Eq. (B.42) separate the variables, we can integrate each individual term along the geometry invariant ξ_3-direction over one pitch length p. The orthogonality of the modes induces that terms with $k\neq k'$ vanish. Dividing the integral by p, we get,

$$\begin{aligned}\sum_{k=-\infty}^{\infty} \|f_k\|^2 &\Big(\left(\partial_t(\tilde{\boldsymbol{\mu}}\,\boldsymbol{h}_{\parallel,k})\,,\boldsymbol{h}_{\parallel,k}\right)_{\Omega} + \left(\partial_t(\tilde{\boldsymbol{\mu}}\,\boldsymbol{h}_{\perp,k})\,,\boldsymbol{h}_{\parallel,k}\right)_{\Omega}\\ &+ \left(\partial_t(\tilde{\boldsymbol{\mu}}\,\boldsymbol{h}_{\parallel,k})\,,\boldsymbol{h}_{\perp,k}\right)_{\Omega} + \left(\partial_t(\tilde{\boldsymbol{\mu}}\,\boldsymbol{h}_{\perp,k})\,,\boldsymbol{h}_{\perp,k}\right)_{\Omega}\Big),\end{aligned} \tag{B.47}$$

where integrals are performed on a 2D domain. Equations for different values of k are decoupled.

Eddy current term

The second term of Eq. (B.41), $(\tilde{\boldsymbol{\rho}}\,\mathbf{curl}\,\boldsymbol{h}\,,\mathbf{curl}\,\boldsymbol{h}')_{\Omega_{\mathrm{c,3D}}}$ expands as the following double sum

$$\begin{aligned}\sum_{k=-\infty}^{\infty}\sum_{k'=-\infty}^{\infty}&\left(\tilde{\boldsymbol{\rho}}\,\mathbf{curl}\,(\boldsymbol{h}_{\parallel,k}f_k)\,,\mathbf{curl}\,(\boldsymbol{h}_{\parallel,k'}f_{k'})\right)_{\Omega_{\mathrm{c,3D}}}+\left(\tilde{\boldsymbol{\rho}}\,\mathbf{curl}\,(\boldsymbol{h}_{\perp,k}f_k)\,,\mathbf{curl}\,(\boldsymbol{h}_{\parallel,k'}f_{k'})\right)_{\Omega_{\mathrm{c,3D}}}\\&+\left(\tilde{\boldsymbol{\rho}}\,\mathbf{curl}\,(\boldsymbol{h}_{\parallel,k}f_k)\,,\mathbf{curl}\,(\boldsymbol{h}_{\perp,k'}f_{k'})\right)_{\Omega_{\mathrm{c,3D}}}+\left(\tilde{\boldsymbol{\rho}}\,\mathbf{curl}\,(\boldsymbol{h}_{\perp,k}f_k)\,,\mathbf{curl}\,(\boldsymbol{h}_{\perp,k'}f_{k'})\right)_{\Omega_{\mathrm{c,3D}}}\,.\end{aligned}\tag{B.48}$$

Using Eq. (5.27) for the curl, we get the following expression for each $k,k'\in\mathbb{Z}$,

$$\begin{aligned}&\left(\tilde{\boldsymbol{\rho}}\,f_k\,\mathbf{curl}\,\boldsymbol{h}_{\parallel,k}\,,f_{k'}\,\mathbf{curl}\,\boldsymbol{h}_{\parallel,k'}\right)_{\Omega_{\mathrm{c,3D}}}+\left(\tilde{\boldsymbol{\rho}}\,\frac{\partial f_k}{\partial\xi_3}\hat{\boldsymbol{e}}_{\xi_3}\times\boldsymbol{h}_{\parallel,k}\,,f_{k'}\,\mathbf{curl}\,\boldsymbol{h}_{\parallel,k'}\right)_{\Omega_{\mathrm{c,3D}}}\\&+\left(\tilde{\boldsymbol{\rho}}\,f_k\,\mathbf{curl}\,\boldsymbol{h}_{\parallel,k}\,,\frac{\partial f_{k'}}{\partial\xi_3}\hat{\boldsymbol{e}}_{\xi_3}\times\boldsymbol{h}_{\parallel,k'}\right)_{\Omega_{\mathrm{c,3D}}}+\left(\tilde{\boldsymbol{\rho}}\,\frac{\partial f_k}{\partial\xi_3}\hat{\boldsymbol{e}}_{\xi_3}\times\boldsymbol{h}_{\parallel,k}\,,\frac{\partial f_{k'}}{\partial\xi_3}\hat{\boldsymbol{e}}_{\xi_3}\times\boldsymbol{h}_{\parallel,k'}\right)_{\Omega_{\mathrm{c,3D}}}\\&+\left(\tilde{\boldsymbol{\rho}}\,f_k\mathbf{curl}\,\boldsymbol{h}_{\perp,k}\,,f_{k'}\,\mathbf{curl}\,\boldsymbol{h}_{\parallel,k'}\right)_{\Omega_{\mathrm{c,3D}}}+\left(\tilde{\boldsymbol{\rho}}\,f_k\mathbf{curl}\,\boldsymbol{h}_{\perp,k}\,,\frac{\partial f_{k'}}{\partial\xi_3}\hat{\boldsymbol{e}}_{\xi_3}\times\boldsymbol{h}_{\parallel,k'}\right)_{\Omega_{\mathrm{c,3D}}}\\&+\left(\tilde{\boldsymbol{\rho}}\,f_k\,\mathbf{curl}\,\boldsymbol{h}_{\parallel,k}\,,f_{k'}\mathbf{curl}\,\boldsymbol{h}_{\perp,k'}\right)_{\Omega_{\mathrm{c,3D}}}+\left(\tilde{\boldsymbol{\rho}}\,\frac{\partial f_k}{\partial\xi_3}\hat{\boldsymbol{e}}_{\xi_3}\times\boldsymbol{h}_{\parallel,k}\,,f_{k'}\mathbf{curl}\,\boldsymbol{h}_{\perp,k'}\right)_{\Omega_{\mathrm{c,3D}}}\\&+\left(\tilde{\boldsymbol{\rho}}\,f_k\mathbf{curl}\,\boldsymbol{h}_{\perp,k}\,,f_{k'}\mathbf{curl}\,\boldsymbol{h}_{\perp,k'}\right)_{\Omega_{\mathrm{c,3D}}}\,.\end{aligned}\tag{B.49}$$

We can integrate each term along the geometry invariant ξ_3-direction over one pitch length p (and dividing by p), use the mode property Eq. (B.45), and exploit the mode orthogonality. For $k=0$, because $\partial_{\xi_3}f_0=0$, only terms for $k'=0$ survive, and they are decoupled from all other terms (for $k\neq 0$). These terms are

$$\begin{aligned}&\|f_0\|^2\left(\tilde{\boldsymbol{\rho}}\,\mathbf{curl}\,\boldsymbol{h}_{\parallel,0}\,,\mathbf{curl}\,\boldsymbol{h}_{\parallel,0}\right)_{\Omega_{\mathrm{c}}}+\|f_0\|^2\left(\tilde{\boldsymbol{\rho}}\,\mathbf{curl}\,\boldsymbol{h}_{\perp,0}\,,\mathbf{curl}\,\boldsymbol{h}_{\parallel,0}\right)_{\Omega_{\mathrm{c}}}\\&+\|f_0\|^2\left(\tilde{\boldsymbol{\rho}}\,\mathbf{curl}\,\boldsymbol{h}_{\parallel,0}\,,\mathbf{curl}\,\boldsymbol{h}_{\perp,0}\right)_{\Omega_{\mathrm{c}}}+\|f_0\|^2\left(\tilde{\boldsymbol{\rho}}\,\mathbf{curl}\,\boldsymbol{h}_{\perp,0}\,,\mathbf{curl}\,\boldsymbol{h}_{\perp,0}\right)_{\Omega_{\mathrm{c}}}\,.\end{aligned}\tag{B.50}$$

For $k\neq 0$, only one term of the sum on k' survives, either $k'=k$, or $k'=-k$. Indeed, Eq. (B.45) induces the coupling of the modes k and $-k$. For each value of $k\neq 0$, in Eq. (B.49), the only terms that remain are

$$\begin{aligned}&\|f_k\|^2\left(\tilde{\boldsymbol{\rho}}\,\mathbf{curl}\,\boldsymbol{h}_{\parallel,k}\,,\mathbf{curl}\,\boldsymbol{h}_{\parallel,k}\right)_{\Omega_{\mathrm{c}}}+\alpha k\|f_{-k}\|^2\left(\tilde{\boldsymbol{\rho}}\,\hat{\boldsymbol{e}}_{\xi_3}\times\boldsymbol{h}_{\parallel,k}\,,\mathbf{curl}\,\boldsymbol{h}_{\parallel,-k}\right)_{\Omega_{\mathrm{c}}}\\&+\alpha(-k)\|f_k\|^2\left(\tilde{\boldsymbol{\rho}}\,\mathbf{curl}\,\boldsymbol{h}_{\parallel,k}\,,\hat{\boldsymbol{e}}_{\xi_3}\times\boldsymbol{h}_{\parallel,-k}\right)_{\Omega_{\mathrm{c}}}+\alpha^2k^2\|f_{-k}\|^2\left(\tilde{\boldsymbol{\rho}}\,\hat{\boldsymbol{e}}_{\xi_3}\times\boldsymbol{h}_{\parallel,k}\,,\hat{\boldsymbol{e}}_{\xi_3}\times\boldsymbol{h}_{\parallel,k}\right)_{\Omega_{\mathrm{c}}}\\&+\|f_k\|^2\left(\tilde{\boldsymbol{\rho}}\,\mathbf{curl}\,\boldsymbol{h}_{\perp,k}\,,\mathbf{curl}\,\boldsymbol{h}_{\parallel,k}\right)_{\Omega_{\mathrm{c}}}+\alpha(-k)\|f_k\|^2\left(\tilde{\boldsymbol{\rho}}\,\mathbf{curl}\,\boldsymbol{h}_{\perp,k}\,,\hat{\boldsymbol{e}}_{\xi_3}\times\boldsymbol{h}_{\parallel,-k}\right)_{\Omega_{\mathrm{c}}}\\&+\|f_k\|^2\left(\tilde{\boldsymbol{\rho}}\,\mathbf{curl}\,\boldsymbol{h}_{\parallel,k}\,,\mathbf{curl}\,\boldsymbol{h}_{\perp,k}\right)_{\Omega_{\mathrm{c}}}+\alpha k\|f_{-k}\|^2\left(\tilde{\boldsymbol{\rho}}\,\hat{\boldsymbol{e}}_{\xi_3}\times\boldsymbol{h}_{\parallel,k}\,,\mathbf{curl}\,\boldsymbol{h}_{\perp,-k}\right)_{\Omega_{\mathrm{c}}}\\&+\|f_k\|^2\left(\tilde{\boldsymbol{\rho}}\,\mathbf{curl}\,\boldsymbol{h}_{\perp,k}\,,\mathbf{curl}\,\boldsymbol{h}_{\perp,k}\right)_{\Omega_{\mathrm{c}}}\,.\end{aligned}\tag{B.51}$$

These terms are coupled with the same set of term but with the opposite value of k, $k^\star=-k$, which sums up to a total of eighteen individual terms for the eddy current contribution, for each value of $|k|\neq 0$.

Appendix C

Additional figures

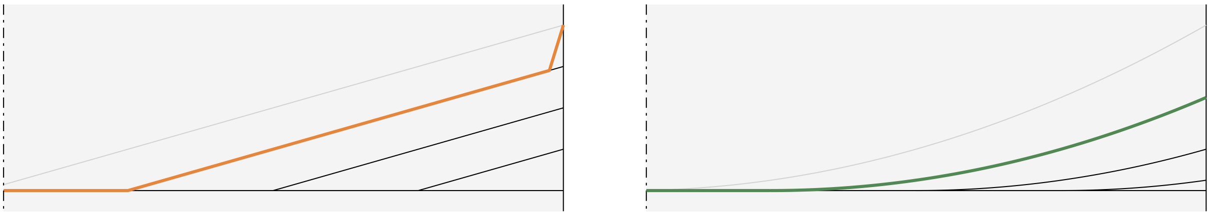

(a) Magnetic field - h-ϕ-formulation - 0th order.

(d) Vector potential - a-formulation - 0th order.

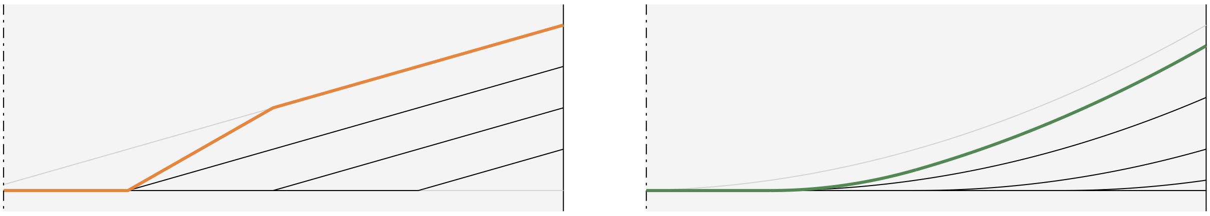

(b) Magnetic field - h-ϕ-formulation - 1st order.

(e) Vector potential - a-formulation - 1st order.

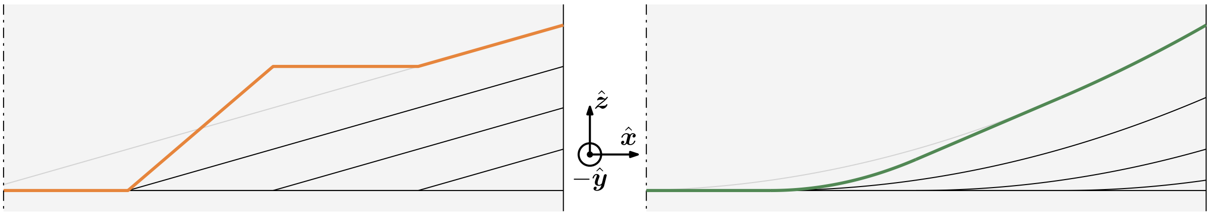

(c) Magnetic field - h-ϕ-formulation - 2nd order.

(f) Vector potential - a-formulation - 2nd order.

Figure C.1: Illustration of the initial iterates (colored bold curves) with the different extrapolation orders for choosing the initial estimate of a given time step. Simple 1D bar problem with a high n value, during the first flux penetration with a linear ramp of applied field. In each subfigure, the successive thin curves going upwards are successive previous solutions and the gray curve is the next exact solution. The Dirichlet boundary conditions are imposed after extrapolation. (a)-(b)-(c) Vertical z-component of $\boldsymbol{h}$ for the h-ϕ-formulation. (d)-(e)-(f) Out-of-plane y-component of $\boldsymbol{a}$ for the a-formulation.

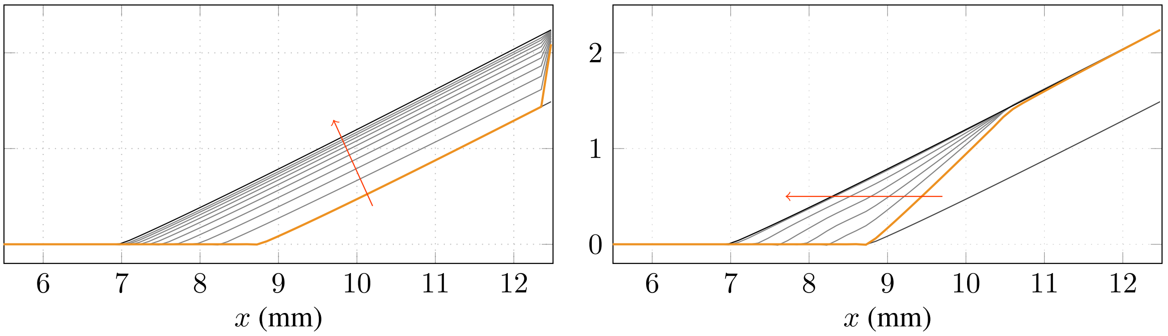

(a) h-ϕ-formulation - 0th order extrapolation.

(b) h-ϕ-formulation - 1st order extrapolation.

Figure C.2: Evolution (upwards) of the numerical Newton-Raphson iterations during one time step for the h-ϕ-formulation and two extrapolation orders, during the first flux penetration. The ordinate axis corresponds to the z-component of $\boldsymbol{b}$ (T). The orange arrows indicate the direction of evolution. Closest curves in (a) are each separated by 10 iterations. Closest curves in (b) are each separated by 5 iterations. The lowest curves represent the solution at the previous time step and the thick orange curves correspond to the initial iterate, as shown in Fig. C.1(a)-(b).

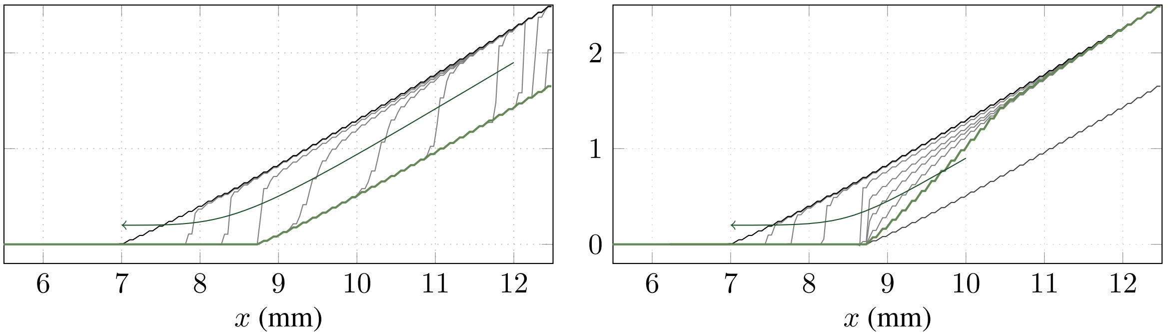

(a) a-formulation - 0th order extrapolation.

(b) a-formulation - 1st order extrapolation.

Figure C.3: Evolution (upwards) of the numerical Picard iterations during one time step for the a-formulation and two extrapolation orders, during the first flux penetration. The ordinate axis corresponds to the z-component of $\boldsymbol{b}$ (T). The green arrows indicate the direction of evolution. Successive curves are not separated by a constant number of iterations. The lowest curves represent the solution at the previous time step and the thick green curves correspond to the initial iterate, as shown in Fig. C.1(d)-(e).

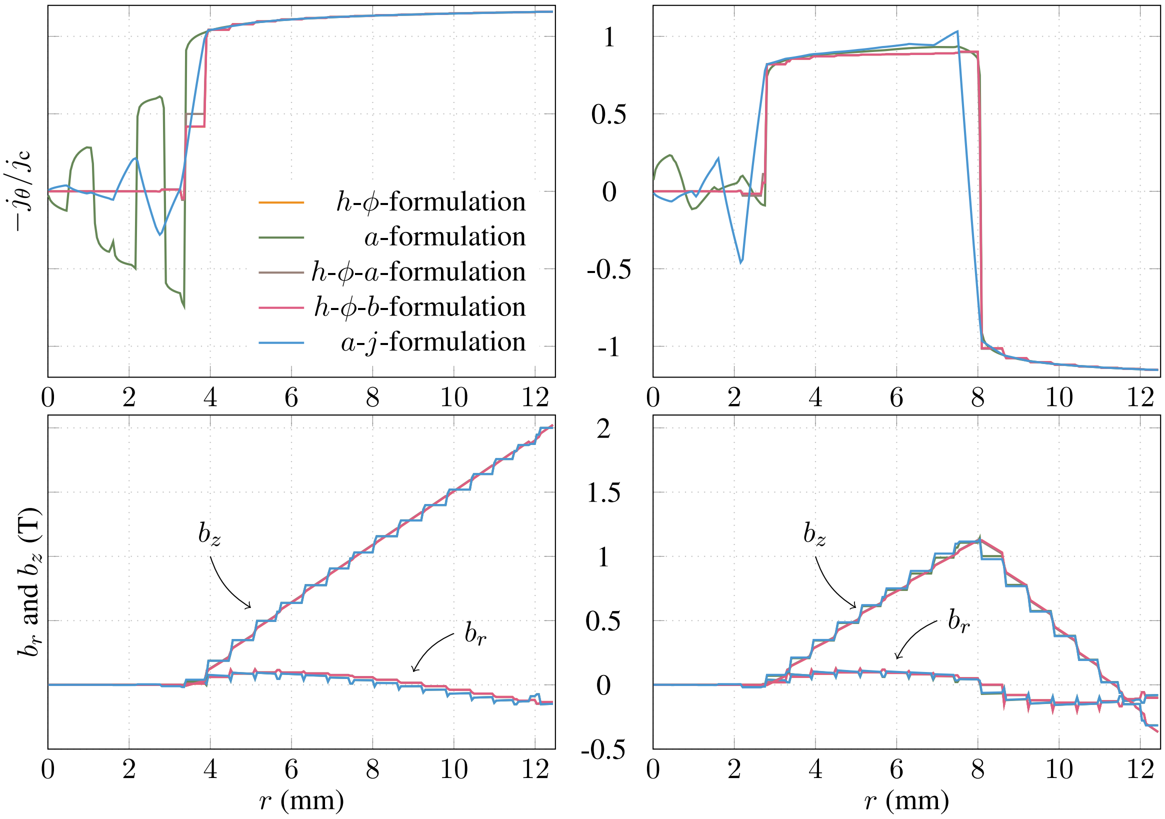

Figure C.4: Azimuthal current density (up) and magnetic flux density r and z-components (down) along the mid-height horizontal segment in the T2S cylinder ("Cut 1" of Fig. 4.19(a)) at time $t = t_1$ (left) and $t = t_2$ (right). Results of five formulations are presented. Medium mesh resolution: $\alpha = 2$ (see Section 4.4.2). The legend is the same for all figures.

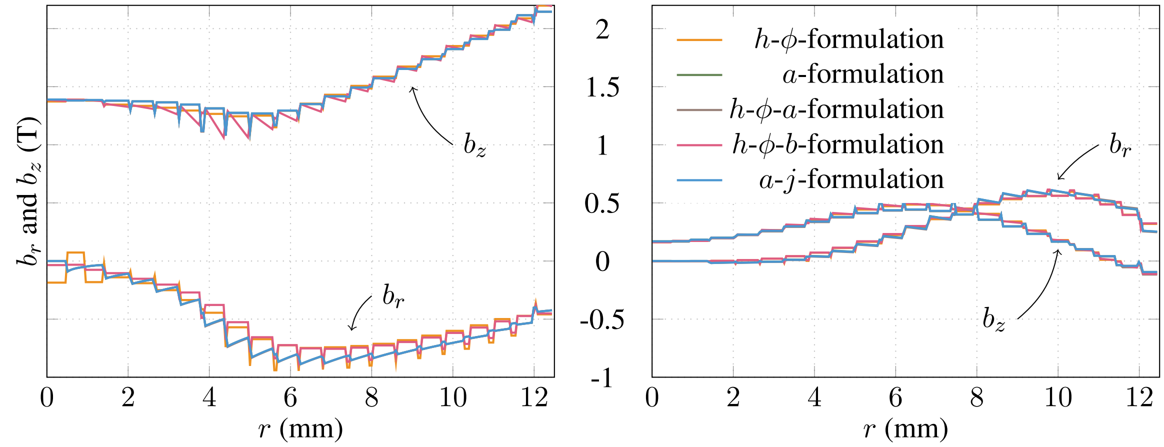

Figure C.5: Magnetic flux density components along the mid-height horizontal segment in the SFM cylinder ("Cut 2" of Fig. 4.19(a)) at time $t = t_1$ (left) and $t = t_2$ (right). Results of five formulations are presented. Medium mesh resolution: $\alpha = 2$ (see Section 4.4.2). The legend is the same for both figures.

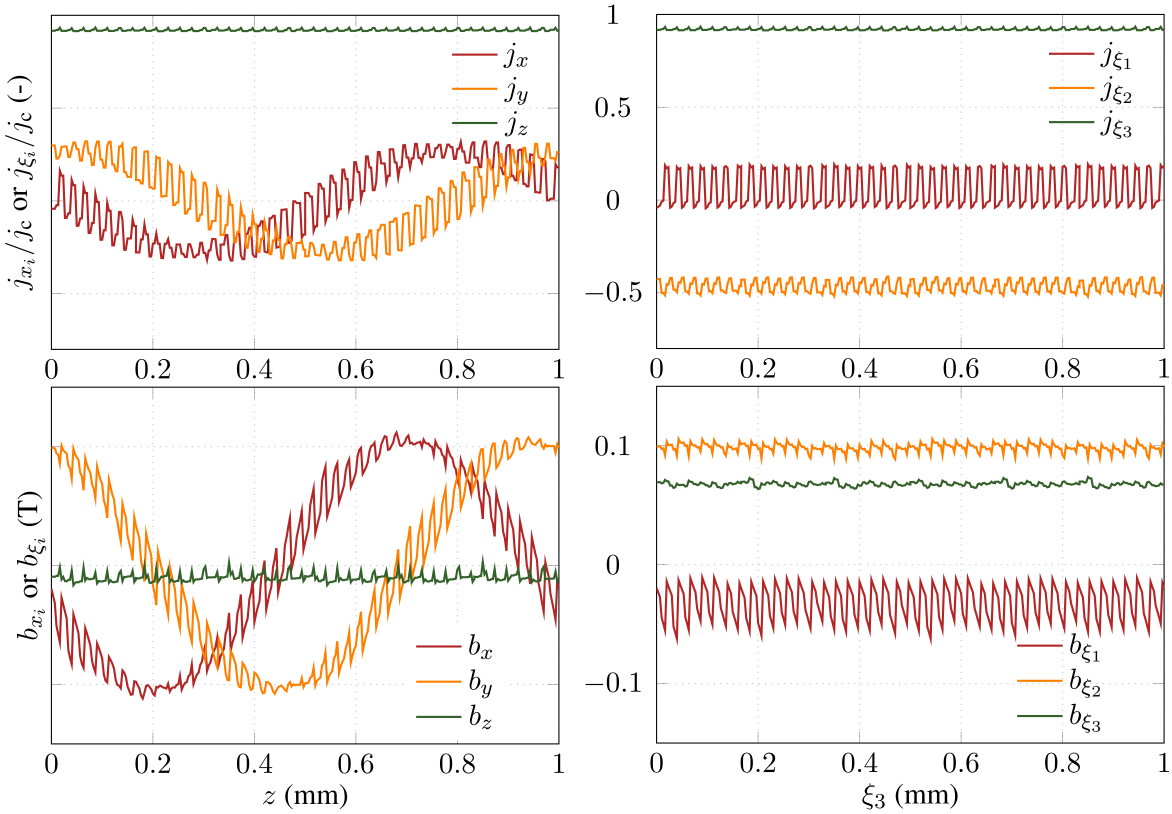

Figure C.6: Current density (up) and magnetic flux density (down) along the helicoidal fiber of pitch length p passing at point $\boldsymbol{x} = \big(r\cos(\theta), r\sin(\theta), 0\big)$, with $r = R_\ell + 0.7R_\mathrm{f}$ and $\theta = \pi/50$, from $z = 0$ to $z = p$. (Left) Three components of the vectors in the $\boldsymbol{x}$-space. (Right) Three components of the vectors in the $\boldsymbol{\xi}$-space. Solution of the 3D model with the h-ϕ-formulation on a coarse tetrahedral mesh involving 16 556 DOFs, solution at $t = T/4$.

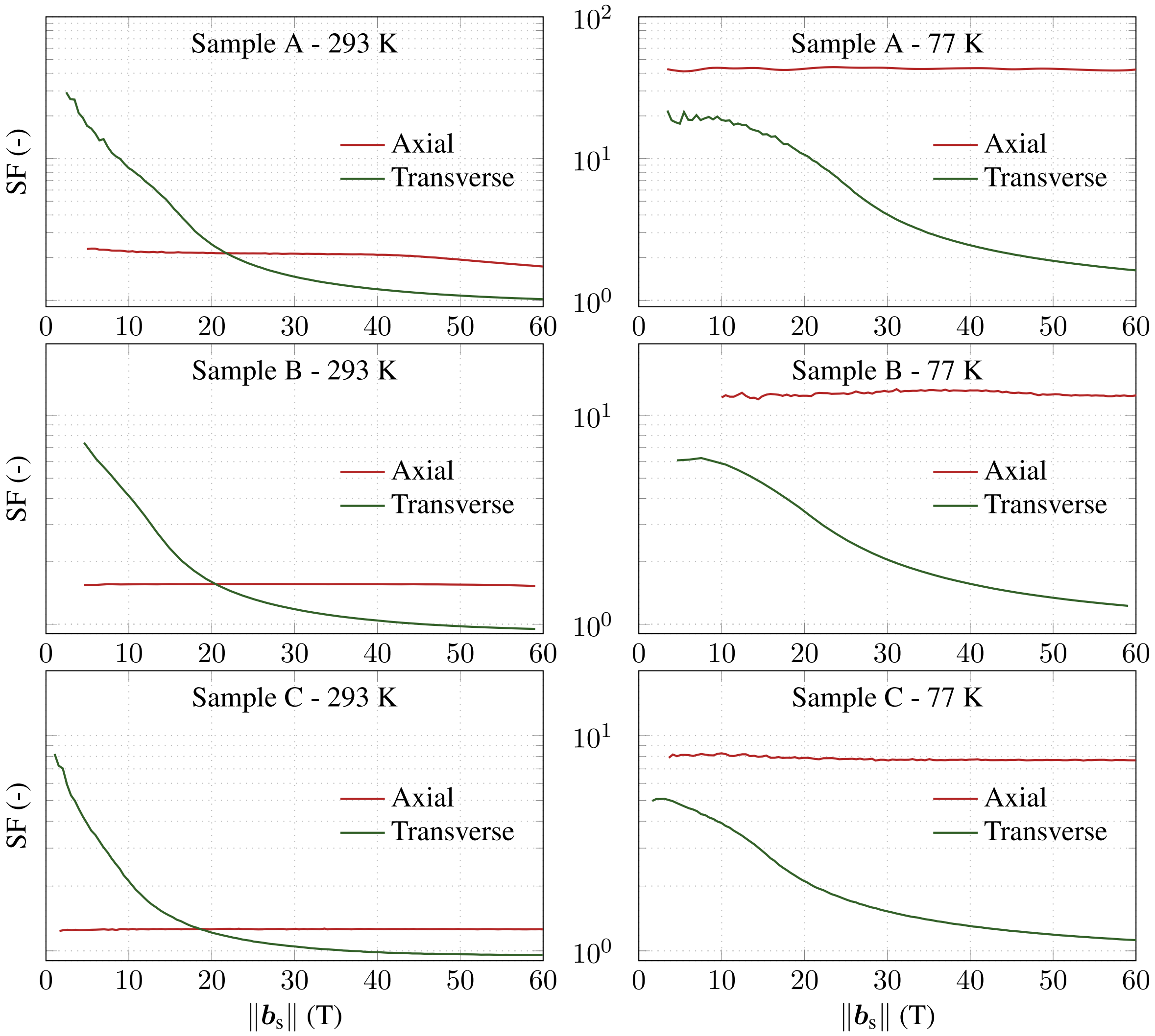

Figure C.7: Experimental measurements of shielding factors for samples A (up), B (middle), and C (down), at room temperature (left) and 77 K (right), in both axial and transverse configurations. Applied field up to 60 mT, at a rate of 0.75 mT/s. Data from [242].

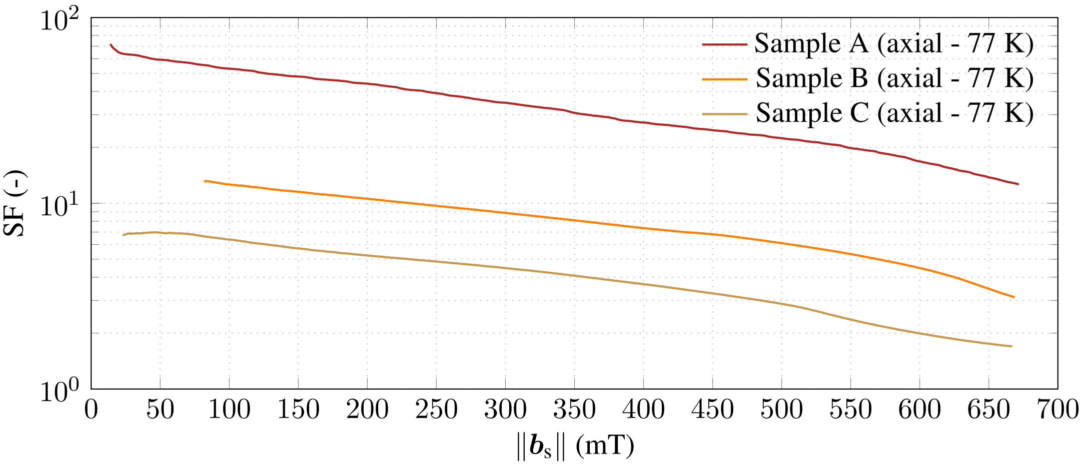

Figure C.8: Experimental measurements of shielding factors for samples A,B, and C at 77 K in the axial configuration. Applied field up to 670 mT, at a rate of 5 mT/s. Data from [242].

Bibliography

[1] H. Kamerlingh Onnes, “The superconductivity of mercury,” *Comm. Phys. Lab. Univ. Leiden*, vol. 122, pp. 122–124, 1911.

[2] W. Meissner and R. Ochsenfeld, “Ein neuer effekt bei eintritt der supraleitfähigkeit,” *Naturwissenschaften*, vol. 21, no. 44, pp. 787–788, 1933.

[3] A. A. Abrikosov, “The magnetic properties of superconducting alloys,” *Journal of Physics and Chemistry of Solids*, vol. 2, no. 3, pp. 199–208, 1957.

[4] A. Campbell and D. Cardwell, “Bulk high temperature superconductors for magnet applications,” *Cryogenics*, vol. 37, no. 10, pp. 567–575, 1997.

[5] C. Yao and Y. Ma, “Superconducting materials: Challenges and opportunities for large-scale applications,” *Iscience*, vol. 24, no. 6, p. 102541, 2021.

[6] B. Shen, F. Grilli, and T. Coombs, “Overview of H-formulation: A versatile tool for modeling electromagnetics in high-temperature superconductor applications,” *IEEE access*, vol. 8, pp. 100403–100414, 2020.

[7] C. Barth, *High temperature superconductor cable concepts for fusion magnets*, vol. 7. KIT Scientific Publishing, 2014.

[8] O. Brüning, P. Collier, P. Lebrun, S. Myers, R. Ostojic, J. Poole, and P. Proudlock, “LHC design report: Volume I, the LHC main ring,” *Reports - CERN*, 2004.

[9] R. G. Sharma, *Superconductivity: Basics and applications to magnets*, vol. 214. Springer Nature, 2021.

[10] J. G. Bednorz and K. A. Müller, “Possible high Tc superconductivity in the Ba-La-Cu-O system,” *Zeitschrift für Physik B Condensed Matter*, vol. 64, no. 2, pp. 189–193, 1986.

[11] M.-K. Wu, J. R. Ashburn, C. Torng, P.-H. Hor, R. L. Meng, L. Gao, Z. J. Huang, Y. Wang, and a. Chu, “Superconductivity at 93 K in a new mixed-phase Y-Ba-Cu-O compound system at ambient pressure,” *Physical review letters*, vol. 58, no. 9, p. 908, 1987.

[12] C. Michel, M. Hervieu, M. Borel, A. Grandin, F. Deslandes, J. Provost, and B. Raveau, “Superconductivity in the Bi-Sr-Cu-O system,” *Zeitschrift für Physik B Condensed Matter*, vol. 68, no. 4, pp. 421–423, 1987.

[13] B. Rozier, *Contribution to electromagnetic and thermal modelling of High Temperature Superconducting REBCO coils for protection purpose*. PhD thesis, Université Grenoble Alpes, 2019.

[14] J. van Nugteren, G. Kirby, J. Murtomäki, G. DeRijk, L. Rossi, and A. Stenvall, “Toward REBCO 20 T+ dipoles for accelerators,” *IEEE Transactions on Applied Superconductivity*, vol. 28, no. 4, pp. 1–9, 2018.

[15] A. Golovashkin, O. Ivanenko, Y. B. Kudasov, K. Mitsen, A. Pavlovsky, V. Platonov, and O. Tatsenko, “Low temperature direct measurements of Hc2 in HTSC using megagauss magnetic fields,” *Physica C: Superconductivity*, vol. 185, pp. 1859–1860, 1991.

[16] D. Arbelaez, E. Barzi, L. Brouwer, B. Cowan, D. Davis, R. Gupta, V. Kashikhin, V. Marinozzi, T. Shen, M. Sumption, *et al.*, “Numerical modeling for superconducting accelerator magnets,” *Snowmass21 LOI*, 2020.

[17] C. Rey, *Superconductors in the power grid: Materials and applications*. Elsevier, 2015.

[18] M. D. Brown, J. Jiang, C. Tarantini, D. Abraimov, G. Bradford, J. Jaroszynski, E. E. Hellstrom, and D. C. Larbalestier, “Prediction of the Jc (B) behavior of Bi-2212 wires at high field,” *IEEE Transactions on Applied Superconductivity*, vol. 29, no. 5, pp. 1–4, 2019.

[19] Y. Zhang, S. Yamano, D. Hazelton, and T. Fukushima, “REBCO HTS wire manufacturing and continuous development at superpower,” in *Mini-Workshop on High Temperature Superconducting Materials and Magnets*, 2018.

[20] J. Zhu, S. Chen, and Z. Jin, “Progress on second-generation high-temperature superconductor tape targeting resistive fault current limiter application,” *Electronics*, vol. 11, no. 3, p. 297, 2022.

[21] M. Paidpilli and V. Selvamanickam, “Development of RE-Ba-Cu-O superconductors in the US for ultra-high field magnets,” *Superconductor Science and Technology*, vol. 35, no. 4, p. 043001, 2022.

[22] J. Rush, C. May-Miller, K. Palmer, N. Rutter, A. Dennis, Y.-H. Shi, D. Cardwell, and J. Durrell, “Transport Jc in bulk superconductors: A practical approach?,” *IEEE Transactions on Applied Superconductivity*, vol. 26, no. 3, pp. 1–4, 2016.

[23] M. D. Ainslie and H. Fujishiro, “Modelling of bulk superconductor magnetization,” *Superconductor Science and Technology*, vol. 28, p. 053002, mar 2015.

[24] J. R. Hull and M. Murakami, “Applications of bulk high-temperature superconductors,” *Proceedings of the IEEE*, vol. 92, no. 10, pp. 1705–1718, 2004.

[25] J. H. Durrell, A. R. Dennis, J. Jaroszynski, M. D. Ainslie, K. G. Palmer, Y. Shi, A. M. Campbell, J. Hull, M. Strasik, E. Hellstrom, *et al.*, “A trapped field of 17.6 T in melt-processed, bulk Gd-Ba-Cu-O reinforced with shrink-fit steel,” *Superconductor Science and Technology*, vol. 27, no. 8, p. 082001, 2014.

[26] M. Ainslie and H. Fujishiro, *Numerical modelling of bulk superconductor magnetisation*. IOP Publishing, 2019.

[27] S. Denis, L. Dusoulier, M. Dirickx, P. Vanderbemden, R. Cloots, M. Ausloos, and B. Vanderheyden, “Magnetic shielding properties of high-temperature superconducting tubes subjected to axial fields,” *Superconductor Science and Technology*, vol. 20, no. 3, p. 192, 2007.

[28] F. Werfel, U. Floegel-Delor, R. Rothfeld, T. Riedel, B. Goebel, D. Wippich, and P. Schirrmeister, “Superconductor bearings, flywheels and transportation,” *Superconductor Science and Technology*, vol. 25, no. 1, p. 014007, 2011.

[29] F. Grilli, "Numerical modeling of HTS applications," *IEEE Transactions on Applied Superconductivity*, vol. 26, no. 3, pp. 1–8, 2016.

[30] A. N. Petrov, *Multiphysics finite element modelling of the AC power loss, fault response and recovery of first generation superconducting cables*. PhD thesis, University of Southampton, 2020.

[31] A. Bossavit, *Computational electromagnetism: variational formulations, complementarity, edge elements*. Academic Press, 1998.

[32] A. Goyal, M. P. Paranthaman, and U. Schoop, "The RABiTS approach: Using rolling-assisted biaxially textured substrates for high-performance YBCO superconductors," *MRS bulletin*, vol. 29, no. 8, pp. 552–561, 2004.

[33] G. Liu, G. Zhang, L. Jing, H. Yu, L. Ai, W. Yuan, and W. Li, "Influence of substrate magnetism on frequency-dependent transport loss in HTS-coated conductors," *IEEE Transactions on Applied Superconductivity*, vol. 27, no. 8, pp. 1–7, 2017.

[34] K. S. Haran, S. Kalsi, T. Arndt, H. Karmaker, R. Badcock, B. Buckley, T. Haugan, M. Izumi, D. Loder, J. W. Bray, *et al.*, "High power density superconducting rotating machines—development status and technology roadmap," *Superconductor Science and Technology*, vol. 30, no. 12, p. 123002, 2017.

[35] L. Bortot, *Simulation of Transient Effects in High-Temperature Superconducting Magnets*. PhD thesis, Technische Universitaet Darmstadt (DE), 2022.

[36] J. Dular, C. Geuzaine, and B. Vanderheyden, "Finite-element formulations for systems with high-temperature superconductors," *IEEE Transactions on Applied Superconductivity*, vol. 30, no. 3, pp. 1–13, 2019.

[37] R. Mataira, M. Ainslie, R. Badcock, and C. Bumby, "Finite-element modelling of no-insulation HTS coils using rotated anisotropic resistivity," *Superconductor Science and Technology*, vol. 33, no. 8, p. 08LT01, 2020.

[38] S. Pandolfi, "New life for an old technology: canted cosine theta magnets," 2017.

[39] G. Kirby, J. Van Nugteren, A. Ballarino, L. Bottura, N. Chouika, S. Clement, V. Datskov, L. Fajardo, J. Fleiter, R. Gauthier, *et al.*, "Accelerator-quality HTS dipole magnet demonstrator designs for the EuCARD-2 5-T 40-mm clear aperture magnet," *IEEE Transactions on Applied Superconductivity*, vol. 25, no. 3, pp. 1–5, 2014.

[40] K. Berger, J. Kapek, A. Colle, M. Stepien, B. Grzesik, T. Lubin, and J. Lévêque, "3-D modeling of coils for pulsed field magnetization of HTS bulk pellets in an electrical machine," *IEEE Transactions on Applied Superconductivity*, vol. 28, no. 4, pp. 1–5, 2018.

[41] R. Apsey, D. Baynham, P. Clee, D. Cragg, N. Cunliffe, R. Hopes, and R. Stovold, "Design of a 5.5 metre diameter superconducting solenoid for the delphi particle physics experiment at lep," *IEEE Transactions on Magnetics*, vol. 21, no. 2, pp. 490–493, 1985.

[42] Y. Yan, T. Qu, and F. Grilli, "Numerical modeling of AC loss in HTS coated conductors and roebel cable using TA formulation and comparison with H formulation," *IEEE Access*, vol. 9, pp. 49649–49659, 2021.

[43] S.-K. Ha, S.-K. Kim, J.-G. Kim, M. Park, I.-K. Yu, S. Lee, K. Sim, and A.-R. Kim, "Transient characteristic analysis of a tri-axial HTS power cable using PSCAD/EMTDC," *IEEE transactions on applied superconductivity*, vol. 23, no. 3, pp. 5400104–5400104, 2012.

[44] M. Takayasu, L. Chiesa, L. Bromberg, and J. Minervini, "Cabling method for high current conductors made of HTS tapes," *IEEE transactions on applied superconductivity*, vol. 21, no. 3, pp. 2340–2344, 2010.

[45] Z. Zhu, *Advanced 3D and 2D Modelling of HTS CORC Cable Based on the TA Formulation for the Propulsion System of Hybrid-electric Aircraft.* PhD thesis, University of Bath, 2020.

[46] V. M. Zermeño and F. Grilli, "3D modeling and simulation of 2G HTS stacks and coils," *Superconductor Science and Technology*, vol. 27, no. 4, p. 044025, 2014.

[47] S. Hahn, D. K. Park, J. Bascunan, and Y. Iwasa, "HTS pancake coils without turn-to-turn insulation," *IEEE transactions on applied superconductivity*, vol. 21, no. 3, pp. 1592–1595, 2010.

[48] Y. Peng, Z. Zeng, D. Zhou, W. Zhao, Z. Jia, Y. Guo, C. Bai, F. Fan, Y. Chen, and C. Cai, "Passive magnetic shielding of stacked joint-free superconducting annular disks made of REBCO tapes," *Journal of Superconductivity and Novel Magnetism*, vol. 34, no. 10, pp. 2493–2501, 2021.

[49] F. Sirois and F. Grilli, "Potential and limits of numerical modelling for supporting the development of HTS devices," *Superconductor Science and Technology*, vol. 28, no. 4, p. 043002, 2015.

[50] F. Huber, W. Song, M. Zhang, and F. Grilli, "The TA formulation: an efficient approach to model the macroscopic electromagnetic behaviour of HTS coated conductor applications," *Superconductor Science and Technology*, vol. 35, no. 4, p. 043003, 2022.

[51] B. De Sousa Alves, *3-D Time-Domain Finite Element Modeling of Nonlinear Conductive and Ferromagnetic Thin Films.* PhD thesis, Polytechnique Montréal, 2021.

[52] F. Grilli, E. Pardo, A. Morandi, F. Gömöry, M. Solovyov, V. M. Zermeño, R. Brambilla, T. Benkel, and N. Riva, "Electromagnetic modeling of superconductors with commercial software: Possibilities with two vector potential-based formulations," *IEEE Transactions on Applied Superconductivity*, vol. 31, no. 1, pp. 1–9, 2020.

[53] S. Brialmont, J. Dular, L. Wéra, J.-F. Fagnard, B. Vanderheyden, C. Geuzaine, S. Hahn, A. Patel, and P. Vanderbemden, "Magnetic shielding up to 0.5 T at 77 K using a stack of high temperature superconducting tape annuli," *Superconductor Science and Technology*, 2023.

[54] R. Brambilla, F. Grilli, L. Martini, M. Bocchi, and G. Angeli, "A finite-element method framework for modeling rotating machines with superconducting windings," *IEEE Transactions on Applied Superconductivity*, vol. 28, pp. 1–11, Aug. 2018.

[55] J. Dular, M. Harutyunyan, L. Bortot, S. Schöps, B. Vanderheyden, and C. Geuzaine, "On the stability of mixed finite-element formulations for high-temperature superconductors," *IEEE Transactions on Applied Superconductivity*, vol. 31, no. 6, pp. 1–12, 2021.

[56] L. Bortot, B. Auchmann, I. C. Garcia, H. De Gersem, M. Maciejewski, M. Mentink, S. Schöps, J. Van Nugteren, and A. P. Verweij, "A coupled A–H formulation for magneto-thermal transients in high-temperature superconducting magnets," *IEEE Transactions on Applied Superconductivity*, vol. 30, no. 5, pp. 1–11, 2020.

[57] J. Dular, K. Berger, C. Geuzaine, and B. Vanderheyden, “What formulation should one choose for modeling a 3D HTS motor pole with ferromagnetic materials?,” *IEEE Transactions on Magnetics*, vol. 58, no. 9, pp. 1–4, 2022.

[58] A. Piwonski, J. Dular, R. S. Rezende, and R. Schuhmann, “2D eddy current boundary value problems for power cables with helicoidal symmetry,” *IEEE Transactions on Magnetics*, 2023.

[59] P. Dular, C. Geuzaine, F. Henrotte, and W. Legros, “A general environment for the treatment of discrete problems and its application to the finite element method,” *IEEE Transactions on Magnetics*, vol. 34, no. 5, pp. 3395–3398, 1998.

[60] C. Geuzaine and J.-F. Remacle, “Gmsh: A 3D finite element mesh generator with built-in pre-and post-processing facilities,” *International journal for numerical methods in engineering*, vol. 79, no. 11, pp. 1309–1331, 2009.

[61] M. Houbart, J.-F. Fagnard, J. Dular, A. Dennis, D. K. Namburi, J. H. Durrell, C. Geuzaine, B. Vanderheyden, and P. Vanderbemden, “Trapped magnetic field distribution above a superconducting linear Halbach array,” *Superconductor Science and Technology*, vol. 35, no. 6, p. 064005, 2022.

[62] J. C. Maxwell, “VIII. a dynamical theory of the electromagnetic field,” *Philosophical transactions of the Royal Society of London*, no. 155, pp. 459–512, 1865.

[63] J. D. Jackson, *Classical electrodynamics*. AAPT, 1999.

[64] D. J. Griffiths, “Introduction to electrodynamics,” 2005.

[65] U. Römer, “Numerical approximation of the magnetoquasistatic model with uncertainties and its application to magnet design,” 2015.

[66] I. Cortes Garcia, S. Schöps, H. D. Gersem, and S. Baumanns, “Systems of differential algebraic equations in computational electromagnetics,” in *Applications of Differential-Algebraic Equations: Examples and Benchmarks*, pp. 123–169, Springer, 2018.

[67] T. Steinmetz, S. Kurz, and M. Clemens, “Domains of validity of quasistatic and quasistationary field approximations,” *COMPEL-The international journal for computation and mathematics in electrical and electronic engineering*, 2011.

[68] “Bureau International des Poids et des Mesures.” `https://www.bipm.org/en/home`. Accessed: 2022-11-19.

[69] M. N. Wilson, “Superconducting magnets,” 1983.

[70] T. P. Orlando, K. A. Delin, and C. J. Lobb, “Foundations of applied superconductivity,” *Physics Today*, vol. 44, no. 6, p. 109, 1991.

[71] J.-F. Fagnard, “Experimental and numerical study of the factors influencing the performances of magnetic screens made of high temperature superconductors,” 2011.

[72] G. Lousberg, *On the magnetic properties of bulk high-temperature superconductors containing an artificial array of holes*. PhD thesis, University of Liège, 2010.

[73] L. N. Cooper, “Bound electron pairs in a degenerate Fermi gas,” *Physical Review*, vol. 104, no. 4, p. 1189, 1956.

[74] F. London and H. London, “The electromagnetic equations of the supraconductor,” *Proceedings of the Royal Society of London. Series A-Mathematical and Physical Sciences*, vol. 149, no. 866, pp. 71–88, 1935.

[75] C. Navau, N. Del-Valle, and A. Sanchez, “Macroscopic modeling of magnetization and levitation of hard type-II superconductors: The critical-state model,” *IEEE Transactions on Applied Superconductivity*, vol. 23, no. 1, pp. 8201023–8201023, 2013.

[76] V. L. Ginzburg and L. D. Landau, “On the theory of superconductivity,” in *On superconductivity and superfluidity*, pp. 113–137, Springer, 2009.

[77] W. D. Gropp, H. G. Kaper, G. K. Leaf, D. M. Levine, M. Palumbo, and V. M. Vinokur, “Numerical simulation of vortex dynamics in type-II superconductors,” *Journal of Computational Physics*, vol. 123, no. 2, pp. 254–266, 1996.

[78] T. Winiecki and C. Adams, “A fast semi-implicit finite-difference method for the TDGL equations,” *Journal of Computational Physics*, vol. 179, no. 1, pp. 127–139, 2002.

[79] L. Burger, “Numerical investigation of the magnetic field distributions in structured superconducting film systems,” 2022.

[80] C. Bean, “Magnetization of hard superconductors,” *Physical review letters*, vol. 8, no. 6, p. 250, 1962.

[81] F. Grilli, E. Pardo, A. Stenvall, D. N. Nguyen, W. Yuan, and F. Gomory, “Computation of losses in HTS under the action of varying magnetic fields and currents,” *IEEE Transactions on Applied Superconductivity*, vol. 24, pp. 78–110, feb 2014.

[82] J. Rhyner, “Magnetic properties and AC-losses of superconductors with power law current—voltage characteristics,” *Physica C: Superconductivity*, vol. 212, no. 3-4, pp. 292–300, 1993.

[83] F. Sirois, F. Grilli, and A. Morandi, “Comparison of constitutive laws for modeling high-temperature superconductors,” *IEEE Transactions on Applied Superconductivity*, vol. 29, no. 1, pp. 1–10, 2018.

[84] E. Zeldov, N. Amer, G. Koren, A. Gupta, M. McElfresh, and R. Gambino, “Flux creep characteristics in high-temperature superconductors,” *Applied physics letters*, vol. 56, no. 7, pp. 680–682, 1990.

[85] E. Zeldov, “Flux creep and vortex potential well structure in high-temperature superconductors,” *Physica A: Statistical Mechanics and its Applications*, vol. 168, no. 1, pp. 260–267, 1990.

[86] G. Escamez, “AC losses in superconductors: a multi-scale approach for the design of high current cables,” tech. rep., Universite de Grenoble, 2016.

[87] A. K. Ghosh, “V–I transition and n-value of multifilamentary LTS and HTS wires and cables,” *Physica C: Superconductivity*, vol. 401, no. 1-4, pp. 15–21, 2004.

[88] X. Zhang, Z. Zhong, J. Geng, B. Shen, J. Ma, C. Li, H. Zhang, Q. Dong, and T. Coombs, “Study of critical current and n-values of 2g hts tapes: Their magnetic field-angular dependence,” *Journal of Superconductivity and Novel Magnetism*, vol. 31, no. 12, pp. 3847–3854, 2018.

[89] R. P. Feynman, R. B. Leighton, and M. L. Sands, *The Feynman Lectures on Physics: electromagnetism and matter*, vol. 2. Addison-Wesley Publishing Company, 1963.

[90] K. Jacques, *Energy-Based Magnetic Hysteresis Models-Theoretical Development and Finite Element Formulations*. PhD thesis, University of Liège, 2018.

[91] F. Delince, *Modélisation des régimes transitoires dans les systèmes comportant des matériaux magnétiques non linéaires et hystérétiques*. PhD thesis, University of Liege, 1994.

[92] M. Philippe, *Magnetic properties of structures combining bulk high temperature superconductors and soft ferromagnetic alloys*. PhD thesis, 2015.

[93] E. H. Brandt and M. Indenbom, "Type-II-superconductor strip with current in a perpendicular magnetic field," *Physical review B*, vol. 48, no. 17, p. 12893, 1993.

[94] J. R. Clem and A. Sanchez, "Hysteretic AC losses and susceptibility of thin superconducting disks," *Physical Review B*, vol. 50, no. 13, p. 9355, 1994.

[95] D. Shantsev, Y. Galperin, and T. Johansen, "Scaling and exact solutions for the flux creep problem in a slab superconductor," *Physical Review B*, vol. 65, no. 18, p. 184512, 2002.

[96] G. P. Mikitik, Y. Mawatari, A. T. S. Wan, and F. Sirois, "Analytical methods and formulas for modeling high temperature superconductors," *IEEE Transactions on Applied Superconductivity*, vol. 23, pp. 8001920–8001920, April 2013.

[97] A. M. Campbell, "An introduction to numerical methods in superconductors," *Journal of superconductivity and novel magnetism*, vol. 24, no. 1-2, pp. 27–33, 2011.

[98] M. Ainslie, F. Grilli, L. Quéval, E. Pardo, F. Perez-Mendez, R. Mataira, A. Morandi, A. Ghabeli, C. Bumby, and R. Brambilla, "A new benchmark problem for electromagnetic modelling of superconductors: the high-Tc superconducting dynamo," *Superconductor Science and Technology*, vol. 33, no. 10, p. 105009, 2020.

[99] H. Fukai, M. Tomita, M. Murakami, and T. Nagatomo, "Numerical simulation of trapped magnetic field for bulk superconductor," *Physica C: Superconductivity*, vol. 357, pp. 774–776, 2001.

[100] A. Aydıner and E. Yanmaz, "Numerical calculation of trapped magnetic field for square and cylindrical superconductors," *Superconductor Science and Technology*, vol. 18, no. 7, p. 1010, 2005.

[101] Z. Shen, M. D. Ainslie, A. M. Campbell, and D. A. Cardwell, "Computation of the field in an axial gap, trapped-flux type superconducting electric machine," *IEEE Transactions on Applied Superconductivity*, vol. 25, no. 3, pp. 1–5, 2014.

[102] L. Prigozhin and V. Sokolovsky, "Fast fourier transform-based solution of 2D and 3D magnetization problems in type-ii superconductivity," *Superconductor Science and Technology*, vol. 31, no. 5, p. 055018, 2018.

[103] L. Prigozhin and V. Sokolovsky, "Solution of 3D magnetization problems for superconducting film stacks," *Superconductor Science and Technology*, vol. 31, no. 12, p. 125001, 2018.

[104] L. Prigozhin and V. Sokolovsky, "Spectral method for inhomogeneous superconducting strip problems and magnetic flux pump modeling," in *8th International Workshop on Numerical Modelling of High Temperature Superconductors (Nancy, France)*, 2022.

[105] L. Prigozhin and V. Sokolovsky, "Fast solution of the superconducting dynamo benchmark problem," *Superconductor Science and Technology*, vol. 34, no. 6, p. 065006, 2021.

[106] A. Bossavit, "Numerical modelling of superconductors in three dimensions: a model and a finite element method," *IEEE transactions on magnetics*, vol. 30, no. 5, pp. 3363–3366, 1994.

[107] E. Pardo and M. Kapolka, “3D computation of non-linear eddy currents: Variational method and superconducting cubic bulk,” *Journal of Computational Physics*, vol. 344, pp. 339–363, 2017.

[108] E. Pardo and M. Kapolka, “3D magnetization currents, magnetization loop, and saturation field in superconducting rectangular prisms,” *Superconductor Science and Technology*, vol. 30, no. 6, p. 064007, 2017.

[109] M. Kapolka and E. Pardo, “3D modelling of macroscopic force-free effects in superconducting thin films and rectangular prisms,” *Superconductor Science and Technology*, vol. 32, no. 5, p. 054001, 2019.

[110] J. Ruuskanen, A. Stenvall, V. Lahtinen, and E. Pardo, “Electromagnetic nonlinearities in a Roebel-cable-based accelerator magnet prototype: Variational approach,” *Superconductor Science and Technology*, vol. 30, no. 2, p. 024008, 2016.

[111] P. Monk *et al.*, *Finite element methods for Maxwell’s equations*. Oxford University Press, 2003.

[112] C. Carpenter, “Comparison of alternative formulations of 3-dimensional magnetic-field and eddy-current problems at power frequencies,” in *Proceedings of the Institution of Electrical Engineers*, vol. 124, pp. 1026–1034, IET, 1977.

[113] O. Biro, “Edge element formulations of eddy current problems,” *Computer Methods in Applied Mechanics and Engineering*, vol. 169, no. 3, pp. 391–405, 1999.

[114] G. Meunier, *The finite element method for electromagnetic modeling*, vol. 33. John Wiley & Sons, 2010.

[115] O. Biro and K. Preis, “On the use of the magnetic vector potential in the finite-element analysis of three-dimensional eddy currents,” *IEEE Transactions on magnetics*, vol. 25, no. 4, pp. 3145–3159, 1989.

[116] R. Brambilla, F. Grilli, and L. Martini, “Development of an edge-element model for AC loss computation of high-temperature superconductors,” *Superconductor Science and Technology*, vol. 20, pp. 16–24, nov 2006.

[117] J. Webb and B. Forghani, “The low-frequency performance of H-phi and T-omega methods using edge elements for 3D eddy current problems,” *IEEE transactions on magnetics*, vol. 29, no. 6, pp. 2461–2463, 1993.

[118] A. Stenvall, V. Lahtinen, and M. Lyly, “An H-formulation-based three-dimensional hysteresis loss modelling tool in a simulation including time varying applied field and transport current: the fundamental problem and its solution,” *Superconductor Science and Technology*, vol. 27, no. 10, p. 104004, 2014.

[119] B. de Sousa Alves, V. Lahtinen, M. Laforest, and F. Sirois, “Thin-shell approach for modeling superconducting tapes in the H-φ finite-element formulation,” *Superconductor Science and Technology*, vol. 35, no. 2, p. 024001, 2021.

[120] B. de Sousa Alves, M. Laforest, and F. Sirois, “3D finite-element thin-shell model for high-temperature superconducting tapes,” *IEEE Transactions on Applied Superconductivity*, vol. 32, no. 3, pp. 1–11, 2022.

[121] N. Amemiya, S.-i. Murasawa, N. Banno, and K. Miyamoto, “Numerical modelings of superconducting wires for AC loss calculations,” *Physica C: Superconductivity*, vol. 310, no. 1-4, pp. 16–29, 1998.

[122] F. Grilli, S. Stavrev, Y. LeFloch, M. Costa-Bouzo, E. Vinot, I. Klutsch, G. Meunier, P. Tixador, and B. Dutoit, "Finite-element method modeling of superconductors: From 2-D to 3-D," *IEEE Transactions on Appiled Superconductivity*, vol. 15, pp. 17–25, mar 2005.

[123] A. Campbell, "A direct method for obtaining the critical state in two and three dimensions," *Superconductor Science and Technology*, vol. 22, no. 3, p. 034005, 2009.

[124] G. P. Lousberg, M. Ausloos, C. Geuzaine, P. Dular, P. Vanderbemden, and B. Vanderheyden, "Numerical simulation of the magnetization of high-temperature superconductors: a 3D finite element method using a single time-step iteration," *Superconductor Science and Technology*, vol. 22, p. 055005, mar 2009.

[125] J.-F. Fagnard, M. Morita, S. Nariki, H. Teshima, H. Caps, B. Vanderheyden, and P. Vanderbemden, "Magnetic moment and local magnetic induction of superconducting/ferromagnetic structures subjected to crossed fields: experiments on GdBCO and modelling," *Superconductor Science and Technology*, vol. 29, no. 12, p. 125004, 2016.

[126] G. P. Lousberg, M. Ausloos, C. Geuzaine, P. Dular, P. Vanderbemden, and B. Vanderheyden, "Simulation of the highly non linear properties of bulk superconductors: finite element approach with a backward Euler method and a single time step," in *Proceedings of the Fourth International Conference on ACOMEN*, 2008.

[127] H. Zhang, M. Zhang, and W. Yuan, "An efficient 3D finite element method model based on the T–A formulation for superconducting coated conductors," *Superconductor Science and Technology*, vol. 30, no. 2, p. 024005, 2016.

[128] G. Hajiri, K. Berger, M. R. Koblischka, A. Koblischka-Veneva, Q. Nouailhetas, and J. Lévêque, "Numerical modelling of a compact trapped field magnet using an HTSc tape as energizing coil during PFM," in *8th International Workshop on Numerical Modelling of High Temperature Superconductors (Nancy, France)*, 2022.

[129] A. Stenvall and T. Tarhasaari, "An eddy current vector potential formulation for estimating hysteresis losses of superconductors with FEM," *Superconductor Science and Technology*, vol. 23, p. 125013, nov 2010.

[130] J. W. Barrett and L. Prigozhin, "Electric field formulation for thin film magnetization problems," *Superconductor Science and Technology*, vol. 25, no. 10, p. 104002, 2012.

[131] M. Beck, Y. K. Tsui, Y. Shi, A. R. Dennis, D. A. Cardwell, D. Moseley, J. H. Durrell, and M. D. Ainslie, "Dynamics of magnetic flux propagation in bulk, single grain superconducting rings during pulsed field magnetisation," *Superconductor Science and Technology*, 2022.

[132] P. Dular, *Modélisation du champ magnétique et des courants induits dans des systèmes tridimensionnels non linéaires*. PhD thesis, University of Liège, 1994.

[133] P. Dular, F. Henrotte, F. Robert, A. Genon, and W. Legros, "A generalized source magnetic field calculation method for inductors of any shape," *IEEE Transactions on Magnetics*, vol. 33, no. 2, pp. 1398–1401, 1997.

[134] P. Dular, P. Kuo-Peng, C. Geuzaine, N. Sadowski, and J. Bastos, "Dual magnetodynamic formulations and their source fields associated with massive and stranded inductors," *IEEE Transactions on Magnetics*, vol. 36, no. 4, pp. 1293–1299, 2000.

[135] P. Hillion, “Remark on Maxwell’s divergence equations,” *COMPEL-The international journal for computation and mathematics in electrical and electronic engineering*, vol. 18, no. 1, pp. 77–83, 1999.

[136] M. H. Nayfeh and M. K. Brussel, *Electricity and magnetism*. Courier Dover Publications, 2015.

[137] C. Geuzaine, *High order hybrid finite element schemes for Maxwell’s equations taking thin structures and global quantities into account*. PhD thesis, 2001.

[138] S. Schöps, H. De Gersem, and T. Weiland, “Winding functions in transient magnetoquasistatic field-circuit coupled simulations,” *COMPEL: The international journal for computation and mathematics in electrical and electronic engineering*, 2013.

[139] A. Arsenault, F. Sirois, and F. Grilli, “Implementation of the H-phi formulation in COMSOL multiphysics for simulating the magnetization of bulk superconductors and comparison with the H-formulation,” *IEEE Transactions on Applied Superconductivity*, vol. 31, no. 2, pp. 1–11, 2020.

[140] A. Bossavit, “Two dual formulations of the 3-D eddy-currents problem,” *COMPEL-The international journal for computation and mathematics in electrical and electronic engineering*, 1985.

[141] A. Bossavit, “Whitney forms: A class of finite elements for three-dimensional computations in electromagnetism,” *IEE Proceedings A-Physical Science, Measurement and Instrumentation, Management and Education-Reviews*, vol. 135, no. 8, pp. 493–500, 1988.

[142] M. Pellikka, S. Suuriniemi, L. Kettunen, and C. Geuzaine, “Homology and cohomology computation in finite element modeling,” *SIAM Journal on Scientific Computing*, vol. 35, no. 5, pp. B1195–B1214, 2013.

[143] L. Kettunen, K. Forsman, and A. Bossavit, “Formulation of the eddy current problem in multiply connected regions in terms of h,” *International journal for numerical methods in engineering*, vol. 41, no. 5, pp. 935–954, 1998.

[144] F. Henrotte and K. Hameyer, “An algorithm to construct the discrete cohomology basis functions required for magnetic scalar potential formulations without cuts,” *IEEE transactions on magnetics*, vol. 39, no. 3, pp. 1167–1170, 2003.

[145] I. Babuška, “The finite element method with Lagrangian multipliers,” *Numerische Mathematik*, vol. 20, no. 3, pp. 179–192, 1973.

[146] E. Creusé, P. Dular, and S. Nicaise, “About the gauge conditions arising in finite element magnetostatic problems,” *Computers & Mathematics with Applications*, 2018.

[147] D. F. Griffiths and D. J. Higham, *Numerical methods for ordinary differential equations: initial value problems*, vol. 5. Springer, 2010.

[148] A. Nicolet and F. Delincé, “Implicit Runge-Kutta methods for transient magnetic field computation,” *IEEE transactions on Magnetics*, vol. 32, no. 3, pp. 1405–1408, 1996.

[149] J. C. Butcher, *Numerical methods for ordinary differential equations*. John Wiley & Sons, 2016.

[150] V. Berinde, “Approximating fixed points of Lipschitzian generalized pseudo-contractions,” 2002.

[151] F. E. Browder and W. V. Petryshyn, “Construction of fixed points of nonlinear mappings in Hilbert space,” *Journal of Mathematical Analysis and Applications*, vol. 20, no. 2, pp. 197–228, 1967.

[152] V. Berinde and F. Takens, *Iterative approximation of fixed points*, vol. 1912. Springer, 2007.

[153] T. J. Ypma, "Historical development of the Newton–Raphson method," *SIAM review*, vol. 37, no. 4, pp. 531–551, 1995.

[154] P. Deuflhard, *Newton methods for nonlinear problems: affine invariance and adaptive algorithms*, vol. 35. Springer Science & Business Media, 2005.

[155] C. Geuzaine, A. Kameni, and A. Stenvall, "Superconductors." `https://gitlab.onelab.info/doc/models/wikis/Superconductors`. Accessed: 2019-02-01.

[156] A. Aitken, "XX.—studies in practical mathematics. II. the evaluation of the latent roots and latent vectors of a matrix," *Proceedings of the Royal Society of Edinburgh*, vol. 57, pp. 269–304, 1938.

[157] F. B. Hildebrand, *Introduction to numerical analysis*. Courier Corporation, 1987.

[158] C. T. Kelley, *Iterative methods for linear and nonlinear equations*. SIAM, 1995.

[159] J. Nocedal and S. J. Wright, *Numerical optimization*. Springer, 1999.

[160] A. Granas and J. Dugundji, *Fixed point theory*, vol. 14. Springer, 2003.

[161] G. Sanderson, "From Newton's method to Newton's fractal (which Newton knew nothing about)," *YouTube, uploaded by 3Blue1Brown*, 2021.

[162] G. Sanderson, "Beyond the Mandelbrot set, an intro to holomorphic dynamics," *YouTube, uploaded by 3Blue1Brown*, 2021.

[163] E. Vinot, *Modélisation des supraconducteurs HTC Applications au calcul des pertes AC*. PhD thesis, Institut National Polytechnique de Grenoble-INPG, 2000.

[164] P. Dular, J.-F. Remacle, F. Henrotte, A. Genon, and W. Legros, "Magnetostatic and magnetodynamic mixed formulations compared with conventional formulations," *IEEE Transactions on Magnetics*, vol. 33, no. 2, pp. 1302–1305, 1997.

[165] P. Alotto, F. Delfino, P. Molfino, M. Nervi, and I. Perugia, "A mixed face-edge finite element formulation for 3D magnetostatic problems," *IEEE transactions on magnetics*, vol. 34, no. 5, pp. 2445–2448, 1998.

[166] F. Brezzi and K.-J. Bathe, "A discourse on the stability conditions for mixed finite element formulations," *Computer methods in applied mechanics and engineering*, vol. 82, no. 1-3, pp. 27–57, 1990.

[167] D. Boffi, F. Brezzi, M. Fortin, *et al.*, *Mixed finite element methods and applications*, vol. 44. Springer, 2013.

[168] F. Liang, S. Venuturumilli, H. Zhang, M. Zhang, J. Kvitkovic, S. Pamidi, Y. Wang, and W. Yuan, "A finite element model for simulating second generation high temperature superconducting coils/stacks with large number of turns," *Journal of Applied Physics*, vol. 122, no. 4, p. 043903, 2017.

[169] Y. Wang, M. Zhang, F. Grilli, Z. Zhu, and W. Yuan, "Study of the magnetization loss of CORC® cables using a 3D TA formulation," *Superconductor Science and Technology*, vol. 32, no. 2, p. 025003, 2019.

[170] P. Dular, C. Geuzaine, and W. Legros, "A natural method for coupling magnetodynamic h-formulations and circuit equations," *IEEE transactions on magnetics*, vol. 35, no. 3, pp. 1626–1629, 1999.

[171] É. Béchet, N. Moës, and B. Wohlmuth, "A stable lagrange multiplier space for stiff interface conditions within the extended finite element method," *International Journal for Numerical Methods in Engineering*, vol. 78, no. 8, pp. 931–954, 2009.

[172] J. H. Bramble, "A proof of the inf–sup condition for the Stokes equations on Lipschitz domains," *Mathematical Models and Methods in Applied Sciences*, vol. 13, no. 03, pp. 361–371, 2003.

[173] B. P. Lamichhane, "Higher order mortar finite elements with dual Lagrange multiplier spaces and applications," 2006.

[174] C. Bernardi, N. Debit, and Y. Maday, "Coupling finite element and spectral methods: First results," *Mathematics of Computation*, vol. 54, no. 189, pp. 21–39, 1990.

[175] B. I. Wohlmuth, "Iterative solvers based on domain decomposition," in *Discretization Methods and Iterative Solvers Based on Domain Decomposition*, pp. 85–176, Springer, 2001.

[176] O. C. Zienkiewicz, R. L. Taylor, and J. Z. Zhu, *The finite element method: its basis and fundamentals*. Elsevier, 2005.

[177] J. Lohi and L. Kettunen, "Whitney forms and their extensions," *Journal of Computational and Applied Mathematics*, vol. 393, p. 113520, 2021.

[178] F. Rapetti and A. Bossavit, "Whitney forms of higher degree," *SIAM Journal on Numerical Analysis*, vol. 47, no. 3, pp. 2369–2386, 2009.

[179] R. Hiptmair, "Higher order Whitney forms," *Progress in Electromagnetics Research*, vol. 32, pp. 271–299, 2001.

[180] D. Chapelle and K.-J. Bathe, "The inf-sup test," *Computers & structures*, vol. 47, no. 4-5, pp. 537–545, 1993.

[181] F. Brezzi, "On the existence, uniqueness and approximation of saddle-point problems arising from Lagrangian multipliers," *Publications mathématiques et informatique de Rennes*, no. S4, pp. 1–26, 1974.

[182] H. Brezis, "Analyse fonctionnelle," *Théorie et applications*, 1983.

[183] S. Ramaswamy, "The Lax-Milgram theorem for Banach spaces, I," *Proceedings of the Japan Academy, Series A, Mathematical Sciences*, vol. 56, no. 10, pp. 462–464, 1980.

[184] D. Malkus, "Eigenproblems associated with the discrete LBB condition for incompressible finite elements," *International Journal of Engineering Science*, vol. 19, no. 10, pp. 1299–1310, 1981.

[185] K.-J. Bathe, "The inf–sup condition and its evaluation for mixed finite element methods," *Computers & structures*, vol. 79, no. 2, pp. 243–252, 2001.

[186] W. Bao, X. Wang, and K.-J. BATHE, "On the inf–sup condition of mixed finite element formulations for acoustic fluids," *Mathematical Models and Methods in Applied Sciences*, vol. 11, no. 05, pp. 883–901, 2001.

[187] K.-J. Bathe, A. Iosilevich, and D. Chapelle, "An inf-sup test for shell finite elements," *Computers & Structures*, vol. 75, no. 5, pp. 439–456, 2000.

[188] K. Van Bockstal, *Numerical techniques for partial differential equations in superconductivity and thermoelasticity*. PhD thesis, Ghent University, 2015.

[189] M. Laforest, “The p-CurlCurl: Spaces, traces, coercivity and a Helmholtz decomposition in Lp,” *arXiv preprint arXiv:1808.05976*, 2018.

[190] N. El-Abbasi and K.-J. Bathe, “Stability and patch test performance of contact discretizations and a new solution algorithm,” *Computers & Structures*, vol. 79, no. 16, pp. 1473–1486, 2001.

[191] J. Pitkäranta, “Boundary subspaces for the finite element method with Lagrange multipliers,” *Numerische Mathematik*, vol. 33, no. 3, pp. 273–289, 1979.

[192] E. Berrospe-Juarez, V. M. Zermeño, F. Trillaud, and F. Grilli, “Real-time simulation of large-scale HTS systems: multi-scale and homogeneous models using the T–A formulation,” *Superconductor Science and Technology*, vol. 32, no. 6, p. 065003, 2019.

[193] A. Royer, E. Béchet, and C. Geuzaine, “Gmsh-Fem: an efficient finite element library based on Gmsh,” in *14th World Congress on Computational Mechanics (WCCM), ECCOMAS Congress 2020*, Scipedia, 2021.

[194] “Life-HTS: Liège university finite element models for high-temperature superconductors,” *www.life-hts.uliege.be*.

[195] “HTS modelling.” `http://www.htsmodelling.com`. Accessed: 2019-02-01.

[196] A. Shadowitz, *The electromagnetic field.* Courier Corporation, 2012.

[197] T. L. Chow, *Introduction to electromagnetic theory: a modern perspective.* Jones & Bartlett Learning, 2006.

[198] F. Henrotte, B. Meys, H. Hedia, P. Dular, and W. Legros, “Finite element modelling with transformation techniques,” *IEEE transactions on magnetics*, vol. 35, no. 3, pp. 1434–1437, 1999.

[199] L. Burger, C. Geuzaine, F. Henrotte, and B. Vanderheyden, “Modelling the penetration of magnetic flux in thin superconducting films with shell transformations,” *COMPEL-The international journal for computation and mathematics in electrical and electronic engineering*, vol. 38, no. 5, pp. 1441–1452, 2019.

[200] V. M. Rodriguez-Zermeno, N. Mijatovic, C. Træholt, T. Zirngibl, E. Seiler, A. B. Abrahamsen, N. F. Pedersen, and M. Sorensen, “Towards faster FEM simulation of thin film superconductors: a multiscale approach,” *IEEE Transactions on Applied Superconductivity*, vol. 21, no. 3, pp. 3273–3276, 2010.

[201] P. R. Amestoy, I. S. Duff, J.-Y. L’Excellent, and J. Koster, “MUMPS: a general purpose distributed memory sparse solver,” in *International Workshop on Applied Parallel Computing*, pp. 121–130, Springer, 2000.

[202] L. Shampine, “Reichelt MW,” *The MATLAB ODE Suite. SIAM J Sci Comput*, vol. 18, pp. 1–22, 1997.

[203] L. F. Shampine, M. W. Reichelt, and J. A. Kierzenka, “Solving index-1 DAEs in MATLAB and simulink,” *SIAM review*, vol. 41, no. 3, pp. 538–552, 1999.

[204] MATLAB, *version 7.10.0 (R2018a).* Natick, Massachusetts: The MathWorks Inc., 201.

[205] M. Philippe, J.-F. Fagnard, S. Kirsch, Z. Xu, A. Dennis, Y.-H. Shi, D. A. Cardwell, B. Vanderheyden, and P. Vanderbemden, “Magnetic characterisation of large grain, bulk Y–Ba–Cu–O superconductor–soft ferromagnetic alloy hybrid structures,” *Physica C: Superconductivity*, vol. 502, pp. 20–30, 2014.

[206] M. Philippe, M. D. Ainslie, L. Wera, J.-F. Fagnard, A. Dennis, Y. Shi, D. A. Cardwell, B. Vanderheyden, and P. Vanderbemden, "Influence of soft ferromagnetic sections on the magnetic flux density profile of a large grain, bulk Y–Ba–Cu–O superconductor," *Superconductor Science and Technology*, vol. 28, no. 9, p. 095008, 2015.

[207] M. Philippe, J.-F. Fagnard, L. Wéra, M. Morita, S. Nariki, H. Teshima, H. Caps, B. Vanderheyden, and P. Vanderbemden, "Influence of crossed fields in structures combining large grain, bulk (RE) BCO superconductors and soft ferromagnetic discs," in *Journal of Physics: Conference Series*, vol. 695, p. 012003, IOP Publishing, 2016.

[208] B. Douine, C.-H. Bonnard, F. Sirois, K. Berger, A. Kameni, and J. Lévêque, "Determination of j_c and n-value of HTS pellets by measurement and simulation of magnetic field penetration," *IEEE Transactions on Applied Superconductivity*, vol. 25, no. 4, pp. 1–8, 2015.

[209] C. Multiphysics, "Introduction to COMSOL multiphysics®," *COMSOL Multiphysics, Burlington, MA, accessed Feb*, vol. 9, p. 2018, 1998.

[210] F. Grilli, R. Brambilla, F. Sirois, A. Stenvall, and S. Memiaghe, "Development of a three-dimensional finite-element model for high-temperature superconductors based on the H-formulation," *Cryogenics*, vol. 53, pp. 142–147, 2013.

[211] P. Dłotko, B. Kapidani, S. Pitassi, and R. Specogna, "Fake conductivity or cohomology: Which to use when solving eddy current problems with h-formulations?," *IEEE Transactions on Magnetics*, vol. 55, no. 6, pp. 1–4, 2019.

[212] A. Arsenault, B. de Sousa Alves, and F. Sirois, "COMSOL implementation of the H-phi-formulation with thin cuts for modeling superconductors with transport currents," *IEEE Transactions on Applied Superconductivity*, vol. 31, no. 6, pp. 1–9, 2021.

[213] W. Carr Jr, "AC loss in a twisted filamentary superconducting wire. I," *Journal of Applied Physics*, vol. 45, no. 2, pp. 929–934, 1974.

[214] C. Christopherson and G. Riley Jr, "Development of twisted high-temperature superconductor composite conductors," *Applied physics letters*, vol. 66, no. 17, pp. 2277–2279, 1995.

[215] G. Escamez, F. Sirois, V. Lahtinen, A. Stenvall, A. Badel, P. Tixador, B. Ramdane, G. Meunier, R. Perrin-Bit, and C.-E. Bruzek, "3D numerical modeling of AC losses in multifilamentary MgB2 wires," *IEEE Transactions on Applied Superconductivity*, vol. 26, no. 3, pp. 1–7, 2016.

[216] A. Nicolet, F. Zolla, and S. Guenneau, "Modelling of twisted optical waveguides with edge elements," *The European Physical Journal Applied Physics*, vol. 28, no. 2, pp. 153–157, 2004.

[217] A. Nicolet and F. Zolla, "Finite element analysis of helicoidal waveguides," in *6th International Conference on Computational Electromagnetics*, pp. 1–3, VDE, 2006.

[218] A. Nicolet, F. Zolla, Y. O. Agha, and S. Guenneau, "Leaky modes in twisted microstructured optical fibers," *Waves in Random and Complex Media*, vol. 17, no. 4, pp. 559–570, 2007.

[219] A. Nicolet, A. B. Movchan, S. Guenneau, and F. Zolla, "Asymptotic modelling of weakly twisted electrostatic problems," *Comptes Rendus Mécanique*, vol. 334, no. 2, pp. 91–97, 2006.

[220] K. Hazim, G. Parent, S. Duchesne, A. Nicolet, and C. Geuzaine, "2D electrostatic modeling of twisted pairs," *COMPEL-The international journal for computation and mathematics in electrical and electronic engineering*, 2021.

[221] A. Stenvall, F. Grilli, and M. Lyly, “Current-penetration patterns in twisted superconductors in self-field,” *IEEE transactions on applied superconductivity*, vol. 23, no. 3, pp. 8200105–8200105, 2012.

[222] V. Lahtinen and A. Stenvall, “Toward two-dimensional simulations of hysteresis losses in partially coupled superconducting wires,” *IEEE transactions on applied superconductivity*, vol. 24, no. 3, pp. 1–5, 2013.

[223] A. Stenvall, T. Tarhasaari, F. Grilli, P. Raumonen, M. Vojenčiak, and M. Pellikka, “Manifolds in electromagnetism and superconductor modelling: Using their properties to model critical current of twisted conductors in self-field with 2D model,” *Cryogenics*, vol. 53, pp. 135–141, 2013.

[224] T. Satiramatekul and F. Bouillault, “Numerical modeling of superconducting filaments for coupled problem,” *IEEE transactions on magnetics*, vol. 46, no. 8, pp. 3229–3232, 2010.

[225] T. Satiramatekul, *Contribution à la modélisation de l’aimantation des brins supraconducteurs*. PhD thesis, Paris 11, 2005.

[226] A. Kameni, L. Makong, F. Bouillault, and P. J. Masson, “Reduced model to compute AC losses of twisted multifilamentary superconductors,” *IEEE Transactions on Applied Superconductivity*, vol. 29, no. 7, pp. 1–6, 2019.

[227] D. A. Clarke, “A primer on tensor calculus,” *Saint mary’s University, Halifax NS, Canada*, 2011.

[228] J. T. Wheeler, “Not so classical mechanics,” 2018.

[229] Y. Ould Agha, *Transformations géométriques réelles et complexes: application à la recherche de modes à pertes dans des fibres optiques microstructurées*. PhD thesis, Aix-Marseille 1, 2007.

[230] M. M. Hardy, *Geometric transformation for double helical wire rods*. PhD thesis, 2004.

[231] W. Wang and K. Wang, “Geometric modeling for swept volume of moving solids,” *IEEE Computer graphics and Applications*, vol. 6, no. 12, pp. 8–17, 1986.

[232] J. Claycomb and J. Miller Jr, “Superconducting magnetic shields for SQUID applications,” *Review of Scientific Instruments*, vol. 70, no. 12, pp. 4562–4568, 1999.

[233] J. H. Durrell, M. D. Ainslie, D. Zhou, P. Vanderbemden, T. Bradshaw, S. Speller, M. Filipenko, and D. A. Cardwell, “Bulk superconductors: a roadmap to applications,” *Superconductor Science and Technology*, vol. 31, p. 103501, sep 2018.

[234] K. Takahata, S. Nishijima, M. Ohgami, T. Okada, S. Nakagawa, and M. Yoshiwa, “Magnetic shielding by a tubular superconducting winding in parallel and transverse fields,” *IEEE Transactions on Magnetics*, vol. 25, no. 2, pp. 1889–1892, 1989.

[235] T. Sasaki and I. Itoh, “Magnetic shielding by Nb-Ti multilayer cylinder,” *Cryogenics*, vol. 36, no. 7, pp. 497–506, 1996.

[236] J.-F. Fagnard, S. Elschner, J. Bock, M. Dirickx, B. Vanderheyden, and P. Vanderbemden, “Shielding efficiency and E (J) characteristics measured on large melt cast Bi-2212 hollow cylinders in axial magnetic fields,” *Superconductor Science and Technology*, vol. 23, no. 9, p. 095012, 2010.

[237] P. Yang, W. Yang, and J. Chen, “Fabrication and properties of single domain GdBCO superconducting rings by a buffer aided Gd+ 011 TSIG method,” *Superconductor Science and Technology*, vol. 30, no. 8, p. 085003, 2017.

[238] P. Yang, J.-F. Fagnard, P. Vanderbemden, and W. Yang, “Magnetic shielding of a short thick GdBCO tube fabricated by the buffer aided top-seeded infiltration and growth method,” *Superconductor Science and Technology*, vol. 32, no. 11, p. 115015, 2019.

[239] J.-F. Fagnard, B. Vanderheyden, E. Pardo, and P. Vanderbemden, “Magnetic shielding of various geometries of bulk semi-closed superconducting cylinders subjected to axial and transverse fields,” *Superconductor Science and Technology*, vol. 32, no. 7, p. 074007, 2019.

[240] J.-F. Fagnard, M. Dirickx, G. Levin, P. Barnes, B. Vanderheyden, and P. Vanderbemden, “Use of second generation coated conductors for efficient shielding of DC magnetic fields,” *Journal of Applied Physics*, vol. 108, no. 1, p. 013910, 2010.

[241] L. Wera, J.-F. Fagnard, G. Levin, B. Vanderheyden, and P. Vanderbemden, “A comparative study of triaxial and uniaxial magnetic shields made out of YBCO coated conductors,” *Superconductor Science and Technology*, vol. 28, no. 7, p. 074001, 2015.

[242] S. Brialmont, J. Dular, B. Vanderheyden, C. Geuzaine, S. Hahn, A. Patel, and P. Vanderbemden, “Annuli of coated conductors with a ferromagnetic substrate: magnetic shielding properties at 77 K and at room temperature,” in *8th International Workshop on Numerical Modelling of High Temperature Superconductors (Nancy, France)*, 2022.

[243] J. Gyselinck and P. Dular, “A time-domain homogenization technique for laminated iron cores in 3D finite-element models,” *IEEE transactions on magnetics*, vol. 40, no. 2, pp. 856–859, 2004.

[244] S. Hahn, J. Voccio, D. K. Park, K.-M. Kim, M. Tomita, J. Bascunan, and Y. Iwasa, “A stack of YBCO annuli, thin plate and bulk, for micro-NMR spectroscopy,” *IEEE transactions on applied superconductivity*, vol. 22, no. 3, pp. 4302204–4302204, 2011.

[245] A. Patel, S. Hahn, J. Voccio, A. Baskys, S. Hopkins, and B. Glowacki, “Magnetic levitation using a stack of high temperature superconducting tape annuli,” *Superconductor Science and Technology*, vol. 30, no. 2, p. 024007, 2016.

[246] S. Brialmont, J.-F. Fagnard, B. Vanderheyden, F. Mazaleyrat, S. Hahn, A. Patel, and P. Vanderbemden, “Measurement of magnetic hysteresis loops of the Ni-5at.%-W alloy substrate as a function of temperature in a stack of 2G HTS-coated conductor annuli,” *IEEE Transactions on Applied Superconductivity*, vol. 32, no. 8, pp. 1–10, 2022.

[247] D. Uglietti, H. Kitaguchi, S. Choi, and T. Kiyoshi, “Angular dependence of critical current in coated conductors at 4.2 K and magnet design,” *IEEE transactions on applied superconductivity*, vol. 19, no. 3, pp. 2909–2912, 2009.

[248] C. Senatore, C. Barth, M. Bonura, M. Kulich, and G. Mondonico, “Field and temperature scaling of the critical current density in commercial REBCO coated conductors,” *Superconductor Science and Technology*, vol. 29, no. 1, p. 014002, 2015.

[249] J. Wang, H. Lin, Y. Huang, and X. Sun, “A new formulation of anisotropic equivalent conductivity in laminations,” *IEEE Transactions on Magnetics*, vol. 47, no. 5, pp. 1378–1381, 2011.

[250] I. Niyonzima, R. Sabariego, P. Dular, and C. Geuzaine, “Finite element computational homogenization of nonlinear multiscale materials in magnetostatics,” *IEEE Transactions on Magnetics*, vol. 48, no. 2, pp. 587–590, 2012.

[251] A. Buffa and S. Christiansen, “A dual finite element complex on the barycentric refinement,” *Mathematics of Computation*, vol. 76, no. 260, pp. 1743–1769, 2007.

[252] X. Xu, Z. Huang, W. Li, X. Huang, M. Wang, Z. Hong, and Z. Jin, “3D finite element modelling on racetrack coils using the homogeneous TA formulation,” *Cryogenics*, vol. 119, p. 103366, 2021.

[253] P. W. Gross, P. W. Gross, P. R. Kotiuga, and R. P. Kotiuga, *Electromagnetic theory and computation: a topological approach*, vol. 48. Cambridge University Press, 2004.

[254] P. Dular, J.-Y. Hody, A. Nicolet, A. Genon, and W. Legros, “Mixed finite elements associated with a collection of tetrahedra, hexahedra and prisms,” *IEEE Transactions on Magnetics*, vol. 30, no. 5, pp. 2980–2983, 1994.

[255] R. A. Adams and J. J. Fournier, *Sobolev spaces*. Elsevier, 2003.

Erratum

- 2023, July 20th: Added a factor $1/(1-f)$ in Eq. (5.47).